frontiers | Research Topics

Role of the Southern Ocean in atmospheric pCO_2 change: observations, simulations and paleorecords

Edited by
Zhifang Xiong, Di Qi, Xu Zhang, Thomas Algeo and Jun Zhao

Published in
Frontiers in Marine Science

ISSN 1664-8714
ISBN 978-2-8325-5862-1
DOI 10.3389/978-2-8325-5862-1

About Frontiers

Frontiers is more than just an open access publisher of scholarly articles: it is a pioneering approach to the world of academia, radically improving the way scholarly research is managed. The grand vision of Frontiers is a world where all people have an equal opportunity to seek, share and generate knowledge. Frontiers provides immediate and permanent online open access to all its publications, but this alone is not enough to realize our grand goals.

Frontiers journal series

The Frontiers journal series is a multi-tier and interdisciplinary set of open-access, online journals, promising a paradigm shift from the current review, selection and dissemination processes in academic publishing. All Frontiers journals are driven by researchers for researchers; therefore, they constitute a service to the scholarly community. At the same time, the *Frontiers journal series* operates on a revolutionary invention, the tiered publishing system, initially addressing specific communities of scholars, and gradually climbing up to broader public understanding, thus serving the interests of the lay society, too.

Dedication to quality

Each Frontiers article is a landmark of the highest quality, thanks to genuinely collaborative interactions between authors and review editors, who include some of the world's best academicians. Research must be certified by peers before entering a stream of knowledge that may eventually reach the public - and shape society; therefore, Frontiers only applies the most rigorous and unbiased reviews. Frontiers revolutionizes research publishing by freely delivering the most outstanding research, evaluated with no bias from both the academic and social point of view. By applying the most advanced information technologies, Frontiers is catapulting scholarly publishing into a new generation.

What are Frontiers Research Topics?

Frontiers Research Topics are very popular trademarks of the *Frontiers journals series*: they are collections of at least ten articles, all centered on a particular subject. With their unique mix of varied contributions from Original Research to Review Articles, Frontiers Research Topics unify the most influential researchers, the latest key findings and historical advances in a hot research area.

Find out more on how to host your own Frontiers Research Topic or contribute to one as an author by contacting the Frontiers editorial office: frontiersin.org/about/contact

Role of the Southern Ocean in atmospheric pCO_2 change: observations, simulations and paleorecords

Topic editors

Zhifang Xiong — First Institute of Oceanography, Ministry of Natural Resources, China

Di Qi — Jimei University, China

Xu Zhang — Institute of Tibetan Plateau Research, Chinese Academy of Sciences (CAS), China

Thomas Algeo — University of Cincinnati, United States

Jun Zhao — Second Institute of Oceanography, Ministry of Natural Resources, China

Citation

Xiong, Z., Qi, D., Zhang, X., Algeo, T., Zhao, J., eds. (2025). *Role of the Southern Ocean in atmospheric pCO_2 change: observations, simulations and paleorecords*. Lausanne: Frontiers Media SA. doi: 10.3389/978-2-8325-5862-1

Table of contents

frontiers | Frontiers in Marine Science

TYPE Editorial
PUBLISHED 17 December 2024
DOI 10.3389/fmars.2024.1531887

OPEN ACCESS

EDITED AND REVIEWED BY
Eric 'Pieter Achterberg,
Helmholtz Association of German Research Centres (HZ), Germany

*CORRESPONDENCE
Zhifang Xiong
zhfxiong@fio.org.cn

RECEIVED 21 November 2024
ACCEPTED 25 November 2024
PUBLISHED 17 December 2024

CITATION
Xiong Z, Zhang X, Qi D, Zhao J and Algeo TJ (2024) Editorial: Role of the Southern Ocean in atmospheric pCO_2 change: observations, simulations and paleorecords.
Front. Mar. Sci. 11:1531887.
doi: 10.3389/fmars.2024.1531887

Editorial: Role of the Southern Ocean in atmospheric pCO_2 change: observations, simulations and paleorecords

Zhifang Xiong[1,2]*, Xu Zhang[3], Di Qi[4], Jun Zhao[5] and Thomas J. Algeo[6,7,8]

[1]Key Laboratory of Marine Geology and Metallogeny, First Institute of Oceanography, Ministry of Natural Resources, Qingdao, China, [2]Laboratory for Marine Geology, Qingdao Marine Science and Technology Center, Qingdao, China, [3]British Antarctic Survey, Cambridge, United Kingdom, [4]Polar and Marine Research Institute, Jimei University, Xiamen, China, [5]Key Laboratory of Marine Ecosystem Dynamics, Second Institute of Oceanography, Ministry of Natural Resources, Hangzhou, China, [6]Department of Geosciences, University of Cincinnati, Cincinnati, OH, United States, [7]State Key Laboratories of Biogeology and Environmental Geology, & Geological Processes and Mineral Resources, China University of Geosciences, Wuhan, China, [8]State Key Laboratory of Oil and Gas Reservoir Geology and Exploitation, Chengdu University of Technology, Chengdu, China

KEYWORDS

ventilation, productivity, iron dynamics, overturning circulation, carbon cycle, sea ice, Antarctic icesheet

Editorial on the Research Topic
Role of the Southern Ocean in atmospheric pCO_2 change: observations, simulations and paleorecords

The Southern Ocean plays a key role in atmospheric CO_2 sequestration, accounting for ~40-50% of the anthropogenic CO_2 absorbed by the modern ocean (Landschützer et al., 2015; Gruber et al., 2019). The Southern Ocean also played a critical role in modulating variation in the atmospheric partial pressure of carbon dioxide (pCO_2) in the geologic past on both orbital and millennial timescales (Anderson et al., 2009; Sigman et al., 2010; Gottschalk et al., 2016). Moreover, the Southern Ocean influences atmospheric and oceanic circulation in the tropics remotely, including low-latitude atmospheric CO_2 exchange (Sarmiento et al., 2004; Hendry and Brzezinski, 2014; Sigman et al., 2021). Thus, the Southern Ocean is a key component of the global climate system through its influence on atmospheric CO_2 variations at a range of timescales (Fischer et al., 2010; Rae et al., 2018; Dong et al., 2024). However, the processes and mechanisms of Southern Ocean influence on atmospheric pCO_2 and global climate changes are still not well understood. To fill this gap, this Research Topic integrates the results of modern observations, paleoclimate data, and model simulations to promote a comprehensive understanding of the significance of the Southern Ocean in global climate change from the perspective of the carbon cycle.

This Research Topic collected 12 articles, including 11 original research articles and 1 perspective article. The articles focus on *in-situ* analyses of carbon and other nutrients and watermass factors, recent advances in simulation of the effects of overturning circulation on atmospheric pCO_2, and palaeoceanographic reconstructions of carbon cycle (-related) processes. These articles can be classified into the three themes explored below.

Modern processes

Li et al. analyzed sea-surface temperature (SST) data from the Southern Ocean since 1870 to resolve why SSTs have been cooling since 1980 despite a global warming trend (Yang et al., 2023). They found that three main modes [i.e., the Global Temperature Anomaly, Atlantic Multidecadal Oscillation (AMO), and El Niño-Southern Oscillation (ENSO)] can explain over 70% of SST variability. The negative phase of the AMO and the positive phase of the ENSO counteract the effects of global warming, resulting in a cooling trend in Southern Ocean SSTs since 1980.

Zhang et al. identified strong seasonal variations of siliceous microplankton fluxes and radiolarian assemblages from a sediment trap, which are dominated by seasonality in sea ice cover and plankton community composition in Prydz Bay polynya, Antarctica. The results of this study provide new insights concerning the fluxes and assemblages of siliceous microplankton as carbon-cycle proxies in the geological past (Ragueneau et al., 2000; Tréguer et al., 2018).

Huang et al. analyzed iron (Fe) speciation and examined the relationship of highly reactive Fe (Fe_{HR}) and organic carbon in surface sediments from Prydz Bay and the adjacent Southern Ocean. They discovered that the Fe_{HR} to total Fe (Fe_T) ratios are lowest for the surface sediments in the global ocean due to weak bedrock weathering and slow glacier melting. They proposed that the influence of Fe_{HR} on sedimentary organic matter significantly varies across different sedimentary environments and sediment categories.

Wu et al. analyzed grain size, coarse fraction lithology, and clay mineral composition of surface sediments to constrain their provenance and delivery mode in the Ross Sea, Antarctica. They identified four types of bulk sediments, classified three sorts of coarse fractions, and quantified the distribution of clay minerals. Their findings reveal that surface sediments were mainly transported by icebergs and bottom currents. This study demonstrates the dynamic character of glaciers draining into the Ross Sea, underscoring their potential contribution to future sea-level rise under global warming conditions.

Yang D. et al. reconstructed spatio-temporal variations of organic matter sources and environmental changes from surface and core sediments in the Ross Sea, Antarctica. They revealed distinct spatial patterns of organic matter sources related to production of marine phytoplankton and bacteria and terrestrial bryophytes, and inputs of mid-latitude dust and low-latitude higher plant leaf waxes. They also indicated obvious temporal variations of organic matter sources consistent with ice shelf dynamics since the Last Glacial Maximum (LGM).

Yang W. et al. used observational data of physical properties and carbon chemistry in the ocean-surface watermass to explore the influence of sea ice melting on surface pCO_2 in the western Arctic Ocean. They discovered distinct controls on surface pCO_2 variability of the Chukchi Sea continental shelf and the Canada Basin, with biological production being the dominant influence in the former area and various factors including biological production, ice meltwater dilution, air-sea CO_2 exchange, and surface temperature being the dominant influences in the latter area. Hopefully, similar studies will be undertaken in the future in the Southern Ocean, where sea ice frequently grows and melts.

Model simulations

Menviel and Spence discussed the impact of the Southern Ocean circulation on atmospheric pCO_2 based on the merging of published and newly performed simulations. Both strengthening and poleward shift of the Southern Hemispheric Westerlies can lead to natural CO_2 outgassing. Enhanced Antarctic Bottom Water formation/transport can decrease deep-water natural dissolved inorganic carbon (DIC) concentrations and increase surface-ocean natural DIC concentrations. This study provides a new perspective on past, present and future relationships between changes in atmospheric CO_2 and Southern Ocean circulation resulting from both dynamic and buoyancy forcing.

Palaeoceanographic records

Hu et al. used surface productivity and deep redox proxies to constrain variations in the deep respired carbon pool of the Cosmonaut Sea, Antarctica, and its impact on the glacial atmospheric pCO_2 budget. They found that waxing and waning of the respired carbon pool contributed to drawdown of atmospheric pCO_2 during the LGM and rising atmospheric pCO_2 during the Last Deglaciation, respectively.

Chen et al. suggested that weathered material from the Prydz Bay and Enderby Land coastlines is the main source of sediment to the Cosmonaut Sea, Antarctica. They also discussed the synchronization of East Antarctic Icesheet dynamics with changes in Antarctic climate since the LGM. The results of this study and Hu et al. are a critical supplement for palaeoceanographic research in the Cosmonaut Sea, which is rarely studied.

Lei et al. examined the historical impacts of Circumpolar Deep Water (CDW) on organic matter and ice-rafted debris (IRD) with a palaeoceanographic record from the Amundsen Sea, Antarctica. They identified six environmental events characterized by covariation among CDW intensity, organic carbon concentrations and isotopes, and IRD concentrations since ~6 ka. This study highlights the importance of the CDW in the regional environmental evolution of the Southern Ocean.

Kim et al. investigated glacial-interglacial changes in oceanic environments and depositional processes, linking them to icesheet/ice shelf variations using two sediment cores from the Bellingshausen Sea continental rise. They demonstrated that sediment composition, surface productivity, deep-ocean redox conditions, and bottom-water formation manifest a pronounced glacial cycle, which was closely linked to icesheet dynamics.

Kenlee et al. performed Fe speciation analyses in cores from the subtropical (18-33°N) Atlantic Ocean core that are dominated by eolian dust from the Sahara Desert. They suggested that dust fluxes decrease but bioavailability of eolian Fe increases with the distance of atmospheric transport. Proximal and distal sediments show inverse Fe speciation patterns (i.e., high versus low Fe_{HR}/Fe_T, respectively), which are linked to lower Fe solubility and primary production in the water column and to greater carbonate dilution/dissolution at proximal versus distal sites. This study underscores the significance of Fe dynamics in regulating glacial-interglacial atmospheric pCO_2 variation in multiple oceanic regions, particularly in the Southern Ocean, where variation in dust delivery on glacial-interglacial timescales is pronounced (Lamy et al., 2014; Martínez-García et al., 2014).

Concluding remarks

The influence of the Southern Ocean on atmospheric pCO_2 and global climate evolution is complicated, being related not only to the carbon cycle but also to the nitrogen and silicon cycles, sulfur and oxygen cycles, iron cycle, hydrological cycle, and icesheet/ice shelf dynamics. The articles collected on this Research Topic represent state-of-the-art investigations into the above-mentioned biogeochemical and dynamic processes at a range of timescales based on modern observations, paleoclimate data, and model simulations. These collective efforts are of great scientific significance in providing new insights concerning the role of the Southern Ocean in modulating variations in atmospheric pCO_2 and global climate in the past, present and future. Despite the progress made by the studies in this Research Topic, key scientific issues remain incompletely understood and will require further investigation in the future in order to achieve a better understanding of the role of the Southern Ocean in global climate change from the perspective of the carbon cycle.

Author contributions

ZX: Conceptualization, Funding acquisition, Writing – original draft. XZ: Writing – review & editing. DQ: Writing – review & editing. JZ: Writing – review & editing. TA: Conceptualization, Writing – review & editing.

Funding

The author(s) declare that financial support was received for the research, authorship, and/or publication of this article. This study was supported by the National Natural Science Foundation of China (grant no. 42076232), the Impact and Response of Antarctic Seas to Climate Change (grant no. IRASCC2020-2022-01-03-02), and the Taishan Scholars Project Funding (grant nos. TS20190963 and TSQN202211265). We thank all the authors, reviewers, editors, staff who have participated in this Research Topic.

Conflict of interest

The authors declare that the research was conducted in the absence of any commercial or financial relationships that could be construed as a potential conflict of interest.

Publisher's note

References

Anderson, R. F., Ali, S., Bradtmiller, L. I., Nielsen, S. H. H., Fleisher, M. Q., Anderson, B. E., et al. (2009). Wind-driven upwelling in the Southern Ocean and the deglacial rise in atmospheric CO_2. *Science* 323, 1443–1448. doi: 10.1126/science.1167441

Dong, Y., Bakker, D. C. E., Bell, T. G., Yang, M., Landschützer, P., Hauck, J., et al. (2024). Direct observational evidence of strong CO_2 uptake in the Southern Ocean. *Sci. Adv.* 10, eadn5781. doi: 10.1126/sciadv.adn5781

Fischer, H., Schmitt, J., Lüthi, D., Stocker, T. F., Tschumi, T., Parekh, P., et al. (2010). The role of Southern Ocean processes in orbital and millennial CO_2 variations - A synthesis. *Quaternary Sci. Rev.* 29, 193–205. doi: 10.1016/j.quascirev.2009.06.007

Gottschalk, J., Skinner, L. C., Lippold, J., Vogel, H., Frank, N., Jaccard, S. L., et al. (2016). Biological and physical controls in the Southern Ocean on past millennial-scale atmospheric CO_2 changes. *Nat. Commun.* 7, 11539. doi: 10.1038/ncomms11539

Gruber, N., Landschützer, P., and Lovenduski, N. S. (2019). The variable Southern Ocean carbon sink. *Annu. Rev. Mar. Sci.* 11, 159–186. doi: 10.1146/annurev-marine-121916-063407

Hendry, K. R., and Brzezinski, M. A. (2014). Using silicon isotopes to understand the role of the Southern Ocean in modern and ancient biogeochemistry and climate. *Quaternary Sci. Rev.* 89, 13–26. doi: 10.1016/j.quascirev.2014.01.019

Lamy, F., Gersonde, R., Winckler, G., Esper, O., Jaeschke, A., Kuhn, G., et al. (2014). Increased dust deposition in the Pacific Southern Ocean during glacial periods. *Science* 343, 403–407. doi: 10.1126/science.1245424

Landschützer, P., Gruber, N., Haumann, F. A., Rödenbeck, C., Bakker, D. C. E., van Heuven, S., et al. (2015). The reinvigoration of the Southern Ocean carbon sink. *Science* 349, 1221–1224. doi: 10.1126/science.aab2620

Martínez-García, A., Sigman, D. M., Ren, H., Anderson, R. F., Straub, M., Hodell, D. A., et al. (2014). Iron fertilization of the Subantarctic Ocean during the last ice age. *Science* 343, 1347–1350. doi: 10.1126/science.1246848

Rae, J. W. B., Burke, A., Robinson, L. F., Adkins, J. F., Chen, T., Cole, C., et al. (2018). CO_2 storage and release in the deep Southern Ocean on millennial to centennial timescales. *Nature* 562, 569–573. doi: 10.1038/s41586-018-0614-0

Ragueneau, O., Tréguer, P., Leynaert, A., Anderson, R. F., Brzezinski, M. A., DeMaster, D. J., et al. (2000). A review of the Si cycle in the modern ocean: recent progress and missing gaps in the application of biogenic opal as a paleoproductivity proxy. *Global Planetary Change* 26, 317–365. doi: 10.1016/S0921-8181(00)00052-7

Sarmiento, J. L., Gruber, N., Brzezinski, M. A., and Dunne, J. P. (2004). High-latitude controls of thermocline nutrients and low latitude biological productivity. *Nature* 427, 56–60. doi: 10.1038/nature02127

Sigman, D. M., Fripiat, F., Studer, A. S., Kemeny, P. C., Martínez-García, A., Hain, M. P., et al. (2021). The Southern Ocean during the ice ages: A review of the Antarctic surface isolation hypothesis, with comparison to the North Pacific. *Quaternary Sci. Rev.* 254, 106732. doi: 10.1016/j.quascirev.2020.106732

Sigman, D. M., Hain, M. P., and Haug, G. H. (2010). The polar ocean and glacial cycles in atmospheric CO_2 concentration. *Nature* 466, 47–55. doi: 10.1038/nature09149

Tréguer, P., Bowler, C., Moriceau, B., Dutkiewicz, S., Gehlen, M., Aumont, O., et al. (2018). Influence of diatom diversity on the ocean biological carbon pump. *Nat. Geosci.* 11, 27–37. doi: 10.1038/s41561-017-0028-x

Yang, H., Lohmann, G., Stepanek, C., Wang, Q., Huang, R. X., Shi, X., et al. (2023). Satellite-observed strong subtropical ocean warming as an early signature of global warming. *Commun. Earth Environ.* 4, 178. doi: 10.1038/s43247-023-00839-w

frontiers | Frontiers in Marine Science

TYPE Original Research
PUBLISHED 29 March 2023
DOI 10.3389/fmars.2023.1142061

OPEN ACCESS

EDITED BY
Khan M. G. Mostofa,
Tianjin University, China

REVIEWED BY
Zhaokai Xu,
Institute of Oceanology (CAS), China
Pier Christian van der Merwe,
University of Tasmania, Australia

*CORRESPONDENCE
Jun Zhao
jzhao@sio.org.cn

SPECIALTY SECTION
This article was submitted to Marine Biogeochemistry, a section of the journal Frontiers in Marine Science

RECEIVED 11 January 2023
ACCEPTED 20 March 2023
PUBLISHED 29 March 2023

CITATION
Huang W, Guo X, Zhao J, Li D, Hu J, Zhang H, Zhang C, Han Z, Sun W, Sun Y and Pan J (2023) Low content of highly reactive iron in sediments from Prydz Bay and the adjacent Southern Ocean: Controlling factors and implications for sedimentary organic carbon preservation. *Front. Mar. Sci.* 10:1142061. doi: 10.3389/fmars.2023.1142061

Low content of highly reactive iron in sediments from Prydz Bay and the adjacent Southern Ocean: Controlling factors and implications for sedimentary organic carbon preservation

Wenhao Huang[1,2], Xiaoze Guo[1,2,3], Jun Zhao[1,2*], Dong Li[1,2], Ji Hu[1,2], Haifeng Zhang[1,2], Cai Zhang[1,2], Zhengbing Han[2], Weiping Sun[2], Yongge Sun[3] and Jianming Pan[1,2]

[1]Key Laboratory of Marine Ecosystem Dynamics, Ministry of Natural Resources, Hangzhou, China, [2]Second Institute of Oceanography, Ministry of Natural Resources, Hangzhou, China, [3]Institute of Environmental and Biogeochemistry (eBig), School of Earth Sciences, Zhejiang University, Hangzhou, China

Examining iron (Fe) speciation in marine sediments is critical to understand Fe and carbon biogeochemical cycling in polar regions. In this study, we investigated the speciation of Fe in sediments from Prydz Bay and the adjacent Southern Ocean, and examined the factors controlling Fe speciation and its relationship with total organic carbon (TOC). Our results reveal that unreactive silicate Fe (Fe_U) is the dominant pool of total Fe (Fe_T), followed by poorly reactive sheet silicate Fe (Fe_{PRS}), reducible crystalline Fe oxides (Fe_{ox2}), easily reducible amorphous/poorly crystalline Fe oxides (Fe_{ox1}), and magnetite (Fe_{mag}), with carbonate-associated ferrous Fe (Fe_{carb}) being the smallest pool. The highly reactive Fe (Fe_{HR})/Fe_T ratios (0.13 $\pm$ 0.06) in our study area are among the lowest end-member globally, primarily due to weak bedrock weathering and slow glacier melting. The Fe_{ox1}/Fe_T ratios are similar to those in continental shelf and marginal seas containing highly weathered materials, while the Fe_{ox2}/Fe_T ratios are significantly lower. This result implicates that low temperature inhibits the aging of iceberg melting-sourced Fe_{ox1} potentially, and accordingly the regulation of weathering on the Fe_{HR}/Fe_T ratio is mainly reflected in Fe_{ox2}/Fe_T ratio. There are no significant correlations between TOC and Fe_{HR}, Fe_{carb}, Fe_{ox1} or Fe_{ox2} in the research region. Four distinct patterns of TOC/Fe_{HR} ratio can be discerned by summarizing the global data set: (a) high TOC/Fe_{HR} ratios (> 2.5) are likely the result of high marine primary productivity and low chemically weathered source materials; (b) low TOC/Fe_{HR} ratios (< 0.6) are caused by high rates of Fe_{HR} inputs and OC remineralization; (c) mid-range TOC/Fe_{HR} ratios (0.6 – 2.5) typical of most river particulates and marginal sea sediments indicate the same Fe_{HR} and OC sources and/or interactions between each other; (d) both low TOC and Fe_{HR} content is the result of low marine primary productivity and weak chemical weathering. Our findings provide new insights into the relationship between Fe_{HR} and TOC in polar sediments.

KEYWORDS

Fe speciation, highly reactive Fe, Southern Ocean, marine sediment, organic carbon

1 Introduction

The role of iron (Fe) speciation, rather than its total amount, is critical in Fe biogeochemical processes such as activity, migration, and bioavailability in marine sediments (Tagliabue et al., 2017). Due to its diverse mineralogy, crystallography, morphology, and chemical composition, Fe exhibits significant oxidation-reduction and adsorption reactivities (Kostka and Iii, 1994; Thamdrup, 2000). The sequential separation of different Fe species from the reaction phase is the foundation of Fe biogeochemistry (Poulton and Raiswell, 2005). Marine sediments serve as both a crucial Fe sink and source (Wadley et al., 2014; Homoky et al., 2016). The characteristics of Fe speciation in sediments are influenced by multiple factors, including the mixing of source materials with varying intensities of chemical weathering, bedrock type, redox conditions, pH values, chemical properties of organic matter, and diagenesis (Canfield, 1989; Poulton and Raiswell, 2005; Konhauser et al., 2011; Wehrmann et al., 2014; Thomasarrigo et al., 2019; Wei et al., 2021; Pasquier et al., 2022). Furthermore, highly reactive Fe (Fe_{HR}, operationally defined as Fe (oxyhydr)oxides and carbonates that readily react with sulfide to form sulfide minerals and eventually pyrite [Canfield, 1989]) in sediments has a significant impact on the biogeochemical cycling and fate of carbon (C) and other trace elements (Tagliabue et al., 2017). Therefore, the analysis of Fe speciation in sediments and the identification of controlling factors are crucial in studying Fe and C biogeochemical cycles.

Early studies demonstrated that Antarctic glacial sediments, which contain poorly chemically weathered material, exhibit significantly lower Fe_{HR} content and Fe_{HR}/total Fe (Fe_T) ratios compared to terrestrial riverine particulates (Poulton and Raiswell, 2002; Raiswell et al., 2006). Recent studies on polar regions have revealed that glacial runoff meltwater contributes additional Fe_{HR} to coastal Antarctic waters (Bhatia et al., 2013; Hawkings et al., 2014; Wehrmann et al., 2014; Lyons et al., 2015; Dinniman et al., 2020), presenting a promising opportunity to enhance primary productivity in the Southern Ocean and accelerate carbon dioxide consumption from the atmosphere in this region (Blain et al., 2007). Correspondingly, the Fe_{HR} content and Fe_{HR}/Fe_T ratio in Antarctic marine sediments may rise (Henkel et al., 2018). Given the increasing melting rate of Antarctic glaciers in recent decades (Shepherd et al., 2018), these impacts may become more significant. However, limited data on Fe species in Antarctic sediments pose challenges in assessing the impact of glacial melting on the biogeochemical cycles of Fe and C in polar regions under the context of global warming.

The natural process of "Fe fertilization", which involves the transport of more Fe_{HR} to the ocean due to increased glacial melting, not only enhances the transport of organic carbon (OC) to the deep sea (Pollard et al., 2009), but also has the potential to promote sedimentary OC burial. OC-Fe_{HR} complexes formed by the combination of Fe_{HR} and OC exhibit long-term preservation potential (Lalonde et al., 2012; Faust et al., 2021), and their formation is therefore significant for improving the burial efficiency of marine sedimentary OC and mitigating global warming (Salvadó et al., 2015). However, the proportion of OC in OC-Fe_{HR} complexes to total OC (TOC) ($f_{OC\text{-}Fe}$) in global marine surface sediments varies widely (0.5% – 80%) (Lalonde et al., 2012; Longman et al., 2021; Longman et al., 2022). Fe speciation and Fe_{HR} content in different sedimentary environments are significantly differ, which may be a crucial factor influencing the degree of OC-Fe_{HR} complexing (Ma et al., 2018; Faust et al., 2021). Therefore, investigating the species composition of Fe_{HR} in Antarctic marine sediments and its potential relationship with OC preservation is of great significance for comprehending the OC-Fe_{HR} coupling mechanism and evaluating the response of the Antarctic C cycle to climate change.

Prydz Bay is the largest bay in the Indian Ocean sector of Antarctica. Its seaward perimeter is delineated by two shallower water depth banks, namely Fram Bank to the northwest and Four Ladies Bank to the northeast. The continental shelf region in Prydz Bay is comparable to that of the Weddell Sea and the Ross Sea, which are the two major Antarctic coastal seas and have the most productive coastal polynyas (Arrigo et al., 2015). However, Prydz Bay has fewer ice-free zones (Campbell et al., 1993) and less ice shelf melting (Shepherd et al., 2018; The IMBIE team, 2018), leading to weak chemical weathering and low Fe_{HR} inputs. The accumulation of marine materials in the surface sediments of Prydz Bay is primarily driven by primary production, as indicated by the distribution of chlorophyll a in surface waters and sedimentary TOC and total nitrogen (TN) (Vaz and Lennon, 1996; Liu et al., 2014). Therefore, Prydz Bay and the adjacent Southern Ocean provide an ideal area for studying Fe speciation and its relationship with OC, given the specific geographical environment and material source conditions.

In this study, we conducted the sequential extraction of Fe species and measured TOC, Fe_T, grain size and specific surface area (SSA) in 20 surface sediments from Prydz Bay and the adjacent Southern Ocean. The aim was to characterize the distribution of Fe species, particularly Fe_{HR}, and speculate on its controlling factors. Additionally, we preliminarily discussed the relationship between TOC and Fe speciation in the research region and the implications from a global perspective.

2 Materials and methods

2.1 Sampling procedure

During the 24th to 29th Chinese National Antarctic Research Expeditions (CHINARE-24 to -29, 2007 – 2013), a total of 20 surface sediment samples were collected from Prydz Bay and the adjacent Southern Ocean (Figure 1; Table 1). The box sampler was used to collect the sediment samples, and the topmost 0 – 1 cm layer was considered as the surface sample. The samples were

Abbreviations: Fe_{carb}, carbonate associated ferrous Fe; Fe_{ox1}, easily reducible amorphous/poorly crystalline Fe oxides (ferrihydrite, lepidocrocite); Fe_{ox2}, reducible crystalline Fe oxides (goethite, akaganéite, hematite); Fe_{mag}, magnetite; Fe_{PRS}, poorly reactive sheet silicate Fe; Fe_T, Total Fe; Fe_{HR}, Highly reactive Fe ($Fe_{carb} + Fe_{ox1} + Fe_{ox2} + Fe_{mag}$); Fe_U, Unreactive silicate Fe ($Fe_T - Fe_{HR} - Fe_{PRS}$); SSA, Specific surface area; TOC, Total organic carbon; $f_{OC\text{-}Fe}$, Proportion of OC in OC-Fe_{HR} complexes to TOC.

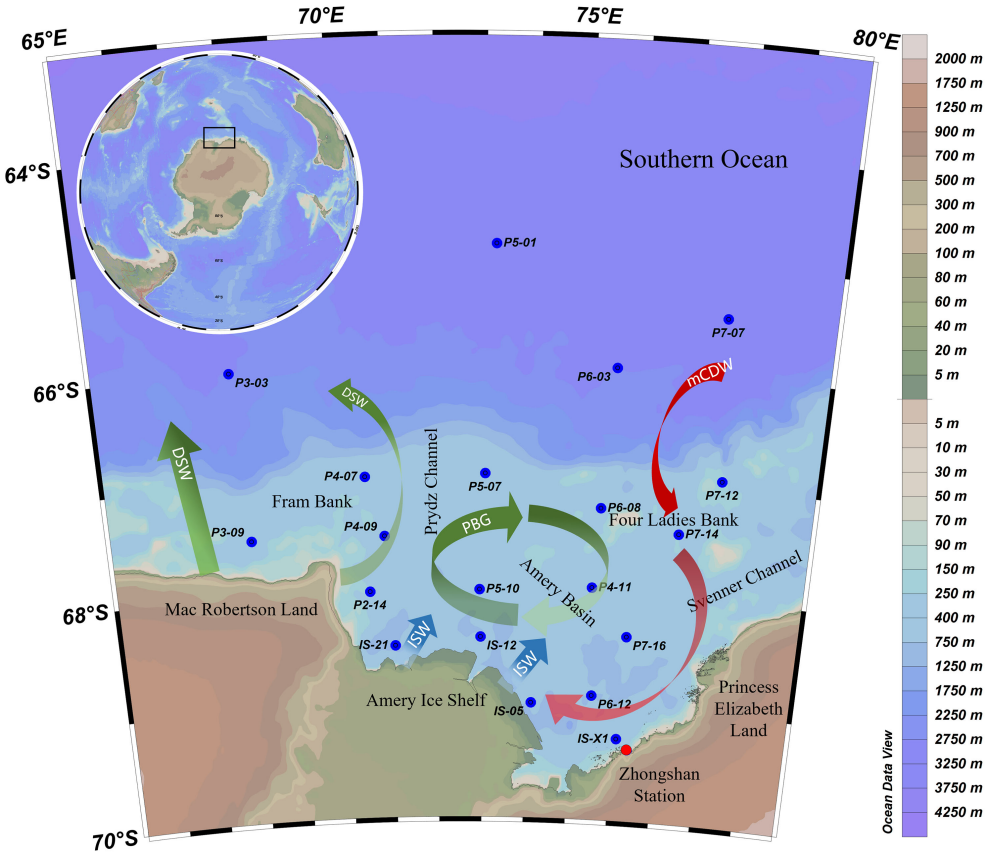

FIGURE 1
Surface sediment sampling stations in Prydz Bay and the adjacent Southern Ocean during the 24th to 29th Chinese National Antarctic Research Expeditions (CHINARE-24 to -29). The circumfluence map is modified after Williams et al. (2016). PBG, Prydz Bay Gyre; mCDW, modified Circumpolar Deep Water; DSW, Dense Shelf Water; ISW, Ice Shelf Water.

TABLE 1 Sampling information, sand, clay, silt and categories of surface sediment from Prydz Bay and the adjacent Southern Ocean.

Station	Longitude (°E)	Latitude (°S)	Water Depth (m)	Cruise	Silt (%)	Sand (%)	Clay (%)	Category
P4-09	70.87	67.52	285	CHINARE-29	22.1	72.7	5.12	Coarse
P4-07	70.49	66.99	293	CHINARE-29	25.5	68.7	5.75	
P7-12	78.00	66.94	218	CHINARE-29	41.3	51.5	7.15	Medium
IS-05	74.11	68.99	707	CHINARE-24	39.5	50.6	9.84	
IS-21	71.05	68.49	777	CHINARE-27	51.5	38.6	9.88	
P5-07	73.02	66.97	510	CHINARE-29	48.2	40.0	11.8	
P7-14	77.18	67.44	312	CHINARE-29	45.9	37.1	17.1	
P5-10	72.92	68.00	642	CHINARE-29	62.3	21.1	16.5	Fine
P7-16	76.20	68.38	559	CHINARE-29	65.1	17.5	17.5	
P3-09	68.01	67.51	251	CHINARE-29	72.8	15.3	11.9	
IS-12	72.95	68.42	748	CHINARE-27	72.4	14.1	13.5	
P2-14	70.52	68.01	496	CHINARE-25	69.0	18.1	12.9	
P4-11	75.38	67.96	491	CHINARE-24	81.9	2.75	15.4	

(Continued)

TABLE 1 Continued

Station	Longitude (°E)	Latitude (°S)	Water Depth (m)	Cruise	Silt (%)	Sand (%)	Clay (%)	Category
IS-X1	76.11	69.28	/	CHINARE-27	79.5	3.69	16.8	
P6-12	75.49	68.91	700	CHINARE-29	75.1	8.14	16.7	
P6-08	75.49	67.25	386	CHINARE-29	66.8	8.29	24.9	
P6-03	75.68	65.99	2920	CHINARE-29	60.7	12.9	26.4	
P7-07	77.82	65.48	3250	CHINARE-29	61.5	11.7	26.9	Ultra-fine
P5-01	73.21	64.90	3421	CHINARE-29	55.5	16.8	27.7	
P3-03	67.81	66.00	2689	CHINARE-29	51.0	9.03	40.0	

immediately frozen at –20°C and transported to the laboratory where they were stored at the same temperature until analysis.

2.2 Grain size and specific surface area analysis

The sediment grain size was analyzed using a laser particle size analyzer (Malven Mastersizer 3000, UK) with an analysis range of 0.01 – 3500 μm and a precision better than 1%. Approximately 1 g of wet sediment was placed into pure water and mixed well with ultrasonication. The bulk sediment samples were then separated into 3 standard size fractions: sand (> 63 μm), silt (4 – 63 μm), and clay (< 4 μm). The freeze-dried sediments were heated in a muffle oven at 350°C for 12 h to remove organic matter. The SSA of the sediments was measured by the static volumetric method using an automatic analyzer (Bessed 3H-2000 PS1, China) with an analysis range of > 0.005 m^2/g and a precision better than 1%.

2.3 TOC analysis

The TOC content in the sediments was determined using an elemental analyzer–isotope ratio mass spectrometer (EA–IRMS) (Thermo Delta V advantage, US). The freeze-dried sediment samples were analyzed after removing carbonates by acid fumigation and oven drying at 60°C for 24 h (Harris et al., 2001). The precision of the reference material (Acetanilide) was ± 0.23% (n = 5). One sample was selected to run as replicates in parallel (P7-16), and the relative standard deviation (RSD) of TOC measurements was < 16% (n = 2, Table S2).

2.4 Total Fe and Al determination

The Fe_T and Al content were analyzed using an inductively coupled plasma–atomic emission spectrometer (ICP–AES) (Thermo Fisher IRIS Intrepid II XSP, US). The freeze-dried sediment samples were placed in a polytetrafluoroethylene inner tank, which was immersed in nitric acid and leached with deionized water. The samples were then digested with mixed HF–$HClO_4$–HNO_3 acids (guaranteed reagent) in a microwave digestion instrument. The acid was expelled, and the volume was calibrated by adding Rhodium. The Fe_T and Al content in the digestion fluid were determined by subtracting blanks. Reference materials (GBW07314 [offshore marine sediments, The State Bureau of Quality and Technical Supervision of China], GBW07103 [granite rock composition analysis reference materials, The State Bureau of Quality and Technical Supervision of China] and GSP-2 [granodiorite powdered reference materials, USGS]) were also digested using the same method for quality control. The recovery efficiencies of Fe_T and Al for the reference materials were 100.2% – 101.9% and 100.1% – 100.4%, respectively. Replicates were analyzed for two samples (P4-07, P7-07), and the RSDs were ≤ 5.3% (n = 2, Table S2).

2.5 Fe speciation

Fe species analyses, including carbonate associated ferrous Fe (Fe_{carb}), easily reducible amorphous/poorly crystalline Fe oxides (Fe_{ox1}), reducible crystalline Fe oxides (Fe_{ox2}), magnetite (Fe_{mag}), and poorly reactive sheet silicate Fe (Fe_{PRS}), were conducted following the methods of Poulton and Canfield (2005) and März et al. (2012) as shown in Table S1. Briefly, the surface sediments were homogenized after freeze-drying, weighed accurately to 0.1 g, and then sequentially extracted by adding the respective reagents necessary for each Fe species to the centrifuge tube containing the sediments. The tubes were centrifuged at 4800 rpm for 10 min and the supernatants were transferred into PET bottles for Fe species analysis. The sediment residuals from the previous step were then washed twice with distilled water, which was added to the extracted supernatants. The Fe content in the supernatants was determined on a flame atomic absorption spectrophotometer (ZEE nit 700P, Germany). The RSDs for 10 samples were < 6.5% for Fe_{carb}, < 8.2% for Fe_{ox1}, < 4.9% for Fe_{ox2}, < 13% for Fe_{mag} (n = 3); and the RSDs for 2 samples was < 5.5% for Fe_{PRS} (n = 2) (Table S2). The sediments exhibited no observable indications of Fe sulfides (black mottles), leading to the assumption that pyrite-bound Fe was insignificant (März et al., 2012) and was not subject to analysis in this study. Here, we established $Fe_{HR} = Fe_{carb} + Fe_{ox1} + Fe_{ox2} + Fe_{mag}$ as per Poulton and Canfield (2005). Consequently, the equation for unreactive silicate Fe (Fe_U) was: $Fe_U = Fe_T - (Fe_{HR} + Fe_{PRS})$.

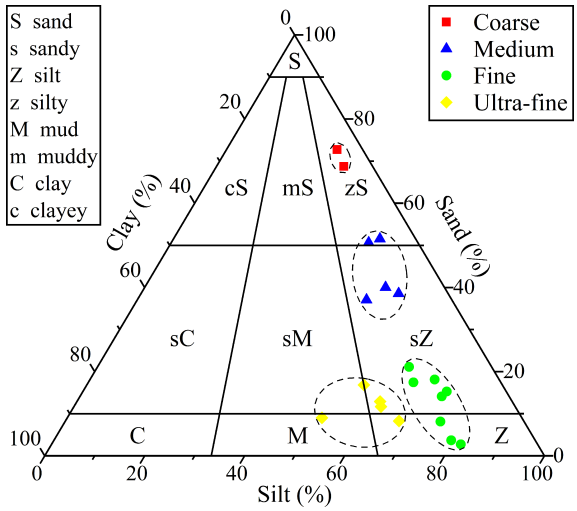

FIGURE 2
Classification of surface sediments in Prydz Bay and the adjacent Southern Ocean. Samples are classified into 4 categories based on a cluster analysis: "Coarse" (red squares), "Medium" (blue triangles), "Fine" (green dots) and "Ultra-fine" (yellow diamonds).

2.6 Statistical analyses

To establish relationships between the measured parameters, a Pearson correlation analysis and a two-tailed test of significance were conducted using the statistical software SPSS (Version 25). Additionally, a cluster analysis was performed using the same software. One-way analysis of variance with a 95% confidence interval ($p < 0.05$) was used to identify statistically significant differences.

3 Results

3.1 Grain size and grouping

The sediment composition in the study area is analyzed in terms of the content of clay (5.12% – 40.0%), sand (2.75% – 72.7%), and silt (22.1% – 81.9%). Silt is found to be the dominant component, accounting for an average of 57.4% of the sediment volume (Table S3). Sandy silt is identified as the main sediment type in the study area (Figure 2) according to the sediment classification method of Folk (1980). Cluster analysis of grain size results in the division of sediment samples into 4 categories: "Coarse", "Medium", "Fine" and "Ultra-fine", as shown in Figure 2. The "Coarse" category includes 2 stations from Fram Bank, the "Medium" category includes 5 stations from the Amery Ice Shelf front, Four Ladies Bank and Prydz Channel, the "Fine" category includes 8 stations from the Cape Darnley polynya and Amery Basin, and the "Ultra-fine" category includes 5 stations from the deep Southern Ocean and Four Ladies Bank (Table 1).

3.2 SSA, TOC and OC loading

The SSA of the sediment samples ranges from 1.78 to 41.2 m^2/g. The highest SSA is found in the "Ultra-fine" sediment category

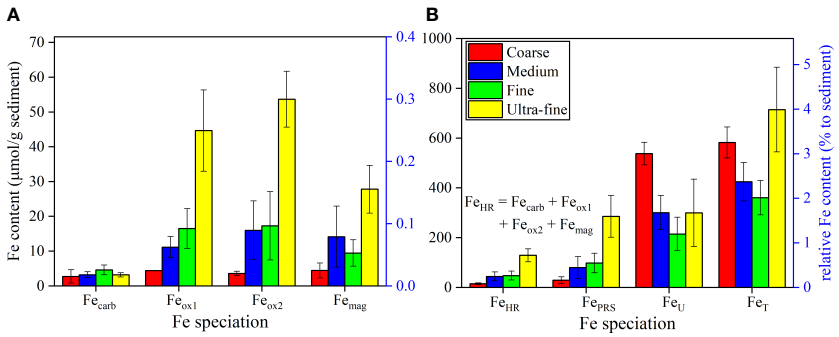

FIGURE 3
The average content of **(A)** Fe_{carb}, Fe_{ox1}, Fe_{ox2}, Fe_{mag} and **(B)** Fe_{HR}, Fe_{PRS}, Fe_U, Fe_T in "Coarse", "Medium", "Fine" and "Ultra-fine" categories of sediments from Prydz Bay and the adjacent Southern Ocean. Note: $Fe_{HR} = Fe_{carb} + Fe_{ox1} + Fe_{ox2} + Fe_{mag}$.

(33.9 ± 8.13 m^2/g), followed by "Fine" (17.7 ± 4.86 m^2/g) and "Medium" (8.57 ± 4.06 m^2/g) sediments. The "Coarse" sediment category has the lowest SSA (1.87 ± 0.128 m^2/g) (Table S3).

The TOC content ranges from 0.13% to 1.65%, similar to values (0.14% – 1.20%) in Liu et al. (2014). The "Fine" sediment category has significantly ($p < 0.005$) higher TOC content (1.02% ± 0.35%) than the other 3 categories (0.19% ± 0.02%, 0.32% ± 0.28%, 0.34% ± 0.19% for "Coarse", "Medium" and "Ultra-fine", respectively) (Table S3).

The OC loading (i.e., the TOC/SSA ratio) ranges from 0.04 to 1.29 mg/m^2. The "Coarse" sediment category has the highest OC loading (0.99 ± 0.18 mg/m^2), followed by "Fine" (0.62 ± 0.33 mg/m^2), "Medium" (0.38 ± 0.21 mg/m^2), and "Ultra-fine" (0.12 ± 0.11 mg/m^2) sediments (Table S3).

3.3 Total Fe and Fe speciation

The Fe_T content ranges from 1.22% to 5.19% (2.72% ± 0.993%), and is significantly ($p < 0.01$) higher in the "Ultra-fine" category sediments (3.99% ± 0.950%) than "Fine" (2.01% ± 0.387%) and "Medium" (2.37% ± 0.430%) sediments, with the middle value in "Coarse" category (3.25% ± 0.348%) (Table S3).

The characteristics of Fe speciation are reported in Table S3. A comparison of the average yields of various Fe pools and their ratios to Fe_T in the 4 grain size categories are shown in Figure 3. Fe_U is the largest Fe pool (290 ± 125 μmol/g), followed by Fe_{PRS} (134 ± 105 μmol/g) and Fe_{HR} (64.0 ± 43.7 μmol/g) (Figure 3B). Within Fe_{HR}, the content of Fe_{ox2} (24.7 ± 19.4 μmol/g) and Fe_{ox1} (21.0 ± 15.9 μmol/g) is significantly ($p < 0.001$) higher than Fe_{carb} (3.70 ± 1.31 μmol/g), with Fe_{mag} in the mid-range of these values (14.7 ± 9.99 μmol/g) (Figure 3A).

Regarding different grain size categories, Fe_{ox1}, Fe_{ox2}, Fe_{mag}, Fe_{HR} and Fe_{PRS} content is all significantly ($p < 0.01$) higher in "Ultra-fine" sediments (44.6 ± 11.7, 53.7 ± 8.02, 27.8 ± 6.87, 129 ± 26.0, 285 ± 83.6 μmol/g, respectively) than "Coarse" (4.37 ± 0.0778, 3.59 ± 0.601, 4.42 ± 2.16, 15.1 ± 3.37, 29.5 ± 13.5 μmol/g, respectively), "Medium" (11.1 ± 3.04, 16.0 ± 8.44, 14.1 ± 8.82, 44.4 ± 17.7, 80.0 ± 43.9 μmol/g, respectively) and "Fine" (16.5 ± 5.73, 17.2 ± 9.82, 9.43 ± 3.79, 47.7 ± 17.9, 98.0 ± 39.1 μmol/g, respectively) categories. Fe_U is significantly ($p < 0.01$) higher in "Coarse" sediments (538 ± 45.5 μmol/g) than in "Medium" (300 ± 68.6 μmol/g), "Fine" (215 ± 67.4 μmol/g) and "Ultra-fine" (300 ± 135 μmol/g) sediments, while there is no significant difference ($p > 0.05$) in Fe_{carb} (2.72 ± 1.90, 3.20 ± 0.830, 4.59 ± 1.41 and 3.16 ± 0.605 μmol/g for "Coarse", "Medium", "Fine" and "Ultra-fine" categories, respectively) (Figure 3).

4 Discussion

4.1 Fe_{HR} characteristics and controlling factors

4.1.1 Control of weak weathering and slow glacier melting on low Fe_{HR}/Fe_T ratio

In the sediments from Prydz Bay and the adjacent Southern Ocean, there is a significant positive correlation between Fe_{HR} and Fe_T, as well as between Fe_{HR} and Al ($R^2 = 0.55$, $p < 0.001$; $R^2 = 0.31$, $p < 0.05$; Figure S1). This finding is consistent with the global riverine and glacial particulates, implying that Fe_{HR} are closely associated with Fe-bearing aluminosilicate minerals (Poulton and Raiswell, 2002; Poulton and Raiswell, 2005). The Fe_{HR}/Fe_T ratios in the research region (0.13 ± 0.06) are similar to those in Antarctic

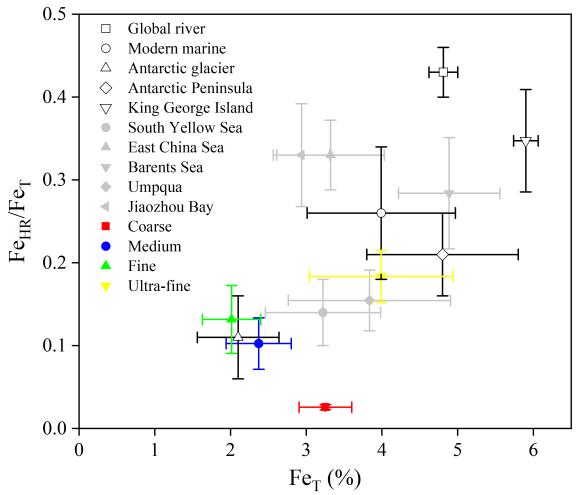

FIGURE 4
Comparison of Fe_{HR}/Fe_T and Fe_T in "Coarse", "Medium", "Fine" and "Ultra-fine" categories of sediments from Prydz Bay and the adjacent Southern Ocean with global riverine particulates and modern marine sediments, Antarctic glaciers (Raiswell and Canfield, 1998; Poulton and Raiswell, 2002), off the western Antarctic Peninsula (Burdige and Christensen, 2022), off King George Island (Henkel et al., 2018), South Yellow Sea (Ma et al., 2018), East China Sea (Zhu et al., 2012), Barents Sea (Faust et al., 2021), Umpqua (Roy et al., 2013) and the Jiaozhou Bay (Zhu et al., 2015). Data are averages of surface sediments (0 – 2 cm) by recalculation of Henkel et al. (2018) and Burdige and Christensen (2022).

glacial particulates (0.11 ± 0.05), and lower than those in global river particulates (0.43 ± 0.03) and modern marine sediments (0.26 ± 0.08) (Figure 4) (Poulton and Raiswell, 2002). This result suggests that the sediments in our study area are mainly influenced by weak chemical weathering. Generally, during chemical weathering, the easily solubilized major elements (such as Na, K, Ca, etc.) in rock minerals are leached, while the insoluble elements, such as Al and Fe, are enriched. As a result, Fe forms insoluble mineral phases (mainly Fe oxides) that continuously adsorb on the surface of parent rock minerals (Martin and Meybeck, 1979; Canfield, 1997). Therefore, the degree of chemical weathering can determine the Fe_{HR} content as well as the Fe_{HR}/Fe_T ratio (Poulton and Raiswell, 2002; Wei et al., 2021).

River and glacier particulates are known to represent the high and low end-members of weathering intensity, respectively, and their mixing in varying proportions determines the Fe_{HR}/Fe_T ratio characteristics of sediments in different marine environments (Poulton and Raiswell, 2005). In the research region, the Fe_{HR}/Fe_T ratios belong to the lower end-member compared to other polar sediments (Figure 4). For example, in the Arctic Barents Sea, off the Antarctic Peninsula and King George Island, the Fe_{HR}/Fe_T ratios of surface sediments (shallower than 2 cm) are 0.28 ± 0.07, 0.21 ± 0.05 and 0.35 ± 0.06, respectively (Henkel et al., 2018; Faust et al., 2021; Burdige and Christensen, 2022), all significantly ($p < 0.01$) higher than our result (0.13 ± 0.06) (Figure 4). This difference can be attributed to the differences in the glacier melting and the bedrock weathering. In our study region, the ice-free area is small and the glacier melting rate is slow (Campbell et al., 1993; The IMBIE team, 2018). However, in the Arctic Barents Sea, off the Antarctic Peninsula and King George Island, there are larger ice-free zones and higher glacier melting rates (Stammerjohn et al., 2008; Screen and Simmonds, 2010; Rueckamp et al., 2011; The IMBIE team, 2018). Therefore, intense weathering process occurs: the runoff formed from ice melting continuously erodes the bedrock, producing soluble Fe^{2+} and secondary nanoparticulates, which are then oxidized and aged into Fe oxides, and transported to the marginal seas along with the runoff (Henkel et al., 2018). This situation is similar to those in rivers of middle and low latitudes, which can continuously transport Fe-containing particulates with high Fe_{HR}/Fe_T ratio. Besides, the Fe_{HR}/Fe_T ratios are significantly ($p < 0.05$) higher off King George Island (Figure 4), probably due to the semi-enclosed bay topography, which is conducive to Fe_{HR} enrichment, similar to the Jiaozhou Bay and Bohai Sea (Zhu et al., 2015; Wang et al., 2019).

Our findings demonstrate that the Fe_{HR}/Fe_T ratios vary across the 4 grain size-based sediment categories in the study area. Specifically, the Fe_T content in "Coarse" sediments (3.25% ± 0.348%) is comparable to that of the Earth's crust (3.5%) (Taylor, 1964), and the Fe_{HR}/Fe_T ratios are extremely low (0.03 ± <0.005), representing minimal weathering of the input material from the Antarctic continent. In "Medium" and "Fine" sediments, the Fe_T content (2.37% ± 0.430% and 2.01% ± 0.387%, respectively) and Fe_{HR}/Fe_T ratios (0.10 ± 0.03 and 0.13 ± 0.04, respectively) are comparable to those of the Antarctic glacial particulates (2.10% ± 0.539% and 0.11 ± 0.05) (Poulton and Raiswell, 2002), indicating that sediments along the shelf of Prydz Bay primarily originate from the weak weathering Antarctic continent. While in "Ultra-fine" sediments, mainly from the deep Southern Ocean, the Fe_T content (3.99% ± 0.950%) is comparable to that of global deep sea sediments (4.29% ± 0.98%), and the Fe_{HR}/Fe_T ratios (0.18 ± 0.03) are slightly lower than those in global deep sea sediments (0.25 ± 0.10) (Poulton and Raiswell, 2002), indicating relatively enhanced weathering in this sediment category.

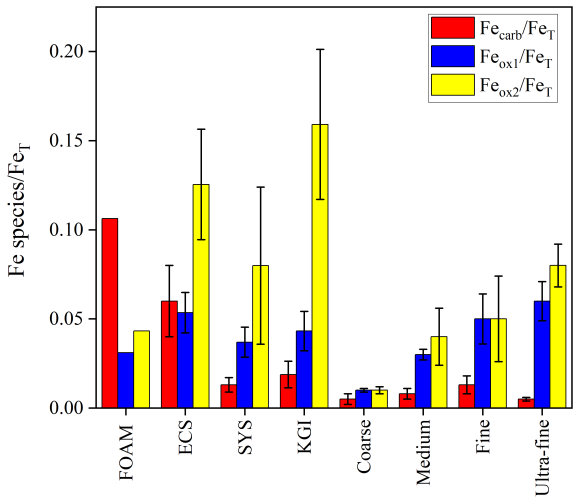

FIGURE 5
Fe_{carb}/Fe_T, Fe_{ox1}/Fe_T and Fe_{ox2}/Fe_T ratios in "Coarse", "Medium", "Fine" and "Ultra-fine" categories of sediments from Prydz Bay and the adjacent Southern Ocean, as well as in sediments from FOAM (friends of anoxic mud) (Canfield, 1989), the ECS (East China Sea) (Zhu et al., 2012), SYS (South Yellow Sea) (Ma et al., 2018) and KGI (King George Island) (Henkel et al., 2018). Data are averages of surface sediments (0 – 2 cm) by recalculation of Canfield (1989) and Henkel et al. (2018).

4.1.2 Indications of the relative content of Fe_{carb}, Fe_{ox1} and Fe_{ox2}

The Fe_{carb}/Fe_T ratios of the 4 grain size-based sediment categories in our research region (0.005 ± 0.003, 0.008 ± 0.003, 0.013 ± 0.005 and 0.005 ± 0.001 for "Coarse", "Medium", "Fine" and "Ultra-fine" categories, respectively) exhibit similarity ($p > 0.05$) to values from oxygen-rich sedimentary environments (e.g., 0.013 ± 0.004 and 0.019 ± 0.007 for the South Yellow Sea and off King George Island, respectively) (Henkel et al., 2018; Ma et al., 2018), but are significantly ($p < 0.001$) lower than those from anoxic or hypoxic sedimentary environments (e.g., 0.11 and 0.06 ± 0.02 for FOAM and the East China Sea, respectively) (Canfield, 1989; Zhu et al., 2012) (Figure 5). Generally, in an Fe-rich and sulfide-free hypoxic or anoxic environment, intense microbially-mediated dissimilatory Fe reduction promotes the transformation of Fe_{ox1} and Fe_{ox2} to Fe(II) (Canfield, 1989; Mathew et al., 2022). Under neutral pH and oxidizing conditions, Fe(II) can rapidly oxidize to Fe(III) and hydrolyze to Fe (hydrogen)oxides (Konhauser et al., 2011; Ma et al., 2018). Therefore, our results indicate that the formation and accumulation of Fe(II) are restricted in oxygen-rich Antarctic marine environments (Meijers et al., 2010; Katsumata et al., 2015).

Interestingly, the Fe_{ox2}/Fe_T ratios of the 4 categories in our research region (0.01 ± <0.005, 0.04 ± 0.02, 0.05 ± 0.02 and 0.08 ± 0.01 for "Coarse", "Medium", "Fine" and "Ultra-fine" categories, respectively) are significantly ($p < 0.001$) lower than those in highly weathered marginal seas, such as the East China Sea and off King George Island (0.13 ± 0.03 and 0.16 ± 0.04) (Zhu et al., 2012; Henkel et al., 2018). However, the Fe_{ox1}/Fe_T ratios (0.03 ± <0.005, 0.05 ± 0.01 and 0.06 ± 0.01 for "Medium", "Fine" and "Ultra-fine" categories, respectively) are similar ($p > 0.05$) to those from the East China Sea, South Yellow Sea, and off King George Island (0.05 ± 0.01, 0.04 ± 0.01 and 0.04 ± 0.01) (Zhu et al., 2012; Henkel et al., 2018; Ma et al., 2018) (Figure 5).

There are 3 potential explanations for the observed differences in patterns between Fe_{ox1}/Fe_T and Fe_{ox2}/Fe_T. Firstly, the transformation of Fe_{ox1} to Fe_{ox2} in the sediments of our study area is restricted. Generally, the initial Fe oxides in the redox cycle are highly reactive and amorphous: i.e., Fe_{ox1}. Over time, Fe_{ox1} gradually transforms into more stable and crystalline Fe oxides: i.e., Fe_{ox2} (Senn et al., 2017). However, the half-life of Fe oxides aging in low temperature environments (< 0°C) is 4 – 6 times longer than in mid-latitude areas (15°C – 20°C) (Canfield et al., 1992; Raiswell and Canfield, 1998; Schwertmann et al., 2004). Considering the relatively new surface sediment ages in the continental shelf of Prydz Bay (Wu et al., 2017), the insufficient conversion time may be responsible for the low Fe_{ox2}/Fe_T ratios observed.

Secondly, there may be additional Fe_{ox1} sources in the study area. Icebergs are considered to be an important Fe_{HR} source to the Southern Ocean (Lin et al., 2011; Raiswell et al., 2016; Raiswell et al., 2018). The Fe in icebergs is often isolated by the ice, limiting Fe contact with water and organic matter and preventing Fe from further aging (Raiswell et al., 2016; Raiswell et al., 2018). Therefore, a high content of ferrihydrite exists in icebergs and may rapidly settle into sediments during melting by scavenging. However, due to a lack of systematic studies, it is still impossible to quantitatively assess the importance of iceberg contributions to sedimentary Fe pools, especially Fe_{ox1}.

Finally, the dynamic equilibrium of the conversion between the transformation from Fe_{ox1} to Fe_{ox2} promoted by aging and the transformation from Fe_T to Fe_{ox1} promoted by chemical weathering (Schwertmann et al., 2004; Poulton and Raiswell, 2005) also explains our Fe_{ox1}/Fe_T results. In summary, these results demonstrate that the regulation of Fe_{HR}/Fe_T ratio by weathering is mainly reflected in the control of Fe_{ox2}/Fe_T ratio rather than Fe_{ox1}/Fe_T ratio.

4.2 Relationship between Fe_{HR} and TOC

The correlation between Fe_{HR} and TOC was investigated in the sediments of Prydz Bay and the adjacent Southern Ocean. Results show a significant negative correlation between TOC and Al, and TOC and Fe_T ($R^2 = 0.53$, $p < 0.01$; $R^2 = 0.35$, $p < 0.01$, Figures S2A, B). The source of Fe in the sediments is mainly from weak-weathered rock of the Antarctic continent (see section 4.1), while TOC is mainly derived from primary production by phytoplankton based on organic biomarkers (Zhao et al., 2014) and TOC/TN ratios (Liu et al., 2014). Therefore, the negative correlations indicate significant differences in the sources of TOC (biogenic) versus Al and Fe_T (lithogenic), and the dilution relationship between each other.

Previous studies have shown that TOC is often positively correlated with Fe_{HR} in surface sediments from riverine particulates, glaciers and marginal seas (Poulton and Raiswell, 2005; Zhu et al., 2012; Roy et al., 2013; Zhu et al., 2015). However, there is no significant ($p > 0.05$) correlation between the TOC and Fe_{HR}, Fe_{carb}, Fe_{ox1} or Fe_{ox2} content in the sediments of our study area (Figures S2C–F), possibly due to the complex sedimentary environment. Based on a wide range of samples, we summarize and classify the relationship between TOC and Fe_{HR} in different sedimentary environments around the world (Figure 6), as follows.

The first scenario pertains to high TOC/Fe_{HR} ratios (> 2.5), observed in "Fine" sediments with elevated TOC content (1.02% ± 0.35%) and high OC loading (TOC/SSA = 0.62 ± 0.33 mg/m^2) in this study (Table S3), as well as in anoxic environments like the Black Sea (Wijsman et al., 2001; Jessen et al., 2017). Usually, the extremely high TOC content and TOC/Fe_{HR} ratios in anoxic environments are due to the reduced remineralization of TOC (Jessen et al., 2017). In contrast, "Fine" sediments are mainly located in the center of Prydz Bay, with shallow water depths (251 – 748 m), and high primary productivity (412 mmol C m^{-2} d^{-1}), summer particulate deposition fluxes (2515 ± 1828 μmol C m^{-2} d^{-1}) and sedimentation rates (2.9 – 8.7 g C m^{-2} a^{-1}) (Behrenfeld and Falkowski, 1997; Yu et al., 2009; Han, 2018). These conditions favor high OC accumulation rates and OC loading (Blair and Aller, 2012). However, the effect of dilution by marine OC on Fe_{HR} content is more significant due to the low Fe_{HR} content caused by inputs of relatively unweathered materials, as described in section 4.1. It should be noted that, unlike in anoxic environments, the situation in our study area is a novel discovery in oxygen-rich polar

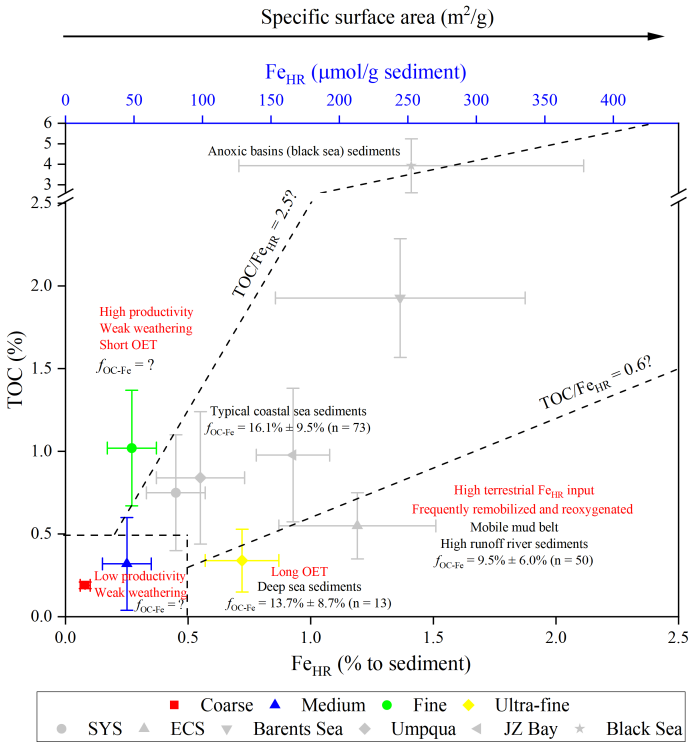

FIGURE 6
Diagram of the relationship between the content of TOC and Fe_{HR}. Specific ranges of TOC/Fe_{HR} ratios characterize different sedimentary environments, and reflect the degree of OC-Fe_{HR} complexing in different environments. Data related to OC/Fe_{HR} ratios are derived from this study, Wijsman et al. (2001); Roy et al. (2013); Jessen et al. (2017); Ma et al. (2018); Faust et al. (2021) and Zhu et al. (2012); Zhu et al. (2015). The f_{OC-Fe} data are from Lalonde et al. (2012); Shields et al. (2016); Ma et al. (2018); Faust et al. (2021) and Zhao et al. (2018). OET, oxygen-exposure time; SYS, South Yellow Sea; ECS, East China Sea, JZ Bay, the Jiaozhou Bay. Data are averages of surface sediments (0 – 2 cm) by recalculation of Jessen et al. (2017); Faust et al. (2021) (stations 393, 506 and 448), Shields et al. (2016) and Wijsman et al. (2001) (station 19).

marine environments and may have significant global implications for the long-term preservation of marine OC (Liu et al., 2014).

The second scenario pertains to low TOC/Fe_{HR} ratios (< 0.6), observed in suspended particulates of rivers with high discharge rates (the Amazon River and the Yellow River) (Poulton and Raiswell, 2005) and deep-sea sediments (Lalonde et al. (2012) and this study). In the former, there are substantial inputs of terrestrial materials (OC and Fe_{HR}) to the ocean; however, more than 90% of the OC is remineralized into CO_2 (Aller and Blair, 2006), and most Fe_{HR} is oxidized and crystallized into hematite, which has relatively poor bioavailability (Zhao et al., 2018, and references therein), due to frequent physical transformations and rapid redox cycling. In the latter, such as "Ultra-fine" sediments in this study, the prolonged oxygen exposure time of OC in deeper waters (> 3000 m) promotes OC remineralization, and the enhanced weathering leads to more Fe_{HR} development (Poulton and Raiswell, 2002).

The third scenario pertains to sediments with both low TOC and Fe_{HR} content, such as "Coarse" and "Medium" sediments in this study, and in icebergs (Poulton and Raiswell, 2005). The former are usually located at the front edge of Amery Ice Shelf or in shallow waters where sea ice cover persists for extended periods, resulting in low rates of OC deposition (1.1 – 5.7 g C m^{-2} a^{-1}) (Yu et al., 2009) and limited TOC accumulation in sediments (Mayer, 1994; Blair and Aller, 2012). Additionally, weak weathering hinders the development of Fe_{HR}.

The final scenario pertains to mid-range TOC/Fe_{HR} ratios (0.6 – 2.5), including typical riverine particulates and marginal shelf sediments (Poulton and Canfield, 2005; Roy et al., 2013). In this scenario, there is a significant positive correlation between TOC and Fe_{HR}, as both are derived from terrestrial sources and interact with each other to form OC-Fe_{HR} complexes through adsorption/coprecipitation. These complexes are then transported to the coastal and shelf sediments and preserved for extended periods (Faust et al., 2021). Therefore, mid-range TOC/Fe_{HR} ratios represent the characteristics of the residual portion of relatively stable terrestrial OC (Poulton and Raiswell, 2005; Lalonde et al., 2012; Roy et al., 2013; Faust et al., 2021).

Based on the preceding discussion, we have deduced that the TOC/Fe_{HR} ratios to some extent can reflect the degree of OC-Fe_{HR} complexing in various environments. This implies that the contribution of Fe_{HR} to OC preservation may differ across different sedimentary settings. For example, in continental shelf marginal sea sediments with mid-range TOC/Fe_{HR} ratios, the f_{OC-Fe} is 16.1% ± 9.5% (n = 73) (Lalonde et al., 2012; Salvadó et al., 2015; Shields et al., 2016; Ma et al., 2018; Faust et al., 2021). In the mobile mud area of the Changjiang Estuary, characterized by low TOC/Fe_{HR} ratios, the f_{OC-Fe} is only 8.1% ± 4.2% (n = 26) (Zhao et al., 2018). In the deep-sea sediments with prolonged oxygen exposure, the f_{OC-Fe} is 13.7% ± 8.7% (n = 13) (Longman et al., 2022). Therefore, we propose that the f_{OC-Fe} may exhibit significant

variation across different sediment categories in Prydz Bay and the adjacent Southern Ocean. However, research on the $f_{OC\text{-}Fe}$ in Antarctic marine sediments is scarce, with only one Antarctic deep sea sediment out of 406 samples worldwide (Lalonde et al., 2012; Longman et al., 2022). Further research on the $f_{OC\text{-}Fe}$ in Antarctic marine sediments is necessary in consideration of the low Fe_{HR}/Fe_T ratios and complex TOC/Fe_{HR} ratios.

5 Conclusion

The Fe_{HR}/Fe_T ratios observed in marine sediments from Prydz Bay and the adjacent Southern Ocean are similar to those in the Antarctic glacial particulates, but lower than those in global riverine particulates and modern marine sediments. This suggests that Fe_{HR} is mainly derived from the Antarctic bedrock with weak weathering. Our Fe_{HR}/Fe_T ratios are also lower than those in sediments from the Arctic Barents Sea, off the Antarctic Peninsula and King George Island, likely due to the slower glacier melting. The Fe_{ox1}/Fe_T ratios in our study area are equivalent to, those in sediments from other continental shelf marginal seas with intense weathering, but the Fe_{ox2}/Fe_T ratios are lower. This indicates that there is a potential inhibitory effect of low temperatures on aging of iceberg melting Fe_{ox1}, and the regulation of weathering on Fe_{HR}/Fe_T ratio is mainly reflected in Fe_{ox2}/Fe_T ratio. There is no significant correlation between TOC and Fe_{HR}, Fe_{carb}, Fe_{ox1} or Fe_{ox2} content, due to the complex and diverse sedimentary environments in the research region: "Fine" sediments with high TOC/Fe_{HR} ratios, TOC content, OC loading and low Fe_{HR} content, "Ultra-fine" sediments with contrary characteristics, and "Medium" and "Coarse" sediments with both low TOC and Fe_{HR} content.

Data availability statement

The original contributions presented in the study are included in the article/Supplementary Material. Further inquiries can be directed to the corresponding author.

Author contributions

WH and JZ made substantial contributions to draft the manuscript. XG and WH made substantial contributions to the data analysis. DL, JH, HZ, CZ, ZH, WS, YS and JP made substantial contributions to participate the manuscript discussion. All authors contributed to the article and approved the submitted version.

Funding

This research was jointly supported by the National Natural Science Foundation of China (NSFC) (Nos. 41976228, 42276255, 41976227, 42176227), the Scientific Research Fund of the Second Institute of Oceanography, MNR (No. JG1805), National Polar Special Program "Impact and Response of Antarctic Seas to Climate Change" (Nos. IRASCC 01-01-02A and 02-02), and the China Scholarship Council (No. 201704180017).

Acknowledgments

The authors would like to thank Dr. Jihao Zhu for helping in Fe_T determination, and Ms. Huijuan Zhang for grain size measurements. We also extend thanks to the *R/V Xuelong* crews who devoted their time and effort to sample sediments in the CHINARE-24 to -29.

Conflict of interest

The authors declare that the research was conducted in the absence of any commercial or financial relationships that could be construed as a potential conflict of interest.

Publisher's note

All claims expressed in this article are solely those of the authors and do not necessarily represent those of their affiliated organizations, or those of the publisher, the editors and the reviewers. Any product that may be evaluated in this article, or claim that may be made by its manufacturer, is not guaranteed or endorsed by the publisher.

Supplementary material

The Supplementary Material for this article can be found online at: https://www.frontiersin.org/articles/10.3389/fmars.2023.1142061/full#supplementary-material

References

Aller, R. C., and Blair, N. E. (2006). Carbon remineralization in the Amazon–guianas tropical mobile mudbelt: A sedimentary incinerator. *Cont. Shelf Res.* 26, 2241–2259. doi: 10.1016/j.csr.2006.07.016

Arrigo, K. R., Van Dijken, G. L., and Strong, A. L. (2015). Environmental controls of marine productivity hot spots around Antarctica. *J. Geophys. Res. Oceans* 120, 5545–5565. doi: 10.1002/2015jc010888

Behrenfeld, M. J., and Falkowski, P. G. (1997). Photosynthetic rates derived from satellite-based chlorophyll concentration. *Limnol. Oceanogr.* 42, 1–20. doi: 10.2307/2838857

Bhatia, M. P., Kujawinski, E. B., Das, S. B., Breier, C. F., Henderson, P. B., and Charette, M. A. (2013). Greenland Meltwater as a significant and potentially bioavailable source of iron to the ocean. *Nat. Geosci.* 6, 274–278. doi: 10.1038/ngeo1746

Blain, S., Queguiner, B., Armand, L., Belviso, S., Bombled, B., Bopp, L., et al. (2007). Effect of natural iron fertilization on carbon sequestration in the southern ocean. *Nature* 446, 1070–1074. doi: 10.1038/nature05700

Blair, N. E., and Aller, R. C. (2012). The fate of terrestrial organic carbon in the marine environment. *Ann. Rev. Mar. Sci.* 4, 401–423. doi: 10.1146/annurev-marine-120709-142717

Burdige, D. J., and Christensen, J. P. (2022). Iron biogeochemistry in sediments on the western continental shelf of the Antarctic peninsula. *Geochim. Cosmochim. Acta* 326, 288–312. doi: 10.1016/j.gca.2022.03.013

Campbell, I. B., Balks, M. R., and Claridge, G. G. C. (1993). A simple visual technique for estimating the impact of fieldwork on the terrestrial environment in ice-free areas of Antarctica. *Polar Rec* 29, 321–328. doi: 10.1017/S0032247400023974

Canfield, D. E. (1989). Reactive iron in marine sediments. *Geochim. Cosmochim. Acta* 53, 619–632. doi: 10.1016/0016-7037(89)90005-7

Canfield, D. E. (1997). The geochemistry of river particulates from the continental USA: Major elements. *Geochim. Cosmochim. Acta* 61, 3349–3365. doi: 10.1016/S0016-7037(97)00172-5

Canfield, D. E., Raiswell, R., and Bottrell, S. H. (1992). The reactivity of sedimentary iron minerals toward sulfide. *Amer. J. Sci.* 292, 659–683. doi: 10.2475/ajs.292.9.659

Dinniman, M. S., St-Laurent, P., Arrigo, K. R., Hofmann, E. E., and Van Dijken, G. L. (2020). Analysis of iron sources in Antarctic continental shelf waters. *J. Geophys. Res. Oceans* 125, 1–19. doi: 10.1029/2019jc015736

Faust, J. C., Tessin, A., Fisher, B. J., Zindorf, M., Papadaki, S., Hendry, K. R., et al. (2021). Millennial scale persistence of organic carbon bound to iron in Arctic marine sediments. *Nat. Commun.* 12, 275. doi: 10.1038/s41467-020-20550-0

Folk, R. L. (1980). *Petrology of sedimentary rocks* (Austin Texas: Hemphill Publishing Company), 184pp.

Han, Z.-B. (2018). *"Biological pump" and its response to changes in sea ice in the Prydz Bay, East Antarctic* (Wuhan: China University of Geosciences) 135.

Harris, D., Horwáth, W., and Kessel, C. V. (2001). Acid fumigation of soils to remove carbonates prior to total organic carbon or carbon-13 isotopic analysis. *Soil Sci. Soc Amer. J.* 65, 1853–1856. doi: 10.2136/sssaj2001.1853

Hawkings, J. R., Wadham, J. L., Tranter, M., Raiswell, R., Benning, L. G., Statham, P. J., et al. (2014). Ice sheets as a significant source of highly reactive nanoparticulate iron to the oceans. *Nat. Commun.* 5, 3929. doi: 10.1038/ncomms4929

Henkel, S., Kasten, S., Hartmann, J. F., Silva-Busso, A., and Staubwasser, M. (2018). Iron cycling and stable fe isotope fractionation in Antarctic shelf sediments, king George island. *Geochim. Cosmochim. Acta* 237, 320–338. doi: 10.1016/j.gca.2018.06.042

Homoky, W. B., Weber, T., Berelson, W. M., Conway, T. M., Henderson, G. M., Van Hulten, M., et al. (2016). Quantifying trace element and isotope fluxes at the ocean-sediment boundary: A review. *Philos. Trans. A Math. Phys. Eng. Sci.* 374, 1–43. doi: 10.1098/rsta.2016.0246

Jessen, L. G., Lichtschlag, A., Ramette, A., Pantoja, S., Rossel, E. P., Schubert, C. J., et al. (2017). Hypoxia causes preservation of labile organic matter and changes seafloor microbial community composition (Black Sea). *Sci. Adv.* 3, e1601897. doi: 10.1126/sciadv.1601897

Katsumata, K., Nakano, H., and Kumamoto, Y. (2015). Dissolved oxygen change and freshening of Antarctic bottom water along 62°S in the Australian-Antarctic basin between 1995/1996 and 2012/2013. *Deep Sea Res. II Top. Stud. Oceanogr.* 114, 27–38. doi: 10.1016/j.dsr2.2014.05.016

Konhauser, K. O., Kappler, A., and Roden, E. E. (2011). Iron in microbial metabolisms. *Elements* 7, 89–93. doi: 10.1002/chin.201227254

Kostka, J. E., and Iii, G. (1994). Partitioning and speciation of solid phase iron in saltmarsh sediments. *Geochim. Cosmochim. Acta* 58, 1701–1710. doi: 10.1016/0016-7037(94)90531-2

Lalonde, K., Mucci, A., Ouellet, A., and Gélinas, Y. (2012). Preservation of organic matter in sediments promoted by iron. *Nature* 483, 198–200. doi: 10.1038/nature10855

Lin, H., Rauschenberg, S., Hexel, C. R., Shaw, T. J., and Twining, B. S. (2011). Free-drifting icebergs as sources of iron to the weddell sea. *Deep Sea Res. II Top. Stud. Oceanogr.* 58, 1392–1406. doi: 10.1016/j.dsr2.2010.11.020

Liu, R., Yu, P., Hu, C. Y., Han, Z. B., and Pan, J. M. (2014). Contents and distributions of organic carbon and total nitrogen in sediments of prydz bay, Antarctic. *Acta Oceanol. Sin.* 36, 118–125. doi: 10.3969/j.issn.0253-4193.2014.04.003

Longman, J., Faust, J. C., Bryce, C., Homoky, W. B., and März, C. (2022). Organic carbon burial with reactive iron across global environments. *Global Biogeochem. Cycles* 36, e2022GB007447. doi: 10.1029/2022gb007447

Longman, J., Gernon, T. M., Palmer, M. R., and Manners, H. R. (2021). Tephra deposition and bonding with reactive oxides enhances burial of organic carbon in the Bering Sea. *Global Biogeochem. Cycles* 35, e2021GB007140. doi: 10.1029/2021gb007140

Lyons, W. B., Dailey, K. R., Welch, K. A., Deuerling, K. M., Welch, S. A., and Mcknight, D. M. (2015). Antarctic Streams as a potential source of iron for the southern ocean. *Geology* 43, 1003–1006. doi: 10.1130/g36989.1

Ma, W. W., Zhu, M.-X., Yang, G.-P., and Li, T. (2018). Iron geochemistry and organic carbon preservation by iron (oxyhydr)oxides in surface sediments of the East China Sea and the south yellow Sea. *J. Mar. Syst.* 178, 62–74. doi: 10.1016/j.jmarsys.2017.10.009

Martin, J. M., and Meybeck, M. (1979). Elemental mass-balance of material carried by major world rivers. *Mar. Chem.* 7, 173–206. doi: 10.1016/0304-4203(79)90039-2

März, C., Poulton, S. W., Brumsack, H. J., and Wagner, T. (2012). Climate-controlled variability of iron deposition in the central Arctic ocean (southern mendeleev ridge) over the last 130,000 years. *Chem. Geol.* 330-331, 116–126. doi: 10.1016/j.chemgeo.2012.08.015

Mathew, D., Gireeshkumar, T. R., Udayakrishnan, P. B., Shameem, K., Nayana, P. M., Deepulal, P. M., et al. (2022). Geochemical speciation of iron under nearshore hypoxia: A case study of alappuzha mud banks, southwest coast of India. *Cont. Shelf Res.* 238, 104686. doi: 10.1016/j.csr.2022.104686

Mayer, L. M. (1994). Surface area control of organic carbon accumulation in continental shelf sediments. *Geochim. Cosmochim. Acta* 58, 1271–1284. doi: 10.1016/0016-7037(94)90381-6

Meijers, A. J. S., Klocker, A., Bindoff, N. L., Williams, G. D., and Marsland, S. J. (2010). The circulation and water masses of the Antarctic shelf and continental slope between 30 and 80°E. *Deep Sea Res. II Top. Stud. Oceanogr.* 57, 723–737. doi: 10.1016/j.dsr2.2009.04.019

Pasquier, V., Fike, D. A., Révillon, S., and Halevy, I. (2022). A global reassessment of the controls on iron speciation in modern sediments and sedimentary rocks: A dominant role for diagenesis. *Geochim. Cosmochim. Acta* 335, 211–230. doi: 10.1016/j.gca.2022.08.037

Pollard, R. T., Salter, I., Sanders, R. J., Lucas, M. I., Moore, C. M., Mills, R. A., et al. (2009). Southern ocean deep-water carbon export enhanced by natural iron fertilization. *Nature* 457, 577–580. doi: 10.1038/nature07716

Poulton, S. W., and Canfield, D. E. (2005). Development of a sequential extraction procedure for iron: Implications for iron partitioning in continentally derived particulates. *Chem. Geol.* 214, 209–221. doi: 10.1016/j.chemgeo.2004.09.003

Poulton, S. W., and Raiswell, R. (2002). The low-temperature geochemical cycle of iron: From continental fluxes to marine sediment deposition. *Amer. J. Sci.* 302, 774–805. doi: 10.2475/ajs.302.9.774

Poulton, S. W., and Raiswell, R. (2005). Chemical and physical characteristics of iron oxides in riverine and glacial meltwater sediments. *Chem. Geol.* 218, 203–221. doi: 10.1016/j.chemgeo.2005.01.007

Raiswell, R., and Canfield, D. E. (1998). Sources of iron for pyrite formation in marine sediments. *Amer. J. Sci.* 298, 219–245. doi: 10.2475/ajs.298.3.219

Raiswell, R., Hawkings, J. R., Benning, L. G., Baker, A. R., Death, R., Albani, S., et al. (2016). Potentially bioavailable iron delivery by iceberg-hosted sediments and atmospheric dust to the polar oceans. *Biogeosciences* 13. doi: 10.3389/feart.2018.00222

Raiswell, R., Hawkings, J., Elsenousy, A., Death, R., Tranter, M., and Wadham, J. (2018). Iron in glacial systems: Speciation, reactivity, freezing behavior, and alteration during transport. *Front. Earth Sci.* 6. doi: 10.3389/feart.2018.00222

Raiswell, R., Tranter, M., Benning, L. G., Siegert, M., De'ath, R., Huybrechts, P., et al. (2006). Contributions from glacially derived sediment to the global iron (oxyhydr) oxide cycle: Implications for iron delivery to the oceans. *Geochim. Cosmochim. Acta* 70, 2765–2780. doi: 10.1016/j.gca.2005.12.027

Roy, M., Mcmanus, J., Goñi, M. A., Chase, Z., Borgeld, J. C., Wheatcroft, R. A., et al. (2013). Reactive iron and manganese distributions in seabed sediments near small mountainous rivers off Oregon and California (USA). *Cont. Shelf Res.* 54, 67–79. doi: 10.1016/j.csr.2012.12.012

Rueckamp, M., Braun, M., Suckro, S., and Blindow, N. (2011). Observed glacial changes on the king George island ice cap, Antarctica, in the last decade. *Global Planet. Change* 79, 99–109. doi: 10.1016/j.gloplacha.2011.06.009

Salvadó, J. A., Tesi, T., Andersson, A., Ingri, J., Dudarev, O. V., Semiletov, I. P., et al. (2015). Organic carbon remobilized from thawing permafrost is resequestered by reactive iron on the Eurasian Arctic shelf. *Geophys. Res. Lett.* 42, 8122–8130. doi: 10.1002/2015gl066058

Schwertmann, U., Stanjek, H., and Becher, H. H. (2004). Long-term *in vitro* transformation of 2-line ferrihydrite to goethite/hematite at 4, 10, 15 and 25°C. *Clay Miner.* 39, 433–438. doi: 10.1180/0009855043940145

Screen, J. A., and Simmonds, I. (2010). Increasing fall-winter energy loss from the Arctic ocean and its role in Arctic temperature amplification. *Geophys. Res. Lett.* 37, L16707. doi: 10.1029/2010gl044136

Senn, A.-C., Kaegi, R., Hug, S. J., Hering, J. G., Mangold, S., and Voegelin, A. (2017). Effect of aging on the structure and phosphate retention of Fe(III)-precipitates formed by Fe(II) oxidation in water. *Geochim. Cosmochim. Acta* 202, 341–360. doi: 10.1016/j.gca.2016.12.033

Shepherd, A., Fricker, H. A., and Farrell, S. L. (2018). Trends and connections across the Antarctic cryosphere. *Nature* 558, 223–232. doi: 10.1038/s41586-018-0171-6

Shields, M. R., Bianchi, T. S., Gélinas, Y., Allison, M. A., and Twilley, R. R. (2016). Enhanced terrestrial carbon preservation promoted by reactive iron in deltaic sediments. *Geophys. Res. Lett.* 43, 1149–1157. doi: 10.1002/2015gl067388

Stammerjohn, S. E., Martinson, D. G., Smith, R. C., and Iannuzzi, R. A. (2008). Sea Ice in the western Antarctic peninsula region: Spatio-temporal variability from ecological and climate change perspectives. *Deep Sea Res. II Top. Stud. Oceanogr.* 55, 2041–2058. doi: 10.1016/j.dsr2.2008.04.026

Tagliabue, A., Bowie, A. R., Boyd, P. W., Buck, K. N., Johnson, K. S., and Saito, M. A. (2017). The integral role of iron in ocean biogeochemistry. *Nature* 543, 51–59. doi: 10.1038/nature21058

Taylor, S. R. (1964). Abundance of chemical elements in the continental crust: A new table. *Geochim. Cosmochim. Acta* 28, 1273–1285. doi: 10.1016/0016-7037(64)90129-2

Thamdrup, B. (2000). Bacterial manganese and iron reduction in aquatic sediments. *Adv. Microbial Ecol.* 16, 41–84. doi: 10.1007/978-1-4615-4187-5_2

The IMBIE team (2018). Mass balance of the Antarctic ice sheet from 1992 to 2017. *Nature* 558, 219–222. doi: 10.1038/s41586-018-0179-y

Thomasarrigo, L. K., Kaegi, R., and Kretzschmar, R. (2019). Ferrihydrite growth and transformation in the presence of ferrous iron and model organic ligands. *Environ. Sci. Technol.* 53, 13636–13647. doi: 10.1021/acs.est.9b03952

Vaz, R., and Lennon, G. W. (1996). Physical oceanography of the prydz bay region of Antarctic waters. *Deep Sea Res. I Oceanogr. Res. Pap.* 43, 603–641. doi: 10.1016/0967-0637(96)00028-3

Wadley, M. R., Jickells, T. D., and Heywood, K. J. (2014). The role of iron sources and transport for southern ocean productivity. *Deep Sea Res. I Oceanogr. Res. Pap.* 87, 82–94. doi: 10.1016/j.dsr.2014.02.003

Wang, D., Zhu, M. X., Yang, G. P., and Ma, W. W. (2019). Reactive iron and iron-bound organic carbon in surface sediments of the river-dominated bohai Sea (China) versus the southern yellow Sea. *J. Geophys. Res. Biogeosci.* 124, 79–98. doi: 10.1029/2018jg004722

Wehrmann, L. M., Formolo, M. J., Owens, J. D., Raiswell, R., Ferdelman, T. G., Riedinger, N., et al. (2014). Iron and manganese speciation and cycling in glacially influenced high-latitude fjord sediments (West spitsbergen, svalbard): Evidence for a benthic recycling-transport mechanism. *Geochim. Cosmochim. Acta* 141, 628–655. doi: 10.1016/j.gca.2014.06.007

Wei, G.-Y., Chen, T., Poulton, S. W., Lin, Y.-B., He, T., Shi, X., et al. (2021). A chemical weathering control on the delivery of particulate iron to the continental shelf. *Geochim. Cosmochim. Acta* 308, 204–216. doi: 10.1016/j.gca.2021.05.058

Wijsman, J. W. M., Middelburg, J. J., and Heip, C. H. R. (2001). Reactive iron in black Sea sediments: Implications for iron cycling. *Mar. Geol.* 172, 167–180. doi: 10.1016/S0025-3227(00)00122-5

Williams, G. D., Herraiz-Borreguero, L., Roquet, F., Tamura, T., Ohshima, K. I., Fukamachi, Y., et al. (2016). The suppression of Antarctic bottom water formation by melting ice shelves in prydz bay. *Nat. Commun.* 7, 12577. doi: 10.1038/ncomms12577

Wu, L., Wang, R., Xiao, W., Ge, S., Chen, Z., and Krijgsman, W. (2017). Productivity-climate coupling recorded in pleistocene sediments off prydz bay (East Antarctica). *Palaeogeogr. Palaeoclimatol. Palaeoecol.* 485, 260–270. doi: 10.1016/j.palaeo.2017.06.018

Yu, P., Hu, C., Liu, X., Pan, J., and Zhang, H. (2009). Modern sedimentation rates in Prydz Bay, Antarctic. *Acta Sedimentol. Sin.* 27, 1172–1177.

Zhao, J., Peter, H.-U., Zhang, H., Han, Z., Hu, C., Yu, P., et al. (2014). Short- and long-term response of phytoplankton to ENSO in prydz bay, Antarctica: Evidences from field measurements, remote sensing data and stratigraphic biomarker records. *J. Ocean Univ. China* 13, 437–444. doi: 10.1007/s11802-014-2231-3

Zhao, B., Yao, P., Bianchi, T. S., Shields, M. R., Cui, X. Q., Zhang, X. W., et al. (2018). The role of reactive iron in the preservation of terrestrial organic carbon in estuarine sediments. *J. Geophys. Res. Biogeosci.* 123, 3556–3569. doi: 10.1029/2018jg004649

Zhu, M.-X., Hao, X.-C., Shi, X.-N., Yang, G.-P., and Li, T. (2012). Speciation and spatial distribution of solid-phase iron in surface sediments of the East China Sea continental shelf. *Appl. Geochem.* 27, 892–905. doi: 10.1016/j.apgeochem.2012.01.004

Zhu, M.-X., Huang, X.-L., Yang, G.-P., and Chen, L.-J. (2015). Iron geochemistry in surface sediments of a temperate semi-enclosed bay, north China. *Estuar. Coast. Shelf Sci.* 165, 25–35. doi: 10.1016/j.ecss.2015.08.018

frontiers | Frontiers in Marine Science

TYPE Original Research
PUBLISHED 20 April 2023
DOI 10.3389/fmars.2023.1135900

OPEN ACCESS

EDITED BY
Peng Lin,
University of Georgia, United States

REVIEWED BY
Fengming Chang,
Institute of Oceanology (CAS), China
Lanlan Zhang,
South China Sea Institute of Oceanology (CAS), China

*CORRESPONDENCE
Rujian Wang
rjwang@tongji.edu.cn
Jianming Pan
jmpan@sio.org.cn

SPECIALTY SECTION
This article was submitted to Marine Biogeochemistry, a section of the journal Frontiers in Marine Science

RECEIVED 02 January 2023
ACCEPTED 20 March 2023
PUBLISHED 20 April 2023

CITATION
Zhang H, Wang R, Han Z, Sun Y, Fan G, Zhao J, Hu J, Ren J and Pan J (2023) Seasonal variations of siliceous microplankton fluxes and radiolarian assemblages linked to environmental conditions in Prydz Bay polynya, Eastern Antarctica.
Front. Mar. Sci. 10:1135900.
doi: 10.3389/fmars.2023.1135900

Seasonal variations of siliceous microplankton fluxes and radiolarian assemblages linked to environmental conditions in Prydz Bay polynya, Eastern Antarctica

Haifeng Zhang[1,2], Rujian Wang[1]*, Zhengbing Han[2], Yongming Sun[3], Gaojing Fan[4], Jun Zhao[2], Ji Hu[2], Jian Ren[2] and Jianming Pan[2,5]*

[1]State Key Laboratory of Marine Geology, Tongji University, Shanghai, China, [2]Key Laboratory of Marine Ecosystem Dynamics, Second Institute of Oceanography, Ministry of Natural Resources, Hangzhou, China, [3]College of Oceanic and Atmospheric Sciences, Ocean University of China, Qingdao, China, [4]Key Laboratory of Polar Science, MNR, Polar Research Institute of China, Shanghai, China, [5]Ocean College, Zhejiang University, Zhoushan, China

Siliceous microplankton is an effective proxy for connecting modern and past marine environments; however, radiolarians have been understudied in Prydz Bay, Eastern Antarctica. This study investigated the changes in the siliceous microbiota fluxes and radiolarian assemblages captured in a 1-year time-series sediment trap (February 2014 to February 2015, ~490 m water depth) in the polynya of Prydz Bay. The results exhibited the strong seasonality in the radiolarian assemblages and the fluxes of radiolarians, diatoms, silicoflagellates and sponge spicules, with low numbers in winter and high numbers in summer. Seasonal variations in the sea ice and plankton community were critical in these patterns. The total radiolarian flux (TRF) displayed three peaks with higher flux than the annual average TRF over the year, all of which occurred in summer. These TRF peaks were mainly driven by seasonal fluctuations of sea ice, primary productivity, grazing pressure caused by phytophagous zooplankton and resuspension of small radiolarians in the surface sediments induced by modified Circumpolar Deep Water (mCDW) intrusion onto the shelf. There were also two notable low-TRF stages, mainly related to full sea-ice coverage and high grazing pressure. Two dominant assemblages were recognized by means of Q-factor analysis. Dominant assemblage one was composed of three small-sized taxa, *Antarctissa* sp., *Phormacantha hystrix* and *Plectacantha oikiskos*, which could be used as a proxy for primary productivity in the Marginal Ice Zone (MIZ) in Prydz Bay. Dominant assemblage two was

composed of *Antarctissa strelkovi* and *Antarctissa denticulata*, with *A. strelkovi* dominating. The high flux and high relative abundance of *A. strelkovi* marked the extension of Ice Shelf Water (ISW) to the shelf area in Prydz Bay. These findings will provide new insights and reliable proxies for modern and paleoceanographic research in the Southern Ocean.

KEYWORDS

Prydz Bay, siliceous microplankton flux, radiolarian assemblage, seasonal variation, polynya, primary productivity, Ice Shelf Water

1 Introduction

The Southern Ocean, a key area for study of the interactions between seawater, sea ice, and the atmosphere and their effects on the climate system, plays a key role in the global carbon and silicon cycles (e.g., Xiao et al., 2016; Meredith et al., 2019; Huguenin et al., 2022). In recent decades, the marine environment and ecosystem of the Southern Ocean have undergone remarkable and rapid changes, of which sea ice is a crucial variate (e.g., Schmidt et al., 2018; Meredith et al., 2019). The MIZ is the transition zone between the open (ice-free) ocean and dense pack ice, where sea-ice algae contributes to the biological pump *via* the seeding of sea-ice-edge blooms (Szymanski and Gradinger, 2016; Yoshida et al., 2020; Louw et al., 2022). These blooms are thought to account for approximately 50% of total primary production of MIZ, despite the composition of the phytoplankton community is still debated (Deppeler and Davidson, 2017; Louw et al., 2022).

Coastal polynyas in the waters around the Antarctica continent are also unique marine ecosystems with low ice cover and high rates of primary production due to the combination of high sunlight and high nutrients, especially iron supply (e.g., Arrigo et al., 2015; McCormack et al., 2017).These areas support critical food sources for abundant top predators, including seals, penguins, and albatross. In austral spring and summer, the surface waters of polynya and their primary producers also undergo processes experienced in the MIZ. For example, sea ice algae varies dramatically in a short period of time in response to light, temperature, pH, and nutrient and gas concentrations (Arrigo, 2017; McMinn, 2017; Yoshida et al, 2020), which in turn cause changes in the feeding strategies of phytophagous zooplankton (copepods and krill) to cope with temporally and spatially changing food availability (Yang et al., 2013). This process has an important impact on the biological pump efficiency and its seasonal variations in polynya areas (Han, 2018; Yang et al., 2019).

Prydz Bay is the largest shelf sea in Eastern Antarctica, contains one of the most productive Antarctic coastal polynyas characterized by high localized primary productivity and zooplankton abundance (Arrigo and van Dijken, 2003; Yang et al., 2019), making it a window to study the marine ecosystem, biological pump efficiency and carbon cycle of the Southern Ocean (Arrigo et al., 2015; Han et al, 2019). The coastal polynyas in Prydz Bay are also believed to be one of important sources in the formation of Antarctic Bottom Water, with supercooled water originating from the Amery Ice Shelf (AIS) and West Ice Shelf (WIS) (Shi et al., 2011; Williams et al., 2016; Ohshima et al., 2022). This supercooled water, known as Ice Shelf Water (ISW), has been studied in terms of its spatial distribution and source (e.g., Yabuki et al., 2006; Shi et al., 2011; Zheng et al., 2011; He et al., 2016), yet there is still a lack of effective indicators for the northward extension of ISW and the associated records of ice shelf expansion over a longer time scale. In this regard, radiolarians in water and sediment may provide a potential solution to this problem.

Siliceous microplankton is an important agent of organic carbon cycling in the global ocean (Matul and Mohan, 2017), with radiolarians being a key group of planktonic communities that connect the micro-food loop and ocean food web (Steineck and Casey, 1990; Suzuki and Not, 2015). Radiolarians play important roles in various marine ecosystems and have been identified as powerful tools for paleoceanographic study (Takahashi, 1991), particularly in high-latitude areas of the Antarctic Ocean that lack calcareous sediments (Abelmann and Gowing, 1997). Their wide range of biodiversity and unique ecosystem regime provide a potentiality for paleoclimate study in the Southern Ocean (Lawler et al., 2021; Lowe et al., 2022). Knowledge of radiolarian ecology is essential for paleoceanographic reconstructions (Takahashi, 1991), and the time-series moored sediment trap is an effective way to assess the production rate, seasonality and distribution pattern of radiolarians in the water column. In the past few decades, sediment traps have been widely used to observe annual and seasonal changes of radiolarians and to study their ecological significance and relationship with the marine environment in Northern Hemisphere oceans (e.g., Boltovskoy et al., 1996; Takahashi et al., 2000; Ikenoue et al., 2012; Matul and Mohan, 2017). By contrast, only a few studies have been devoted to modern radiolarians in the Southern Ocean, mainly focusing on their spatial and temporal distributions in the Atlantic sector. These studies have shown that the obvious seasonal variations of radiolarians, characterized by short-term flux pulses during the austral summer, which are linked to variations in sea-ice coverage and also affected by phytoplankton production, "scavenging" by zooplankton grazers (e.g., krill and copepods), and lateral transport (e.g., Abelmann, 1992a; Abelmann and Gowing, 1997; Suzuki and Not, 2015; Boltovskoy, 2017). Additionally, distinct differences in the species composition were observed in the neritic and pelagic environments. For example, the relative abundances of

the *Antarctissa denticulata/strelkovi* group were 50% and 36% in the upper and lower traps in the Drake Passage, respectively, but these species rarely appeared in the traps sited in the Bransfield Strait and the Powell Basin (Abelmann, 1992b).

In Prydz Bay, previous trap-based studies have focused on particle fluxes, primary production and the biological pump, the trace element compositions, and the particulate barium flux and its relationship with export production (Sun et al., 2013; Sun et al., 2016; Han et al., 2018; Han et al., 2019). However, radiolarian fluxes and their seasonal changes in this area are still poorly understood. This paper presents the first 1-year settling flux record of radiolarians and other siliceous mircoplankton obtained from a sediment trap deployed in the polynya of Prydz Bay from February 2014 to February 2015. The specific objectives of this study are to reveal the seasonal variation of radiolarian flux and its relationship with the marine environment, and to investigate the seasonal variations of the dominant radiolarian species/assemblages and their ecological significance in Prydz Bay.

2 Regional setting

The Prydz Bay Gyre, a closed cyclonic gyre, is characterized by modern surface circulation in Prydz Bay (Figures 1A, B). It is mainly located on the shelf area and is fed by broad inflows from the northeast (Smith and Tréguer, 1994), as well as some water from the Antarctic Coastal Current, a westward current that flows along the front of the AIS and exits near Cape Darnley, bringing cold water from the WIS (Smith et al., 1984; Nunes Vaz and Lennon, 1996). The Antarctic Slope Current flows westward along the continental shelf break in the north of the bay (Smith et al., 1984; Mathiot et al., 2011). Between the Antarctic Slope Current and Antarctic Circumpolar Current, the cyclonic Antarctic Divergence Zone intrudes into the shelf and brings up the relatively warm and salty Circumpolar Deep Water (Yabuki et al., 2006; Williams et al., 2016).

Five water masses are present around Prydz Bay (e.g., Smith et al., 1984; Yabuki et al., 2006). It has been suggested that the water mass on the shelf is relatively simple and stable, typically composed of Antarctic Surface Water, Shelf Water, modified Circumpolar Deep Water (mCDW) and ISW (Figures 1C, D) (e.g., Yabuki et al., 2006; Williams et al., 2016; Guo et al., 2019). The Antarctic Surface Water can be divided into the Summer Surface Water (SSW) and Winter Water. The SSW is spread above the seasonal thermocline of a vast area of Prydz Bay south of 62°S, with a thickness of 20 to 50 m, while the Winter Water is a thin layer of cold, salty water under the SSW, mainly occurring north of the slope (e.g., Chen et al., 2014; Guo et al., 2019). The mCDW can intrude into the shelf across Four Ladies Bank or through the Prydz Channel (Figures 1B–D) (e.g., Yabuki et al., 2006; Williams et al., 2016; Liu et al., 2018; Guo et al., 2019). The Shelf Water is the "memory" of the cold winter water ($T < -1.5$°C) under the SSW, while the ISW is a "supercooled" water mass formed by internal cooling beneath the ice shelves (Yabuki et al., 2006; Shi et al., 2011), and plays an important role in the marine environmental system of Prydz Bay (Smith and Tréguer, 1994; Williams et al., 2016). Recent studies have revealed that the ISW occurs mainly below the seasonal thermocline along the front of the AIS, with a maximum depth of 600 m. This water mass is divided horizontally into several discrete water cores, exhibiting temporal and spatial variations (Zheng et al., 2011). Although most of the ISW is concentrated west of 73°E, it can also be observed east of 73°E during some summers, and is believed to originate from the WIS (Zheng et al., 2011; Williams et al., 2016).

Recent studies have reported the distribution and structural characteristics of nutrients in Prydz Bay and its adjacent areas, with a generalized pattern of a "front" along the shelf edge, featuring high nutrient levels in the inner bay to the south of the front and low levels in the slope and deep sea areas to the north (e. g. Chen et al., 2017). The silicate content, which is closely related to radiolarian production, displays similar characteristics. The 50 μmol kg^{-1} contour of silicate on the shelf appears at approximately 50 m, and then not differing markedly with increasing depth (Figure 1E).

Chlorophyll *a* (*chl*-a) concentrations in the surface water of Prydz Bay during summer follow a similar pattern to that of nutrients, being high in the shelf area and low in the deep sea area. This pattern was confirmed by measurements obtained during cruises conducted by Chinese National Antarctic Research Expedition (e.g., Liu and Chen, 2003). Furthermore, *chl-a* exhibits obvious seasonal and regional changes, as demonstrated by the remote-sensing *chl*-a concentration data for 2014–2015 (Figure 2A). This variation is mainly controlled by the seasonal changes of sea ice, water temperature, sunlight duration and nutrient content (e.g., Sun et al., 2012).

Sea ice extends to approximately 57°S during winter and generally retreats back to the inner bay in summer, but some multi-year sea ice may exist in coastal areas (Figure 2B). In the austral summer, sea ice undergoes bidirectional melting because of the polynyas in Prydz Bay, retreating from north to south in the outer bay and from south to north in the inner bay (Zheng and Shi, 2011). Sea ice in Prydz Bay is reported to generally begin thawing in October, with the most rapid decrease in the sea-ice concentration (SIC) in November. This melting is primarily manifested internally within the sea ice. From December, melting is mainly observed as a decrease in sea-ice coverage area. March is the primary stage of sea-ice growth, which is characterized by rapid expansion of the sea-ice edge and increasing SIC in polynyas (Zheng and Shi, 2011; and reference therein).

3 Material and methods

3.1 Sediment trap samples

A mooring system was deployed for 1 year at Station M8 (68.49°S, 75.38°E, 620 m water depth) in Prydz Bay polynya from February 27, 2014 to February 12, 2015 (Han, 2018). This system carried a Mark78H-21 sediment trap (McLane Inc., East Falmouth, Massachusetts, USA), an RBRsolo T temperature sensor (moored at ~282 m, RBR Ltd., Ottawa, Canada) and an SBE37-SM conductivity–temperature–depth sensor (moored at ~582 m, Sea-Bird Scientific, Bellevue, Washington, USA) (Figure 1). The time-series trap with 21 rotary sample cups was installed at ~490 m water depth. The cups were filled with filtered seawater that had been pre-

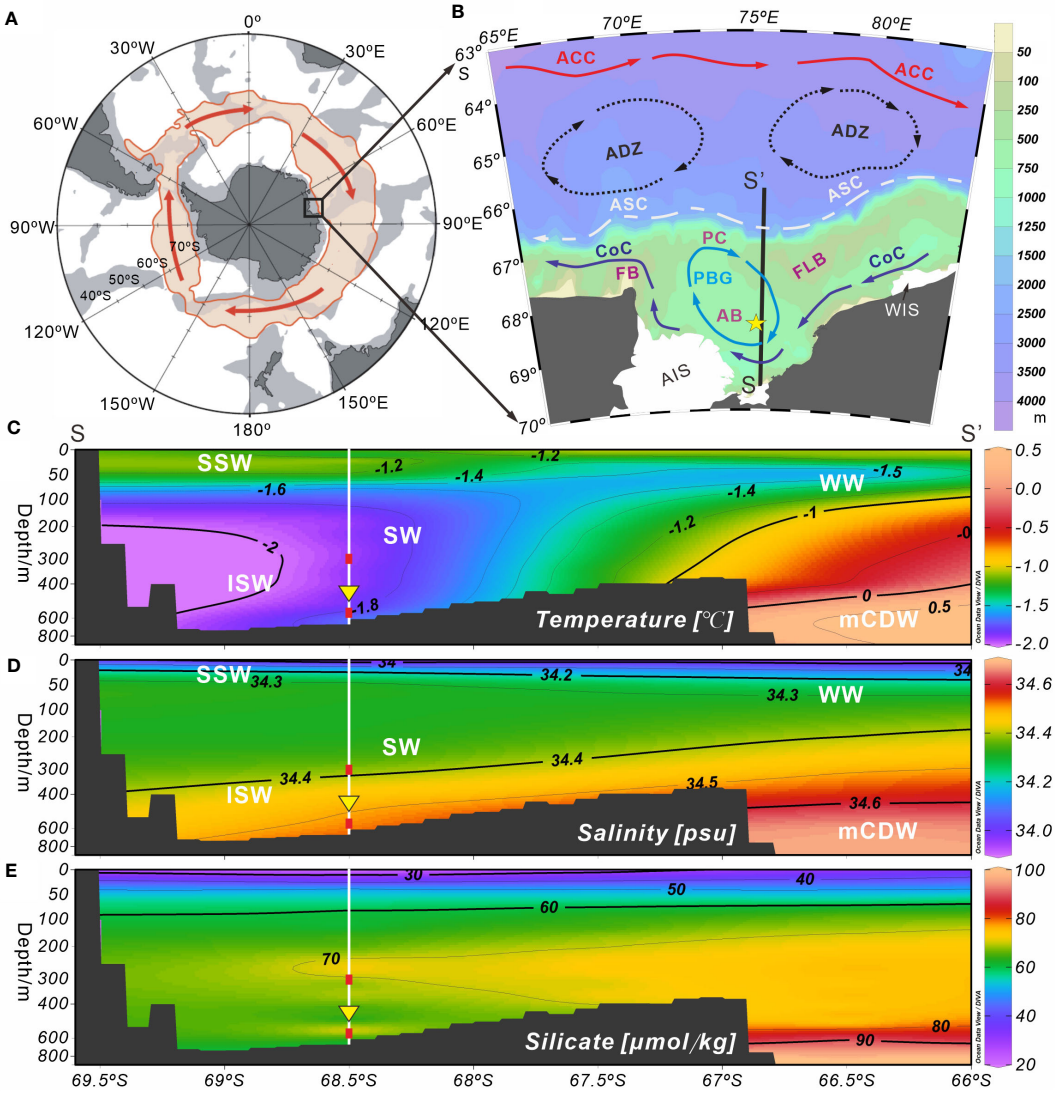

FIGURE 1
Schematic plots of the survey station and environmental setting of Prydz Bay and adjacent areas, Eastern Antarctica. **(A)** Schematic diagram of the Antarctic region. The light red shaded area of the closed loop represents the flow width of the ACC. **(B)** Station M8 (yellow five-pointed star) and modern surface circulation (arrows) in Prydz Bay. The black solid line (SS') represents the hydrological location of section 75.5°E in **(C–E)**. Major current systems (modified from Wu et al., 2019; Zhu et al., 2019): ACC, Antarctic Circumpolar Current; ADZ, Antarctic Divergence Zone; ASC, Antarctic Slope Current; CoC, Antarctic Coastal Current; PBG, Prydz Bay Gyre. Major geomorphic units: PC, Prydz Channel; FLB, Four Ladies Bank; FB, Fram Bank; AB, Amery Basin; AIS, Amery Ice Shelf; WIS, West Ice Shelf. **(C–E)** show the water masses and their temperature, salinity and silicate profiles (section 75.5°E) near Station M8. The data set representing the climatological annual mean between 1955 and 2010, were obtained from the World Ocean Atlas 2018 (https://odv.awi.de/data/ocean/world-ocean-atlas-2018). Major water masses: SSW, Summer Surface Water; WW, Winter Water; SW, Shelf Water; ISW, Ice Shelf Water; mCDW, modified Circumpolar Deep Water. White vertical solid lines indicate the location of Station M8. Red squares mark the depths at which the temperature sensors were installed, and yellow inverted triangles indicate the position of the sediment trap.

treated with 1.67% mercuric chloride solution to prevent degradation of organic matter by microbial activity (Han et al., 2019). Because of the differences in primary productivity and SIC in Prydz Bay during austral summer and winter, the sampling interval was set at approximately 1 week (7 to 9 days) from December to February and at half a month or 1 month (15 or 30 days) between March and November (Table S1). After recovery of the trap, all samples were sieved using a 1-mm mesh nylon sieve to remove zooplankton swimmers. Particulates < 1 mm were then divided into equal aliquots with a McLane wet sample divider (WSD-10). Radiolarian and diatom slides were produced from 19 of the samples; however, this was not possible for cups 6 and 8 due to insufficient sample size.

3.2 Slide preparation and identification

Quantitative radiolarian and diatom slides were prepared according to the methods developed based on the previous studies (Wang et al., 2006; Zhang et al., 2009; Ren et al., 2021; Ran et al., 2022). Subsamples of each aliquot (1/32 to 3/32,

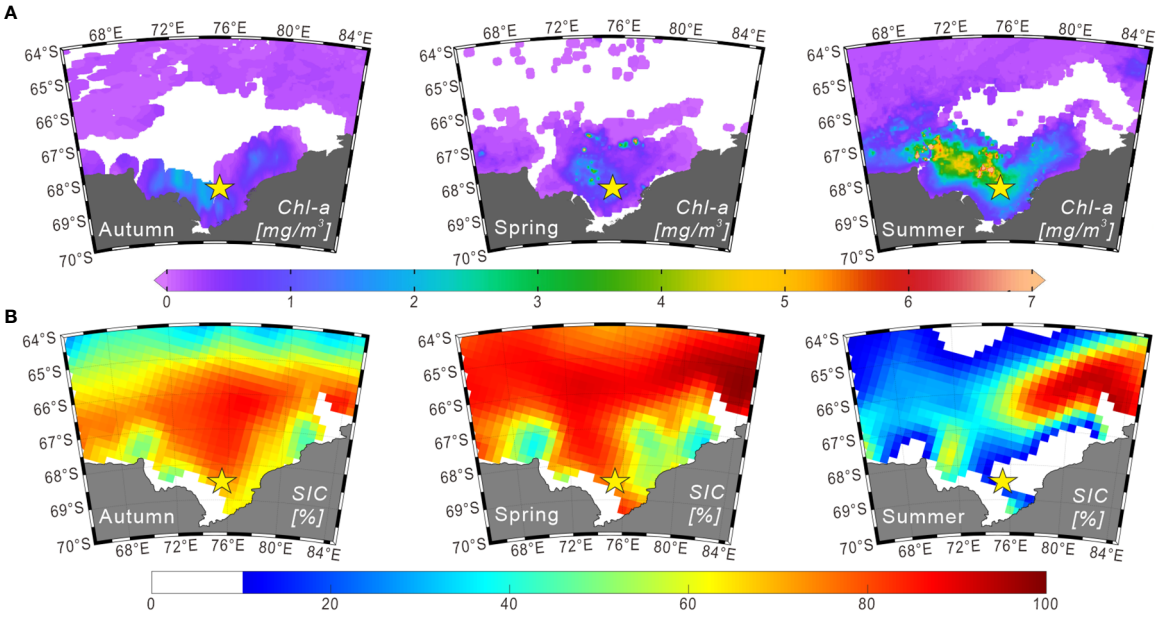

FIGURE 2
Seasonal distributions of chlorophyll *a* and sea-ice concentrations (2014–2015) in Prydz Bay and adjacent areas. **(A)** Seasonal chlorophyll *a* concentration data in the surface ocean derived from Aqua-MODIS products (https://oceanwatch.pifsc.noaa.gov/erddap/griddap). The durations of autumn, spring and summer were defined as March 01 to June 01, 2014; September 01 to December 01, 2014; and December 01, 2014 to March 01, 2015, respectively. **(B)** Seasonal sea-ice concentration data obtained from the climatology data set (2014–2015) of the National Snow and Ice Data Center (https://nsidc.org). The durations of autumn, spring and summer were defined as March–April–May, September–October–November, and December–January–February of 2014 and 2015, respectively.

depending on sample amount) were treated with HCl (~10%) and H_2O_2 (~30%) to generate residues. The mixtures were then stirred and diluted with distilled water four times to remove excess HCl and H_2O_2, as well as the reaction solution. The remaining particles were collected to a constant volume of 50 or 100 mL for slides.

For each radiolarian slide, an aliquot of a known amount (1 to 40 mL, depending on the particulate content) of the residue was dropped on a cover glass (24 × 50 mm) settled in a Petri dish containing gelatin solution. For each diatom slide, an aliquot of a known amount (0.1 to 3 mL, depending on the particle content) of the residue was diluted to 20 mL and mixed with 2 mL gelatin solution, then dropped on two cover glasses (24 × 24 mm) settled in a Petri dish. After 1 h (for radiolarian slides) or 24 h (for diatom slides) of settling time, the supernatant in the dish was removed with bibulous paper. When the materials had completely dried, each cover glass was transferred onto a labeled slide. These permanent slides were mounted with NOA61 UV-sensitive glue (nD = ~1.56, Norland Products, Inc, USA).

All the radiolarians (refer to polycystine radiolarian in this paper), sponge spicules and lithogenic debris in each radiolarian slide were counted under a Leica DM 750 light microscope at ×200 magnification. Radiolarians were identified from plates in references (e.g., Petrushevskaya, 1967; Petrushevskaya, 1971; Takahashi, 1991; Abelmann, 1992a; Abelmann, 1992b; Boltovskoy, 1999; Boltovskoy et al., 2010) and an online radiolarian website (http://www.radiolaria.org). Sponge spicules were mainly identified according to two books (Boury-Esnault and Rutzler, 1997; Hooper and van Soest, 2002). Lithogenic debris (< 1 mm) was counted directly. Diatoms and silicoflagellates in each diatom slide were counted with a Motic BA410E microscope at ×400 or ×1000 magnification, and were mainly identified using the plates of Zielinski (1993). Only siliceous specimens with intact main bodies (> 2/3 shell) were counted.

3.3 Statistical data analysis

3.3.1 Total particle fluxes

The total radiolarian flux (TRF) in each sample was calculated using the following equation:

$$\mathrm{TRF} = \frac{N \times S}{n \times s \times f \times A \times T}$$

where TRF is expressed in skeletons m^{-2} day^{-1}, N is the total number of radiolarians counted under the microscope, S is the area of the petri dish (mm^2), n is the number of fields of vision in which radiolarians were counted under the microscope, s is the area of one field of vision (mm^2), f is the proportion of the sample used for the quantitative slide, A is the area of the funnel mouth (m^2) of sediment trap, and T is the duration of each sampling interval (days).

Similarly, the totals of diatom flux (TF_{diatom}), silicoflagellate flux (TF_{silico}), sponge spicule flux (TF_{ss}), lithogenic debris flux (TF_{litho}), and each identified radiolarian species flux (SF) in each sample were estimated using this formula.

3.3.2 Relative abundance

The relative abundance (RA) of every identified radiolarian species in each sample was calculated by the following equation:

$$RA = \frac{N_a}{N} \times 100\,\%$$

where *Na* represents the number of specimens of a given radiolarian species identified in a sample, and *N* represents the total number of all radiolarian specimens identified in the same sample. This parameter can reflect the contribution of each species to TRF in each sample to some extent.

3.3.3 Q-mode factor analysis

Due to the limited sample material for radiolarians analysis from the sediment trap (splits of 1/32 to 3/32 of the total sample), fewer than 300 radiolarians could be counted in some samples, particularly samples collected during winter at times of low flux. Therefore, conventional Q-factor analysis, which involves selecting species with relative abundance > 2% (Wang et al., 2006), was not suitable for studying changes in radiolarian assemblages. To address this issue, two new parameters, the average contribution rate (ACR) and relative contribution rate (RCR), were introduced to screen the dominant species/assemblages of radiolarians and to reduce statistical deviation caused by insufficient sample size. They were calculated as described below.

(1) First, the average TRF and SF values for all 19 samples (i.e., annual average, 290 days in total) were calculated and referred to as $TRF_{ave.}$ and $SF_{ave.}$, respectively.

(2) Second, the ACR of every species through the year (ACR_{SF}) were estimated, representing the average contribution rate of each species to all radiolarian assemblages over the year, using the following equation:

$$ACR_{SF} = SF_{ave.}/TRF_{ave.} \times 100\,\%$$

(3) Third, the RCR of every species in each sample (RCR_{SF}) was estimated, representing the ratio of each SF in every sampling interval to $TRF_{ave.}$, reflecting the time series variation of the contribution of each species to the total radiolarian flux. This was calculated using the following equation:

$$RCR_{SF} = SF/TRF_{ave.} \times 100\,\%$$

Species with ACR_{SF} > 2% in at least one sample are identified as dominant species, and their RCR_{SF} were analyzed by the Q-factor analysis module (CABFAC) of the PAST software (version 4.06b) (Hammer et al., 2001).

4 Results

4.1 Seasonal variation of TRF

TRF in Prydz Bay polynya from 2014 to 2015 was low in winter and high in summer, exhibiting time-series variation that was notably different from that of total mass flux (TMF) after October 2014 (Figures 3B, C). The $TRF_{ave.}$ of 19 samples was 4070 skeletons m^{-2} d^{-1}. Three radiolarian flux peaks (RFP) with high TRF (> $TRF_{ave.}$) were observed throughout the year, contributing 55.5% of the total annual radiolarian count (Table 1; Figure 3C). Specifically, the highest TRF of the year (30850 skeletons m^{-2} d^{-1}) was observed during the first RFP period (RFP-1) in late summer to early autumn 2014 (February 27 to March 14), which was five to six times greater than the maximum values in later peaks, and represented 39.2% of total annual radiolarian count. After late March 2014, TRF decreased sharply with the rapid increase of SIC (Figures 3A, C). During autumn and winter (March 14 to September 10, 2014), the average TRF was only 2070 skeletons m^{-2} d^{-1}. After October, TRF increased markedly, and the second RFP peak (RFP-2) occurred in late spring 2014 (November 9 to December 1). The average TRF during RFP-2 was approximately 5420 skeletons m^{-2} d^{-1}, contributing 10.1% of the total annual radiolarian count (Table 1; Figure 3C). Subsequently, during the early summer (December 1, 2014 to January 19, 2015), there was a low-TRF stage lasting 7 weeks, with an average of only 1360 skeletons m^{-2} d^{-1}, even lower than the rate in winter. From that time, TRF increased again, and the third RFP (RFP-3) occurred in mid-summer (January 19 to February 3), with an average of ca. 4850 skeletons m^{-2} d^{-1}, representing 6.2% of total annual radiolarian count (Table 1; Figure 3C). In the last sampling interval of the year, TRF was approximately 3650 skeletons m^{-2} d^{-1}.

4.2 Seasonal variation of other particle fluxes

The time-series changes of TF_{diatom} and TF_{silico} also showed seasonality, high in summer and low in winter (Figures 3D, E), similar to TMF but different from TRF (Figures 3B, C). The annual average values were 53.6×10^6 valves m^{-2} d^{-1} for TF_{diatom} and 0.8×10^6 skeletons m^{-2} d^{-1} for TF_{silico} (Table 2). In detail, both diatoms and silicoflagellates exhibited flux peaks during RFP-1, which were also their highest fluxes of the year, with TF_{diatom} and TF_{silico} of approximately 535.1×10^6 valves m^{-2} d^{-1} and 9.0×10^6 skeletons m^{-2} d^{-1}, respectively, representing 51.7% and 55.4% of the total annual counts of diatoms and silicoflagellates, respectively (Table 2). Subsequently, both types of microbiota experienced a long low-flux stage lasting 9 months, and displayed second flux peaks simultaneously with TMF in the middle of summer 2014 (December 15 to 29). During these sampling intervals, the average TF_{diatom} and TF_{silico} were 172.4×10^6 valves m^{-2} d^{-1} and 1.3×10^6 skeletons m^{-2} d^{-1}, respectively, accounting for approximately 15.5% and 7.5% of total annual diatoms and silicoflagellates, respectively (Table 2; Figures 3D, E). Both of these fluxes were much lower than those during RFP-1.

The seasonal variation of TF_{ss} was notably different from those of other siliceous microplankton (Figures 3C–F). The annual average TF_{ss} was approximately 0.7×10^3 spicules m^{-2} d^{-1}, with a maximum of ca. 6.0×10^3 spicules m^{-2} d^{-1} occurring from late autumn to early summer (November 24 to December 1) (Table 2; Figure 3F). Over the same period, TF_{litho} also exhibited the highest peak of the year, with a maximum of approximately 5.0×10^5 particles m^{-2} d^{-1},

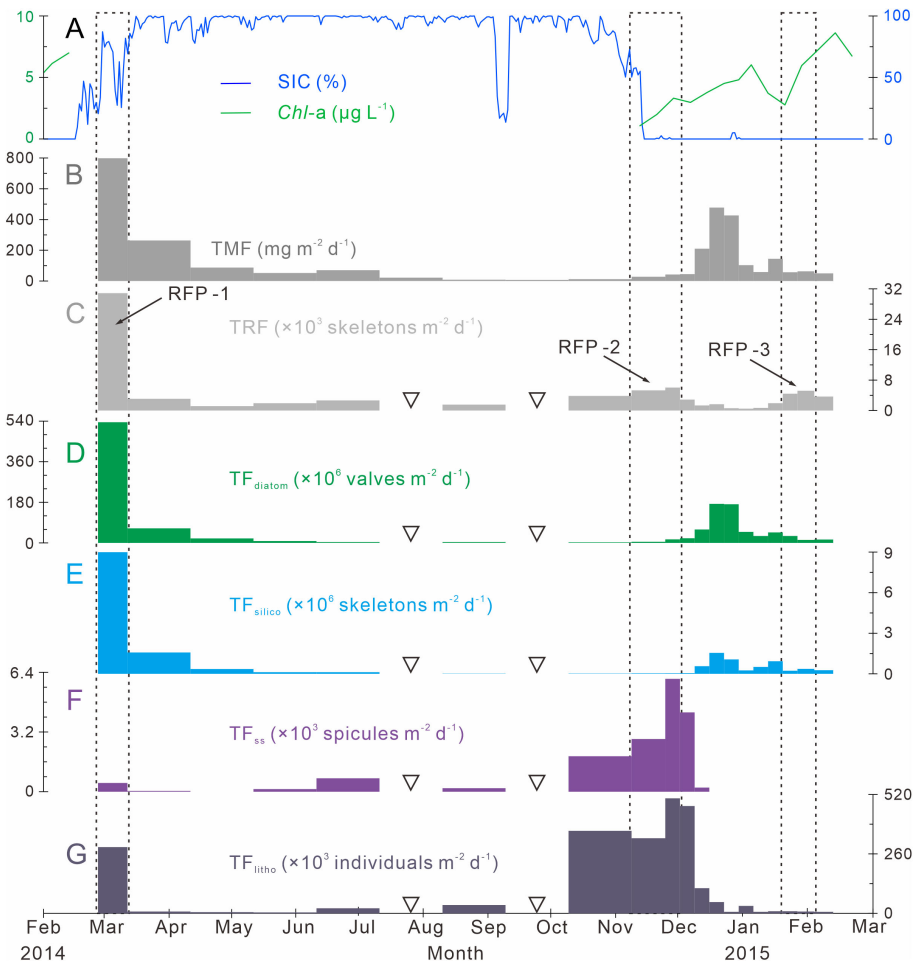

FIGURE 3
Time-series variations of particle fluxes, SIC (%) and *Chl*-a (μg L^{-1}) in Prydz Bay polynya. **(A)** Distributions of SIC (%) and *Chl*-a (μg L^{-1}). SIC data were retrieved from the University of Bremen (http://www.iup.uni-bremen.de:8084/amsr2); *Chl*-a data from the Aqua-MODIS products (http://hermes.acri.fr). **(B)** TMF, total mass flux (Han, 2018). **(C)** TRF, total radiolarian flux. RFP-1–3 are three radiolarian flux peaks (black dotted lines). **(D)** TF_{diatom}, total diatom flux. **(E)** TF_{silico}, total silicoflagellate flux. **(F)** TF_{ss}, total sponge spicule flux. **(G)** TF_{litho}, total lithogenic debris (< 1 mm) flux. The width of each bar in the histogram indicates the sampling interval, and black hollow inverted triangles mark samples that were not analyzed because the sample size was too small.

and another peak occurred at the same time as RFP-1, with approximately 2.9 × 10^5 particles m^{-2} d^{-1}. The annual average TF_{litho} was ca. 1.1 × 10^5 particles m^{-2} d^{-1} (Table 2; Figure 3G).

4.3 Q-mode factor analysis

Following the method outlined in section 3.3.3, 15 dominant radiolarian species were recognized with ACR_{SF} > 2% (Figures 4B, C, 5); the sum of these ACRs was 85.2%. A Q-mode factor analysis based on the RCR values of these 15 species yielded two varimax factors (Table 3), which explained 84.3% of the total population information. Factor one was composed of three small taxa: *Antarctissa* sp., *Phormacantha hystrix* and *Plectacantha oikiskos* (Figures 5A–E), with ACR values of 15.0%, 13.1% and 10.6%, respectively. Factor two was composed of *Antarctissa strelkovi* and *Antarctissa denticulata* (Figures 5F–I), with ACR values of 12.4% and 2.7%, respectively. The sum of these five ACR values was 53.8% (Table 3; Figure 4C).

4.4 Variations of the two dominant assemblages

Dominant assemblage one, i.e., factor one, was the most abundant assemblage in Prydz Bay polynya, with an annual average flux of approximately 1570 skeletons m^{-2} d^{-1}. This assemblage exhibited time-series variation similar to that of TRF (Figures 3C, 4B, 6A). During RFP-1, the flux of dominant assemblage one (FDA1) reached its maximum value (10440 skeletons m^{-2} d^{-1}) of the year (Figure 6A), as did the fluxes of the three small taxa of assemblage one (Figure 4B). Of these taxa, the flux of *Antarctissa* sp. was approximately 4180 skeletons m^{-2} d^{-1}, which was also the highest flux of all radiolarian taxa, while the

TABLE 1 Seasonal variations of TRF from the trap in Prydz Bay polynya.

No.	Sampling period	Season	Total days	Sampling intervals	Ave. TRF*	Contr. rate to total Rads**	Ratio to $TRF_{ave.}$***	Stage
1	2014.02.27-03.14	Late summer to early autumn	15	1	30850	39.2%	7.6	RFP-1
2	2014.03.14-09.10	Autumn to winter	150	5	2070	26.3%	0.5	
3	2014.10.10-11.09	Early spring	30	1	3790	9.6%	0.9	
4	2014.11.09-12.01	Late spring	22	2	5420	10.1%	1.3	RFP-2
5	2014.12.01-2015.01.19	Early to middle summer	49	7	1360	5.7%	0.3	
6	2015.01.19-02.03	Mid-summer	15	2	4850	6.2%	1.2	RFP-3
7	2015.02.03-02.12	Late summer	9	1	3650	2.8%	0.9	
8	2014.02.27-2015.02.12	Annual	290	19	4070****	100%	1	

*Average flux of radiolarians during the sampling period (unit: skeletons m^{-2} d^{-1}); note that a sampling period may contain more than one sampling interval. Ave. TRF is calculated by summing (TRF value × number of days) for all sampling intervals within the sampling period, and dividing this value by the total number of sampling days during the sampling period. The data are rounded to the nearest ten digits.

**Contribution to the total number of radiolarians, i.e., the proportion of radiolarians during the sampling period to the total number of radiolarians for the year. The contribution is calculated as Ave. TRF multiplied by the total number of sampling days, then divided by the total annual sinking radiolarians (290 days multiplied by 4070 skeletons m^{-2} d^{-1}). The sum of these numbers is slightly less than 100% because of rounding during the operation.

***Ratio of the average radiolarian flux during the sampling period to $TRF_{ave.}$, which is calculated by Ave. TRF divided by $TRF_{ave.}$ (4070 skeletons m^{-2} d^{-1}). According to this parameter, there were three radiolarian flux peaks for which this value was greater than one.

****$TRF_{ave.}$ is calculated by the sum of TRF in each of the 19 sampling intervals multiplied by the corresponding number of sampling days, then divided by the total number of sampling days (290 days).

fluxes of *P. hystrix* and *P. oikiskos* were 3480 and 2780 skeletons m^{-2} d^{-1}, respectively (Table 4; Figure 4B). From April to September, FDA1 experienced a low-flux stage similar to TRF, and then gradually increased from October and reached its second peak of the year during RFP-2 (Figure 6A). However, FDA1 and the fluxes of its three taxa during RFP-2 were markedly lower than those during RFP-1, with FDA1 of approximately 2850 skeletons m^{-2} d^{-1} and taxon fluxes of ca. 1250 skeletons m^{-2} d^{-1} (*Antarctissa* sp.), 880 skeletons m^{-2} d^{-1} (*P. hystrix*) and 720 skeletons m^{-2} d^{-1} (*P. oikiskos*) (Table 4; Figure 4B). From December to the following February, their fluxes exhibited a synchronous decline from peaks to low values. Although slight increases were observed during RFP-3 in mid-January 2015, they did not reach the same peak as RFP-2, and the average FDA1 was only approximately 510 skeletons m^{-2} d^{-1} (Table 4; Figure 6B).

Dominant assemblage two, i.e., factor two, was composed of *A. strelkovi* and *A. denticulata*, showed time-series changes that were different from those of TRF (Figures 3C, 4B, 6B). The flux of dominant assemblage two (FDA2) was lower than that of FDA1 (Figures 6A, B), with an annual average value of ca. 620 skeletons m^{-2} d^{-1} (Table 4). Two peaks of FDA2 occurred during RFP-1 and RFP-3, with average values of 4640 and 3370 skeletons m^{-2} d^{-1}, respectively. In the last sampling interval of the year, FDA2 reached 2350 skeletons m^{-2} d^{-1}, much higher than the value of 80 skeletons m^{-2} d^{-1} during RFP-2 (Table 4; Figures 4B, 6B). In the other 13 sampling intervals, the average FDA2 was less than 150 skeletons

TABLE 2 Seasonal features of the fluxes of siliceous microorganisms and lithogenic debris from the trap in Prydz Bay polynya.

No.	Particle fluxes	Annual		First flux peak			Second flux peak		
		Ave.*	Max.	Sampling period	Ave.**	Contr. rate to total fluxes***	Sampling period	Ave.**	Contr. rate to total fluxes***
1	Diatom/×10^6 vales m^{-2} d^{-1}	53.6	535.1	2014.02.27-03.14	535.1	51.7%	2014.12.15-12.29	172.4	15.5%
2	Silicoflagellate/×10^6 skeletons m^{-2} d^{-1}	0.8	9.0	2014.02.27-03.14	9.0	55.4%	2014.12.15-12.29	1.3	7.5%
3	Sponge spine/×10^3 spicules m^{-2} d^{-1}	0.7	6.0	2014.02.27-03.14	4.6	32.9%	2014.11.09-12.08	3.9	53.8%
4	Lithogenic debris/×10^5 individuals m^{-2} d^{-1}	1.1	5.0	2014.02.27-03.14	2.9	14.2%	2014.11.09-12.08	4.1	38.2%

*Annual average flux.

**Average flux in the corresponding sampling period.

***Contribution to total fluxes, representing the proportion of particles (siliceous particles and lithogenic debris) during the corresponding sampling period to the total annual sinking fluxes. Calculations are as in Table 1.

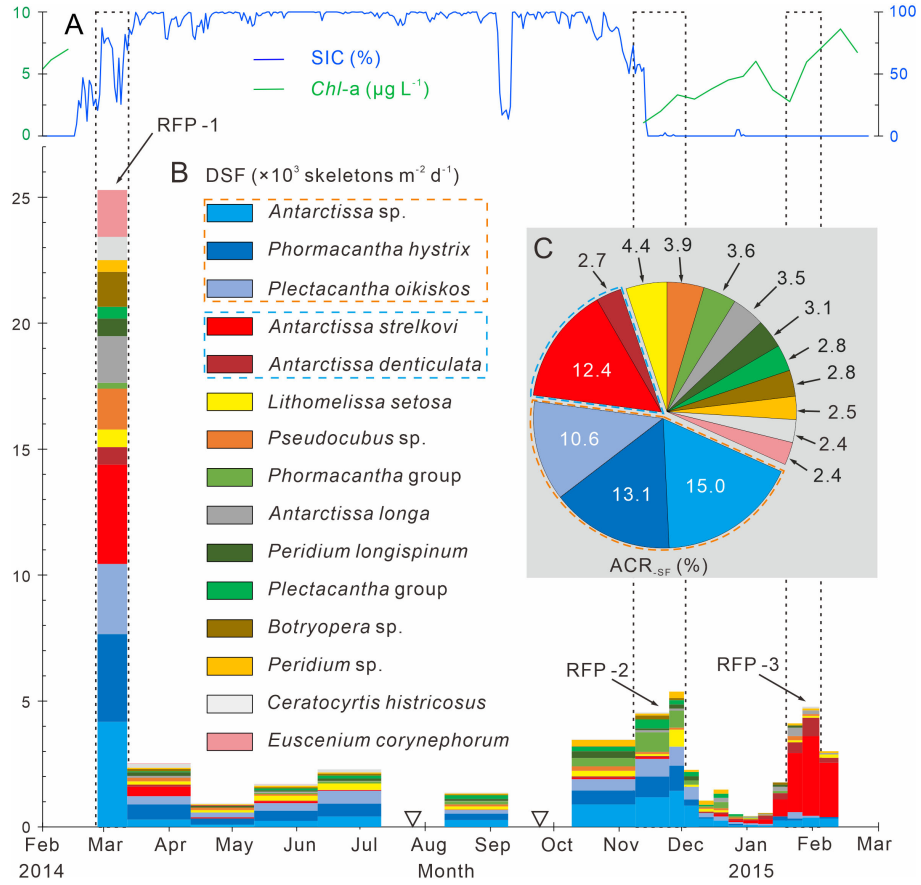

FIGURE 4
Time-series variations of the dominant species fluxes, SIC (%) and *Chl*-a (μg L^{-1}) in Prydz Bay polynya. **(A)** SIC (%) and *Chl*-a (μg L^{-1}). SIC data were retrieved from the University of Bremen (http://www.iup.uni-bremen.de:8084/amsr2); *Chl*-a data from the Aqua-MODIS products (http://hermes.acri.fr). **(B)** DSF, dominant species flux. RFP-1–3 are the three radiolarian flux peaks, (black dotted boxes). The width of each histogram box indicates the sampling interval, and black hollow inverted triangles mark samples that were not analyzed because the sample size was too small. Orange and blue dotted boxes indicate dominant assemblages one and two, respectively. **(C)** ACR_{-SF}, average contribution of each species flux.

m^{-2} d^{-1} (Figure 6B). Notably, *A. strelkovi* dominated this assemblage, with the flux of *A. strelkovi* in each sample being much higher than that of *A. denticulata* (Table 4; Figures 4B, C). The annual average flux of *A. strelkovi* was approximately 510 skeletons m^{-2} d^{-1}, almost five times that of *A. denticulata*. The maximum flux of *A. strelkovi* was ca. 3940 skeletons m^{-2} d^{-1} during RFP-1, whereas the maximum for *A. denticulata* was only 590 skeletons m^{-2} d^{-1} in RFP-3 (Table 4; Figure 4B).

The relative abundances of the two dominant assemblages exhibited opposite trends, with obvious seasonal changes (Figure 6C). During RFP-1, the relative abundance of dominant assemblage one (RADA1) was approximately 33.8%, slightly lower than the annual average (35.7%). RADA1 maintained an upward trend and reached its maximum value (55.9%) in RFP-2, with an average value of 53.5% during that interval (Table 4). During the same period, the relative abundance of dominant assemblage two (RADA2) gradually decreased from 15.0% to 0%, averaging 1.1% during RFP-2 (Table 4; Figure 6C). Following the end of RFP-2, RADA1 decreased rapidly, reaching a minimum (8.5%) of the year by the end of RFP-3, with an average value of 10.8% during that interval. Simultaneously, RADA2 increased steeply, reaching a maximum of 74.7% in RFP-3, with an average of 68.5% (Table 4; Figure 6B).

5 Discussion

5.1 Seasonal variability of TRF and its controlling factors

5.1.1 RFP-1 during late summer 2014

In the late summer of 2014, the dramatic changes in sea ice during RFP-1 (February 27 to March 14, 2014) likely contributed to the peak in siliceous microbiota fluxes (except for TF_{ss}) at the same time as TMF (Figure 3). The daily SIC data showed that sea ice began to grow from February 17, 2014 at Station M8, with dramatic daily fluctuations and SIC was more than 80% to March 14, 2014 (Figure 3A), suggesting the rapid sea-ice gain and melting *in situ* during this period, rather than drifting from other area. During periods of dramatic changes in daily SIC, the coagulation of effective ballast and large amounts of organic matter (90% diatoms) had a marked effect on TMF (Han et al., 2019), consistent with the fluxes

TABLE 3 ACR_{SF} and varimax factor score matrix of dominant radiolarian species from the trap in Prydz Bay polynya.

Specie Name	ACR_{SF}/%	Factor 1	Factor 2
Antarctissa sp.	***15.0***	***2.488***	0.305
Phormacantha hystrix	***13.1***	***1.809***	0.047
Antarctissa strelkovi	***12.4***	-0.391	***3.637***
Plectacantha oikiskos	***10.6***	***1.688***	0.173
Lithomelissa setosa	4.4	0.792	0.011
Pseudocubus sp.	3.9	0.495	0.158
Phormacantha group	3.6	0.835	0.043
Antarctissa longa	3.5	0.170	0.540
Peridium longispinum	3.1	0.420	0.016
Plectacantha group	2.8	0.641	-0.038
Botryopera sp.	2.8	0.184	0.202
Antarctissa denticulata	***2.7***	0.026	***1.126***
Peridium sp.	2.5	0.500	0.012
Ceratocyrtis histricosus	2.4	0.240	0.048
Euscenium corynephorum	2.4	0.084	0.115

The bold values represent the factor scores of the five dominant taxa recognized in factors 1 and 2, respectively.

of diatoms and silicoflagellates (Figures 3D, E). The abundant organic matter was also beneficial to radiolarians, as evidenced by the notable positive correlations of the numbers of diatoms and silicoflagellates with the number of radiolarians in the trap, with correlation coefficients (R^2) of 0.70 and 0.84, respectively (Table 5). However, these relationships are rapidly decoupled when the data for RFP-1 are removed (Table 5), further confirming the importance of phytoplankton to radiolarian production during RFP-1.

Furthermore, the grazing pressure of radiolarians during RFP-1 may have been lower. Previous studies in western Antarctica suggested that at least some copepods stop feeding and become dormant in early March (Schnack-Schiel et al., 1991), and cultivation experiments in Prydz Bay have also shown that copepods mainly feed on ciliates in the shelf area near Station M8 during the late austral summer, with low consumption of the phytoplankton standing stock. Phytoplankton thus mainly supplied the predation demand of micro-zooplankton (Li et al., 2001; Yang et al., 2013). This is further supported by the lowest flux of zooplankton swimmers in the same trap in March (Yang et al., 2019), as well as 13 of 15 dominant species reaching their highest flux over the year at that time (Figure 4B). Similarly, the fluxes of two dominant assemblages both exhibited their highest values of the year at the same time (Table 4; Figures 6A, B), indicating that the radiolarian fauna had a general advantage in competition during RFP-1.

5.1.2 Low TRF during autumn to winter in 2014

The 6-month low-TRF stage in autumn and winter (late March to late September, 2014) was mainly attributed to the full sea-ice coverage in the polynya (Figures 3A, C), which reduced solar radiation and limited photosynthesis by phytoplankton below the sea ice, resulting in a shortage of food for radiolarians. Additionally, the abundance of zooplankton in the waters below the sea ice was not very low, and some zooplankton (such as krill) may have shifted their feeding strategy from herbivory during summer to omnivory during autumn and winter (Nicol et al., 2004; Yang et al., 2019), further inhibiting the production of radiolarians. This causal relationship between the low TRF and the full ice-coverage and related zooplankton activity was more prominent in autumn (mid-March to mid-May).

Following mid-May, resuspension of surface sediments caused by mCDW invasion may have been the primary cause of the increasing trend of TRF (Figures 3C, F, G, 6D, E). Previous studies have suggested that the mean current velocity at the mooring site was < 10 cm s^{-1} (Nunes Vaz and Lennon, 1996), making lateral advection of particulate material negligible (Yang et al., 2019). During winter, mCDW invades the shelf area near 75°E across Four Ladies Bank, and can even advance to the front of the AIS (Yabuki et al., 2006; Herraiz-Borreguero et al., 2015; Williams et al., 2016). The temperature sensor at 582 m depth on the mooring recorded two warming events in the deep water during autumn and late winter 2014 (Figure 6E), which may have been caused by mCDW invasion from the eastern Amery Basin (Herraiz-Borreguero et al., 2015). This invasion could have transported some radiolarian remains in surface sediments from Four Ladies Bank and/or the *in situ* seafloor into the trap. For instance, the flux and relative abundance of dominant assemblage one increased simultaneously (Figures 6A, C). This process is strongly supported by the synchronous increases of TF_{ss} and TF_{litho} (Figures 3F, G). Sponge spicules, the hard parts of sponges (marine sessile multicellular animals; Hooper and van Soest,

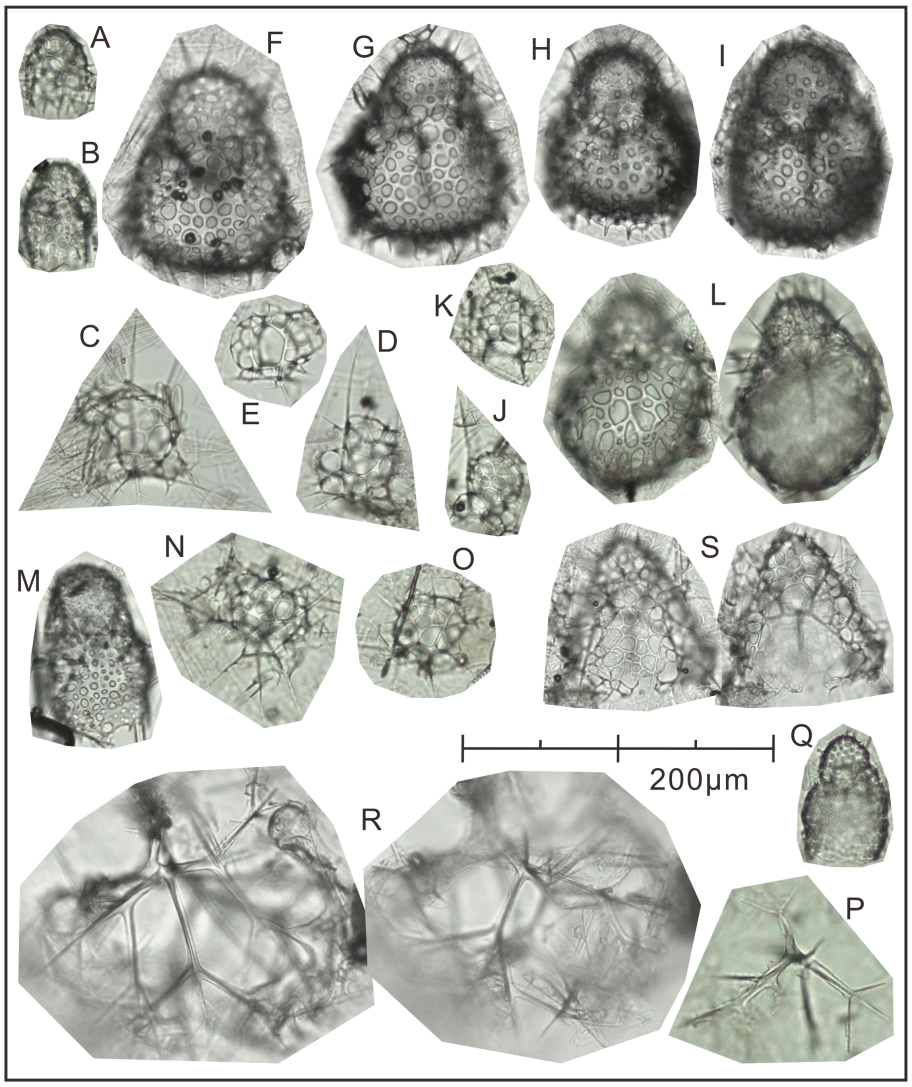

FIGURE 5
The plate of 15 dominant species identified at Station M8 in Prydz Bay polynya. **(A)** *Antarctissa* sp., Summer; **(B)** *Antarctissa* sp., Autumn; **(C)** *Phormacantha hystrix*, Summer; **(D)** *Phormacantha hystrix*, Spring; **(E)** *Plectacantha oikiskos*, Summer; **(F, G)** *Antarctissa strelkovi*, Summer; **(H)** *Antarctissa denticulata*, Summer; **(I)** *Antarctissa denticulata*, Autumn; **(J)** *Peridium longispinum*, Autumn; **(K)** *Peridium* sp., Autumn; **(L)** *Antarctissa longa*, Autumn; **(M)** *Botryopera* sp., Summer; **(N)** *Phormacantha* group, Autumn; **(O)** *Plectacantha* group, Autumn; **(P)** *Pseudocubus* sp., Autumn; **(Q)** *Lithomelissa setosa*, Spring; **(R)** *Euscenium corynephorum*, Autumn; **(S)** *Ceratocyrtis histricosus*, Summer.

2002), can only be derived from surface sediments. Similarly, surface sediment is a main source of lithogenic debris, the other being material released into the sea from melting sea ice (Han et al., 2018).

The similar effects of resuspension and lateral transport of mCDW invasion on the radiolarian remains and lithogenic debris may be related to their close particle size. Grain size analysis showed that the surface sediments from the eastern part of Prydz Bay consist mainly of clay and fine silt (Wang et al., 2015), which is close to the three small-sized taxa of dominant assemblage one (*Antarctissa* sp., *P. hystrix* and *P. oikiskos*) in the trap (Figures 5A–E), generally about 50-70μm (Petrushevskaya, 1967; Nimmergut and Abelmann, 2002). Furthermore, the radiolarian results analyzed in surface sediments from Prydz Bay shelf area reveal that they also constitute a dominant assemblage (Zhang et al., in preparation). This assemblage abundance is strongly and weakly positively correlated with silt and clay content, respectively, indicating a similar distribution pattern.

Simultaneously, we observed that the mCDW invasion did not lead to a significant increase in TF_{diatom} and TF_{silico} in the trap (Figures 3D, E), despite the fact that they are abundant in surface sediments in Prydz Bay shelf. This may be attributed to the differential settling over time caused by the differences in size and mass between radiolarian and diatom. Previous studies reported that the average sedimentation rate of radiolarians in water column was < 0.1 cm s^{-1}, which was much faster than that of diatoms and silicoflagellates (Takahashi, 1987; Liang and Ran, unpublished data). Additionally, the diatom assemblages on the shelf area tend to be smaller and less silicified (Taylor et al., 1997). This may result in the resuspended diatoms and silicoflagellates drifting in the water for a longer period of time.

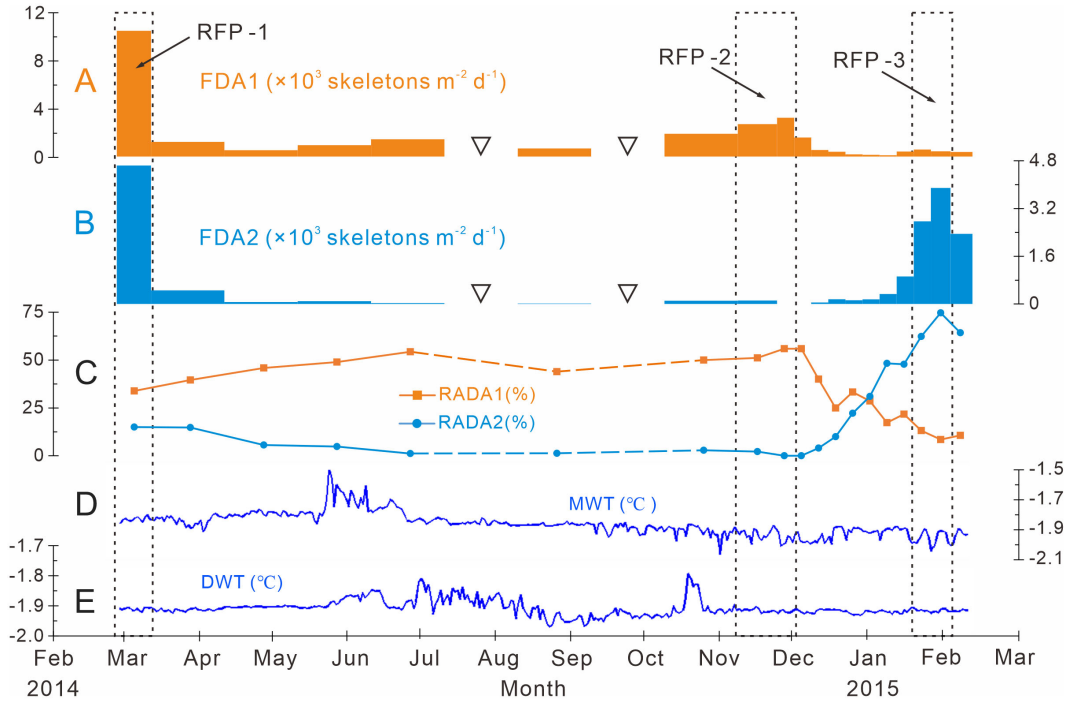

FIGURE 6
Time-series variations of the fluxes and relative abundances of the dominant assemblages with water temperatures measured at Station M8 in Prydz Bay polynya. **(A)** FDA1, flux of dominant assemblage one (the group of small-sized taxa). **(B)** FDA2, flux of dominant assemblage two. **(C)** RADA1, relative abundance of dominant assemblage one; RADA2, relative abundance of dominant assemblage two. **(D)** MWT, medium-depth water temperature recorded by a sensor moored at 282 m. **(E)**, DWT, deep-water temperature recorded by a sensor moored at 582 m. The data sets in **(D)** and **(E)** were provided by the National Arctic and Antarctic Data Center (http://www.chinare.org.cn). The black dotted boxes indicate RFP-1–3. The width of the histogram bars indicates the sampling intervals, and the black hollow inverted triangles indicate samples that were not analyzed because the sample size was too small.

It is worth noting that the temperature sensor at 282 m depth on the mooring, located above the trap (Figures 1C–E), recorded a mCDW invasion event around June 2014 (Figure 6D). The mCDW may have invaded to the shelf area through the Prydz Channel during this period (Chen et al., 2014), with a shallower invasion depth and undisturbed the surface sediments. This may be the causation of the absence of increased fluxes for radiolarian, lithogenic debris and sponge spicules around this period.

5.1.3 TRF fluctuations in spring to summer of 2014 and 2015

The rapid decoupling of TRF from TF_{diatom} and TF_{silico} during RFP-2 (November 9 to December 1, 2014) may have been related to the anomalous retreat of sea ice and resuspension of surface sediments (Figures 3A, C–G, 6E). During normal years, the melting of sea ice dumps abundant ice algae into the water, and the sinking flux of diatoms increases due to the ballast effect of

TABLE 4 Seasonal variations of dominant species fluxes from the trap in Prydz Bay polynya.

Sampling period	Stage	Ave. flux of dominant specie/skeletons·m^{-2}·d^{-1} *					RADA1	RADA2	RA of *A. strelkovi***
		Dominant assemblage one			Dominant assemblage two				
		Antarctissa sp.	*P. hystrix*	*P. oikiskos*	*A. strelkovi*	*A. denticulata*			
2014.02.27-03.14	RFP-1	4180	3480	2780	3940	700	33.8%	15.1%	12.8%
2014.11.09-12.01	RFP-2	1250	880	720	50	30	53.5%	1.1%	0.7%
2015.01.19-02.03	RFP-3	310	40	160	2780	590	10.8%	68.7%	56.7%
2014.02.27-2015.02.12	Annual	610	530	430	510	110	35.7%	21.7%	16.2%

*The average flux is calculated as in Table 1, and the data are rounded to the nearest ten digits.
**The relative abundance of *A. strelkovi* was estimated as described in section 3.2.2.

TABLE 5 Correlations between TRF and TF_{diatom}, and TRF and TF_{silico} in the trap in Prydz Bay polynya.

Variables	TRF			
	Data of RFP-1 included		Data of RFP-1 not included	
	R^2	p	R^2	p
TF_{diatom}	0.71	0.04	0.20	< 0.01
TF_{silico}	0.85	0.05	0.12	< 0.01

lithogenic materials (Han et al., 2019), providing plentiful prey for zooplankton. However, the SIC data showed that the sea ice around Station M8 started to melt after late October 2014, and its coverage suddenly decreased from 55.1% (November 12) to 10.9% (November 13) (Figure 3A), likely due to the physical process of the sea ice "drifting" away under the effect of ocean currents or wind (Han, 2018; Han et al., 2019). This created an ice-free open water area nearly a month earlier than in previous years (Han et al., 2019), which increased the amount of solar radiation reaching the surface waters and the temperature of those waters, and enhanced the stratification of the upper ocean, elevating the photosynthetic efficiency of phytoplankton and the exploitation of nutrients (Schmidt et al., 2018). As a result, the surface primary productivity recovered quickly, as confirmed by the increase of *chl*-a (Figure 3A), providing abundant prey for radiolarians. Previous studies have suggested that krill and copepods, representative of the dominant zooplankton in Prydz Bay, had a low ingestion rate of phytoplankton during the early stage of sea-ice melting, because the copepods (mainly *Calanoides acutus*) were still in a state of dormancy under the ice, whereas the krill (mainly *Euphausia crystallorophias*) showed a modest preference for ciliates (Yang et al., 2013). Thus, TRF increased rapidly due to the adequate prey and lower grazing pressure during RFP-2.

In addition, a warming event lasting approximately 10 days in late October 2014 was recorded by the temperature sensor on the mooring (Figure 6E), likely related to the mCDW invasion from the eastern Amery Basin. This invasion may have caused resuspension and lateral transport of surface sediments, as occurred in the southwestern Weddell Sea (Abelmann and Gersonde, 1991), thus resulting in increased TF_{ss}, TF_{litho} and TRF (Figures 3C, F, G). The increased TRF was mainly contributed by the small-sized taxa such as dominant assemblage one (Figures 6A, C), which was close to the silt in the surface sediments in terms of particle size. However, resuspended diatoms and silicoflagellates may have been unable to settle into the trap in a short period due to their low settling velocity (Takahashi, 1987), as observed in the South China Sea (Liang and Ran, unpublished data).

An intriguing phenomenon during RFP-2 was that TF_{diatom} and TF_{silico} were low, and their increases were even one month later than that of TRF (Figures 3C–E), similar to the results from a trap in the southwestern Weddell Sea (Abelmann and Gersonde, 1991). This lag of TF_{diatom} may have been related to changes in the phytoplankton community during this period. Previous studies have suggested that there may be a phytoplankton bloom dominated by *Phaeocystis* and/or some naked flagellates before diatom mass production in the Southern Ocean MIZ during the early stage of sea-ice melting (e.g., Abelmann and Gersonde, 1991; Garrison et al., 2005; Dumont et al., 2009; Arrigo et al., 2014; Smith et al., 2014; van Leeuwe et al., 2018). Furthermore, there is a so-called "retention system" that is characterized by heavy copepod grazing and re-mineralization of the produced matter in the upper ocean, which decreases the downward-sinking flux (Abelmann and Gersonde, 1991; and references therein). However, more work is needed to verify whether this process is applicable to Prydz Bay. Additionally, during the anomalous retreating process of sea ice, large amounts of ice algae (including diatoms if any) sealed in the bottom of the ice were "carried" away with sea ice drift before they could be dumped into the polynya waters, resulting in the low TF_{diatom}, TF_{silico} and TMF.

Following RFP-2, another low-TRF stage lasting 7 weeks (December 1, 2014 to January 19, 2015) was observed in sharp contrast to the high TF_{diatom} and TF_{silico} (Figures 3C–E). This decoupling may have been linked to the increased grazing pressure caused by the activities of herbivorous predators (krill and copepods) in mid-summer. During this period, there was a large area of open water with high *chl-a* concentration in the polynya (Figures 2, 3A), and the high fluxes of phytoplankton dominated by diatoms and silicoflagellates exhibited their second peaks (Figures 3D, E). This increase in phytoplankton may have induced a rapid increase in the zooplankton biomass and daily grazing (Li and Yang, 2017), which is strongly supported by the increased abundance of zooplankton predators (krill, large copepods and small copepods) and their different types of fecal pellets in the same trap (Nicol et al., 2004; Yang et al., 2017; Yang et al., 2019). The scavenging of these predators in the water resulted in greater grazing pressure on radiolarians (Abelmann, 1992a). Additionally, the delayed settling of resuspended diatoms and silicoflagelates during RFP-2 also contributed to their subsequent high fluxes.

During RFP-3, *chl*-a in the surface ocean rose quickly, and TF_{diatom} and TF_{silico} were also notably higher than their values in winter and RFP-2, indicating that there could have been more prey for radiolarians (Figures 3A–E). Moreover, FDA2 and RADA2 peaked steeply, while RADA1 decreased to its lowest value, despite FDA1 being slightly higher than in the low-TRF stage. Therefore, RFP-3 may have been mainly related to the increased primary productivity and a change in the dominant radiolarian species (Figures 3A–E, 6A–C).

5.2 Ecological and environmental significance of the dominant radiolarian assemblages

5.2.1 Dominant assemblage one as a primary productivity proxy in the MIZ

The small-sized group, dominant assemblage one in the M8 trap, was composed of three taxa (*Antarctissa* sp., *P. oikiskos* and *P. hystrix*) (Figures 5A–E). *P oikiskos* and *P. hystrix*, which are morphologically similar, are typical bipolar species and are often treated as the *P. oikiskos/P. hystrix* group (Petrushevskaya, 1967; Petrushevskaya, 1971). This group is typically found in neritic coastal environments with fjord topography and steep shelves in the Southern Ocean, such as the Powell Basin and Bransfield Strait (Abelmann, 1992a; Abelmann, 1992b). In the Ross Sea, it is used to indicate a nearshore environment with high primary productivity and drastic changes in water depth and topography, and has even been used as a proxy of the MIZ with active seasonal sea-ice changes (Nishimura et al., 1997; Teng and Wang, 2019). This is consistent with reports of this group in the high latitudes of the Northern Hemisphere, where it is thought to inhabit a cold-water, highly productive neritic sea with complex terrain such as steep shelves and fjords (Jørgensen, 1905; Nimmergut and Abelmann, 2002; Abelmann and Nimmergut, 2005; Wang et al., 2006). *Antarctissa* sp. is rarely reported in the Southern Ocean, but is common in open water formed after sea-ice melting in the Sea of Okhotsk. This taxon is most abundant in the subsurface minimum-temperature zone (50–130 m), and is considered to be an index for the Sea of Okhotsk dichothermal layer and for the presence of pronounced summer sea-surface stratification linked to primary productivity (Nimmergut and Abelmann, 2002).

In this study, the average flux of the small-sized group was approximately 1570 skeletons m^{-2} d^{-1} (Table 4), representing 38.7% of the total annual radiolarian count (Table 3; Figures 4B, C). During RFP-1 and RFP-2, there were dramatic sea-ice changes, the flux and relative abundance of the small-sized group and its members were notably higher than the values during RFP-3 in the ice-free period (Figures 4A, B, 6A, C). Although *chl*-a data was missing because of rapid sea-ice fluctuations during RFP-1 (Figure 3A), TMF, TF_{diatom} and TF_{silico} all indicated that the primary productivity of the upper ocean was almost the highest of the year at that time (Figures 3A–E), which was beneficial to radiolarian fauna. After the full ice-coverage winter, sea-ice melting accelerated after October 24, 2014, resulting in the transport of fresh, cold water into the polynya and the enhanced stratification of the upper ocean. This water input was favorable for the recovery of phytoplankton primary production and for the growth of *Antarctissa* sp. (Nimmergut and Abelmann, 2002). During RFP-2, the SIC decreased sharply from 55.1% to 10.9% in one day, and open water then appeared in the polynya (Figure 3A). Higher sea-surface temperature and enhanced light efficiency provided the environmental basis for rapid rises in primary productivity and *chl*-a, which supplied rich, fresh food for *Antarctissa* sp., the dominant taxa feeding primarily on bacteria or relatively fresh phytoplankton debris from the high-productivity surface waters (Abelmann and Nimmergut, 2005). In the MIZ, the assemblage was composed of juveniles and small-sized taxa able to respond quickly to food availability (Swanberg and Eide, 1992; Bjørklund et al., 1998). These factors, together with the lower predation rate by zooplankton (Yang et al, 2013), the possible dominance of the existing phytoplankton community by *Phaeocystis* and/or naked flagellates, and the "retention system" (Abelmann and Gersonde, 1991; and references therein), created a favorable marine environment for growth of small-sized taxa. This was reflected in the second flux peak of the small-sized group and the highest value of RADA1 (55.9%) (Table 4; Figures 4B, 6A, C). Thus, this small-sized group can be used as a proxy for surface primary productivity in the MIZ in Prydz Bay.

5.2.2 *Antarctissa strelkovi* as a proxy for extension of cold Ice Shelf Water

Although *A. strelkovi* and *A. denticulata* (Figures 5F–I) were classified into the same assemblage by Q-factor analysis, *A. strelkovi* may record more representative environmental information than *A. denticulata* in Prydz Bay, and its seasonal variations also appear to be a stronger indication of local characteristics. The flux and average contribution rate of *A. strelkovi* were much higher than those of *A. denticulata* (Table 3; Figures 4B, C). In addition, the two species have markedly different living habits. *A. strelkovi* is restricted to the Antarctic Ocean and is not encountered in warm-water regions. This species is typically found in cold (< 2°C) shallow water with abundant dissolved silicate (Petrushevskaya, 1967). The results of opening/closing net samples collected from 0 to 1000 m showed that the species is restricted to the Antarctic Surface Water and has its highest loadings in the uppermost 200 m of the water (Abelmann and Gowing, 1997). In the MIZ, *A. strelkovi* prefers surface water shallower than 100 m, but can also migrate downward to 385 m in the shelf area (Morley and Stepien, 1985). In other words, *A. strelkovi* is mainly concentrated in environments with temperatures < 1.5°C and high levels of dissolved silicate (50–70 μmol L^{-1}) (Abelmann and Gowing, 1997). Therefore, neither seawater temperature nor silicate content was the limiting factor in Prydz Bay polynya (Figure 1D). *A. denticulata* is also a typical dominant species in the Antarctic cold water group, and was often treated as the *A. denticulata/strelkovi* group in earlier studies (e.g., Abelmann, 1992a; Abelmann, 1992b; Boltovskoy, 1999; Boltovskoy et al., 2010). It is an abundant and typical species in deep-water sediments of the open ocean, with relative abundance of up to 20%–30%. However, its abundance is at most 24% in coastal areas with ice-raft deposits (Petrushevskaya, 1967) and only approximately 3%–5% in shelf areas such as Prydz Bay (Zhu et al., 2019; Zhang et al., in preparation).

Based on this information, *A. strelkovi* in dominant assemblage two is thought to have a greater environmental significance and highly sensitive to cold water masses in the study area. There were two peaks of the *A. strelkovi* flux over the year, in RFP-1 and RFP-3 (Figure 4B). The species' relative abundance in RFP-1 (12. 8%) was much lower than that in RFP-3 (56.7%) and lower than its annual average (16.2%) (Table 4), indicating that *A. strelkovi* had no competitive advantage relative to other radiolarians during RFP-1. During winter, the mCDW invaded the shelf area across Four Ladies Bank and caused significant

warming in the medium-depth and deep waters (Figures 6D, E), which could have caused resuspension and movement of sediment from the bank or *in situ* seafloor to the trap. However, this process did not change the decreasing *A. strelkovi* flux and relative abundance, likely due to its larger skeleton size (150-170 µm) compared to members of the small-sized group (Figures 5A–I) (Jørgensen, 1905; Petrushevskaya, 1967).

As spring and summer arrived, the surface seawater temperature and phytoplankton productivity increased due to the melting of sea ice (Figure 2B), resulting in great silicate consumption. This may have prompted *A. strelkovi* to migrate to the middle-deep ocean, where the temperature is lower and the silicate levels higher (Figure 7). In addition, the temperature sensor at 282 m showed that the medium-depth ocean was affected by cold water masses after mid-September 2014, particularly after mid-January 2015 (Figure 6D). In Prydz Bay, these cold waters mainly originated from the supercooled water under the ice shelf, i.e., the ISW (Figures 7A, B). The remarkable low-temperature characteristics of this water had a marked cooling effect on the waters of the shelf area. Herraiz-Borreguero et al. (2015) noted that the ISW flows into the small circulation under the AIS from the northeast and then flows out from the west. Some studies have suggested that the ISW developed in front of the AIS mainly occurs west of 73°E, while the ISW in the area east of 73°E may originate from the WIS in eastern Prydz Bay (Zheng et al., 2011; Williams et al., 2016). Notably, the flux of *A. strelkovi* started to rise in synchrony with cooling after September; in particular, the steep increase in the relative abundance of this species from December onward indicates sensitivity to the cooling process of the medium-depth waters (Figures 4B, 6B). More significantly and directly, the water at 282 m cooled by 0.2°C (down to as low as −2°C) during RFP-3 (January 19 to February 3 2015), which is a typical feature of ISW. At the same time, the flux and relative abundance of *A. strelkovi* rapidly peaked (Figures 4B, 6B), indicating that this dominant species, which prefers a cold, high-silicate environment, was notably sensitive to supercooled water from the ice shelf during periods of open water and high surface seawater temperatures in the polynya during summer. In conclusion, the high flux and high relative abundance of *A. strelkovi* in Prydz Bay mainly records the process of ISW invasion to the shelf area in summer.

6 Conclusions

The 1-year flux record of siliceous microplankton acquired in a time-series trap (February 2014 to February 2015, ~490 m) moored in Prydz Bay, Eastern Antarctica, highlights the strong seasonality of radiolarian, diatom, silicoflagellate and sponge spicule fluxes and radiolarian assemblages. All fluxes were low in winter and high in summer and were closely related to the particular marine environment of the study area, especially seasonal variations in sea ice and the plankton community.

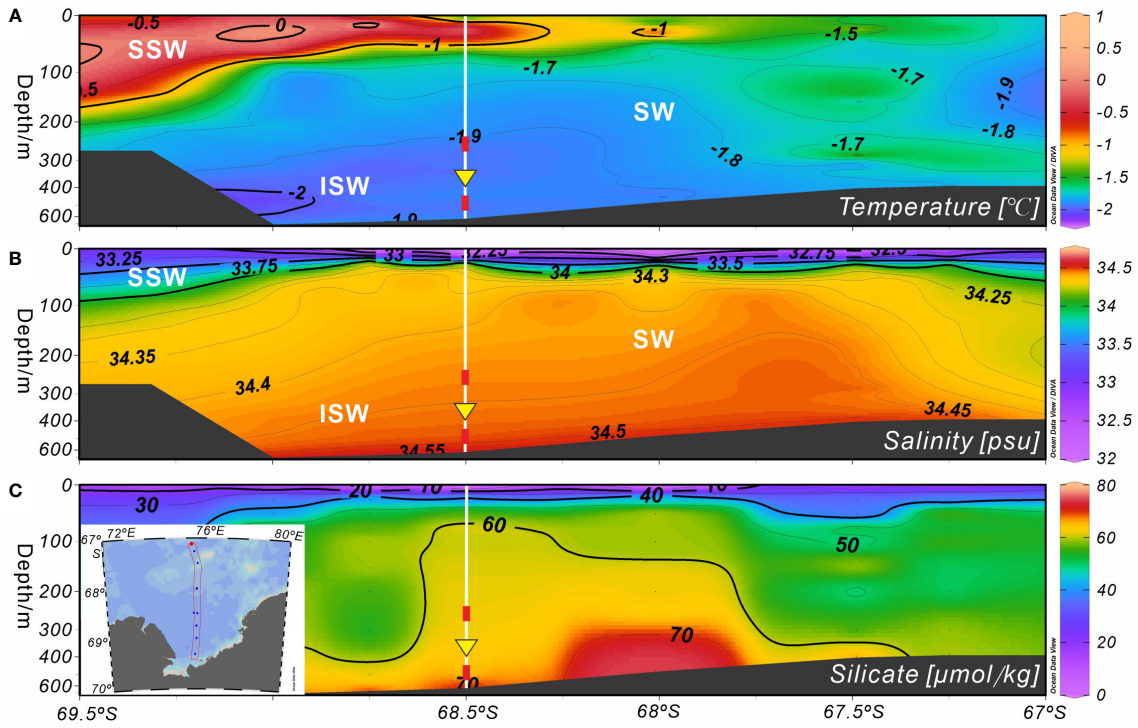

FIGURE 7
Marine environmental profiles of Section 75.5°E on the shelf of Prydz Bay in late summer 2015. **(A, B)** Temperature and salinity profiles showing the locations of water masses. **(C)** Silicate profile. Major water masses: SSW, Summer Surface Water; SW, Shelf Water; ISW, Ice Shelf Water. White vertical solid lines indicate the location of Station M8, red rectangles mark the depths of the temperature sensors, and yellow inverted triangles indicate the position of the sediment trap. The data set was provided by the National Arctic and Antarctic Data Center (http://www.chinare.org.cn), and was obtained during the 31st cruise of CHINARE from February 28 to March 1, 2015.

Three TRF peaks (> $TRF_{ave.}$) were observed over the year, all in the summer season and referred as to RFP-1, RFP-2 and RFP-3. The other two notable low-TRF intervals were identified, one in winter and another in mid-summer. During RFP-1 in early March 2014 (late summer), TRF was the highest of the year, five to six times greater than those in RFP-2 (early summer 2014–2015) and RFP-3 (mid-to-late summer), coinciding with the maximum values of TF_{diatom}, TF_{silico} and TMF. This result can be attributed to the increased primary productivity and decreased grazing pressure related to the rapid fluctuation of sea ice in situ. The generally low siliceous microbiota fluxes in autumn and winter (late March to late September) were mainly constrained by the harsh environment resulting from full sea-ice coverage. The resuspension of surface sediments caused by mCDW intrusion onto the shelf played an important role in the increased radiolarian flux. Decoupling of radiolarian and siliceous phytoplankton fluxes during RFP-2 was mainly related to the abnormal sea-ice retreat in early summer of 2014–2015. The enhanced competitive advantage of the small-sized radiolarian group, the mCDW invasion and the bloom of non-diatom-dominated phytoplankton communities were also important factors. During mid-summer (December 2014 to early January 2015), radiolarians exhibited a low-flux stage lasting 7 weeks, in sharp contrast to the second flux peaks of diatoms and silicoflagellates, mainly related to the increased grazing pressure caused by the activities of herbivorous predators. RFP-3 was mainly related to the increase of surface primary productivity and a change in the dominant radiolarian assemblages.

Two dominant radiolarian assemblages were recognized by Q-factor analysis of 15 dominant radiolarian species, with markedly differences in fluxes and relative abundances. Dominant assemblage one, referred to as the small-sized group, was composed of *Antarctissa* sp., *P. oikiskos* and *P. hystrix*, and showed high fluxes during RFP-1 and RFP-2. Its relative abundance was greatest during RFP-2, with a preceding upward trend and a subsequent rapid decrease, suggesting that it can be used as a proxy for primary productivity in the MIZ of Prydz Bay. Dominant assemblage two was composed of *A. strelkovi* and *A. denticulata*, with *A. strelkovi* dominating. The flux of *A. strelkovi* was high during RFP-1 and RFP-3, but its relative abundance was opposite to that of the small-sized group, being lowest during RFP-1 and highest during RFP-3. This suggests that the high flux and high relative abundance of *A. strelkovi* may record the extension of ISW onto the shelf in Prydz Bay.

Data availability statement

The original contributions presented in the study are included in the article/Supplementary Material. Further inquiries can be directed to the corresponding authors.

Author contributions

HZ performed the analyses of sediment trap samples and wrote the first version of the manuscript, RW conceived the sample experiments, manuscript structure and revised the text, ZH performed the TMF experiments and the statistical analysis of marine environmental data, YS supported the processing and plotting of the temperature sensors data, GF performed the data processing and plotting of sea-ice concentration and chlorophyll-a, JZ and JH collected and treated the samples, JR supported the diatom identification and revised the manuscript, and JP organized the project implementation. All authors contributed to the article and approved the submitted version.

Funding

The study was financially supported by National Natural Science Foundation of China (Grant nos. 42030401, 41506223, 41976228, 42276255), Scientific Research Fund of the Second Institute of Oceanography, MNR, (Grant nos. JG2211), and National Polar Special Program “Impact and Response of Antarctic Seas to Climate Change” (Grant nos. IRASCC 01-01-02A, IRASCC 02-02).

Acknowledgments

We thank all the cruise members of cruise 30th and 31st of Chinese National Antarctic Research Expedition (CHINARE) for deployment and recovery of the mooring. We thank Chengcheng Shen and Xinfeng Dai from SIO for their valuable suggestions on the manuscript and identification of sponge spicules. Yang Guang (Institute of Oceanology, Chinese Academy of Sciences), Guijun Guo (First Institute of Oceanography, MNR) and Jiuxin Shi (Ocean University of China) are acknowledged for their analytical support and suggestions on the zooplankton data, water masses and temperature data. We also wish to thank the reviewers for their valuable comments that allowed us to improve the manuscript.

Conflict of interest

The authors declare that the research was conducted in the absence of any commercial or financial relationships that could be construed as a potential conflict of interest.

Publisher’s note

Supplementary material

The Supplementary Material for this article can be found online at: https://www.frontiersin.org/articles/10.3389/fmars.2023.1135900/full#supplementary-material

References

Abelmann, A. (1992a). Radiolarian flux in Antarctic waters (Drake passage, Powell basin, bransfield strait). *Polar Biol.* 12, 357–372. doi: 10.1007/BF00243107

Abelmann, A. (1992b). Radiolarian taxa from southern-ocean sediment traps (Atlantic sector). *Polar Biol.* 12, 373–385. doi: 10.1007/bf00243108

Abelmann, A., and Gersonde, R. (1991). Biosiliceous particle flux in the southern ocean. *Mar. Chem.* 35, 503–536. doi: 10.1016/S0304-4203(09)90040-8

Abelmann, A., and Gowing, M. M. (1997). Spatial distribution pattern of living polycystine radiolarian taxa–baseline study for paleoenvironmental reconstructions in the southern ocean (Atlantic sector). *Mar. Micropaleontol.* 30, 3–28. doi: 10.1016/S0377-8398(96)00021-7

Abelmann, A., and Nimmergut, A. (2005). Radiolarians in the Sea of Okhotsk and their ecological implication for paleoenvironmental reconstructions. *Deep Sea Res. Part II: Top. Stud. Oceanogr.* 52, 2302–2331. doi: 10.1016/j.dsr2.2005.07.009

Arrigo, K. R. (2017). "Sea Ice as a habitat for primary producers," in *Sea Ice, Third Edition*. Ed. D. N. Thomas (Chichester: John Wiley & Sons, Ltd), 352–369. doi: 10.1002/9781118778371.ch14

Arrigo, K. R., Brown, Z. W., and Mills, M. M. (2014). Sea Ice algal biomass and physiology in the amundsen Sea, Antarctica. *Elementa: Sci. Anthropocene.* 2, 28. doi: 10.12952/journal.elementa.000028

Arrigo, K. R., and van Dijken, G. L. (2003). Phytoplankton dynamics within 37 Antarctic coastal polynya systems. *J. Geophys. Res.* 108 (C8), 3271. doi: 10.1029/2002JC001739

Arrigo, K. R., van Dijken, G. L., and Strong, A. L. (2015). Environmental controls of marine productivity hot spots around Antarctica. *J. Geophys. Res.: Oceans.* 120, 5545–5565. doi: 10.1002/2015JC010888

Bjørklund, K. R., Cortese, G., Swanberg, N. R., and Schrader, H. J. (1998). Radiolarian faunal provinces in surface sediments of the Greenland, Iceland and Norwegian (GIN) seas. *Mar. Micropaleontol.* 35, 105–140. doi: 10.1016/S0377-8398(98)00013-9

Boltovskoy, D. (1999). "Radiolaria polycystina," in *South Atlantic zooplankton*. Ed. D. Boltovskoy (Leiden: Backhuys Publishers), 149–212.

Boltovskoy, D. (2017). Vertical distribution patterns of radiolaria polycystina (Protista) in the world ocean: living ranges, isothermal submersion and settling shells. *J. Plankton Res.* 39, 330–349. doi: 10.1093/plankt/fbx003

Boltovskoy, D., Kling, S. A., Takahashi, K., and Bjørklund, K. (2010). World atlas of distribution of recent polycystina (radiolaria). *Palaeontol. Electron.* 13, 131–142. doi: 10.1016/j.palaeo.2009.11.002

Boltovskoy, D., Oberhänsli, H., and Wefer, G. (1996). Radiolarian assemblages in the eastern tropical Atlantic: patterns in the plankton and in sediment trap samples. *J. Mar. Syst.* 8, 31–51. doi: 10.1016/0924-7963(95)00038-0

Boury-Esnault, N., and Rutzler, K. (1997). *Thesaurus of sponge morphology* (Washington, D.C: Smithsonian Institution Press).

Chen, J. Y., Han, Z. B., Hu, C. Y., Sun, W. P., and Zhang, H. S. (2017). Distribution and seasonal depletion of nutrients in prydz bay, Antarctica (in Chinese with English abstract). *Chin. J. Polar Res.* 29, 327–337. doi: 10.13679/j.jdyj.2017.3.327

Chen, H. X., Lin, L. N., and Shi, J. X. (2014). Study on water masses in prydz bay and its adjacent sea area (in Chinese with English abstract). *Acta Oceanol. Sinica.* 36, 1–8. doi: 10.3969/j.issn.0253-4193.2014.07.001

Deppeler, S. L., and Davidson, A. T. (2017). Southern ocean phytoplankton in a changing climate. *Front. Mar. Sci.* 4. doi: 10.3389/fmars.2017.00040

Dumont, I., Schoemann, V., Lannuzel, D., Chou, L., Tison, J.-L., and Becquevort, S. (2009). Distribution and characterization of dissolved and particulate organic matter in Antarctic pack ice. *Polar Biol.* 32, 733–750. doi: 10.1007/s00300-008-0577-y

Garrison, D. L., Gibson, A., Coale, S. L., Gowing, M. M., Okolodkov, Y. B., Fritsen, C. H., et al. (2005). Sea-Ice microbial communities in the Ross Sea: autumn and summer biota. *Mar. Ecol. Prog. Ser.* 300, 39–52. doi: 10.3354/meps300039

Guo, G. J., Shi, J. X., Gao, L. B., Tamura, T., and Williams, G. D. (2019). Reduced Sea ice production due to upwelled oceanic heat flux in prydz bay, East Antarctica. *Geophys. Res. Lett.* 46, 4782–4789. doi: 10.1029/2018gl081463

Hammer, Ø., Harper, D. A. T., and Ryan, P. D. (2001). PAST: paleontological statistics software package for education and data analysis. *Palaeontol. Electron.* 4, 9. https://palaeo-electronica.org/2001_1/past/past.pdf.

Han, Z. B. (2018). *"Biological pump" and its response to changes in sea ice in the prydz bay, East Antarctica (in Chinese with English abstract) [Doctoral dissertation]* (Wuhan: China University of Geosciences).

Han, Z. B., Hu, C. Y., Sun, W. P., Zhao, J., Pan, J. M., Fan, G. J., et al. (2019). Characteristics of particle fluxes in the prydz bay polynya, Eastern Antarctica. *Sci. China Earth Sci.* 62, 657–670. doi: 10.1007/s11430-018-9285-6

Han, Z. B., Sun, W. P., Fan, G. J., HU, C. Y., Pan, J. M., Zhao, J., et al. (2018). Sinking particle fluxes during austral summer in the prydz bay polynya, Antarctica (in Chinese with English abstract). *China Environ. Sci.* 38, 1923–1934. doi: 10.19674/j.cnki.issn1000-6923.2018.0218

He, W., Cheng, L. Q., and Gao, G. P. (2016). Spatial distribution and seasonal variation of ice shelf water between 2001 and 2002 at amery ice shelf, Antarctica (in Chinese with English abstract). *J. Shanghai Ocean University* 25, 753–766. doi: 10.12024/jsou.20151201622

Herraiz-Borreguero, L., Coleman, R., Allison, I., Rintoul, S. R., Craven, M., and Williams, G. D. (2015). Circulation of modified circumpolar deep water and basal melt beneath the amery ice shelf, East Antarctica. *J. Geophys. Res.: Oceans* 120, 3098–3112. doi: 10.1002/2015jc010697

Hooper, J. N. A., and van Soest, R. W. M. (2002). *Systema Porifera: a guide to the classification of sponges* (New York: Kluwer Academic/Plenum Publishers).

Huguenin, M. F., Holmes, R. M., and England, M. H. (2022). Drivers and distribution of global ocean heat uptake over the last half century. *Nat. Commun.* 13, 4921. doi: 10.1038/s41467-022-32540-5

Ikenoue, T., Takahashi, K., and Tanaka, S. (2012). Fifteen year time-series of radiolarian fluxes and environmental conditions in the Bering Sea and the central subarctic pacific 1990–2005. *Deep. Res. Part II Top. Stud. Oceanogr.* 61–64, 17–49. doi: 10.1016/j.dsr2/2011.12.003

Jørgensen, E. (1905). "The protist plankton and the diatoms in bottom samples. VII. radiolaria," in *Hydrographical and biological investigations in Norwegian fiords*. Ed. O. Nordgaard (Bergen: Bergen Museum Skrifter), 114–141. https://www.radiolaria.org/plate.php?pl_id=6.

Lawler, K. A., Cortese, G., Civel-Mazens, M., Bostock, H., Crosta, X., Leventer, A., et al. (2021). The southern ocean radiolarian (SO-RAD) dataset: a new compilation of modern radiolarian census data. *Earth Syst. Sci. Data.* 13, 5441–5453. doi: 10.5194/essd-2021-148

Li, C. L., Sun, S., Zhang, G. T., and Ji, P. (2001). Summer feeding activities of zooplankton in prydz bay, Antarctica. *Polar Biol.* 24, 892–900. doi: 10.1007/s003000100292

Li, C. L., and Yang, G. (2017). Progress of Chinese zooplankton ecology research in prydz bay, Antarctica. *Adv. Polar Sci.* 28, 120–128. doi: 10.13679/j.advps.2017.2.00120

Liu, Z. L., and Chen, Z. Y. (2003). The distribution feature of size-fractionated chlorophyll *a* and primary productivity in prydz bay and its north sea area during the austral summer (in Chinese with English abstract). *Chin. J. Polar Sci.* 14, 81–89. doi: 10.3969/j.issn.1674-9928.2003.02.001

Liu, C. Y., Wang, Z. M., Cheng, C., Wu, Y., Xia, R. B., Li, B. R., et al. (2018). On the modified circumpolar deep water upwelling over the four ladies bank in prydz bay, East Antarctica. *J. Geophys. Res.: Oceans* 123, 7819–7838. doi: 10.1029/2018JC014026

Louw, S. D. V., Walker, D. R., and Fawcett, S. E. (2022). Factors influencing sea-ice algae abundance, community composition, and distribution in the marginal ice zone of the southern ocean during winter. *Deep Sea Res. Part I: Oceanogr. Res. Pap.* 185, 103805. doi: 10.1016/j.dsr.2022.103805

Lowe, V., Cortese, G., Lawler, K.-A., Civel-Mazens, M., and Bostock, H. C. (2022). Ecoregionalisation of the southern ocean using radiolarians. *Front. Mar. Sci.* 9. doi: 10.3389/fmars.2022.829676

Mathiot, P., Goosse, H., Fichefet, T., Barnier, B., and Gallée, H. (2011). Modelling the seasonal variability of the Antarctic slope current. *Ocean Sci.* 7, 455–470. doi: 10.5194/os-7-455-2011

Matul, A., and Mohan, R. (2017). Distribution of polycystine radiolarians in bottom surface sediments and its relation to summer sea temperature in the high-latitude north Atlantic. *Front. Mar. Sci.* 4. doi: 10.3389/fmars.2017.00330

McCormack, S., Melbourne-Thomas, J., Trebilco, R., Blanchard, J., and Constable, A. (2017). "Simplification of complex ecological networks — species aggregation in Antarctic food web models," in *Proceedings of the 22nd International Congress on Modelling and Simulation*, Hobart. https://mssanz.org.au/modsim2017/B3/mccormack.pdf.

McMinn, A. (2017). Ice acidification: a review of the effects of ocean acidification on sea ice microbial communities. *Biogeosciences* 14, 3927–3935. doi: 10.5194/bg-2017-111

Meredith, M., Sommerkorn, M., Cassotta, S., Derksen, C., Ekaykin, A., Hollowed, A., et al. (2019). "Polar regions," in *IPCC special report on the ocean and cryosphere in a changing climate*. Ed. H.-O. Pörtner, et al (Cambridge: Cambridge University Press), 203–320. doi: 10.1017/9781009157964.005

Morley, J. J., and Stepien, J. C. (1985). Antarctic Radiolaria in late winter/early spring weddell Sea waters. *Micropaleontol.* 31, 365–371. doi: 10.2307/1485593

Nicol, S., Virtue, P., King, R., Davenport, S. R., Mcgaffin, A. F., and Nichols, P. (2004). Condition of *Euphausia crystallorophias* off East Antarctica in winter in comparison to other seasons. *Deep Sea Res. II Top. Stud. Oceanogr.* 51, 2215–2224. doi: 10.1016/j.dsr2.2004.07.002

Nimmergut, A., and Abelmann, A. (2002). Spatial and seasonal changes of radiolarian standing stocks in the Sea of Okhotsk. *Deep Sea Res. I Oceanogr. Res. Pap.* 49, 463–493. doi: 10.1016/S0967-0637(01)00074-7

Nishimura, A., Nakaseko, K., and Okuda, Y. (1997). A new coastal water radiolarian assemblage recovered from sediment samples from the Antarctic ocean. *Mar. Micropaleontol.* 30, 29–44. doi: 10.1016/S0377-8398(96)00019-9

Nunes Vaz, R. A., and Lennon, G. W. (1996). Physical oceanography of the prydz bay region of Antarctic waters. *Deep Sea Res. I Oceanogr. Res. Pap.* 43, 603–641. doi: 10.1016/0967-0637(96)00028-3

Ohshima, K. I., Fukamachi, Y., Ito, M., Nakata, K., Simizu, D., Ono, K., et al. (2022). Dominant frazil ice production in the cape darnley polynya leading to Antarctic bottom water formation. *Sci. Adv.* 8, eadc9174. doi: 10.1126/sciadv.adc9174

Petrushevskaya, M. G. (1967). "Radiolarians of orders spumellaria and nassellaria of the Antarctic region (from material of the soviet Antarctic expedition)," in *Studies of marine fauna IV(XII): Biological reports of the soviet Antarctic expedition, (1955-1958)*. Eds. A. P. Andriyashev and P. V. Ushakov (Leningrad: Academy of Sciences of the USSR, Zoological Institute), (translated from Russian and published by Israel Program for Scientific Translations [1968]), 3, 2–186. https://www.radiolaria.org/plate.php?pl_id=31.

Petrushevskaya, M. G. (1971). "Radiolaria in the plankton and recent sediments from the Indian ocean and Antarctic," in *The micropalaeontology of oceans*. Eds. B. M. Funnell and W. R. Riedel (Cambridge: Cambridge University Press), 319–329.

Ran, L. H., Ma, W. T., Wiesner, M. G., Wang, Y. T., Chen, J. F., Zhang, L. L., et al. (2022). Sediment resuspension as a major contributor to sinking particles in the northwestern south China Sea: evidence from observations and modeling. *Front. Mar. Sci.* 9. doi: 10.3389/fmars.2022.819340

Ren, J., Chen, J. F., Li, H. L., Wiesner, M. G., Bai, Y. C., Sicre, M. A., et al. (2021). Siliceous micro- and nanoplankton fluxes over the northwind ridge and their relationship to environmental conditions in the western Arctic ocean. *Deep Sea Res. Part I: Oceanogr. Res. Pap.* 174, 103568. doi: 10.1016/j.dsr.2021.1

Schmidt, K., Brown, T. A., Belt, S. T., Ireland, L. C., Taylor, K. W. R., Thorpe, S. E., et al. (2018). Do pelagic grazers benefit from sea ice? insights from the Antarctic sea ice proxy $IPSO_{25}$. *Biogeosciences* 15, 1987–2006. doi: 10.5194/bg-15-1987-2018

Schnack-Schiel, S., Hagen, W., and Mizdalski, E. (1991). Seasonal comparison of *Caianoides acutus* and *Calanus propinquus* (Copepoda: Calanida) in the southeastern weddell Sea, Antarctica. *Mar. Eco. Prog. Ser.* 70, 17–27. doi: 10.3354/meps070017

Shi, J. X., Cheng, Y. Y., Jiao, Y. T., and Hou, J. Q. (2011). Supercooled water in austral summer in prydz bay, Antarctica. *Chin. J. Oceanol. Limnol.* 29, 427–437. doi: 10.1007/s00343-010-0011-5

Smith, W. O.Jr., Ainley, D. G., Arrigo, K. R., and Dinniman, M. S. (2014). The oceanography and ecology of the Ross Sea. *Annual. Rev. Mar. Sci.* 6, 469–487. doi: 10.1146/annurev-marine-010213-135114

Smith, N. R., Dong, Z. Q., Kerry, K. R., and Wright, S. (1984). Water masses and circulation in the region of prydz bay, Antarctica. *Deep Sea Res. Part A. Oceanogr. Res. Pap.* 31, 1121–1147. doi: 10.1016/0198-0149(84)90016-5

Smith, N., and Tréguer, P. (1994). "Physical and chemical oceanography in the vicinity of prydz bay, Antarctica," in *Southern ocean ecology: The BIOMASS perspective*. Ed. S. Z. El-Sayed (Cambridge: Cambridge University Press), 25–45.

Steineck, P. L., and Casey, R. E. (1990). "Ecology and paleobiology of foraminifera and radiolaria," in *Ecology of marine Protozoa*. Ed. G. M. Capriulo (Oxford: Oxford University Press), 89–138.

Sun, W. P., Han, Z. B., Hu, C. Y., and Pan, J. M. (2013). Particulate barium flux and its relationship with export production on the continental shelf of prydz bay, east Antarctica. *Mar. Chem.* 157, 86–92. doi: 10.1016/j.marchem.2013.08.002

Sun, W. P., Han, Z. B., Hu, C. Y., and Pan, J. M. (2016). Source composition and seasonal variation of particulate trace element fluxes in prydz bay, East Antarctica. *Chemosphere* 147, 318–327. doi: 10.1016/j.chemosphere.2015.12.10

Sun, W. P., Hu, C. Y., Han, Z. B., Pan, J. M., and Weng, H. X. (2012). Distribution of nutrients and chl *a* in prydz bay during the austral summer of 2011 (in Chinese with English abstract). *Chin. J. Polar Res.* 24, 178–186. doi: 10.3724/SP.J.1084.2012.0017

Suzuki, N., and Not, F. (2015). "Biology and ecology of radiolaria," in *Marine protists: Diversity and dynamics*. Eds. S. Ohtsuka, T. Suzaki, T. Horiguchi, et al (Tokyo: Springer), 179–222. doi: 10.1007/978-4-431-55130-0_8

Swanberg, N. R., and Eide, L. K. (1992). The radiolarian fauna at the ice edge in the Greenland Sea during summe. *J. Mar. Res.* 50, 297–320. doi: 10.1357/002224092784797674

Szymanski, A., and Gradinger, R. (2016). The diversity, abundance and fate of ice algae and phytoplankton in the Bering Sea. *Polar Biol.* 39, 309–325. doi: 10.1007/s00300-015-1783-z

Takahashi, K. (1987). "Silicoflagellates and actiniscus: vertical fluxes at pacific and Atlantic sediment trap stations," in *Ocean biocoenosis series No.2*. Ed. S. Honjo (Massachusetts: Woods Hole Oceanographic Institution), 1–35.

Takahashi, K. (1991). "Radiolaria: flux, ecology, and taxonomy in the pacific and Atlantic," in *Ocean biocoenosis series 3*. Ed. S. Honjo (Massachusetts: Woods Hole Oceanographic Institution), 1–177.

Takahashi, K., Fujitani, N., Yanada, M., and Maita, Y. (2000). Long-term biogenic particle fluxes in the Bering Sea and the central subarctic pacific ocean 1990-1995. *Deep. Res. Part II Top. Stud. Oceanogr.* 47, 1723–1759. doi: 10.1016/s0967-0637(00)00002-9

Taylor, F., McMinn, A., and Franklin, D. (1997). Distribution of diatoms in surface sediments of prydz bay, Antarctica. *Mar. Micropaleontol.* 32, 209–229. doi: 10.1016/s0377-8398(97)00021-2

Teng, Y., and Wang, R. J. (2019). Biogenic silica and radiolarian assemblages in the surface sediments of Ross Sea, Antarctica and their implications on marine environment and ecology (in Chinese with English abstract). *Acta Micropalaeontol. Sinica.* 36, 377–398. doi: 10.16087/j.cnki.1000-0674.2019.04.008

van Leeuwe, M., Tedesco, L., Arrigo, K. R., Assmy, P., Stefels, J., Meiners, K. M., et al. (2018). Microalgal community structure and primary production in Arctic and Antarctic sea ice: A synthesis. *Elementa: Sci. Anthropocen.* 2, 000028. doi: 10.1525/elementa.267

Wang, H. Z., Chen, Z. H., Wang, C. J., Liu, H. L., Zhao, R. J., Tang, Z., et al. (2015). Characteristics of grain size in surface sediments from the continental shelf, prydz bay, and implications for sedimentary environment. (in Chinese with English abstract). *Chin. J. Polar Res.* 4, 421–428. doi: 10.13679/j.jdyj.2015.4.421

Wang, R. J., Xiao, W. S., Li, Q. Y., and Chen, R. H. (2006). Polycystine radiolarians in surface sediments from the Bering Sea green belt area and their ecological implication for paleoenvironmental reconstructions. *Mar. Micropaleontol.* 59, 135–152. doi: 10.1016/j.marmicro.2006.02.002

Williams, G., Herraiz-Borreguero, L., Roquet, F., Tamura, T., Ohshima, K. I., Fukamachi, Y., et al. (2016). The suppression of Antarctic bottom water formation by melting ice shelves in prydz bay. *Nat. Commun.* 7, 12577. doi: 10.1038/ncomms12577

Wu, L., Wang, R. J., Krijgsman, W., Chen, Z. H., Xiao, W. S., Ge, S. L., et al. (2019). Deciphering color reflectance data of a 520-kyr sediment core from the southern ocean: Method application and paleoenvironmental implications. *Geochem. Geophys. Geosy.* 20, 2808–2826. doi: 10.1029/2019GC008212

Xiao, W. S., Esper, O., and Gersonde, R. (2016). Last glacial - Holocene climate variability in the Atlantic sector of the southern ocean. *Quat. Sci. Rev.* 135, 115–137. doi: 10.1016/j.quascirev.2016.01.023

Yabuki, T., Suga, T., Hanawa, K., Matsuoka, K., Kiwada, H., and Watanabe, T. (2006). Possible source of the Antarctic bottom water in the prydz bay region. *J. Oceanogr.* 62, 649–655. doi: 10.1007/s10872-006-0083-1

Yang, G., Han, Z. B., Pan, J. M., Zhou, K. L., Wang, Y. Q., and Li, C. L. (2019). Contribution of zooplankton faecal pellets to carbon transport of the mesopelagic layers in the polynya region of prydz bay, Antarctica. *Estuar. Coast. Shelf Sci.* 222, 139–146. doi: 10.1016/j.ecss.2019.04.006

Yang, G., Li, C. L., Sun, S., Zhang, C. X., and He, Q. (2013). Feeding of dominant zooplankton in prydz bay, Antarctica, during austral spring/summer: food availability and species responses. *Polar Biol.* 36, 1701–1707. doi: 10.1007/s00300-013-1387-4

Yang, G., Li, C. L., Wang, Y. Q., and Wang, Y. (2017). Vertical profiles of zooplankton community structure in prydz bay, Antarctica, during the austral summer of 2012/2013. *Polar Biol.* 40, 1101–1114. doi: 10.1007/s00300-016-2037-4

Yoshida, K., Seger, A., Kennedy, F., McMinn, A., and Suzuki, K. (2020). Freezing, melting and light stress on the photophysiology of ice algae: ex situ incubation of the ice algal diatom *Fragilariopsis cylindrus* (Bacillariophyceae) using an ice tank. *J. Phycol.* 56, 1323–1338. doi: 10.1111/jpy.13036

Zhang, L. L., Chen, M. H., Xiang, R., Zhang, J. L., Liu, C. J., Huang, L. M., et al. (2009). Distribution of polycystine radiolarians in the northern south China Sea in September 2005. *Mar. Micropaleontol.* 70, 20–38. doi: 10.1016/j.marmicro.2008.10.002

Zheng, S. J., and Shi, J. ,. X. (2011). The characteristic of sea ice growth and melt in the prydz bay region, Antarctica (in Chinese with English abstract). *Periodical Ocean Univ. China* 41, 009–016. doi: 10.16441/j.cnki.hdxb.2011.z2.002

Zheng, S. J., Shi, J. X., Jiao, Y. T., and Ge, R. F. (2011). Spatial distribution of ice shelf water in front of the amery ice shelf, Antarctica in summer. *Chin. J. Ocean. Limnol.* 29, 1325. doi: 10.1007/s00343-011-0318-x

Zhu, L. L., Zhang, H. F., Pan, J. M., Hu, J., Zhu., Q. H., and Zhang, H. S. (2019). Radiolarian assemblages and their distribution characteristics in surface sediments of prydz bay (in Chinese with English abstract). *Mar. Geol. Quat. Geol.* 39, 96–106. doi: 10.16562/j.cnki.0256-1492.2019010702

Zielinski, U. (1993). *Quantitative estimation of palaeoenvironment the Antarctic surface water in the late transfer functions with diatoms [Doctoral dissertation]* (Bremen: Alfred-Wegener-Institut für Polar- und Meeresforschung).

frontiers | Frontiers in Marine Science

TYPE Original Research
PUBLISHED 15 May 2023
DOI 10.3389/fmars.2023.1183516

OPEN ACCESS

EDITED BY
Zhifang Xiong,
Ministry of Natural Resources, China

REVIEWED BY
Li Wu,
Guangdong Ocean University, China
Shuzhuang Wu,
Université de Lausanne, Switzerland

*CORRESPONDENCE
Sunghan Kim
delongksh@kopri.re.kr

RECEIVED 10 March 2023
ACCEPTED 02 May 2023
PUBLISHED 15 May 2023

CITATION
Kim S, Bak Y-S, Prebble JG, Kang M-I, Kim S, Park J, Lee MK, Lee JI, Yoo K-C and Moon HS (2023) Glacial-interglacial changes in oceanic conditions and depositional process in the continental rise in response to ice sheet (shelf) variation in Bellingshausen Sea, Antarctica.
Front. Mar. Sci. 10:1183516.
doi: 10.3389/fmars.2023.1183516

Glacial-interglacial changes in oceanic conditions and depositional process in the continental rise in response to ice sheet (shelf) variation in Bellingshausen Sea, Antarctica

Sunghan Kim[1]*, Young-Suk Bak[2], Joseph G. Prebble[3], Myung-Il Kang[1], Sookwan Kim[4], Jinku Park[1], Min Kyung Lee[1], Jae Il Lee[1], Kyu-Cheul Yoo[1] and Heung Soo Moon[1]

[1]Korea Polar Research Institute, Incheon, Republic of Korea, [2]Department of Earth and Environmental Sciences, Jeonbuk National University, Jeonju, Republic of Korea, [3]Department of Surface Geosciences, GNS Science, Lower Hutt, New Zealand, [4]Korea Institute of Ocean Science and Technology, Busan, Republic of Korea

Antarctic continental margin sediments are eroded from the shelf and transported to the slope/rise in association with changing ice sheet configuration. Understanding the dynamics of this transport pathway is important for utilizing distal deep-sea sedimentary archives to determine past changes in the Antarctic ice sheet. However, these connections are poorly understood. Here we present multi-proxy records of two sediment cores (BS17-GC01 and BS17-GC02) from the Bellingshausen Sea continental rise, to explore relationships between depositional regime and ice sheet dynamics. Two cores show depositional/sedimentological variations on glacial-interglacial scales. Biogenic sediments were deposited during MIS 1, 5, and 7 under open ocean conditions. Glacial to deglacial sediments were laminated as a result of varying intensity of bottom currents. Terrestrially derived sediments are inferred to be transported from shelf both as grounded ice advanced during glacial expansion, and as ice retreated during deglacial periods. Sediment color shifted to brown after deglacial periods with high Mn/Ti and occurrence of bioturbation, indicating increasing bottom water oxygenation in the study area. Since surface water production started to increase from deglacial periods, we infer increased bottom water oxygenation in this setting is due to ventilation (i.e., Antarctic Bottom Water (AABW) formation), implying that AABW formation was increased during interglacial periods from deglacial period whereas was decreased during glacial periods. Thus, sedimentary/depositional changes in BS17-GC01 and BS17-GC02 are closely linked to ice sheet dynamics during the late Quaternary.

KEYWORDS

Bellingshausen Sea, surface diatom production, contourite, lamination, ice sheet variation

1 Introduction

The stability of the West Antarctic Ice Sheet (WAIS) is strongly influenced by variability of the surrounding ocean (Golledge et al., 2012; Pritchard et al., 2012; De Conto and Pollard, 2016). The spatial and temporal pattern of ice sheet advance/retreat across the continental shelf is largely a function of ocean water mass exchange along the glacial front. On glacial/interglacial timescales, this water mass exchange is influenced by the geomorphology (e.g., Dinniman et al., 2011; Lavoie et al., 2015), which is in turn influenced by tectonic process, glacier dynamics, bottom currents, and sediment input. However, sedimentary deposits that could be used to reconstruct glacial dynamics on glacial/interglacial timescales are fragmentary and cryptic in this setting. Although the Antarctic continental shelf contains a valuable record of deglacial to recent ice dynamics (e.g., De Santis et al., 1995; Domack et al., 1999), the advance of erosional ice sheets to the shelf break during the Last Glacial Maximum (LGM) (Anderson et al., 2002; Ó Cofaigh et al., 2014; The RAISED Consortium et al., 2014) means that LGM and older archives are rare on the continental shelf. For the most part, LGM and older sediments have been eroded and transported to the upper slope and continental rise (e.g., Anderson, 1999; Dowdeswell et al., 2002; Dowdeswell et al., 2008; Noormets et al., 2009). It is these deep-sea archives we must interpret, to understand ice dynamics during the LGM and older times.

It is normally recognized that dense shelf water formation, occurred by brine rejection in association with high sea ice formation in Antarctic coastal polynyas, is related to the formation of Antarctic Bottom Water (AABW), which is the densest water mass (Tamura et al., 2008). As a result, AABW is characterized by high oxygen concentration (Gordon, 2009). It is reported that AABW formation restarted or intensified at the end of glacial periods, that is deglacial periods, when grounded ice began to retreat on the shelf (Wu et al., 2018; Jimenez-Espejo et al., 2020). Since the production of AABW is related to shelf cavities (Wu et al., 2018; Jimenez-Espejo et al., 2020), these deep-sea archives will provide information on bottom water redox condition variations on glacial-interglacial time scale.

In this study, we use two sedimentary records from the continental rise of the Bellingshausen Sea, to infer changes in oceanographic conditions and sediment depositional process, in response to ice sheet variation on the Bellingshausen Sea continental shelf. To do this, we analyze lithology, physical properties (magnetic susceptibility (MS), grain density, and color reflectance), geochemical proxies ($CaCO_3$, total organic carbon (TOC), biogenic opal concentrations, and C/N ratio), paleontological records (diatoms and palynomorphs), manganese/titanium (Mn/Ti) ratio, zirconium/rubidium (Zr/Rb) ratio, and grain size records with grains >1 mm.

2 Depositional setting

In the Bellingshausen Sea, a wide sediment fan is formed directly seaward of the shelf break (Figure 1), reflecting the large amount of sediment that has been transported from the shelf to slope and rise areas by this pathway (Dowdeswell et al., 2008). Because of intermittent and erosional sediment input (i.e., gravity flows), the sample sites on the fan are not an ideal archive infer paleoenvironmental changes associated with the neighboring ice sheet. Moreover, application of environmental proxies from this upper- to middle-slope depositional environment is hampered by the coarse sediment originating from the ice margin during glacial periods (e.g., Dowdeswell et al., 2008 and references therein). Because drift sediments are well developed from the western Antarctic Peninsula to Bellingshausen Sea sector of the Antarctic margin (Rebesco et al., 2002; Hillenbrand et al., 2008a), previous studies have focused on the influence of bottom currents on this region and depositional environment, with a particular emphasis on interpreting cores collected from close to the shelf break (Pudsey and Camerlenghi, 1998; Lucchi et al., 2002; Lucchi and Rebesco, 2007; Hillenbrand et al., 2021).

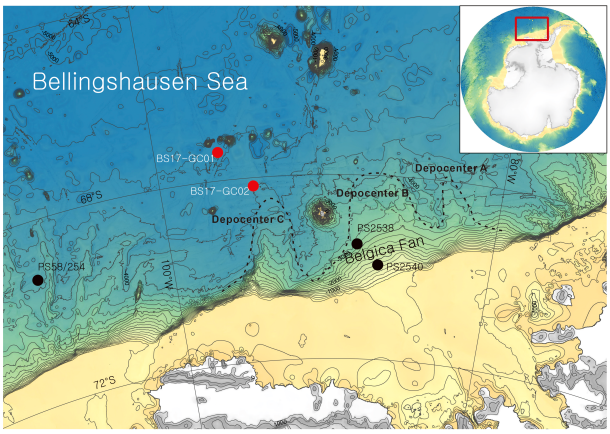

FIGURE 1
Location map of the study area in the Bellingshausen Sea continental margin, West Antarctica, with core locations for BS17-GC01 and BS17-GC02 (red circles) and previously reported cores (black circles). Dashed lines indicate sediment depocenters from Scheuer et al. (2006).

Along western Antarctic Peninsula to Bellingshausen Sea sector of the Antarctic margin, sedimentation during glacial periods includes, (faintly) laminated sediments with less biogenic components, deposited by a combination of contourite, meltwater plumite, and distal turbidite mechanisms (Hillenbrand et al., 2021 and references therein). The northern extent of these glacial facies is not yet established, due to lack of distal, deep water core records from the Bellingshausen Sea.

Surface sediments of the nearby sea, Amundsen Sea, shows a regional variability; most notably difference between east and west (Hillenbrand et al., 2003). To date, most research effort has been on the area east of the Peter I. Island (e.g., Pudsey and Camerlenghi, 1998; Lucchi et al., 2002; Hillenbrand et al., 2003; Hillenbrand et al., 2009; Hillenbrand et al., 2021). Understanding the accumulation of sedimentary records from the west, which are likely to represent a different mode of deposition given the distinct surficial sediments, is necessary to obtain a complete picture of paleoceanographic evolution of the Bellingshausen Sea region during the late Quaternary.

3 Material and methods

Two gravity cores were collected from the continental rise of the Bellingshausen Sea by IBR/V *Araon* during the ANA07D cruise in 2017; 217 cm-long BS17-GC01 (67°22.8947′S, 96°23.2464′W, 4627 m water depth) and 846 cm-long BS17-GC02 (68°09.4940′S, 94°34.7988′W, 4361 m water depth) (Figure 1). The two cores were stored cold before being opened, described, and sub-sampled at the Korea Polar Research Institute (KOPRI). Core photos and chemical elements were measured by ITRAX core scanner at KOPRI. X-radiographs were taken from 8 cm x 30 cm x 1 cm slabs at KOPRI. Physical properties, geochemical proxies, and grain size analysis were performed at KOPRI. Analysis of diatom assemblages was performed at Jeonbuk National University and palynology analysis was performed at GNS Science. All data for BS17-GC01 and BS17-GC02 are in Supplementary Tables 1, 2, respectively.

3.1 Physical properties (magnetic susceptibility, color reflectance, and grain density)

The Magnetic Susceptibility (MS) for BS17-GC01 and BS17-GC02 was measured at 1 cm-intervals on split half core sections using a Bartington MS-2B susceptibility meter. The MS values for BS17-GC01 was reported in Kim et al. (2022a). Color reflectances a* and b*, which reflect the balance between red (+) and green (-) and yellow (+) and blue (-), respectively, were measured at 1 cm intervals on split half core sections of two cores by spectrophotometry. The grain density was measured at 10 cm intervals for BS17-GC02 and 4 cm intervals for BS17-GC01 using a gas pycnometer (AccuPyc II 1340). All physical properties were measured at KOPRI.

3.2 Geochemical proxies (biogenic opal, TOC, and $CaCO_3$ concentrations)

All geochemical proxies for BS17-GC01 and BS17-GC02 were measured at 2 cm intervals on 1 cm thick sub-samples at KOPRI. Biogenic silica concentration was measured using a Continuous Flow Analyzer (SKALAR SANplus Analyzer) with wet-alkaline extraction method modified from DeMaster (1981) following the method of Kim et al. (2018a). Biogenic opal concentration was calculated by multiplying biogenic silica concentration by 2.4 (Mortlock and Froelich, 1989). The relative error of biogenic silica concentration in sediment samples is less than 1%. Total inorganic carbon (TIC) concentration was measured using UIC CO_2 coulometer (Model CM5240). $CaCO_3$ concentration was calculated by multiplying TIC concentration by 8.333. The relative standard deviation for $CaCO_3$ concentration is ±1%. Total carbon (TC) and total nitrogen (TN) concentrations were measured by an Organic Elemental Analyzer (FLASH 2000 NC Analyzer) with an analytical precision less than ±0.1% and ±0.16%, respectively. TOC concentration was calculated by the difference between TC and TIC. C/N ratio was calculated as TOC/TN.

3.3 Diatom assemblage analysis

Fifty samples were analyzed at 10 cm intervals for brown units and 50 cm intervals for gray units for BS17-GC02 and twenty-two samples were analyzed at 10 cm intervals for BS17-GC01. Due to the predominant occurrence of *Fragilariopsis kerguelensis*, in the intervals of high biogenic opal concentration, up to 200 diatom specimens were counted. The other intervals had extremely low diatom abundances due to poor preservation, 200 microscope fields of view were observed and counted. The sample preparation and diatom counting methods followed Bak et al. (2018). The quantitative analysis of the diatom slides followed the procedures described in Scherer (1994). Absolute abundance was calculated using the following equation: abundance = ((A × B)/(C × D))/E, where A is the number of specimens counted, B is the area of the settling chamber, C is the number of microscope fields of view, D is the area of the field of view, and E is the sample mass.

3.4 Palynology analysis

Because both cores have brown-gray color alterations and BS17-GC02 has more color cycles, only core BS17-GC02 was examined for palynology. 13 samples were selected from dark brown, brown, and gray units. Samples were dried and weighed. Cold 10% HCl was added to the dried sample to remove carbonates, followed by 24 hours in cold 52% HF and a second cold wash in 10% HCl. Samples were placed in an ultrasonic bath for up to a minute, sieved through a 6 µm mesh to remove small particulate material, and mounted on glass slides in glycerine jelly. A single lycopodium tablet (batch 1061) was introduced during processing to determine absolute palynomorph abundance. Palynology was performed at the GNS Science palynology laboratory.

All counts were completed on a light microscope at 400x magnification. For this study, 100 palynomorph specimens were counted for each sample where possible. The entire slide was scanned for samples in which palynomorphs were rare.

3.5 Grain size analysis and count of grains >1 mm

After removing biogenic components (organic matter, biogenic silica, $CaCO_3$) from bulk sediments using 34% H_2O_2, 2N NaOH, and 10% HCl, respectively, grain size was analyzed at 8 cm intervals for BS17-GC02 and at 4 cm intervals for BS17-GC01. Grain size was analyzed using a laser diffraction instrument (Mastersizer 3000, Malvern) at KOPRI. The classification of sediments follows that of Folk and Ward (1957).

X-radiographs of center slices (1 cm thick x 8 cm width x 30 cm length) removed from each core section. Then, grains >1 mm in diameter were manually counted every 1 cm on the X-radiograph images.

3.6 Mn/Ti and Zr/Rb ratios

The distribution of chemical elements for both cores was determined non-destructively using an ITRAX core scanner at KOPRI. Following the procedure of Croudace et al. (2006), we analyzed at 5 mm intervals with a 3 kW Mo X-ray tube under 30 kV and 30 mA with a dwell time of 5 seconds. In this study, we focus on Mn, Ti, Zr, and Rb elemental XRF peak area intensities measured in total counts per second (CPS). The elemental data are presented as Mn/Ti and Zr/Rb ratios to account for changes in water content or physical properties.

4 Chronology

4.1 BS17-GC02

Previous studies of sediment accumulation in the Western Antarctic Peninsula region have aligned high MS intervals containing low biological production with glacial periods and assigned low MS intervals containing high biological production to interglacial periods (e.g., Pudsey and Camerlenghi, 1998; Pudsey, 2000; Hillenbrand et al., 2009; Hillenbrand et al., 2021). BS17-GC02 showed a similar lithologic pattern to previous cores collected from the western Antarctic Peninsula (e.g., Pudsey and Camerlenghi, 1998; Pudsey, 2000; Lucchi et al., 2002; Hillenbrand et al., 2009). Recently, Hillenbrand et al. (2021) established age models for cores from the study area by a combination of correlating $\delta^{18}O$ data of planktonic foraminifera with LR04 (Lisiecki and Raymo, 2005), Marine Tephra B (MIS 5/6 boundary at ~130 ka; Hillenbrand et al., 2008b), and accelerator mass spectrometry (AMS) ^{14}C dates. This chronological result was consistent with previous chronological frames. Thus, we apply the chronological scheme in Hillenbrand et al. (2021) for the BS17-GC02 age model. A bioturbated biogenic interval at core top (0–35 cm) likely corresponds to interglacial MIS 1, the next biogenic interval (348–398 cm) likely corresponds to interglacial MIS 5, and the deeper biogenic interval (660–698 cm) likely corresponds to interglacial MIS 7. We infer the intervening intervals correspond to the glacial periods MIS 2–4, 6, and 8. However, as it is acknowledged in Hillenbrand et al. (2021), it is not established that the biogenic interval spans the entire MIS 5 and MIS 7 intervals, (or represent only MIS 5e MIS 7e, respectively). We also acknowledge that there is some uncertainty in MIS boundaries in this study due to gradational/bioturbated contacts.

AMS ^{14}C dates were obtained using planktonic foraminifera, *Neogloboquadrina pachyderma* (sin.), at 354 cm and 372 cm (Kim et al., 2022b). The two radiocarbon ages were calibrated using CALIB 7.1 (Stuiver and Reimer, 1993) with the MARINE13 dataset (Reimer et al., 2013) using a constant marine reservoir effect of 1300 years, consistent with previous Southern Ocean and Western Antarctic Peninsula studies (e.g., Domack et al., 2001; Pugh et al., 2009; Kilfeather et al., 2011; Xiao et al., 2016). The calibrated ages were 20.6 ka at 354 cm and 37.5 ka at 372 cm. These carbon dates are inconsistent with the chronological scheme described above, which assigns the interval 354–372 cm to interglacial MIS 5. Although planktonic foraminifera ^{14}C dates have been previously reported from cores collected from the western Antarctic Peninsula region, (Hillenbrand et al., 2021), we note our dates are the first reported from the first sub-surface $CaCO_3$ interval. As a result, we have limited opportunity to assess the reliability and lateral reproducibility of the two AMS ^{14}C dates we report. Thus, in this study, we follow the established regional chronology by ignoring the two AMS ^{14}C dates for BS17-GC02 we obtained, but note that further investigation of the regional-scale chronological scheme of the western Antarctic Peninsula may be warranted, along with further investigation using radiometric dating approaches (Pudsey and Camerlenghi, 1998; Lucchi et al., 2002; Lucchi and Rebesco, 2007; Hillenbrand et al., 2021).

4.2 BS17-GC01

The correlation between MS values and the European Project for Ice Coring in Antarctica (EPICA) Dronning Maud Land (EDML) ice core dust record (Fischer et al., 2007) has been used for age establishment of Scotia Sea sediment cores, although there has been debate about the causal mechanisms that isochronously connect the two settings (e.g., Pugh et al., 2009; Weber et al., 2012; Xiao et al., 2016; Kim et al., 2018b; Shin et al., 2020). Kim et al. (2022a) established an age model for BS17-GC01 by correlating MS values to EDML ice core dust record. In that scheme, the biogenic interval at the upper part of the core (0–35 cm) corresponded to MIS 1, the 35–217 cm interval corresponded to MIS 2–4; 35–78 cm for MIS 2, 78–189 cm for MIS 3, and 189–217 cm for MIS 4.

5 Results

5.1 Lithology and physical properties

5.1.1 BS17-GC02

BS17-GC02 sediments alternated between decimeter-scale bioturbated diatom-bearing mud with foraminifera (interglacial MIS 1, 5, and 7), and meter-scale laminated mud inferred to be of terrestrial origin (MIS 2–4, 6, and 8). The biogenic intervals were composed of dark brown diatom-bearing mud, overlain by gray mud with foraminifera. These intervals are characterized by decreasing biogenic opal concentration up-section, with a gradual/bioturbated contact (Figure 2). The laminated intervals can be divided into two units; a gray unit, overlain by a brown unit (Figure 2). We infer gray intervals correspond to glacial periods and brown intervals were likely deposited during periods of ice retreat (i.e., deglacial period) (Figure 2).

MS values at BS17-GC02 show fluctuating values from 20 to 1500 10^{-5} SI (Figure 2A). MS values were constantly low (<100 10^{-5} SI) during interglacial MIS 1, 5, and 7. In contrast, MS values were high and variable during MIS 2–4, 6, and 8 (Figure 2A). In spite of color difference between the brown and gray units, there was no significant difference in MS values during MIS 2–4, 6, and 8 (Figure 2A).

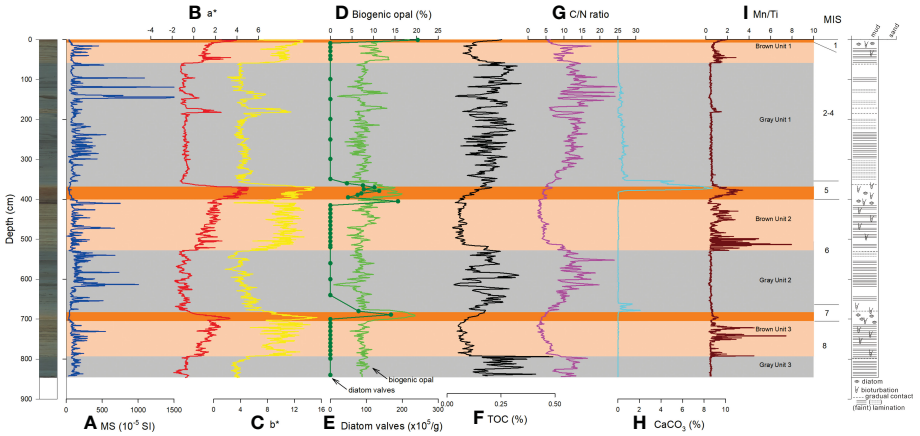

FIGURE 2
Downcore variations of **(A)** MS, **(B)** a*, **(C)** b*, **(D)** biogenic opal concentration, **(E)** diatom valves, **(F)** TOC concentration, **(G)** C/N ratio, **(H)** $CaCO_3$ concentration, **(I)** Mn/Ti ratio of BS17-GC02. Core photo image and lithologic log are shown on the left and right, respectively. MIS: Marine Isotope Stage.

Grain density (g/cm^3) of BS17-GC02 ranges mostly from 2.4 to 2.7 (Figure 3E). Grain density values were noticeably low during interglacial MIS 1, 5, and 7 (Figure 3E).

Color reflectance (a* and b* values) of BS17-GC02 was high in the brown intervals inferred to have been deposited under deglacial to interglacial conditions, and low in the gray intervals inferred to have been deposited under glacial conditions (Figures 2B, C). Maximum a* and b* values were found in the dark brown intervals (interglacial MIS 1, 5, and 7) (Figure 2). Mn/Ti ratios showed increased values from deglacial to interglacial periods (Figure 2I). However, Mn/Ti ratios from interglacial MIS 1, 5, and 7 were not higher than those observed during deglacial periods (Figure 2I).

5.1.2 BS17-GC01

BS17-GC01 showed alternating deposition between bioturbated (diatom-bearing) mud (corresponding to MIS 1 and 3) and faintly laminated/structureless sandy mud (corresponding to MIS 2 and 4) (Figure 4). The brown units are composed of bioturbated mud overlying intermittently laminated mud. In contrast to BS17-GC02, diatom frustules were found during MIS 1 only (Figure 4). The gray units are composed of structureless sandy mud, overlying faintly laminated mud (Figure 4).

MS values from BS17-GC01 were also constantly low (<100 10^{-5} SI) during interglacial MIS 1 and MIS 3 (Figure 4A), but were high during MIS 2 and 4.

Grain density (g/cm^3) of BS17-GC01 ranges mostly from 2.6 to 2.7 (Figure 5F). Grain density showed relatively low values during MIS 1 and 3 (Figure 5F).

Color reflectance (a* and b* values) from BS17-GC01 showed high values in brown intervals (inferred to be deposited during deglacial to interglacial periods) and low values in gray intervals inferred to represent deposition under glacial conditions (Figures 4B, C). Maximum a* and b* values were recorded at the upper part of brown intervals (Figures 4B, C). Mn/Ti ratios showed increased values during MIS 1 and 3, relative to sediment deposited during MIS 2 and 4 time (Figure 4I).

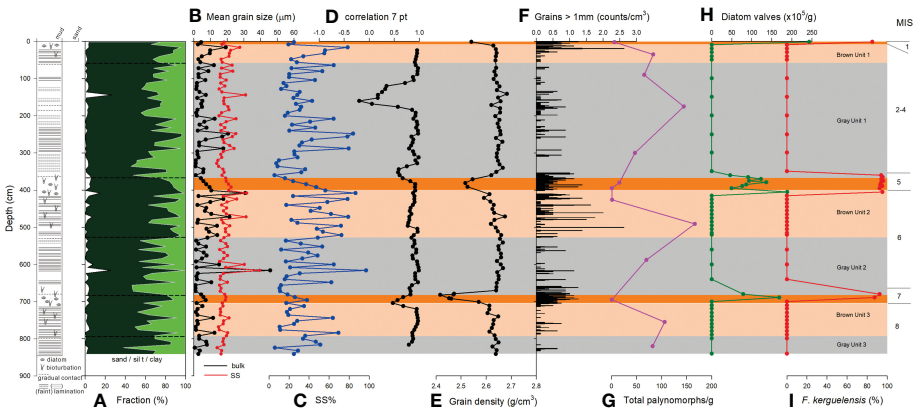

FIGURE 3
Downcore variations of **(A)** fraction of sand (white), silt (dark green), and clay (green), **(B)** MGS of bulk sediment (black) and SS (red), **(C)** SS% in mud fraction, **(D)** 7 point-running correlation between SS MGS and SS%, **(E)** grain density, **(F)** grains >1 mm, **(G)** total palynomorphs, **(H)** total diatom valves, and **(I)** relative abundance of *F. kerguelensis* of BS17-GC02. Lithologic log is shown on the left. MIS, Marine Isotope Stage.

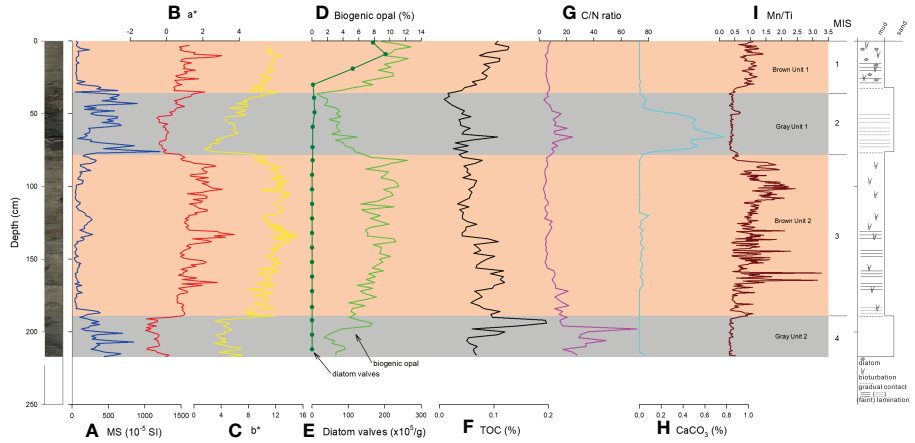

FIGURE 4
Downcore variations of **(A)** MS (Kim et al., 2022a), **(B)** a*, **(C)** b*, **(D)** biogenic opal concentration, **(E)** diatom valves, **(F)** TOC concentration, **(G)** C/N ratio, **(H)** $CaCO_3$ concentration, **(I)** Mn/Ti ratio of BS17-GC01. Core photo image and lithologic log are shown on the left and right, respectively. MIS, Marine Isotope Stage.

5.2 Geochemical measurements (biogenic opal, TOC, $CaCO_3$, and C/N ratio)

5.2.1 BS17-GC02

In BS17-GC02, biogenic opal concentrations showed high values (15–20%) during interglacial MIS 1, 5, and 7, and low values (<10%) during MIS 2–4, 6, and 8 (Figure 2D). TOC values were high, though variable, (0.3%) in the gray laminated glacial intervals (Figure 2F). TOC concentrations showed minimum values during deglacial periods, and increased during interglacial MIS 1, 5, and 7 (Figure 2F). In general, C/N ratios co-varied with TOC; high during glacial MIS 2–4, 6, and 8, low/moderate during deglacial periods, and low/increasing during interglacial MIS 1, 5, and 7 (Figure 2G). $CaCO_3$ concentrations were generally very low (~0%), but increased $CaCO_3$ concentrations were observed occurred right above biogenic opal peaks of interglacial MIS 5 and 7 (Figure 2H).

5.2.2 BS17-GC01

In BS17-GC01, elevated concentrations of biogenic opal were observed in sediments deposited during interglacial MIS 1 (10–12%) and MIS 3 (8–10%), whereas low concentrations (<5%) were observed during MIS 2 and 4 (Figure 4D). TOC concentrations were generally lower than BS17-GC02 (<0.2%). Except for a brief peak (0.2%) in MIS 4, TOC concentrations were relatively increased during MIS 1 and 3, compared to MIS 2 and 4 (Figure 4F). C/N ratios were lower during MIS 1 and 3, than MIS 2 and 4 (Figure 4G). $CaCO_3$ was generally absent in the core, but a trace amount (0.6–0.8%) was observed in sediments deposited during MIS 2 (Figure 4H).

5.3 Diatom and palynology record

5.3.1 BS17-GC02

Twenty-four diatom species belonging to 10 genera were identified in BS17-GC02. Diatoms were abundant (46–243 10^5 valves/g) during interglacial MIS 1, 5, and 7, and were absent in other lithologies (Figure 3H). *Fragilariopsis kerguelensis*, an open ocean species (Crosta et al., 2005; Xiao et al., 2016), dominated the assemblages (85–95%) (Figure 3I). Other minor species were found together with *F. kerguelensis* during interglacial MIS 1, 5, and 7 and were absent in the other intervals (Table S2).

Palynomorphs concentrations of BS17-GC02 are very low (<165 palynomorphs/g sediment) in all 13 samples examined (Figure 3G). Although the palynomorph abundance was extremely low (~10 specimens/g) in the dark brown units, these samples contained *Impagidinium pallidum*. This is one of the few forms of dinoflagellate cyst observed in modern high southern latitudes core top samples, and is inferred to be *in situ* (Esper and Zonneveld, 2007; Prebble et al., 2013). Intervals with a palynomorph concentration of >45 palynomorphs/g contains a mixture of dinoflagellate cyst and pollen forms characteristic of pre-Quaternary Antarctic Sediments of Eocene-Miocene age (Truswell, 1983; Askin, 2000; Askin and Raine, 2000). These dinoflagellate cysts include *Hystrichosphaeridium* spp., *Enneadocysta*, *Operculodinium* spp., and *Spinidinium* spp., while pollen includes various types of *Nothofagidites*, *Podocarpidites* spp., trilete, and monolete spores (Table S2).

5.3.2 BS17-GC01

Eighteen diatom species belonging to 12 genera were identified in BS17-GC01. Diatoms were abundant (112–202 $x10^5$/g) during MIS 1, and were very rare to absent during MIS 2–4 (Figure 5H). During MIS 3, biogenic opal concentration was relatively high. In contrast, diatoms samples from sediments of MIS 3 were barren. *F. kerguelensis* was dominant (83–100%) in most samples were diatoms were present (Figure 5I). At 59 cm, the relative abundance of *F. kerguelensis* was reduced to 55%. In that sample, *Dactyliosolen antarcticus* (22%), *Eucampia antarctica* sp. (11%), and *Paralia sulcata* (11%) were more common (Figure 5I, Table S1).

5.4 Grain size analysis and grains >1 mm

5.4.1 BS17-GC02

Sediments of BS17-GC02 are dominated by mud fraction (Figure 3A), with silt fraction higher than clay fraction (Figure 3A). Laminated intervals are characterized by a marked increase in mean grain size (MGS), driven by an increase in silt fraction. The MGS was generally less than 20 µm (Figure 3B). In addition, sortable silt (SS: 10–63 µm) MGS showed a consistent variation pattern with MGS (Figure 3B).

Grains >1 mm are found throughout BS17-GC02 (Figure 3F), and occur more frequently during deglacial periods, with highest frequency during interglacial MIS 1, 5, and 7 (Figure 3).

5.4.2 BS17-GC01

The mud fraction is dominant (>95%) during MIS 1 and 3, whereas sand content sharply increased (up to 40%) during MIS 2 and 4 (Figure 5A). As a result, MGS increased during MIS 2 and 4. SS MGS also showed consistent pattern with MGS variation (Figure 5B).

Interestingly, grains >1 mm were found during MIS 1 and 3, but not found during MIS 2 and 4 (Figure 5G).

6 Discussion

6.1 Glacial periods

6.1.1 Deep-water site BS17-GC02 ice covered and likely anoxic during glacials

During glacial periods gray laminated mud was deposited at BS17-GC02. This mud was characterized by fluctuating MS values, low a* and b* values, low biogenic opal concentration, high but fluctuating TOC concentration, high C/N ratios, low $CaCO_3$ concentration, low Mn/Ti, fluctuating MGS, high grain density, dispersed grains >1 mm, increased total palynomorphs represented by reworked species, and an absence of diatoms (Figures 2, 3). These characteristics are very similar to sediments deposited on the western Antarctic Peninsula continental slope/rise during glacial periods (Pudsey and Camerlenghi, 1998; Lucchi et al., 2002; Lucchi and Rebesco, 2007; Hillenbrand et al., 2021). In the western Antarctic Peninsula region, laminated sediments, with reduced biogenic component deposited during glacial periods have previously been interpreted as being deposited by a combination of contourite, meltwater plumite, and distal turbidites (Hillenbrand et al., 2021 and references therein). We infer broadly similar deposition mechanisms for BS17-GC02, although since this site is located further north (~300 km from shelf break) than other previously reported cores on the drift, we infer influence from meltwater plumite to be low.

Sortable Silt MGS has previously been used as a proxy for bottom current speed in a range of deep water settings (e.g., McCave and Hall, 2006; McCave et al., 2017; Wu et al., 2018; McCave and Andrews, 2019; Hillenbrand et al., 2021). Since SS MGS and percentage of sortable silt in mud generally covaries in the core ($r > 0.5$) (Figure 3D), we follow the approach of previous authors in this region and apply SS MGS as a proxy for bottom current speed at BS17-GC02 (McCave and Andrews, 2019; Hillenbrand et al., 2021). Recently, modified sediment grain size distributions free of IRD influence to recalculate SS MGS have been introduced to sediments including IRDs in the polar regions (Stevenard et al., 2023). The ln(Zr/Rb) ratio is considered and is used as a grain-size proxy free of sandy IRD influence in Antarctic sediment cores (Wu et al., 2020; Stevenard et al., 2023). Since ln(Zr/Rb) ratio of BS17-GC01 showed a good consistence with SS MGS (Figure 5), we did not recalculate SS MGS free of IRD influence in this study. SS MGS data showed a mean value of 19 µm with standard deviation of 4 µm, indicating a relatively small glacial-interglacial changes in bottom-current velocity (Figure 3B). This is consistent with previous study results (Pudsey and Camerlenghi, 1998; Vautravers et al., 2013; Hillenbrand et al., 2021).

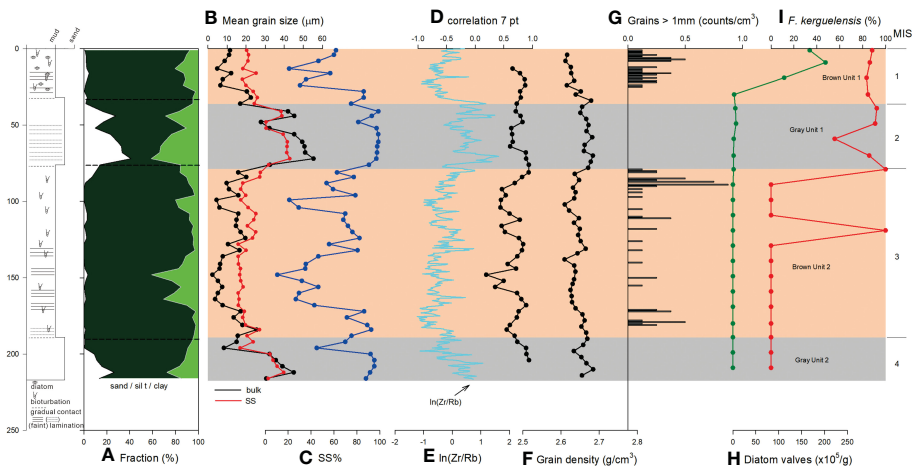

FIGURE 5
Downcore variations of **(A)** fraction of sand (white), silt (dark green), and clay (green), **(B)** MGS of bulk sediment (black) and SS (red), **(C)** SS% in mud fraction, **(D)** 7 point-running correlation between SS MGS and SS%, **(E)** ln(Zr/Rb), **(F)** grain density, **(G)** grains >1 mm, **(H)** total diatom valves, and **(I)** relative abundance of *F. kerguelensis* of BS17-GC01. Lithologic log is shown on the left. MIS, Marine Isotope Stage.

TOC concentrations at BS17-GC02 increased during glacial periods (Figure 2F). Hillenbrand et al. (2021) reported increased refractory TOC during glacial periods in the glacial sediments in the western Antarctic Peninsula. C/N ratios are indicative of the degree of marine vs terrestrial organic matter because marine organic matter has lower C/N ratios than those of terrestrial organic matter (Lamb et al., 2006 and references therein). Despite the lack of extant terrestrial vegetation and unique soils on present day Antarctica, this relationship has also been used to infer changes in organic matter source on glacial-interglacial time scales in the Ross Sea and the Scotia Sea, where analysis of sediment cores showed high C/N ratios during glacial periods (Kim et al., 2020a; Kim et al., 2020b; Ha et al., 2022). In addition, high C/N ratios are found in subglacial to proximal depositional environments in the Antarctic sediments (Smith et al., 2019). Thus, high C/N ratios in laminated gray mud at BS17-GC02 suggest that the high TOC concentration is related to the reworked TOC from shelf regions during advance of grounded ice. Palynomorph assemblages also support down slope reworking (Figure 3G). MS values are commonly observed to correlate to proxies of terrestrial input in the Antarctic sediment cores, often showing high values during glacial periods (Leventer et al., 1996; Pudsey and Camerlenghi, 1998; Hillenbrand and Cortese, 2006; Hillenbrand et al., 2009; Kim et al., 2020a; Kim et al., 2020b; Hillenbrand et al., 2021). We infer this relationship is also likely to hold in the present setting, and interpret intervals of increased and fluctuating MS values to indicate terrestrial sediment input from the shelf region (Figure 2A).

In the modern Southern Ocean south of the Polar Front, biogenic opal production is controlled by sea ice (Chase et al., 2015). During glacial periods, a northward expansion of both summer and winter sea ice coverage around the Antarctic margin has been proposed (Gersonde et al., 2005), along with northward migration of oceanic fronts (Kemp et al., 2010; Manoj and Thamban, 2015; Roberts et al., 2017). The sedimentary signature of these glacial sediments is terrigenous laminated/stratified mud with rare IRD, and a low proportion of biogenic components (biogenic opal and $CaCO_3$) (Hillenbrand et al., 2021). We infer the low biological productivity of surface waters during glacial periods in our study area is likely related to extended sea ice conditions coinciding with northward front migration. Lucchi and Rebesco (2007) and Hillenbrand et al. (2021) also proposed that perennial sea ice condition in the south of BS17-GC02 during glacial periods.

Normalized Mn/Ti ratios in marine sediments have been used as an indicator of relative bottom water oxygenation in deep ocean settings (e.g., Jaccard et al., 2016; Wagner and Hendy, 2017; Wu et al., 2018). Mn/Ti was constantly low during glacial periods, consistent with low oxygen conditions (Figure 2I). Although Hillenbrand et al. (2021) proposed progressively decreasing bottom water oxygenation in glacial-aged sediment cores on the drift off the western Antarctic Peninsula, they inferred conditions remained oxic throughout. We acknowledge that Mn/Ti is uncalibrated, and because other redox sensitive elements were not measured in this study and by Hillenbrand et al. (2021), it is difficult to be confident about the exact oxygenation state of the bottom water during glacial periods. However, we note that in our cores, laminations deposited during glacial periods were well preserved without bioturbation, suggesting that the bottom water oxygen may have been too low to support benthic organisms. We infer that bottom water oxygen concentration was low during glacial periods in our study area (dysoxic to anoxic), consistent with conclusions of other workers from around the Antarctic continent supporting ceased/decreased AABW formation (e.g., Jaccard and Galbraith, 2012; Galbraith and Jaccard, 2015; Jaccard et al., 2016; Wagner and Hendy, 2017; Wu et al., 2018). Bottom water oxygenation is related to ventilation and export production (Kim et al., 2011; Jaccard and Galbraith, 2012; Galbraith and Jaccard, 2015; Jaccard et al., 2016; Kim et al., 2017; Wagner and Hendy, 2017; Wu et al., 2018). Although increased TOC is refractory, the relatively high TOC concentration has potential to draw down bottom water oxygen in the study area. The decomposition of the elevated TOC input may additionally draw down dissolved oxygen concentration of the bottom water during glacial periods. Thus, the dysoxic to anoxic bottom water condition was ascribed to ceased/decreased oxygen-rich AABW formation and additional decomposition of elevated organic matter during glacial periods.

A schematic of the inferred depositional environments during the interglacial phase is shown in Figure 6A.

6.1.2 Glacial deposition at BS17-GC01

There is a brown interval, corresponding to MIS 3, at BS17-GC01. Mn/Ti ratio showed high values in both brown intervals (MIS 1 and 3) (Figure 4I). We infer these ratio values are consistent with oxic bottom water condition at BS17-GC01 site during MIS 3, coinciding with increased opal concentrations during this time. However, no diatoms or other bio-siliceous fragments were observed (Figure 7). However, due to the presence of black colored volcanic sand sized grains we infer the origin of the opal is volcanic. Volcanic grains are vitric in BS17-GC01 (Figure S1). This means that they are volcanic glass shards which are amorphous and uncrystallized product of rapidly cooling magma. As a result, they may have low MS values (Li and Fu, 2019) and tend to be extracted by we-alkaline method. In addition, Zulaikah and Nurlaily (2018) reported volcanic ash has lower MS values than classic sand and/or silt. High C/N ratios also indicate that reworked sediments are dominant.

During MIS 2, diatom production was low, but the assemblage was dominated by *F. kerguelensis* (Figures 5H, I), with occurrences of *Eucampia antarctica* sp., an indicator BS17-GC01 probably covered by seasonal, but not perennial, sea ice during that time (Crosta et al., 2005; Xiao et al., 2016) (Table S1). Increased gravelly IRDs (grains >1 mm) were observed only during MIS 3 which is relatively warmer climate during the last glacial period MIS 2 and MIS 4 (Figure 5G). The absence of gravelly IRDs at BS17-GC01 indicates that gravelly IRDs were probably limited to BS17-GC02 site during MIS 2 and 4.

SS MGS showed increased values up to 40 μm during MIS 2 and 4 (Figure 5B). This indicates that the bottom current intensified during MIS 2 and 4 at distal continental rise site. That is, bottom current speed was higher at BS17-GC01 than that at BS17-GC02 during MIS 2 and 4. ln(Zr/Rb) data are largely in agreement with SS MGS data, supporting stronger bottom current at BS17-GC01 site.

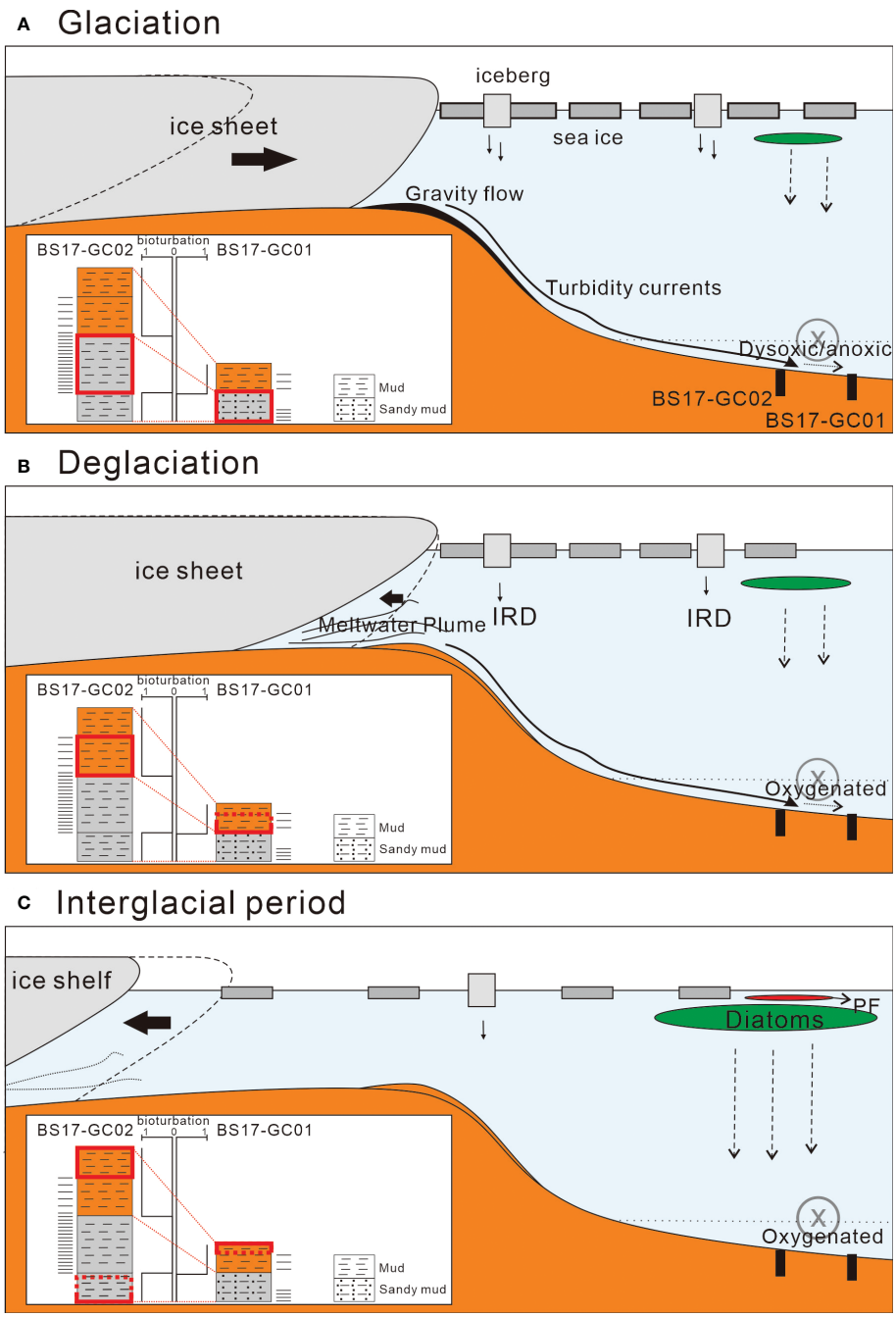

FIGURE 6
Schematic depositional models of **(A)** glaciation phase, **(B)** deglaciation phase, and **(C)** fully retreated phase (late/warm interglacial period) in the Bellingshausen Sea continental rise. PF, planktonic foraminifers and IRD, ice rafted debris.

In both the Scotia and Bellingshausen Seas, the increased MS values during glacial periods are related to sand- to coarse silt-sized grains (16–250 μm) having high MS values, implying that MS could be used to infer IRD transport in this setting (Kim et al., 2018b; Kim et al., 2020b; Shin et al., 2020; Kim et al., 2022a). Kim et al. (2020b) proposed that different source regions between glacial and deglacial/interglacial periods could result in different IRD with different characteristics deposited at the sites. Kim et al. (2022a) proposed that sand- to coarse silt-sized grains, entrapped into grounded ice while advancing, were mainly deposited on the continental shelf during ice shelf development during deglacial to interglacial periods by sub ice shelf melting. In contrast, icebergs during glacial periods still contains the sand- to coarse silt-sized grains and were drifted into the deep basin. We infer that IRD was delivered to BS17-GC01 throughout the last glacial period, but the size characteristics if the IRD was unique during MIS 3. However, it was reported that very

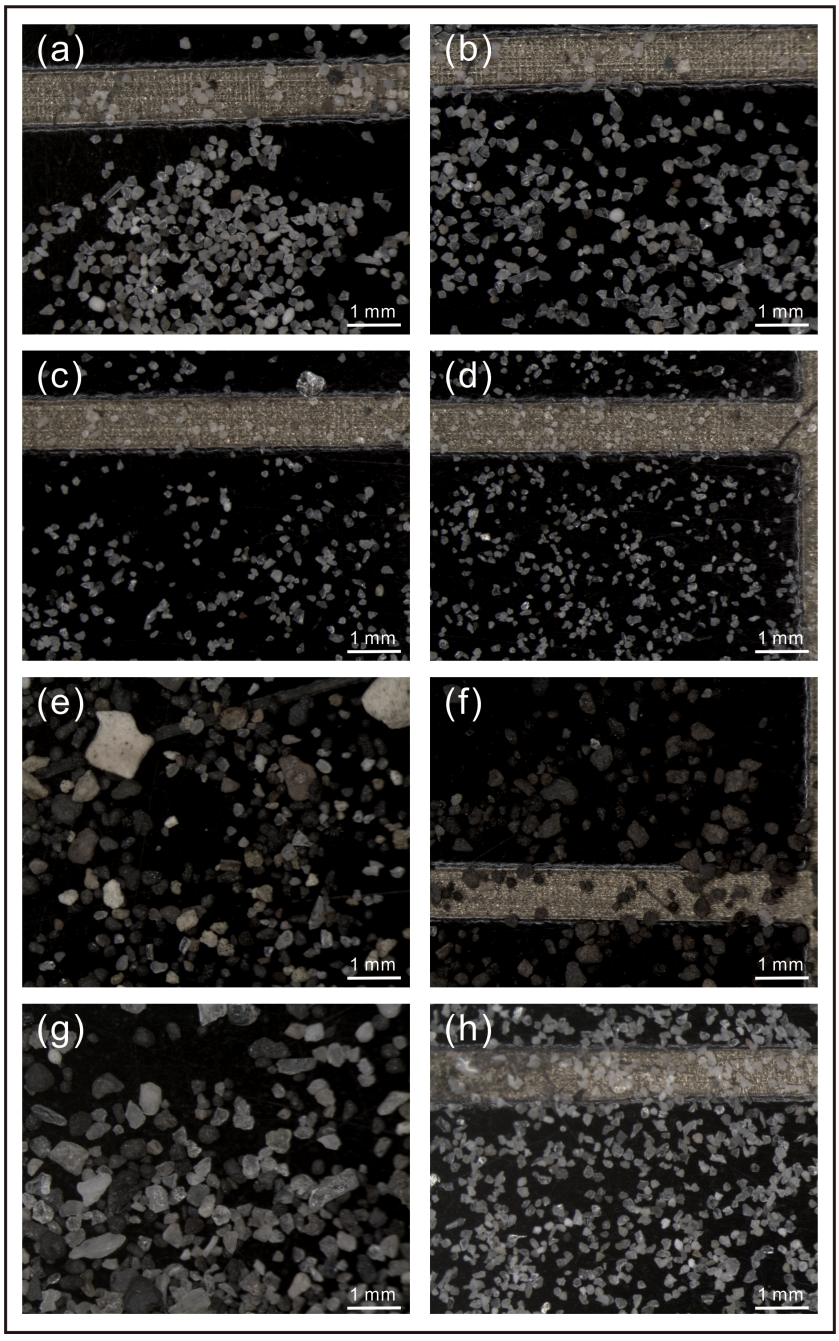

FIGURE 7
Microscopic photos of grains >63 μm of BS17-GC01 at **(A)** 0 cm, **(B)** 20 cm, **(C)** 50 cm, **(D)** 70 cm, **(E)** 110 cm, **(F)** 140 cm, **(G)** 170 cm, and **(H)** 200 cm. 0 cm and 20 cm belong to MIS 1, 50 cm and 70 cm belong to MIS 2, 110 cm, 140 cm, and 170 cm belong to MIS 3, and 200 cm belongs to MIS 4.

fine sands can be sorted by bottom current in the Drake Passage where (Wu et al., 2021). Nonetheless, sand sized grains are difficult to be transported from source areas considering the directions of currents and sinking rate of sand grains. SS MGS values during MIS 2 and 4 are ~40 μm (Figure 5B), which is similar to those reported in the Drake Passage (Wu et al., 2021). Thus, possibility of sorting sand sized grains by bottom current cannot be ruled out.

A schematic of the inferred depositional environments during the glaciation phase is shown in Figure 7A.

6.2 Deglacial periods

6.2.1 BS17-GC02

During deglacial periods, brown laminated mud was deposited at BS17-GC02. This mud was characterized by fluctuating MS values, high a* and b* values, low/decreased C/N ratios, high Mn/Ti, fluctuating MGS, high grain density, and disperse grains >1 mm. Biological characteristics of the interval included low biogenic opal, TOC, $CaCO_3$, an absence of diatoms, and increased total

palynomorphs represented by reworked species (Figures 2, 3). These characteristics are similar to those observed in other deglacial settings (Hillenbrand et al., 2021).

The overall sedimentary characteristics between glacial and deglacial periods in this setting are quite similar (Hillenbrand et al., 2021; this study). Thus, deglacial brown laminated mud at BS17-GC02 is considered mainly contourites as well. However, we infer that the down-slope sediment transportation mechanism is different between glacial and deglacial periods. Down-slope sediment transportation occurred by the advance of grounded ice across the shelf during glacial periods (Hillenbrand et al., 2021), but occurred by sediment-rich subglacial melt water out as grounded ice retreats across the shelf during deglacial periods.

Other outstanding difference between the two periods are sediment color and elemental composition; gray with low Mn/Ti during glacial periods vs brown with high Mn/Ti during deglacial periods (Figure 2I). Elevated Mn has been widely reported from the Southern Ocean during deglacial periods, and attributed to high-oxygen conditions (Jaccard and Galbraith, 2012; Galbraith and Jaccard, 2015; Jaccard et al., 2016; Wagner and Hendy, 2017; Wu et al., 2018): we infer the increased Mn/Ti rations during deglacials at BS17-GC02 arises from increased bottom water oxygenation. This is consistent with observations of rapidly increasing bottom-water oxygen oxygenation during glacial termination at other sites along the western Antarctic Peninsula (Hillenbrand et al., 2021) and in Prydz Bay (Wu et al., 2018).

We are intrigued by the constantly low TOC concentrations (Figure 2F). It has previously been suggested that TOC minima in these settings could imply low (1–2 cm/kyr) sedimentation rates or minimum input of refractory organic material (Hillenbrand et al., 2021). A few deci-meter to meter scale deposits during deglacial periods implies that high sedimentation rates although we cannot define the glacial-deglacial-interglacial boundary precisely in this study. The thickness of glacial terminations of previously reported cores also showed similar sedimentation (Hillenbrand et al., 2021). In the Scotia Sea surface diatom production started to increase from deglacial periods with sea ice retreat (Sprenk et al., 2013; Xiao et al., 2016; Kim et al., 2020b). As sea ice is the main controlling factor for surface diatom production in the Southern Ocean (Chase et al., 2015), surface diatom production should have increased during deglacial periods with sea ice decrease although the signal of increased production is not clear in sediments. This is supported by C/N ratios. The last deglacial period showed TOC minima with low to moderate C/N ratios indicating some sediment input from the shelf region (Figures 2F, G). However, the two previous deglacial intervals showed low C/N ratios indicating that organic carbon relatively more originates from surface water by biological production. However, decomposition of non-refractory organic matter under oxic bottom water conditions can draw down TOC concentration (Hillenbrand et al., 2021). This likely results in low TOC concentrations in the sediment. Thus, TOC minima with low to moderate C/N ratios indicates increased proportion of marine organic matter and increased decomposition of the organic matter under oxic bottom water conditions during deglacial periods. Co-occurrence of bioturbation and laminated mud during deglacial periods suggests depositional alternation between lamination as a combination of distal turbidite and contourite leaving high sedimentation and bioturbated hemipelagic deposition leaving low sedimentation. This seems to be related to discontinuous retreat of ice sheet/shelf on the shelf.

A schematic of the inferred depositional environments during the interglacial phase is shown in Figure 6B.

6.2.2 BS17-GC01

The faintly laminated, bioturbated brown interval at BS17-GC01 is considered to represent deposition during the last deglacial period (Figure 4). MS values sharply decreased into the last deglacial, accompanied by an increase in biogenic opal concentration (Figures 4A, D). We infer this represents an increase in diatom production, while the assemblage contains increasing frequency of the (mainly) open water species *F. kerguelensis* (Figure 5H). Although C/N ratios of BS17-GC02 showed moderate values, those of BS17-GC01 showed low values (Figures 2G, 4G). This means that BS17-GC01 site became open ocean condition earlier than BS17-GC02, as expected. The long distance of BS17-GC01 from the shelf break can additionally result in less terrestrial influence than BS17-GC02. Mn/Ti started to increase with a* and b* increases, indicating oxygenated bottom water condition at BS17-GC01 site (Figures 4B, C, I).

A schematic of the inferred depositional environments during the deglaciation phase is shown in Figure 6B.

6.3 Interglacial periods

6.3.1 Interglacial periods from site BS17-GC02

During interglacial periods, dark brown to gray biogenic bearing mud is deposited at BS17-GC02. It is characterized by minimum of MS values, high a* and b* values, increased biogenic opal concentration, increasing TOC concentration, increasing C/N ratios (but still low), increased $CaCO_3$ concentration (right after biogenic opal), high Mn/Ti, fluctuating MGS, low grain density, abundant grains >1 mm, decreased total palynomorphs represented by modern like species, and increased diatoms consisting mainly of *F. kerguelenesis* (Figures 2, 3). These characteristics are similar to those of peak to moderate (late) interglacial periods in the western Antarctic Peninsula (Hillenbrand et al., 2021).

As previous studies in the Amundsen and Bellingshausen Seas reported increased surface diatom productivity during interglacial periods (Hillenbrand et al., 2009; Hillenbrand et al., 2021), biogenic opal concentration showed its maxima within dark brown intervals, indicated by the maxima of a* and b* (Figures 2B, C). TOC concentration increased but C/N ratio was still low, implying that export production increase is related to increased surface water diatom production (Figures 2F, G). Total diatom valves also significantly increased during interglacial periods (Figure 2I). The dominant species is *F. kerguelensis*, an open ocean species indicating Antarctic Circumpolar Current influence (Zielinski and Gersonde, 1997; Abelmann et al., 2006; Xiao et al., 2016). In addition, total palynomorph, composed of reworked species, is significantly reduced but few species living modern like open ocean conditions

was observed (Figure 3G). MS values were constantly low and grain density decreased, implying less terrestrial input and increased biogenic component under open ocean conditions during interglacial periods.

Occurrence of grains >1 mm was focused on the interglacial periods implying that gravelly IRD input likely increased during interglacial periods in the Bellingshausen Sea (Figure 3F). Mn/Ti ratio was also elevated, but not higher than those during deglacial periods despite its darker brown color (Figure 2I). Although TOC concentrations were similar to those observed during glacial periods, interglacial sediments are characterized by brown color, bioturbation, and high Mn/Ti (Figure 2I). These characteristics suggest bottom water at BS17-GC02 remained oxygenated during interglacial periods. We conclude that the main factor to control bottom water oxygenation in this setting is bottom water formation, not surface production, which draws down dissolved oxygen by decomposition, in the Bellingshausen Sea. An increase in $CaCO_3$ concentration, mainly composed of planktonic foraminifera *N. pachyderma*, overlies biogenic opal maxima at BS17-GC02 during MIS 5 and 7 coincident with change of sediment color changed into gray across a gradual bioturbated boundary (Figure 2). However, neither $CaCO_3$ peak nor gray colored sediment were observed in MIS 1. This suggests that increased $CaCO_3$ intervals may include also the early part of glacial periods. This is consistent with previous reports that high biogenic intervals correspond to glacial to early part of glacial periods (Hillenbrand et al., 2021).

A schematic of the inferred depositional environments during the interglacial phase is shown in Figure 6C.

6.3.2 Interglacial periods from site BS17-GC01

Although biogenic opal concentration maxima occurred in peak interglacial periods of BS17-GC01, marked by dark brown intervals corresponding maximum of a* and b*, dark brown intervals were not observed in the core (Figure 4). Biogenic opal concentration showed high values and total diatom valves, consisting of mainly *F. kerguelensis* (~90%), were outstandingly high, indicating increased surface diatom production under open ocean conditions (Figures 4D, 5H, and 5I). Grain density showed decreased values, also supporting increased biological composition at BS17-GC01. Biogenic opal and TOC concentration at BS17-GC01 was lower than BS17-GC02. This is consistent with lower grain density values at BS17-GC02 than those at BS17-GC01 (Figures 3E, 5F). $CaCO_3$ concentrations of BS17-GC01 and BS17-GC02 during MIS 1 were very low although those of BS17-GC02 during MIS 5 and 7 were relatively high (Figures 2H, 4H). Since core top $CaCO_3$ concentration increase was found from some cores not all, indicating some local effect (Hillenbrand et al., 2021).

Decreased SS MGS values and ln(Zr/Rb) during MIS 1 indicates that bottom current was intensified during MIS 2 and 4 at BS17-GC01 site. The last glacial-Holocene Antarctic Circumpolar Current flow speed differences in the Drake Passages showed different pattern according to its latitude (McCave et al., 2014). In addition, glacial-interglacial frontal migration in the Southern Ocean was reported (Kemp et al., 2010; Manoj and Thamban, 2015; Roberts et al., 2017). Thus, the bottom water intensity change on glacial-interglacial scale at the study site is also considered to be related to glacial-interglacial frontal migration. As McCave et al. (2014) and Kim et al. (2020b) reported increased SS MGS from the south of the Polar Front close to slope/rise boundary, BS17-GC01 record might reflect intensified southwestward flowing bottom current influence.

A schematic of the inferred depositional environments during the interglacial phase is shown in Figure 6C.

7 Conclusions

In this study, we documented glacial-interglacial succession from two sediment cores from the Bellingshausen Sea continental rise to understand glacial-interglacial changes in oceanographic conditions and depositional process in response to ice sheet dynamics. The followings are the main conclusions:

1. Surface diatom production started to increase from deglacial periods as ice sheet/shelf retreated, reaching a maximum during interglacials MIS 1, 5, and 7. In MIS 5 and MIS 7, the maxima of diatom productivity was overlain by a $CaCO_3$ peak (but not in MIS 1). Low diatom production is thought to be related to the influence of extensive sea ice. Low MS values also indicate that input of terrestrial material was lowest during MIS 1, 5, and 7. However, frequent occurrence of IRD grains indicate active ice shelf calving on the shelf during interglacial periods.
2. Terrestrially-derived, laminated mud was dominant during glacial and deglacial periods. During glacial periods, gray laminated mud was observed, with increased refractory TOC, low Mn/Ti, and lacking bioturbation, implying dysoxic bottom water conditions. In contrast, we infer, brown laminated mud with increased Mn/Ti and intermittent bioturbation observed in sediments deposited during deglacial periods, implies oxic bottom water conditions.
3. Increased bottom water oxygenation endured during interglacial periods until surface diatom production increased. Thus, we infer the main factor controlling bottom water oxygenation in this setting is the degree of AABW formation; increased during interglacial and decreased during glacial periods.
4. A strong correlation between SS MGS and %SS imply that SS at two cores can be used as a proxy for bottom current intensity, despite IRD influence. Laminated mud during glacial to deglacial periods is likely a result of varying bottom current intensity.

Data availability statement

The original contributions presented in the study are included in the article/Supplementary Material. Further inquiries can be directed to the corresponding author.

Author contributions

The co-authors' contributions are the following: ML and HM helped to obtain two cores and data interpretation. Y-SB conducted diatom analysis. JoP conducted palynology record. M-IK conducted IRD counting. JiP helped interpretation of the modern oceanographic conditions. JL, K-CY, and SuK helped data interpretation and result discussion. All authors reviewed the manuscript.

Funding

This research was supported by KOPRI grant funded by the Ministry of Oceans and Fisheries (PE23090). JP was supported by the New Zealand Government MBIE Antarctic Science Platform contract ID ANTA1801. This work was also supported by the National Research of Korea (NRF) grant funded by the Korea government (MSIT) (No. 2022R1A2C1091796).

Acknowledgments

We would like to thank the crew and scientific party of the IBR/V *Araon* for all their help during the gravity coring on board. We would like to thank KOPRI laboratory members for all their help during experimental measurements. We appreciate the handling editor ZX and two reviewers for their important and constructive comments to improve data interpretation and manuscript structure. This research was supported by KOPRI grant funded by the Ministry of Oceans and Fisheries (PE23090). JP was supported by the New Zealand Government MBIE Antarctic Science Platform contract ID ANTA1801. This work was also supported by the National Research of Korea (NRF) grant funded by the Korea government (MSIT) (No. 2022R1A2C1091796).

Conflict of interest

The authors declare that the research was conducted in the absence of any commercial or financial relationships that could be construed as a potential conflict of interest.

Publisher's note

Supplementary material

The Supplementary Material for this article can be found online at: https://www.frontiersin.org/articles/10.3389/fmars.2023.1183516/full#supplementary-material

SUPPLEMENTARY FIGURE 1
Microscopic images of **(A)** BS17-GC01 1cm (x400), **(B)** BS17-GC02 1 cm (x400), **(C)** BS17-GC01 109 cm (x200), and **(D)** BS17-GC01 109 cm (x400). (A) and **(B)** belong to MIS 1 showing biogenic components. **(C)** and **(D)** belong to MIS 3 showing volcanic shards.

SUPPLEMENTARY TABLE 1
physical properties (magnetic susceptibility (MS), grain density, and color reflectance), geochemical proxies ($CaCO_3$, total organic carbon (TOC), biogenic opal concentrations, and C/N ratio), paleontological record (diatoms), and grain size records with grains >1 mm for BS17-GC01.

SUPPLEMENTARY TABLE 2
physical properties (magnetic susceptibility (MS), grain density, and color reflectance), geochemical proxies ($CaCO_3$, total organic carbon (TOC), biogenic opal concentrations, and C/N ratio), paleontological records (diatoms and palynomorphs), and grain size records with grains >1 mm for BS17-GC02.

References

Abelmann, A., Gersonde, R., Cortese, G., Kuhn, G., and Smetacek, V. (2006). Extensive phytoplankton blooms in the Atlantic sector of the glacial southern ocean. *Paleoceanography* 21, PA1013. doi: 10.1029/2005PA001199

Anderson, J. B. (1999). *Antarctic Marine geology* (Cambridge: Cambridge University Press).

Anderson, J. B., Shipp, S. S., Lowe, A. L., Wellner, J. S., and Mosola, A. B. (2002). The Antarctic ice sheet during the last glacial maximum and its subsequent retreat history: a review. *Quat. Sci. Rev.* 21, 49–70. doi: 10.1016/S0277-3791(01)00083-X

Askin, R. A. (2000). Spores and pollen from the McMurdo sound erratics, Antarctica. *Antarct. Res. Ser.* 76, 161–181. doi: 10.1029/AR076p0161

Askin, R. A., and Raine, J. I. (2000). Oligocene and early Miocene terrestrial palynology of the cape roberts drillhole CRP-2/2A, Victoria land basin, Antarctica. *Terra Antarctica* 7, 493–501. doi: 10.1029/AR076p0161

Bak, Y.-S., Yoo, K.-C., Lee, J. I., and Yoon, H. I. (2018). Glacial-interglacial records from sediments in Powell basin, Antarctica. *Antarct. Sci.* 30, 371–378. doi: 10.1017/S0954102018000408

Chase, Z., Kohfeld, K. E., and Matsumoto, K. (2015). Controls on biogenic silica burial in the southern ocean. *Global Biogeochm. Cycles* 29, 1599–1616. doi: 10.1002/2015GB005186

Crosta, X., Romero, O., Armand, L. K., and Pichon, J. J. (2005). The biogeography of major diatom taxa in southern ocean sediments: 2. open ocean related species. *Palaeogeogr. Palaeoclimatol. Palaeoecol.* 223, 66–92. doi: 10.1016/j.palaeo.2005.03.028

Croudace, I. W., Rindby, A., and Rothwell, R. G. (2006). "ITRAX: description and evaluation of a new multi-function X-ray core scanner," in *Geological society*, vol. 267. (London: Special Publicatios), 51–63.

De Conto, R. M., and Pollard, D. (2016). Contribution of Antarctica to past and future sea level rise. *Nature* 531, 591–597. doi: 10.1038/nature17145

DeMaster, D. J. (1981). The supply and accumulation of silica in the marine environment. *Geochim. Cosmochim. Acta* 5, 1715–1732. doi: 10.1016/0016-7037(81)90006-5

De Santis, L., Anderson, J. B., Brancolini, G., and Zayatz, I. (1995). "Seismic record of late oligocene through Miocene glaciation on the central and Eastern continental shelf of the Ross Sea," in *Geology and seismic stratigraphy of the Antarctic margin*, vol. 68 . Eds. A. K. Cooper, P. F. Barker and G. Brancolini (American Geophysical Union Antarctic Research Series), 235–260.

Dinniman, M. S., Klinck, J. M., and Smith, W. O.Jr. (2011). A model study of circumpolar deep water on the West Antarctic peninsula and Ross Sea continental shelves. *Deep-Sea Res. II* 58, 1508–1523. doi: 10.1016/j.dsr2.2010.11.013

Domack, E. W., Jacobson, E. A., Shipp, S., and Anderson, J. B. (1999). Late pleistocene–Holocene retreat of the West Antarctic ice-sheet system in the Ross Sea: part 2–sedimentologic and stratigraphic signature. *GSA Bull.* 111, 1517–1536. doi: 10.1130/0016-7606(1999)111<1517:LPHROT>2.3.CO;2

Domack, E. W., Leventer, A., Dunbar, R., Taylor, F., Brachfeld, S., Sjunneskog, C., et al. (2001). Chronology of the palmer deep site, Antarctic peninsula: a Holocene

palaeoenvironmental reference for the circum-Antarctic. *Holocene* 11, 1–9. doi: 10.1191/095968301673881493

Dowdeswell, J. A., Ó Cofaigh, C., Noormets, R., Larter, R. D., Hillenbrand, C.-D., Benetti, S., et al. (2008). A major trough-mouth fan on the continental margin of the bellingshausen Sea, West Antarctica: the belgica fan. *Mar. Geol.* 252, 129–140. doi: 10.1016/j.margeo.2008.03.017

Dowdeswell, J. A., Ó Cofaigh, C., Taylor, J., Kenyon, N. H., Mienert, J., and Wilken, M. (2002). "On the architecture of high-latitude continental margins: the influence of ice-sheet and sea-ice processes in the polar north Atlantic," in *Glacier-influenced sedimentation on high-latitude continental margins*, vol. 203 . Eds. J. A. Dowdeswell and C. Ó Cofaigh (London: Geological Society, Special Publication), 33–54.

Esper, O., and Zonneveld, K. A. F. (2007). The potential of organic-walled dinoflagellate cysts for the reconstruction of past sea-surface conditions in the southern ocean. *Mar. Micropaleontol.* 65, 185–212. doi: 10.1016/j.marmicro.2007.07.002

Fischer, H., Fundel, F., Ruth, U., Twarloh, B., Wegner, A., Udisti, R., et al. (2007). Reconstruction of millennial changes in dust emission, transport and regional sea ice coverage using the deep EPICA ice cores from the Atlantic and Indian ocean sector of Antarctica. *Earth Planet. Sci. Lett.* 260, 340–354. doi: 10.1016/j.epsl.2007.06.014

Folk, R. L., and Ward, W. C. (1957). Brazos river bar [Texax]; a study in the significance of grain size parameters. *J. Sediment. Res.* 27, 3–26. doi: 10.1306/74D70646-2B21-11D7-8648000102C1865D

Galbraith, E. D., and Jaccard, S. L. (2015). Deglacial weakening of the oceanic soft tissue pump: global constraints from sedimentary nitrogen isotopes and oxygenation proxies. *Quat. Sci. Rev.* 109, 38–48. doi: 10.1016/j.quascirev.2014.11.012

Gersonde, R., Crosta, X., Abelmann, A., and Armand, L. (2005). Sea-Surface temperature and sea ice distribution of the southern ocean at the EPILOG last glacial maximum – a circum-Antarctic view based on siliceous microfossil records. *Quat. Sci. Rev.* 24, 869–896. doi: 10.1016/j.quascirev.2004.07.015

Golledge, N. R., Fogwill, C. J., Mackintosh, A. N., and Buckley, K. M. (2012). Dynamics of the last glacial maximum Antarctic ice sheet and its response to ocean forcing. *Proc. Natl. Acad. Sci.* 109, 16052-16056 doi: 10.1073/pnas.1205385109

Gordon, A. L. (2009). "Bottom water formation," in *Ocean currents*. Eds. J. H. Steele, S. A. Thorpe and K. K. Turekian (Associated Press), 263–269.

Ha, S., Colizza, E., Torricella, F., Langone, L., Giglio, F., Kuhn, G., et al. (2022). Glaciomarine sediment deposition on the continental slope and rise of the central Ross Sea since the last glacial maximum. *Mar. Geol.* 445, 106752. doi: 10.1016/j.margeo.2022.106752

Hillenbrand, C.-D., Camerlenghi, A., Cowan, E. A., Hernández-Molina, F. J., Lucchi, R. G., Rebesco, M., et al. (2008a). The present and past bottom-current flow regime around the sediment drifts on the continental rise west of the Antarctic peninsula. *Mar. Geol.* 255, 55–63. doi: 10.1016/j.margeo.2008.07.004

Hillenbrand, C.-D., and Cortese, G. (2006). Polar stratification: a critical view from the southern ocean. *Palaeogeogr. Palaeoclimatol. Palaeoecol.* 242, 240–252. doi: 10.1016/j.palaeo.2006.06.001

Hillenbrand, C.-D., Crowhurst, S. J., Williams, M., Hodell, D. A., McCave, I. N., Ehrmann, W., et al. (2021). New insights from multi-proxy data from the West Antarctic continental rise: implications for dating and interpreting late quaternary paleoenvironmental records. *Quat. Sci. Rev.* 257, 106842. doi: 10.1016/j.quascirev.2021.106842

Hillenbrand, C.-D., Grobe, H., Diekmann, B., Kuhn, G., and Fütterer, D. J. (2003). Distribution of clay minerals and proxies for productivity in surface sediments of the bellingshausen and amundsen seas (West Antarctica) – relation to modern environmental conditions. *Mar. Geol.* 193, 253–271. doi: 10.1016/S0025-3227(02)00659-X

Hillenbrand, C.-D., Kuhn, G., and Frederichs, T. (2009). Record of a mid-pleistocene depositional anomaly in West Antarctic continental margin sediments: an indicator for ice-sheet collapse? *Quat. Sci. Rev.* 28, 1147–1159. doi: 10.1016/j.quascirev.2008.12.010

Hillenbrand, C.-D., Moreton, S. G., Caburlotto, A., Pudsey, C. J., Lucchi, R. G., Smellie, J. L., et al. (2008b). Volcanic time-markers for marine isotopic stages 6 and 5 in southern ocean sediments and Antarctic ice cores: implications for tephra correlations between palaeoclimatic records. *Quat. Sci. Rev.* 27, 518–540. doi: 10.1016/j.quascirev.2007.11.009

Jaccard, S. L., and Galbraith, E. D. (2012). Large Climate-driven changes of oceanic oxygen concentrations during the last deglaciation. *Nat. Geosci.* 5, 151–156. doi: 10.1038/ngeo1352

Jaccard, S. L., Galbraith, E. D., Martínez-García, A., and Anderson, R. F. (2016). Covariation of deep southern ocean oxygenation and atmospheric CO_2 through the last ice age. *Nature* 530, 207–210. doi: 10.1038/nature16514

Jimenez-Espejo, F. J., Presti, M., Kuhn, G., McKay, R., Crosta, X., Escutia, C., et al. (2020). Late pleistocene oceanographic and depositional variations along the Wilkes land margin (East Antarctica) reconstructed with geochemical proxies in deep-sea sediments. *Glob. Planet. Change* 184, 103045. doi: 10.1016/j.gloplacha.2019.103045

Kemp, A. E. S., Grigorov, I., Pearce, R. B., and Naveira Garabato, A. C. (2010). Migration of the Antarctic polar front through the mid-pleistocene transition: evidence and climatic implications. *Quat. Sci. Rev.* 29, 1993–2009. doi: 10.1016/j.quascirev.2010.04.027

Kilfeather, A. A., Ó Cofaigh, C., Lloyd, J. M., Dowdeswell, J. A., Xu, S., and Moreton, S. G. (2011). Ice-stream retreat and ice-shelf history in Marguerite trough, Antarctic peninsula: sedimentological and foraminiferal signatures. *Geol. Soc Am. Bull.* 123, 997–1015. doi: 10.1130/B30282.1

Kim, S., Khim, B.-K., Ikehara, K., Itaki, T., Shibahara, A., and Yamamoto, M. (2017). Millennial-scale changes of surface and bottom water conditions in the northwestern pacific during the last deglaciation. *Glob. Planet. Change* 154, 33–43. doi: 10.1016/j.gloplacha.2017.04.009

Kim, S., Khim, B.-K., Uchida, M., Itaki, T., and Tada, R. (2011). Millennial-scale paleoceanographic events and implication for the intermediate-water ventilation in the northern slope area of the Bering Sea during the last 71 kyrs. *Global. Planet. Change* 79, 89–98. doi: 10.1016/j.gloplacha.2011.08.004

Kim, S., Lee, J. I., McKay, R. M., Yoo, K. C., Bak, Y. S., Lee, M. K., et al. (2020a). Late pleistocene paleoceanographic changes in the Ross Sea – glacial-interglacial variations in paleoproductivity, nutrient utilization, and deep-water formation. *Quat. Sci. Rev.* 239, 106356. doi: 10.1016/j.quascirev.2020.106356

Kim, S., Lee, M. K., Shin, J. Y., Yoo, K. C., Lee, J. I., Kang, M. I., et al. (2022a). Variation in magnetic susceptibility in the bellingshausen Sea continental rise since the last glacial period and implications for terrigenous material input mechanisms. *Palaeogeogr. Palaeoclimatol. Palaeoecol.* 594, 110948. doi: 10.1016/j.palaeo.2022.110948

Kim, S., McKay, R. M., Lee, J. I., Yoo, K. C., Lee, M. K., and Moon, H. S. (2022b). Bioturbation supplying young carbon into West Antarctic continental margin sediment. *Palaeogeogr. Palaeoclimatol. Palaeoecol.* 602, 111161 doi: 10.1016/j.palaeo.2022.111161

Kim, S., Yoo, K. C., Lee, J. I., Khim, B. K., Bak, Y. S., Lee, M. K., et al. (2018a). Holocene Paleoceanography of bigo bay, west Antarctic peninsula: connections between surface water productivity and nutrient utilization and its implication for surface-deep water mass exchange. *Quat. Sci. Rev.* 192, 59–70. doi: 10.1016/j.quascirev.2018.05.028

Kim, S., Yoo, K. C., Lee, J. I., Lee, M. K., Kim, K., and Yoon, H. I. (2018b). Relationship between magnetic susceptibility and sediment grain size since the last glacial period in the southern ocean off the northern Antarctic peninsula – linkages between the cryosphere and atmospheric circulation. *Palaeogeogr. Palaeoclimatol. Palaeoecol.* 505, 359–370. doi: 10.1016/j.palaeo.2018.06.016

Kim, S., Yoo, K. C., Lee, J. I., Roh, Y. H., Bak, Y. S., Um, I. K., et al. (2020b). Paleoceanographic changes in the southern ocean off elephant island since the last glacial period: links between surface water productivity, nutrient utilization, bottom water currents, and ice-rafted debris. *Quat. Sci. Rev.* 249, 106563. doi: 10.1016/j.quascirev.2020.106563

Lamb, A. L., Wilson, G. P., and Leng, M. J. (2006). A review of coastal palaeoclimate and relative sea-level reconstructions using $\delta^{13}C$ and C/N ratios in organic material. *Earth Sci. Rev.* 75, 29–57. doi: 10.1016/j.earscirev.2005.10.003

Lavoie, C., Domack, E. W., Pettit, E. C., Scambos, T. A., Larter, R. D., Schenke, H.-W., et al. (2015). Configuration of the northern Antarctic peninsula ice sheet at LGM based on a new synthesis of seabed imagery. *Cryosphere* 9, 613–629. doi: 10.5194/tc-9-613-2015

Leventer, A., Domack, E. W., Ishman, S. E., Brachfeld, S., McClennen, C. E., and Manley, P. (1996). Productivity cycles of 200–300 years in the Antarctic peninsula region: understanding linkages among the sun, atmosphere, oceans, sea ice, and biota. *Geol. Soc Am. Bull.* 108, 1626–1644. doi: 10.1130/0016-7606(1996)108<1626:PCOYIT>2.3.CO;2

Li, Z., and Fu, G. (2019). Application of magnetic susceptibility parameters in research of igneous rock in chepaizi. *J. Phys. Conf. Ser.* 1176, 42068. doi: 10.1088/1742-6596/1176/042068

Lisiecki, L. E., and Raymo, M. E. (2005). A pliocene-pleistocene stack of 57 globally distributed benthic $\delta^{18}O$ records. *Paleoceanography* 20, PA1003. doi: 10.1029/2004PA001071

Lucchi, R. G., and Rebesco, M. (2007). "Glacial contourites on the Antarctic peninsula margin: insight for palaeoenvironmental and palaeoclimatic conditions," in *Economic and palaeoceanographic significance of contourite deposits*, vol. 276 . Eds. A. R. Viana and M. Rebesco (London: Geological Society, Special Publications), 111–127.

Lucchi, R. G., Rebesco, M., Camerlenghi, A., Busetti, M., Tomadin, L., Villa, G., et al. (2002). Mid-late pleistocene glacimarine sedimentary processes of a high-latitude, deep-sea sediment drift (Antarctic peninsula pacific margin). *Mar. Geol.* 189, 343–370. doi: 10.1016/S0025-3227(02)00470-X

Manoj, M. C., and Thamban, M. (2015). Shifting frontal regimes and its influence on bioproductivity variations during the late quaternary in the Indian sector of southern ocean. *Deep-Sea Res. II* 118, 261–274. doi: 10.1016/j.dsr2.2015.03.011

McCave, I. N., and Andrews, J. T. (2019). Distinguishing current effects in sediments delivered to the ocean by ice. i. principles, methods and examples. *Quat. Sci. Rev.* 212, 92–107. doi: 10.1016/j.quascirev.2019.03.031

McCave, I. N., Crowhurst, S. J., Kuhn, G., Hillenbrand, C.-D., and Meredith, M. P. (2014). Minimal change in Antarctic circumpolar current flow speed between the last glacial and Holocene. *Nat. Geosci* 7, 113-116. doi: 10.1038/NGEO2037

McCave, I. N., and Hall, I. R. (2006). Size sorting in marine muds: processes, pitfalls and prospects for palaeoflow-speed proxies. *Geochem. Geophys. Geosyst* 7, Q10N05. doi: 10.1029/2006GC001284

McCave, I. N., Thornalley, D. J. R., and Hall, I. R. (2017). Relation of sortable silt grain size to deep-sea current speeds: calibration of the 'Mud current meter'. *Deep-Sea Res. Part I* 127, 1–12. doi: 10.1016/j.dsr.2017.07.003

Mortlock, R. A., and Froelich, P. N. (1989). A simple method for the rapid determination of opal in pelagic marine sediments. *Deep-Sea Res.* 36, 1415–1426. doi: 10.1016/0198-0149(89)90092-7

Noormets, R., Dowdeswell, J. A., Larter, R. D., Ó Cofaigh, C., and Evans, J. (2009). Morphology of the upper continental slope in the bellingshausen and amundsen seas – implications for sedimentary processes at the shelf edge of West Antarctica. *Mar. Geol.* 258, 100–114. doi: 10.1016/j.margeo.2008.11.011

Ó Cofaigh, C., Davies, B. J., Livingstone, S. J., Smith, J. A., Johnson, J. S., Hocking, E. P., et al. (2014). Reconstruction of ice-sheet changes in the Antarctic peninsula since the last glacial maximum. *Quat. Sci. Rev.* 100, 87–110. doi: 10.1016/j.quascirev.2014.06.023

Prebble, J. G., Crouch, E. M., Carter, L., Cortese, G., Bostock, H., and Neil, H. (2013). An expanded modern dinoflagellate cyst dataset for the southwest pacific and southern hemisphere with environmental associations. *Mar. Micropaleontol.* 101, 33–48. doi: 10.1016/j.marmicro.2013.04.004

Pritchard, H. D., Ligtenberg, S. R. M., Fricker, H. A., Vaughan, D. G., Broeke, M. R., and van den, Padman, L. (2012). Antarctic Ice sheet loss driven by basal melting of ice shelves. *Nature* 484, 502–505. doi: 10.1038/nature10968

Pudsey, C. J. (2000). Sedimentation on the continental rise west of the Antarctic peninsula over the last three glacial cycles. *Mar. Geol.* 167, 313–338. doi: 10.1016/S0025-3227(00)00039-6

Pudsey, C. J., and Camerlenghi, A. (1998). Glacial-interglacial deposition on a sediment drift on the pacific margin of the Antarctic peninsula. *Antarct. Sci.* 10, 286–308. doi: 10.1017/S0954102098000376

Pugh, R. S., MaCave, I. N., Hillenbrand, C.-D., and Kuhn, G. (2009). Circum-Antarctic age modeling of quaternary marine cores under the Antarctic circumpolar current: ice core dust-magnetic correlation. *Earth Planet. Sci. Lett.* 284, 113–123. doi: 10.1016/j.epsl.2009.04.016

Rebesco, M., Pudsey, C., Canals, M., Camerlenghi, A., Barker, P., Estrada, F., et al. (2002). "Sediment drift and deep-sea channel systems, Antarctic peninsula pacific margin," in *Deep-water contourite systmes: modern drifts and ancient series, seismic and sedimentary characteristics*, vol. 22 . Eds. D. A. V. Stow, C. J. Pudsy, J. A. Howe, J. C. Faugères. and A. R. Viana (London, Memoirs: Geological Society), 353–371.

Reimer, P. J., Bard, E., Bayliss, A., Beck, J. W., Blackwell, P. G., Ramsey, C. B., et al. (2013). IntCal13 and Marine13 radiocarbon age calibration curves 0-50,000 years cal BP. *Radiocarbon* 55, 1869–1887. doi: 10.2458/azu_js_rc.55.16947

Roberts, J., McCave, I. N., McClymont, E. L., Kender, S., Hillenbrand, C. D., Matano, R., et al. (2017). Earth planet. *Sci. Lett.* 474, 397–408. doi: 10.1016/j.epsl.2017.07.004

Scherer, R. P. (1994). A new method for the determination of absolute abundance of diatoms and other silt-sized sedimentary particles. *J. Paleolimnol.* 12, 171–180. doi: 10.1007/BF00678093

Scheuer, C., Gohl, K., Larter, R. D., Rebesco, M., and Udintsev, G. (2006). Variability in Cenozoic sedimentation along the continental rise of the Bellingshausen Sea, West Antarctica. *Mar. Geol.* 227, 279–298.

Shin, J. Y., Kim, S., Zhao, X., Yoo, K. C., Yu, Y., Lee, J. I., et al. (2020). Particle-size dependent magnetic properties of Scotia Sea sediments since the last glacial maximum: glacial ice-sheet discharge controlling magnetic proxeis. *Palaeogeogr. Palaeoclimatol. Palaeoecol.* 557, 109906. doi: 10.1016/j.palaeo.2020.109906

Smith, J. A., Graham, A. G. C., Post, A. L., Hillenbrand, C.-D., Bart, P. J., and Powell, R. D. (2019). The marine geological imprint of Antarctic ice shelves. *Nat. Commun.* 10, 5635. doi: 10.1038/s41467-019-1349605

Sprenk, D., Weber, M. E., Kuhn, G., Rosén, P., Frank, M., Molina-Kescher, M., et al. (2013). Southern ocean bioproductivity during the last glacial cycle–new detection method and decadal-scale insight from the Scotia Sea. *Geol. Soc London. Spec. Publ.* 381, 245–261. doi: 10.1144/SP381.17

Stevenard, N., Govin, A., Kissel, C., and Toer, A. (2023). Correction of the IRD influence for paleo-current flow speed reconstructions in hemipelagic sediments. *Paleoceanography Paleoclimatology* 38, e2022PA004500. doi: 10.1029/2022PA004500

Stuiver, M., and Reimer, P. J. (1993). Extended ^{14}C data base and revised CALIB 3.0 ^{14}C age calibration program. *Radiocarbon* 35, 215–230. doi: 10.1017/S0033822200013904

Tamura, T., Ohshima, K. I., and Nihashi, S. (2008). Mapping of sea ice production for Antarctic coastal polynyas. *Geophys. Res. Lett.* 35, L07606. doi: 10.1029/2007/GL032903

The RAISED Consortium, Bentley, M. J., Ó Cofaigh, C., Anderson, J. B., Conway, H., Davies, B., et al. (2014). A community-based geological reconstruction of Antarctic ice sheet deglaciation since the last glacial maximum. *Quat. Sci. Rev.* 100, 1–9. doi: 10.1016/j.quascirev.2014.06.025

Truswell, E. M. (1983). Recycled Cretaceous and tertiary pollen and spores in Antarctic marine sediments: a catalogue. *Palaeontogr. Abt. B.* 186, 121–174.

Vautravers, M. J., Hodell, D. A., Channell, J. E. T., Hillenbrand, C.-D., Hall, M., Smith, J. A., et al. (2013). "Palaeoenvironmental records from the West Antarctic peninsula drift sediments over the last 75 ka," in *Antarctic Palaeoenvironmnets and earth-surface processes*, vol. 318 . Eds. M. J. Hambrey, P. F. Barker, P. J. Barrett, V. Bowman, B. Davies, J. L. Smellie and M. Tranter (Geol. Soc. London Special Publ), 263–276. doi: 10.1144/SP381.12

Wagner, M., and Hendy, I. L. (2017). Trace metal evidence for a poorly ventilated glacial southern ocean. *Quat. Sci. Rev.* 170, 109–120. doi: 10.1016/j.quascirev.2017.06.014

Weber, M. E., Kuhn, G., Sprenk, D., Rolf, C., Ohlwein, C., and Ricken, W. (2012). Dust transport from Patagonia to Antarctica–a new stratigraphic approach from the Scotia Sea and its implications for the last glacial cycle. *Quat. Sci. Rev.* 36, 177–188. doi: 10.1016/j.quascirev.2012.01.016

Wu, S., Lembke-Jene, L., Lamy, F., Arz, H. W., Nowaczyk, N., Xiao, W., et al. (2021). Orbital- and millennial-scale Antarctic circumpolar current variability in drake passage over the past 140,000 years. *Nat. Commun.* 12, 3948. doi: 10.1038/s41467-021-24264-9

Wu, L., Wang, R., Xiao, W., Krijgsman, W., Li, Q., Ge, S., et al. (2018). Late quaternary deep stratification-climate coupling in the southern ocean: implications for changes in abyssal carbon storage. *Geochem. Geophys. Geosyst* 19, 379-395. doi: 10.1002/2017GC007250

Wu, L., Wilson, D. J., Wang, R., Yin, X., Chen, Z., Xiao, W., et al. (2020). Evaluating Zr/Rb ratio from XRF scanning as an indicator of grain-size variations of glaciomarine sediments in the southern ocean. *Geochem. Geophys. Geosyst* 21, e2020GC009350. doi: 10.1029/2020GC009350

Xiao, W., Frederichs, T., Gersonde, R., Kuhn, G., Esper, O., and Zhang, X. (2016). Constraining the dating of late quaternary marine sediment records from the Scotia Sea (Southern ocean). *Quat. Geochronol.* 31, 97–118. doi: 10.1016/j.quageo.2015.11.003

Zielinski, U., and Gersonde, R. (1997). Diatom distribution in southern ocean surface sediments (Atlantic sector): implications for paleoenvironmental reconstructions. *Palaeogeogr. Palaeoclimatol. Palaeoecol.* 129, 213–250. doi: 10.1016/S0031-0182(96)00130-7

Zulaikah, S., and Nurlaily, I. P. (2018). Magnetic domain distribution analysis of volcanic material from the 2017 eruptions of mount agung, Indonesia. *J. Phys. Conf. Ser.* 1093, 12029. doi: 10.1088/1742-6596/1093/1/012029

frontiers | Frontiers in Marine Science

TYPE Original Research
PUBLISHED 16 October 2023
DOI 10.3389/fmars.2023.1215048

OPEN ACCESS

EDITED BY
Xu Zhang,
Chinese Academy of Sciences (CAS), China

REVIEWED BY
Xuyuan Ai,
Max Planck Institute for Chemistry, Germany
Yunhai Li,
Ministry of Natural Resources, China

*CORRESPONDENCE
Xibin Han
hanxibin@sio.org.cn

RECEIVED 01 May 2023
ACCEPTED 25 September 2023
PUBLISHED 16 October 2023

CITATION
Hu L, Zhang Y, Wang Y, Ma P, Wu W, Ge Q, Bian Y and Han X (2023) Paleoproductivity and deep-sea oxygenation in Cosmonaut Sea since the last glacial maximum: impact on atmospheric CO_2. *Front. Mar. Sci.* 10:1215048. doi: 10.3389/fmars.2023.1215048

Paleoproductivity and deep-sea oxygenation in Cosmonaut Sea since the last glacial maximum: impact on atmospheric CO_2

Liangming Hu[1,2], Yi Zhang[1,2], Yizhuo Wang[3], Pengyun Ma[4], Wendong Wu[5], Qian Ge[1,2], Yeping Bian[1,2] and Xibin Han[1,2]*

[1]Key Laboratory of Submarine Geosciences, Ministry of Natural Resources, Hangzhou, China, [2]Second Institute of Oceanography, Ministry of Natural Resources, Hangzhou, China, [3]Institute of Sedimentary Geology, Chengdu University of Technology, Chengdu, China, [4]College of Geodesy and Geomatics, Shandong University of Science and Technology, Qingdao, China, [5]School of Mechanical Engineering, Shanghai Jiao Tong University, Shanghai, China

The paleoproductivity in the Southern Ocean plays a crucial role in controlling the atmospheric CO_2 concentration. Here, we present the sediment record of gravity core ANT37-C5/6-07, which was retrieved from the Cosmonaut Sea (CS), Indian Ocean sector of the Southern Ocean. We found that the change in the oxygen concentration in the CS bottom water is strongly correlated with the atmospheric CO_2 fluctuations since the Last Glacial Maximum (LGM). Based on the change in the export production, we reconstructed the evolution history of the deep-water ventilation/upwelling in the study area. During the LGM, a large amount of respiratory carbon was stored in the deep Southern Ocean due to the effect of the low export productivity and restricted ventilation. The oxygen concentration was also low at this time. Despite the increase in paleoproductivity, the biological pump efficiency remained at a low level during the Last Deglaciation. Vast quantities of CO_2 were released into the atmosphere through enhanced upwelling. The recovery of ventilation during this period facilitated the supply of oxygen-rich surface water to the deep ocean. Moreover, signals were identified during the transitions between the Heinrich Stage 1 (HS1), Antarctic Cold Reverse (ACR), and Younger Drays (YD) periods. During the Holocene, the productivity increased overall, and the oxygen in the bottom water was consumed but still remained at a high level. This may have been caused by the enhanced ventilation and/or the prevalence of East Cosmonaut Polynya (ECP) near Cape Ann.

KEYWORDS

paleoproductivity, oxygenation, last glacial maximum, carbon cycling, Cosmonaut Sea

1 Introduction

The Southern Ocean covers approximately 20% of the global ocean area, accounts for 30–40% of the global oceanic net CO_2 absorption and serves as an important carbon sink region (Gao et al., 2001). The Southern Ocean could exert a substantial control on the partial pressure of CO_2, due to its leverage on the efficiency of the global soft-tissue pump through which the photosynthetic production, sinking and remineralization of organic matter store dissolved inorganic carbon (DIC) in the ocean's interior (Sarmiento and Nicolas, 2006; Jaccard et al., 2016). The atmosphere-ocean carbon cycle is inextricably linked to ocean production in all sectors and at all times (Jaccard et al., 2005; Sigman et al., 2010). In the southern part of the Antarctic Polar Front, the surface productivity tends to decrease during cold periods and increase during warm periods (Bonn et al., 1998; Anderson et al., 2009). Marine primary productivity refers to the ability of marine upper plankton to convert inorganic carbon into organic carbon (Raynaud et al., 1992; Graham et al., 2015). By studying marine paleoproductivity, we can gain insights into the CO_2 exchange between the ocean and atmosphere, providing a better understanding of the biogeochemical cycle of carbon in atmosphere-ocean-benthic sediment systems (Paytan et al., 1996; Lin et al., 1999).

Previous research has established that marine diatoms are responsible for the majority of the primary production in the Southern Ocean (DeMaster et al., 1991). As the primary producer in Antarctic coastal waters, diatoms assimilate dissolved Si and CO_2 in water for growth, consequently providing over 75% of the Southern Ocean's export productivity (Quéguiner et al., 1991; Nelson et al., 1995). Silica productivity in seawater mainly consists of biogenic opal and organic matter (Bonn et al., 1998). Following their demise, the remains of diatoms detach from the surface seawater and sink to the seafloor, making Si a crucial component in governing the carbon cycle in the Southern Ocean (Tréguer, 2002). Biogenic silicon is a valuable proxy and is closely associated with climatic conditions (Armand et al., 2005; Crosta et al., 2005; Esper et al., 2010; Esper and Gersonde, 2014a; Esper and Gersonde, 2014b). Hence, it is widely used in the studies of paleoproductivity and the carbon cycle in the Southern Ocean (Agnihotri et al., 2008; Hu et al., 2022). Moreover, the exportation, sedimentation, and preservation of biogenic silicon are closely related to the occurrence of marine barite ($BaSO_4$) in sediments, and there is a strong correlation between the accumulation of biogenic barium and the carbon output to the deep sea (Dymond et al., 1992). Consequently, researchers have conducted many investigations on the paleoproductivity in the Southern Ocean, using biogenic barium as an alternative indicator (Dehairs et al., 1991; Bonn et al., 1998; Fagel et al., 2002).

Reconstructing changes in bottom water oxygenation in the past can provide a better understanding of the relevant processes. The remineralization of organic matter leads to significant changes in the dissolved oxygen concentration, in conjunction with variations in respiratory carbon storage (Hoogakker et al., 2015; Jaccard et al., 2016; Jacobel et al., 2017; Anderson et al., 2019). The temporal evolution of bottom water oxygenation can be reconstructed qualitatively using the distribution of redox-sensitive metals in marine sediments (Calvert and Pedersen, 1996; Nameroff et al., 2002). Enhanced ventilation, particularly in high-latitude regions, plays a significant role in the provision and recovery of the oxygen content in deep ocean layers (Schmittner et al., 2008; Ridgwell and Schmidt, 2010; Amsler et al., 2022). As a result, identifying the redox environment in the deep Southern Ocean is essential to understanding the changes in deep-sea ventilation and surface water productivity (Pailler et al., 2002; Li et al., 2010; Jaccard et al., 2016).

While previous studies have gained a regionally integrated understanding of the leverage the Southern Ocean bears on the air-sea partitioning of CO_2 across the last deglacial termination, observations are largely based on records from the southern Atlantic. Records from the Pacific and Indian sectors of the Southern Ocean are consistent with the first-order paleoceanographic evolution, but regional specificities exist. In particular, it remains unclear how export production patterns vary regionally in the Indian sector of the Southern Ocean, and they are characterized by a complex frontal structure (Durgadoo et al., 2008).

Based on the connections to the global ocean, the overturning circulation of the Southern Ocean has been usefully separated into "upper" and "lower" cells (Toggweiler et al., 2006). Previous studies in the Indian Ocean sector focused on the SAZ and the AZ near the Polar Front and reflected the changes in the upper cell of the Southern Ocean ventilation (Ai et al., 2020; Sigman et al., 2021; Amsler et al., 2022). Based on five sediment cores encompassing the Subantarctic and Antarctic zones in the southwestern Indian Ocean, Amsler et al. (2022) argued that regional changes in the export of siliceous phytoplankton to the deep sea may have entailed a secondary influence on oxygen levels at the water–sediment interface, especially in the SAZ near the Polar Front. Although these records highlight the role that the Indian Ocean sector played in the air–sea partitioning of CO_2 on glacial–interglacial timescales, they are still insufficient to reveal the impact of the lower cell, which ventilates the deeper limb of the Southern Ocean's overturning circulation. In the western Cosmonaut Sea, recent studies were conducted by Hu et al. (2022) and Li et al. (2021). Based on a study of core ANT36-C4-05, Hu et al. (2022) argued that the paleoproductivity of the Cosmonaut Sea has fluctuated strongly since the Middle Holocene, and its evolution trend is basically consistent with the temperature change in the Antarctica, which is greatly restricted by the change in the sea ice range. Li et al. (2021) compared the diatom data for two cores from the western Cosmonaut Sea to other records from the Southern Ocean to reveal the climatic response of the ice-proximal environment to the melting of the ice sheet from the Last Glacial Maximum (LGM) to the Holocene. Both investigations were carried out in the Antarctic Zone of the Cosmonaut Sea, far from the coast.

Based on the baseline research on oceanography, krill, and the environment-West (BROKE-West) survey, Westwood et al. (2010) reported that the rate of primary productivity was significantly higher within the marginal ice zone compared to the open ocean.

The region between 50°E and 60°E has been reported to be a region of converging flow because the Antarctic Slope Current (ASC) is directed northwestward by the topography along the Mawson Coast and meets the Antarctic Circumpolar Current (ACC) north of Cape Ann (Williams et al., 2010). Based on observational and satellite data, Anilkumar et al. (2014) found that the Chl *a* content is high in the coastal region between 52°E and 60°E, with the maximum occurring between 52°E and 54°E. This region is located in the southern part of the ACC, making it an important upwelling region associated with the atmospheric Antarctic Divergence (Williams et al., 2010). Since the upwelling caused by the Antarctic Divergence draws circumpolar deep water (CDW) into the surface waters, it is sometimes co-located with the southern boundary (SB) of the ACC. This upwelling feature is thought to be associated with increased biological activity in all trophic levels (Nicol and Foster, 2003). Moreover, the region offshore of Cape Darnley immediately to the west has high oxygen concentrations and bottom-intensified flows, suggestive of local bottom-water formation that can extend westward to ~30°E (Meijers et al., 2010).

Overall, the productivity in the Cosmonaut Sea coastal region north of Cape Ann has significant regional characteristics and is closely related to the lower layer of the circulation system in the Indian Ocean sector. There is great potential in using the sedimentary records of the Cosmonaut Sea since the LGM to learn about the evolution of climate-driven biogeochemistry. In this study, we established a chronological framework for the top segment of core ANT37-C5/6-07. Based on suitable proxies of paleoproductivity and bottom-water oxygenation, we aimed to reconstruct the co-evolution of the paleoproductivity and deep-water ventilation in the Cosmonaut Sea since the LGM and to reveal their impact and feedback on the carbon cycle in the Indian Ocean sector of the Southern Ocean.

2 Regional setting

The Cosmonaut Sea is part of the Indian Ocean sector of the Southern Ocean, spanning 30–60°E. It is bordered by the Enderby Land to the south, the Cooperation Sea to the east, and the Gunnerus Ridge to the west, and it is adjacent to the Riiser-Larsen Sea (Figure 1) (Hu et al., 2022). There are mainly three small bays along the coast, namely, the Amundsen Bay, the Casey Bay, and the Lützow-Holm Bay from east to west. The Cosmonaut Sea is located in the middle of two large bays, the Weddell Bay and the Prydz Bay, which create two major circulation systems around the study area, the East Weddell Gyre and the Prydz Bay Gyre, respectively (Heywood et al., 1999; Meijers et al., 2010). The bottom edge of the Amery Ice Shelf in the Prydz Bay may extend to the area near the eastern coast of the Cosmonaut Sea (Wong et al., 1985).

The ocean current system in the Cosmonaut Sea area exhibits a complex pattern (Hu et al., 2022). The region has three distinct banded fronts: the southern front of the ACC (sACCf), the SB, and the Antarctic Slope Front (ASF) from north to south (Meijers et al., 2010). The ASF is effectively the result of the deepening of the T_{min} layer over the upper continental slope toward the shelf break (Williams et al., 2010). A strong westward current, associated with the horizontal pressure gradient of the ASF, is referred to as the Antarctic Slope Current (ASC). The main feature of the ASC is a strong jet that is generally located over the upper continental slope at depths of 750–1250 m. The surface circulation consists of the eastward flowing ACC and the westward flowing Antarctic Coastal Current (CC) (Figure 1). The Antarctic Coastal Current flows westward through the Cosmonaut Sea from the Prydz Bay, forming two branches at the Gunnerus Ridge. One continues westward, while the other branch creates an anticyclonic circulation that deflects to the northeast (Bibik et al., 1988).

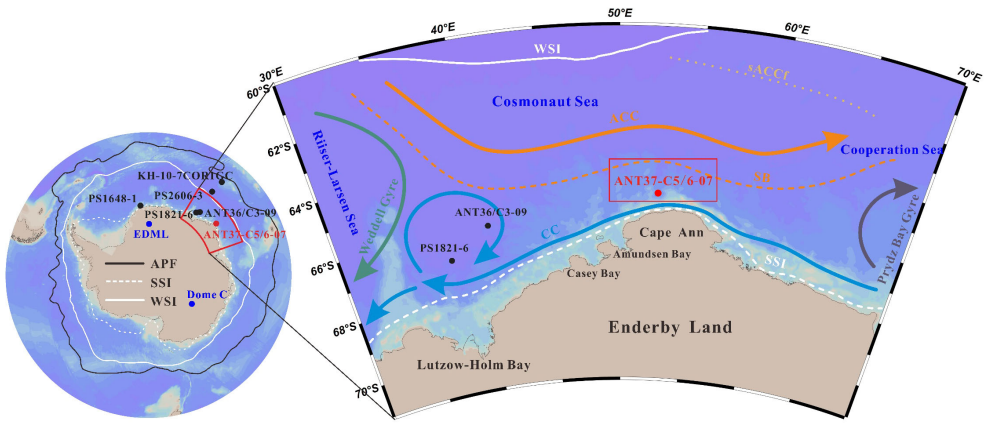

FIGURE 1
Regional setting and locations of the studied and referenced cores. The black solid line indicates the location of the Antarctic Polar Front (APF) (Orsi et al., 1995). The white solid line and the white dashed line indicate the average extent of the modern winter sea ice (WSI) and summer sea ice (SSI), respectively (Comiso, 2003). The ocean circulation patterns of the Antarctic Circumpolar Current (ACC) and the coastal current (CC) are indicated by the orange and blue arrows, respectively (modified after Hunt et al., 2007). The green and gray arrows indicate the Weddell Gyre and the Prydz Bay Gyre, respectively (modified after Hu et al., 2022). The golden dotted line indicates the southern front of the ACC (sACCf) (Hu et al., 2022). The southern boundary of the ACC (SB) is denoted by the orange dashed line (Hunt et al., 2007). The red rectangle represents the position of the ECP (Comiso and Gordon, 1996).

The ACC predominantly consists of the CDW, which is transported eastward around Antarctica, connecting the Atlantic, Indian, and Pacific oceans (Williams et al., 2010). The lower CDW originates from North Atlantic Deep Water, while the upper CDW consists of Indian Deep Water and Pacific Deep Water (Talley, 2013). The Southern Ocean also has a meridional overturning circulation that transports the CDW southward toward the Antarctic continental slope where it shoals and is transformed into cold and fresh Antarctic surface water (AASW). Part of the ACC water mass mixes with the shelf water near the front edge of the continental shelf in the eastern Cosmonaut Sea (Bibik et al., 1988; Klyausov and Lanin, 1988). The dense shelf water sinks off Cape Darnley, forming the Cape Darnley bottom water (CDBW), which contributes to the Antarctic bottom water (AABW) (Aoki et al., 2020). Based on lowered-acoustic Doppler current profiler (LADCP) data, Meijers et al. (2010) reported the occurrence of westward-flowing AABW high on the continental slope. This westward-flowing region at the bottom has been found to become progressively deeper and covers our sampling point.

The East Antarctic Ice Sheet was relatively stable during the Last Deglaciation, so, the Cosmonaut Sea was mainly affected by the melt water from the West Antarctic Ice Sheet (Li et al., 2021). Previous studies have pointed out that winter sea ice (WSI) can extend northward to 60°S, while the range of the summer sea ice (SSI) in the Indian Ocean zone of the Southern Ocean has remained relatively unaltered from the LGM to the present day (Gersonde et al., 2005). Based on more than 20 years of satellite observation data, Comiso and Gordon (1996) reported a long-lasting polynya near Cape Ann in the Cosmonaut Sea. Polynyas are areas of persistent open water or reduced ice concentration surrounded by sea ice (Smith et al., 1990; Morales Maqueda et al., 2004). The West Cosmonaut Polynya (WCP) occurs west of 45°E, which is formed by storms. The east polynya, located in the coastal region north of Cape Ann, is known as the East Cosmonaut Polynya (ECP) (Prasad et al., 2005). Previous studies have suggested that ocean forcing and/or divergent winds may have contributed to the formation of the ECP (Comiso and Gordon, 1996; Arbetter et al., 2004; Bailey et al., 2004).

3 Materials and methods

3.1 Sample collection

Gravity core ANT37-C5/6-07 was obtained off the coast of Cape Ann (65°21.27'S, 52°35.69'E) in the Cosmonaut Sea during the 37th Chinese Antarctica Expedition. The core site is located north of the modern SSI and south of the WSI range. Cape Ann is the northernmost promontory on the Antarctic continent where the surfaces of Antarctic glaciers reach, except for the Antarctic Peninsula (Comiso and Gordon, 1996). The sampling point is located on the continental ridge at a water depth of 2825 m. The top of the core is shown as grayish olive green, and the lithology is dominated by clayey silt. As shown in the X-radiographic image (Figure 2), there is no obvious sedimentary hiatus in the core. The entire core was divided into four segments with similar lengths. The first segment at the top (length of 91 cm) was used in this study.

3.2 Dating

Reliably dating glaciomarine sediments deposited on the Antarctic shelf since the LGM is challenging due to the scarcity of calcareous (micro-) fossils and the recycling of fossil organic matter. Therefore, accelerator mass spectrometry (AMS) ^{14}C-dating is commonly performed on the acid-insoluble organic fraction (AIO) of marine sediments (Licht and Andrews, 2002; Hillenbrand et al., 2010; Hu et al., 2022). The AIO primarily consists of diatomaceous organic matter, and

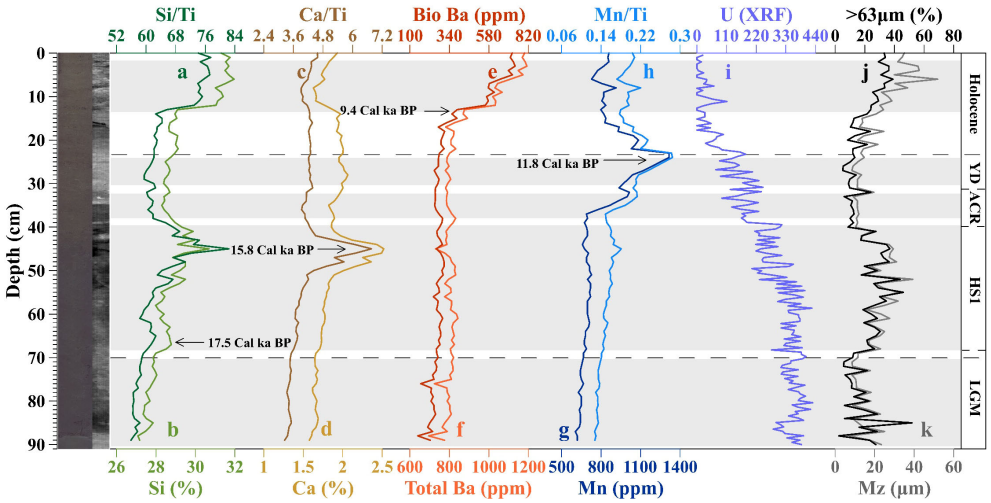

FIGURE 2
Downcore distribution patterns of the paleoproductivity proxies, oxygenation proxies, and the percentage of >63 μm grains in the core sediments. **(A)** Si/Ti ratios, **(B)** Si content, **(C)** Ca/Ti ratios, **(D)** Ca content, **(E)** Bio Ba content, **(F)** Total Ba content, **(G)** Mn content, **(H)** Mn/Ti ratios, **(I)** U (XRF) content, **(J)** percentage of >63 μm grains, and **(K)** mean grain size of core sediments.

it is assumed to provide reliable age models for sediment cores retrieved from the Southern Ocean (Licht and Andrews, 2002). We selected sediment samples from six layers (1 cm, 12 cm, 32 cm, 45 cm, 68 cm, and 91 cm) in the top segment and conducted radioactive ^{14}C-dating analysis of these samples at the Beta Analytic Testing Laboratory, Miami (Table 1).

3.3 Paleoproductivity proxies

The main elements in the bulk samples were analyzed via X-ray fluorescence spectrometry (XRF), while the trace elements were analyzed using an Elan DRC-e inductively coupled plasma mass spectrometry (ICP-MS) with a sampling resolution of 1 cm. The sediment grain size was determined using a Mastersizer 2000 analyzer. In addition, we also used an XRF core scanner (ITRAX) to collect optical and X-radiographic images and to obtain high-resolution element profiles of the core. Since only biogenic barium from discrete barite particles (associated with decaying organic matter) provides information on the export of organic matter to the seafloor, the impacts of barium from other sources must be eliminated (Dehairs et al., 1980; Dymond et al., 1992). Investigations of various sedimentary environments have shown that the main impact comes from terrigenous debris, which varies widely between 200 and 1000 ppm (Dymond et al., 1992; Gingele and Dahmke, 1994; Stroobants et al., 1991). A normative approach is commonly used to distinguish between detrital barium and biogenic barium (Bio Ba) (Dymond et al., 1992; Gingele and Dahmke, 1994). The correlation between Al and Ti in the samples is high (R^2 = 0.7894) (Figure 3E), and the downcore distribution patterns of both are highly consistent (Figures 3A, B), indicating the absence of significant biogenic Al. Therefore, the barium/aluminum ratio and the barium/titanium ratio were used for the correction of the debris end. The equations for calculating the biogenic barium content are as follows:

$$Bio\ Ba = Ba_{total} - Al_{sam} \times (Ba/Al)_{ter} \quad (1)$$

$$Bio\ Ba = Ba_{total} - Ti_{sam} \times (Ba/Ti)_{ter} \quad (2)$$

where Bio Ba denotes biogenic barium, and Ba_{total}, Al_{sam}, and Ti_{sam} are the total Ba, total Al, and total Ti contents in the sediment sample, respectively. $(Ba/Al)_{ter}$ and $(Ba/Ti)_{ter}$ are used to indicate the abundance of Ba in the continental crust. The Ba/Al ratio of aluminum silicate in the global crust is 0.005–0.01, the average value method was used to obtain a value of 0.0075 according to previous studies (Dymond et al., 1992; Hu et al., 2022). The $(Ba/Ti)_{ter}$ value is 0.126 (Turekian and Wedepohl, 1961). We assumed that the composition of the terrestrial materials related to the barium content was constant in time and space (Bonn et al., 1998). Figure 3 shows that there is no significant difference between the distribution patterns of Bio Ba calculated using $(Ba/Al)_{ter}$ and $(Ba/Ti)_{ter}$. However, the range of the Bio Ba values calculated using $(Ba/Al)_{ter}$ is closer to that obtained in a previous study in the Indian Ocean sector of the Southern Ocean (Figures 4G–I) (Bonn et al., 1998), so we chose to use the Bio Ba content obtained using Eq. (1).

In addition, we also used the ratios of Si and Ca to Ti to indicate changes in the paleoproductivity, thereby eliminating the impact of the terrigenous clastic input (Cheshire and Thurow, 2005; Agnihotri et al., 2008). Finally, we selected Bio Ba and Si/Ti as alternative proxies of the siliceous productivity, and Ca/Ti as an alternative proxy of biogenic calcium carbonate and the calcareous productivity.

3.4 Oxygenation proxies

The concentration of redox sensitive elements (RSEs) in sediments can reflect the oxygen content at the water-sediment interface and in bottom water and has been widely used as an alternative indicator of the redox environment in the deep ocean (Calvert and Pedersen, 1993; Brown et al., 2000). Under reducing or suboxidizing conditions, Mn is dissolved in water as ionic Mn(II). While under oxidizing conditions, it produces Mn oxides/hydroxides in the form of Mn(III) or Mn(IV), which are precipitated and enriched in the sediments (Calvert and Pedersen, 1993; Calvert and Pedersen, 1996). When the deposition environment becomes a suboxidizing or even anoxic environment again, the Mn hydroxide will be reduced to Mn(II) (Mn^{2+} or $MnCl^{+}$) and will migrate upward or downward in the sediment column (Middelburg et al., 1987; Brumsack, 1989; Morford et al., 2001). Another characteristic of Ti is that it is almost unaffected by changes in the redox conditions of seawater. We used the Mn/Ti ratio to eliminate the dilution effect of terrestrial debris components (Wang et al., 2018).

In oxygenated environments, uranium (U) is present as soluble U (VI). When the seawater becomes oxygen-depleted, the U is reduced and is precipitated as insoluble U(IV) in the form of

TABLE 1 AMS ^{14}C data and the calibrated calendar ages for the top 91 cm of core ANT37-C5/6-07.

Lab ID	Depth (cm)	Material	^{14}C age (a BP)	Calibrated age (a BP)	Old carbon age (a)	Calendar age (Cal a BP)
616427	0–1	Organic carbon	5300 ± 30	2118	2118	0
664982	11–12	Organic carbon	13230 ± 50	11486	2118	9368
664983	31–32	Organic carbon	18410 ± 60	18035	2118	15917
616428	44–45	Organic carbon	18210 ± 50	17774	2118	15656
664984	67–68	Organic carbon	19810 ± 80	19280	2118	17162
616430	90–91	Organic carbon	27830 ± 120	28116	2118	25998

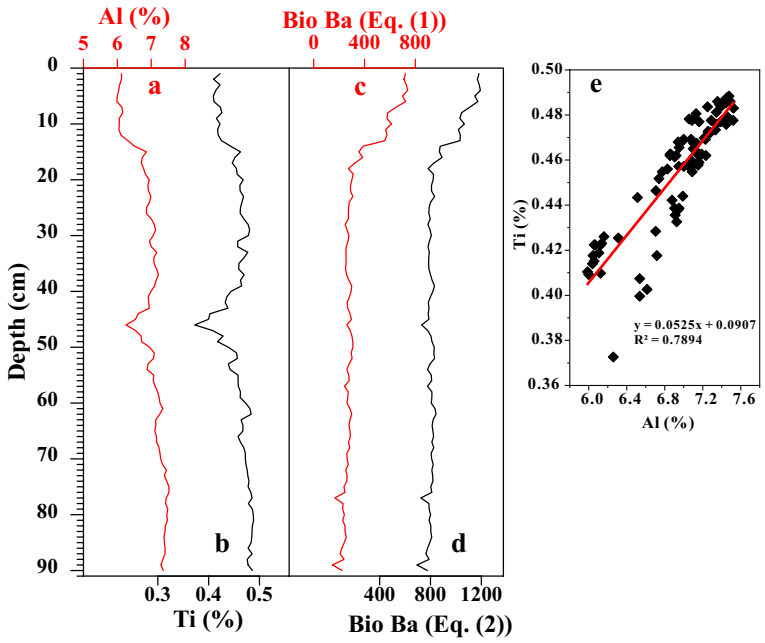

FIGURE 3
Effects of different Ba/Al and Ba/Ti ratios (Eqs. (1) and (2)) on computing the detrital barium background from the Batotal values. **(A)** Al content, **(B)** Ti content, **(C)** Bio Ba content (Eq. (1)), **(D)** Bio Ba content (Eq. (2)), and **(E)** the correlation between Ti (%) and Al (%) of core sediments.

uraninite (Morford and Emerson, 1999). Under reducing conditions, the decrease in the U concentration of the sediment porewater will create a concentration gradient between the bottom water and the uppermost sediment layers. This gradient leads to the diffusion of the dissolved U into the sediment and to the precipitation of authigenic U (aU) phases (Langmuir, 1978). And the authigenic fraction typically amounts for > 60% of the total U (Amsler et al., 2022). Therefore, the Mn/Ti ratio and U content (data collected from the XRF core scanner) were used as two proxies of the oxygenation of bottom water in this study.

4 Results

4.1 Chronology

The AMS ^{14}C dating results for the selected three layers are presented in Table 1. We found that an age reversal occurred at 32 cm. We speculate that at ~16 Cal ka BP, there may have been a sudden intensify of terrestrial material input, resulting in the interference of terrestrial-derived old carbon in this layer. The age model obtained after removing the data from this layer is consistent with that calculated through Bacon age-depth modelling tool, which indicates that this age reversal has a minimal impact on our study. Therefore, we rounded off the data for that layer. The test age was corrected using the Calib 8.2.0 (Stuiver and Reimer, 1993) procedure and the Marine 20 calibration dataset (Heaton et al., 2020). According to previous studies, a delta R value of 1120 for carbon storage correction was used (Yoshida and Moriwaki, 1979; Takano et al., 2012). After the correction and fitting, the corrected ages of the samples from the top segment of the core were obtained: 2118 Cal a BP at 1 cm and 28116 Cal a BP at 91 cm.

Similarly, AMS ^{14}C dating of the AIO from surface seafloor sediments around Antarctica has frequently yielded ages of several thousand years (Andrews et al., 1999; Pudsey et al., 2006). The occurrence of old surface ages combined with the potential error of downcore AIO ages complicates the reliability of ^{14}C-based age models for post-LGM sedimentary sequences south of the APF (Hillenbrand et al., 2010). Usually, down-core AIO ages are corrected by subtracting the age of the top of the core (Andrews et al., 1999; Pudsey et al., 2006). Hu et al. (2022) determined the downcore distribution pattern of $^{210}Pb_{ex}$ in the top 20 cm section of adjacent core ANT36-C4-05. They found that the specific activity of $^{210}Pb_{ex}$ decreased exponentially from the surface to a depth of 4 cm, and it fluctuated within the range of the background values below 4 cm. Therefore, the surface layer of the core is considered to be modern sediment, and the age of the top of the core is 0 Cal a BP. An age of 2118 a was used as the old carbon age for the correction in this study, and the final calendar ages of each layer were obtained after removing the influence of the old carbon storage (Table 1). After calculating the calendar age, we obtained the accumulation rate of the top 91 cm of the core (Figure 5). Our data are similar to those of a previous study of adjacent cores (Bonn, 1995).

4.2 Characteristics of the paleoproductivity proxies

As shown in Figure 2, during the LGM, the values of the alternative indicators of paleoproductivity fluctuated within narrow ranges and typically remained at a relatively low level.

In the early stage of the Last Deglaciation, there was no significant change in the Bio Ba value and Ca/Ti ratio (Figures 2C, E), while the Si/

10.3389/fmars.2023.1215048

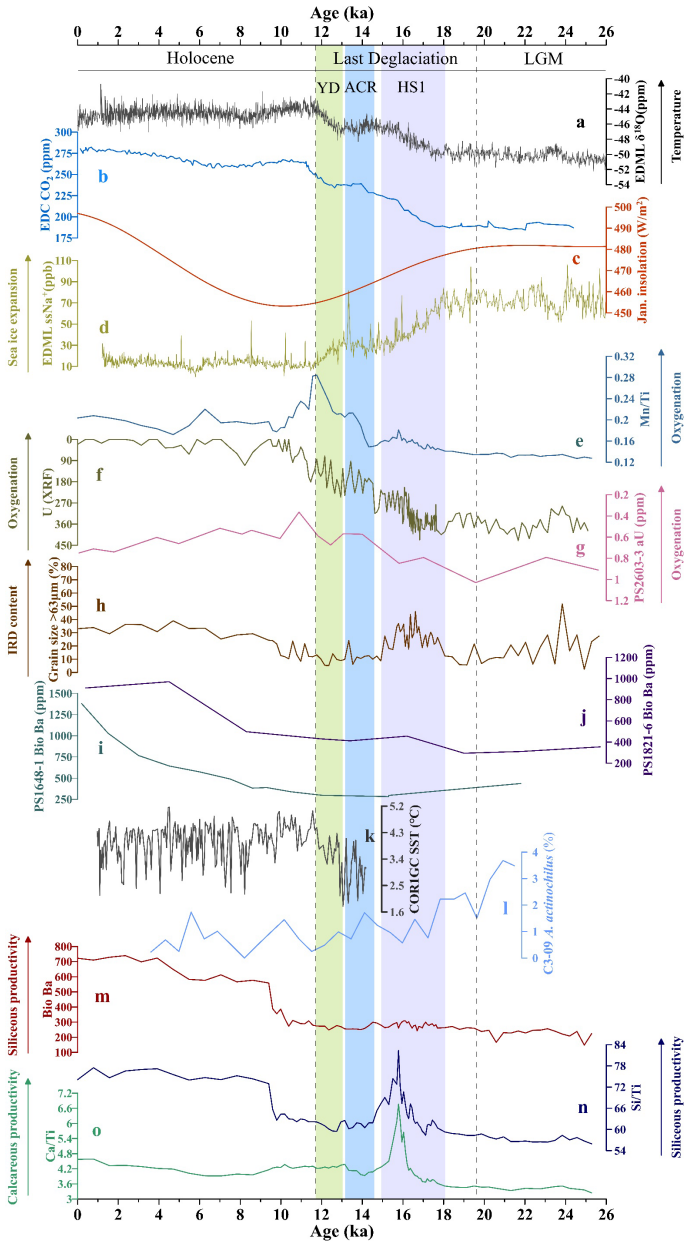

FIGURE 4
Comprehensive comparison of paleoproductivity and oxygenation proxies of our samples with records from ice cores and other sediment cores. **(A)** EDML $\delta^{18}O$ content (EpicaCommunityMembers, 2006), **(B)** EDC CO_2 content (Monnin et al., 2004; Schmitt et al., 2012), **(C)** summer insolation in the Southern Hemisphere at 65°S (Laskar et al., 2004), **(D)** EDML $ssNa^+$ content (Fischer et al., 2007), **(G)** authigenic uranium (aU) concentrations of core PS2603-3 (Amsler et al., 2022), **(I, J)** Bio Ba contents in cores PS1648-1 and PS1821-6 (Bonn, 1995), **(K)** sea surface temperature record of core KH-10-7COR1GC (Orme et al., 2020), **(L)** *Actinocyclus actinochilus* abundance of core ANT36/C3-09 (Li et al., 2021). **(E)** Mn/Ti ratios, **(F)** U content (XRF), **(H)** percentage of >63 μm grains, **(M)** Bio Ba content, **(N)** Si/Ti ratios, and **(O)** Ca/Ti ratios of core sediments.

Ti ratio exhibited a minor peak at ~19.1 Cal ka BP, followed by a decline before entering Heinrich Stage 1 (HS1, 18–14.6 Cal ka BP) (Figure 2A). During HS1 (corresponding to the W2 warm period in the Southern Hemisphere) (Siani et al., 2013), all of the paleoproductivity proxies exhibited increasing trends, but the Bio Ba curve remained relatively flat. The Si/Ti and Ca/Ti ratios reached high peaks in the middle stage of HS1 (~15.9 Cal ka BP), whereas the Bio Ba curve had a low value during this period. During the Antarctic Cold Reverse period (ACR, 13.1–14.7 Cal ka BP), all of the paleoproductivity proxies exhibited a decline to varying degrees, with the most significant reductions occurring in the Si/Ti and Ca/Ti ratios. After the ACR, the Ca/Ti curve exhibited a stable change, while the Bio Ba value and Si/Ti ratio began to increase slightly, continuing until the end of the Younger Drays period (YD, 11.7–13.1 Cal ka BP). Overall, the levels of all three paleoproductivity proxies were higher during the Last Deglaciation than during the LGM, despite the low Si/Ti and Ca/Ti values at the end of the Last Deglaciation.

During the Holocene, the changes in all of the paleoproductivity proxies can be categorized into two distinct stages. In the Early and Middle Holocene, both the Bio Ba value and Si/Ti ratio began to

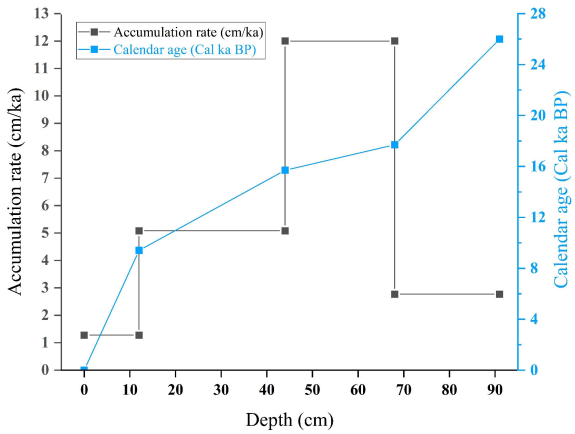

FIGURE 5
Accumulation rates and calibrated calendar ages for the top 91 cm of core ANT37-C5/6-07.

increase significantly and remained at high levels (Figures 2A, E), while the Ca/Ti ratio slowly decreased (Figure 2C). In the second stage (since the Middle Holocene, at ~6.6 Cal ka BP), the Bio Ba value and Si/Ti ratio underwent another slight increase. Although the Ca/Ti ratio remained at a relatively low level during the Late Holocene, it also exhibited an overall increasing trend.

4.3 Characteristics of the oxygenation proxies

As shown in Figure 2, the Mn/Ti ratio was relatively low during the LGM and began to increase during the Last Deglaciation. Similar to the paleoproductivity proxies, a significant peak occurred at ~15.8 Cal ka BP (Figure 2H). However, during the transition to the ACR, the increase in the Mn/Ti ratio became stagnant. Subsequently, from the YD period to the Holocene, the Mn/Ti ratio exhibited a rapid rebound, and the highest peak occurred at ~11.8 Cal ka BP. The change in the U content (XRF) was opposite to that of the Mn/Ti ratio (Figure 2I). It remained at a high value during the LGM. During the Last Deglaciation, it exhibited a continuous decreasing trend, and it remained at a low level during the Holocene. However, there is an absence of the large oxygenation peak in the U content (XRF) around 12 Cal ka BP. Our sampling point is located very close to the continental shelf, and the high Al and Ti contents at depths of 15-40 cm in the sediment core indicate a strong input of terrestrial material during this interval. This may have led to the significant deviation between the actual aU content and the total U content, which resulted in the absence of the peak point of U (XRF) curve.

5 Discussion

5.1 Source of the organic matter

Most regions of the Southern Ocean have a low primary productivity, which is typical of high nutrient and low chlorophyll oceans (Smith, 1991; Moore and Abbott, 2000; Gao and Chen, 2002). The total organic carbon (TOC) content within the upper 91 cm of core ANT37-C5/6-07 ranges from 0.10% to 0.63%, with an average value of 0.38%, which is close to those of other cores in the Cosmonaut Sea (Bonn, 1995; Yang et al., 2022). The downcore distribution pattern of the total nitrogen (TN) content is comparable to that of the TOC, with a strong positive correlation ($R^2 = 0.8687$) (Figure 6D). This indicates that the source of the organic matter in the core sediments was relatively stable, and the sources of the TOC and TN were consistent (Liu et al., 2014).

The ratio of the total organic carbon to the total nitrogen (TOC/TN) and the $\delta^{13}C$ content were used to determine whether the source of the organic matter in the marine sediments was terrestrial or oceanic (Prahl et al., 1994; Thornton and McManus, 1994; Meyers, 1997; Sampei and Matsumoto, 2001; Ogrinc et al., 2005). The TOC/TN ratio of organic matter derived from marine phytoplankton is typically 3–8, while that of organic matter from terrestrial sources is typically ≥20 (Emerson and Hedges, 1988; Gao et al., 2008). Marine organic carbon has a classic range of $\delta^{13}C$ value of −22 ‰ to −19 ‰ (Fontugne and Jouanneau, 1987), but previous studies have reported that the $\delta^{13}C$ value of the organic matter in Southern Ocean sediments tends to be more negative (Macko and Pereira, 1990; Harada et al., 1995; Domack et al., 1999; Domack et al., 2001; Kulbe et al., 2001; Berg et al., 2013; Han et al., 2015; Learman et al., 2016). This suggests that relying solely on the $\delta^{13}C$ values may not provide an accurate reference for the origin of the organic matter in Southern Ocean sediments. Therefore, in addition to the TOC/TN ratio and $\delta^{13}C$ value, we also utilized an end-component mixing model to estimate the proportions of the terrestrial and marine organic matter inputs (Eqs. (3)–(6)) (Mei et al., 2015):

$$TOC_{ter}(\%) = (\delta^{13}C_{mar} - \delta^{13}C_{sam})/(\delta^{13}C_{mar} - \delta^{13}C_{ter}) \times TOC_{sam}(\%) \quad (3)$$

$$TOC_{mar}(\%) = TOC_{sam}(\%) - TOC_{ter}(\%) \quad (4)$$

$$TOC_{mar-con}(\%) = TOC_{mar}(\%)/TOC_{sam}(\%) \times 100\% \quad (5)$$

$$TOC_{ter-con}(\%) = 1 - TOC_{mar-con}(\%) \quad (6)$$

where TOC_{ter} (%) and TOC_{mar} (%) are the percentages of terrestrial and oceanic organic carbon, respectively, $TOC_{ter\text{-}con}$ (%) and $TOC_{mar\text{-}con}$ (%) are the contributions of terrestrial and oceanic organic carbon, respectively, and TOC_{sam} (%) is the total organic carbon content of the sediment samples. $\delta^{13}C_{mar}$ is the $\delta^{13}C$ value of the sea-source organic matter endmember, which is the comprehensive level (−26.04‰) of the plankton, benthic organic matter, and seawater particulate organic matter in the Southern Ocean (Kopczyńska et al., 1995; Frazer, 1996; Gillies et al., 2012; Berg et al., 2013; Zhang et al., 2017). $\delta^{13}C_{ter}$ is the $\delta^{13}C$ value of the terrestrial organic matter endmember, which is taken from the cold vegetation on the Antarctic continent (−21.54‰) (Strauch et al., 2011). $\delta^{13}C_{sam}$ is the $\delta^{13}C$ value of the organic matter in the core sediments.

10.3389/fmars.2023.1215048

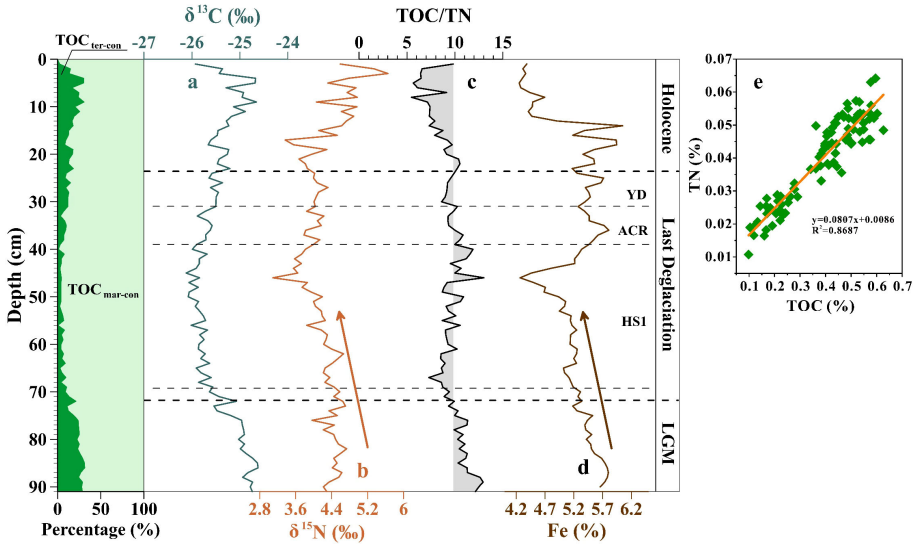

FIGURE 6
Downcore distribution patterns of the terrestrial and oceanic contribution ratios of the TOC, **(A)** δ13C, **(B)** δ15N, **(C)** TOC/TN ratios, **(D)** Fe content, and **(E)** the correlation between TOC (%) and TN (%).

According to the calculation results of the endmember mixing model (Table 2), the $TOC_{mar\text{-}con}$ (%) of the organic matter in the core sediments is 68.47%–99.46%, with an average value of 86.15%. Moreover, the TOC/TN ratio of the core organic matter is 5.48–13.01 (Figure 6C), with an average value of 9.51, which is very biased toward the TOC/TN ratio of marine organic matter (Thunell et al., 1992). Therefore, we believe that the vast majority of the organic matter came from marine export productivity, although the organic matter in core ANT37-C5/6-07 is interfered using the terrestrial input (Figure 6).

5.2 Changes in the paleoproductivity and the oxygenation

5.2.1 Last glacial maximum

The LGM occurred at approximately 19–26.5 Cal ka BP. During this period, the global temperature was relatively low, with an average temperature decrease of about 3–4°C. This period was characterized by the presence of massive continental ice sheets in both the Northern and Southern hemispheres (Adkins et al., 2002). In the seasonal sea ice regions surrounding the Antarctic continental margin, the main factors controlling the productivity are the lighting conditions, water ventilation, and sea ice cover (Anderson et al., 2002). During glacial to interglacial cycles, the sea ice cover fluctuates synchronously with the deep-ocean oxygen isotope records and Antarctic temperature, indirectly affecting the export production by regulating variables such as the lighting conditions, nutrient availability, and mixed layer depth (Dieckmann and Hellmer, 2003; Wolff et al., 2006; Bouttes et al., 2010; Abram et al., 2013). The sea salt Na^+ ($ssNa^+$) data from the EPICA DML (EDML) ice core serve as a proxy for sea ice expansion in the Indian Ocean sector of the Southern Ocean (Schüpbach et al., 2013). During the LGM, EDML-$ssNa^+$ content indicates that the Southern Ocean's sea ice coverage was extremely extensive (Figure 4D) (Fischer et al., 2007). The high abundance of *A. actinochilus* is also indicative of a cold environment and sea-ice expansion in the Cosmonaut Sea (Figure 4L) (Li et al., 2021). In the Antarctic coastal area, the >63 μm components of the marine sediments are typically deemed to be ice raft debris (IRD) (Diekmann and Kuhn, 1999; Liu et al., 2015; Lei et al., 2021). The IRD content reached a large peak during the early LGM (~25 Cal ka BP) (Figure 4H), signifying that sea ice expansion in the Cosmonaut Sea may have peaked during this period.

All the available proxies for core ANT37-C5/6-07 indicate that the paleoproductivity was extremely low during the LGM (Figures 4M–O), and the Bio Ba contents of cores PS1821-6 and PS1648-1 were also at a low value (Figures 4I, J) (Bonn, 1995). Even though the summer insolation in the Southern Hemisphere at 65°S was high (Figure 4C), the sea ice cover hindered the penetration of sunlight into the ocean and significantly reduced the amount of sunlight received by the

TABLE 2 Total organic carbon (TOC), percentages of terrestrial and oceanic organic carbon, and their contributions for the top 91 cm of core ANT37-C5/6-07.

	TOC (%)	TOC_{mar} (%)	TOC_{ter} (%)	$TOC_{mar\text{-}con}$ (%)	$TOC_{ter\text{-}con}$ (%)
Value range	0.10–0.63	0.07–0.57	0–0.18	68.47–99.46	0.54–31.53
Average value	0.38	0.33	0.05	86.15	13.85

surface ocean (Abram et al., 2013). The EDML-$\delta^{18}O$ content (Figure 4A) (EpicaCommunityMembers, 2006) also indicates the occurrence of low temperatures during the LGM, which severely limited the surface export productivity. However, the proportion of the Antarctic sea-ice algae in the phytoplankton in the surface ocean covered by sea ice may have increased during the LGM (Figure 4L). Ice algae, though usually not a significant contributor to the organic matter in benthic sediments, may have resulted in less negative $\delta^{13}C$ values during the LGM (Figure 6A) due to their relatively high $\delta^{13}C$ values (−15‰ to −8‰) (Gibson et al., 1999). The $\delta^{15}N$ value of sediment is often used to identify the nitrate bioavailability, and an increase in its value corresponds to an increase in the nutrient utilization by phytoplankton in the surface seawater (Francois et al., 1992; Altabet and Francois, 1994). The high $\delta^{15}N$ values during the LGM (Figure 6B) suggest that the nutrient utilization rate was relatively high despite the low paleoproductivity. However, the photosynthesis of phytoplankton should be hindered under thick sea ice coverage and lead to lower $\delta^{15}N$ values (Studer et al., 2015). This indicates that the nutrient supply may have been limited because of the weakened deep-water upwelling in the Cosmonaut Sea during this period (Kim et al., 2020), which is the major reason of the low export productivity at this time.

The Mn/Ti ratio was low during the LGM, while the U content (XRF) was high (Figures 4E, F), indicating significant depletion of oxygen due to pre-formed carbon storage and insufficient replenishment (Jaccard and Galbraith, 2012). The same evidence of the low oxygen content of the bottom water was obtained for the southwestern part of the Indian Ocean sector (Figure 4G) (Amsler et al., 2022). The radioactive ^{14}C ages indicate that poor ventilation conditions occurred in the deep sea during the LGM (Sarnthein et al., 2013; Skinner et al., 2017). The formation and activity of the sea ice in the Southern Ocean hindered gas exchange between the atmosphere and ocean and led to increased vertical stratification of the water column (Adkins et al., 2002; Watson and Naveira Garabato, 2006; Bouttes et al., 2010; Wolff et al., 2010; Adkins, 2013; Ferrari et al., 2014). Despite the fact that the solubility of oxygen increases at colder temperatures, it was difficult for the higher oxygen concentration surface water to reach the deeper layer to achieve refreshment and replenishment. Moreover, the bottom water (rich in nutrients) in the Cosmonaut Sea also failed to reach the surface ocean, which contributed to the extremely low export production. In summary, during the LGM, the paleoproductivity of the Cosmonaut Sea and the oxygenation level of the bottom water were primarily controlled by the constraints imposed by poor ventilation conditions.

Another impact of sea ice expansion was the northward movement of the upwelling zone in the Southern Ocean, which enhanced the sequestration of the respiratory carbon in the deep water along the coast of Antarctica, thereby reducing the amount of CO_2 emitted into the atmosphere (Toggweiler, 1999; Sigman and Boyle, 2000; Toggweiler et al., 2006; Watson et al., 2015). The biopump efficiency was found to be high during this period (Keir, 1988). In addition to the physical mechanisms, such as weakened ventilation and the northward movement of the upwelling zone, biogeochemical changes also played a positive role in the storage of carbon dioxide (François et al., 1997; Sigman and Boyle, 2000; Galbraith and Jaccard, 2015; Sigman et al., 2021). Due to the more comprehensive assimilation and utilization of nutrients (Figure 6B) and/or the relatively higher supply of iron containing terrestrial material (Figure 6D), more efficient biological carbon pumps were created in the Cosmonaut Sea during the LGM, further inhibiting the emission of CO_2 in the deep ocean (Studer et al., 2015; Gottschalk et al., 2016; Ai et al., 2020; Galbraith and Skinner, 2020).

5.2.2 Last deglaciation

It is widely believed that the Last Deglaciation began at 18–20 Cal ka BP, and the onset occurred later in East Antarctica than in West Antarctica (Fudge et al., 2013). The paleoproductivity proxy values in core ANT37-C5/6-07 began to increase significantly after 19.6 Cal ka BP (Figures 4N, O), and the oxygen content also exhibited a synchronous increase at this time (Figures 4E, F). Simultaneously, wind dust records from the EDML ice core also began to decrease from the peak. These data comprehensively indicate that the Last Deglaciation may have begun at ~19.6 Cal ka BP in the Southern Hemisphere (Jae Il et al., 2010; Yang et al., 2021).

The initial increase in the biogenic silicon content at the end of the last glacial period may have been due to the large consumption of siliceous nutrients in the water bodies south of the Antarctic Polar Front (Figure 4N) (Dumont et al., 2020). During HS1, the EDML-ssNa$^+$ value (Figure 4D), the IRD content (Figure 4H), and *A. actinochilus* abundance in core ANT36/C3-09 (Figure 4L) significantly decreased, indicating that the sea ice retreat process in the Cosmonaut Sea may have been approaching the end (Li et al., 2021). The sharp increases in Si/Ti and Ca/Ti ratios further suggest a rapid increase in the export productivity in the Cosmonaut Sea, which was likely due to significant amounts of nutrients and respiratory carbon reaching the surface ocean via the upwelling of deep water (Skinner et al., 2010; Jaccard et al., 2016; Gottschalk et al., 2020). With the decrease in the sea ice coverage, the surface layer of the Cosmonaut Sea received sufficient sunlight and the temperature increased in the Southern Hemisphere (Figure 4A), which may contribute to high levels of paleoproductivity (Frank et al., 2000; Kohfeld et al., 2005; Anderson et al., 2009; Jaccard et al., 2013; Thöle et al., 2019). In contrast, the $\delta^{15}N$ value continued to decline during HS1 and remained at a relatively low value (Figure 6B), indicating lower nutrient utilization compared to that during the LGM. This suggests that the decisive factor of increasing productivity was the increase in the nutrient supply from the lower layer of the Cosmonaut Sea, which also serves as evidence of enhanced ventilation (Kim et al., 2020). Macko and Estep (1984) argued that the oxidation of bottom water may lead to a decrease in bulk sedimentary $\delta^{15}N$ by suppressing the N isotope effect associated with denitrification (which generally produces low $\delta^{15}N$ NH_4^+). For instance, at ~12 Cal ka BP and ~16 Cal ka BP, two low values of $\delta^{15}N$ were observed in the core sediments, corresponding to the oxidation of bottom water during these two periods. However, empirical data, including the sediment trap results, suggest that even in slowly accumulating regions of the ocean, bulk sedimentary $\delta^{15}N$ records will primarily reflect changes in the $\delta^{15}N$ of exported N in most cases, rather than differential alteration (Robinson et al., 2012).

It should be noted that the Bio Ba values for core ANT37-C5/6-07 did not exhibit a significant peak during HS1 (Figure 4K), which is comparable with the data for cores PS1648-1 and PS1821-6 from the west of Cosmonaut Sea (Figures 4I, J) (Bonn, 1995). The preservation of biogenic barium is highly sensitive to changes in the paleoenvironmental conditions. When the sedimentary environment becomes oxygen or sulfate depleted, the solubility of $BaSO_4$ will greatly increase (McManus et al., 1998; Anderson et al., 2002; Beek et al., 2003; Tribovillard et al., 2006). McManus et al. (1998) argued that the Ba arriving at the seafloor under conditions of high carbon export and low bottom water oxygen may be poorly preserved—even in environments not showing significant porewater sulfate depletion. Poor preservation of Ba may also be indicated by high levels of aU. As shown in the Figure 7, during ~14–18 Cal ka BP, the Si/Ti ratios, U content (XRF), and TOC contents in the core sediments were relatively high, indicating the existence of such conditions of high organic carbon export and relatively low bottom-water oxygen, which led to the absence of a peak in the Bio Ba value during the middle stage of HS1.

An increase in the export productivity will lead to an increase in the consumption of oxygen via the decomposition of organic matter in the water body to some extent, causing a decrease in the oxygen content (Yamamoto et al., 2015). However, all of the records from the Cosmonaut Sea reveal that the oxygen content of the bottom water increased during this period (Figures 4E–G), indicating that the impact of organic matter remineralization on the oxygen content was minor (Amsler et al., 2022). To maintain oxygen levels, fresh and oxygen-rich surface seawater should be injected deep into the Cosmonaut Sea. We propose that the improved ventilation of the Southern Ocean during HS1, which was driven by the reduced generation of the North Atlantic Deep Water and the weakened Atlantic Meridional Overturning Circulation, played a major role in the increased oxygenation of the bottom water (McManus et al., 2004). The increase in water column temperature reduced the accumulation of respired carbon and possibly shifted the organic matter respiration to the upper water column, thereby decreasing the sinking flux of the organic matter to the abyss (Matsumoto, 2007). A deglacial decrease in the oceanic nutrient inventory could have also contributed to the reduction of the amount of organic matter available for respiration (Jaccard and Galbraith, 2012).

More importantly, it is crucial to note that the intensification of upwelling can result in an imbalance of the surface seawater's CO_2 budget. At the beginning of the last glacial termination period (TERM I) at ~17.5 Cal ka BP, radioactive carbon depleted CO_2 that was formed during the LGM and locked in the deep Southern Ocean was released into the atmosphere via the enhanced ventilation (Burke and Robinson, 2011; Bauska et al., 2016; Basak et al., 2018; Rae et al., 2018). Although the growth of phytoplankton was stimulated by the elevated nutrient levels, they were unable to completely assimilate and fix the dissolved carbon. This was evidenced by the low $\delta^{15}N$ values, indicating a low efficiency of the biological pump during this period, which permitted a considerable amount of CO_2 to escape into the atmosphere (Sigman et al., 2010; Studer et al., 2015).

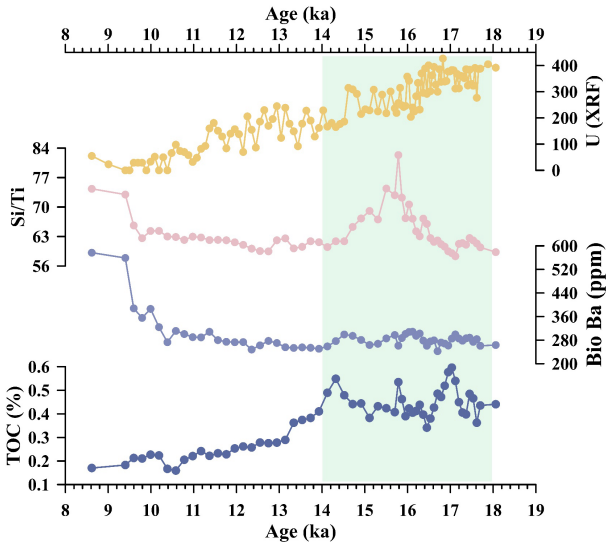

FIGURE 7
U content (XRF), Si/Ti ratios, Bio Ba content, and TOC content of core sediments during 8.6–18.1 Cal ka BP.

In the Southern Hemisphere, there was a cold period, which interrupted the warming trend near the deglacial midpoint, i.e., the ACR (14.7–13.1 Cal ka BP) (Shakun et al., 2012). The EDML-ssNa$^+$ value and *A. actinochilus* abundance rebounded during the ACR (Figures 4D, L), indicating that the sea ice resumed activity. The decrease in the summer insolation at 65°S (Figure 4C), coupled with the reflection from the sea ice and the temperature regulation (Figures 4A, K), limited the surface productivity of the Southern Ocean. The decrease in the productivity output also means that the nutrient supplementation in the surface seawater was deficient during the ACR, which may have been associated with the weakening of upwelling (Jaccard et al., 2013). This corresponded to a temporary cessation of the increase in the atmospheric CO_2 content (Figure 4B). The changes in the Mn/Ti ratio and U content (XRF) in core ANT37-C5/6-07 and the aU content in core PS2603-3 stagnated during the ACR (Figures 4E–G), indicating that the supplementation of the oxygen content in the deep Cosmonaut Sea was interrupted, which is further proof of the weakened ventilation in the study area.

During the YD, there was a notable improvement in the oxygenation levels of the bottom water in the Cosmonaut Sea (Figures 4E, F), but the improvement of the export productivity was very minimal (Figures 4M–O). The efficiency of the biological pump remained consistent with that during the ACR, i.e., it remained at a low level. The atmospheric CO_2 content continued to rise as it was supplemented by deep sea respiratory carbon (Figure 4B). In conclusion, during the HS1 period, the booming productivity of the Cosmonaut Sea was attributed to the favorable sunlight conditions and the increase in the nutrient supply by the enhanced ventilation, the latter also greatly facilitated the gas exchange between the surface and deep waters. However, during the latter half of the Last Deglaciation, the decrease in sunlight

intensity in the high-latitude regions of the Southern Hemisphere dominated the surface productivity of the Cosmonaut Sea.

5.2.3 Holocene

During the Early Holocene, the records in core ANT37-C5/6-07 indicate that a significant increase in siliceous productivity occurred (Figures 4M, N). However, the Ca/Ti ratio, which had previously been consistent with the Si/Ti ratio, exhibited a decreasing trend. The oxygen concentration of the bottom water remained high during the Early and Middle Holocene. Since the Middle Holocene (~5.5 Cal ka BP), the paleoproductivity in the Cosmonaut Sea has been comprehensively improved and maintained at a high level. The Bio Ba patterns of cores PS1648-1 and PS1821-6 are similar to that of core ANT37-C5/6-07 (Figures 4I, J, M). This suggests that the change in paleoproductivity may have been a more widespread phenomenon in the Indian Ocean sector of the Southern Ocean, rather than a regional characteristic.

We found that changes in the paleoproductivity were consistent with the variations in the summer solar radiation at 65°S in the Southern Hemisphere (Figure 4C), which helps to explain the widespread conditions mentioned above. During the Holocene, the amount of summer insolation in the high-latitude region in the Southern Hemisphere increased significantly. The retreat of the sea ice led to a reduction in the sunlight blocking efficiency, thus prolonging surface water exposure, which may have been one of the causes of the significant increase in the productivity in the Cosmonaut Sea since ~ 9.4 Cal ka BP (Boyd et al., 2001; Denis et al., 2010; Cheah et al., 2013). Furthermore, the utilization rate of nutrients indicated by the $\delta^{15}N$ values in the core reached a high level (Figure 6B), which was decoupled from Fe availability (Figure 6D) and was closely linked to the rapid increase in surface productivity during this time period. The existence of a tightly coupled glacier-sea ice-ocean system driven by insolation changes throughout the Holocene has also been revealed by the sedimentary records of the Adélie Land in the East Antarctica (Crosta et al., 2008; Denis et al., 2009a; Denis et al., 2009b; Denis et al., 2010). The high oxygen content of the bottom water of the Cosmonaut Sea suggests that deep-water ventilation has been favorable during the Holocene. Despite the negative effects of both the high export productivity (Figures 4M, N) and the increase in temperature (Figure 4K), the enhanced ventilation dominated the level of oxygenation, leading to the overall high oxygen content of the Cosmonaut Sea bottom water during the Holocene.

The East Cosmonaut Sea Polynya (ECP) may be another important driving factor of the local paleoproductivity and oxygenation changes. Comiso and Gordon (1996) reported that the ECP occurs regularly on a long-term basis, with an average central position at 65°S (range of 64–66°S) and 52°E (range of 42–57°E) near Cape Ann during winter in the Southern Hemisphere. This polynya is among the most persistent polynyas in the Southern Ocean, and it has been observed almost every year since the availability of satellite passive microwave data in December 1972. The formation of the ECP may have been triggered by either ocean forcing (Comiso and Gordon, 1996) or offshore divergent winds (Arbetter et al., 2004; Bailey et al., 2004) or a combination of both processes (Figure 7) (Prasad et al., 2005). The unique configuration of the coastline plays an important role in this process (Comiso and Gordon, 1996; Prasad et al., 2005). Due to the vast northward extension of Cape Ann, the westward flowing CC and the eastward flowing ACC form a high level of boundary forcing in this region. According to climatological data, it has been argued that this offshore location experienced upwelling of the warm salty CDW, which broke the original sea ice cover, and may have also played a key role in promoting deep-sea ventilation (Figure 8) (Prasad et al., 2005). The newly formed sea ice is constantly pushed off the coast by strong katabatic winds (Francis et al., 2019). The increase in the IRD content in the core sediments since ~9.4 Cal ka BP was likely caused by the continuous offshore transportation, dissolution, and release of detrital materials carried by fragmented sea ice (Figure 4H).

A previous study has shown that the chlorophyll-*a* concentration is higher in the Maud Rise Polynya than in the surrounding region during austral spring (von Berg et al., 2020). Jena and Pillai (2020) suggested that this could be the result of the improved irradiance conditions and increased iron supply through upwelling after the formation of polynyas. During the Holocene, the sea surface temperature of the Cosmonaut Sea was higher than during the Last Glacial Maximum, and there was a decrease in the abundance of *A. actinochilus* (Figures 4K, L), which indicates a decrease in sea ice concentration during this period. Based on the positive impact of the polynya system on the local export productivity and deep-water ventilation, combined with the increase in the IRD content of the benthic sediments, we speculate that the formation and development history of the ECP can be traced back to ~9.4 Cal ka BP, but we still lack more evidence of changes in ECP on the millennial scale. In general, the Cosmonaut Sea region was in a well-ventilated state during the Holocene.

6 Conclusions

Valuable proxies reveal that the paleoproductivity and oxygen levels were low in the Cosmonaut Sea during the LGM. Furthermore, the nutrient utilization rate by the phytoplankton in the surface seawater was at a relatively high level. This indicates that the Cosmonaut Sea deep water was in a state of weak ventilation, which hindered the nutrient supply to the surface ocean. The pre-formed carbon storage led to significant oxygen consumption, while the respiratory CO_2 formed was trapped in the deep Southern Ocean. This likely contributed to the low atmospheric CO_2 content during the LGM period.

During the Last Deglaciation, a significant increase in the export productivity was caused by the increase in the nutrient supply from the deep Cosmonaut Sea. However, the utilization rate of nutrients was low, indicating the inefficient assimilation of nutrients and dissolved CO_2 by the phytoplankton in the surface seawater. A large amount of respiratory CO_2 was released into the atmosphere via the enhanced ventilation. In addition, the supplementation of the dissolved oxygen from the surface water exceeded the consumption caused by the increased export productivity, leading to an improvement in the degree of oxygenation. However, there were noticeable interruptions

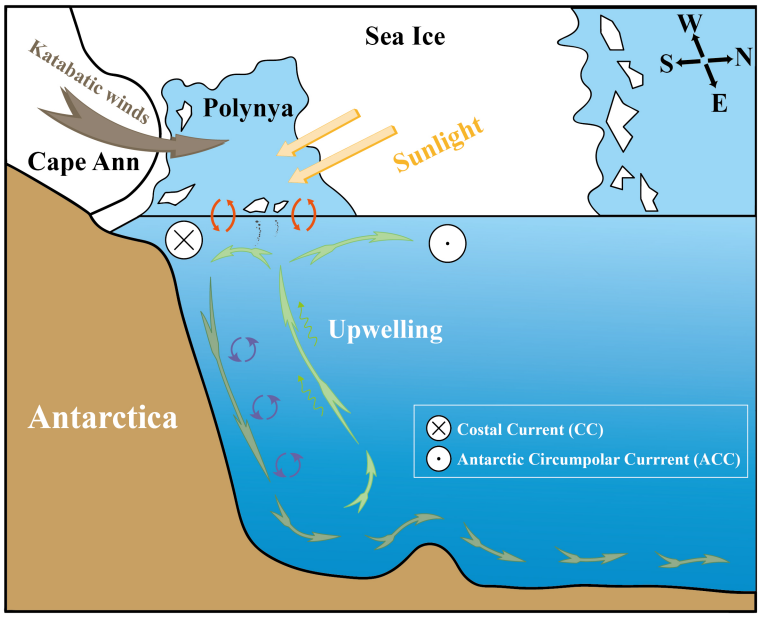

FIGURE 8
Enhanced ventilation under the East Cosmonaut Polynya conditions since the Holocene.

during the Last Deglaciation, which were triggered by the transitions from the HS1 to the ACR.

The paleoproductivity in the Cosmonaut Sea experienced two increases in the Early Holocene and Middle Holocene respectively. We speculate that the changes in the summer insolation at high southern latitudes have significantly contributed to the increased productivity. After the Middle Holocene, there was a comprehensive improvement in the productivity within the Indian Ocean sector of the Southern Ocean, accompanied by a simultaneous increase in the nutrient utilization rates. The replenishment of oxygen dominated the changes in the oxygen content of the bottom-water, which was potentially related to the enhanced ventilation during the Holocene and/or the formation of the East Cosmonaut Sea Polynya.

Data availability statement

The raw data supporting the conclusions of this article will be made available by the authors, without undue reservation.

Author contributions

The contribution from the authors are as follows: LH: methodology, data analysis and visualization, paper writing. YZ: conceptualization of the study and data acquisition. YW: methodology, data acquisition and data curation. PM: data analysis and data visualization. WW: methodology and data curation. QG: core chronology methodology, funding acquisition. YB: methodology, data curation and paper revision. XH: investigation, methodology, paper revision and funding acquisition. All authors contributed to the article and approved the submitted version

Funding

This research is funded by National Key R&D Program of China (2022YFC2905500), Impact and Response of Antarctic Seas to Climate Change (IRASCC2020-2022).

Acknowledgments

We are very grateful to all of the scientific expedition staff, especially the teachers and students of the Marine Geology and the Geophysics Working Group, and all of the crew of the R/V "XUELONG2" icebreaker for their hard work in sampling during the 37th Chinese Antarctic Research Expedition. We sincerely thank the Chinese Arctic and Antarctic Administration and Polar Research Institute of China for their great help in this research.

Conflict of interest

The authors declare that the research was conducted in the absence of any commercial or financial relationships that could be construed as a potential conflict of interest.

Publisher's note

All claims expressed in this article are solely those of the authors and do not necessarily represent those of their affiliated organizations, or those of the publisher, the editors and the reviewers. Any product that may be evaluated in this article, or claim that may be made by its manufacturer, is not guaranteed or endorsed by the publisher.

References

Abram, N. J., Wolff, E. W., and Curran, M. A. J. (2013). A review of sea ice proxy information from polar ice cores. *Quat. Sci. Rev.* 79, 168–183. doi: 10.1016/j.quascirev.2013.01.011

Adkins, J. F. (2013). The role of deep ocean circulation in setting glacial climates. *Paleoceanography* 28 (3), 539–561. doi: 10.1002/palo.20046

Adkins, J. F., McIntyre, K., and Schrag, D. P. (2002). The salinity, temperature, and $\delta^{18}O$ of the glacial deep ocean. *Science* 298 (5599), 1769–1773. doi: 10.1126/science.1076252

Agnihotri, R., Altabet, M. A., Herbert, T. D., and Tierney, J. E. (2008). Subdecadally resolved paleoceanography of the Peru margin during the last two millennia. *Geochem. Geophys. Geosystems* 9 (5), Q05013. doi: 10.1029/2007GC001744

Ai, X. E., Studer, A. S., Sigman, D. M., Martínez-García, A., Fripiat, F., Thöle, L. M., et al. (2020). Southern Ocean upwelling, Earth's obliquity, and glacial-interglacial atmospheric CO_2 change. *Science* 370 (6522), 1348–1352. doi: 10.1126/science.abd2115

Altabet, M. A., and Francois, R. (1994). Sedimentary nitrogen isotopic ratio as a recorder for surface ocean nitrate utilization. *Glob. Biogeochem. Cycles* 8 (1), 103–116. doi: 10.1029/93GB03396

Amsler, H. E., Thöle, L. M., Stimac, I., Geibert, W., Ikehara, M., Kuhn, G., et al. (2022). Bottom water oxygenation changes in the Southwestern Indian Ocean as an indicator for enhanced respired carbon storage since the last glacial inception. *Climate Past* 18 (8), 1797–1813. doi: 10.5194/cp-18-1797-2022

Anderson, R. F., Ali, S., Bradtmiller, L. I., Nielsen, S. H. H., Fleisher, M. Q., Anderson, B. E., et al. (2009). Wind-driven upwelling in the southern ocean and the deglacial rise in atmospheric CO_2. *Science* 323 (5920), 1443–1448. doi: 10.1126/science.1167441

Anderson, R. F., Chase, Z., Fleisher, M. Q., and Sachs, J. (2002). The Southern Ocean's biological pump during the Last Glacial Maximum. *Deep Sea Res. Part II: Topical Stud. Oceanography* 49 (9), 1909–1938. doi: 10.1016/S0967-0645(02)00018-8

Anderson, R. F., Sachs, J. P., Fleisher, M. Q., Allen, K. A., Yu, J., Koutavas, A., et al. (2019). Deep-sea oxygen depletion and ocean carbon sequestration during the last ice age. *Glob. Biogeochem. Cycles* 33 (3), 301–317. doi: 10.1029/2018GB006049

Andrews, J. T., Domack, E. W., Cunningham, W. L., Leventer, A., Licht, K. J., Jull, A. J. T., et al. (1999). Problems and possible solutions concerning radiocarbon dating of surface marine sediments, ross sea, Antarctica. *Quat. Res.* 52 (2), 206–216. doi: 10.1006/qres.1999.2047

Anilkumar, N., Chacko, R., Sabu, P., Pillai, H. U. K., George, J. V., and Achuthankutty, C. T. (2014). Biological response to physical processes in the Indian Ocean sector of the Southern Ocean: a case study in the coastal and oceanic waters. *Environ. Monit. Assess.* 186 (12), 8109–8124. doi: 10.1007/s10661-014-3990-4

Aoki, S., Katsumata, K., Hamaguchi, M., Noda, A., Kitade, Y., Shimada, K., et al. (2020). Freshening of antarctic bottom water off cape darnley, East Antarctica. *J. Geophysical Research: Oceans* 125 (8), e2020JC016374. doi: 10.1029/2020JC016374

Arbetter, T. E., Lynch, A. H., and Bailey, D. A. (2004). Relationship between synoptic forcing and polynya formation in the Cosmonaut Sea: 1. Polynya climatology. *J. Geophysical Research: Oceans* 109 (C4), C04022. doi: 10.1029/2003JC001837

Armand, L. K., Crosta, X., Romero, O., and Pichon, J.-J. (2005). The biogeography of major diatom taxa in Southern Ocean sediments: 1. Sea ice related species. *Palaeogeogr. Palaeoclimatol. Palaeoecol.* 223 (1), 93–126. doi: 10.1016/j.palaeo.2005.02.015

Bailey, D. A., Lynch, A. H., and Arbetter, T. E. (2004). Relationship between synoptic forcing and polynya formation in the Cosmonaut Sea: 2. Regional climate model simulations. *J. Geophysical Research: Oceans* 109 (C4), C04022. doi: 10.1029/2003JC001838

Basak, C., Fröllje, H., Lamy, F., Gersonde, R., Benz, V., Anderson, R., et al. (2018). Breakup of last glacial deep stratification in the South Pacific. *Science* 359, 900–904. doi: 10.1126/science.aao2473

Bauska, T. K., Baggenstos, D., Brook, E. J., Mix, A. C., Marcott, S. A., Petrenko, V. V., et al. (2016). Carbon isotopes characterize rapid changes in atmospheric carbon dioxide during the last deglaciation. *Proc. Natl. Acad. Sci. U.S.A.* 113 (13), 3465–3470. doi: 10.1073/pnas.1513868113

Beek, P., Reyss, J.-L., Bonté, P., and Schmidt, S. (2003). Sr/Ba in barite: A proxy of barite preservation in marine sediments? *Mar. Geol.* 199, 205–220. doi: 10.1016/S0025-3227(03)00220-2

Berg, S., Leng, M. J., Kendrick, C. P., Cremer, H., and Wagner, B. (2013). Bulk sediment and diatom silica carbon isotope composition from coastal marine sediments off East Antarctica. *Silicon* 5 (1), 19–34. doi: 10.1007/s12633-012-9113-3

Bibik, V. A., Maslennikov, V. V., Pelevin, A. S., Polonsky, V. E., and Solyankin, E. V. (1988). "The current system and the distribution of waters of different modifications in the Cosmonaut Sea," in *Interdisciplinary investigations of pelagic ecosystem in the commonwealth and cosmonaut seas*. Eds. T. G. Lubimova, R. R. Makarov, V. V. Maslennikov, E. Z. Samyshev, V. A. Bibik and T. G. Tarverdieva (Moscow: VNIRO Publishers), 16–43.

Bonn, W. J. (1995). "Biogenopal und biogenes Barium als Indikatoren für spätquartäre Produktivitätsänderungen am antarktischen Kontinentalhang, atlantischer Sektor (Biogenic opal and barium: Indicators for late Quarternary changes in productivity at the Antarctic continental margin, Atlantic Sector)," in *Berichte zur polarforschung = Reports on polar research* (Bremerhaven, Germany: Alfred-Wegener-Institut für Polar- und Meeresforschung), 1–186.

Bonn, W. J., Gingele, F. X., Grobe, H., Mackensen, A., and Fütterer, D. K. (1998). Palaeoproductivity at the Antarctic continental margin: Opal and barium records for the last 400 ka. *Palaeogeogr. Palaeoclimatol. Palaeoecol.* 139 (3), 195–211. doi: 10.1016/S0031-0182(97)00144-2

Bouttes, N., Paillard, D., and Roche, D. M. (2010). Impact of brine-induced stratification on the glacial carbon cycle. *Clim. Past* 6 (5), 575–589. doi: 10.5194/cp-6-575-2010

Boyd, P. W., Crossley, A. C., DiTullio, G. R., Griffiths, F. B., Hutchins, D. A., Queguiner, B., et al. (2001). Control of phytoplankton growth by iron supply and irradiance in the subantarctic Southern Ocean: Experimental results from the SAZ Project. *J. Geophysical Research: Oceans* 106 (C12), 31573–31583. doi: 10.1029/2000JC000348

Brown, E. T., Le Callonnec, L., and German, C. R. (2000). Geochemical cycling of redox-sensitive metals in sediments from lake Malawi: A diagnostic paleotracer for episodic changes in mixing depth. *Geochimica Cosmochimica Acta* 64 (20), 3515–3523. doi: 10.1016/S0016-7037(00)00460-9

Brumsack, H. J. (1989). Geochemistry of recent TOC-rich sediments from the Gulf of California and the Black Sea. *Geologische Rundschau* 78 (3), 851–882. doi: 10.1007/BF01829327

Burke, A., and Robinson, L. (2011). The Southern ocean's role in carbon exchange during the last deglaciation. *Sci. (New York N.Y.)* 335, 557–561. doi: 10.1126/science.1208163

Calvert, S. E., and Pedersen, T. F. (1993). Geochemistry of Recent oxic and anoxic marine sediments: Implications for the geological record. *Mar. Geol.* 113 (1), 67–88. doi: 10.1016/0025-3227(93)90150-T

Calvert, S. E., and Pedersen, T. F. (1996). Sedimentary geochemistry of manganese; implications for the environment of formation of manganiferous black shales. *Econ. Geol.* 91 (1), 36–47. doi: 10.2113/gsecongeo.91.1.36

Cheah, W., McMinn, A., Griffiths, F. B., Westwood, K. J., Wright, S. W., and Clementson, L. A. (2013). Response of phytoplankton photophysiology to varying environmental conditions in the sub-antarctic and polar frontal zone. *PLoS One* 8 (8), e72165. doi: 10.1371/journal.pone.0072165

Cheshire, H., and Thurow, J. W. (2005). Late Quaternary climate change record from two long sediment cores from Guaymas Basin, Gulf of California. *J. Quat. Sci.* 20 (5), 457–469. doi: 10.1002/jqs.944

Comiso, J. C. (2003). "Large-scale characteristics and variability of the global sea ice cover," in *Sea ice*. (Oxford: Blackwell), 112–142.

Comiso, J. C., and Gordon, A. L. (1996). Cosmonaut polynya in the Southern Ocean: Structure and variability. *J. Geophysical Research: Oceans* 101 (C8), 18297–18313. doi: 10.1029/96JC01500

Crosta, X., Denis, D., and Ther, O. (2008). Sea ice seasonality during the Holocene, Adélie Land, East Antarctica. *Mar. Micropaleontol.* 66 (3), 222–232. doi: 10.1016/j.marmicro.2007.10.001

Crosta, X., Romero, O., Armand, L. K., and Pichon, J.-J. (2005). The biogeography of major diatom taxa in Southern Ocean sediments: 2. Open ocean related species. *Palaeogeogr. Palaeoclimatol. Palaeoecol.* 223 (1), 66–92. doi: 10.1016/j.palaeo.2005.03.028

Dehairs, F., Chesselet, R., and Jedwab, J. (1980). Discrete suspended particles of barite and the barium cycle in the open ocean. *Earth Planetary Sci. Lett.* 49 (2), 528–550. doi: 10.1016/0012-821X(80)90094-1

Dehairs, F., Stroobants, N., and Goeyens, L. (1991). Suspended barite as a tracer of biological activity in the Southern Ocean. *Mar. Chem.* 35 (1), 399–410. doi: 10.1016/S0304-4203(09)90032-9

DeMaster, D. J., Nelson, T. M., Harden, S. L., and Nittrouer, C. A. (1991). The cycling and accumulation of biogenic silica and organic carbon in Antarctic deep-sea and continental margin environments. *Mar. Chem.* 35 (1), 489–502. doi: 10.1016/S0304-4203(09)90039-1

Denis, D., Crosta, X., Barbara, L., Massé, G., Renssen, H., Ther, O., et al. (2010). Sea ice and wind variability during the Holocene in East Antarctica: Insight on middle-high latitude coupling. *Quat. Sci. Rev.* 29 (27), 3709–3719. doi: 10.1016/j.quascirev.2010.08.007

Denis, D., Crosta, X., Schmidt, S., Carson, D. S., Ganeshram, R. S., Renssen, H., et al. (2009a). Holocene glacier and deep water dynamics, Adélie Land region, East Antarctica. *Quat. Sci. Rev.* 28 (13), 1291–1303. doi: 10.1016/j.quascirev.2008.12.024

Denis, D., Crosta, X., Schmidt, S., Carson, D. S., Ganeshram, R. S., Renssen, H., et al. (2009b). Holocene productivity changes off Adélie Land (East Antarctica). *Paleoceanography* 24 (3), PA3207. doi: 10.1029/2008PA001689

Dieckmann, G. S., and Hellmer, H. H. (2003). "The importance of sea ice: An overview," in *Sea ice*. (Oxford: Blackwell), 1–21.

Diekmann, B., and Kuhn, G. (1999). Provenance and dispersal of glacial–marine surface sediments in the Weddell Sea and adjoining areas, Antarctica: Ice-rafting versus current transport. *Mar. Geol.* 158 (1), 209–231. doi: 10.1016/S0025-3227(98)00165-0

Domack, E. W., Jacobson, E. A., Shipp, S., and Anderson, J. B. (1999). Late Pleistocene–Holocene retreat of the West Antarctic Ice-Sheet system in the Ross Sea:

Part 2—Sedimentologic and stratigraphic signature. *GSA Bull.* 111 (10), 1517–1536. doi: 10.1130/0016-7606(1999)111<1517:LPHROT>2.3.CO;2

Domack, E., Leventer, A., Dunbar, R., Taylor, F., Brachfeld, S., and Sjunneskog, C. (2001). Chronology of the Palmer Deep site, Antarctic Peninsula: a Holocene palaeoenvironmental reference for the circum-Antarctic. *Holocene* 11 (1), 1–9. doi: 10.1191/095968301673881493

Dumont, M., Pichevin, L., Geibert, W., Crosta, X., Michel, E., Moreton, S., et al. (2020). The nature of deep overturning and reconfigurations of the silicon cycle across the last deglaciation. *Nat. Commun.* 11 (1), 1534. doi: 10.1038/s41467-020-15101-6

Durgadoo, J. V., Lutjeharms, J. R. E., Biastoch, A., and Ansorge, I. J. (2008). The conrad rise as an obstruction to the antarctic circumpolar current. *Geophysical Res. Lett.* 35 (20), L20606. doi: 10.1029/2008GL035382

Dymond, J., Suess, E., and Lyle, M. (1992). Barium in deep-sea sediment: A geochemical proxy for paleoproductivity. *Paleoceanography* 7 (2), 163–181. doi: 10.1029/92PA00181

Emerson, S., and Hedges, J. I. (1988). Processes controlling the organic carbon content of open ocean sediments. *Paleoceanography* 3 (5), 621–634. doi: 10.1029/PA003i005p00621

EpicaCommunityMembers (2006). One-to-one coupling of glacial climate variability in Greenland and Antarctica. *Nature* 444 (7116), 195–198. doi: 10.1038/nature05301

Esper, O., and Gersonde, R. (2014a). New tools for the reconstruction of Pleistocene Antarctic sea ice. *Palaeogeogr. Palaeoclimatol. Palaeoecol.* 399, 260–283. doi: 10.1016/j.palaeo.2014.01.019

Esper, O., and Gersonde, R. (2014b). Quaternary surface water temperature estimations: New diatom transfer functions for the Southern Ocean. *Palaeogeogr. Palaeoclimatol. Palaeoecol.* 414, 1–19. doi: 10.1016/j.palaeo.2014.08.008

Esper, O., Gersonde, R., and Kadagies, N. (2010). Diatom distribution in southeastern Pacific surface sediments and their relationship to modern environmental variables. *Palaeogeogr. Palaeoclimatol. Palaeoecol.* 287 (1), 1–27. doi: 10.1016/j.palaeo.2009.12.006

Fagel, N., Dehairs, F., André, L., Bareille, G., and Monnin, C. (2002). Ba distribution in surface Southern Ocean sediments and export production estimates. *Paleoceanography* 17 (2), 1–1-1-20. doi: 10.1029/2000PA000552

Ferrari, R., Jansen, M. F., Adkins, J. F., Burke, A., Stewart, A. L., and Thompson, A. F. (2014). Antarctic sea ice control on ocean circulation in present and glacial climates. *Proc. Natl. Acad. Sci.* 111 (24), 8753–8758. doi: 10.1073/pnas.1323922111

Fischer, H., Fundel, F., Ruth, U., Twarloh, B., Wegner, A., Udisti, R., et al. (2007). Reconstruction of millennial changes in dust emission, transport and regional sea ice coverage using the deep EPICA ice cores from the Atlantic and Indian Ocean sector of Antarctica. *Earth Planetary Sci. Lett.* 260 (1), 340–354. doi: 10.1016/j.epsl.2007.06.014

Fontugne, M. R., and Jouanneau, J.-M. (1987). Modulation of the particulate organic carbon flux to the ocean by a macrotidal estuary: Evidence from measurements of carbon isotopes in organic matter from the Gironde system. *Estuarine Coast. Shelf Sci.* 24 (3), 377–387. doi: 10.1016/0272-7714(87)90057-6

Francis, D., Eayrs, C., Cuesta, J., and Holland, D. (2019). Polar cyclones at the origin of the reoccurrence of the maud rise polynya in austral winter 2017. *J. Geophysical Research: Atmospheres* 124 (10), 5251–5267. doi: 10.1029/2019JD030618

Francois, R., Altabet, M. A., and Burckle, L. H. (1992). Glacial to interglacial changes in surface nitrate utilization in the Indian Sector of the Southern Ocean as recorded by sediment δ^{15}N. *Paleoceanography* 7 (5), 589–606. doi: 10.1029/92PA01573

François, R., Altabet, M. A., Yu, E.-F., Sigman, D. M., Bacon, M. P., Frank, M., et al. (1997). Contribution of Southern Ocean surface-water stratification to low atmospheric CO_2 concentrations during the last glacial period. *Nature* 389 (6654), 929–935. doi: 10.1038/40073

Frank, M., Gersonde, R., van der Loeff, M. R., Bohrmann, G., Nürnberg, C. C., Kubik, P. W., et al. (2000). Similar glacial and interglacial export bioproductivity in the Atlantic Sector of the Southern Ocean: Multiproxy evidence and implications for glacial atmospheric CO_2. *Paleoceanography* 15 (6), 642–658. doi: 10.1029/2000PA000497

Frazer, T. K. (1996). Stable isotope composition (δ^{13}C and δ^{15}N) of larval krill, Euphausia superba, and two of its potential food sources in winter. *J. Plankton Res.* 18 (8), 1413–1426. doi: 10.1093/plankt/18.8.1413

Fudge, T. J., Steig, E. J., Markle, B. R., Schoenemann, S. W., Ding, Q., Taylor, K. C., et al. (2013). Onset of deglacial warming in West Antarctica driven by local orbital forcing. *Nature* 500 (7463), 440–444. doi: 10.1038/nature12376

Galbraith, E. D., and Jaccard, S. L. (2015). Deglacial weakening of the oceanic soft tissue pump: global constraints from sedimentary nitrogen isotopes and oxygenation proxies. *Quat. Sci. Rev.* 109, 38–48. doi: 10.1016/j.quascirev.2014.11.012

Galbraith, E. D., and Skinner, L. C. (2020). The biological pump during the last glacial maximum. *Ann. Rev. Mar. Sci.* 12, 559–586. doi: 10.1146/annurev-marine-010419-010906

Gao, Z.-Y., and Chen, L.-Q. (2002). Study of carbon cycling in the southern ocean: A review. *World Sci-Tech R D* 04), 41–48. doi: 10.16507/j.issn.1006-6055.2002.04.012

Gao, X.-L., Chen, S.-Y., Ma, F.-J., Dang, A.-C., and Long, A.-M. (2008). Distribution and source characteristics of carbon and nitrogen and their burial fluxes in two core sediments from western Nansha Islands sea area. *J. Trop. Oceanography* 27 (03), 38–44.

Gao, Z.-Y., Chen, L.-Q., and Wang, W.-Q. (2001). Air-sea fluxes and the distribution of sink and source of CO2 between 80°W and 80°E in the Southern Ocean. *Chin. J. Polar Res.* 13 (3), 263–269.

Gersonde, R., Crosta, X., Abelmann, A., and Armand, L. (2005). Sea-surface temperature and sea ice distribution of the Southern Ocean at the EPILOG Last Glacial Maximum—a circum-Antarctic view based on siliceous microfossil records. *Quat. Sci. Rev.* 24 (7), 869–896. doi: 10.1016/j.quascirev.2004.07.015

Gibson, J. A. E., Trull, T., Nichols, P. D., Summons, R. E., and McMinn, A. (1999). Sedimentation of ^{13}C-rich organic matter from Antarctic sea-ice algae: A potential indicator of past sea-ice extent. *Geology* 27 (4), 331–334. doi: 10.1130/0091-7613(1999)027<0331:SOCROM>2.3.CO;2

Gillies, C. L., Stark, J. S., and Smith, S. D. A. (2012). Research article: small-scale spatial variation of δ^{13}C and δ^{15}N isotopes in Antarctic carbon sources and consumers. *Polar Biol.* 35 (6), 813–827. doi: 10.1007/s00300-011-1126-7

Gingele, F., and Dahmke, A. (1994). Discrete barite particles and barium as tracers of paleoproductivity in south Atlantic sediments. *Paleoceanography* 9 (1), 151–168. doi: 10.1029/93PA02559

Gottschalk, J., Michel, E., Thöle, L. M., Studer, A. S., Hasenfratz, A. P., Schmid, N., et al. (2020). Glacial heterogeneity in Southern Ocean carbon storage abated by fast South Indian deglacial carbon release. *Nat. Commun.* 11 (1), 6192. doi: 10.1038/s41467-020-20034-1

Gottschalk, J., Skinner, L. C., Lippold, J., Vogel, H., Frank, N., Jaccard, S. L., et al. (2016). Biological and physical controls in the Southern Ocean on past millennial-scale atmospheric CO_2 changes. *Nat. Commun.* 7 (1), 11539. doi: 10.1038/ncomms11539

Graham, R. M., De Boer, A. M., van Sebille, E., Kohfeld, K. E., and Schlosser, C. (2015). Inferring source regions and supply mechanisms of iron in the Southern Ocean from satellite chlorophyll data. *Deep Sea Res. Part I: Oceanographic Res. Papers* 104, 9–25. doi: 10.1016/j.dsr.2015.05.007

Han, X.-B., Zhao, J., Chu, F.-Y., Pan, J.-M., Tang, L.-G., Xu, D., et al. (2015). The source of organic matter and its sedimentary environment of the bottom surface sediment in northeast waters to Antarctic Peninsula based on the biomarker features. *Haiyang Xuebao* 37 (8), 26–38. doi: 10.3969/j.issn.0253-4193.2015.08.003

Harada, N., Handa, N., Fukuchi, M., and Ishiwatari, R. (1995). Source of hydrocarbons in marine sediments in Lützow-Holm Bay, Antarctica. *Org. Geochem.* 23 (3), 229–237. doi: 10.1016/0146-6380(94)00124-J

Heaton, T. J., Köhler, P., Butzin, M., Bard, E., Reimer, R. W., Austin, W. E. N., et al. (2020). Marine20—The marine radiocarbon age calibration curve (0–55,000 cal BP). *Radiocarbon* 62 (4), 779–820. doi: 10.1017/RDC.2020.68

Heywood, K. J., Sparrow, M. D., Brown, J., and Dickson, R. R. (1999). Frontal structure and Antarctic Bottom Water flow through the Princess Elizabeth Trough, Antarctica. *Deep Sea Res. Part I: Oceanographic Res. Papers* 46 (7), 1181–1200. doi: 10.1016/S0967-0637(98)00108-3

Hillenbrand, C.-D., Smith, J. A., Kuhn, G., Esper, O., Gersonde, R., Larter, R. D., et al. (2010). Age assignment of a diatomaceous ooze deposited in the western Amundsen Sea Embayment after the Last Glacial Maximum. *J. Quat. Sci.* 25 (3), 280–295. doi: 10.1002/jqs.1308

Hoogakker, B. A. A., Elderfield, H., Schmiedl, G., McCave, I. N., and Rickaby, R. E. M. (2015). Glacial–interglacial changes in bottom-water oxygen content on the Portuguese margin. *Nat. Geosci.* 8 (1), 40–43. doi: 10.1038/ngeo2317

Hu, B.-Y., Long, F.-J., Han, X.-B., Zhang, Y.-C., Hu, L.-M., Xiang, B., et al. (2022). The evolution of paleoproductivity since the Middle Holocene in the Cosmonaut Sea, Antarctic. *Earth Sci. Front.* 29 (4), 113–122. doi: 10.13745/j.esf.sf.2022.1.12

Hunt, B. P. V., Pakhomov, E. A., and Trotsenko, B. G. (2007). The macrozooplankton of the Cosmonaut Sea, east Antarctica (30°E–60°E), 1987–1990. *Deep Sea Res. Part I: Oceanographic Res. Papers* 54 (7), 1042–1069. doi: 10.1016/j.dsr.2007.04.002

Jaccard, S. L., and Galbraith, E. D. (2012). Large climate-driven changes of oceanic oxygen concentrations during the last deglaciation. *Nat. Geosci.* 5 (2), 151–156. doi: 10.1038/ngeo1352

Jaccard, S. L., Galbraith, E. D., Martínez-García, A., and Anderson, R. F. (2016). Covariation of deep Southern Ocean oxygenation and atmospheric CO_2 through the last ice age. *Nature* 530 (7589), 207–210. doi: 10.1038/nature16514

Jaccard, S. L., Haug, G. H., Sigman, D. M., Pedersen, T. F., Thierstein, H. R., and Röhl, U. (2005). Glacial/interglacial changes in subarctic north pacific stratification. *Science* 308 (5724), 1003–1006. doi: 10.1126/science.1108696

Jaccard, S. L., Hayes, C. T., Martínez-García, A., Hodell, D. A., Anderson, R. F., Sigman, D. M., et al. (2013). Two modes of change in southern ocean productivity over the past million years. *Science* 339 (6126), 1419–1423. doi: 10.1126/science.1227545

Jacobel, A. W., McManus, J. F., Anderson, R. F., and Winckler, G. (2017). Repeated storage of respired carbon in the equatorial Pacific Ocean over the last three glacial cycles. *Nat. Commun.* 8 (1), 1727. doi: 10.1038/s41467-017-01938-x

Jae Il, L., Bak, Y.-S., Yoo, K.-C., Hyoun Soo, L., Ho Il, Y., and Suk Hee, Y. (2010). Climate changes in the South Orkney Plateau during the last 8600 years. *Holocene* 20 (3), 395–404. doi: 10.1177/0959683609353430

Jena, B., and Pillai, A. N. (2020). Satellite observations of unprecedented phytoplankton blooms in the Maud Rise polynya, Southern Ocean. *Cryosphere* 14 (4), 1385–1398. doi: 10.5194/tc-14-1385-2020

Keir, R. S. (1988). On the Late Pleistocene ocean geochemistry and circulation. *Paleoceanography* 3 (4), 413–445. doi: 10.1029/PA003i004p00413

Kim, S., Yoo, K.-C., Lee, J. I., Roh, Y. H., Bak, Y.-S., Um, I.-K., et al. (2020). Paleoceanographic changes in the Southern Ocean off Elephant Island since the last

glacial period: Links between surface water productivity, nutrient utilization, bottom water currents, and ice-rafted debris. *Quat. Sci. Rev.* 249, 106563. doi: 10.1016/j.quascirev.2020.106563

Klyausov, A. V., and Lanin, V. I. (1988). "On the near-shelf frontal zone in the Commonwealth and Cosmonaut Seas," in *Interdisciplinary investigations of pelagic ecosystem in the commonwealth and cosmonaut seas*. Eds. T. G. Lubimova, R. R. Makarov, V. V. Maslennikov, E. Z. Samyshev, V. A. Bibik and T. G. Tarverdieva (Moscow: VNIRO Publishers), 56–62.

Kohfeld, K. E., Quéré, C. L., Harrison, S. P., and Anderson, R. F. (2005). Role of marine biology in glacial-interglacial CO_2 cycles. *Science* 308 (5718), 74–78. doi: 10.1126/science.1105375

Kopczyńska, E. E., Goeyens, L., Semeneh, M., and Dehairs, F. (1995). Phytoplankton composition and cell carbon distribution in Prydz Bay, Antarctica: relation to organic particulate matter and its $\delta^{13}C$ values. *J. Plankton Res.* 17 (4), 685–707. doi: 10.1093/plankt/17.4.685

Kulbe, T., Melles, M., Verkulich, S. R., and Pushina, Z. V. (2001). East antarctic climate and environmental variability over the last 9400 years inferred from marine sediments of the bunger oasis. *Arctic Antarctic Alpine Res.* 33 (2), 223–230. doi: 10.2307/1552223

Langmuir, D. (1978). Uranium solution-mineral equilibria at low temperatures with applications to sedimentary ore deposits. *Geochimica Cosmochimica Acta* 42 (6, Part A), 547–569. doi: 10.1016/0016-7037(78)90001-7

Laskar, J., Robutel, P., Joutel, F., Gastineau, M., Correia, A. C. M., and Levrard, B. (2004). A long-term numerical solution for the insolation quantities of the Earth. *Astronomy Astrophysics* 428, 261–285. doi: 10.1051/0004-6361:20041335

Learman, D. R., Henson, M. W., Thrash, J. C., Temperton, B., Brannock, P. M., Santos, S. R., et al. (2016). Biogeochemical and Microbial Variation across 5500 km of Antarctic Surface Sediment Implicates Organic Matter as a Driver of Benthic Community Structure. *Front. Microbiol.* 7. doi: 10.3389/fmicb.2016.00284

Lei, Z.-Y., Ge, Q., Chen, D., Zhang, Y.-C., Han, X.-B., Ye, L.-M., et al. (2021). The paleoclimatic significance and sources of sediments from the Amundsen Sea in West Antarctic since Mid-Holocene. *Earth Sci. Front.* 29 (4), 179–190. doi: 10.13745/j.esf.sf.2022.1.7

Li, C., Love, G. D., Lyons, T. W., Fike, D. A., Sessions, A. L., and Chu, X.-L. (2010). A stratified redox model for the ediacaran ocean. *Science* 328 (5974), 80–83. doi: 10.1126/science.1182369

Li, Q.-M., Xiao, W.-S., Wang, R.-J., and Chen, Z.-H. (2021). Diatom based reconstruction of climate evolution through the Last Glacial Maximum to Holocene in the Cosmonaut Sea, East Antarctica. *Deep Sea Res. Part II: Topical Stud. Oceanography* 194, 104960. doi: 10.1016/j.dsr2.2021.104960

Licht, K. J., and Andrews, J. T. (2002). The ^{14}C record of late pleistocene ice advance and retreat in the central ross sea, Antarctica. *Arctic Antarctic Alpine Res.* 34, 324–333.

Lin, H.-L., Lai, C.-T., Ting, H.-C., Wang, L., Sarnthein, M., and Hung, J.-J. (1999). Late Pleistocene nutrients and sea surface productivity in the South China Sea: a record of teleconnections with Northern hemisphere events. *Mar. Geol.* 156 (1), 197–210. doi: 10.1016/S0025-3227(98)00179-0

Liu, H.-L., Chen, Z.-H., Ge, S.-L., Xiao, W.-S., Wang, H.-Z., Tang, Z., et al. (2015). Late Quaternary sedimentary records and paleoceanographic implications from the core on continental slope off the Prydz Bay, East Antarctic. *Mar. Geology Quaternary Geology* 35 (03), 209–217. doi: 10.3724/SP.J.1140.2015.03209

Liu, R.-J., Yu, P.-S., Hu, C.-Y., Han, Z.-B., and Pan, J.-M. (2014). Contents and distributions of organic carbon and total nitrogen in sediments of Prydz Bay, Antarctic. *Acta Oceanologica Sin.* 36 (4), 118–125.

Macko, S. A., and Estep, M. L. F. (1984). Microbial alteration of stable nitrogen and carbon isotopic compositions of organic matter. *Org. Geochem.* 6, 787–790. doi: 10.1016/01466380(84)90100-1

Macko, S., and Pereira, C. (1990). Neogene paleoclimate development of the antarctic weddell sea region: Organic geochemistry. *Proceedings of the Ocean Drilling Program, Scientific Results* 113, 881–897. doi: 10.2973/odp.proc.sr.113.190.1990

Matsumoto, K. (2007). Biology-mediated temperature control on atmospheric pCO2 and ocean biogeochemistry. *Geophys. Res. Lett.* 34 (20), L20605. doi: 10.1029/2007GL031301

McManus, J., Berelson, W. M., Klinkhammer, G. P., Johnson, K. S., Coale, K. H., Anderson, R. F., et al. (1998). Geochemistry of barium in marine sediments: implications for its use as a paleoproxy. *Geochimica Cosmochimica Acta* 62 (21), 3453–3473. doi: 10.1016/S0016-7037(98)00248-8

McManus, J. F., Francois, R., Gherardi, J. M., Keigwin, L. D., and Brown-Leger, S. (2004). Collapse and rapid resumption of Atlantic meridional circulation linked to deglacial climate changes. *Nature* 428 (6985), 834–837. doi: 10.1038/nature02494

Mei, J., Wang, R.-J., Zhang, T.-L., Xiao, W.-S., Chen, Z.-H., Chen, J.-F., et al. (2015). Paleoceanopraphic records of core 08P31 on the Chukchi Plateau, Weatern Arctic Ocean. *Haiyang Xuebao* 37 (5), 121–135. doi: 10.3969/j.issn.0253-4193.2015.05.012

Meijers, A. J. S., Klocker, A., Bindoff, N. L., Williams, G. D., and Marsland, S. J. (2010). The circulation and water masses of the Antarctic shelf and continental slope between 30 and 80°E. *Deep Sea Res. Part II: Topical Stud. Oceanography* 57 (9), 723–737. doi: 10.1016/j.dsr2.2009.04.019

Meyers, P. A. (1997). Organic geochemical proxies of paleoceanographic, paleolimnologic, and paleoclimatic processes. *Org. Geochem.* 27 (5), 213–250. doi: 10.1016/S0146-6380(97)00049-1

Middelburg, J. J., De Lange, G. J., and van der Weijden, C. H. (1987). Manganese solubility control in marine pore waters. *Geochimica Cosmochimica Acta* 51 (3), 759–763. doi: 10.1016/0016-7037(87)90086-X

Monnin, E., Steig, E. J., Siegenthaler, U., Kawamura, K., Schwander, J., Stauffer, B., et al. (2004). Evidence for substantial accumulation rate variability in Antarctica during the Holocene, through synchronization of CO_2 in the Taylor Dome, Dome C and DML ice cores. *Earth Planetary Sci. Lett.* 224 (1), 45–54. doi: 10.1016/j.epsl.2004.05.007

Moore, J. K., and Abbott, M. R. (2000). Phytoplankton chlorophyll distributions and primary production in the Southern Ocean. *J. Geophysical Research: Oceans* 105 (C12), 28709–28722. doi: 10.1029/1999JC000043

Morales Maqueda, M. A., Willmott, A. J., and Biggs, N. R. T. (2004). Polynya dynamics: A review of observations and modeling. *Rev. Geophysics* 42 (1), RG1004. doi: 10.1029/2002RG000116

Morford, J. L., and Emerson, S. (1999). The geochemistry of redox sensitive trace metals in sediments. *Geochimica Cosmochimica Acta* 63 (11), 1735–1750. doi: 10.1016/S0016-7037(99)00126-X

Morford, J. L., Russell, A. D., and Emerson, S. (2001). Trace metal evidence for changes in the redox environment associated with the transition from terrigenous clay to diatomaceous sediment, Saanich Inlet, BC. *Mar. Geol.* 174 (1), 355–369. doi: 10.1016/S0025-3227(00)00160-2

Nameroff, T. J., Balistrieri, L. S., and Murray, J. W. (2002). Suboxic trace metal geochemistry in the Eastern Tropical North Pacific. *Geochimica Cosmochimica Acta* 66 (7), 1139–1158. doi: 10.1016/S0016-7037(01)00843-2

Nelson, D. M., Tréguer, P., Brzezinski, M. A., Leynaert, A., and Quéguiner, B. (1995). Production and dissolution of biogenic silica in the ocean: Revised global estimates, comparison with regional data and relationship to biogenic sedimentation. *Glob. Biogeochem. Cycles* 9 (3), 359–372. doi: 10.1029/95GB01070

Nicol, S., and Foster, J. (2003). Recent trends in the fishery for Antarctic krill. *Aquat. Living Resour.* 16 (1), 42–45. doi: 10.1016/S0990-7440(03)00004-4

Ogrinc, N., Fontolan, G., Faganeli, J., and Covelli, S. (2005). Carbon and nitrogen isotope compositions of organic matter in coastal marine sediments (the Gulf of Trieste, N Adriatic Sea): indicators of sources and preservation. *Mar. Chem.* 95 (3), 163–181. doi: 10.1016/j.marchem.2004.09.003

Orme, L. C., Crosta, X., Miettinen, A., Divine, D. V., Husum, K., Isaksson, E., et al. (2020). Sea surface temperature in the Indian sector of the Southern Ocean over the Late Glacial and Holocene. *Clim. Past* 16 (4), 1451–1467. doi: 10.5194/cp-16-1451-2020

Orsi, A. H., Whitworth, T., and Nowlin, W. D. (1995). On the meridional extent and fronts of the Antarctic Circumpolar Current. *Deep Sea Res. Part I: Oceanographic Res. Papers* 42 (5), 641–673. doi: 10.1016/0967-0637(95)00021-W

Pailler, D., Bard, E., Rostek, F., Zheng, Y., Mortlock, R., and van Geen, A. (2002). Burial of redox- metals and organic matter in the equatorial Indian Ocean linked to precession. *Geochimica Cosmochimica Acta* 66 (5), 849–865. doi: 10.1016/S0016-7037(01)00817-1

Paytan, A., Kastner, M., and Chavez, F. P. (1996). Glacial to interglacial fluctuations in productivity in the equatorial pacific as indicated by marine barite. *Science* 274 (5291), 1355. doi: 10.1126/science.274.5291.1355

Prahl, F. G., Ertel, J. R., Goni, M. A., Sparrow, M. A., and Eversmeyer, B. (1994). Terrestrial organic carbon contributions to sediments on the Washington margin. *Geochimica Cosmochimica Acta* 58 (14), 3035–3048. doi: 10.1016/0016-7037(94)90177-5

Prasad, T. G., McClean, J. L., Hunke, E. C., Semtner, A. J., and Ivanova, D. (2005). A numerical study of the western Cosmonaut polynya in a coupled ocean–sea ice model. *J. Geophysical Research: Oceans* 110 (C10), C10008. doi: 10.1029/2004JC002858

Pudsey, C. J., Murray, J. W., Appleby, P., and Evans, J. (2006). Ice shelf history from petrographic and foraminiferal evidence, Northeast Antarctic Peninsula. *Quaternary Sci. Rev.* 25 (17), 2357–2379. doi: 10.1016/j.quascirev.2006.01.029

Quéguiner, B., Tréguer, P., and Nelson, D. M. (1991). The production of biogenic silica in the Weddell and Scotia Seas. *Mar. Chem.* 35 (1), 449–459. doi: 10.1016/S0304-4203(09)90036-6

Rae, J. W. B., Burke, A., Robinson, L. F., Adkins, J. F., Chen, T., Cole, C., et al. (2018). CO_2 storage and release in the deep Southern Ocean on millennial to centennial timescales. *Nature* 562 (7728), 569–573. doi: 10.1038/s41586-018-0614-0

Raynaud, D., Barnola, J. M., Chappellaz, J., Zardini, D., Jouzel, J., and Lorius, C. (1992). Glacial-interglacial evolution of greenhouse gases as inferred from ice core analysis: A review of recent results. *Quat. Sci. Rev.* 11 (4), 381–386. doi: 10.1016/0277-3791(92)90020-9

Ridgwell, A., and Schmidt, D. N. (2010). Past constraints on the vulnerability of marine calcifiers to massive carbon dioxide release. *Nat. Geosci.* 3 (3), 196–200. doi: 10.1038/ngeo755

Robinson, R. S., Kienast, M., Luiza Albuquerque, A., Altabet, M., Contreras, S., De Pol Holz, R., et al. (2012). A review of nitrogen isotopic alteration in marine sediments. *Paleoceanography* 27 (4), PA4203. doi: 10.1029/2012PA002321

Sampei, Y., and Matsumoto, E. (2001). C/N ratios in a sediment core from Nakaumi Lagoon, southwest Japan - Usefulness as an organic source indicator -. *Geochem. J.* 35 (3), 189–205. doi: 10.2343/geochemj.35.189

Sarmiento, J. L., and Nicolas, G. (2006). *Ocean biogeochemical dynamics* (Princeton: Princeton University Press). doi: 10.2307/j.ctt3fgxqx

Sarnthein, M., Schneider, B., and Grootes, P. M. (2013). Peak glacial ^{14}C ventilation ages suggest major draw-down of carbon into the abyssal ocean. *Climate Past* 9 (6), 2595–2614. doi: 10.5194/cp-9-2595-2013

Schmitt, J., Schneider, R., Elsig, J., Leuenberger, D., Lourantou, A., Chappellaz, J., et al. (2012). Carbon isotope constraints on the deglacial CO_2 rise from ice cores. *Science* 336 (6082), 711–714. doi: 10.1126/science.1217161

Schmittner, A., Oschlies, A., Matthews, H. D., and Galbraith, E. D. (2008). Future changes in climate, ocean circulation, ecosystems, and biogeochemical cycling simulated for a business-as-usual CO_2 emission scenario until year 4000 AD. *Glob. Biogeochem. Cycles* 22 (1), GB1013. doi: 10.1029/2007GB002953

Schüpbach, S., Federer, U., Kaufmann, P., Albani, S., Barbante, C., Stocker, T., et al. (2013). High-resolution mineral dust and sea ice proxy records from the Talos Dome ice core. *Climate Past* 9, 2789–2807. doi: 10.5194/cp-9-2789-2013

Shakun, J. D., Clark, P. U., He, F., Marcott, S. A., Mix, A. C., Liu, Z., et al. (2012). Global warming preceded by increasing carbon dioxide concentrations during the last deglaciation. *Nature* 484 (7392), 49–54. doi: 10.1038/nature10915

Siani, G., Michel, E., De Pol-Holz, R., DeVries, T., Lamy, F., Carel, M., et al. (2013). Carbon isotope records reveal precise timing of enhanced Southern Ocean upwelling during the last deglaciation. *Nat. Commun.* 4 (1), 2758. doi: 10.1038/ncomms3758

Sigman, D. M., and Boyle, E. A. (2000). Glacial/interglacial variations in atmospheric carbon dioxide. *Nature* 407 (6806), 859–869. doi: 10.1038/35038000

Sigman, D. M., Fripiat, F., Studer, A. S., Kemeny, P. C., Martínez-García, A., Hain, M. P., et al. (2021). The Southern Ocean during the ice ages: A review of the Antarctic surface isolation hypothesis, with comparison to the North Pacific. *Quat. Sci. Rev.* 254, 106732. doi: 10.1016/j.quascirev.2020.106732

Sigman, D. M., Hain, M. P., and Haug, G. H. (2010). The polar ocean and glacial cycles in atmospheric CO_2 concentration. *Nature* 466 (7302), 47–55. doi: 10.1038/nature09149

Skinner, L. C., Fallon, S., Waelbroeck, C., Michel, E., and Barker, S. (2010). Ventilation of the deep southern ocean and deglacial CO_2 rise. *Science* 328 (5982), 1147–1151. doi: 10.1126/science.1183627

Skinner, L. C., Primeau, F., Freeman, E., de la Fuente, M., Goodwin, P. A., Gottschalk, J., et al. (2017). Radiocarbon constraints on the glacial ocean circulation and its impact on atmospheric CO_2. *Nat. Commun.* 8 (1), 16010. doi: 10.1038/ncomms16010

Smith, W. O. (1991). Nutrient distributions and new production in polar regions: parallels and contrasts between the Arctic and Antarctic. *Mar. Chem.* 35 (1), 245–257. doi: 10.1016/S0304-4203(09)90020-2

Smith, S. D., Muench, R. D., and Pease, C. H. (1990). Polynyas and leads: An overview of physical processes and environment. *J. Geophysical Research: Oceans* 95 (C6), 9461–9479. doi: 10.1029/JC095iC06p09461

Strauch, G., Haendel, D., Maass, I., Mühle, K., and Runge, A. (2011). Isotope variations of hydrogen, carbon and nitrogen in florae from the Schirmacher Oasis, East Antarctica. *Isotopes Environ. Health Stud.* 47 (3), 280–285. doi: 10.1080/10256016.2011.600455

Stroobants, N., Dehairs, F., Goeyens, L., Vanderheijden, N., and Van Grieken, R. (1991). Barite formation in the Southern Ocean water column. *Mar. Chem.* 35 (1), 411–421. doi: 10.1016/S0304-4203(09)90033-0

Studer, A. S., Sigman, D. M., Martínez-García, A., Benz, V., Winckler, G., Kuhn, G., et al. (2015). Antarctic Zone nutrient conditions during the last two glacial cycles. *Paleoceanography* 30 (7), 845–862. doi: 10.1002/2014PA002745

Stuiver, M., and Reimer, P. J. (1993). Extended ^{14}C data base and revised CALIB 3.0 ^{14}C age calibration program. *Radiocarbon* 35 (1), 215–230. doi: 10.1017/S0033822200013904

Takano, Y., Tyler, J. J., Kojima, H., Yokoyama, Y., Tanabe, Y., Sato, T., et al. (2012). Holocene lake development and glacial-isostatic uplift at Lake Skallen and Lake Oyako, Lützow-Holm Bay, East Antarctica: Based on biogeochemical facies and molecular signatures. *Appl. Geochem.* 27 (12), 2546–2559. doi: 10.1016/j.apgeochem.2012.08.009

Talley, L. D. (2013). Closure of the global overturning circulation through the Indian, Pacific, and Southern Oceans: Schematics and transports. *Oceanography* 26 (1), 80–97. doi: 10.5670/oceanog.2013.07

Thöle, L. M., Amsler, H. E., Moretti, S., Auderset, A., Gilgannon, J., Lippold, J., et al. (2019). Glacial-interglacial dust and export production records from the Southern Indian Ocean. *Earth Planetary Sci. Lett.* 525, 115716. doi: 10.1016/j.epsl.2019.115716

Thornton, S. F., and McManus, J. (1994). Application of organic carbon and nitrogen stable isotope and C/N ratios as source indicators of organic matter provenance in estuarine systems: Evidence from the tay estuary, scotland. *Estuarine Coast. Shelf Sci.* 38 (3), 219–233. doi: 10.1006/ecss.1994.1015

Thunell, R. C., Miao, Q.-M., Calvert, S. E., and Pedersen, T. F. (1992). Glacial-holocene biogenic sedimentation patterns in the South China sea: Productivity variations and surface water pCO_2. *Paleoceanography* 7 (2), 143–162. doi: 10.1029/92PA00278

Toggweiler, J. R. (1999). Variation of atmospheric CO2 by ventilation of the ocean's deepest water. *Paleoceanography* 14 (5), 571–588. doi: 10.1029/1999PA900033

Toggweiler, J. R., Russell, J. L., and Carson, S. R. (2006). Midlatitude westerlies, atmospheric CO_2, and climate change during the ice ages. *Paleoceanography* 21 (2), PA2005. doi: 10.1029/2005PA001154

Tréguer, P. (2002). Silica and the cycle of carbon in the ocean. *Comptes Rendus Geosci.* 334 (1), 3–11. doi: 10.1016/S1631-0713(02)01680-2

Tribovillard, N., Algeo, T. J., Lyons, T., and Riboulleau, A. (2006). Trace metals as paleoredox and paleoproductivity proxies: An update. *Chem. Geol.* 232 (1), 12–32. doi: 10.1016/j.chemgeo.2006.02.012

Turekian, K. K., and Wedepohl, K. H. (1961). Distribution of the elements in some major units of the earth's crust. *GSA Bull.* 72 (2), 175–192. doi: 10.1130/0016-7606(1961)72[175:DOTEIS]2.0.CO;2

von Berg, L., Prend, C. J., Campbell, E. C., Mazloff, M. R., Talley, L. D., and Gille, S. T. (2020). Weddell sea phytoplankton blooms modulated by sea ice variability and polynya formation. *Geophys. Res. Lett.* 47 (11), e2020GL087954. doi: 10.1029/2020GL087954

Wang, J.-K., Li, T.-G., Xiong, Z.-F., Chang, F.-M., Qin, B.-B., Wang, L.-M., et al. (2018). Sedimentary geochemical characteristics of the Redox-sensitive elements in Ross Sea, Antarctic: Implications for paleoceanography. *Mar. Geology Quaternary Geology* 38 (5), 112–121. doi: 10.16562/j.cnki.0256-1492.2018.05.011

Watson, A. J., and Naveira Garabato, A. C. (2006). The role of Southern Ocean mixing and upwelling in glacial-interglacial atmospheric CO_2 change. *Tellus B* 58 (1), 73–87. doi: 10.1111/j.1600-0889.2005.00167.x

Watson, A. J., Vallis, G. K., and Nikurashin, M. (2015). Southern Ocean buoyancy forcing of ocean ventilation and glacial atmospheric CO_2. *Nat. Geosci.* 8 (11), 861–864. doi: 10.1038/ngeo2538

Westwood, K. J., Brian Griffiths, F., Meiners, K. M., and Williams, G. D. (2010). Primary productivity off the Antarctic coast from 30°–80°E; BROKE-West surve. *Deep Sea Res. Part II: Topical Stud. Oceanography* 57 (9), 794–814. doi: 10.1016/j.dsr2.2008.08.020

Williams, G. D., Nicol, S., Aoki, S., Meijers, A. J. S., Bindoff, N. L., Iijima, Y., et al. (2010). Surface oceanography of BROKE-West, along the Antarctic margin of the south-west Indian Ocean (30–80°E). *Deep Sea Res. Part II: Topical Stud. Oceanography* 57 (9), 738–757. doi: 10.1016/j.dsr2.2009.04.020

Wolff, E. W., Barbante, C., Becagli, S., Bigler, M., Boutron, C. F., Castellano, E., et al. (2010). Changes in environment over the last 800,000 years from chemical analysis of the EPICA Dome C ice core. *Quat. Sci. Rev.* 29 (1), 285–295. doi: 10.1016/j.quascirev.2009.06.013

Wolff, E. W., Fischer, H., Fundel, F., Ruth, U., Twarloh, B., Littot, G. C., et al. (2006). Southern Ocean sea-ice extent, productivity and iron flux over the past eight glacial cycles. *Nature* 440 (7083), 491–496. doi: 10.1038/nature04614

Wong, A. P. S., Bindoff, N. L., and Forbes, A. (1985). "Ocean-ice shelf interaction and possible bottom water formation in prydz bay, Antarctica," in *Ocean, ice, and atmosphere: Interactions at the antarctic continental margin*. Eds. S. S. Jacobs and R. F. Weiss (Washington, DC: American Geophysical Union), 173–187.

Yamamoto, A., Abe-Ouchi, A., Shigemitsu, M., Oka, A., Takahashi, K., Ohgaito, R., et al. (2015). Global deep ocean oxygenation by enhanced ventilation in the Southern Ocean under long-term global warming. *Glob. Biogeochem. Cycles* 29 (10), 1801–1815. doi: 10.1002/2015GB005181

Yang, Z.-F., Chen, M., Tang, Z., Zheng, M.-F., and Qiu, Y.-S. (2022). The sedimentation, bioturbation and organic matter degradation as revealed by excess ^{230}Th and ^{210}Pb in the Cosmonaut Sea. *Deep Sea Res. Part II: Topical Stud. Oceanography* 198, 105049. doi: 10.1016/j.dsr2.2022.105049

Yang, C.-L., Chen, Z.-H., Xiao, W.-S., Wang, X., Ju, M.-S., Cui, Y.-C., et al. (2021). Paleoproductivity and its environmental constraints in the Scotia Sea, Antarctica since 34 ka BP. *Haiyang Xuebao* 43 (03), 116–125. doi: 10.12284/hyxb2021051

Yoshida, Y., and Moriwaki, K. (1979). Some consideration on elevated coastal features and their dates around syowa station, Antarctica. *Memoirs Natl. Institute Polar Res. Special issue* 13, 220–226.

Zhang, Y., Li, C.-L., Yang, G., Wang, Y.-Q., Tao, Z.-C., Zhang, Y.-S., et al. (2017). Ontogenetic diet shift in Antarctic krill (Euphausia superba) in the Prydz Bay: A stable isotope analysis. *Acta Oceanologica Sin.* 36 (12), 67–78. doi: 10.1007/s13131-017-1049-4

frontiers | Frontiers in Marine Science

TYPE Perspective
PUBLISHED 08 January 2024
DOI 10.3389/fmars.2023.1328534

OPEN ACCESS

EDITED BY
Zhifang Xiong,
Ministry of Natural Resources, China

REVIEWED BY
Yingxu Wu,
Jimei University, China
Tianyu Chen,
Nanjing University, China

*CORRESPONDENCE
Laurie Menviel
l.menviel@unsw.edu.au

RECEIVED 26 October 2023
ACCEPTED 08 December 2023
PUBLISHED 08 January 2024

CITATION
Menviel L and Spence P (2024) Southern Ocean circulation's impact on atmospheric CO_2 concentration. *Front. Mar. Sci.* 10:1328534. doi: 10.3389/fmars.2023.1328534

Southern Ocean circulation's impact on atmospheric CO_2 concentration

Laurie Menviel[1,2]* and Paul Spence[2,3]

[1]Climate Change Research Centre, University of New South Wales, Sydney, NSW, Australia, [2]The Australian Centre for Excellence in Antarctic Science, University of Tasmania, Hobart, TAS, Australia, [3]Institute for Marine and Antarctic Studies and Australian Antarctic Program Partnership, University of Tasmania, Hobart, TAS, Australia

In the context of past and present climate change, the Southern Ocean (SO) has been identified as a crucial region modulating the concentration of atmospheric CO_2. The sustained upwelling of carbon-rich deep waters and inefficient nutrient utilization at the surface of the SO leads to an outgassing of natural CO_2, while anthropogenic CO_2 is entrained to depth during the formation of Antarctic Bottom water (AABW), Antarctic intermediate water (AAIW) and sub-Antarctic mode water (SAMW). Changes to the SO circulation resulting from both dynamic and buoyancy forcing can alter the rate of upwelling as well as formation and subsequent transport of AABW, AAIW and SAMW, thus impacting the air-sea CO_2 exchange in the SO. Models of all complexity robustly show that stronger southern hemispheric (SH) westerlies enhance SO upwelling, thus leading to stronger natural CO_2 outgassing, with a sensitivity of 0.13 GtC/yr for a 10% increase in SH westerly windstress. While the impact of changes in the position of the SH westerly winds was previously unclear, recent simulations with high-resolution ocean/sea-ice/carbon cycle models show that a poleward shift of the SH westerlies also enhances natural CO_2 outgassing with a sensitivity of 0.08GtC/yr for a 5° poleward shift. While enhanced AABW transport reduces deep ocean natural DIC concentration and increases surface natural DIC concentration, it acts on a multi-decadal timescale. Future work should better constrain both the natural and anthropogenic carbon cycle response to changes in AABW and the compound impacts of dynamic and buoyancy changes on the SO marine carbon cycle.

KEYWORDS

Southern Ocean, carbon cycle, atmospheric CO2, Antarctic Bottom Water (AABW), Southern hemisphere westerlies

1 Introduction

Despite covering only about 25% of the world's ocean surface, the Southern Ocean (SO, south of 35°S) is one of today's largest sink of both anthropogenic carbon and excess heat, accounting for ~40% of the oceanic anthropogenic carbon uptake and ~72% of the excess heat uptake (Sabine et al., 2004; Mikaloff-Fletcher et al., 2006; Shi et al., 2018). This oversized role is due to the unique overturning circulation of the SO that brings deep water up to the surface and leads to the formation of deep and intermediate water masses. A key driver of this overturning are the strong westerly winds that peak in strength around 55°S and are bounded by easterly winds on their Antarctic and subtropical flanks. These winds create a divergent surface flow and steeply tilted isopycnals that outcrop south of the maximum westerly wind stress to allow old, nutrient rich Circumpolar Deep Water (CDW) to upwell from mid-depths to the surface (Figure 1A). Due to Ekman transport within the westerly wind belt, Antarctic surface waters move equatorwards, freshen and warm. As a result, there is an outgassing of natural CO_2 south of the sub-Antarctic front and particularly south of the polar front. As CDW equilibrates with the atmosphere, its dissolved inorganic carbon (DIC) is consumed by phytoplankton, thus decreasing the surface water pCO_2, leading to an oceanic uptake of atmospheric CO_2, a process referred to as the biological pump (Talley, 2013).

The CDW that rises to the SO surface is replaced by downward flows of surface waters in other regions. In the current context of elevated atmospheric CO_2 concentration, these downward flows entrain carbon, and particularly anthropogenic carbon, as well as heat in the SO interior (Frölicher et al., 2015; Gruber et al., 2019), primarily within Antarctic Intermediate Water (AAIW), but also within Antarctic Bottom Water (AABW) and sub-Antarctic Mode Water (SAMW) (Figure 1B). AAIW subducts along isopycnals into the SO interior equatorward of the sub-Antarctic front where wind driven surface flows converge. Winter deepening of the mixed layer north of the Antarctic Circumpolar Current (ACC) leads to the formation of SAMW, which overlays AAIW (Morrison et al., 2022). Closer to Antarctica, dense shelf waters, the precursor of AABW are formed on the Antarctic continental shelf in the Ross Sea, Weddell Sea, Prydz Bay, and Adelie Land (Purkey et al., 2018), through brine rejection and ocean/ice-shelf interactions.

Observational products suggest that the SO total (sum of anthropogenic and natural) CO_2 fluxes exhibit large decadal-scale variability (LeQuéré et al., 2007; Matear and Lenton, 2008; Landschützer et al., 2015; Bushinsky et al., 2019; Gruber et al., 2019; Keppler and Landschützer, 2019; Gruber et al., 2023), with a lower than expected total CO_2 uptake in the 1990s and early 2000s (LeQuéré et al., 2007; Landschützer et al., 2015; Gruber et al., 2019) and probably during the mid-2010s (Bushinsky et al., 2019; Gruber et al., 2019; Keppler and Landschützer, 2019; Landschützer et al., 2020). The main hypothesis to explain the stagnation in the CO_2 uptake observed in the 1990s and early 2000s is the concurrent positive SAM trend (LeQuéré et al., 2007; Lovenduski et al., 2008; Resplandy et al., 2015; Gruber et al., 2023), which corresponds to a strengthening and poleward shift of the SH westerlies. As the CO_2 uptake re-invigorated, particularly between 2002 and 2012, other hypotheses to explain the variability emerged such as regional wind variability associated with the zonal wave number 3 pattern (Keppler and Landschützer, 2019), solubility effects (Landschützer et al. 2015) and changes in atmospheric CO_2 growth rate (McKinley et al., 2020). While hindcast experiments support a dominant role of the SAM in modulating the SO CO_2 fluxes (Gruber et al., 2019; Hauck et al., 2020; Menviel et al., 2023), they underestimate the observed SO CO_2 flux variability. This could be due to an underestimation of Southern Ocean stratification (de Lavergne et al., 2014), potentially linked to enhanced Antarctic basal melt rates (Adusumilli et al., 2020), which would weaken AABW formation and transport (Li, 2023). The individual and compound roles of changes in SH westerly wind strength and position, and AABW formation and transport on the marine carbon cycle need to be fully understood to constrain changes in SO CO_2 fluxes.

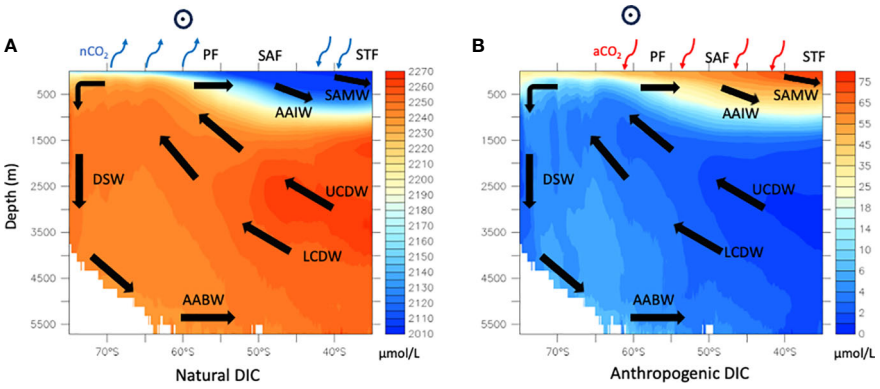

FIGURE 1
Schematic showing zonally averaged Southern Ocean **(A)** natural DIC and **(B)** anthropogenic DIC concentration (µmol/L) averaged over years 2017-2021 in the ACCESS-OM2-01 simulation. Blue and red arrows at the ocean's surface represent the natural and anthropogenic CO_2 fluxes, respectively, and the westerly wind is represented by a circle above. PF, SAF and STF are the positions of the Polar Front, Subantarctic Front and Subtropical Front, respectively. Thick black arrows in the ocean interior represent the circulation of water masses: Dense Shelf Water (DSW), Antarctic Bottom Water (AABW), Lower Circumpolar Deep Water (LCDW), Upper Circumpolar Deep Water (UCDW), Antarctic Intermediate Water (AAIW), and Subantarctic Mode Water (SAMW).

While overall the SO has mitigated the rise in atmospheric CO_2 since at least the 1980s, SO CO_2 outgassing has been suggested to induce an increase in atmospheric CO_2 during deglaciations as well as past abrupt climate change events (Anderson et al., 2009; Skinner et al., 2010; Watson et al., 2015; Rae et al., 2018; Shuttleworth et al., 2021; Gray et al., 2023). SO stratification during glacial periods, potentially arising from a large sea-ice cover, weaker and/or equatorward shifted SH westerlies would allow a carbon accumulation in the deep ocean (Toggweiler et al., 2006; Menviel et al., 2017). The breakdown of this stratification during deglaciations and Antarctic warm events, i.e. millennial-scale warm periods over Antarctica and the Southern Ocean (Buizert and Members, 2015), would lead to a SO CO_2 outgassing and an increase in atmospheric CO_2 of up to 20 ppm (Ahn and Brook, 2008; Marcott et al., 2014; Menviel et al., 2018; Bauska et al., 2021). An improved understanding of the interplay between SO circulation and marine carbon cycle is however needed to refine our understanding of these past climate change events.

Here we provide a perspective on past, present and future relationship between changes in atmospheric CO_2 and SO circulation arising from both changes in surface wind and buoyancy. We also present recent advances and future work.

2 Southern hemispheric westerly winds

There is a general consensus that stronger SH westerly winds enhance SO natural CO_2 outgassing by increasing the upward transport of DIC-rich CDW, thus leading to an increase in atmospheric CO_2 (Gottschalk et al., 2020). This DIC increase mostly arises from the advective upwelling of CDW along isopycnals into the mixed layer, although increased vertical diffusion at the base of the mixed layer could also significantly contribute to the higher surface DIC (Dufour et al., 2013). Enhanced upwelling of CDW can also enhance primary production, which acts to increase the export of organic carbon to depth, thus lowering atmospheric CO_2 (Menviel, 2008; Hauck et al., 2013). However, most studies found this negative feedback to only have a small impact on the CO_2 fluxes (Dufour et al., 2013) and to mostly impact carbon uptake north of the sub-Antarctic front (Menviel et al., 2023).

Depending on the pCO_2 of the upwelled water, the magnitude of the negative biological feedback as well as the resolution of the ocean model used, which can impact the outcrop area of deep water and SO circulation response, a 10% strengthening of the SH westerly wind stress has been found to lead to a 2.7 ppm +/- 0.5 ppm CO_2 increase (Menviel et al., 2008; Menviel et al., 2015; Huiskamp et al., 2016; Lauderdale et al., 2017; Menviel et al., 2018; Gottschalk et al., 2019). While Toggweiler et al. (2006) hypothesized that a poleward shift of the SH westerly should enhance the SO CO_2 outgassing, simulations performed with coarse resolution models led to mixed results, with a poleward SH westerly shift leading to both an increase and a decrease in atmospheric CO_2 depending on the model used (Gottschalk et al., 2019).

Most modelling studies that assessed the impact of SH westerly changes on the marine carbon cycle were performed with models that could not resolve mesoscale eddies (Lenton and Matear, 2007; Lovenduski et al., 2007; Lovenduski et al., 2008; Menviel, 2008; Tschumi et al., 2011; Dufour et al., 2013; Hauck et al., 2013; Völker and Köhler, 2013; Huiskamp et al., 2016; Lauderdale et al., 2017). Mesoscale eddies are prevalent in the SO, particularly downstream of topographic features that intercept the path of the Antarctic Circumpolar Current (ACC) (Sokolov and Rintoul, 2009; Frenger et al., 2015). In the SO, eddy induced transports oppose the Ekman-driven overturning transport via eddy compensation. Eddy-permitting and eddy-rich models have thus highlighted the role of eddy compensation in mitigating the Southern Ocean overturning change due to increased wind stress (Meredith et al., 2012; Morrison and Hogg, 2013). It has further been suggested that climate models that did not use a variable eddy parametrization coefficient most likely overestimated the wind-driven response (Gent, 2016).

A recent study (Menviel et al., 2023) assessed the impact of changes in the strength and position of the SH westerlies on SO CO_2 fluxes, associated with a positive trend of the SAM over the last 42 years in a global eddy-rich model (ACCESS-OM2-01, 0.1° resolution, 75 vertical levels) forced by the 55-year Japanese Reanalysis for driving oceans (JRA55-do) (Tsujino et al., 2018). This simulation shows that positive phases of the SAM (stronger and poleward shifted SH westerlies) lead to enhanced SO CO_2 outgassing south of the polar front, and reduced CO_2 uptake north of the sub-Antarctic front. The CO_2 outgassing is maximum over topography features such as over the eastern part of the Southeast Indian Ridge, east of the Drake Passage and over the Southwest Indian Ridge, which could be due to enhanced eddy mixing over topography linked to the merging of multiple jets.

Here, we synthesize these results and merge them with other experiments performed with the suite of ACCESS-OM2 models. This includes the ACCESS-OM2 (1° and 50 vertical levels) and ACCESS-OM2-01 (0.1° and 75 vertical levels) forced by the JRA55-do reanalysis over the period 1958 to 2021 (Tsujino et al., 2018; Kiss et al., 2020) as well as four idealized perturbation experiments performed with the ACCESS-OM2-025 (0.25° and 50 vertical levels), in which the SH near surface wind speeds are abruptly modified (Hogg et al., 2017). The zonally uniform and temporally steady perturbations are applied to the CORE-NYF 6-hourly wind field between 27°S and 70°S with smoothing within 5° latitude of the perturbation boundaries. The perturbations include i) a 20% increase in SH westerly windstress between 32°S and 65°S, ii) a 20% increase with a 4° poleward shift, iii) a ~16% decrease, and iv) a ~4° equatorward shift of the SH westerly windstress. The first three idealized experiments are integrated for 42 years, while the last one is run for 125 years (Gray et al., 2023).

In all the simulations performed with the suite of ACCESS-OM2 models, stronger and poleward shifted SH westerlies lead to enhanced CO_2 outgassing south of the polar front (Figure 1). A robust linear relationship is obtained between the natural SO CO_2 flux and mean SO windstress (Figure 2A). The SO CO_2 outgassing increases by 13 ± 3 GtC/yr per N/m^2 (therefore ~0.13 GtC/yr per 10% windstress increase). These results show that an eddy-rich

model displays a similar sensitivity to changes in SO upwelling than a coarse-resolution model with a varying isopycnal thickness diffusivity (Kiss et al., 2020).

While the relationship between the position of the maximum SO windstress and SO CO_2 fluxes is weak, there is still a significant relationship, with enhanced SO CO_2 outgassing as the SH westerlies shift poleward, with a sensitivity of 0.016 ± 0.04 GtC/° latitude (Figure 2B). As the SH westerlies move poleward, so does the divergence, which leads to a steepening of heavier isopycnals, thus increasing the upwelling pathway of carbon-rich deep-waters (Toggweiler et al., 2006; Gray et al., 2023).

While many modelling studies assessed the impact of SH westerly changes on natural CO_2 fluxes, the impact on anthropogenic CO_2 fluxes has been less studied. Nevertheless, the results suggest that stronger SH westerlies also enhance the uptake of anthropogenic CO_2 in the SO, but the amplitude of this enhanced SO anthropogenic CO_2 uptake is only one third of the associated enhanced natural CO_2 outgassing (Lovenduski et al., 2008; Menviel et al., 2023). As such stronger SH westerlies reduce the total SO CO_2 uptake.

3 Antarctic bottom water transport

AABW is the densest large-scale water mass in the global ocean and it fills roughly 35% of the global ocean volume. As AABW moves northward in the abyss, it upwells through diapycnal mixing in the sub-tropics and tropics into deep waters (Talley, 2013). These deep waters, i.e. North Atlantic Deep Water (NADW), Indian Deep Water (IDW) and Pacific Deep Water (PDW) are then often upwelled at the surface of the Southern Ocean as CDW. Changes in AABW formation and transport, can arise from changes in SH westerlies, but also changes in sea-ice cover and polynya opening. For example, a poleward strengthening of the SH westerlies in the ACCESS-OM2-025 enhances the northward transport of sea-ice, thus leading to enhanced AABW formation and transport (Hogg et al., 2017; Menviel et al., 2018). On the contrary, stronger polar easterlies increase the build-up of sea ice over the continental shelf, which reduces AABW formation (Jeong et al., 2022; Schmidt et al., 2023). Changes in buoyancy forcing resulting from changes in sea-ice formation can also affect AABW formation and transport. Polynya openings in the Antarctic coastal zone trigger large deep-ocean convection events, which strengthen the lower overturning cell (Hogg et al., 2017; Jeong et al., 2022). On the other hand, reduced sea-ice formation and associated warmer conditions can decrease the density of surface waters, thus increasing stratification and decreasing the formation of AABW (Choudhury et al., 2022; Zhou et al., 2023).

In turn, changes in AABW formation and transport affect the oceanic DIC concentration and atmospheric CO_2. Figure 3 shows zonally averaged DIC anomalies in two experiments which feature stronger AABW transport, but one is generated by surface SO salinification in an Earth system model of intermediate complexity, LOVECLIM (Menviel et al., 2015) (△AABW=+14 Sv, Figures 3A, B) and the other by a poleward strengthening of the SH westerlies in the ACCESS-OM2-025 (△AABW=+11 Sv, Figures 3C–F). In both cases, enhanced AABW transport leads to a natural DIC decrease in the deep ocean (Figures 3A, C). This arises i) from a decrease in remineralized DIC (Figures 3B, D), i.e. a decrease in the amount of carbon that can accumulate in the deep ocean resulting from a lower residence time of AABW; and ii) from a larger proportion of southern sourced waters with lower DIC concentration being advected to the deep North Pacific. The deep North Pacific indeed host the oldest watermass with the highest DIC concentration. As this enhanced lower overturning cell reduces deep ocean DIC concentration, it leads to an increase in DIC concentration above 1500m depth north of 40°S and in the mixed layer of the Southern Ocean (Figures 3A, C), thus resulting in a weaker vertical DIC gradient.

The differences in simulated DIC anomalies between the SO salinification and SH westerly poleward strengthening experiments could be attributed i) to the different length of the experiments (100 years vs 50 years): the DIC anomaly needs more than 50 years to

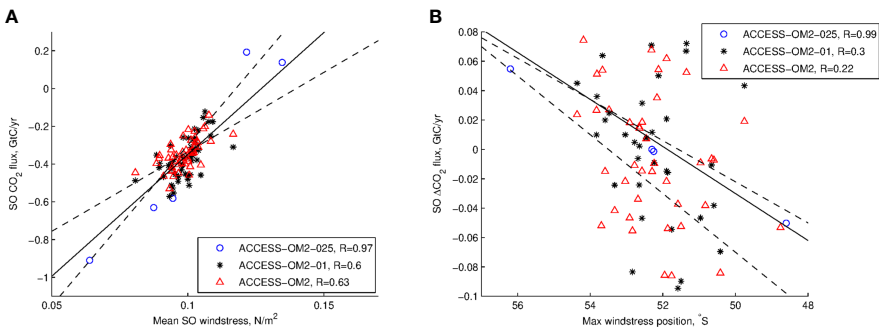

FIGURE 2
Relationship between SO natural CO_2 flux (south of 35°S) and SO windstress as simulated in experiments performed with ACCESS-OM2 models at 0.1° (black stars, ACCESS-OM2-01), 0.25° (blue circles, ACCESS-OM2-025) and 1° (red triangles, ACCESS-OM2) resolution. (left) SO natural CO_2 flux as a function of SO windstress (averaged between 35°S-65°S), with a slope of 13 ± 3 GtC.m^2/N across all experiments and R values of 0.97, 0.6 and 0.63 for the experiments performed with the ACCESS-OM2-025, ACCESS-OM2-01 and ACCESS-OM2, respectively. (right) SO residual natural CO_2 flux as a function of location of the maximum SO windstress with a slope of 0.016 ± 0.04 GtC/° latitude. The R values are of 0.99, 0.3 and 0.22 for the experiments performed with the ACCESS-OM2-025, ACCESS-OM2-01 and ACCESS-OM2, respectively. The residual natural CO_2 flux was calculated by subtracting the impact of changes in the strength of the westerly windstress as per the relationship defined on the left.

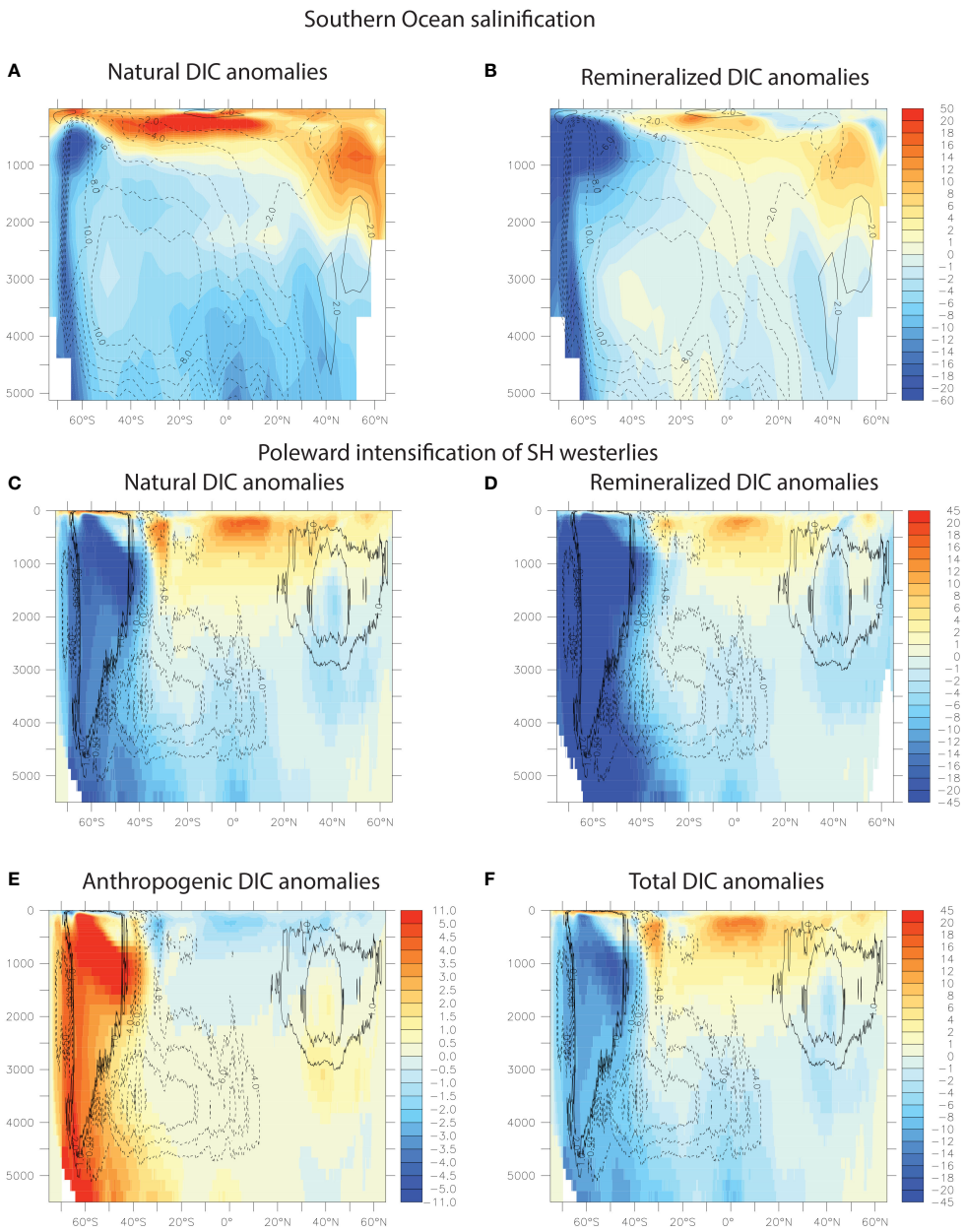

FIGURE 3
Zonally-averaged **(A)** natural DIC and **(B)** remineralized DIC anomalies (mmol/m^3) after 100 years for the SO salinification experiment performed with the Earth system model of intermediate complexity LOVECLIM (Menviel et al., 2015). Zonally-averaged **(C)** natural DIC, **(D)** remineralized DIC, **(E)** anthropogenic DIC and **(F)** total DIC anomalies (mmol/m^3) after 50 years for the poleward intensified SH westerlies (+20% and 4° poleward shift) experiment performed with the ACCESS-OM2-025 (Menviel et al., 2018). Overlaid are the global overturning streamfunction anomalies (Sv).

reach the deep North Pacific; ii) the poleward strengthening of the winds enhance the upper overturning cell (Hogg et al., 2017) (Figure 3C); and iii) the poleward strengthening of the SH westerlies leads to the opening of a polynya, which triggers a large deep-ocean convection event in SO.

Even though the preformed carbon entrained in the downwelling branch of AABW can increase, thus also leading to a significant increase in anthropogenic DIC concentration in the Southern Ocean (Figure 3E), this cannot compensate for the loss of natural DIC (Figure 3C) thus leading to negative total DIC anomalies (Figure 3F).

4 Discussion

Both dynamical and buoyancy changes can impact SO circulation and thus the SO CO_2 air-sea gas exchange, as well as the oceanic DIC distribution. As changes in the strength and position of the SH westerlies modulate the upwelling of carbon-rich deep-waters to the surface of the SO, it has long been suggested that changes in the SH westerlies could modulate the atmospheric CO_2 concentration (Russell et al., 2006; Toggweiler et al., 2006). While coarse resolution models consistently showed that stronger SH westerlies enhance the SO natural CO_2 outgassing (Gottschalk et al., 2019), the

lack of representation of mesoscale eddies within these modelling framework cast doubts on this result. In addition, due to the misrepresentation of AABW formation and the coarse resolution of the models used, the impact of changes in the position of SH westerlies on SO CO_2 flux was debated (Gottschalk et al., 2019). New results obtained with an eddy-rich model, which correctly forms dense-shelf water, show that mesoscale eddies do not significantly diminish the carbon cycle response to the wind-driven circulation and that poleward shifted SH westerlies enhance the SO natural CO_2 outgassing (Menviel et al., 2023).

In line with this, present-day hindcast simulations have suggested that changes in SH westerlies associated with the SAM were the dominant factor modulating the SO air-sea CO_2 exchange (Lenton and Matear, 2007; Lovenduski et al., 2007; Lovenduski et al., 2008). However, these simulations have not been able to reproduce the observational-based estimates contemporary CO_2 fluxes in SO (Lequere et al., 2018; Gruber et al., 2019; Hauck et al., 2020), even with eddy-rich ocean models (Menviel et al., 2023) forced with atmospheric reanalyses. Gloege et al. (2021) found that the decadal-scale variability in SO contemporary CO_2 flux could be overestimated by 30% due to undersampling. On the other hand, hindcast simulations could also underestimate the variability due to an overestimation of negative feedbacks (e.g. biological). The impact of changes in the strength and position of the SH westerlies should be further studied in eddy-permitting or eddy-resolving models that include complex ecosystem models.

The underestimation of the decadal-scale CO_2 variability could also be due to a poor representation of changes in buoyancy forcing, for example arising from enhanced Antarctic basal melt rates (Adusumilli et al., 2020), that could weaken AABW (Li, 2023). Buoyancy gain on the Antarctic shelf through either increased meltwater or warming will weaken the formation of AABW, and its subsequent transport (Menviel et al., 2010; Bintanja et al., 2013; Li, 2023). As a water mass ages, it accumulates remineralized nutrients. Weaker AABW transport increases the remineralized nutrient content in the deep ocean, which has been shown to increase the vertical DIC gradient and reduce SO natural CO_2 outgassing (Ito and Follows, 2005; Menviel et al., 2015). Future hindcast simulations should thus also include changes in Antarctic basal melt rates, with the caveat that the present-day carbon cycle could still be responding to changes that occurred decades ago.

In addition, as most models used to study the impact of changes in the oceanic circulation form AABW through deep-ocean convection, the impact of changes in dense-shelf water formation on the marine carbon cycle needs to be studied. In particular, the transport pathway of carbon from the abyss into deep waters and back to the surface as a function of bottom and deep water masses transport and volume should be better constrained. While both changes in SO upwelling strength and AABW formation can impact atmospheric CO_2, the marine carbon cycle response timescales are different: the SH westerlies impact the SO CO_2 outgassing within just a few months (Lenton and Matear, 2007; Menviel et al., 2023), while changes in AABW formation and transport only significantly impact air-sea CO_2 fluxes on a multi-decadal timescale (Menviel et al., 2018).

Finally, buoyancy and dynamic SO forcing can oppose each other, thus leading to a complex time-evolving oceanic circulation and thus marine carbon cycle response. In the context of past, present and future climate change, the individual and compound effects of changes in SH westerly, sea-ice formation and melt, formation of SO watermasses and the marine carbon cycle need to be better constrained to understand the resultant changes in atmospheric CO_2.

Data availability statement

The datasets presented in this study can be found in the Dryad repository https://datadryad.org/stash/share/E21b0EPD0x4ZXYb5JUt41sM42fEqhdA40hl8bnC1-2Y.

Author contributions

LM: Conceptualization, Formal Analysis, Investigation, Methodology, Writing – original draft. PS: Conceptualization, Methodology, Writing – review & editing.

Funding

The author(s) declare financial support was received for the research, authorship, and/or publication of this article. This project was supported by the Australian Research Council (ARC), including grants FT180100606, FT190100413, and SR200100008.

Acknowledgments

The authors thank the Consortium for Ocean-Sea Ice Modelling in Australia (COSIMA; http://www.cosima.org.au) for making the ACCESS-OM2 suite of models available at https://github.com/COSIMA/accessom2. Model runs were undertaken with the assistance of resources from the National Computational Infrastructure (NCI), which is supported by the Australian Government.

Conflict of interest

The authors declare that the research was conducted in the absence of any commercial or financial relationships that could be construed as a potential conflict of interest.

Publisher's note

References

Adusumilli, S., Fricker, H., Medley, B., Padman, L., and Siegfried, M. (2020). Interannual variations in meltwater input to the Southern Ocean from Antarctic ice shelves. *Nat. Geosciences* 13, 616–620. doi: 10.1038/s41561-020-0616-z

Ahn, J., and Brook, E. (2008). Atmospheric $CO_{2\ and}$ climate on millennial time scales during the last glacial period. *Science* 322, doi:10.1126/science.1160832.

Anderson, R. F., Ali, S., Bradtmiller, L., Nielsen, S., Fleisher, M., Anderson, B., et al. (2009). Wind-driven upwelling in the Southern Ocean and the deglacial rise in Atmospheric CO_2. *Science* 323, 1443–1448.

Bauska, T., Brook, E., and Marcott, S. (2021). Abrupt changes in the global carbon cycle during the last glacial period. *Nat. Geosci.* 14, 91–96. doi: 10.1038/s41561-020-00680-2

Bintanja, R., van Oldenborgh, G., and Drijfhout, S. (2013). Important role for ocean warming and increased ice-shelf melt in antarctic sea-ice expansion. *Nat. Geosci.* 6, 376–379.

Buizert, C., and Members, W. D. P. (2015). Precise interpolar phasing of abrupt climate change during the last ice age. *Nature* 520, 661–665. doi: 10.1038/nature14401

Bushinsky, S. M., Landschützer, P., Rödenbeck, C., Gray, A. R., Baker, D., Mazloff, M. R., et al. (2019). Reassessing southern ocean air-sea CO2 flux estimates with the addition of biogeochemical float observations. *Global Biogeochemical Cycles* 33, 1370–1388. doi: 10.1029/2019GB006176

Choudhury, D., Menviel, L., Meissner, K. J., Yeung, N. K. H., Chamberlain, M., and Ziehn, T. (2022). Marine carbon cycle response to a warmer southern ocean: the case of the last interglacial. *Climate Past* 18, 507–523. doi: 10.5194/cp-18-507-2022

de Lavergne, C., Palter, J., Galbraith, E., Bernardello, R., and Marinov, I. (2014). Cessation of deep convection in the open Southern Ocean under anthropogenic climate change. *Nat. Climate Change* 4, 278–282. doi: 10.1038/NCLIMATE2132

Dufour, C. O., Sommer, J. L., Gehlen, M., Orr, J. C., Molines, J.-M., Simeon, J., et al. (2013). Eddy compensation and controls of the enhanced sea-to-air CO2 flux during positive phases of the Southern Annular Mode. *Global Biogeochemical Cycles* 27, 950–961. doi: 10.1002/gbc.20090

Frenger, I., Münnich, M., Gruber, N., and Knutti, R. (2015). Southern Ocean eddy phenomenology. *J. Geophysical Research: Oceans* 120, 7413–7449. doi: 10.1002/2015JC011047

Frölicher, T. L., Sarmiento, J. L., Paynter, D. J., Dunne, J. P., Krasting, J. P. , and Winton, M. (2015). Dominance of the southern ocean in anthropogenic carbon and heat uptake in CMIP5 models. *J. Climate* 28, 862–886. doi: 10.1175/JCLI-D-14-00117.1

Gent, P. R. (2016). Effects of southern hemisphere wind changes on the meridional overturning circulation in ocean models. *Annu. Rev. Mar. Sci.* 8, 79–94. doi: 10.1146/annurev-marine-122414-033929

Gloege, L., McKinley, G. A., Landschützer, P., Fay, A. R., Frölicher, T. L., Fyfe, J. C., et al. (2021). Quantifying errors in observationally based estimates of ocean carbon sink variability. *Global Biogeochemical Cycles* 35, e2020GB006788. doi: 10.1029/2020GB006788

Gottschalk, J., Battaglia, G., Fischer, H., Frölicher, T. L., Jaccard, S. L., Jeltsch-Thömmes, A., et al. (2019). Mechanisms of millennial-scale atmospheric co2 change in numerical model simulations. *Quaternary Sci. Rev.* 220, 30–74. doi: 10.1016/j.quascirev.2019.05.013

Gottschalk, J., Skinner, L. C., Jaccard, S. L., Menviel, L., Nehrbass-Ahles, C., and Waelbroeck, C. (2020). Southern Ocean link between changes in atmospheric CO2 levels and northern-hemisphere climate anomalies during the last two glacial periods. *Quaternary Sci. Rev.* 230, 106067. doi: 10.1016/j.quascirev.2019.106067

Gray, W. R., de Lavergne, C., Jnglin Wills, R. C., Menviel, L., Spence, P., Holzer, M., et al. (2023). Poleward shift in the southern hemisphere westerly winds synchronous with the deglacial rise in co2. *Paleoceanography Paleoclimatology* 38, e2023PA004666. doi: 10.1029/2023PA004666

Gruber, N., Bakker, D., DeVries, T., Gregor, L., Hauck, J., Landschützer, P., et al. (2023). Trends and variability in the ocean carbon sink. *Nat.Rev Earth Environ.* 4, 119–134. doi: 10.1038/s43017-022-00381-x

Gruber, N., Landschützer, P., and Lovenduski, N. (2019). The variable Southern Ocean carbon sink. *Annu. Rev. Mar. Sci.* 11, 159–186.

Hauck, J., Völker, C., Wang, T., Hoppema, M., Losch, M., and Wolf-Gladrow, D. A. (2013). Seasonally different carbon flux changes in the southern ocean inresponse to the southern annular mode. *Global Biogeochemical Cycles* 27, 1236–1245. doi: 10.1002/2013GB004600

Hauck, J., Zeising, M., Le Quéré, C., Gruber, N., Bakker, D. C. E., Bopp, L., et al. (2020). Consistency and challenges in the ocean carbon sink estimate for the global carbon budget. *Front. Mar. Sci.* 7. doi: 10.3389/fmars.2020.571720

Hogg, A., Spence, P., Saenko, O., and Downes, S. (2017). The energetics of southern ocean upwelling. *J. Phys. Oceanogr.* 47, 135–153.

Huiskamp, W. N., Meissner, K. J., and d'Orgeville, M. (2016). Competition between ocean carbon pumps in simulations with varying Southern Hemisphere westerly wind forcing. *Climate Dynamics* 46, 3463–3480. doi: 10.1007/s00382-015-2781-0

Ito, T., and Follows, M. (2005). Preformed phosphate, soft tissue pump and atmospheric CO_2. *J. Mar. Res.* 63, 813–839.

Jeong, H., Turner, A. K., Roberts, A. F., Veneziani, M., Price, S. P., Asay-Davis, X. S., et al. (2022). Southern ocean polynyas and dense water formation in a high-resolution, coupled earth system model. *Cryosphere Discussions* 2022, 1–32. doi: 10.5194/tc-2022-133

Keppler, L., and Landschützer, P. (2019). Regional wind variability modulates the southern ocean carbon sink. *Sci. Rep.* 9, 7384. doi: 10.1038/s41598-019-43826-y

Kiss, A. E., Hogg, A. M., Hannah, N., Boeira Dias, F., Brassington, G. B., Chamberlain, M. A., et al. (2020). ACCESS-OM2 v1.0: a global ocean–sea ice model at three resolutions. *Geoscientific Model. Dev.* 13, 401–442. doi: 10.5194/gmd-13-401-2020

Landschützer, P., Gruber, N., and Bakker, D. (2020). *An observation-based global monthly gridded sea surface pCO2 product from 1982 onward and its monthly climatology (NCEI Accession 0160558)*. (NOAA: NOAA National Centers for Environmental Information). doi: 10.7289/V5Z899N6

Landschützer, P., Gruber, N., Haumann, F. A., Rödenbeck, C., Bakker, D. C. E., van Heuven, S., et al. (2015). The reinvigoration of the Southern Ocean carbon sink. *Science* 349, 1221–1224. doi: 10.1126/science.aab2620

Lauderdale, J. M., Williams, R. G., Munday, D. R., and Marshall, D. P. (2017). The impact of Southern Ocean residual upwelling on atmospheric CO2 on centennial and millennial timescales. *Climate Dynamics* 48, 1611–1631. doi: 10.1007/s00382-016-3163-y

Lenton, A., and Matear, R. (2007). Role of the southern annular mode (SAM) in southern ocean CO_2 uptake. *Global Biogeochemical Cycles* 21. doi: 10.1029/2006GB002714

Lequere, C., Andrew, R. M., Friedlingstein, P., Sitch, S., Hauck, J., Pongratz, J., et al. (2018). Global carbon budget 2018. *Earth System Sci. Data* 10, 2141–2194. doi: 10.5194/essd-10-2141-2018

LeQuéré, C., Rödenbeck, C., Buitenhuis, E., Conway, T., Langenfelds, R., Gomez, A., et al. (2007). Saturation of the Southern Ocean CO_2 sink due to recent climate change. *Science* 316, 1735–1738.

Li, E. M. H. A. S. R. A. M. (2023). Abyssal ocean overturning slowdown and warming driven by Antarctic meltwater. *Nature* 615, 841–847. doi: 10.1038/s41586-023-05762-w

Lovenduski, N., Gruber, N., and Doney, S. (2008). Toward a mechanistic understanding of the decadal trends in the Southern Ocean carbon sink. *Global Biogeochemical Cycles* 22GB3016. doi: 10.1029/2007GB003139

Lovenduski, N., Gruber, N., Doney, S., and Lima, I. (2007). Enhanced CO_2 outgassing in the Southern Ocean from a positive phase of the Southern Annular Mode. *Global Biogeochemical Cycles* 21. doi: 10.1029/2006GB002900

Marcott, S., Bauska, T., Buizert, C., Steig, E., Rosen, J., Cuffey, K., et al. (2014). Centennial-scale changes in the global carbon cycle during the last deglaciation. *Nature* 514, 616–619. doi: 10.1038/nature13799

Matear, R., and Lenton, A. (2008). Impact of historical climate change on the southern ocean carbon cycle. *J. Climate* 21, 5820–5834. doi: 10.1175/2008JCLI2194.1

McKinley, G. A., Fay, A. R., Eddebbar, Y. A., Gloege, L., and Lovenduski, N. S. (2020). External forcing explains recent decadal variability of the ocean carbon sink. *AGU Adv.* 1, e2019AV000149. doi: 10.1029/2019AV000149

Menviel, L. (2008). Climate-carbon cycle interactions on millennial to glacial timescales as simulated by a model of intermediate complexity, LOVECLIM. Ph.D. thesis (University of Hawai'i).

Menviel, L., Mouchet, A., Meissner, K., Joos, F., and England, M. (2015). Impact of oceanic circulation changes on atmospheric $\delta^{13}CO_2$. *Global Biogeochemical Cycles* 29, 1944–1961. doi: 10.1002/2015GB005207

Menviel, L. C., Spence, P., Kiss, A. E., Chamberlain, M. A., Hayashida, H., England, M. H., et al. (2023). Enhanced Southern Ocean CO_2 outgassing as a result of stronger and poleward shifted southern hemispheric westerlies. *EGUsphere* 2023, 1–27. doi: 10.5194/egusphere-2023-390

Menviel, L., Spence, P., Yu, J., Chamberlain, M., Matear, R., Meissner, K., et al. (2018). Southern Hemisphere westerlies as a driver of the early deglacial atmospheric CO_2 rise. *Nat. Commun.* 92503. doi: 10.1038/s41467-018-04876-4

Menviel, L., Timmermann, A., Mouchet, A., and Timm, O. (2008). Climate and marine carbon cycle response to changes in the strength of the southern hemispheric westerlies. *Paleoceanography* 23. doi: 10.1029/2008PA001604

Menviel, L., Timmermann, A., Mouchet, A., and Timm, O. (2010). Climate and biogeochemical response to a rapid melting of the West-Antarctic Ice Sheet during interglacials and implications for future climate. *Paleoceanography* 25, doi:10.1029/2009PA001892.

Menviel, L., Yu, J., Joos, F., Mouchet, A., Meissner, K., and England, M. (2017). Poorly ventilated deep ocean at the Last Glacial Maximum inferred from carbon isotopes: a data-model comparison study. *Paleoceanography* 32, 2–17. doi: 10.1002/2016PA003024

Meredith, M. P., Garabato, A. C. N., Hogg, A. M. , and Farneti, R. (2012). Sensitivity of the overturning circulation in the southern ocean to decadal changes in wind forcing. *J. Climate* 25, 99–110. doi: 10.1175/2011JCLI4204.1

Mikaloff-Fletcher, S., Gruber, N., Jacobson, A., Doney, S., Dutkiewicz, S., Gerber, M., et al. (2006). Inverse estimates of anthropogenic CO_2 uptake, tranport, and storage by the ocean. *Global Biogeochemical Cycles* 20, GB2002. doi: 10.1029/2005GB002530

Morrison, A., and Hogg, A. (2013). On the relationship between southern ocean overturning and ACC transport. *J. Phys. Oceanogr.* 43, 140–148. doi: 10.1175/JPO-D-12-057.1

Morrison, A. K., Waugh, D. W., Hogg, A. M., Jones, D. C., and Abernathey, R. P. (2022). Ventilation of the southern ocean pycnocline. *Annu. Rev. Mar. Sci.* 14, 405–430. doi: 10.1146/annurev-marine-010419-011012

Purkey, S. G., Smethie, W. M., Gebbie, G., Gordon, A. L., Sonnerup, R. E., Warner, M. J., et al. (2018). A synoptic view of the ventilation and circulation of antarctic bottom water from chlorofluorocarbons and natural tracers. *Annu. Rev. Mar. Sci.* 10, 503–527. doi: 10.1146/annurev-marine-121916-063414

Rae, J., Burke, A., Robinson, L., Adkins, J., Chen, T., Cole, C., et al. (2018). CO_2 storage and release in the deep Southern Ocean on millennial to centennial timescales. *Nature* 562, 569–573. doi: 10.1038/s41586-018-0614-0

Resplandy, L., Séférian, R., and Bopp, L. (2015). Natural variability of CO2 and O2 fluxes: What can we learn from centuries-long climate models simulations? *J. Geophysical Research: Oceans* 120, 384–404. doi: 10.1002/2014JC010463

Russell, J. L., Dixon, K. W., Gnanadesikan, A., Stouffer, R. J., and Toggweiler, J. R. (2006). The southern hemisphere westerlies in a warming world: Propping open the door to the deep ocean. *J. Climate* 19, 6382–6390. doi: 10.1175/JCLI3984.1

Sabine, C., Feely, R., Gruber, N., Key, R., Lee, K., Bullister, J., et al. (2004). The oceanic sink of anthropogenic CO_2. *Science* 305, 367–371.

Schmidt, C., Morrison, A. K., and England, M. H. (2023). Wind- and sea-ice-driven interannual variability of antarctic bottom water formation. *J. Geophysical Research: Oceans* 128, e2023JC019774. doi: 10.1029/2023JC019774

Shi, J.-R., Xie, S.-P., and Talley, L. D. (2018). Evolving relative importance of the southern ocean and north atlantic in anthropogenic ocean heat uptake. *J. Climate* 31, 7459–7479. doi: 10.1175/JCLI-D-18-0170.1

Shuttleworth, R., Bostock, H., Chalk, T., Calvo, E., Jaccard, S., Pelejero, C., et al. (2021). Early deglacial co2 release from the sub-antarctic atlantic and pacific oceans. *Earth Planetary Sci. Lett.* 554, 116649. doi: 10.1016/j.epsl.2020.116649

Skinner, L., Fallon, S., Waelbroeck, C., Michel, E., and Barker, S. (2010). Ventilation of the deep Southern Ocean and deglacial CO_2 rise. *Science* 328, 1147–1151.

Sokolov, S., and Rintoul, S. R. (2009). Circumpolar structure and distribution of the antarctic circumpolar current fronts: 1. mean circumpolar paths. *J. Geophysical Research: Oceans* 114. doi: 10.1029/2008JC005108

Talley, L. D. (2013). Closure of the global overturning circulation through the Indian, pacific, and southern oceans: Schematics and transports. *Oceanography* 26, 80–97.

Toggweiler, J., Russell, J., and Carson, S. (2006). Midlatitude westerlies, atmospheric CO_2, and climate change during ice ages. *Paleoceanography* 21, PA2005. doi: 10.1029/2005PA001154

Tschumi, T., Joos, F., Gehlen, M., and Heinze, C. (2011). Deep ocean ventilation, carbon isotopes, marine sedimentation and the deglacial CO_2 rise. *Climate Past* 7, 771–800. doi: 10.5194/cp-7-771-2011

Tsujino, H., Urakawa, S., Nakano, H., Small, R. J., Kim, W. M., Yeager, S. G., et al. (2018). JRA-55 based surface dataset for driving ocean–sea-ice models (JRA55-do). *Ocean Model.* 130, 79–139. doi: 10.1016/j.ocemod.2018.07.002

Völker, C., and Köhler, P. (2013). Responses of ocean circulation and carbon cycle to changes in the position of the Southern Hemisphere westerlies at Last Glacial Maximum. *Paleoceanography* 28, 726–739. doi: 10.1002/2013PA002556

Watson, A., Vallis, G., and Nikurashin, M. (2015). Southern Ocean buoyancy forcing of ocean ventilation and glacial atmospheric CO_2. *Nat. Geosci.* 8, 861–864. doi: 10.1038/ngeo2538

Zhou, S., Meijers, A., Meredith, M., Abrahamsen, E. P., Holland, P. R., Silvano, A., et al. (2023). Slowdown of Antarctic Bottom Water export driven by climatic wind and sea-ice changes. *Nat. Clim. Change* 13, 701–709. doi: 10.1038/s41558-023-01695-4

frontiers | Frontiers in Marine Science

TYPE Original Research
PUBLISHED 08 January 2024
DOI 10.3389/fmars.2023.1284750

OPEN ACCESS

EDITED BY
Zhifang Xiong,
Ministry of Natural Resources, China

REVIEWED BY
Grant Bigg,
The University of Sheffield, United Kingdom
Thomas Algeo,
University of Cincinnati, United States

*CORRESPONDENCE
Qian Ge
qge@sio.org.cn

RECEIVED 30 August 2023
ACCEPTED 15 December 2023
PUBLISHED 08 January 2024

CITATION
Lei Z, Ge Q, Chen D, Zhang Y and Han X (2024) Impact of circumpolar deep water on organic carbon isotopes and ice-rafted debris in West Antarctic: a case study in the Amundsen Sea.
Front. Mar. Sci. 10:1284750.
doi: 10.3389/fmars.2023.1284750

Impact of circumpolar deep water on organic carbon isotopes and ice-rafted debris in West Antarctic: a case study in the Amundsen Sea

Ziyan Lei[1,2,3], Qian Ge[1,2]*, Dong Chen[1,2], Yongcong Zhang[1,2] and Xibin Han[1,2]

[1]Key Laboratory of Submarine Geosciences, Ministry of Natural Resources, Hangzhou, China, [2]Second Institute of Oceanography, Ministry of Natural Resources, Hangzhou, China, [3]Department of Oceanography and Coastal Science, Louisiana State University, Baton Rouge, LA, United States

This research delves into the interaction between carbon isotopes, ice-rafted debris (IRD), and Circumpolar Deep Water (CDW) in the Amundsen Sea, West Antarctic. Utilizing sediment core ANT36-A11-04, we traced the source of the organic matter though an analysis of the total organic carbon (TOC), stable carbon isotopes ($\delta^{13}C_{org}$), and nitrogen content. We identified six environmental events in this region since the Mid-Holocene, which were discerned through a comparative analysis of the $\delta^{13}C_{org}$, TOC, and IRD content. These events were closely linked to variations in the intensity of the CDW. Notably, the synchronous occurrence of a negative shift in the $\delta^{13}C_{org}$ value and increases in TOC and IRD highlight the significant impact of CDW intrusion, underlining the pivotal role of the CDW in the regional environmental evolution. Specifically, intensified upwelling of the CDW was correlated with increased heat and nutrients, enhanced glacier melting, phytoplankton blooms, higher TOC content, augmented deposition of IRD, and finally resulted in a negative shift in the $\delta^{13}C_{org}$ value. We present a comprehensive picture of the local environmental evolution in the Amundsen Sea, characterized as a marine-glacial-biological coupling model, thereby contributing to a broader understanding of Antarctic environmental dynamics.

KEYWORDS

paleoenvironment, evolution pattern, organic matter, geochemistry, sediment

Highlights

- The organic matter source of the sediments in Core ANT36-A11-04 was analyzed.
- The 6000-yr paleoenvironmental evolution was reconstructed via indicators.
- Six events were identified via indexes and corresponding records.
- Circumpolar Deep Water plays a key role in environmental evolution.

1 Introduction

The Antarctic environment is experiencing significant transformations. Recent satellite data reveal that over the last two decades, the West Antarctic Ice Sheet (WAIS) has been diminishing at an alarming rate of 100–200 Gt per year. This decline contributes to a rise in sea level of approximately 0.25–0.26 mm per year (Joughin and Alley, 2011). Notably, the Amundsen Sea region exhibits pronounced changes, with the Pine Island and Thwaites ice shelves experiencing the most substantial mass losses. These shelves, as floating extensions of the ice sheet, play a crucial role in buttressing the ice sheet. Their melting leads to accelerated flow of the upstream glaciers into the ocean, significantly impacting global sea levels (Gudmundsson et al., 2019; Naughten et al., 2023). The vulnerability of the WAIS to warm, moist oceanic air and sub-shelf currents is a key factor driving these changes (Jenkins et al., 2010; Nicolas and Bromwich, 2011). In the Amundsen Sea, the melting of the ice shelf is predominantly influenced by the upwelling of the Circumpolar Deep Water (CDW). This warmer water not only transports heat and nutrients but also plays a vital role in shaping the regional sea ice dynamics and ecosystems (Nakayama et al., 2014; Nakayama et al., 2018; van Manen et al., 2022).

Research on the CDW in the Amundsen Sea has predominantly concentrated on modeling the intrusion of the CDW and examining variations in the temperature and salinity within the water column (Thoma et al., 2008; Nakayama et al., 2013; Mallett et al., 2018). However, there is a notable gap in research on the historical evolution of the CDW and its correlations with various indicators in sediment and ice-rafted debris (IRD). We aim to shed light on the paleoenvironmental shifts in the Amundsen Sea and to investigate how organic components and IRD respond to the influence of the CDW. This approach enables us to unravel the underlying mechanisms driving environmental changes in this region.

2 Materials and methods

Sediment samples were collected from push core ANT36-A11-04, which was obtained during the 36th Chinese National Antarctic Research Expedition (2019–2020). The sampling site, situated at a depth of 500 meters in the Amundsen Sea, West Antarctic (117.835° W, 72.028°S) is depicted in Figure 1. Following the collection, these samples were meticulously preserved at 4°C in a freezer, pending analysis. The processing in the laboratory adhered strictly to the

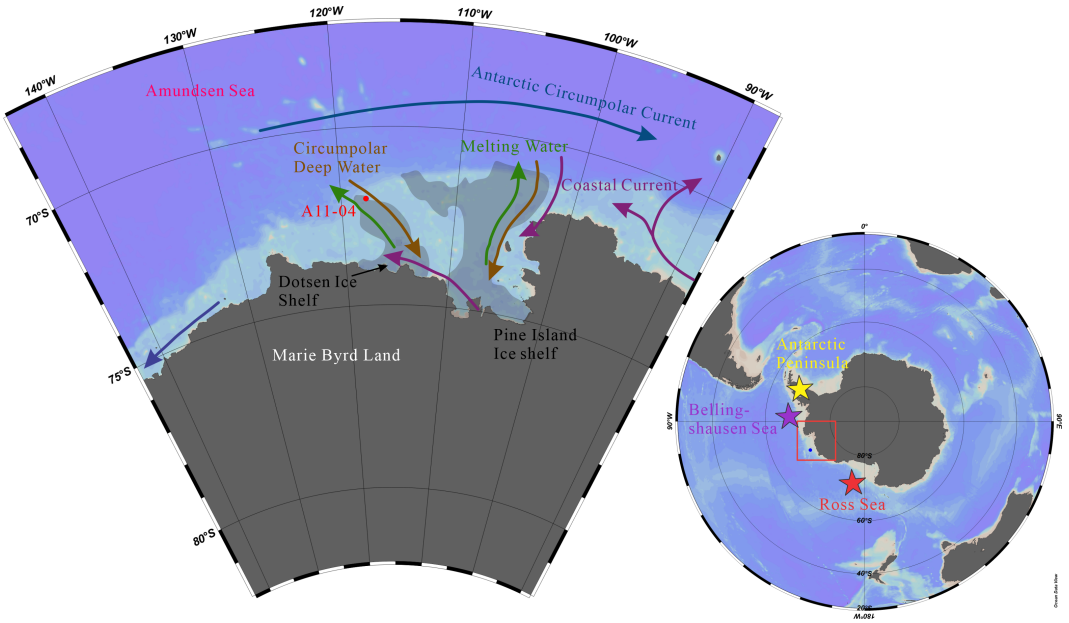

FIGURE 1
Map of the currents and station. The map on the right side is an overall map of the Antarctic. The red rectangle is the study area in the Amundsen Sea, the yellow star denotes Antarctic Peninsula, the purple star denotes the Bellingshausen Sea, and the red star denotes the Ross Sea. The map on the left side is a detailed map of the study area. The arrows represent the currents. The purple arrow is the costal current, green arrow is melting water, the brown arrow is the Circumpolar Deep Water, and the deep blue arrow is the Antarctic Circumpolar Current. The two grey shaded areas are the two biggest ice shelves in this region.

Specifications for oceanographic survey - Part 8: marine geology and geophysics survey (Liu et al., 2007). The core was 38 cm long and characterized by a dark grayish-brown hue. It was sectioned at 1-cm intervals, resulting in the attainment and analysis of 36 distinct samples.

Antarctica shelf sediments typically lack calcareous foraminifera, which are commonly used in radiocarbon dating due to their well-established reservoir adjustments (Smith et al., 2014). Consequently, dating the acid insoluble organic (AIO) fraction becomes necessary. However, bulk AIO dates often face contamination risks from ancient organic matter eroded from the Antarctica continent (Licht et al., 1996; Anderson and Andrews et al., 1999; Ohkouchi and Eglinton, 2006) or the redistribution of older shelf sediments (Domack et al., 1999), potentially leading to anomalously older radiocarbon ages. Despite these challenges, several studies have effectively employed AIO fraction dates to establish deglacial chronologies for the Antarctica shelf (Domack et al., 1999; Licht and Andrews, 2002; Mosola and Anderson, 2006; Heroy and Anderson, 2007; Hillenbrand et al., 2010; Smith et al., 2011; Licht and Hemming, 2017).

For core ANT36-A11-04, we implemented a rigorous dating methodology, integrating sedimentological and geochemical data to identify optimal horizons for accurate ^{14}C dating. Notable shifts in these data, potentially indicative of significant environmental changes (Figure 2), guided the selection of six samples for accelerator mass spectrometry (AMS) ^{14}C dating at Beta Laboratories, USA (Table 1), complemented by ^{210}Pb dating methods (Figure 3). Age corrections were made using the Calib 8.2 program (Stuiver and Reimer, 1993). It was assumed that the regional marine offset (ΔR) was 900 ± 100, which is consistent with the global marine reservoir effect and previous studies conducted in the Amundsen Sea Embayment (Lowe and Anderson, 2002; Hillenbrand et al., 2010).

Grain size analysis was conducted using a Malvern 2000 laser particle size analyzer at the Second Institute of Oceanography, Ministry of Natural Resources, Hangzhou, Zhejiang Province, China, following the Specifications for oceanographic survey - Part 8: marine geology and geophysics survey (Liu et al., 2007).

The organic carbon and nitrogen contents and isotope compositions were also analyzed at the Second Institute of Oceanography. Freeze-dried samples were milled to a size of less than 120 μm. Excess 1 M hydrochloric acid was added to the samples, which were then left to react for 24 hours to remove the carbonate. After neutralizing the samples with deionized water, the samples were lyophilized. For the $\delta^{13}C_{org}$ and organic carbon content analyses, 1–4 mg of the treated samples were wrapped in tin cups, while the nitrogen content analysis required a ten-fold increase in the sample weight. Isotope ratio mass spectrometry (Thermo Delta Plus AD, Germany) was used to conduct the $\delta^{13}C_{org}$ analysis of the sediments, and the results were calibrated against standards USGS-24, GBW4407, and IAEA-N-1. The $\delta^{13}C_{org}$ data have an accuracy of ±0.2‰ in reference to the Pee Dee Belemnite (PDB) international standard. The organic carbon and nitrogen contents were analyzed using an Elementar Vario (Germany), with an analytical accuracy of ±0.01%.

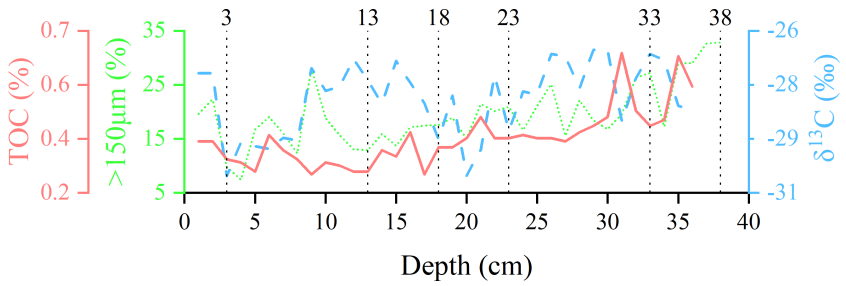

FIGURE 2
Comparison of grain size and geochemistry for the sediments in core ANT36-A11-04. The red solid line denotes the total organic carbon (TOC), the green dot line denotes the > 150 μm particle content, and the blue dash line denotes the $\delta^{13}C_{org}$.

TABLE 1 Dating results and sedimentation rate for sediment in core ANT36-A11-04 or financial relationships that could be construed as a potential conflict of interest.

Depth (cm)	AMS ^{14}C (cal yr B.P.)	Calibrated Age (a)	Old Carbonate Age (a)	Calendar Age (cal yr B.P)	Sedimentation rate (cm/kyr)
2–3	5100 ± 30	4096	4096	0	6.66
12–13	6730 ± 30	6047	4096	1951	
17–18	8310 ± 30	7693	4096	3597	3.04
22–23	9450 ± 30	8979	4096	4883	3.04
32–33	10230 ± 50	9951	4096	5855	10.29
37–38	10400 ± 30	10245	4096	6149	17.01

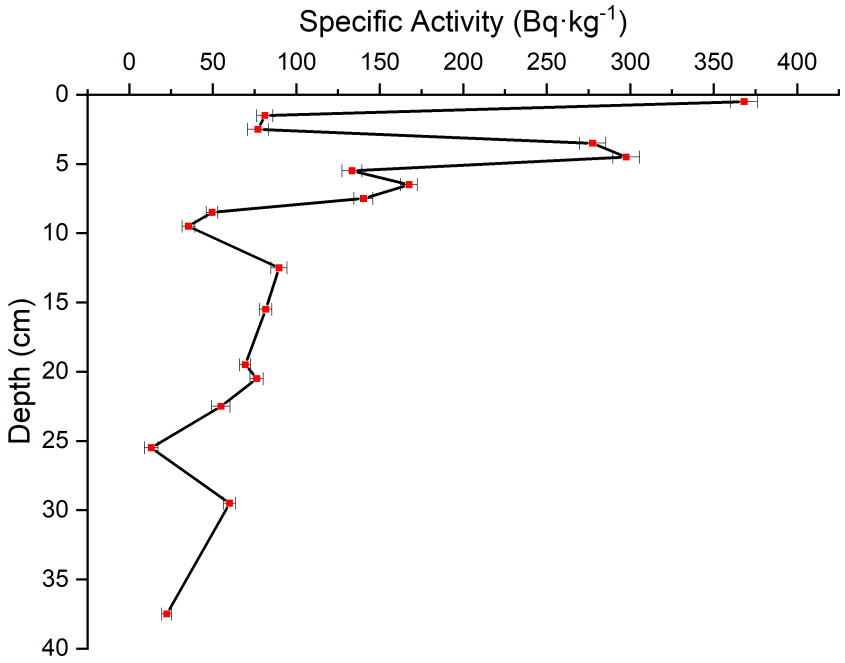

FIGURE 3
$^{210}Pb_{ex}$ profile of sediment in core ANT36-A11-04.

3 Results

3.1 Chronology

Figure 3 shows that there is a distinct exponential decrease in the excess 210Pb activity from the surface to a depth of 10 cm in the sediment from core ANT36-A11-04. It stabilizes at background levels below this depth. This trend suggests that the uppermost layer is indicative of recent sedimentation. Via age calibration using the Calib 8.2 software, we estimate that the calendar age of the sediment at depths of 2–3 cm is approximately 4096 years before present (B.P.). In light of the 210Pb activity profile, this age is interpreted as the old carbon age for this region. As a result, all of the AMS ^{14}C dating results were corrected by subtracting the age of the top of the core (4096 cal yr B.P.) Through linear interpolation and extrapolation of these corrected ages, we estimate that the calendar age at the base of the sediment is 6149 cal yr B.P. The sedimentation rates (Table 1) range from 3.0 cm/kyr to 17.0 cm/kyr. The limited quantity of sediment in the lowermost layers (36 cm to 38 cm) precluded the acquisition of data on the organic carbon, nitrogen, and carbon isotopes, but grain size analysis was conducted. Consequently, in the subsequent analyses, the age of the 35-cm layer, approximately 6031 cal yr B.P., is uniformly adopted as the representative age of the bottom layer.

3.2 Organic carbon content, nitrogen content, and organic carbon isotopes

In core ANT36-A11-04, the total organic carbon (TOC) content varied notably, ranging from 0.26% to 0.66%, with an average of 0.38% (Figure 4). The TOC content peaked between 6000 and 5200 cal yr B.P., reached the highest level, and subsequently remained a lower range of 0.26–0.45% after 5200 cal yr B.P. Regarding the total nitrogen (TN) content, it oscillated between 0.02% to 0.06%. A distinct shift occurred around 4000 cal yr B.P., that is, from 6000 to 4000 cal yr B.P., the TN content varied between 0.04% and 0.06%, with an average of 0.05%. After 4000 cal yr B.P., it ranged from 0.02% to 0.04%, with an average of 0.03%. The carbon to nitrogen ratio (C/N) also fluctuated, ranging from 6.6 to 17.9, with an overall average of 10.78. The $\delta^{13}C_{org}$ value underwent significant variation, ranging from –30.75‰ to –26.33‰, with an average of –28.07‰. The lowest and highest $\delta^{13}C_{org}$ values occurred at 177 cal yr B.P. and 5369 cal yr B.P., respectively.

3.3 Grain size

Figure 5 depicts the changes in the grain size and compositional characteristics of the sediments in core ANT36-A11-04. The sediment composition varied. Silt was predominant (average of 41.2%), followed by sand (38.7%) and clay (19.9%). The grain size composition characteristics can be categorized into two distinct stages. From 3600 cal yr B.P. onwards, the mean grain size (Mz), skewness, kurtosis, and sand content generally remained below the average values, with a notable exception around 1500 cal yr B.P. when they exceeded the average values. Conversely, during this stage, the silt and clay contents exhibited inverse trends. The sorting coefficient, skewness, and kurtosis exhibited minimal variation, suggesting a more uniform grain size distribution. In contrast, from 6149 to 3600 cal yr B.P, the Mz, skewness, kurtosis, and sand content consistently exceeded the average values, while the silt and clay contents were lower. During this period, the average skewness was 0.56, indicative of right-skewness, and the average kurtosis was 2.32.

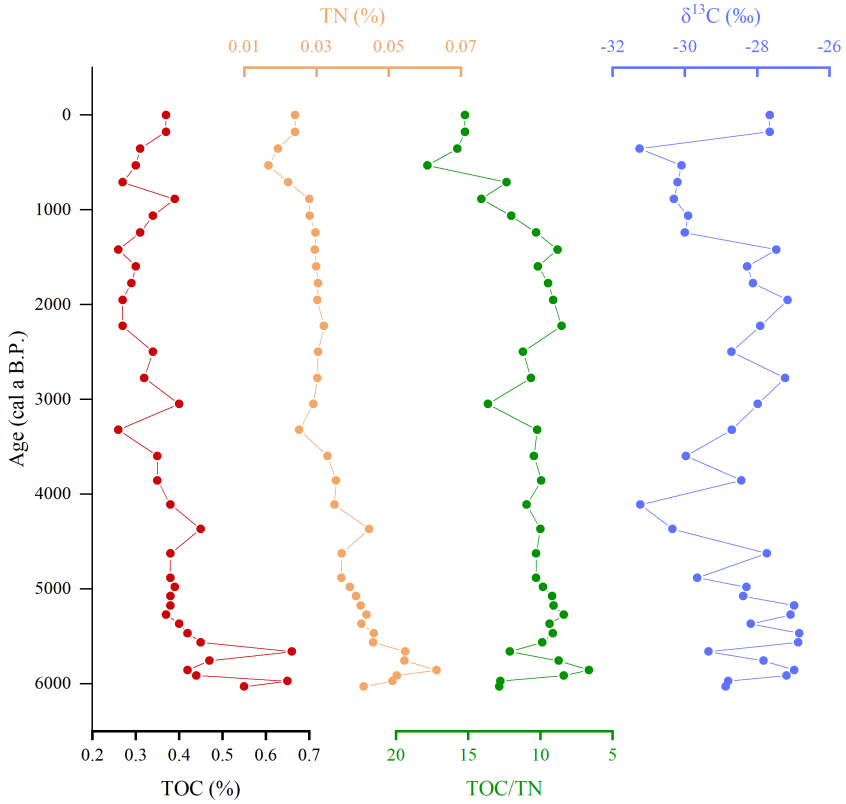

FIGURE 4
Vertical variations in TOC, TN, C/N, and $\delta^{13}C$ for the sediments in core ANT36-A11-04.

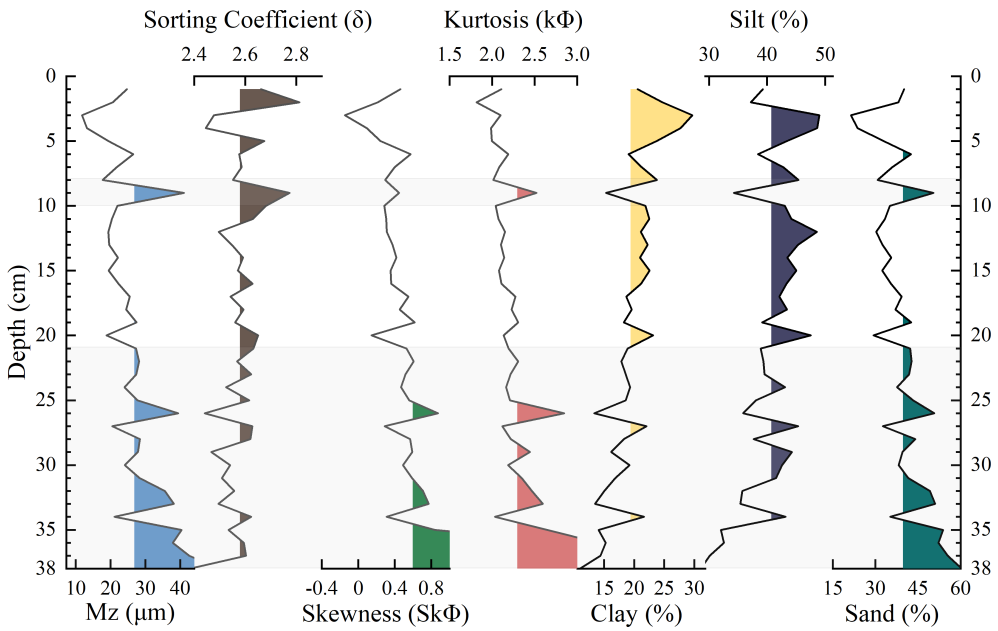

FIGURE 5
Grain size characteristics of sediments in core ANT36-A11-04. The colorful shaded area represents that this layer is beyond the average value. The grey shaded area denotes that the data within these depths are distinct from the data for the other depths.

This earlier phase was characterized by higher levels of skewness, kurtosis, and sand-grade components, implying that the provenance of the sand-grade components was distinct from that in the later stage.

4 Discussion

4.1 TOC and $\delta^{13}C_{org}$ profiles: indicators of paleoenvironmental conditions

The Antarctic environment imparts distinct characteristics to the stable carbon isotope compositions of marine organic materials, markedly differing from those at lower latitudes. The notably low (depleted) $\delta^{13}C_{org}$ values of Antarctic plankton have been attributed to several factors: the low water temperature and resultant high CO_2 availability (Rau et al., 1989), the specific species composition of the plankton, and the upwelling of deep water (Lupton and Craig, 1981; Spezie, 1999). In Antarctic waters, the surface-water CO_2 concentrations can be up to 2.5 times higher than those in equatorial waters, primarily due to the lower temperatures. This increase in the CO_2 concentration, coupled with the temperature decrease, likely contributes to the reduction in the $\delta^{13}C_{org}$ values at higher latitudes. Additionally, the upwelling of deep waters, which are enriched in dissolved CO_2 with low $\delta^{13}C$ values due to the remineralization of organic matter, further influences this biological processing in the surface water. Consequently, $\delta^{13}C_{org}$ is a potential indicator of environmental change and is a focal point in this study.

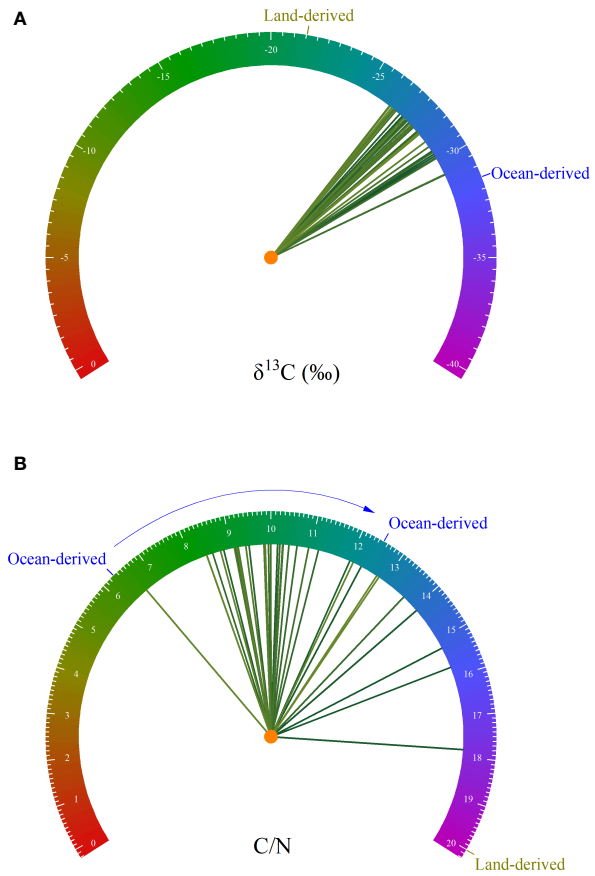

FIGURE 6
Organic matter source discriminant diagram for core ANT36-A11-04. **(A)** $\delta^{13}C_{org}$ value and endmember value of the sediments in core ANT36-A11-04 (Shultz and Calder, 1976; Minoura et al., 1997). The region delineated by the blue arrow, marking the range of 6.3 to 12.4, suggests a marine origin for the organic matter. A C/N ratio of greater than 20 indicates that the organic matter has a terrestrial origin. **(B)** C/N value and end-member value of the organic matter in ANT36-A11-04 (Albuquerque and Mozeto, 1997; Stein and Fahl, 2000). The values close to the blue area signify a marine source for the organic matter, while proximity to the green area indicates a terrestrial source.

The study area is predominantly influenced by the colonial haptophyte *Phaeocystis antarctica*, known for its specific organic carbon isotope ratio ($\delta^{13}C_{org}$). This ratio typically ranges between –28.34‰ and –29.86‰ (Delmont et al., 2014; Ducklow et al., 2015), which is very consistent with our data (i.e., –30.75‰ to –26.33‰, average of –28.07‰). These findings suggest that marine phytoplankton made a significant contribution to the organic carbon in the sediment in core ANT36-A11-04. To ascertain the organic carbon source, we used a $\delta^{13}C_{org}$ value of –31.5‰ for West Antarctic phytoplankton as the marine endmember, and a value of –23.6‰ for East Antarctic terrestrial mosses, lichens, and freshwater lake algae as the terrestrial endmember (Shultz and Calder, 1976; Minoura et al., 1997). Our analysis revealed that the organic carbon in the core predominantly originated from marine sources (Figure 6). Furthermore, due to the fact that terrestrial plants are composed of nitrogen-poor lignin and cellulose, while marine organisms are contain nitrogen-rich proteins marine and terrestrial sources of organic matter have distinct C/N values. Terrestrial plants typically have C/N values of > 20 (Albuquerque and Mozeto, 1997), whereas that of high-latitude marine phytoplankton ranges from 6.3 to 12.5 (Stein and Fahl, 2000). As depicted in Figure 6, C/N values of > 20 suggest a terrestrial plant origin, while values of 6.3–12.5 indicate a contribution from marine phytoplankton. The average C/N value of 10.8 for the core suggests a primarily marine phytoplankton source. However, the variation in the C/N values from 6.6 to 17.8 implies possible terrestrial inputs or the influences of early diagenesis or grain size effects, as evidenced by the correlation between the C/N ratio and Mz of 0.42, $p = 0.03$. Consequently, marine sources were the dominant contributors to the core's organic carbon content.

The TOC content is intricately linked to primary productivity in the marine environment. Enhanced primary productivity is often correlated with an increase in the TOC content (Island, 2001; Khim et al., 2004; Mendonça et al., 2017). In high-latitude regions, the primary productivity exhibits notable seasonal and spatial variations and is primarily governed by light availability and climatic fluctuations. Consequently, the TOC content is a potential indicator of environmental change, reflecting alterations in the underlying productivity dynamics.

4.2 Tracing paleoenvironmental dynamics and underlying mechanisms in the Amundsen Sea since the mid-Holocene

Previous studies in the Ross Sea (Yongbin et al., 2021) and the Amundsen Sea (Hillenbrand et al., 2009) have established that the

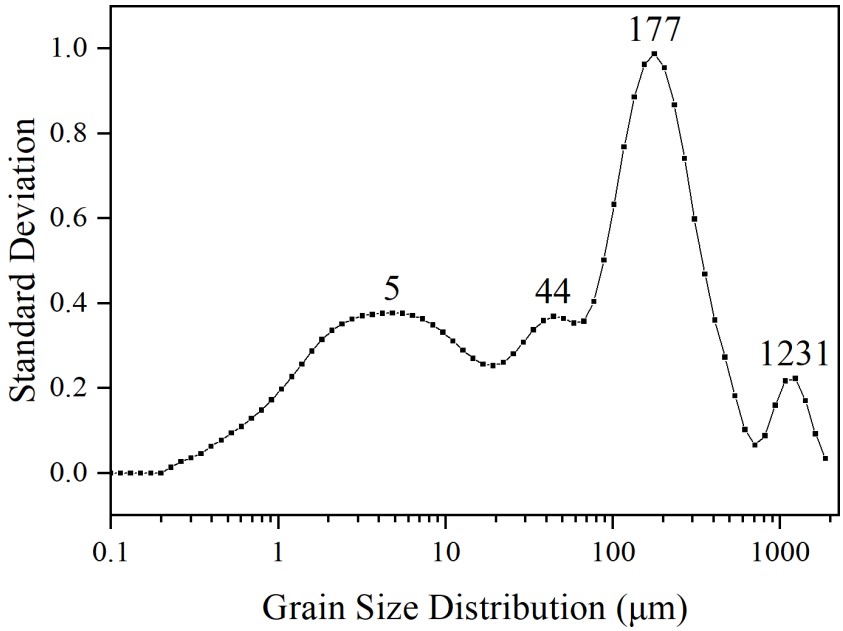

FIGURE 7
Grain size-standard deviation diagram of sediment in core ANT36-A11-04.

IRD variation was closely linked to environmental changes, making IRD a key indicator of glacial activity in the West Antarctic region. In high-latitude regions, the > 150 μm grain-size fraction in sediments is commonly used as a proxy for IRD. Our analysis of core ANT36-A11-04 (Figure 7) indicates that the 67–707 μm grain size interval was the most sensitive to environmental changes, with a pronounced peak at 177 μm. Thus, the > 150 μm fraction was selected as the IRD proxy in this study.

Through integration of multiple proxies, including the Cd/P ratio (indicative of CDW intensity) (Xu et al., 2021), $\delta^{13}C_{org}$ of organic matter and TOC content for core ANT36-A11-04, and the > 150 μm grain size (IRD proxy), we reconstructed the paleoenvironmental history of the Amundsen Sea. Spanning over 6,000 years, the core recorded six distinct environmental events (I–VI; Figure 8). Generally, the TOC and IRD trends corresponded with the variations in the intensity of the CDW. During 6000–3000 cal yr B.P, the TOC, IRD, and CDW decreased from the highest points to the average states. This pattern suggests a strong interconnection between the TOC, IRD, and CDW, that is, both the TOC and IRD decreased as the intensity of the CDW decreased, underscoring the influence of the CDW on these parameters. Additionally, there were noticeable peaks in both the TOC and IRD during the six periods studied. This trend was inversely reflected in the $\delta^{13}C_{org}$ record, suggesting that the $\delta^{13}C_{org}$ variations were associated with the TOC and IRD variations, and the CDW was also a potential influencing factor.

Our environmental evolution model (Figure 9) proposes that the upwelling of the relatively warm CDW contributed to accelerated glacier melting, enhancing sea ice melting and the subsequent release of IRD. The melting of sea ice facilitated a rapid exchange between the ocean and the atmosphere, leading to a marked negative shift in the $\delta^{13}C_{org}$ value of the marine plankton (Rau et al., 1989; Yager et al., 2016). Additionally, the influx of heat and nutrients associated with the CDW likely stimulated phytoplankton blooms, contributing to an increase in the TOC.

During event I (5800–5500 cal yr B.P), as illustrated in Figure 8, there was a concurrent peak in the TOC, and the > 150 μm particle size content coincided with a low $\delta^{13}C_{org}$ value. This pattern is indicative of an increased supply of IRD, potentially linked to intensified sea ice melting (Sakamoto et al., 2005). This period corresponded with a documented reduction in the sea ice content in the Weddell Sea, as evidenced by the abundance of foraminifera *F. curta* (Mezgec et al., 2017). A subsequent decline in the Cd/P ratio pointed to weakening of the intensity of the CDW, which likely led to diminished heat transfer to the sea surface. This reduction in heat transfer could have resulted in decreased ice shelf melting or augmented sea ice coverage (Thoma et al., 2008; Guo et al., 2019). Consequently, this led to a decrease in the supply of IRD and lower availability of light and nutrients, which in turn resulted in a decrease in the TOC. The observed decrease in the $\delta^{13}C_{org}$ value was influenced by multiple factors (Rau et al., 1989; Goericke and Fry, 1994; Annett et al., 2007). When phytoplankton absorb carbon from the inorganic carbon pool, they are more inclined to absorb lighter isotopes at higher inorganic carbon concentrations (Mook et al., 1974). These factors were linked to the changes in the CDW, as a decline in the intensity of the CDW resulted in decreased heat and nutrient transport to the sea surface (Fei et al., 2019; Xu et al., 2021).

The subsequent events, II (5100–4600 cal yr B.P), III (3900–3200 cal yr B.P), IV (2600–2000 cal yr B.P), V (1800–1300 cal yr B.P), and VI (1100–500 cal yr B.P), exhibited similar patterns. The IRD and TOC exhibited opposite patterns compared to that of the $\delta^{13}C_{org}$. The presence of an IRD deposition pattern was evident in the sediment in core ANT36-A11-04, which is consistent with the ice retreat-associated IRD input events in the Ross Sea and the Amundsen Sea (Hillenbrand et al., 2009; Yongbin et al., 2021). This pattern can be

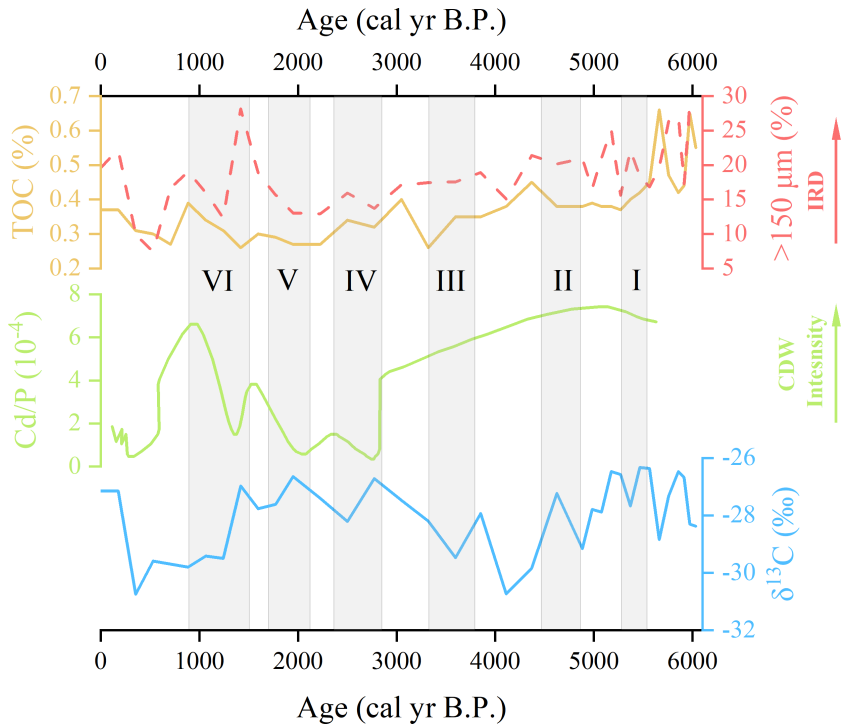

FIGURE 8
The response relationship between $\delta^{13}C_{org}$ and the environment and its potential mechanism. The yellow solid line denotes the TOC content in core ANT36-A11-04, the red dashed line indicates the > 150 μm fraction content in the core, the green solid line denotes the Cd/P ratio within the penguin ornithogenic sediments from the Ross Sea, which indicates the intensity of the CDW (Xu et al., 2021), and the blue solid line denotes the $\delta^{13}C_{org}$ of the organic matter within the core sediments.

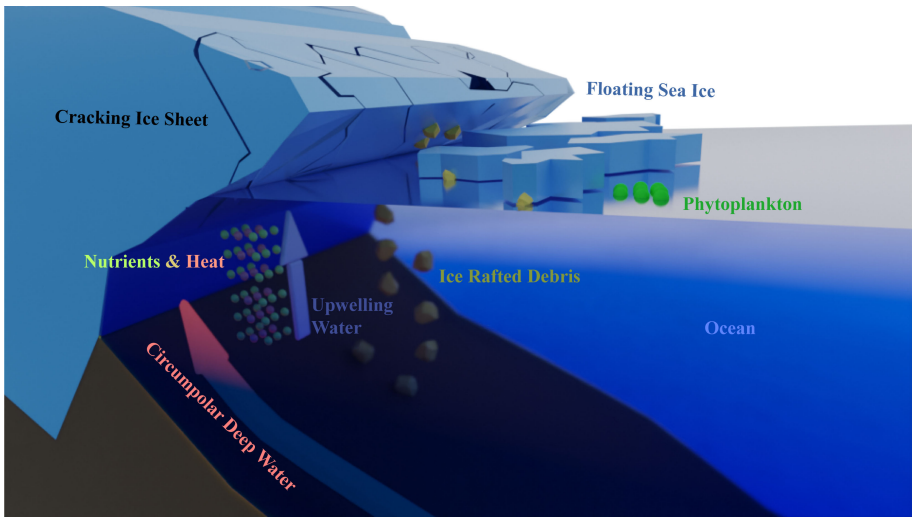

FIGURE 9
Environmental evolution pattern. The Circumpolar Deep Water (CDW) (depicted in red) intruded beneath the ice shelf (depicted as a blue opaque polyhedron with cracking details). The upwelling CDW is shown as upwelling water (indicated by the dark blue arrow), which carries both nutrients (shown as small green spheres) and heat (shown as red spheres) toward the sea surface. This upwelling fostered the proliferation of phytoplankton (illustrated as larger green spheres) near the floating sea ice. Additionally, this process contributed to the melting of the ice shelf and sea ice, leading to the release of ice-rafted debris (yellow and brown particles), which then became incorporated into the ocean sediments.

attributed to the influence of the upwelling of warm CDW on the ice shelves in the Amundsen Sea sector. As the grounding line of the ice shelves retreated, significant amounts of land-derived detritus were unloaded, leading to IRD deposition events and the formation of glacial debris deposits on the continental shelf (Anderson et al., 2014). When the heat flux decreased and the sea ice coverage expanded, the melting of icebergs slowed, resulting in decreased IRD deposition, reduced primary production, and a lower TOC.

Our analysis of the sediment in core ANT36-A11-04 suggests that the CDW profoundly impacted the local environmental changes, including the sea ice dynamics, blooming of phytoplankton, and IRD deposition (Figure 9). The core record illustrates that the close association between the CDW, $\delta^{13}C_{org}$, and IRD values suggests that the CDW played a critical role in the regional environmental evolution process. The reduction in the intensity of the CDW resulted in a decreased water temperature, reduced ice shelf melting, diminished IRD input, and a reduced production rate of organically derived phytoplankton. In summary, the existence of this coupled model emphasizes the importance of the CDW in the environmental changes in the Amundsen Sea region.

5 Conclusions

Over the past decade, many researchers have found that the atmosphere and ocean currents in West Antarctic played a key role in the environmental evolution in this region. In particular, the CDW deeply influenced the glaciers and ecosystem. To determine the relationship between the CDW and the environmental changes, several analyses were performed in this study. The three main conclusions are presented below.

1. By examining the sediment of core ANT36-A11-04 and integrating prior research findings, it was found that the primary source of the organic matter in the sediment was largely oceanic.
2. The > 150 μm grain size component in core ANT36-A11-04 was utilized as an alternative indicator of IRD, in combination with other indicators such as $\delta^{13}C_{org}$, TOC, and proxy for the CDW. Through these indicators, six environmental events were identified, each with corresponding records in the Antarctic region.
3. By comparing multiple indicators, it was observed that there was a clear response relationship between the $\delta^{13}C_{org}$, IRD, and CDW, indicating that the CDW played a critical role in the regional environmental evolution. The upwelling of the relatively warm CDW led to accelerated glacier melting and increased heat flux, which also enhanced the melting of sea ice. This process resulted in the release and deposition of IRD carried by glacial and sea ice. Furthermore, the heat and nutrients transported by the upwelling water stimulated the proliferation of marine plankton. Additionally, the melting of sea ice enhanced the rapid exchange between the ocean and the atmosphere, ultimately causing a noticeable negative shift in the $\delta^{13}C_{org}$ value of the marine plankton.

Data availability statement

The raw data supporting the conclusions of this article will be made available by the authors, without undue reservation.

Author contributions

ZL: Software, Visualization, Writing – original draft, Writing – review & editing. QG: Funding acquisition, Methodology, Resources, Supervision, Writing – review & editing. DC: Investigation, Validation, Writing – review & editing. YZ: Investigation, Resources, Software, Writing – review & editing. XH: Investigation, Methodology, Resources, Writing – review & editing.

Funding

The author(s) declare financial support was received for the research, authorship, and/or publication of this article. This work was funded by the Impact and Response of Antarctic Seas to Climate Change (IRASCC). This project provided us with cruise and funding for sampling and analysis.

Acknowledgments

Supported by the crew and researchers of the 36th Chinese Antarctic Research Expedition, and it was reviewed by reviewers and editors. We thank them for their patience and time.

Conflict of interest

The authors declare that the research was conducted in the absence of any commercial or financial relationships that could be construed as a potential conflict of interest.

Publisher's note

Supplementary material

The Supplementary Material for this article can be found online at: https://www.frontiersin.org/articles/10.3389/fmars.2023.1284750/full#supplementary-material

References

Albuquerque, A. L. S., and Mozeto, A. A. (1997). C: N: P ratios and stable carbon isotope compositions as indicators of organic matter sources in a riverine wetland system (Moji-guaçu River, São Paulo-Brazil). *Wetlands* 17, 1–9. doi: 10.1007/BF03160713

Anderson, J. B., Conway, H., Bart, P. J., Witus, A. E., Greenwood, S. L., McKay, R. M., et al. (2014). Ross Sea paleo-ice sheet drainage and deglacial history during and since the LGM. *Quat. Sci. Rev.* 100, 31–54. doi: 10.1016/j.quascirev.2013.08.020

Annett, A. L., Carson, D. S., Ganeshram, R. S., and Fallick, A. E. (2007). "Ecological influences on δ13C of particulate matter in seasonally ice-covered Ryder Bay." *Antarctica–Online Proceedings of the 10th ISAES X* edited by A. K. Cooper, C. R. Raymond, et al. USGS Open-File Report 1047 (2007).

Delmont, T. O., Hammar, K. M., Ducklow, H. W., Yager, P. L., and Post, A. F. (2014). Phaeocystis Antarctica blooms strongly influence bacterial community structures in the Amundsen Sea polynya. *Front. Microbiol.* 5. doi: 10.3389/fmicb.2014.00646

Domack, E. W., Jacobson, E. A., Shipp, S., and Anderson, J. B. (1999). Late Pleistocene–Holocene retreat of the West Antarctic Ice-Sheet system in the Ross Sea: Part 2—Sedimentologic and stratigraphic signature. *GSA Bull.* 111, 1517–1536. doi: 10.1130/0016-7606(1999)111<1517:LPHROT>2.3.CO;2

Ducklow, H. W., Wilson, S. E., Post, A. F., Stammerjohn, S. E., Erickson, M., Lee, S., et al. (2015). Particle flux on the continental shelf in the Amundsen Sea Polynya and Western Antarctic PeninsulaAntarctic particle flux. *Elem. Sci. Anthr* 3, 000046. doi: 10.12952/journal.elementa.000046

Fei, X., Zhang, Z., Cheng, Z., and Santosh, M. (2019). Factors controlling the crystal morphology and chemistry of garnet in skarn deposits: A case study from the Cuihongshan polymetallic deposit, Lesser Xing'an Range, NE China. *Am. Mineral.* 104, 1455–1468. doi: 10.2138/am-2019-6968

Goericke, R., and Fry, B. (1994). Variations of marine plankton δ13C with latitude, temperature, and dissolved CO2 in the world ocean. *Glob. Biogeochem. Cycles* 8, 85–90. doi: 10.1029/93GB03272

Gudmundsson, G. H., Paolo, F. S., Adusumilli, S., and Fricker, H. A. (2019). Instantaneous Antarctic ice sheet mass loss driven by thinning ice shelves. *Geophys. Res. Lett.* 46, 13903–13909. doi: 10.1029/2019GL085027

Guo, G., Shi, J., Gao, L., Tamura, T., and Williams, G. D. (2019). Reduced sea ice production due to upwelled oceanic heat flux in Prydz Bay, East Antarctica. *Geophys. Res. Lett.* 46, 4782–4789. doi: 10.1029/2018GL081463

Heroy, D. C., and Anderson, J. B. (2007). Radiocarbon constraints on Antarctic Peninsula ice sheet retreat following the Last Glacial Maximum (LGM). *Quat. Sci. Rev.* 26, 3286–3297. doi: 10.1016/j.quascirev.2007.07.012

Hillenbrand, C.-D., Kuhn, G., and Frederichs, T. (2009). Record of a Mid-Pleistocene depositional anomaly in West Antarctic continental margin sediments: an indicator for ice-sheet collapse? *Quat. Sci. Rev.* 28, 1147–1159. doi: 10.1016/j.quascirev.2008.12.010

Hillenbrand, C.-D., Smith, J. A., Kuhn, G., Esper, O., Gersonde, R., Larter, R. D., et al. (2010). Age assignment of a diatomaceous ooze deposited in the western Amundsen Sea Embayment after the Last Glacial Maximum. *J. Quat. Sci.* 25, 280–295. doi: 10.1002/jqs.1308

Island, G. (2001). South Shetland islands. *Antarct. Sci.* 7, 99–113.

Jenkins, A., Dutrieux, P., Jacobs, S. S., McPhail, S. D., Perrett, J. R., Webb, A. T., et al. (2010). Observations beneath Pine Island Glacier in West Antarctica and implications for its retreat. *Nat. Geosci.* 3, 468–472. doi: 10.1038/ngeo890

Joughin, I., and Alley, R. B. (2011). Stability of the West Antarctic ice sheet in a warming world. *Nat. Geosci.* 4, 506–513. doi: 10.1038/ngeo1194

Anderson, J., and Andrew, J. (1999). Radiocarbon constraints on ice sheet advance and retreat in the Weddell Sea, Antarctica. *Geology* 27 (2), 179–182. doi: 10.1130/0091-7613(1999)027<0179:RCOISA>2.3.CO;2

Khim, B.-K., Yoon, H.-I., Kang, C.-Y., and Zhao, J. (2004). Holocene variations of organic carbon contents in lake Langer of king George island, South Shetland islands, West Antarctica. *Ocean Polar Res.* 26, 507–514. doi: 10.4217/OPR.2004.26.3.507

Licht, K. J., and Andrews, J. T. (2002). The 14C record of late pleistocene ice advance and retreat in the central ross sea, Antarctica. *Arct. Antarct. Alp. Res.* 34, 324–333. doi: 10.1080/15230430.2002.12003501

Licht, K. J., and Hemming, S. R. (2017). Analysis of Antarctic glacigenic sediment provenance through geochemical and petrologic applications. *Quat. Sci. Rev.* 164, 1–24. doi: 10.1016/j.quascirev.2017.03.009

Licht, K.J., Jennings, A.E., Andrews, J.T., and Williams, K.M. (1996). Chronology of late Wisconsin ice retreat from the western Ross Sea Antarctica. *Geology* 24, 223–226.

Liu, S., LI, J., Fang, X., Zhang, H., Yu, Y., Cao, P., et al. (2007). National Standards of People's Republic of China: Specifications for oceanographic survey - Part 8: Marine geology and geophysics survey. *Beijing, China, China Standards Press for China National Standardization Administration*, 139pp. doi: 10.25607/OBP-151

Lowe, A. L., and Anderson, J. B. (2002). Reconstruction of the West Antarctic ice sheet in Pine Island Bay during the Last Glacial Maximum and its subsequent retreat history. *Quat. Sci. Rev.* 21, 1879–1897. doi: 10.1016/S0277-3791(02)00006-9

Lupton, J.E., and Craig, H. (1981). A major helium-3 source at 15°S on the East Pacific Rise. *Science* 214, 13-18. doi: 10.1126/science.214.4516.13

Mallett, H. K., Boehme, L., Fedak, M., Heywood, K. J., Stevens, D. P., and Roquet, F. (2018). Variation in the distribution and properties of Circumpolar Deep Water in the eastern Amundsen Sea, on seasonal timescales, using seal-borne tags. *Geophys. Res. Lett.* 45, 4982–4990. doi: 10.1029/2018GL077430

Mendonça, R., Müller, R. A., Clow, D., Verpoorter, C., Raymond, P., Tranvik, L. J., et al. (2017). Organic carbon burial in global lakes and reservoirs. *Nat. Commun.* 8, 1694. doi: 10.1038/s41467-017-01789-6

Mezgec, K., Stenni, B., Crosta, X., Masson-Delmotte, V., Baroni, C., Braida, M., et al. (2017). Holocene sea ice variability driven by wind and polynya efficiency in the Ross Sea. *Nat Commun* 8, 1334. doi: 10.1038/s41467-017-01455-x

Minoura, K., Hoshino, K., Nakamura, T., and Wada, E. (1997). Late Pleistocene-Holocene paleoproductivity circulation in the Japan Sea: sea-level control on δ13C and δ15N records of sediment organic material. *Palaeogeogr. Palaeoclimatol. Palaeoecol.* 135, 41–50. doi: 10.1016/S0031-0182(97)00026-6

Mook, W. G., Bommerson, J. C., and Staverman, W. H. (1974). Carbon isotope fractionation between dissolved bicarbonate and gaseous carbon dioxide. *Earth Planet. Sci. Lett.* 22, 169–176. doi: 10.1016/0012-821X(74)90078-8

Mosola, A. B., and Anderson, J. B. (2006). Expansion and rapid retreat of the West Antarctic Ice Sheet in eastern Ross Sea: possible consequence of over-extended ice streams? *Quat. Sci. Rev.* 25, 2177–2196. doi: 10.1016/j.quascirev.2005.12.013

Nakayama, Y., Menemenlis, D., Zhang, H., Schodlok, M., and Rignot, E. (2018). Origin of Circumpolar Deep Water intruding onto the Amundsen and Bellingshausen Sea continental shelves. *Nat. Commun.* 9, 3403. doi: 10.1038/s41467-018-05813-1

Nakayama, Y., Schröder, M., and Hellmer, H. H. (2013). From circumpolar deep water to the glacial meltwater plume on the eastern Amundsen Shelf. *Deep Sea Res. Part Oceanogr. Res. Pap.* 77, 50–62. doi: 10.1016/j.dsr.2013.04.001

Nakayama, Y., Timmermann, R., Schröder, M., and Hellmer, H. H. (2014). On the difficulty of modeling Circumpolar Deep Water intrusions onto the Amundsen Sea continental shelf. *Ocean Model.* 84, 26–34. doi: 10.1016/j.ocemod.2014.09.007

Naughten, K. A., Holland, P. R., and De Rydt, J. (2023). Unavoidable future increase in West Antarctic ice-shelf melting over the twenty-first century. *Nat. Clim. Change* 13, 1222–1228. doi: 10.1038/s41558-023-01818-x

Nicolas, J. P., and Bromwich, D. H. (2011). Climate of West Antarctica and influence of marine air intrusions. *J. Clim.* 24, 49–67. doi: 10.1175/2010JCLI3522.1

Ohkouchi, N., and Eglinton, T. I. (2006). Radiocarbon constraint on relict organic carbon contributions to Ross Sea sediments. *Geochem. Geophys. Geosyst.* 7, Q04012. doi: 10.1029/2005GC001097

Rau, G. H., Takahashi, T., and Marais, D. J. D. (1989). Latitudinal variations in plankton δ13C: implications for CO2 and productivity in past oceans. *Nature* 341, 516–518. doi: 10.1038/341516a0

Sakamoto, T., Ikehara, M., Aoki, K., Iijima, K., Kimura, N., Nakatsuka, T., et al. (2005). Ice-rafted debris (IRD)-based sea-ice expansion events during the past 100 kyrs in the Okhotsk Sea. *Deep Sea Res. Part II Top. Stud. Oceanogr.* 52, 2275–2301. doi: 10.1016/j.dsr2.2005.08.007

Shultz, D. J., and Calder, J. A. (1976). Organic carbon 13C12C variations in estuarine sediments. *Geochim. Cosmochim. Acta* 40, 381–385. doi: 10.1016/0016-7037(76)90002-8

Smith, J. A., Hillenbrand, C.-D., Kuhn, G., Klages, J. P., Graham, A. G. C., Larter, R. D., et al. (2014). New constraints on the timing of West Antarctic Ice Sheet retreat in the eastern Amundsen Sea since the Last Glacial Maximum. *Glob. Planet. Change* 122, 224–237. doi: 10.1016/j.gloplacha.2014.07.015

Smith, J. A., Hillenbrand, C.-D., Kuhn, G., Larter, R. D., Graham, A. G., Ehrmann, W., et al. (2011). Deglacial history of the West Antarctic Ice Sheet in the western Amundsen Sea embayment. *Quat. Sci. Rev.* 30, 488–505. doi: 10.1016/j.quascirev.2010.11.020

Spezie, G. (1999). *Oceanography of the ross sea: Antarctica* (Springer).

Stein, R., and Fahl, K. (2000). Holocene accumulation of organic carbon at the Laptev Sea continental margin (Arctic Ocean): sources, pathways, and sinks. *Geo-Mar. Lett.* 20, 27–36. doi: 10.1007/s003670000028

Stuiver, M., and Reimer, P. J. (1993). Extended 14C data base and revised CALIB 3.0 14C age calibration program. *Radiocarbon* 35, 215–230. doi: 10.1017/S0033822200013904

Thoma, M., Jenkins, A., Holland, D., and Jacobs, S. (2008). Modelling circumpolar deep water intrusions on the Amundsen Sea continental shelf, Antarctica. *Geophys. Res. Lett.* 35. doi: 10.1029/2008GL034939

van Manen, M., Aoki, S., Brussaard, C. P. D., Conway, T. M., Eich, C., Gerringa, L. J. A., et al. (2022). The role of the Dotson Ice Shelf and Circumpolar Deep Water as driver and source of dissolved and particulate iron and manganese in the Amundsen Sea polynya, Southern Ocean. *Mar. Chem.* 246, 104161. doi: 10.1016/j.marchem.2022.104161

Xu, Q. B., Yang, L. J., Gao, Y. S., Sun, L. G., and Xie, Z. Q. (2021). 6,000-year reconstruction of modified circumpolar deep water intrusion and its effects on sea ice and penguin in the ross sea. *Geophys. Res. Lett.* 48, e2021GL094545. doi: 10.1029/2021GL094545

Yager, P., Sherrell, R., Stammerjohn, S., Ducklow, H., Schofield, O., Ingall, E., et al. (2016). A carbon budget for the Amundsen Sea Polynya, Antarctica: Estimating net community production and export in a highly productive polar ecosystem. *Elem. Sci. Anthr.* 4, 140. doi: 10.12952/journal.elementa.000140

Yongbin, L., Rujian, W., Li, W. U., and Wenshen, X. (2021). Glacial dynamics evolutions revealed by ice-rafted detritus record from the Ross Sea sector of the Southern Ocean since Late Pleistocene. *Quat. Sci.* 41, 662–677. doi: 10.11928/j.issn.1001-7410.2021.03.04

frontiers | Frontiers in Marine Science

TYPE Original Research
PUBLISHED 11 January 2024
DOI 10.3389/fmars.2023.1324391

OPEN ACCESS

EDITED BY
Di Qi, Jimei University, China

REVIEWED BY
Liang Gao,
China University of Geosciences, China
Jingteng Guo,
Ministry of Natural Resources, China

*CORRESPONDENCE
Rujian Wang
rjwang@tongji.edu.cn

RECEIVED 09 November 2023
ACCEPTED 21 December 2023
PUBLISHED 11 January 2024

CITATION
Wu L, Li L, Wang R, Shao H, Chen Y, Lin Z, Liu Y, Xiao W and Xu R (2024) Grain-size, coarse fraction lithology and clay mineral compositions of surface sediments from Ross Sea, Antarctica: implications for their provenance and delivery mode.
Front. Mar. Sci. 10:1324391.
doi: 10.3389/fmars.2023.1324391

Grain-size, coarse fraction lithology and clay mineral compositions of surface sediments from Ross Sea, Antarctica: implications for their provenance and delivery mode

Li Wu[1,2,3,4], Longwei Li[1,3], Rujian Wang[2]*, Hebin Shao[5], Yi Chen[1], Zipei Lin[1], Yue Liu[1], Wenshen Xiao[2] and Ran Xu[1]

[1]Laboratory for Coastal Ocean Variation and Disaster Prediction, College of Ocean and Meteorology, Guangdong Ocean University, Zhanjiang, Guangdong, China, [2]State Key Laboratory of Marine Geology, Tongji University, Shanghai, China, [3]Key Laboratory of Climate, Resources and Environment in Continental Shelf Sea and Deep Sea of Department of Education of Guangdong Province, Guangdong Ocean University, Zhanjiang, Guangdong, China, [4]Key Laboratory of Space Ocean Remote Sensing and Application, Ministry of Natural Resources, Beijing, China, [5]Key Laboratory for Polar Science of the Ministry of Natural Resources, Polar Research Institute of China, Shanghai, China

Knowledge on spatial distribution, provenance and delivery mode of surface sediment aids in interpretation of nearby sediment records for paleoenvironmental reconstruction. Such knowledge, however, remains largely unknown for the modern Ross Sea, Antarctica: a key region for understanding the dynamical behavior of Antarctic Ice Sheet over geological past. In this study, we address this gap by analyzing the grain-size distribution, coarse fraction (>250 μm) lithology, and clay mineralogy of a set of surface sediment samples covering the whole Ross Sea continental shelf. Our data reveals that the sediments were mostly delivered by icebergs and bottom currents. Iceberg delivery was significantly controlled by factors such as water depth, proximity to the iceberg sources, and invasion of the Modified Circumpolar Deep Water. Bottom current activity was stronger in the Western Ross Sea (WRS) than in the Eastern Ross Sea (ERS), controlled by the formation and transport of Dense Shelf Water. Three major sorts of coarse fraction were identified, including the quartz-rich Iceberg Rafted Detritus (IRD) originating from West Antarctic glaciers and primarily distributed in the ERS, the mafic rocks-rich IRD from the Ferrar Group as well as the McMurdo Volcanic Group and mainly found in the WRS, and deformed silt traced back to the grounding zone of the David Glacier-Dragalski Ice Tongue system. The distribution of clay minerals is dominated by a distinct binary mixing pattern. Smectite and kaolinite are mainly present in the ERS, derived from beneath the West Antarctic Ice Sheet. Higher illite and chlorite contents were found offshore of the Southern Victoria Land, derived from the East Antarctic

craton. Overall, these results demonstrate that the glaciers draining into Ross Sea from both the East and West Antarctic Ice Sheets are highly dynamical in the context of modern climate conditions, with implications for potential contribution to future sea level rise.

KEYWORDS

surface sediment, ross sea, grain-size, iceberg rafted debris, clay mineralogy

1 Introduction

Antarctica hosts the hugest ice sheet on earth, representing a sea level equivalent of approximately 60 m (Fretwell et al., 2013). The potential for partial melting of the Antarctic Ice Sheet to contribute significantly to global sea level rise has garnered increasing attention in the context of ongoing global climate warming (Blackburn et al., 2020; Ge et al., 2022). Ross Sea is one of the largest marginal seas around Antarctica. It serves as a major drainage basin for glaciers derived from both the East Antarctic Ice Sheet (EAIS) and the West Antarctic Ice Sheet (WAIS) (Naish et al., 2001; Naish et al., 2009). Sediment records from the continental shelf of the Ross Sea hold invaluable clues about the dynamical behavior of the glaciers derived from these ice sheets (Anderson et al., 1984; Ehrmann, 1998; Naish et al., 2001; Anderson et al., 2018; Marschalek et al., 2021), which are crucial for deepening our understanding of the global climate system as well as for projections on future climate and sea level change (DeConto and Pollard, 2016; Edwards et al., 2019).

Understanding sediment provenance and delivery modes is paramount in deciphering the signals of paleo-environmental changes embedded in sediment sequences (Junttila et al., 2005; Cowan et al., 2008; Wilson et al., 2018; Wu L. et al., 2021). Analysis of the spatial distribution of sediments offers valuable insights for acquiring such knowledge (Borchers et al., 2011; Shao et al., 2022). In the region of the Ross Sea, these analyses have primarily focused on sediments from the last glacial period (Licht et al., 1999; Licht et al., 2005; Farmer et al., 2006; Halberstadt et al., 2018). For instance, Licht et al. (1999) examined the spatial distribution of tills in the Western Ross Sea (WRS) deposited during the last glacial period. Their findings suggest that even during the Last Glacial Maximum (LGM), the Ross Ice Shelf (RIS) did not extend to the shelf break in the WRS. In another study, Licht et al. (2005) investigated tills deposited across the entire continental shelf of the Ross Sea during the last glacial period and observed that tills in the Eastern Ross Sea (ERS) were rich in quartz and exhibited a finer mean grain-size. In contrast, tills from the WRS contained abundant mafic igneous rock detritus and displayed a coarser mean grain-size. Farmer et al. (2006) conducted further geochemical and isotopic analyses of these tills and identified similarities between tills from the ERS and terrestrial tills from West Antarctica, while tills from the WRS exhibited characteristics akin to rocks from the McMurdo Volcanic Group. Collectively, these findings provide evidence of significant expansion of both the West Antarctic Ice Sheet (WAIS) and East Antarctic Ice Sheet (EAIS) during the last glacial period (Licht et al., 2005; Farmer et al., 2006).

The first preliminary description of the shelf surface sediments in Ross Sea was provided by Anderson et al. (1984). Subsequent studies on such sediments focus primarily on distributions of their biogenic components, including the composition of carbon isotopes (^{14}C and ^{13}C) (Andrews et al., 1999), biological silica/carbonates (Burckle, 2001; Hauck et al., 2012), and diatom assemblages (Cunningham and Leventer, 1998). Distributions of the detrital fractions of these sediments, however, remains largely uninvestigated (Anderson et al., 1984), despite the existence of a few studies regarding the geochemical and isotopic compositions of the surface sediments from Ross Sea involving limited sampling sites (Shao et al., 2022; Wang et al., 2022).

Here, we provide a novel dataset comprising grain-size distribution, coarse fraction (>250 um) lithology, and clay mineralogy measured on a set of surface sediment samples obtained from the Ross Sea continental shelf. This study aims to determine the provenances, distribution patterns, and delivery modes of these sediments which may aid in interpretation of sedimentary records collected from this area.

2 Environmental setting and geological background

Ross Sea is the second largest marginal sea around Antarctica, facing the Pacific Ocean. It is bounded by Marie Byrd Land on the east and the Transantarctic Mountains on the west and south (Figure 1A), serving as outlets of many glaciers derived from both the EAIS and WAIS (Farmer et al., 2006; Rignot et al., 2008).

Currently, the Ross Sea continental shelf south of 78°S is covered by the RIS. It stands as the largest ice shelf on earth with an average ice thickness of ~600 m and an area of 5×10^5 km^2 (Figure 1A) (McKay et al., 2018). The Ross Sea floor north of 78°S deepens landward (southward) with water depth ranging from 200-1000 m and an average of ~500 m. It is featured by several SW/NE-

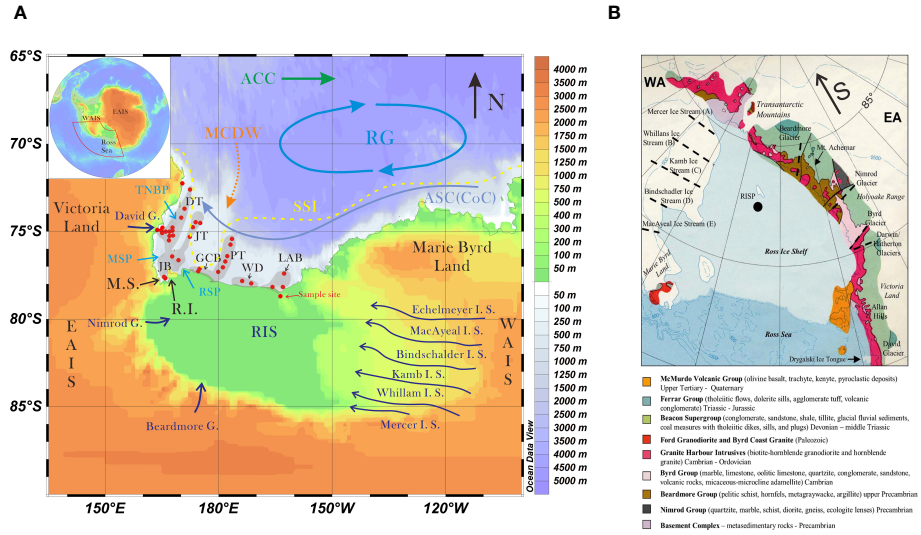

FIGURE 1
(A) Location map displaying the sampling locations and relevant features of the Ross Sea embayment for this study. The abbreviations used are as follows: WAIS (West Antarctic Ice Sheet), EAIS (East Antarctic Ice Sheet), RIS (Ross Ice Shelf), R.I (Ross Island), M.S (McMurdo Sound), RSP (Ross Sea Polynya), MSP (McMurdo Sound Polynya), TNBP (Terra Nova Bay Polynya), David G. (David Glacier), Nimrod G. (Nimrod Glacier), Beardmore G. (Beardmore Glacier), Echelmeyer I. S. (Echelmeyer Ice Stream), MacAyeal I. S. (MacAyeal Ice Stream), Bindschalder I. S. (Bindschalder Ice Stream), Kamb I. S. (Kamb Ice Stream), Whillam I. S. (Whillam Ice Stream), Mercer I. S. (Mercer Ice Stream), DT (Drygalski Trough), JB (Joides Basin), JT (Joides Trough), GCB (Glomar Challenger Basin), PT (Pennell Trough), WD (Whales Deep), LAB (Little American Basin), ASC (Antarctic Slope Current), CoC (Antarctic Coastal Current), RG (Ross Gyre), ACC (Antarctic Circumpolar Current), MCDW (Modified Circumpolar Deep Water), SSI (Summer Sea Ice limit). It should be noted that the Ross Sea is divided into three areas: ERS (eastern Ross Sea), WRS (western Ross Sea), and CRS (central Ross Sea). CRS specifically refers to the area around the PT. ERS and WRS correspond to the eastern and western regions of the PT, respectively, in this study. The oceanic current system is based on Smith et al. (2014). The position of the SSI is determined from modern observations (https://earthdata.nasa.gov). The glacier distributions around the Ross Sea embayment are according to Drewry (1983). The map was generated using Ocean Data View software (R. Schlitzer, 2014; https://odv.awi.de). The inset show the location of the study area in Antarctica. The black lines indicate catchment divides. The blue lines represent glacier flow directions. **(B)** Generalized geologic map illustrating the major bedrock groups in the Ross Sea Embayment, including the Transantarctic Mountains, Victoria Land, and Western Marie Byrd Land. The approximate locations of glaciers and ice streams mentioned in the text are shown as dashed black lines. WA represents West Antarctica, EA represents East Antarctica, and RISP represents core sites of the Ross Ice Shelf Drilling Project. The figure is modified after Licht et al. (2005).

oriented trough-ridge systems that traverse the continental shelf and deep-water basins in front of the RIS.

In the Ross Sea region, the oceanic circulation system comprises four distinct branches (Figure 1A; Smith et al., 2014). The westward-propagating Antarctic Coastal/Slope Currents, under the influence of easterly winds, transport frigid water masses from the eastern sector into the embayment. Adjacent to these currents lies the cyclonic Ross Gyre, a result of shear stress induced by the Easterly and Westerly Winds. Further offshore, the Antarctic Circumpolar Current flows eastward driven by the Westerly Winds.

Sea ice predominates over the entire Ross Sea region during the austral winter, gradually retreating in the austral spring (https://www.earthdata.nasa.gov). Nevertheless, only the Western Ross Shelf (WRS) experiences complete sea ice melt in the austral summer. Katabatic winds prevail along the southwestern coast of the Ross Sea throughout the winter season, propelling newly formed sea ice towards the north (Mezgec et al., 2017). Consequently, a succession of polynya, encompassing the McMurdo Sound Polynya, Ross Polynya, and Terra Nova Bay Polynya, emerge along the southwestern coast and endure until thawing of the sea ice during the austral spring (Mezgec et al., 2017).

The lithologies of bedrocks surrounding the Ross Sea have been inferred based on scattered outcrops (Figure 1B). The study area encompasses a diverse range of rock units, representing seven primary rock groups spanning from the Precambrian to the Quaternary, as illustrated in Figure 1B. The Nimrod Group, originating from the Archean and Early Proterozoic era, constitutes a heterogeneous metamorphic complex comprising both mafic and felsic rock types (Goodge and Fanning, 1999). Overlying the Nimrod Group is the Beardmore Group, predominantly consisting of metasedimentary rocks of upper Precambrian ages (Goodge et al., 2002). The Byrd Group is situated above the Beardmore Group, composed of sedimentary and metasedimentary rocks of Cambrian ages (Myrow et al., 2002). The Beacon Supergroup overlies the Byrd Group and is primarily comprised of sedimentary rocks with ages from the Devonian to the Middle Triassic (Barrett, 1991). The Ferrar Group lies above the Beacon Supergroup, primarily composed of mafic igneous rocks. Lastly, the McMurdo Volcanic Group is situated above the Ferrar Group and is associated with a diverse array of Cenozoic extrusive rock types, including rhyolites and basalts (Kyle, 1990).

3 Materials

This study utilize 42 surface sediment samples obtained from the Ross Sea continental shelf in 2014-2019 on R/V *Xuelong* during the 31st-35th Chinese Antarctic Research Expedition. Various

10.3389/fmars.2023.1324391

TABLE 1 Information of the Ross Sea surface sediment samples used in this study.

Sector	Sample	longitude	latitude	Sampling device	Water Depth (m)
WRS	ANT31R18	163°45.900′E	74°54.780′S	BC	46.0
	ANT31R14	164°48′17″E	74°56′06″S	BC	901.1
	ANT31R08	165°0′43″E	75°0′11″S	BC	691.8
	ANT33I5	165°2′53″E	75°5′13″S	BC	1174.0
	ANT31R02	165°7′59″E	74°47′6″S	BC	719.2
	ANT31JB01	165°34′10″E	77°35′18″S	BC	774.0
	ANT33A1-20	165°53′6″E	77°39′58″S	BC	590.1
	ANT31R09	165°59′53″E	75°0′12″S	BC	1032.1
	ANT31R20	166°50′52″E	75°30′16″S	MC	425.6
	ANT31R16	166°59′50″E	75°15′15″S	MC	486.7
	ANT31R10	167°00′07″E	74°59′68″S	BC	636.0
	ANT33A1-18	167°43′26″E	76°25′16″S	BC	742.8
	ANT31R05	167°46′39″E	74°46′36″S	BC	585.6
	ANT31R11	167°48′20″E	74°56′57″S	BC	449.4
	ANT31R17	167°54′33″E	75°13′49″S	BC	374.4
	ANT35R1-03	168°21′28″E	74°59′43″S	BC	348.6
	ANT32RB15C	168°47′19″E	77°12′7″S	GC	939.8
	ANT33A1-17	169°23′46″E	76°38′10″S	BC	604.5
	ANT33A2-02	170°7′5″E	74°12′22″S	BC	654.0
	ANT31R19	170°23′40″E	72°15′16″S	BC	516.3
	ANT33A2-03	170°58′44″E	73°42′4″S	BC	588.0
	ANT31JB04	172°22′21″E	75°18′04″S	BC	510.8
	ANT33A2-05	172°26′13″E	72°36′18″S	BC	546.2
	ANT31JB05	173°11′17″E	74°45′19″S	BC	496.8
	ANT31JB06	173°54′24″E	74°28′22″S	GC	567.5
	ANT32RB11B	174°35′59″E	77°16′10″S	BC	494.9
	ANT33A1-15	174°57′50″E	77°7′37″S	BC	399.9
	ANT32RB16B	175°07′18″E	74°30′49″S	BC	478.0
CRS	ANT32RB08B	179°51′09″E	77°18′32″S	BC	669.7
	ANT32RB07B	178°54′01″W	77°02′59″S	BC	628.3
	ANT32RB06B	178°14′25″W	76°42′48″S	BC	619.0
	ANT33A1-13	178°1′16″W	77°32′42″S	BC	663.8
	ANT32RB05B	177°43′10″W	76°24′19″S	BC	606.0
	ANT32RB03B	176°52′11″W	75°44′48″S	BC	610.0
	ANT32RB02B	176°29′9″W	75°25′24″S	BC	574.0
ERS	ANT33A1-11	173°47′17″W	77°49′34″S	BC	530.4
	ANT33A1-10	171°22′23″W	77°58′5″S	BC	514.9
	ANT33A1-09	168°57′7″W	78°5′2″S	BC	586.0
	ANT33A1-08	165°47′17″W	78°10′19″S	BC	497.6

(Continued)

TABLE 1 Continued

Sector	Sample	longitude	latitude	Sampling device	Water Depth (m)
	ANT33RS78	163°40′1″W	78°41′38″S	BC	331.1
	ANT33A1-07	163°2′20″W	78°10′5″S	BC	678.8
	ANT33A1-05	162°40′41″W	77°23′46″S	BC	658.3

WRS, Western Ross Sea; CRS, Central Ross Sea; ERS, Eastern Ross Sea; BC, Box corer; MC, Multt-corer; GC, Gravity corer.

sampling techniques, including box corers, multi-corers, and gravity corers were employed to collect these sediments. The samples were the top 0-2 cm from the collected sediments in most cases, with a few exceptions where depths reached 0-5 cm. The sampling locations cover the entire continental shelf, with a focus on the basin and trough area and water depths ranging from 46 to 1174 m (Figure 1; Table 1). The sediment color changes between greenish grey and greyish black, and their composition varies from clayey silt to gravel sands. Biogenic silica is common in most of the sediments in the form of diatoms, sponge spicules, and radiolarians, while carbonates were detected in only a few samples and comprise <10 wt.%.

4 Methods

To carry out this study, we employed various experimental techniques, including measurements of the grain-size distribution, clay mineralogy and abundance and lithology of the coarse fraction of the sediments.

To analyze the sediment grain-size, a series of treatments were carried out. Specifically, 0.13-0.22 g of dry bulk sediment underwent sequential treatments starting with 10% H_2O_2, followed by 1.0 N HCl and finally 2.0 N Na_2CO_3, to successively eliminate organic carbon, carbonates, and biogenic silica. The samples were then dispersed using an ultrasonic bath for 2 minutes following immersion in 25 mL of distilled water. The grain-size measurements were performed using a Laser particle sizer (Malvern Mastersizer 3000), which can analyze grain-sizes ranging from 0.1 μm to 3,500 μm, satisfying our test demand. Duplicate measurements of 10 randomly selected samples showed that reproducibility was better than 5%. This experiment was done at Laboratory for Coastal Ocean Variation and Disaster Prediction, College of Ocean and Meteorology, Guangdong Ocean University.

End Member Modeling Algorithm (EMMA) was employed to deconstruct the grain-size distribution data set. EMMA is designed as an inversion algorithm which posits the input grain-size distributions as combinations of a finite number of end-members (EMs) that possess realistic compositions (Weltje, 1997). Extensive studies have demonstrated the effectiveness of this algorithm in analyzing grain-size distributions across diverse environmental contexts (Prins and Weltje, 1999; Jonkers et al., 2015; Wu et al., 2018).

The fraction with a size smaller than 2 μm was utilized for the analysis of clay minerals, after the removal of carbonates through treatment with 0.5 N HCl (e.g., Wu L. et al., 2021). Analysis was conducted using a PANalytical X'Pert PRO diffractometer equipped with a Ni filter and CuKa radiation at an intensity of 40 mA and voltage of 45 kV. Oriented mounts were prepared for three XRD runs including one following air-drying, one after saturation with ethylene-glycol for 1 day, and one after heating at approximately 490°C for around 120 minutes. Multiple X-ray diffractograms obtained under the above mentioned measurement conditions were compared to identify and interpret clay minerals species (Liu et al., 2003). Peak parameters were semi-quantitatively calculated using the MacDiff software (Petschick, 2000) based on the glycolated curve. The relative abundance of each clay mineral species was primarily estimated by analyzing the area of the (001) series of basal reflections (Holtzapffel, 1985). The distinction between chlorite and kaolinite was made using a peak area ratio at 3.54 Å and 3.57 Å (Holtzapffel, 1985).

The coarse fraction was determined using the procedures outlined by Wang et al. (2013). In brief, approximately 10-15g of dry sediment samples were submerged in deionized water for a period of 2 days. If needed, H_2O_2 was added to facilitate the disaggregation of the sediment. Subsequently, the sediment was rinsed with clean water through a 63 μm mesh, and the residue with particle size >63 μm was subjected to drying at 55°C. The dried residue was then sieved through a 250 μm mesh. The weight percentage of the >250 μm fraction was calculated based on the weight of the original dry sediment.

The lithology of the coarse fraction grains was determined and quantified using a binocular microscope for all samples, focusing on the fraction with a size greater than 250 μm (Wang et al., 2013). In cases where grains larger than 250 μm were scarce, the fraction >154 μm was utilized. A total of more than 400 non-biogenic grains were counted for each sample. Within the coarse fraction, we identified and counted various types of grains, including angular quartz, rounded quartz, plagioclase, K-feldspar, sedimentary rocks, garnet, chert, mafic igneous rocks, mica, hornblende, metamorphic rock, deformed silt, and volcanic ash. Additionally, any encountered lithic grains with unknown lithology were also included in the count, although this specific data is not presented here.

The clay mineralogy and coarse fraction abundance and lithology identification experiments were done at State Key Laboratory for Marine Geology, Tongji University.

5 Results

5.1 Grain-size

The studied sediments consist of clay (5%-30%), silt (30%-82%), and sand (0%-62%), with a mean grain-size ranging from 12 μm to

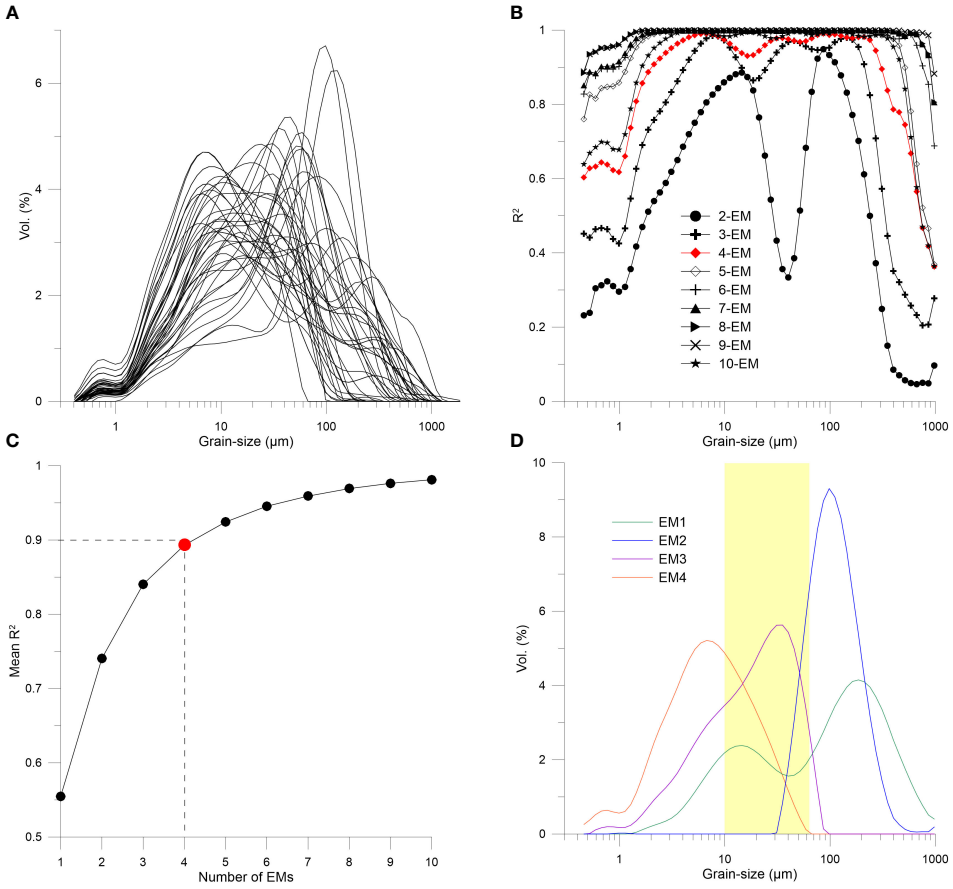

FIGURE 2
Results of end-member modeling for the grain-size dataset of the studied sediments. **(A)** Grain-size distributions of the studied sediments. **(B)** Coefficients of determination (R^2) for each size class of models with 2-10 end members. **(C)** Mean coefficient of determination (R^2_{mean}) for all size classes in each end-member model. **(D)** Grain-size distributions of the modeled end members of the studied sediments. A four-end-member (Four-EM) model was selected to explain the dataset and is depicted in red in **(B, C)**. The sortable silt interval (10-63 μm) is shaded in yellow in **(D)**.

143 μm. The grain-size distribution patterns of the samples are highly variable, without any universal grain-size mode (Figure 2A). The EMMA analysis was performed to identify the primary factors governing the grain-size distributions of the sediments. Figures 2B, C present the coefficients of determination (R^2) plotted versus the grain-size and number of end-members, respectively. As the number of end-members increases, the mean R^2 (R^2_{mean}) also increases (Figure 2C). Amongst the two and three end-member models (R^2_{mean}=0.59 and R^2_{mean}=0.84, respectively), lower R^2 (<0.6) was observed for the grain-size intervals <2 μm, 30–60 μm, and >200 μm (Figure 2B). The four-end-member model (R^2_{mean}=0.9), however, displayed lower R^2 only for the grain-size interval >500 μm. Models containing six or more end-members are better suited to reproduce this coarse fraction. However, for determining the appropriate number of end-members, the coarse end (>500 μm) could be disregarded, as it consists of only a small volume fraction (<2 vol.%) of the samples (Figure 2A; e.g., Stuut et al., 2002), and measurement precision for laser particle sizing in the coarse end is inferior to that of the fine fraction (Jonkers et al., 2015). On the contrary, the mixing model should effectively reproduce the grain-size range between 2 and 500 μm, as it constitutes the majority of the sediment mass (Figure 2A). Thus, the four-end-member model represents the best compromise between R^2 and the number of end-members.

Figure 2D shows the grain-size distributions of the four end-members derived from the Four-EM model. EM1 is characterized by a flat two-modal pattern, with modal sizes at 200 μm and 15 μm, respectively. It has the poorest sorting (2.16). EM2 to EM4 are uni-modal. EM2 has a modal size at 150 μm, and has the best sorting (0.77). EM3 and EM4 peak at 30 μm and 8 μm, with moderate sorting of 1.38 and 1.42, respectively.

The spatial distributions of the four end-members are illustrated in Figure 3. A greater abundance of EM1 (>0.4) is primarily found in the outer shelf region, particularly near the northernmost coast of Victoria Land and the coast of Marie Byrd Land in the WRS and ERS, respectively (Figure 3A). Higher EM2 proportions (>0.2) is predominantly present in the outer shelf of the WRS, extending to some extent in the McMurdo Sound and near the Drygalski Ice Tongue, while being scarce near Marie Byrd Land (Figure 3B). The relatively high concentration of EM3 (>0.3) is exclusively observed in the WRS (<180°E), specifically in the Joides Basin, Drygalski Trough, and Joides Trough (Figure 3C). Higher proportions of EM4 proportions (>0.3) is mainly distributed in the central and eastern regions of the inner continental shelf area,

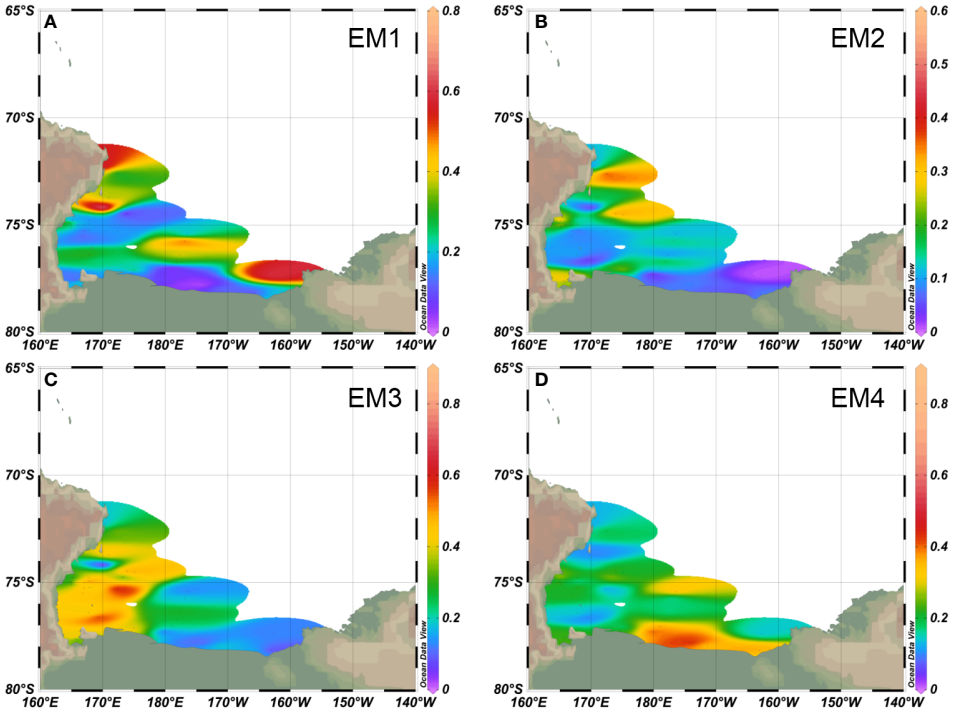

FIGURE 3
Spatial distributions of **(A)** EM1, **(B)** EM2, **(C)** EM3, and **(D)** EM4 derived from EMMA analysis of the grain-size distributions in the studied surface sediment samples.

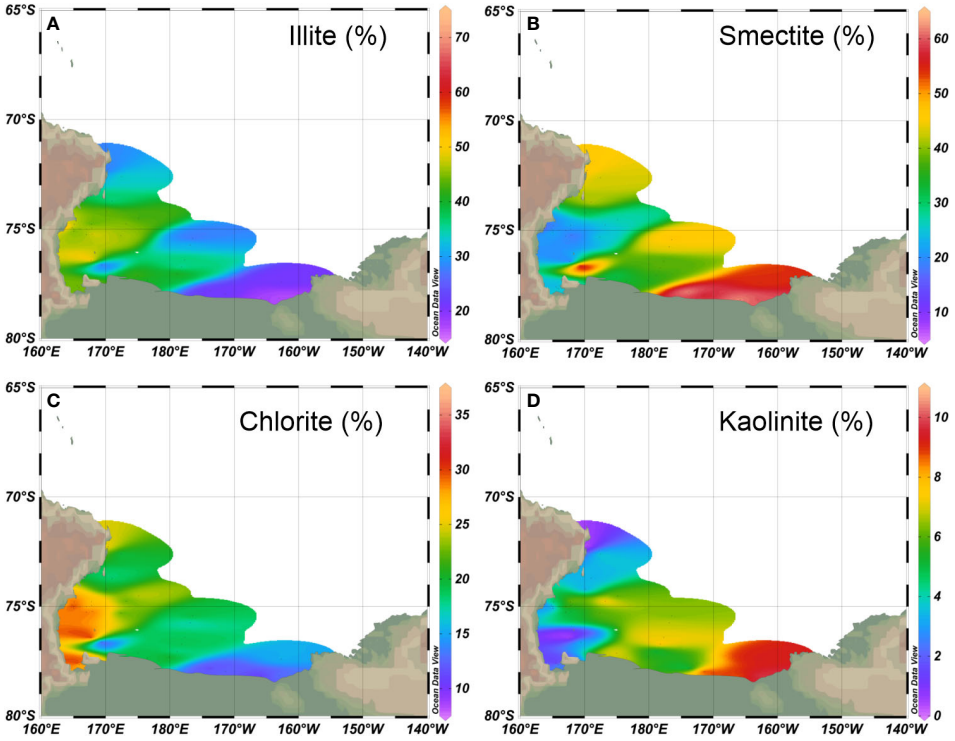

FIGURE 4
Spatial distributions of **(A)** illite, **(B)** smectite, **(C)** chlorite, and **(D)** kaolinite in the studied sediment samples.

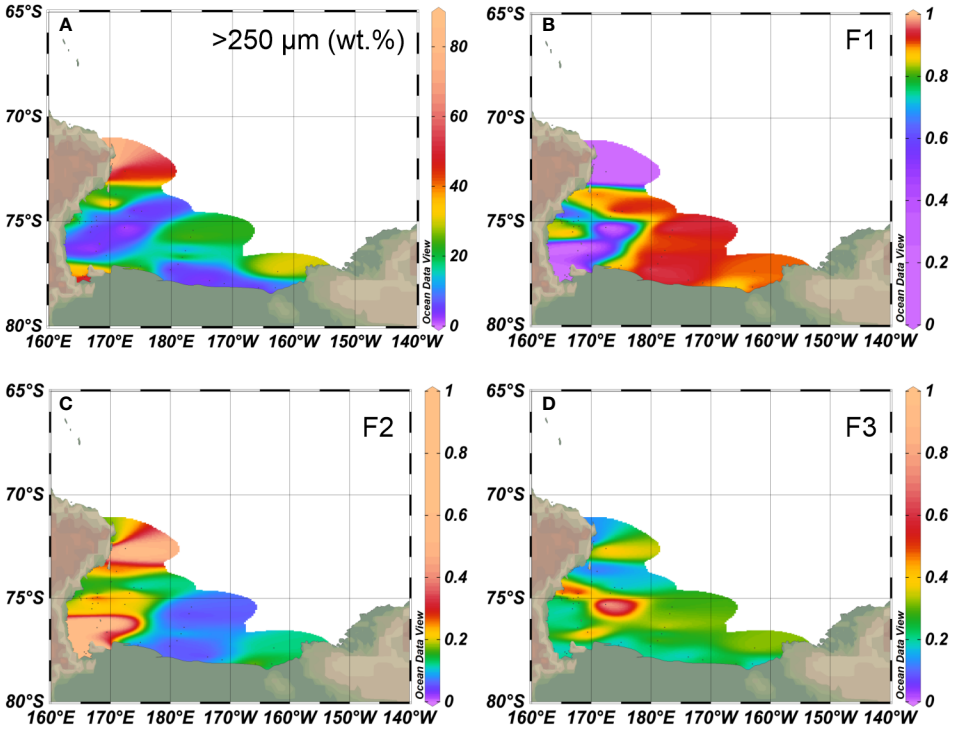

FIGURE 5
Spatial distributions of **(A)** weight percent of the >250 µm fraction derived from wet sieving, and factor scores of Factor 1 (F1), Factor 2 (F2), and Factor 3 (F3) in panels **(B–D)**, respectively, derived from factor analysis of the >250 µm coarse fraction dataset.

encompassing Whales Deep and Little American Basin located in front of the RIS (Figure 3D).

5.2 Clay mineralogy

The clay minerals in the investigated sediments are mainly composed of illite (15%-73%), smectite (5%-64%), chlorite (9%-36%), and trace amount of kaolinite (0-23%). Illite and smectite are the most abundant species in the study area, and their spatial distribution patterns exhibit an interesting contrast (Figure 4). Illite content is relatively higher in the WRS (Figure 4A), whereas smectite content shows a relatively higher concentration mainly in the ERS (Figure 4B). The spatial distribution pattern of chlorite follows a similar trend to that of illite (Figure 4C), while that of kaolinite mirrors that of smectite (Figure 4D).

5.3 Coarse fraction

The abundance of the coarse fraction (>250 µm) obtained through sieving ranges from 0 to 85 wt.% with an average of 17 wt.%. Higher contents are predominantly found in the outer shelf and along the coast of the WRS, while lower contents are observed in front of the RIS, as well as in the Joides Basin and Joides Trough (Figure 5A). The major constituents of the coarse fraction, with a mean content exceeding 10%, include angular quartz, rounded quartz, mafic rocks, and deformed silt (Figure 6A). In order to elucidate the primary factors influencing the spatial distribution of the coarse fraction, a Q-mode Factor Analysis (Klovan and Miesch, 1976) was performed on the dataset representing the lithological composition of the coarse fraction. The analysis yielded a three-Factor model that accounts for over 93% of the data variance (Figure 6B). Each of these three Factors possesses eigenvalues greater than 1, indicating that they explain more variance than any individual raw variable in the dataset (Wu et al., 2019). These three Factors consistently emerge across multiple runs of the Factor Analysis algorithms utilizing different Factor extraction methods. In contrast, the fourth Factor displays instability, with changing factor loadings and scores during these runs. Furthermore, inclusion of the fourth Factor does not significantly enhance the explained variance (Figure 6B), but may introduce additional errors in the results (e.g., Weltje, 1997). Therefore, the three-Factor model represents the optimal compromise between the explained variance and the factor number.

The three identified Factors account for 76.14%, 12.17%, and 5.49% of the data variance, respectively (Figure 6B). Factor 1 is characterized by high loadings of angular quartz and rounded quartz (Figure 6C). Factor 2 displays significant loadings on mafic igneous rocks (Figure 6C). Factor 3 is associated with deformed silt (Figure 6C). With regards to their spatial distribution, higher scores of Factor 1 (>0.9) are mainly observed in the ERS and Central Ross Sea (CRS), extending to the central Victoria Land coast (Figure 5B). In contrast, Factor 2 exhibits higher scores (>0.1) in both the WRS, particularly near the McMurdo Sound and the northernmost part of Victoria Land, and low scores (<0.1) in the CRS (Figure 5C). High scores of Factor 3 (>0.5) predominantly occur in the nearby region of the David Glacier-Drygalski Ice Tongue system in the WRS (Figure 5D).

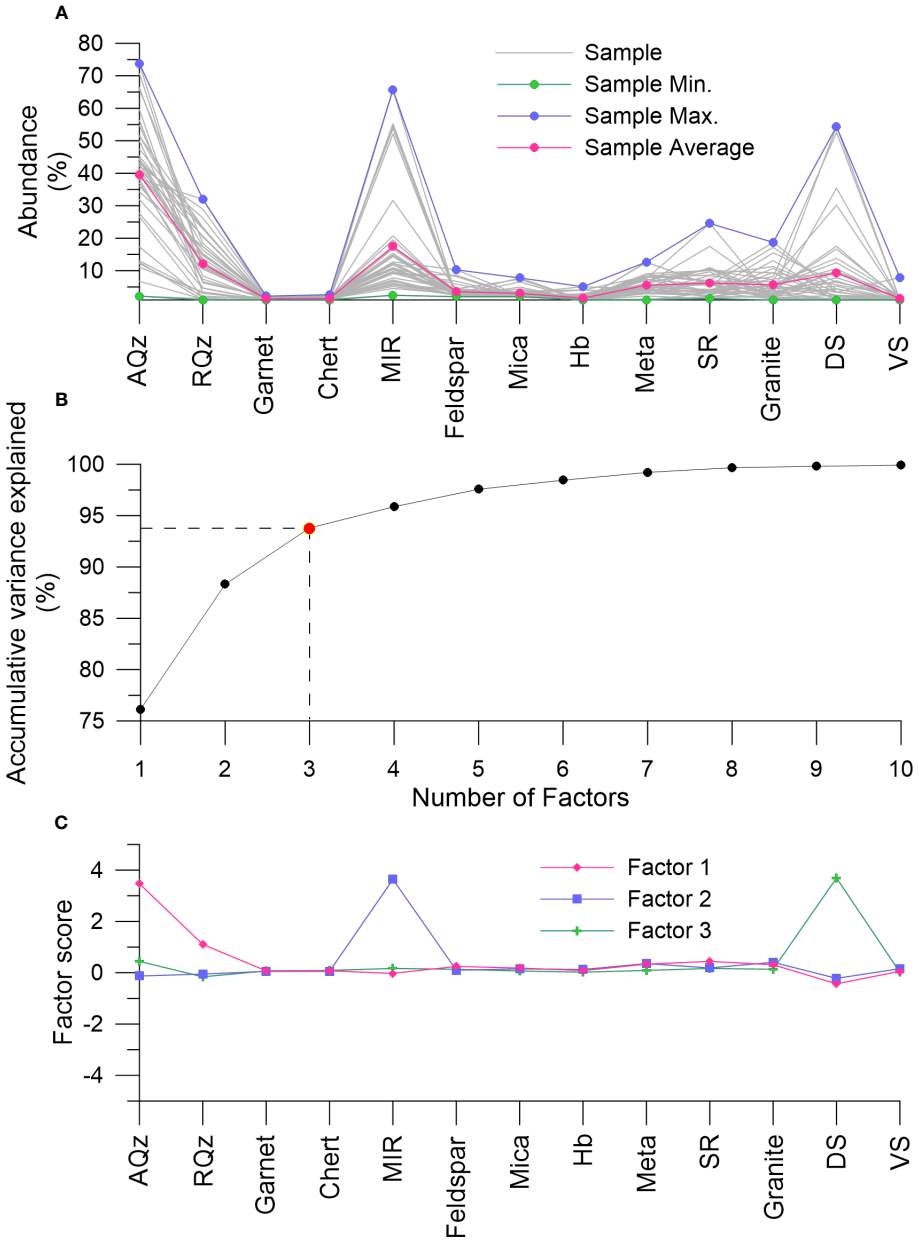

FIGURE 6
Factor analyses of the >250 μm fraction derived from wet sieving. **(A)** Summary of the lithologic composition of the >250 μm fraction. **(B)** Cumulative variance explained by increasing factors (2-10). **(C)** Distribution of factor loadings for the selected three-Factor model. AQz represents angular quartz, RQz represents rounded quartz, MIR represents mafic igneous rock, Hb represents hornblende, Meta represents metamorphic rock, SR represents sedimentary rock, DS represents deformed silt, and VS represents volcanic shards.

6 Discussion

6.1 Sediment delivery mode

6.1.1 Linking grain-size end-members to sediment delivery modes

End-members of sediment grain-size obtained from EMMA analyses have been frequently associated with sediment transport and/or deposition mechanisms in various environmental settings. Previous studies suggest that in the Southern Ocean, oceanic currents, icebergs, sea ice and wind could be potential media that deliver terrestrial sediments to the seas (Pudsey, 1992; Gilbert et al., 1998; McCave et al., 2014; Wu et al., 2018; Wu S. et al., 2021). Sea ice, however, forms in deep water continental shelf (~500 m) in Ross Sea, with little sediment encased. Earlier studies indicate that the WRS coast could be a possible source area for wind-blown dust (Delmonte et al., 2010). Nonetheless, none of the four end-members displays a spatial distribution pattern decreasing seaward from the WRS coast, excluding wind-blown dust as a major contributor to the sediments. Therefore, we associate the grain-size end-members with sediment delivery primarily by icebergs and bottom currents.

In polar oceans, icebergs can carry sediments with a broad range of grain-size compositions. Therefore, the grain-size distribution of IRD is typically described as poorly sorted, even though coarse sediment fractions such as the >150 μm and/or >250 μm fractions from polar oceans are often considered as IRD. This is because sediment of such diameters cannot be moved and sorted by typical oceanic currents (Lamy et al., 2015; Wu et al., 2020). The grain-size distribution of EM1 (Figure 2D) displays poor sorting and bears a resemblance to the previously published grain-size distribution of IRD (Prins et al., 2002; Wu et al., 2018). Moreover, there is a robust correlation between EM1 and the >250 μm component obtained from wet sieving (R=0.63, p<0.01). We thus interpret EM1 as IRD.

EM2 has the best sorting and a relatively coarse mean grain-size (Figure 2D). This grain-size distribution is likely produced by strong current winnowing (e.g., Abuodha, 2003). However, there is a weak positive correlation between EM2 and the sorting parameter of the <150 μm fraction (r=0.31, n = 41), implying that higher EM2 content does not correspond to better sorting of the finer fraction of the sediments. Modern observations indicate that the bottom current velocity of the Ross Sea continental shelf generally remains below 15 cm/s (Jacobs et al., 1970), which is insufficient to transport particles >63 μm (McCave and Hall, 2006). Thus, the good sorting of the relatively coarse EM2 cannot be interpreted as bottom current winnowing lags. Instead, previous studies have identified well-sorted IRD in other ocean areas (Prins et al., 2002; Wang et al., 2023). It is postulated that this IRD may originate from the transport of icebergs in regions with intense hydrodynamics, such as coastal sand beaches (Prins et al., 2002; Wang et al., 2023). In such environments, the sediment itself is sorted well before being entrained in icebergs. Indeed, paleo-beaches forming during Middle Holocene Climate Optimum have been frequently found situating above the modern sea level along the western coast of Ross Sea (Colhoun et al., 1992). EM2 is thus interpreted as IRD delivered by icebergs derived from coastal beaches in the Western coast of Ross Sea.

The grain-size distributions of EM3 and EM4 exhibit significant overlap with the sortable silt interval (10-63 μm) (Figure 2D). This indicates that they can be transported and/or altered by bottom currents in deep-sea environments (McCave and Hall, 2006; McCave et al., 2017). The presence of a larger modal grain-size combined with relatively better sorting suggests that EM3 would likely accumulate in an environment with stronger bottom currents. Conversely, the finer grain-size and slightly poorer sorting of EM4 are indicative of deposition in an environment with weaker hydrodynamics (Jonkers et al., 2015; Wu et al., 2018).

6.1.2 Delivery of IRD

The Ross Sea region has been identified as a significant source of icebergs in the Southern Ocean, and extensive presence of icebergs has been observed in this area (Turnbull, 2006). Indeed, the contents of EM1, EM2 and the wet sieving-based >250 μm fraction in most samples are above zero, suggesting widespread iceberg unloading throughout the sampling area. Iceberg unloading is primarily associated with dynamics of the ice shelf/glacier that produces the iceberg, but might be further influenced by a range of factors such as the sea water temperatures, ocean current pathways,

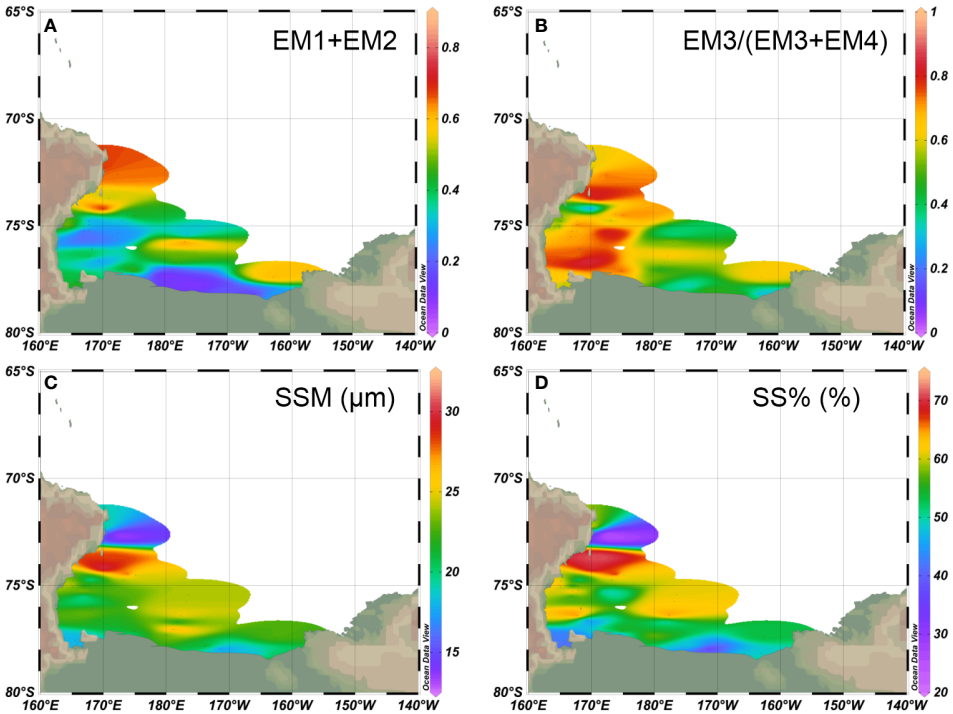

FIGURE 7
Spatial distributions of **(A)** EM1+EM2 and **(B)** EM3/(EM3+EM4) resulting from grain-size EMMA analysis, and **(C)** Sortable Silt mean grain-size (SSM) and **(D)** Sortable Silt percent (SS%) in the studied sediments.

debris type and amount in icebergs, distance from iceberg sources, and geomorphology of the seafloor (Teitler et al., 2010; Cook et al., 2013; Cook et al., 2014; Weber et al., 2014; Wu L. et al., 2021).

Antarctic ice shelves as large as the RIS, are typically devoid of basal debris as most of the debris have been unloaded near their grounding zone prior to calving (Patterson et al., 2014; Smith et al., 2019). This accounts for the extremely low content of IRD immediately in front of the RIS to the east of 178°E (Figures 5A, 7A). The presence of the RIS provides protection against wave and tidal action, whereas the ice shelf-free coastlines of the WRS have experienced intense wave, tide, and storm activity since the Mid-Late Holocene, after the retreat of the RIS to its current position (McKay et al., 2008), favoring the development of beaches (e.g., Colhoun et al., 1992). We noted that the maximum value of EM2 decreased significantly with increasing longitude (Figure 8B), suggesting that EM2 originated from the ice shelf-free western coast of Ross Sea (See Section 6.1.1). Conversely, there was no observable trend in the spatial distribution of EM1 or the wet sieving-based >250 µm fraction across longitudes (Figures 8A, C), in combination with the fact that EM1 and EM2 display dissimilar grain-size distribution patterns (Figure 2D), suggesting that the source regions of EM1 and EM2 are distinct.

On the other hand, we observed a complex relationship between IRD and water depth. When the water depth is below ~660 meters, there is significant variation in the proportion of EM1 and the weight percent of the wet sieving-based >250 µm fraction among different stations, ranging from 0 to 72% and from 0 to 85 wt.%, respectively (Figures 8G, I). However, when the water depth exceeds ~660 meters,

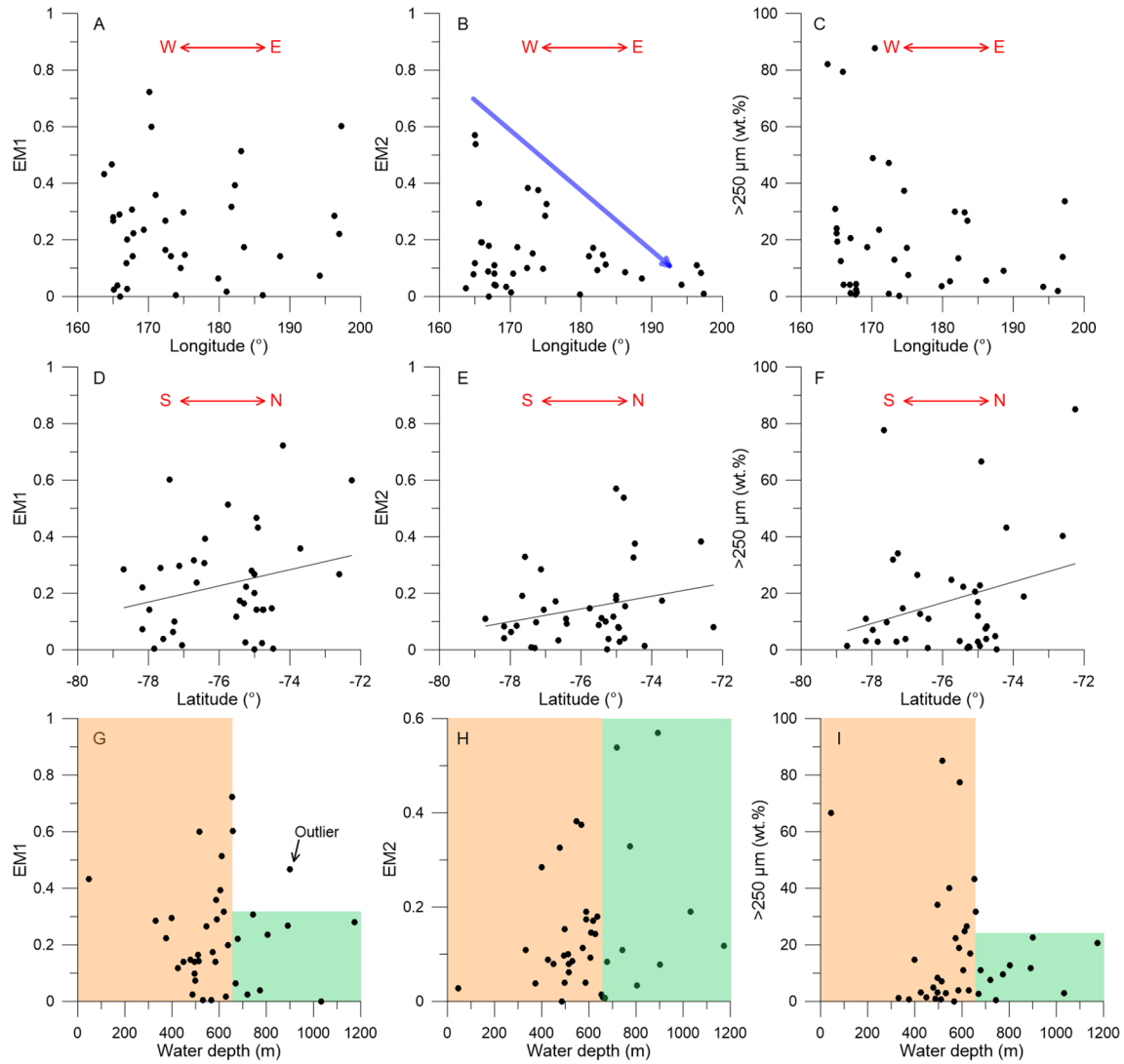

FIGURE 8
Plots of grain-size end-members from EMMA analysis of the studied sediment samples against sampling longitude, latitude, and water depth, respectively. **(A)** EM1 versus longitude. **(B)** EM2 versus longitude. **(C)** Longitude versus the >250 µm fraction derived from wet sieving. **(D)** EM1 versus latitude. **(E)** EM2 versus latitude. **(F)** Latitude versus the >250 µm fraction derived from wet sieving. **(G)** EM1 versus water depth. **(H)** EM2 versus water depth. **(I)** Water depth versus the >250 µm fraction derived from wet sieving. The red double arrows in **(A)** to **(C)** represent west (W) and east **(E)** directions. The red double arrows in **(D)** to **(F)** represent south (S) and north (N) directions. The light orange and light green shades in **(G)** to **(I)** indicate samples deposited in areas with water depth <660 m and >660 m, respectively. The blue arrow in **(B)** indicates a decrease in EM2 proportions with longitude. The black lines in **(D)** to **(F)** represent regression lines.

this variation range abruptly narrows to between 0 and 30%, and between 0 and 22 wt.%, respectively. Notably, there is no such relationship between EM2 and water depth (Figure 8H).

The RIS has an average thickness approximately 600 meters (McKay et al., 2018), implying that large icebergs calved from the RIS are more likely to remain grounded for extended periods when the water depth on the continental shelf is close to this value. This may lead to extended unloading of basal and englacial detritus of the icebergs there and even disturbance of previously deposited sediments, as described by O'Brien and Leitchenkov (1997) for the scenario in Prydz Bay, East Antarctica. In contrast, smaller icebergs could unload their detritus at any water depth deeper than the thickness of their marine portion. This mechanism could explain the complex relationship between water depth and EM1 as well as the >250 μm fraction (Figures 8G, I). The presence of different patterns between EM1 and water depth (Figure 8G), and between EM2 and water depth (Figure 8H), thus may indicate that at least part of EM1 was released from larger icebergs, while EM2 was released from smaller ones.

Additionally, significant positive correlations were observed between all the indicators of IRD and latitude (Figures 8D-F), indicating a tendency for IRD deposition towards the outer shelf, coinciding with the intrusion of MCDW onto the continental shelf (Whitworth and Orsi, 2006). The warmer MCDW that enters the Ross Sea compared to other water masses can enhance the basal melting of icebergs, promoting the release of IRD. Consequently, the overall increase in IRD towards the north suggests that variations in sea water temperature, influenced by the intrusion of MCDW, play a significant role in governing delivery of IRD onto the Ross Sea continental shelf.

6.1.3 Bottom currents

The analysis of sediment grain-size offers valuable insights into the dynamics of sediment transport. In the deep-sea setting, the duration of sediment settling from the water column to the seafloor is relatively brief in comparison to its residence time near the sediment-water interface, particularly in areas characterized by low sedimentation rates. Consequently, when establishing a connection between sediment grain-size and ocean currents, the primary focus lies on discerning variations in the intensity of bottom currents (McCave and Hall, 2006; McCave and Andrews, 2019).

McCave and Hall (2006) proposed using the geometric mean grain-size of the 10-63 μm fraction, which is known as the sortable silt mean (SSM), as a proxy for changes in bottom current strength, provided that it correlates well with the percentage of the sortable silt (SS%). The presence of IRD in high-latitude oceans, however, can complicate this relationship, particularly when bottom current strength is weak (Jonkers et al., 2015; Stevenard et al., 2023). In such cases, coarser components in IRD are not effectively sorted by the bottom current, resulting in an increase in SSM with the addition of coarse component content (Jonkers et al., 2015; Stevenard et al., 2023). In our samples, we found a significant correlation between SSM and SS% (Figures 7C, D, 9A), but an insignificant correlation between SSM and the IRD end-member EM1 (Figure 9B). Interestingly, there was a significant correlation between SSM and EM2 (Figure 9C), and the spatial distribution pattern of SSM overlapped with that of EM2 as well (Figures 3B, 7C), leading to suspicions that the SSM here could be used as a proxies for bottom current strength change (Figure 2D). In view of this, we propose a new index, EM3/(EM3+EM4) (Figure 7B), to evaluate the relative change of local bottom current strength. This index utilizes indicators that reflect transport by relatively strong and weak bottom currents in EMMA end-members, which are unaffected by IRD (e.g., Prins et al., 2002; Jonkers et al., 2015; Wu et al., 2018; Wang et al., 2023).

The EM3/(EM3+EM4) ratio exhibits a significant correlation with both SSM and SS% (Figures 9D, E). However, no significant correlation was observed between the EM3/(EM3+EM4) ratio and any IRD indicator (Figures 9F, G), and the spatial distribution of EM3/(EM3+EM4) (Figure 7B) also differs from that of the IRD indicators (Figures 3A, B). Moreover, a significant negative correlation was found between the EM3/(EM3+EM4) ratio and the sorting of the <100 μm fraction (Figure 9H). This suggests that higher values of EM3/(EM3+EM4) correspond to better sorting of the fine fractions (e.g., Passchier, 2011; Patterson et al., 2014; Wu L. et al., 2021), thus supporting its validity as an indicator for relative changes of the bottom current strength in our study. Higher EM3/(EM3+EM4) values indicate stronger bottom current activities, and vice versa.

Spatially, elevated values of EM3/(EM3+EM4) are predominantly observed in the WRS, particularly in the Joides basin, Joides trough, and the northernmost region of Victoria Land (Figure 7B). This spatial distribution indicates that these specific areas underwent notable activities of relatively strong bottom currents.

In the Southern Ocean, wind stress curl is a crucial factor that influences the oceanic current activities across the water column. Furthermore, the energy derived from the wind stress curl is regulated by sea ice cover (e.g., Toggweiler et al., 2006; McCave et al., 2014). However, we found no correlation between the EM3/(EM3+EM4) ratio and water depth in our samples (Figure 9I). This suggests that the energy that prompts bottom current activity does not originate from the sea surface. Otherwise, shallower sampling stations would display higher bottom current strength due to greater energy gain, resulting in a higher EM3/(EM3+EM4) ratio. Therefore, we propose that bottom current strength in our study is not related to wind stress curl, and other factor(s) must be involved to explain its spatial distribution and variability.

It is well know that the WRS serves as a significant source region for the generation of Antarctic Bottom Water (AABW), accounting approximately for 25% of its overall production (Orsi et al., 2002; Orsi and Wiederwohl, 2009). Formation of AABW in the WRS is closely linked to the rejection of brine resulting from sea ice production within the polynya (Tamura et al., 2008; Gordon et al., 2015). The influx of warm and saline MCDW from the WRS leads to raised salinity within the local water mass. Concurrently, continuous sea ice formation in the polynya further elevates the salinity of the expelled brine. As a result, highly saline brine descends and accumulates in deep water basins on the

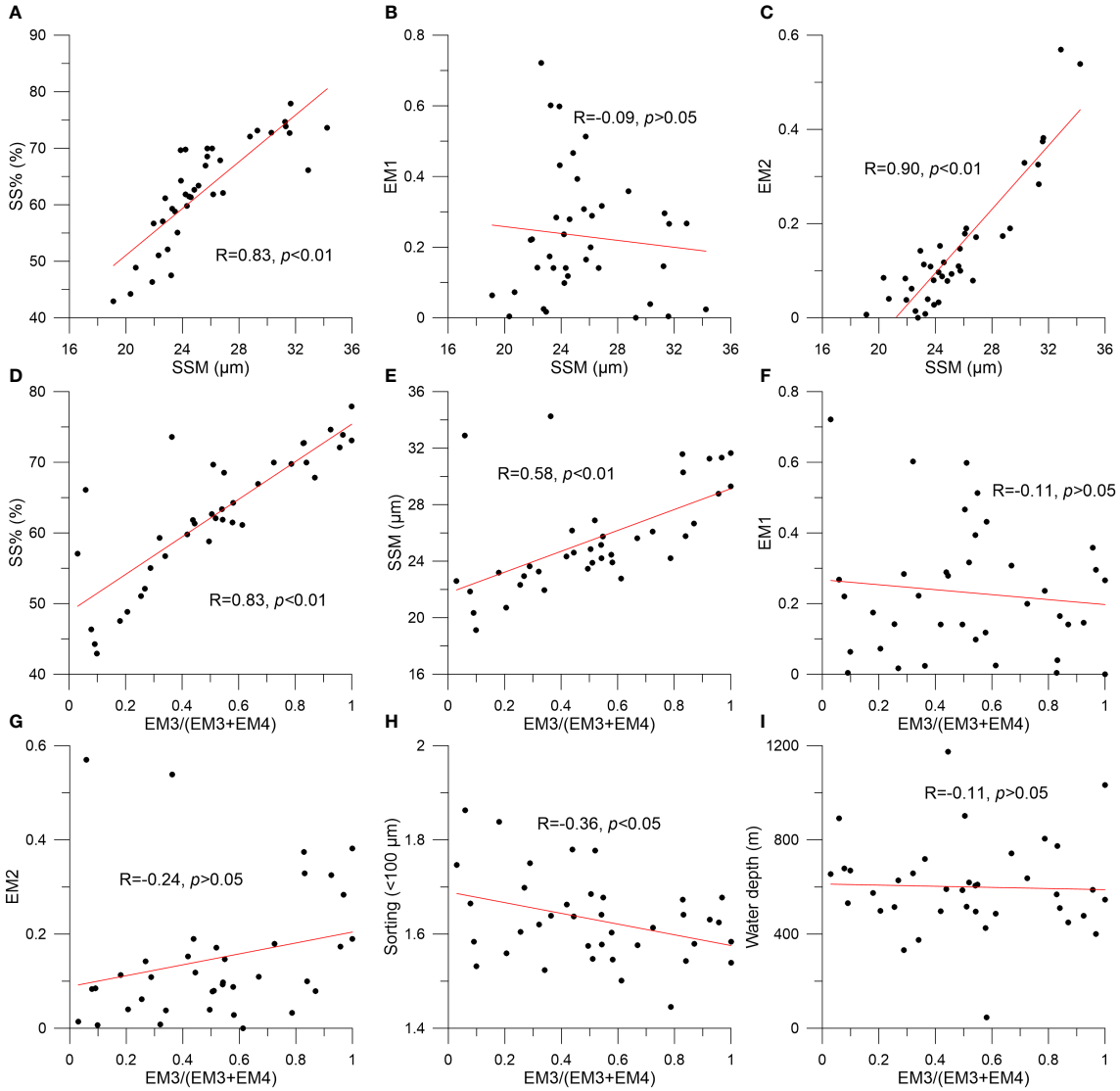

FIGURE 9
Plots of **(A)** SSM versus SS%, **(B)** EM1 versus SSM, **(C)** EM2 versus SSM, **(D)** EM3/(EM3+EM4) versus SS%, **(E)** EM3/(EM3+EM4) versus SSM, **(F)** EM3/(EM3+EM4) versus EM1, **(G)** EM3/(EM3+EM4) versus EM2, **(H)** EM3/(EM3+EM4) versus sorting of the <100 μm fraction, and **(I)** EM3/(EM3+EM4) versus water depth. Red regression lines are shown in these plots.

continental shelf, giving rise to Dense Shelf Water (DSW). Subsequently, the DSW moves northward through submarine canyons and, driven by tidal activity, passes the sills on the outer continental shelf. Eventually, it descends the continental slope, thereby culminating in the formation of AABW (Tamura et al., 2008; Gordon et al., 2015).

Recent observations indicate that the Joides Basin and Joides Trough in the WRS play a pivotal role in the northward advection of DSW generated within the region. Conversely, the Glomar Challenger Basin and areas east of Pennell Trough do not exhibit the presence of this water mass (Gordon et al., 2015). Interestingly, this spatial distribution pattern of DSW closely aligns with the EM3/(EM3+EM4) ratio depicted in our findings (Figure 7B). Hence, we deduce that the stronger activity of bottom currents in the WRS is primarily governed by the formation and transport of DSW.

6.2 Sediment provenances

6.2.1 Clay minerals

Clay minerals in marine sediment serve as valuable indicators of sediment origin due to their small grain-size, enabling easy transportation and distribution through various media (Hillenbrand et al., 2003; Liu et al., 2003; Liu et al., 2007). Illite and chlorite are commonly found in high-latitudes of the Southern Ocean as a result of physical weathering and glacial erosion of basement rocks in Antarctica (Chamley, 1989; Ehrmann, 1991; Ehrmann, 1998). Illite originates from acidic rocks including granulites, gneisses, and granites. Chlorite is derived from igneous and metamorphic rocks that contain chlorite (Chamley, 1989; Hillenbrand et al., 2003). In contrast, smectite and kaolinite form by chemical weathering. Smectite forms through hydrolysis in environments with slow water movement and is often associated

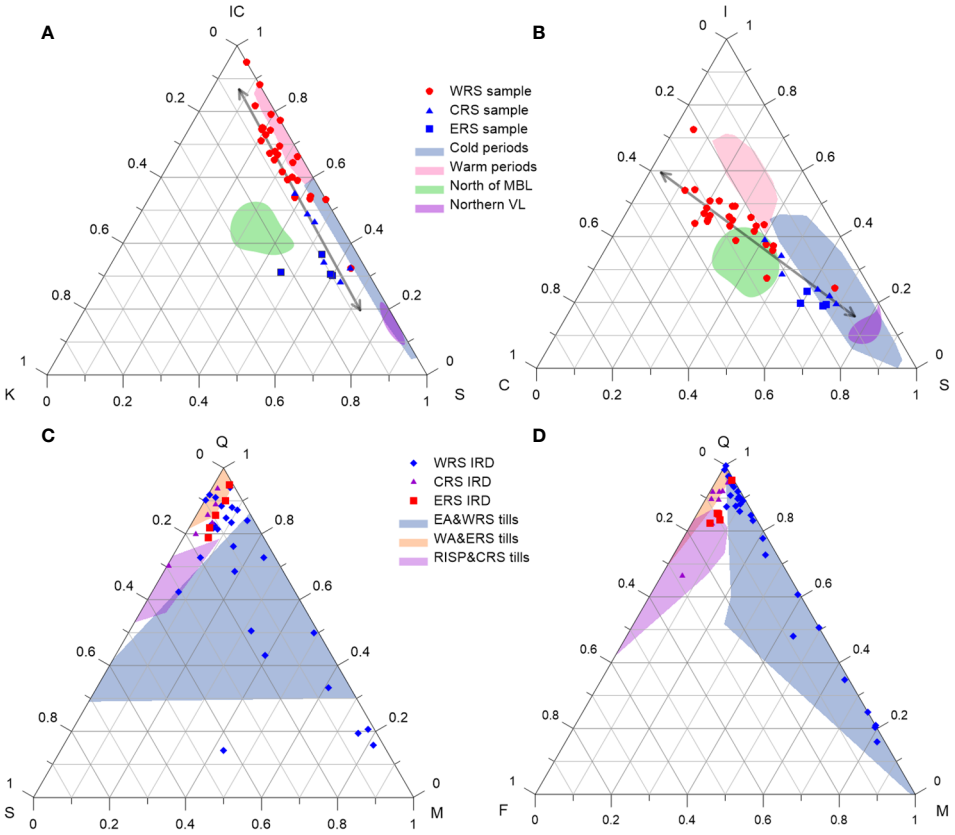

FIGURE 10
Ternary diagrams depicting **(A)** S-IC-K, **(B)** S-I-C, **(C)** Q-M-S, and **(D)** Q-M-F compositions. S, IC, K, and C in **(A, B)** represent smectite, illite plus chlorite, kaolinite, and chlorite, respectively. Q, S, M, and F in **(C, D)** represent quartz, sedimentary rocks, mafic rock grains, and feldspars, respectively. The light green shades in **(A, B)** represent clay mineral compositions of shelf sediments north of MBL (Marie Byrd Land) (Hillenbrand et al., 2003), while the light pink, light blue, and purple shades indicate clay mineral compositions of Cenozoic sediments from the McMurdo Sound (Ehrmann et al., 2003) and sediments from the northernmost coast of Victoria Land (Orombelli et al., 1990). The double arrows in these diagrams depict the binary mixing trends of clay mineral compositions. In **(C, D)**, the light orange, light purple, and light blue shades represent compositions of tills from West Antarctica & ERS (ERS), RISP sites and CRS (CRS), and East Antarctica & WRS (WRS) according to Licht et al. (2005).

with volcanic regions in the Southern Ocean (Petschick et al., 1996). Kaolinite develops through extensive hydrolysis of feldspars in humid and warm environments (Chamley, 1989). The occurrence of kaolinite around Antarctica is usually related to recycling of ancient sediment (Junttila et al., 2005; Borchers et al., 2011).

To identify the source areas of the clay minerals in our samples, we utilized S-IC-K and S-I-C ternary diagrams to analyze our surface sediment data alongside a compilation of previously published data (Figures 10A, B). In the S-IC-K diagram, we observed that surface sediments from the WRS were closer to the IC apex, while those from the Eastern and CRS were closer to the S apex. All samples followed a line adjacent to the IC-S edge (Figure 10A). In the I-S-C diagram, we found that the WRS samples were nearer the I-C edge, while the ERS and CRS samples were closer to the S vertex. Additionally, all samples fell along a line perpendicular to the I-C edge roughly in the middle of the diagram (Figure 10B). These diagrams indicate that the studied sediments were the result of binary mixing between two end-members: an illite- and chlorite-rich end-member, and a smectite-rich end-member. Notably, neither of the end-members overlaps with the clay mineral composition of the surface sediments from the continental shelf north of Marie Byrd Land (Figures 10A, B), suggesting a minimal contribution from the Amundsen Sea via the westward flowing Antarctic Coastal and Slope Currents. Additionally, the contribution of the clay fraction by impinging MCDW from the north could be ruled out as well since the outer shelf samples are located between the two identified end-members in the diagrams. Thus, we conclude that both the illite- and chlorite-rich end-member and the smectite-rich end-member were primarily originated from the Ross Sea Embayment itself, which

is consistent with the results of Nd and Sr isotopic analyses conducted on the clay-sized fractions of the surface sediments within the investigated region by Shao et al. (2022).

The examination of Cenozoic sediment sequences from McMurdo Sound, as documented in previous studies, reveals a correlation between warmer climate conditions and higher concentrations of illite and chlorite, while colder climate conditions are associated with higher concentrations of smectite (Figures 10A, B; Ehrmann et al., 2003). The illite and chlorite components are believed to originate from the Beacon Supergroup on the Southern Victoria Land coast, whereas the smectite component is thought to derive from areas where the McMurdo Volcanic Group outcrops. Our findings support an East Antarctic craton origin for the significant abundance of illite and chlorite in our samples from the WRS, particularly in close proximity to the Southern Victoria Land (Figures 4A, C). However, the overall declining trend of smectite from east to west (Figure 4B) contradicts the notion of a potential origin from the McMurdo Volcanic Group which is located in the WRS (Figure 1B). Instead, it is more reasonable to interpret the spatial distribution of smectite as originating from beneath the glaciers of West Antarctica. This is supported by the presence of Cenozoic mafic volcanic structures beneath the glacier systems that drain into the Ross Sea from the WAIS (Behrendt et al., 1995; Behrendt et al., 2004), as well as the elevated levels of smectite found in tills derived from the Bindschadler Ice Stream and MachAyeal Ice Stream (Figure 1A; Balshaw, 1981). Nevertheless, the sporadic occurrence of high smectite levels in front of Ross Island and near the northernmost coast of Victoria Land likely originates locally due to their proximity to the McMurdo Volcanic Group (Figure 1B). Our study thus highlights the need for caution when considering the origin of smectite in sedimentary records from the Ross Sea, given its potential multiple sources.

The consistency between kaolinite and smectite in terms of spatial distributions in the ERS (Figures 4B, D) may suggest that they were derived from spatially adjacent sources beneath the WAIS. This is supported by the occurrence of kaolinite in sediments from the Amundsen Sea continental shelf where clay minerals were mainly derived from beneath the WAIS as well (Hillenbrand et al., 2003), and the absence of kaolinite from sedimentary records in the WRS (Figure 10A). The lower kaolinite abundance in our samples compared to the sediments from Amundsen Sea indicates less entrainment of ancient chemically weathered sediments filled in the West Antarctica basin (Rooney et al., 1988) by glaciers draining into Ross Sea from the WAIS.

The congruity in spatial distributions between kaolinite and smectite within the ERS (Figures 4B, D) implies that they were likely originated from neighboring sources beneath the WAIS. This is reinforced by the presence of kaolinite in sediments collected from the Amundsen Sea continental shelf, where clay minerals are predominantly derived from beneath the WAIS as well (Hillenbrand et al., 2003), and the absence of kaolinite in sedimentary records within the WRS (Figure 10A; Ehrmann et al., 2003). The lower abundance of kaolinite in our samples, in comparison to the sediments from the Amundsen Sea, suggests a reduced incorporation of ancient chemically weathered sediments, which fill the basin of West Antarctica (Rooney et al., 1988), by glaciers draining into the Ross Sea from the WAIS.

6.2.2 Coarse fractions

The region surrounding the Ross Sea is predominantly covered by thick ice sheets, but exposed outcrops reveal the intricate lithologies of the bedrock. The uneven distribution of rock outcrops presents an opportunity to follow the origin of the coarse-grained IRD through an analysis of its lithological composition (Licht et al., 2005). Despite the intricate and diverse composition within the coarse fraction, Factor Analyses indicate the presence of only three primary components (Figure 6), characterized by high levels of angular and rounded quartz, mafic rock grains, and deformed silt, respectively. These components are likely associated with three main sources that dominate the coarse fraction, enabling the provenance analyses of the coarse fraction to be simplified as based on them.

Factor 1, as evidenced by high loadings of both angular and rounded quartz (Figure 6C), is likely derived from acidic source rocks. In the Antarctic region, quartz is commonly enriched in the IRD fractions compared to other minerals due to its high mechanical hardness, rendering it resistant to breakage during glacial grinding and retains a larger particle size (Wu et al., 2020). Licht et al. (2005) observed that tills beneath the Kamb Ice Stream and Whillans Ice Stream (Figure 1A) contained a high abundance of both angular and rounded quartz but almost an absence of mafic volcanic rocks, despite Cenezoic volcanoes being scattered beneath these glaciers. Furthermore, quartz was the most abundant mineral species in till samples across the ERS and CRS during the Last glacial periods (Figures 10C, D), possibly eroded from the Granite Harbor Intrusives, as well as the granodiorite and granite of Marie Byrd Land (Figure 1B; Licht et al., 2005). In our samples, Factor 1 is predominantly present in the ERS and CRS regions and extends to the central Victoria Land coast. Additionally, in the Q-M-S and Q-M-F diagrams, our ERS and CRS samples mostly occupy the domains of the West Antarctic & ERS tills and the RISP (RIS Drilling Project; Licht et al., 2005) tills, supporting that the quartz-enriched Factor 1 represents a source of icebergs originating from West Antarctica.

Factor 2, characterized by a significant presence of mafic igneous rock grains, is likely indicative of materials primarily derived from a basic volcanic region. Tills in East Antarctica exhibit varying lithologies in comparison to those in West Antarctica (Figures 10C, D), reflecting the diverse composition of bedrock throughout the Transantarctic Mountains (Figure 1B). However, a substantial mafic component is consistently found in most East Antarctic tills, which is believed to originate from the Ferrar Group (Licht et al., 2005). In the Q-M-F ternary diagram, our samples from the WRS align well with the East Antarctic & WRS tills (Figure 10D). In the Q-M-S diagram, however, these samples disperse over a broader range than the East Antarctic & WRS tills

(Figure 10C). Some WRS samples display higher quartz content compared to the remaining samples from the WRS, and their distribution tends to overlap with the West Antarctic & ERS tills, indicating a mixture of materials transported by icebergs from both West and East Antarctica. These particular samples are located between 74°S and 75°S in the WRS (Figure 5B). In contrast, certain WRS samples contain a significantly higher proportion of mafic rock grains than the tills from East Antarctica and the WRS, suggesting an additional source of mafic igneous rocks. These samples are situated between 72°S and 73°S, as well as between 76°S and 78°S (Figure 5C), close to areas where the McMurdo Volcanic Group is exposed (Figure 1). This suggests that the McMurdo Volcanic Group may contribute significantly to the modern IRD found in the WRS.

The moderate scores (0.1-0.2) observed in Factor 2 within the ERS area likely correspond to the presence of Cenozoic mafic volcanic structures underlying the glacier systems that drain into the Ross Sea from the WAIS. However, an apparent discrepancy arises when considering that there is a high abundance of smectite in the clay fraction but a disproportionately low amount of mafic rock grains in the ERS. It has been proposed by Behrendt et al. (1995); Behrendt et al. (2004) that (ancient) glacial erosion likely planed off the mafic volcanic structures in West Antarctica before the development of the current ice streams. Rooney et al. (1988) suggest that the West Antarctic basin, which lies beneath the WAIS, is filled with glacial and marine sediments up to a kilometer thick, masking the volcanic structures. Consequently, the coarse mafic rock grains may be more commonly found in older successions beneath West Antarctica (Licht et al., 2005), making it less accessible to the present glaciers.

Factor 3 exhibits a prominent abundance of deformed silt, which comprises coarse-grained materials that form during the stabilization of a glacier at its grounding zone (Cowan et al., 2012). The prevalence of these materials within the sediment indicates the proximity of the sediment location to a glacier grounding zone (Cowan et al., 2012). Geospatially, the highest score in Factor 3 is primarily observed in the David Glacier-Drygalski Ice Tongue (DG-DIT) area, providing strong evidence for its derivation from beneath this specific glacier system.

The DG-DIT system represents the largest outlet glacier within the Victoria Land section of the EAIS (Frezzotti and Mabin, 1994). Over the past century, this system has undergone numerous calving events (Frezzotti and Mabin, 1994). Consequently, as glaciers detach from this ice tongue, they have a propensity to incorporate deformed silt as basal debris and subsequently disperse it along their drifting trajectories.

To summarize, the clay minerals and coarse fraction (IRD) found in the surface sediments of Ross Sea were sourced from both the West Antarctica and East Antarctica. Provenance analysis exhibits a complementary spatial distribution pattern for these two sediment components. Considering that approximately 50% of the mass loss of the Antarctic Ice Sheet is through iceberg calving (Depoorter et al., 2013), these findings collectively indicate that both the WAIS and the EAIS, which discharge into the Ross Sea Embayment, have maintained a high level of dynamism under the modern climatic conditions.

7 Conclusions and summary

In this investigation, we carried out a series of measurements and analysis on sediment samples collected from the Ross Sea continental shelf to examine the provenance and delivery mode of sediments in the modern Ross Sea environment. We focused on grain-size distribution, lithology of the coarse fraction (>250 μm), and clay mineral composition. Based on our findings, we have made the following main conclusions:

(1) The grain-size distributions of the studied sediments display significant variations. Through EMMA analysis, we identified four distinct sediment types associated with different delivery mechanisms: poorly sorted IRD, well-sorted IRD, and sediments transported by relatively strong and weak bottom currents.

(2) The transport and deposition of IRD in Ross Sea are influenced by factors such as water depth, proximity to the iceberg source area, and seawater temperature resulting from MCDW intrusion. Well-sorted IRD (EM2) originates from sandy beaches in the WRS and is delivered by relatively small icebergs, whereas at least some of the poorly sorted IRD (EM1) originates from large icebergs calved from the RIS.

(3) The EMMA-derived index EM3/(EM3+EM4) reflects relative changes in bottom current strength in the investigated area. It reveals that the WRS experiences stronger bottom current activity compared to the ERS, particularly in the Joides Basin, Joides Trough, and near the northernmost Victoria Land. These findings reflect formation and northward transport of DSW.

(4) The studied sediments contain a high proportion of illite and smectite, a moderate level of chlorite, and a small quantity of kaolinite. These clay minerals primarily originate from the Ross Sea Embayment itself through a binary mixing process. Illite and chlorite predominantly came from the East Antarctic craton, whereas smectite and kaolinite were mainly originated from beneath the WAIS. Additionally, smectite can also be contributed by the McMurdo Volcanic Group.

(5) Factor Analysis on the lithology of the coarse fraction identified three major sources characterized by a high abundance of quartz-rich grains, mafic igneous rock-rich grains, and deformed silt, respectively. The quartz-rich and mafic igneous rock-rich components are predominantly distributed in the ERS and WRS, originating from West Antarctica and East Antarctica, respectively. The deformed silt is mainly found near the David Glacier-Dragalski Ice

Tongue system, highlighting the dynamic nature of this system.

In summary, our findings support the notion that the WRS plays a crucial role as a source area for the formation of AABW. Moreover, our study reveals the dynamic nature of the glaciers draining into the Ross Sea from both the EAIS and WAIS, underscoring their potential contribution to future sea level rise under ongoing climate warming conditions.

Data availability statement

The original contributions presented in the study are included in the article/Supplementary Material. Further inquiries can be directed to the corresponding author.

Author contributions

LW: Conceptualization, Data curation, Formal Analysis, Funding acquisition, Investigation, Methodology, Project administration, Visualization, Writing – original draft. LL: Data curation, Methodology, Software, Visualization, Writing – review & editing. RW: Data curation, Funding acquisition, Resources, Supervision, Validation, Writing – review & editing. HS: Software, Validation, Visualization, Writing – review & editing. YC: Data curation, Methodology, Visualization, Writing – review & editing. ZL: Data curation, Methodology, Software, Visualization, Writing – review & editing. YL: Data curation, Methodology, Software, Validation, Visualization, Writing – review & editing. WX: Data curation, Resources, Supervision, Validation, Writing – review & editing. RX: Data curation, Methodology, Validation, Visualization, Writing – review & editing.

Funding

The author(s) declare financial support was received for the research, authorship, and/or publication of this article. We declare that all sources of funding received for this research have been submitted. LW acknowledges the support from the Chinese National Natural Science Foundation (Grant No. 42276077) and the Open Fund of State Key Laboratory of Marine Geology, Tongji University (Grant No. MGK202207). RW is grateful for the financial support provided by the Chinese National Natural Science Foundation (Grant No. 42030401).

Acknowledgments

We express our deep gratitude to the participants of the 31st-35th Chinese Antarctic Expedition cruise for their assistance in sample retrieval. We also sincerely thank the two reviewers for their constructive comments and suggestions that helped to improve the manuscript and Editor Dr. Qi Di for efficiently handling our manuscript.

Conflict of interest

The authors declare that the research was conducted in the absence of any commercial or financial relationships that could be construed as a potential conflict of interest.

Publisher's note

Supplementary material

The Supplementary Material for this article can be found online at: https://www.frontiersin.org/articles/10.3389/fmars.2023.1324391/full#supplementary-material

References

Abuodha, J. O. Z. (2003). grain-size distribution and composition of modern dune and beach sediments, Malindi Bay coast, Kenya. *J. Afr. Earth Sci.* 36, 41–54. doi: 10.1016/S0899-5362(03)00016-2

Anderson, J., Brake, C., and Myers, N. (1984). Sedimentation on the ross sea continental shelf, Antarctica. *Mar. Geol.* 57, 295–333. doi: 10.1016/0025-3227(84)90203-2

Anderson, J., Simkins, L., Bart, P., Santis, L., Halberstadt, A. R., Olivo, E., et al. (2018). Seismic and geomorphic records of Antarctic Ice Sheet evolution in the Ross Sea and controlling factors in its behaviour. *Geological Society London Special Publications* 475, 223–240. doi: 10.1144/SP475.5

Andrews, J., Domack, E., Cunningham, W., Leventer, A., Licht, K., Jull, A. J., et al. (1999). Problems and possible solutions concerning radiocarbon dating of surface marine sediments, Ross Sea, Antarctica. *Quaternary Res.* 52, 206–216. doi: 10.1006/qres.1999.2047

Balshaw, K. (1981). Antarctic glacial chronology reflected in the Oligocene through Pliocene sedimentary section in the Ross Sea (Houston (IL: Rice University).

Barrett, P. J. (1991). The Devonian to Jurassic Beacon Supergroup of the Transantarctic Mountains and correlatives in other parts of Antarctica. In: Tingey, R.J. (Ed.), *The Geology of Antarctica*. Oxford University Press, New York, pp. 120–152.

Behrendt, J., Blankenship, D., Damaske, D., and Cooper, A. (1995). Glacial removal of late Cenozoic subglacially emplaced volcanic edifices by the West Antarctic ice sheet. *Geology* 23, 1111–1114. doi: 10.1130/0091-7613(1995)023<1111:GROLCS>2.3.CO;2

Behrendt, J., Blankenship, D., Morse, D., and Bell, R. (2004). Shallow-source aeromagnetic anomalies observed over the West Antarctic Ice Sheet compared with coincident bed topography from radar ice sounding - New evidence for glacial "removal" of subglacially erupted late Cenozoic rift-related volcanic edifices. *Global Planetary Change* 42, 177–193. doi: 10.1016/j.gloplacha.2003.10.006

Blackburn, T., Edwards, G., Tulaczyk, S., Scudder, M., Piccione, G., Hallet, B., et al. (2020). Ice retreat in Wilkes Basin of East Antarctica during a warm interglacial. *Nature* 583, 554–559. doi: 10.1038/s41586-020-2484-5

Borchers, A., Voigt, I., Kuhn, G., and Diekmann, B. (2011). Mineralogy of glaciomarine sediments from the Prydz Bay–Kerguelen region: relation to modern depositional environments. *Antarctic Sci.* 23, 164–179. doi: 10.1017/S0954102010000830

Burckle, L. H. (2001). *Distribution of opal in surface sediments, compiled from different sources* (PANGAEA). doi: 10.1594/PANGAEA.58365

Chamley, H. (1989). *Clay sedimentology* (Berlin: Springer), 623.

Colhoun, E. A., Mabin, M. C. G., Adamson, D. A., and Kirk, R. M. (1992). Antarctic ice volume and contribution to sea-level fall at 20,000 yr BP from raised beaches. *Nature* 358, 316–319. doi: 10.1038/358316a0

Cook, C., Flierdt, T., Williams, T., R Hemming, S., Iwai, M., Kobayashi, M., et al. (2013). Dynamic behaviour of the East Antarctic ice sheet during Pliocene warmth. *Nat. Geosci.* 6, 765–769. doi: 10.1038/ngeo1889

Cook, C. P., Hill, D. J., van de Flierdt, T., Williams, T., Hemming, S. R., Dolan, A. M., et al. (2014). Sea surface temperature control on the distribution of far-traveled Southern Ocean ice-rafted detritus during the Pliocene. *Paleoceanography* 29, 533–548. doi: 10.1002/2014PA002625

Cowan, E., Christoffersen, P., and Powell, R. (2012). Sedimentological signature of A deformable bed preserved beneath an ice stream in A late pleistocene glacial sequence, Ross Sea, Antarctica. *J. Sedimentary Res.* 82, 270–282. doi: 10.2110/jsr.2012.25

Cowan, E. A., Hillenbrand, C.-D., Hassler, L. E., and Ake, M. T. (2008). Coarse-grained terrigenous sediment deposition on continental rise drifts: A record of Plio-Pleistocene glaciation on the Antarctic Peninsula. *Palaeogeogr. Palaeoclimatol. Palaeoecol.* 265, 275–291. doi: 10.1016/j.palaeo.2008.03.010

Cunningham, W. L., and Leventer, A. (1998). Diatom assemblages in surface sediments of the Ross Sea: relationship to present oceanographic conditions. *Antarctic Sci.* 10, 134–146. doi: 10.1017/S0954102098000182

DeConto, R. M., and Pollard, D. (2016). Contribution of Antarctica to past and future sea-level rise. *Nature* 531, 591–597. doi: 10.1038/nature17145

Delmonte, B., Baroni, C., Andersson, P. S., Schoberg, H., Hansson, M., Aciego, S., et al. (2010). Aeolian dust in the Talos Dome ice core (East Antarctica, Pacific/Ross Sea sector): Victoria Land versus remote sources over the last two climate cycles. *J. Quaternary Sci.* 25, 1327–1337. doi: 10.1002/jqs.1418

Depoorter, M. A., Bamber, J. L., Griggs, J. A., Lenaerts, J. T. M., Ligtenberg, S. R. M., van den Broeke, M. R., et al. (2013). Calving fluxes and basal melt rates of Antarctic ice shelves. *Nature* 502, 89–92. doi: 10.1038/nature12567

Drewry, D. J. (1983). *Antarctica: glaciological and geophysical folio* (Cambridge University Press, Cambridge Scoot Polar Research Institute).

Edwards, T. L., Brandon, M. A., Durand, G., Edwards, N. R., Golledge, N. R., Holden, P. B., et al. (2019). Revisiting Antarctic ice loss due to marine ice-cliff instability. *Nature* 566, 58–64. doi: 10.1038/s41586-019-0901-4

Ehrmann, W. U. (1991). Implications of sediment composition on the southern Kerguelen Plateau for paleoclimate and depositional environment. *Proc. ODP Sci. Results* 119, 185–210. doi: 10.2973/odp.proc.sr.119.121.1991

Ehrmann, W. (1998). Implications of late Eocene to early Miocene clay mineral assemblages in McMurdo Sound (Ross Sea, Antarctica) on paleoclimate and ice dynamics. *Palaeogeogr. Palaeoclimatol. Palaeoecol.* 139, 213–231. doi: 10.1016/S0031-0182(97)00138-7

Ehrmann, W., Bloemendal, J., Hambrey, M. J., McKelvey, B., and Whitehead, J. (2003). Variations in the composition of the clay fraction of the Cenozoic Pagodroma Group, East Antarctica: implications for determining provenance. *Sedimentary Geol.* 161, 131–152. doi: 10.1016/S0037-0738(03)00069-1

Farmer, L., Licht, K., Swope, R., and Andrews, J. (2006). Isotopic constraints on the provenance of fine-grained sediment in LGM tills from the Ross Embayment, Antarctica. *Earth Planetary Sci. Letters* 249, 90–107. doi: 10.1016/j.epsl.2006.06.044

Fretwell, P., Pritchard, H. D., Vaughan, D. G., Bamber, J., Barrand, N., Bell, R., et al. (2013). Bedmap2: improved ice bed, surface and thickness datasets for Antarctica. *Cryosphere* 7, 375–393. doi: 10.5194/tc-7-375-2013

Frezzotti, M., and Mabin, M. (1994). 20th century behaviour of Drygalski Ice Tongue, Ross Sea, Antarctica. *Ann. Glaciol.* 20, 397–400. doi: 10.3189/1994AoG20-1-397-400

Ge, S., Chen, Z., Liu, Q., Wu, L., Zhong, Y., Liu, H., et al. (2022). Dynamic response of East Antarctic ice sheet to Late Pleistocene glacial–interglacial climatic forcing. *Quaternary Sci. Rev.* 277, 107299. doi: 10.1016/j.quascirev.2021.107299

Gilbert, I. M., Pudsey, C. J., and Murray, J. W. (1998). A sediment record of cyclic bottom-current variability from the northwest Weddell Sea. *Sedimentary Geol.* 115, 185–214. doi: 10.1016/S0037-0738(97)00093-6

Goodge, J., and Fanning, C. (1999). 2.5 b.y. of punctuated Earth history as recorded in a single rock. *Geology* 27, 1007–1010. doi: 10.1130/0091-7613(1999)027<1007:BYOPEH>2.3.CO;2

Goodge, J., Myrow, P., Williams, I., and Bowring, S. A. (2002). Age and provenance of the beardmore group, Antarctica: constraints on rodinia supercontinent breakup. *J. Geol.* 110, 393–406. doi: 10.1086/340629

Gordon, A., Huber, B., and Busecke, J. (2015). Bottom water export from the WRS 2007 through 2010. *Geophys. Res. Letters* 42, 5387–5394. doi: 10.1002/2015GL064457

Halberstadt, A. R., Simkins, L., Anderson, J., Prothro, L., and Bart, P. (2018). Characteristics of the deforming bed: Till properties on the deglaciated Antarctic continental shelf. *J. Glaciol.* 64, 1014–1027. doi: 10.1017/jog.2018.92

Hauck, J., Gerdes, D., Hillenbrand, C.-D., Hoppema, M., Kuhn, G., Nehrke, G., et al. (2012). Distribution and mineralogy of carbonate sediments on Antarctic shelves. *J. Mar. Systems* 90, 77–87. doi: 10.1016/j.jmarsys.2011.09.005

Hillenbrand, C.-D., Grobe, H., Diekmann, B., Kuhn, G., and Fütterer, D. K. (2003). Distribution of clay minerals and proxies for productivity in surface sediments of the Bellingshausen and Amundsen seas (West Antarctica)–Relation to modern environmental conditions. *Mar. Geol.* 193, 253–271. doi: 10.1016/S0025-3227(02)00659-X

Holtzapffel, T. (1985). Les, minéraux argileux: préparation, analyse diffractométrique et determination. *Société géologique du Nord* .12, 1–36.

Jacobs, S. S., Amos, A. F., and Bruchhausen, P. M. (1970). Ross sea oceanography and antarctic bottom water formation. *Deep Sea Res. Oceanographic Abstracts* 17, 935–962. doi: 10.1016/0011-7471(70)90046-X

Jonkers, L., Barker, S., Hall, I. R., and Prins, M. A. (2015). Correcting for the influence of ice-rafted detritus on grain-size-based paleocurrent speed estimates. *Paleoceanography* 30, 1347–1357. doi: 10.1002/2015PA002830

Junttila, J., Ruikka, M., and Strand, K. (2005). Clay-mineral assemblages in high-resolution Plio-Pleistocene interval at ODP Site 1165, Prydz Bay, Antarctica. *Global Planetary Change* 45, 151–163. doi: 10.1016/j.gloplacha.2004.09.007

Klovan, J. E., and Miesch, A. T. (1976). Extended CABFAC and QMODEL computer programs for Q-mode factor analysis of compositional data. *Comput. Geosci.* 1, 161–178. doi: 10.1016/0098-3004(76)90004-2

Kyle, P. R. (1990). "McMurdo volcanic group western Ross Embayment," in *Volcanoes of the antarctic plate and Southern oceans*. Eds. W. E. Le Masurier and J. W. Thomson (Washington, DC: American Geophysical Union), 48–80.

Lamy, F., Arz, H. W., Kilianc, R., Lange, C. B., Lembke-Jene, L., Wengler, M., et al. (2015). Glacial reduction and millennial-scale variations in Drake Passage throughflow. *Proc. Natl. Acad. Sci. United States America* 112, 13496–13501. doi: 10.1073/pnas.1509203112

Licht, K. J., Dunbar, N. W., Andrews, J. T., and Jennings, A. E. (1999). Distinguishing subglacial till and glacial marine diamictons in the WRS, Antarctica: Implications for a last glacial maximum grounding line. *Geological Soc. America Bulletin* 111, 91–103. doi: 10.1130/0016-7606(1999)111<0091:DSTAGM>2.3.CO;2

Licht, K. J., Lederer, J. R., and Jeffrey Swope, R. (2005). Provenance of LGM glacial till (sand fraction) across the Ross embayment, Antarctica. *Quaternary Sci. Rev.* 24, 1499–1520. doi: 10.1016/j.quascirev.2004.10.017

Liu, Z., Trentesaux, A., Clemens, S. C., Colin, C., Wang, P., Huang, B., et al. (2003). Clay mineral assemblages in the northern South China Sea: implications for East Asian monsoon evolution over the past 2 million years. *Mar. Geol.* 201, 133–146. doi: 10.1016/S0025-3227(03)00213-5

Liu, Z., Zhao, Y., Li, J., and Colin, C. (2007). Late Quaternary clay minerals off Middle Vietnam in the western South China Sea: Implications for source analysis and East Asian monsoon evolution. *Sci. China Ser. D: Earth Sci.* 50, 1674–1684. doi: 10.1007/s11430-007-0115-8

Marschalek, J., Zurli, L., Talarico, F., Flierdt, T., Vermeesch, P., Carter, A., et al. (2021). A large West Antarctic ice sheet explains early neogene sea-level amplitude. *Nature* 600, 450–455. doi: 10.1038/s41586-021-04148-0

McCave, I., and Andrews, J. (2019). Distinguishing current effects in sediments delivered to the ocean by ice. I. Principles, methods and examples. *Quaternary Sci. Rev.* 212, 92–107. doi: 10.1016/j.quascirev.2019.03.031

McCave, I., Crowhurst, S., Kuhn, G., Hillenbrand, C., and Meredith, M. (2014). Minimal change in Antarctic Circumpolar Current flow speed between the last glacial and Holocene. *Nat. Geosci.* 7, 113–116. doi: 10.1038/ngeo2037

McCave, I., and Hall, I. (2006). Size sorting in marine muds: Processes, pitfalls, and prospects for paleoflow-speed proxies. *Geochem. Geophys. Geosystems* 7, 1–37. doi: 10.1029/2006GC001284

McCave, I. N., Thornalley, D. J. R., and Hall, I. R. (2017). Relation of sortable silt grain-size to deep-sea current speeds: Calibration of the 'Mud Current Meter. *Deep Sea Res. Part I: Oceanographic Res. Pap.* 127, 1–12. doi: 10.1016/j.dsr.2017.07.003

McKay, R., Dunbar, G., Naish, T., Barrett, P., Carter, L., and Harper, M. (2008). Retreat history of the Ross Ice Sheet (Shelf) since the Last Glacial Maximum from deep-basin sediment cores around Ross Island. *Palaeogeogr. Palaeoclimatol. Palaeoecol. - PALAEOGEOGR PALAEOCLIMATOL* 260, 245–261. doi: 10.1016/j.palaeo.2007.08.015

McKay, R., Santis, L., Kulhanek, D., Ash, J., Beny, F., Browne, I., et al. (2018). International Ocean Discovery Program: Expedition 374 Preliminary Report: Ross Sea West Antarctic Ice Sheet History: Ocean-ice sheet interactions and West Antarctic Ice Sheet vulnerability: clues from the Neogene and Quaternary record of the outer Ross Sea continental margin. *Int. Ocean Discovery Program*, 1–63. doi: 10.14379/iodp.pr.374.2018

Mezgec, K., Stenni, B., Crosta, X., Masson-Delmotte, V., Baroni, C., Braida, M., et al. (2017). Holocene sea ice variability driven by wind and polynya efficiency in the Ross Sea. *Nat. Commun.* 8, 1334. doi: 10.1038/s41467-017-01455-x

Myrow, P. M., Pope, M. C., Goodge, J. W., Fischer, W., and Palmer, A. R. (2002). Depositional history of pre-Devonian strata and timing of Ross orogenic tectonism in the central TransantarcticMountains, Antarctica. *GSA Bulletin* 114 (9):1070–1088. doi: 10.1130/0016-7606(2002)114<1070:DHOPDS>2.0.CO;2

Naish, T., Powell, R., Levy, R., Wilson, G., Scherer, R., Talarico, F., et al. (2009). Obliquity-paced Pliocene West Antarctic ice sheet oscillations. *Nature* 458, 322–328. doi: 10.1038/nature07867

Naish, T. R., Woolfe, K. J., Barrett, P. J., Wilson, G. S., Atkins, C., Bohaty, S. M., et al. (2001). Orbitally induced oscillations in the East Antarctic ice sheet at the Oligocene/Miocene boundary. *Nature* 413, 719–723. doi: 10.1038/35099534

O'Brien, P. E., and Leitchenkov, G. (1997). "Deglaciation of Prydz Bay, East Antarctica, based on echo sounding and topographic features," in *Geology and seismic stratigraphy of the Antarctic margin*, *2*, vol. 71 . Eds. P. F. Barker and A. K. Cooper (American Geophysical Union), 109–126. doi: 10.1029/AR071p0109

Orombelli, G., Baroni, C., and Denton, G. H. (1990). Late cenozoic glacial history of the terra nova bay region, northern Victoria land, Antarctica. *Geografia Fisica e Dinamica Quaternaria* 13, 139–163.

Orsi, A., Smethie, W., and Bullister, J. (2002). On the total input of Antarctic Waters to the deep ocean: A preliminary estimate from chlorofluorocarbon measurements. *J. Geophys. Res. (Oceans)* 107, 1–14. doi: 10.1029/2001JC000976

Orsi, A., and Wiederwohl, C. (2009). A recount of Ross Sea water. *Deep Sea Res. Part II: Topical Stud. Oceanogr.* 56, 778–795. doi: 10.1016/j.dsr2.2008.10.033

Passchier, S. (2011). Linkages between East Antarctic Ice Sheet extent and Southern Ocean temperatures based on a Pliocene high-resolution record of ice-rafted debris off Prydz Bay, East Antarctica. *Paleoceanography* 26, PA4204. doi: 10.1029/2010PA002061

Patterson, M. O., McKay, R., Naish, T., Escutia, C., Jimenez-Espejo, F. J., Raymo, M. E., et al. (2014). Orbital forcing of the East Antarctic ice sheet during the Pliocene and Early Pleistocene. *Nat. Geosci.* 7, 841–847. doi: 10.1038/ngeo2273

Petschick, R. (2000) *MacDiff 4.2.2*. Available at: http://servermac.geologie.uni-frankfurt.de/Rainer.html.

Petschick, R., Kuhn, G., and Gingele, F. (1996). Clay mineral distribution in surface sediments of the South Atlantic: sources, transport, and relation to oceanography. *Mar. Geol.* 130, 203–229. doi: 10.1016/0025-3227(95)00148-4

Prins, M. A., Bouwer, L. M., Beets, C. J., Troelstra, S. R., Weltje, G. J., Kruk, R. W., et al. (2002). Ocean circulation and iceberg discharge in the glacial North Atlantic: Inferences from unmixing of sediment size distributions. *Geology* 30, 555–558. doi: 10.1130/0091-7613(2002)030<0555:OCAIDI>2.0.CO;2

Prins, M. A., and Weltje, G. (1999). "End-member modeling of siliciclastic grain-size distributions: The late Quaternary record of aeolian and fluvial sediment supply to the Arabian Sea and its paleoclimatic significance," in *Numerical experiments in stratigraphy: Recent advances in stratigraphic and sedimentologic computer simulations*, vol. 62. (SEPM (Society for Sedimentary Geology) Special Publication), 91–111. doi: 10.2110/pec.99.62.0091

Pudsey, C. J. (1992). Late quaternary changes in Antarctic bottom water velocity inferred from sediment grain size in the northern Weddell Sea. *Mar. Geol.* 107, 9–33. doi: 10.1016/0025-3227(92)90066-Q

R., Schlitzer. (2014). Available at: https://odv.awi.de.

Rignot, E., Bamber, J., Mr, V. D. B., Davis, C., Li, Y., Wj, V. D. B., et al. (2008). Recent Antarctic ice mass loss from radar interferometry and regional climate modelling. *Nat. Geosci.* 1, 106–110. doi: 10.1038/ngeo102

Rooney, S., Blankenship, D., Alley, R., and Bentley, C. (1988). Seismic-reflection profiling of a widespread till beneath Ice Stream B, West Antarctica (Abstract). *Ann. Glaciol.* 11, 210–210. doi: 10.3189/S0260305500006704

Shao, H., He, J., Wu, L., and Wei, L. (2022). Elemental and Sr–Nd isotopic compositions of surface clay-size sediments in the front end of major ice shelves around Antarctica and indications for provenance. *Deep Sea Res. Part II: Topical Stud. Oceanogr.* 195, 105011. doi: 10.1016/j.dsr2.2021.105011

Smith, W. O., Ainley, D. G., Arrigo, K. R., and Dinniman, M. S. (2014). The oceanography and ecology of the Ross Sea. *Annu. Rev. Mar. Sci.* 6, 469–487. doi: 10.1146/annurev-marine-010213-135114

Smith, J., Graham, A., Post, A., Hillenbrand, C.-D., Bart, P., Powell, R., et al. (2019). The marine geological imprint of Antarctic ice shelves. *Nat. Commun.* 10, 5635. doi: 10.1038/s41467-019-13496-5

Stevenard, N., Govin, A., Kissel, C., and Van Toer, A. (2023). Correction of the IRD influence for paleo-current flow speed reconstructions in hemipelagic sediments. *Paleoceanogr. Paleoclimatol.* 38, e2022PA004500. doi: 10.1029/2022PA004500

Stuut, J.-B. W., Prins, M. A., Schneider, R. R., Weltje, G. J., Jansen, J., and Postma, G. (2002). A 300-kyr record of aridity and wind strength in southwestern Africa: inferences from grain-size distributions of sediments on Walvis Ridge, SE Atlantic. *Mar. Geol.* 180, 221–233. doi: 10.1016/S0025-3227(01)00215-8

Tamura, T., Ohshima, K. I., and Nihashi, S. (2008). Mapping of sea ice production for Antarctic coastal polynyas. *Geophys. Res. Letters* 35, L07606. doi: 10.1029/2007GL032903

Teitler, L., Warnke, D. A., Venz, K. A., Hodell, D. A., Becquey, S., Gersonde, R., et al. (2010). Determination of Antarctic Ice Sheet stability over the last~500 ka through a study of iceberg-rafted debris. *Paleoceanography* 25, PA1202. doi: 10.1029/2008PA001691

Toggweiler, J. R., Russell, J. L., and Carson, S. R. (2006). Midlatitude westerlies, atmospheric CO_2, and climate change during the ice ages. *Paleoceanography* 21, PA2005. doi: 10.1029/2005PA001154

Turnbull, I. (2006). Impact of the inverse barometer effect on iceberg drift in the Ross Sea Region, Antarctica. *AGU Fall Meeting Abstracts*.

Wang, J., Li, T., Tang, Z., Xiong, Z., Liu, Y., Chen, Z., et al. (2022). Relating the composition of continental margin surface sediments from the Ross Sea to the Amundsen Sea, West Antarctica, to modern environmental conditions. *Adv. Polar Sci.* 33, 55–70. doi: 10.13679/j.advps.2021.0005

Wang, R., Polyak, L., Xiao, W., Wu, L., and Li, W. (2023). Middle to Late Quaternary changes in ice rafting and deep current transport on the Alpha Ridge, central Arctic Ocean and their responses to climatic cyclicities. *Global Planetary Change* 220, 104019. doi: 10.1016/j.gloplacha.2022.104019

Wang, R., Xiao, W., März, C., and Li, Q. (2013). Late Quaternary paleoenvironmental changes revealed by multi-proxy records from the Chukchi Abyssal Plain, western Arctic Ocean. *Global Planetary Change* 108, 100–118. doi: 10.1016/j.gloplacha.2013.05.017

Weber, M. E., Clark, P. U., Kuhn, G., Timmermann, A., Sprenk, D., Gladstone, R., et al. (2014). Millennial-scale variability in Antarctic ice-sheet discharge during the last deglaciation. *Nature* 510, 134–138. doi: 10.1038/nature13397

Weltje, G. J. (1997). End-member modeling of compositional data: numerical-statistical algorithms for solving the explicit mixing problem. *Math. Geol.* 29, 503–549. doi: 10.1007/BF02775085

Whitworth, T., and Orsi, A. H. (2006). Antarctic Bottom Water production and export by tides in the Ross Sea. *Geophys. Res. Letters* 33, L12609. doi: 10.1029/2006GL026357

Wilson, D., Bertram, A., R., F., Needham, E., Flierdt, T., Welsh, K. J., et al. (2018). Ice loss from the East Antarctic Ice Sheet during late Pleistocene interglacials. *Nature* 561, 383–386. doi: 10.1038/s41586-018-0501-8

Wu, S., Lembke-Jene, L., Lamy, F., Arz, H., Nowaczyk, N., Xiao, W., et al. (2021). Orbital- and millennial-scale Antarctic Circumpolar Current variability in Drake Passage over the past 140,000 years. *Nat. Commun.* 12, 3948. doi: 10.1038/s41467-021-24264-9

Wu, L., Wang, R., Krijgsman, W., Chen, Z., Xiao, W., Ge, S., et al. (2019). Deciphering color reflectance data of a 520-kyr sediment core from the Southern ocean: method application and paleoenvironmental implications. *Geochem. Geophys. Geosystems* 20, 2808–2826. doi: 10.1029/2019GC008212

Wu, L., Wang, R., Xiao, W., Krijgsman, W., Li, Q., Ge, S., et al. (2018). Late quaternary deep stratification-climate coupling in the Southern ocean: implications for changes in abyssal carbon storage. *Geochem. Geophys. Geosystems* 19, 379–395. doi: 10.1002/2017GC007250

Wu, L., Wilson, D. J., Wang, R., Passchier, S., Krijgsman, W., Yu, X., et al. (2021). Late Quaternary dynamics of the Lambert Glacier-Amery Ice Shelf system, East Antarctica. *Quaternary Sci. Rev.* 252, 106738. doi: 10.1016/j.quascirev.2020.106738

Wu, L., Wilson, D. J., Wang, R., Yin, X., Chen, Z., Xiao, W., et al. (2020). Evaluating zr/rb ratio from XRF scanning as an indicator of grain-size variations of glaciomarine sediments in the Southern ocean. *Geochem. Geophys. Geosystems* 21, e2020GC009350. doi: 10.1029/2020GC009350

frontiers | Frontiers in Marine Science

TYPE Original Research
PUBLISHED 07 February 2024
DOI 10.3389/fmars.2024.1307295

OPEN ACCESS

EDITED BY
Jianfang Chen,
Ministry of Natural Resources, China

REVIEWED BY
Wei-Jen Huang,
National Sun Yat-sen University, Taiwan
Hui Gao,
Guangdong Ocean University, China

*CORRESPONDENCE
Yingxu Wu
yingxu.wu@jmu.edu.cn
Di Qi
qidi@jmu.edu.cn

RECEIVED 04 October 2023
ACCEPTED 09 January 2024
PUBLISHED 07 February 2024

CITATION
Yang W, Zhao Y, Wu Y, Chen Z, Gao X, Lin H, Ouyang Z, Cai W, Chen L and Qi D (2024) The impact of sea ice melt on the evolution of surface pCO_2 in a polar ocean basin. *Front. Mar. Sci.* 11:1307295. doi: 10.3389/fmars.2024.1307295

The impact of sea ice melt on the evolution of surface pCO_2 in a polar ocean basin

Wei Yang[1], Yu Zhao[2], Yingxu Wu[1]*, Zijie Chen[2], Xiang Gao[1], Hongmei Lin[3], Zhangxian Ouyang[4], Weijun Cai[4], Liqi Chen[1] and Di Qi[1]*

[1]Polar and Marine Research Institute, College of Harbor and Coastal Engineering, Jimei University, Xiamen, China, [2]Marine Science College, Nanjing University of Information Science & Technology, Nanjing, China, [3]Key Laboratory of Global Change and Marine-Atmospheric Chemistry of Ministry of Natural Resources (MNR), Third Institute of Oceanography, Xiamen, China, [4]School of Marine Science and Policy, University of Delaware, Newark, DE, United States

The strong CO_2 sink in Arctic Ocean plays a significant role in the global carbon budget. As a high-latitude oceanic ecosystem, the features of sea surface pCO_2 and air-sea CO_2 flux are significantly influenced by sea ice melt; however, our understanding of pCO_2 evolution during sea ice melt remains limited. In this study, we investigate the dynamics of pCO_2 during the progression of sea ice melt in the western Arctic Ocean based on data from two cruises conducted in 2010 and 2012. Our findings reveal substantial spatiotemporal variability in surface pCO_2 on the Chukchi Sea shelf and Canada Basin, with a boundary along the shelf breaks at depths of 250-500 m isobaths. On the Chukchi Sea shelf, strong biological consumption dominates pCO_2 variability. Moreover, in Canada Basin, the pCO_2 dynamics are modulated by various processes. During the active sea ice melt stage before sea ice concentration decreases to 15%, biological production through photosynthetic processes and dilution of ice melt water lead to a reduction in DIC concentration and subsequent decline in pCO_2. Further, these effects are counteracted by the air-sea CO_2 exchange at the sea surface which tends to increase seawater DIC and subsequently elevate surface pCO_2. Compared to the pCO_2 reduction resulting from biological production and dilution effects, the contribution of air-sea CO_2 exchange is significantly lower. The combined effects of these factors have a significant impact on reducing pCO_2 during this stage. Conversely, during the post sea ice melt stage, an increase in pCO_2 resulting from high temperatures and air-sea CO_2 exchange outweighs its decrease caused by biological production. Their combined effects result in a prevailing increase in sea surface pCO_2. We argue that enhanced air-sea CO_2 uptake under high wind speeds also contributes to the high sea surface pCO_2 observed in 2012, during both active sea ice melt stage and post sea ice melt stage. The present study reports, for the first time, the carbonate dynamics and pCO_2 controlling processes during the active sea ice melt stage. These findings have implications for accurate estimation of air-sea CO_2 fluxes and improved modeling simulations within the Arctic Ocean.

KEYWORDS

Western Arctic Ocean, pCO_2 dynamics, sea ice melt, sea ice concentration, wind speed

Highlights

- The decrease in DIC resulting from biological production and dilution of ice melt water tends to reduce pCO_2 during the active sea ice melt stage in Canada Basin, although it is counteracted by CO_2 uptake at the air-sea interface.
- The increase in pCO_2 resulting from high temperatures and air-sea CO_2 exchange outweighs its decrease caused by biological production, leading to elevated sea surface pCO_2 during the post sea ice melt stage in Canada Basin.
- The enhanced air-sea CO_2 uptake under high wind speeds also contributes to the high sea surface pCO_2 observed in 2012, during both active sea ice melt stage and post sea ice melt stage.

1 Introduction

Since the beginning of the first industrial revolution, anthropogenic activities have resulted in substantial carbon emissions into the atmosphere. Consequently, atmospheric carbon dioxide (CO_2) levels have continuous risen from 280 ppm in 1850 to 417 ppm in 2022. However, this increase accounts for only 49% of total carbon emissions, and 29% of emitted CO_2 has been absorbed by surface ocean (Friedlingstein et al., 2022). Due to the high solubility of CO_2 in low-temperature waters, the Arctic Ocean and its adjacent marginal seas serve as a significant CO_2 sink (Anderson and Kaltin, 2016; Yasunaka et al., 2018). Observations and model simulations have indicated that the Arctic Ocean absorbs 58-180 Tg C per year, accounting for 2%-7% of the global oceanic carbon sink (Manizza et al., 2013; Yasunaka et al., 2016; Mortenson et al., 2020). In recent decades, rapid and diverse changes, for example the increased seawater temperature, ice sheet melt, and an extended ice-free period, have occurred in Arctic ecosystems (Screen and Simmonds, 2010; Shepherd et al., 2012; Jeong et al., 2018). These changes exert a significant influence on sea surface pCO_2 and air-sea CO_2 fluxes. For instance, in the context of global warming, the Chukchi Sea has transitioned from being perennially covered by ice to becoming seasonally ice-free during the past two decades, and the summer CO_2 uptake has significantly increased by l.4 ± 0.6 Tg C per decade (Ouyang et al., 2022).

Different from observations made in low/middle latitudinal marginal seas and open oceans, the features of sea surface pCO_2 and air-sea CO_2 flux in Arctic Ocean are significantly influenced by the presence of sea ice (Bates et al., 2011; Qi et al., 2020). During cold seasons, despite the elevated pCO_2 values beneath the sea ice, the air-sea CO_2 exchange is impeded by ice, resulting in relatively low CO_2 fluxes (Schuster et al., 2013; Cross et al., 2014; DeGrandpre et al., 2020). In contrast to observations in cold seasons, the water column stratification ensues during warm seasons when sea ice melts and freshwater input occurs. This leads to a decrease in pCO_2 values and consequently enhances the CO_2 sink at the sea surface (Riedel et al., 2008). Moreover, the mixing of ice melt water featured low pCO_2 values, $CaCO_3$ dissolution, and photosynthesis during algal blooms would further decrease pCO_2 values and facilitate CO_2 dissolving into seawater (Fransson et al., 2009; Geilfus et al., 2012). However, this pCO_2 drawdown would be counteracted by the increased sea surface temperature and the strong CO_2 sink at the sea surface (Burgers et al., 2017; Islam et al., 2017; Pipko et al., 2017). In the seawater carbonate system, a frequent occurrence of high pCO_2 is observed in accordance with elevated SST values due to its decreased solubility at high temperatures (Wanninkhof et al., 2022). Additionally, the air-sea CO_2 exchange at the sea surface tends to increase seawater DIC in the Arctic Ocean, subsequently elevating seawater pCO_2 (Yang et al., 2023). Moreover, changes in wind fields, such as high wind speeds (>10 m/s) and upwelling-favorable wind, tend to upward transport the nutrient enriched water to subsurface. This nutrient supply significantly increases the net primary production (NPP), which consumes DIC and decreases the sea surface pCO_2 (Xu et al., 2023).

As previously mentioned, the spatiotemporal variability of hydrographic features and carbonate parameters during sea ice melt is influenced by various processes; however, their contributions to the dynamics of sea surface pCO_2 remain unclear. Previous studies have reported the pCO_2 dynamics during sea ice melt through model simulations and field measurements (e.g., Nomura et al., 2010; Fransson et al., 2017; DeGrandpre et al., 2020), but limited attention has been devoted to its changes prior to the melting process (DeGrandpre et al., 2020).

The Arctic Ocean serves as a conduit for water exchange between the Pacific and Atlantic oceans, and its biogeochemical cycling is influenced by lateral inputs of nutrients from sources like nutrient-rich inflows through the Barents Sea (North Atlantic) and Chukchi Sea (North Pacific) (Schuster et al., 2013). Characterized by intricate interactions and feedbacks among sea ice, ocean, and atmosphere, the Arctic Ocean plays a crucial role in the global climate system, (Bates et al., 2011). In the context of global warming, there has been a significant decline in seasonal sea ice extent in the Arctic Ocean over the past four decades, accompanied by a more recent year-round decrease in sea ice extent, area, and volume (Polyakov et al., 2020). For instance, arctic sea ice extent has decreased at a rate of 13.1% per decade in September and 2.6% per decade in March; furthermore, the annual mean thickness of sea ice in the central Arctic Ocean reduced from 3.59 m to 1.25 m between 1975 and 2012 (Lindsay and Schweiger, 2015; Garcia-Soto et al., 2021). The reduction of sea ice content would hinder dense water formation while slowing down deep water circulation processes, leading to diminished CO_2 sequestration capacity (Semiletov et al., 2004).

In this study, we investigated the pCO_2 dynamics during two cruises in the western Arctic Ocean using underway measurements downloaded from an online database. Firstly, we identified the dominant processes governing the variations in pCO_2 and subsequently used a 1-D dynamic model to simulate pCO_2 values

in the western Arctic Ocean during sea ice melt. Finally, we quantified changes in pCO_2 between different stages of sea ice melt and elucidated their underlying controlling mechanisms.

2 Data and methods

2.1 Study area

The Arctic Ocean is a distinct basin surrounded by vast continental land masses. Based on hydrographic, topographic, and ocean circulation characteristics, the Arctic Ocean can be classified into various sub-regions such as the Norwegian Sea, Barents Sea, East Siberian Sea, Chukchi Sea, Beaufort Sea and the Canada Basin (Yasunaka et al., 2018). In this study, we divided the western Arctic Ocean into three sub-regions, as (1) the nutrient-rich Chukchi Sea shelf with a latitude range of 65-75°N; (2) the oligotrophic Canada Basin separated from the Chukchi Shelf along the shelf breaks at depths of 250-500 m isobaths; and (3) the Beaufort Sea separated from both the Chukchi Sea and Canada Basin by boundaries defined as longitude 152°W and latitude 72°N (Figure 1). Considering the different sea ice concentration (SIC) values presented in Table 1, we further divided the Canada Basin into two sub-regions, i.e. a sea ice covered zone (>77°N) and a rapid sea ice melt zone (<77°N). In Canada Basin, the water column can be categorized into five primary water masses, namely Pacific Winter Water (PWW), Alaska Coastal Water (ACW), Chukchi Summer Water (CSW), Early-Season Melt Water (ESMW), and Late-Season Melt Water (LSMW). During the warm seasons, ESMW and LSMW exert significant influence on the characteristics of surface water, confirming the impact of sea ice melt water (Qi et al., 2022a).

2.2 Data source

In this study, the *in situ* temperature, salinity, dissolved inorganic carbon (DIC), total alkalinity (TA), air and seawater pCO_2 values in the western Arctic Ocean were obtained from the Climate Variability and Predictability Experiment (CLIVAR) database (https://www.ncei.noaa.gov/access/ocean-carbon-acidification-data-system/oceans/RepeatSections/) (Figure 1). The data were collected during the 4th and 5th Chinese National Arctic Research Expedition (CHINARE) in 2010 and 2012, respectively. Detailed sampling and analysis methods for these two cruises can be found in Ouyang et al. (2020). Wind speed was obtained from JRA-55 reanalysis dataset (http://search.diasjp.net/en/dataset/JRA55), which has a spatial resolution of 0.5625° latitude/longitude and a temporal resolution of 3 hours (Japan Meteorological Agency/Japan, 2013). Near-surface winds were utilized to calculate the high wind frequency (HWF), representing the percentage of time when wind speed exceeds 10 m/s (Xu et al., 2023).

2.3 Air-sea CO_2 flux estimation

The net air-sea CO_2 flux (FCO_2, mmol C m^{-2} d^{-1}) is calculated as (see Equation 1):

$$FCO_2 = k \times a \times (pCO_{2s} - pCO_{2a}) \times (1 - SIC) \quad (1)$$

where k represents the gas transfer velocity (m d^{-1}), a denotes the solubility of CO_2 (mol kg^{-1} atm^{-1}; Weiss, 1974); pCO_{2s} and pCO_{2a} represent the partial pressure of CO_2 in seawater and atmosphere, respectively, and their difference (defined as ΔpCO_2) determines the direction of CO_2 transfer; SIC is the sea ice concentration with values ranging from 0 to 1. Please note that

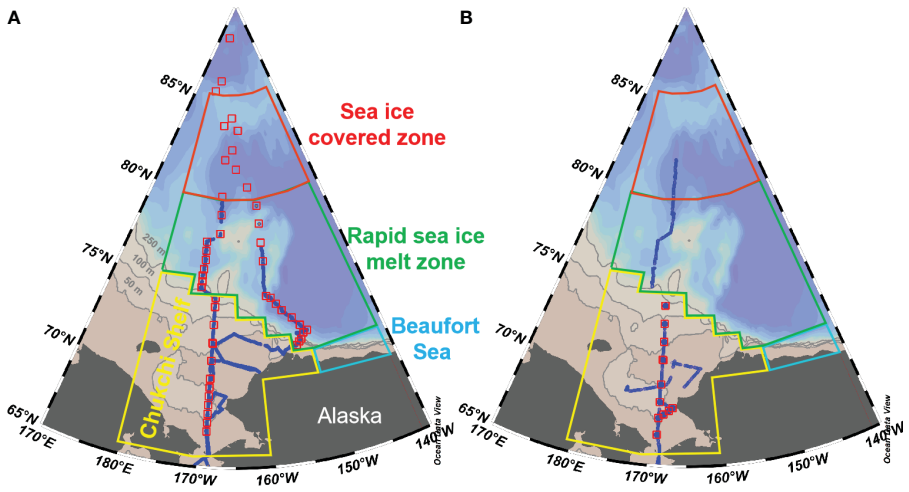

FIGURE 1
Maps showing the location of sampling stations (red squares) and underway measurements (blue dotes) in the western Arctic Ocean during 2010 **(A)** and 2012 **(B)**. Also shown are the boundary of different sub-regions following Ouyang et al. (2022): (1) Chukchi Sea shelf with latitude of 65-75°N, as shown by the yellow line; (2) Canada Basin, separated from the Chukchi Shelf along the 250-500 m isobaths; (3) the Beaufort Sea, separated from the Chukchi Sea and Canada Basin along 152°W and 72°N, respectively. Considering the different sea ice concentrations during warm seasons, we further divided the Canada Basin into two sub-regions with a latitude of 80°N, i.e. the sea ice covered zone and the rapid sea ice melt zone (Ouyang et al., 2022).

TABLE 1 Summary of sea ice concentration (SIC), high wind frequency (HWF) and wind speed in different sub-regions.

Sub-regions	Date	Voyage	SIC	HWF	Wind Speed ($m\ s^{-1}$)
Chukchi Sea	20100720	Forward	0.063	0.081	5.81
	20100829	Return	0.018	0	5.09
	20120718	Forward	0.130	0.019	5.83
	20120907	Return	0.019	0.168	7.44
Sea ice covered zone in Canada Basin	20100730-20100826	Forward and return	0.694	0	3.30
	20120904	Forward and return	0.288	0.042	6.47
Sea ice melt zone in Canada Basin	20100724	Forward	0.524	0.114	5.11
	20100826	Return	0.092	0.021	4.89
	20120906	Return	0	0.194	7.23

Note HWF is high wind frequency (wind speed >10 m s^{-1}).
Please note that these average values were obtained from model simulation following methods described in Xu et al. (2023).

the SIC data utilized in this study were obtained from the NSIDC (Nation Snow and Ice Data Center) database (https://nsidc.org/data/nsidc-0079/versions/3).

The gas transfer velocity was calculated following Wanninkhof (2014), as (see Equation 2):

$$k = 0.251 \times U_{10}^{2} \times (Sc/660)^{-0.5} \quad (2)$$

where U_{10} represents wind speed at 10 m height. *Sc* corresponds to Schmidt number for CO_2, which was determined using equations in Wanninkhof (2014).

2.4 Modeling the pCO_2 values with a 1-D dynamic approach

In this study, a mass balance model was used to simulate the pCO_2 dynamics during sea ice melt. For each simulation step (Δt, 1 day in this study), sea surface pCO_2 was calculated from TA and DIC at the corresponding step. A change in DIC inventory for a time step, Δt, in the surface mixed layer (defined as ΔDIC_t) is calculated as follows (see Equation 3):

$$\Delta DIC_t = (FCO_{2t} + NCP_t) \times \Delta t/(MLD \times \rho) + \Delta DIC_{(diluted)t} \quad (3)$$

where FCO_{2t}, NCP_t, and $\Delta DIC_{(diluted)t}$ indicate the changes in DIC inventory (μmol kg^{-1}) induced by air-sea CO_2 flux (mmol C m^{-2} d^{-1}), net community production (NCP, mmol C m^{-2} d^{-1}), and melt water dilution ($\Delta DIC_{(diluted)t}$, μmol kg^{-1}) at simulation time step t, respectively. MLD (m) and ρ (set as 1.021×10^3 kg m^{-3}) are the mixed layer depth and density of surface seawater.

During the model simulation, we assumed that the dilution of ice melt water will change the concentrations of DIC and TA in the seawater at a same rate, which has been previously proposed and utilized by Qi et al. (2022b). In Arctic Ocean, the TA and DIC values in surface water were set as 1959 μmol kg^{-1} and 1880 μmol kg^{-1}, respectively, which were much higher than that in the ice melt water end-member (TA=400 μmol kg^{-1}, DIC=450 μmol kg^{-1}) (Yang et al., 2023). The mixing of ice melt water have negligible influence on the TA/DIC ratio in surface water, which is close to 1:1. Therefore, any changes in DIC induced by dilution (defined as $\Delta DIC_{(diluted)t}$) can be quantified as follows (see Equation 4):

$$\Delta DIC_{(diluted)t} = (TA_{t+1} - TA_t)/TA_t \times DIC_t \quad (4)$$

where $(TA_{t+1}\text{-}TA_t)/TA_t$ is the changing rate in TA during sea ice melt. And DIC at time step t+1 is iteratively calculated as follows (see Equation 5):

$$DIC_{t+1} = DIC_t + \Delta DIC_t \quad (5)$$

Due to the dilution caused by ice melt water, TA in the seawater decreased continuously from its initial values at a SIC of 95% to low values at a SIC of 0% during the sea ice melt. Subsequently, TA remained constant during the ice free period. With the new DIC and TA for the next simulation step, a new pCO_2 is calculated, and this simulation process repeats until the last day.

3 Results

3.1 Distributions of sea surface temperature, salinity and pCO_2 in the western Arctic Ocean

The surface distributions of temperature (SST), salinity (SSS), and pCO_2 during both cruises are shown in Figure 2, which exhibited significant spatial variability. In 2010, SST ranged from -2.0 to 8.0 °C, exhibiting a latitudinal decreasing trend (Figure 2A). The Chukchi Sea exhibited the highest SST values, followed by the rapid sea ice melt zone and the sea ice covered zone in Canada Basin. This distribution pattern aligns with previous studies conducted by Sun et al. (2017) and Yang et al. (2023), which can be attributed to reduced solar radiation at higher latitudes and the influence of warm Pacific surface water on the Chukchi Sea shelf (Zheng et al., 2021). SSS displayed their highest values on the Chukchi Sea shelf, ranging from 29 to 32.5, while relatively lower values were observed in Canada Basin, ranging from 25.5 to 29 (Figure 2B). As mentioned

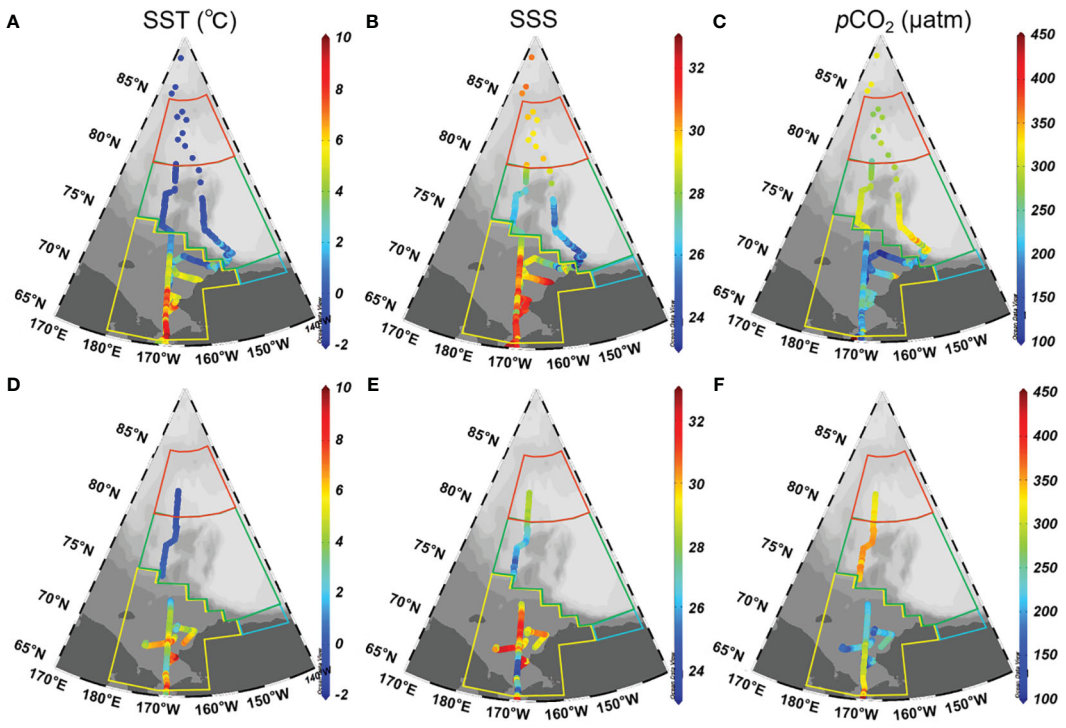

FIGURE 2
Surface distributions of temperature (left panels), salinity (middle panels), and pCO_2 (right panels) in the western Arctic Ocean in 2010 **(A–C)** and 2012 **(D–F)**. In **(A, B)**, SST and SSS observed north of 80° N are sourced from bottle data. In **(C)**, pCO_2 were calculated from DIC and TA using the CO2SYS program (Pierrot et al., 2006), which employed dissociation constants for carbonic acid from Mehrbach et al. (1973), as refitted by Dickson and Millero (1987), along with the dissociation constant for HSO_4^- determined by Dickson (1990). The relationship between total boron and salinity followed Uppstrom (1967).

earlier, high salinity on the Chukchi Sea shelf reflects the influence of Pacific Source Water, whereas low salinity surface water in Canada Basin is likely diluted by ice melt water (Geilfus et al., 2012). The sea surface pCO_2 during this cruise exhibited a range of 100-350 µatm (Figure 2C). Low pCO_2 values were observed on the Chukchi Sea shelf, whereas high values were observed in Canada Basin. On the Chukchi Sea shelf, the low pCO_2 values can be attributed to the high biological production sustained by nutrient-rich Bering Strait through flow (Tu et al., 2021; Zheng et al., 2021). In Canada Basin, sea ice exerts a significant influence on regulating the dynamics of sea surface pCO_2 during both sea ice formation and melt processes. The evolution of sea surface pCO_2 during the sea ice melt will be further quantified in the subsequent discussion.

In 2012, SST, SSS, and pCO_2 ranged -1-7.5 °C, 25.0-32.0, and 180-360 µatm, respectively (Figures 2D–F). Due to the influence of Pacific Water, the Chukchi Sea shelf exhibited significantly higher SST and SSS compared to the Canada Basin, which is consistent with the observations made in 2010. In contrast to the observations in Canada Basin, the sea surface pCO_2 on the Chukchi Sea shelf was observed to be at its lowest level.

3.2 Distributions of SIC, HWF and wind speed in the western Arctic Ocean

As shown in Table 1, the surface water in the northernmost sea ice covered zone was predominantly encompassed by sea ice with SIC values ranging from 0.29 to 0.69 throughout the sampling period. In the rapid sea ice melt zone, distinct SIC values were recorded during these three voyages, ranging from 0 to 0.524. On the Chukchi Sea shelf, there was a minor influence of sea ice melt as evidenced by low SIC values ranging from 0.02 to 0.13. The highest HWF and wind speed were observed during the cruise in 2012.

4 Discussion

4.1 Controlling processes to the dynamics of sea surface pCO_2 in Canada Basin

4.1.1 Temperature effect

During both cruises, the variability of SST ranged from -1.6 °C to 4.0 °C, which could significantly impact the distribution patterns of surface pCO_2. To assess the influence of temperature on pCO_2 variability, we plotted the relationship between $\ln pCO_2$ and SST (Figure 3A). In 2010, a positive correlation was observed with an equation of $\ln pCO_2 = 0.0394 \times SST + 5.7704$ ($R^2 = 0.38$, $p<0.05$). Wanninkhof et al. (2022) suggested an exponential increase in pCO_2 with rising temperature at a rate of 4.13% $°C^{-1}$. Although the observed slope was nearly consistent with the theoretical value of 0.0413, the correlation coefficient is only 0.6 (R=0.6). This result indicates that although temperature is a significant controlling factor, it cannot fully explain the variability in pCO_2 within the

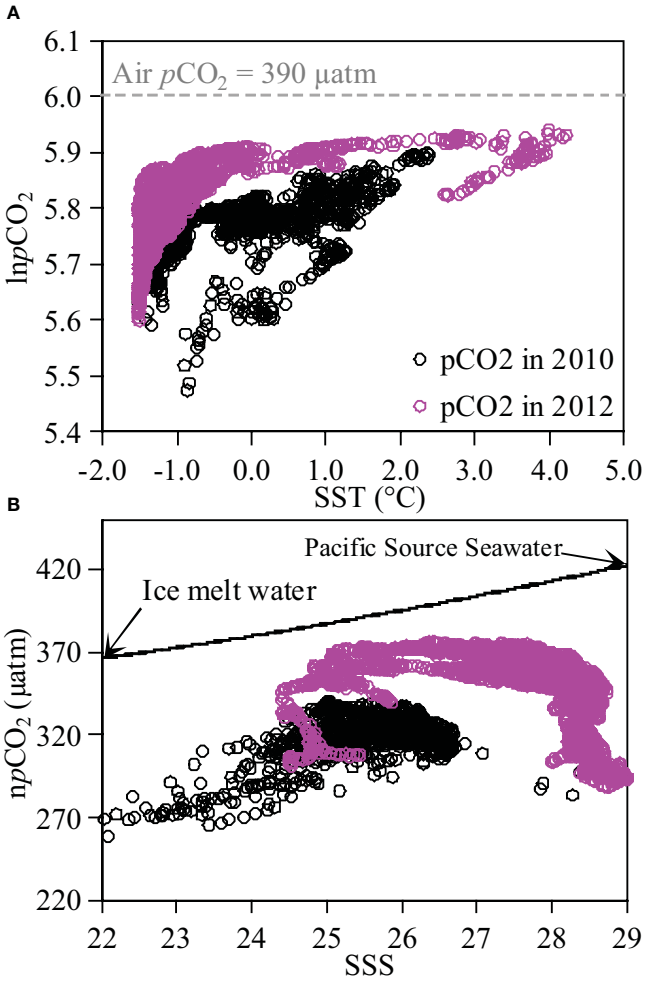

FIGURE 3
Relationships of $\ln pCO_2$ vs. sea surface temperature, SST ($\ln pCO_2$-SST, **(A)** and $npCO_2$ vs. sea surface salinity, SSS ($npCO_2$-SSS, panel b) for surface water in Canada Basin in 2010 and 2012. In panel a, dashed line indicate the logarithm of air pCO_2. In **(B)**, black arrows represent the end-members of ice melt water and Pacific Source Seawater with end-member values sourced from Qi et al. (2020) and Yang et al. (2023); solid line represent the hypothetical conservative mixing line between these two end-members.

Canada Basin. In 2012, there was also a positive correlation relationship between $\ln pCO_2$ and SST for surface water with an equation of $\ln pCO_2 = 0.0702x+5.8696$ ($R^2 = 0.26$, not shown in the figure), but this relationship alone cannot fully explain variation in pCO_2.

4.1.2 Dilution of ice melt water

In Canada Basin, it has been suggested that the offshore surface water is influenced by the dilution of ice melt water and Pacific Source Seawater (Qi et al., 2020). Using end-member values of S=33.215 ± 0.012, TA=2242.2 ± 6.9 µmol kg^{-1}, DIC=2159.1 ± 0.3 µmol kg^{-1} for Pacific Source Seawater and S=0, TA=400 µmol kg^{-1}, DIC=450 µmol kg^{-1} for ice melt water (Yang et al., 2023), we calculated the proportions of ice melt water at different salinities. During both cruises, the fractions of ice melt water ranged from 12.7% to 27.7%. We further calculated the conservative pCO_2 values at different salinities, and the result suggested a pCO_2 value of 368 µatm at salinity of 22, and a pCO_2 value of 411 µatm at salinity of 29. The observed difference in pCO_2 (43 µatm) can be attributed to the dilution effect. We also examined the relationship between $npCO_2$ and SSS to investigate the influence of water mass mixing on the variability of sea surface pCO_2 in Canada Basin (Figure 3B). In this study, $npCO_2$ was normalized to 0 °C following the method of Wanninkhof et al. (2022). Consequently, no significant correlation was observed between $npCO_2$ and SSS, indicating that other processes may exert a stronger impact on the spatial variability of sea surface pCO_2 than mixing during both cruises.

4.1.3 Air-sea CO_2 flux

In Canada Basin, there was an average difference of -25 to -80 µatm between pCO_2 values in surface water and the overlying atmosphere (Table 2), indicating a net uptake of CO_2 during both cruises. Using average SIC values and wind speeds summarized in Table 1, we estimated the air-sea CO_2 flux during the sampling period, and the results are summarized in Table 2. Consequently, the instantaneous air-sea CO_2 fluxes varied from -1.6 to -4.3 mmol C m^{-2} d^{-1} (Table 2; negative values indicate a CO_2 sink). Our estimated CO_2 flux was almost consistent with Yasunaka et al. (2016) of -4 ± 4 mmol

TABLE 2 Summary of sea surface temperature (SST), sea surface salinity (SSS), sea surface pCO_2, air-sea ΔpCO_2, CO_2 flux, and average mixed layer depth (m) in Canada Basin.

Date	Voyage	SST (°C)	SSS	$pCO_{2in\text{-}situ}$ (µatm)	Air-sea ΔpCO_2 (µatm)	CO_2 flux (mmol C m^{-2} d^{-1})	MLD (m)
20100724	Forward	0.3 ± 0.9	25.4 ± 1.8	306 ± 41	-71 ± 41	-1.6 ± 1.6	13.2
20100826	Return	-0.5 ± 1.2	26.8 ± 1.2	292 ± 35	-80 ± 34	-4.3 ± 1.8	16.2
20120906	Return	0.3 ± 0.1	25.8 ± 0.5	351 ± 19	-25 ± 19	-3.3 ± 2.4	18.8

Please note that the mixed layer depth (MLD) during both voyages was obtained using methods described in Xu et al. (2023).

C m^{-2} d^{-1}, Manizza et al. (2019) of -2.5 ± 0.2 mmol C m^{-2} d^{-1}, Bates and Mathis (2009) of -1.7~-4.2 mmol C m^{-2} d^{-1}, and Islam et al. (2017) of -2.5 ± 2.6 mmol C m^{-2} d^{-1} in Arctic Ocean, but was lower than Ouyang et al. (2022) of -5.0 mmol C m^{-2} d^{-1} in Canada Basin, Sun et al. (2017) of -8.6 ± 1.4 mmol C m^{-2} d^{-1} and Burgers et al. (2017) of -12 mmol C m^{-2} d^{-1} in Arctic Ocean.

Here we conducted a preliminary estimation of DIC and subsequently the pCO_2 increase during sea ice melt. Assuming an average CO_2 flux of -3.0 mmol C m^{-2} d^{-1} during these three voyages (Table 2), an ice melt period of 80 days during warm seasons (from DSR=-40 to DSR=40), and an average MLD of 16 m that obtained using methods described in Xu et al. (2023) (Table 2), it can be inferred that the air-sea CO_2 exchange at the sea surface would result in a rise in seawater DIC by 15 µmol kg^{-1}. Based on the definition of Revelle factor (RF), pCO_2 variability caused by the air-sea CO_2 exchange can be calculated as: $RF \times pCO_{2water} \times \Delta DIC_F / DIC_{water}$ (Harry et al., 1979; Egleston et al., 2010). The results suggest that, during sea ice melt, air-sea CO_2 exchange at the sea surface would lead to an increase in seawater pCO_2 by 40 µatm in Canada Basin.

4.1.4 Sea ice concentration

In Canada Basin, a significant negative relationship is observed between SIC and sea surface pCO_2 (pCO_2=-46.14×SIC+343.43, R^2 = 0.47, Figure 4). The surface pCO_2 tends to decrease with increasing SIC, exhibiting lower values in areas where SIC>0.5 and higher values in open water with an SIC of 0. In Arctic ecosystems, low SIC would facilitate CO_2 dissolution into seawater, leading to increased seawater DIC and surface pCO_2. During both cruises, the observed sea surface pCO_2 was measured at 343 µatm when SIC=0, and decreased to 297 µatm when SIC=1. The calculated difference in pCO_2 amounts to 46 µatm.

4.1.5 Biological consumption

In Arctic Ocean, the higher nutrient supply and subsequent biological consumption of DIC result in a significant net uptake of CO_2. Previous studies have reported the NCP values in this region, ranging from 1.88 to 7 mmol C m^{-2} d^{-1} (Cai et al., 2010; Islam et al., 2017; DeGrandpre et al., 2019; Ouyang et al., 2022). Using an NCP value of 1.88 mmol C m^{-2} d^{-1} (Cai et al., 2010), and an ice melt period of 80 days, it can be inferred that biological consumption would lead to a decrease in seawater DIC by 9 µmol kg^{-1} and subsequently reduce seawater pCO_2 by 24 µatm.

4.1.6 Wind speed

In the estimation of air-sea CO_2 flux, higher wind speeds lead to an increased gas transfer velocity, thereby resulting in a higher CO_2 flux (see Equation 2). In Arctic Ocean, the intensified CO_2 sink under high wind speeds would elevate seawater DIC concentrations and subsequently increase pCO_2. Here we utilized the HWF obtained from model simulations to characterize the intensity of wind speeds (for more details on the model simulation, please refer to Xu et al. (2023)), and their respective results were presented in Table 1. Consequently, HWF and wind speeds exhibited notable increases in 2012 than in 2010, which may also contribute to higher pCO_2 in 2012.

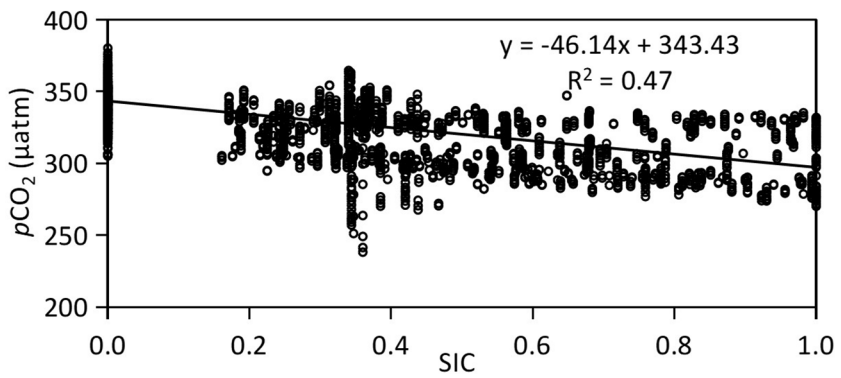

FIGURE 4
Linear relationship between surface pCO_2 and sea ice concentration (SIC) in Canada Basin with data collected during both 2010 and 2012.

4.2 Modeling the sea surface pCO_2 during sea ice melt

4.2.1 Results from a 1-D dynamic model

To assess changes in sea surface pCO_2 during sea ice melt, we utilized the definition of days since ice retreat (DSR) in our results description and model simulation. Firstly, the day of ice retreat (DOR) is defined as the day when SIC falls below 15%. Then, we calculate the temporal difference between DOR and the day of field observation (DOF), which represents DSR. A positive or negative DSR indicates that the corresponding DOR occurred earlier or later than DOF. The specific values of DSR and SIC during these two cruises can be found in the Supplementary Material provided by Qi et al. (2022b).

In the present study, we divided the sampling period during both cruises into three distinct stages, the pre-retreat stage (DSR<-40), an active sea ice melt stage (-40<DSR<0), and a post sea ice melt stage (DSR>0). Consequently, DSR values for pCO_2 measurements in 2010 were predominantly negative (DSR<0), representing an active sea ice melt stage. Conversely, DSR values in 2012 were positive (DSR>0), representing a post sea ice melt stage. As shown in Figure 5, during the active sea ice melt stage in 2010, pCO_2 measurements displayed a scattered distribution pattern; however, they demonstrated an increasing trend during the post sea ice melt stage in 2012.

In order to gain a better understanding of variations in pCO_2 during sea ice melt, we extended our simulation time to the early melt period. Consequently, our modeled results covered the DSR from -50 days to the maximum DSR recorded during these two cruises (50 days). The initial values and model settings were derived from Qi et al. (2022b). Briefly, the initial SST, SSS, pCO_2, and TA were averaged from observations beneath the sea ice for the period 2011-2020 when DSR was less than -40. Their respective values were set at -1.0 °C, 27.1, 330 µatm, and 1959 µmol kg^{-1}. During the sea ice retreat period (-50<DSR<0), we assumed that SST linearly increased from its initial value to the mean SST over -5<DSR<5. Simultaneously, ice concentration linearly decreased from 95% to 0%, while SSS and TA decreased gradually from their initial values to their respective means over -5<DSR<5. The values of SST, SSS, and TA at DSR=0 were set to -0.7 °C, 26, and 1886 µmol kg^{-1}, respectively. During the ice free period (DSR>0), SSS and TA remained constant while allowing SST to increase up to a maximum value of 1.4 °C at DSR=60. A NCP value of 1.88 mmol C m^{-2} d^{-1} was assigned for the period between -40<DSR<50 to reflect weak primary production in the study area (Cai et al., 2010), whereas a value of 0 mmol C m^{-2} d^{-1} was used for the period between -50<DSR<-40. An averaged MLD of 16 m was consistently applied throughout the simulation (Table 2). Two average wind speeds, 4 m s^{-1} recorded during July and August in 2010, and 7 m s^{-1} observed during July, August, and September in 2012, were considered for CO_2 flux estimation and model simulation.

The evolution of seawater pCO_2 during sea ice melt in Canada Basin was simulated with a wind speed of 4.0 m s^{-1}, and their result was shown in Figure 5. During the pre-retreat stage, no significant change was observed in the simulated seawater pCO_2. Subsequently, a decreasing trend in pCO_2 was observed during the active sea ice melt stage. Following this stage, there was a continuous increase in the simulated seawater pCO_2 during the post sea ice melt stage.

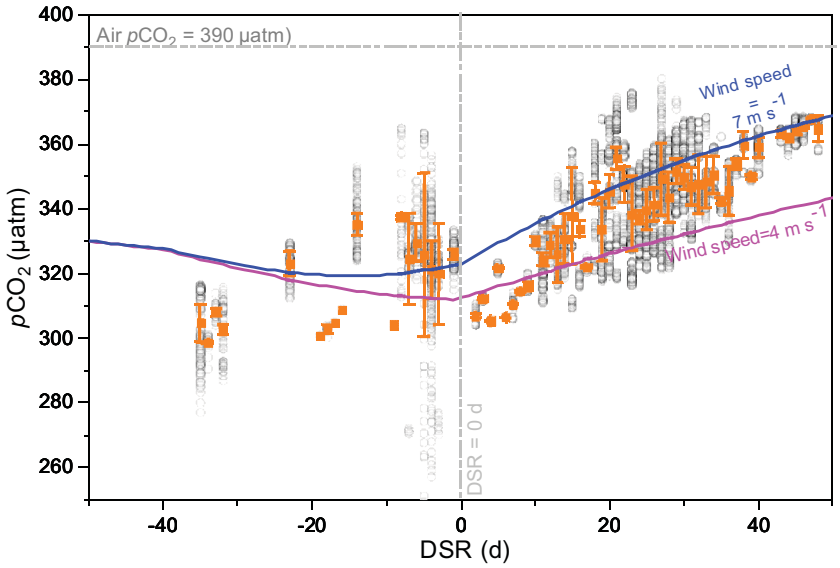

FIGURE 5
Relationships between pCO_2 and days since ice retreat (DSR) in Canada Basin during the cruise both in 2010 and 2012 (gray circles). Orange squares and error bars indicate the average values. During both cruises, DSR values for pCO_2 measurements in 2010 were predominantly negative (DSR<0), representing an active sea ice melt stage. Conversely, DSR values in 2012 were positive (DSR>0), representing a post sea ice melt stage. The horizontal dashed line is the atmospheric pCO_2 of 390 µatm, and the vertical dashed line is DSR=0 d. Solid lines are the simulated seawater pCO_2 using a 1-D dynamic approach at a wind speed of 4 m s^{-1} (pink line) and 7 m s^{-1} (blue line), with initial values and model settings derived from Qi et al. (2022b).

When using a higher wind speed of 7.0 m s^{-1}, it was noted that pCO_2 exhibited a decreasing trend when DSR<-10 but an increasing trend when DSR>-10. In comparison to the pCO_2 values simulated at a wind speed of 4.0 m s^{-1}, the modeled pCO_2 with a wind speed of 7.0 m s^{-1} showed significantly higher values; exhibiting a difference of 11 µatm at DSR=0 and reaching up to 25 µatm at DSR=50.

4.2.2 Quantifying the controlling processes to the pCO_2 dynamics during sea ice melt

Here, we quantified the controlling processes to pCO_2 dynamics during sea ice melt at two stages, the active sea ice melt stage (from DSR=-40 to DSR=0) and the post sea ice melt stage (from DSR=0 to DSR=50), with modeled carbonate parameters at DSR=-40, 0, and 50. To assess the impact of temperature effects on pCO_2 dynamics, we firstly calculated pCO_2 values at different SSTs while keeping DIC and TA constant for each stage. The difference in pCO_2 values represented changes attributed to temperature effects. For biological production and air-sea CO_2 exchange, we first calculated the variability in DIC resulting from the biological consumption (referred to as ΔDIC_{Bio}) and air-sea CO_2 $_{flux}$ (referred to as ΔDIC_{Flux}) as NCP/(MLD×ρ) and FCO_2/(MLD×ρ), respectively. Subsequently, these DIC consumption/addition values were subtracted/added to the observed DIC data (referred to as $DIC^{obs\text{-}Bio}$ and $DIC^{obs\text{-}Flux}$), allowing us to calculate seawater pCO_2 with the new DIC concentrations. The difference between these calculated and observed pCO_2 values indicates changes attributed to biological production and air-sea CO_2 exchange. Finally, the DIC changes resulted from the dilution of ice melt water was estimated as $\Delta DIC\text{-}\Delta DIC_{Bio}\text{-}\Delta DIC_{Flux}$ to balance the overall DIC budget. Its impact on pCO_2 variability could be determined using methods described above.

During the sea ice melt, the contributions of different processes to the dynamics of pCO_2 under a wind speed of 4 m s^{-1} were summarized in Figures 6A. During the active sea ice melt stage, the increase in SST of 0.24 °C only resulted in a rise in pCO_2 by 4 µatm. Over a time scale of 40 days, biological production and air-sea CO_2 exchange led to a decrease and increase in DIC by 5 µmol kg^{-1} and 5 µmol kg^{-1}, respectively, which would alter seawater pCO_2 by -15 µatm and 15 µatm correspondingly. Furthermore, the dilution effect caused by ice melt water further reduced seawater pCO_2 by 16 µatm. Consequently, compared to its reduction resulting from biological production and dilution effects, the contribution of air-sea CO_2 exchange towards increasing pCO_2 was significantly lower. The combined effects of biological production, dilution effects, and air-sea CO_2 exchange have a significant impact on reducing pCO_2 during this stage. During the post sea ice melt stage, there was an observed increase in pCO_2 by 45 µatm. The increase in SST by 2.1 °C would elevate pCO_2 by 32 µatm, while biological production and air-sea CO_2 exchange would lead to a decrease and increase respectively in seawater pCO_2 by 22 µatm and 37 µatm due to variability in DIC of -7 µmol kg^{-1} and 11 µmol kg^{-1}. The influence of ice melt water is negligible during the post sea ice melt stage. Consequently, the increase in pCO_2 resulting from high temperatures and air-sea CO_2 exchange outweighs its decrease caused by biological production. The combined effects of temperature effect, biological production, and air-sea CO_2 exchange result in a prevailing increase in sea surface pCO_2 during the post sea ice melt stage.

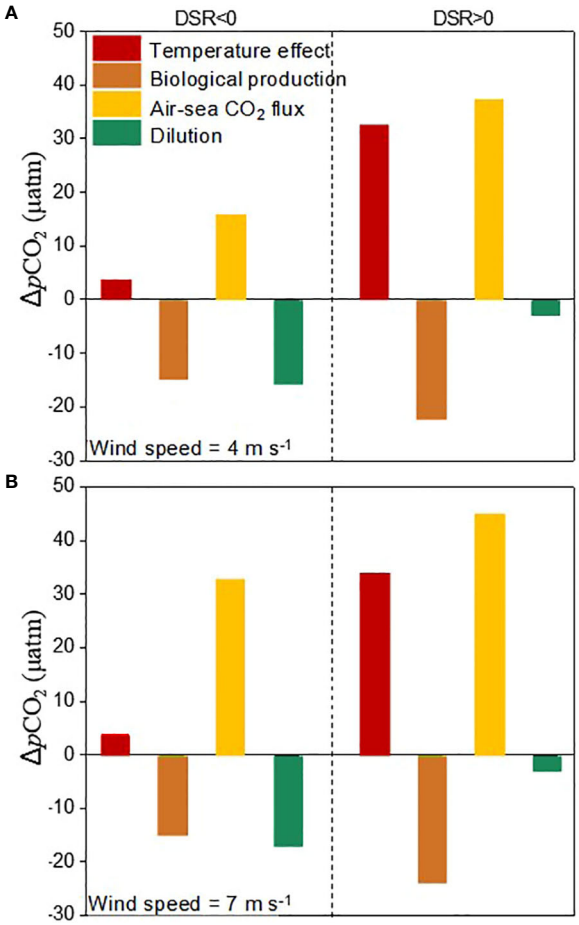

FIGURE 6
Contributions of temperature effect, biological production, air-sea CO_2 flux and the dilution of ice melt water to the changes of sea surface pCO_2 during sea ice melt at a wind speed of 4 m s^{-1} **(A)** and 7 m s^{-1} **(B)**. During the data processing, the modeled carbonate parameters at DSR=-40, 0, and 50 were selected for quantification.

Compared to the average low wind speed of 4.0 m s^{-1} recorded during July and August in 2010, the enhanced CO_2 uptake at a high average wind speed of 7.0 m s^{-1} observed during July, August, and September in 2012 would further increase seawater pCO_2 by 17 µatm during the active sea ice melt stage and by 8 µatm during the post sea ice melt stage, while the contributions of temperature, biological production, and dilution from ice melt water remain constant (Figure 6B). During the active sea ice melt stage, although the presence of sea ice cover hinders air-sea CO_2 exchange at the sea surface, the increased wind speed from 4.0 m s^{-1} to 7.0 m s^{-1} and extremely low pCO_2 values (ranging from 320-330 µatm) tend to facilitate CO_2 dissolution into seawater and subsequently elevate the pCO_2 by 17 µatm. However, this wind-driven enhancement in CO_2 sinking is significantly attenuated with a pCO_2 increase of 8 µatm during the post sea ice melt stage when pCO_2 values are considerably higher (ranging from 330-370 µatm).

4.2.3 Uncertainty analysis

In this study, the initial values utilized in model simulations were derived from a long-time field observation, which may differ from the observed values in a specific year. As previously discussed, we quantified the impact of varying wind speeds on pCO_2 dynamics, ranging from 53 to 77 µatm. Regarding the dilution effect, the mixing of ice melt water contributed to a pCO_2 variability of 18-43 µatm. For biological production, a low NCP of 1.88 mmol C m^{-2} d^{-1} and a high NCP of 7 mmol C m^{-2} d^{-1} was used in our pCO_2 simulation, indicating that biological processes could contribute to a pCO_2 variability of 37-137 µatm. Additionally, temperature effects were found to contribute significantly to a pCO_2 variability of 36-350 µatm. Therefore, careful selection of wind speeds, NCP values and the temperature range is crucial for achieving accurate model simulations.

5 Conclusion

This study presents the dynamics of sea surface pCO_2 during sea ice melt based on field measurements in the western Arctic Ocean. Compared to the pCO_2 reduction resulting from biological production and dilution effects, the contribution of air-sea CO_2 exchange is significantly lower. The combined effects of these factors have a significant impact on reducing pCO_2 during the active sea ice melt stage. In contrast, during the post sea ice melt stage, the increase in pCO_2 resulting from high temperatures and air-sea CO_2 exchange outweighs its decrease caused by biological production, dominating the prevailing increase in sea surface pCO_2. Compared to normal situations with a wind speed of 4.0 m s^{-1}, enhanced CO_2 uptake at a high wind speed of 7.0 m s^{-1} would further elevate seawater pCO_2 during both active and post sea ice melt stages. The increase in pCO_2 with high wind speed was more pronounced during active sea ice melt stage when seawater pCO_2 values were significantly lower. The present study reports, for the first time, the carbonate dynamics and controlling processes that govern pCO_2 dynamics during the active sea ice melt stage. It highlights the crucial role of wind speed in regulating the evolution of surface pCO_2 during sea ice melt.

In the Arctic Ocean, Manizza et al. (2019) also observed an exceptionally low SIC and relatively high levels of pCO_2 in the East Siberian Sea during 2012. Their findings indicated that the melt of sea ice under elevated seawater temperatures resulted in a substantial accumulation of freshwater on the sea surface. The presence of this low-density freshwater led to stratification within the water column, which hindered primary productivity of surface phytoplankton and impeded further reduction of pCO_2 through biotic processes, consequently leading to increased values of sea surface pCO_2. Our study argues that enhanced air-sea CO_2 uptake during periods characterized by high wind speeds also contributed to the elevated levels of sea surface pCO_2 observed in 2012.

Data availability statement

The original contributions presented in the study are included in the article/Supplementary Material. Further inquiries can be directed to the corresponding author.

Author contributions

WY: Conceptualization, Methodology, Validation, Writing – original draft, Writing – review & editing. YZ: Conceptualization, Data curation, Methodology, Software, Validation, Writing – original draft, Writing – review & editing. YW: Conceptualization, Data curation, Methodology, Software, Supervision, Validation, Writing – original draft, Writing – review & editing. ZC: Data curation, Methodology, Software, Validation, Writing – original draft, Writing – review & editing. XG: Data curation, Software, Validation, Writing – original draft, Writing – review & editing. HL: Validation, Writing – original draft, Writing – review & editing. ZO: Conceptualization, Data curation, Methodology, Validation, Writing – original draft, Writing – review & editing. WC: Conceptualization, Methodology, Supervision, Validation, Writing – original draft, Writing – review & editing. LC: Conceptualization, Methodology, Writing – original draft, Writing – review & editing. DQ: Conceptualization, Formal analysis, Funding acquisition, Methodology, Project administration, Supervision, Validation, Writing – original draft, Writing – review & editing.

Funding

The author(s) declare financial support was received for the research, authorship, and/or publication of this article. This work was supported by the National Key Research and Development Program of China (2019YFE0114800), National Natural Science Foundation of China (42176230, 41941013), Fujian Provincial Science and Technology Plan (2022J06026), and and Independent Research Projects of the Southern Marine Science and Engineering Guangdong Laboratory (Zhuhai) (SML2021SP306).

Acknowledgments

We thank the many contributors to the CHINARE dataset as well as the many research vessels and crews that contributed to the collection of data used in this study. We thank the Polar Research Institute of China and the Chinese National Arctic and Antarctic Data Center.

Conflict of interest

The authors declare that the research was conducted in the absence of any commercial or financial relationships that could be construed as a potential conflict of interest.

The handling editor, JC declared a past collaboration with the authors, DQ, YW, WC.

Publisher's note

References

Anderson, L., and Kaltin, S. (2016). Carbon fluxes in the Arctic Ocean-potential impact by climate change. *Polar Res.* 20 (2), 225–232. doi: 10.3402/Q26 polar.v20i2.6521

Bates, N., Cai, J., and Mathis, J. (2011). The ocean carbon cycle in the Western Arctic Ocean: distributions and air-sea fluxes of carbon dioxide. *Oceanography* 24 (3), 186–201. doi: 10.5670/oceanog.2011.71

Bates, N., and Mathis, J. (2009). The Arctic Ocean marine carbon cycle: evaluation of air-sea CO_2 exchanges, ocean acidification impacts and potential feedbacks. *Biogeosciences* 6 (11), 2433–2459. doi: 10.5194/bg-6-2433-2009

Burgers, T., Miller, L., Thomas, H., Else, B., Gosselin, M., and Papakyriakou, T. (2017). Surface water pCO_2 variations and sea-air CO_2 fluxes during summer in the Eastern Canadian Arctic. *J. Geophys. Res.* 122, 9663–9678. doi: 10.1002/2017JC013250

Cai, W., Chen, L., Chen, B., Gao, Z., Lee, S., Chen, J., et al. (2010). Decrease in the CO_2 uptake capacity in an ice-free Arctic Ocean Basin. *Science* 329, 556–559. doi: 10.1126/science.1189338

Cross, J. N., Mathis, J. T., Frey, K. E., Cosca, C. E., Danielson, S. L., and Bates, N. R. (2014). Annual sea-air CO_2 fluxes in the Bering Sea: insights from new autumn and winter observations of a seasonally ice-covered continental shelf. *J. Geophys. Res. Oceans.* 119, 6693–6708. doi: 10.1002/2013JC009579

DeGrandpre, M., Evans, W., Timmermans, M., Krishfield, R., Williams, B., and Steele, M. (2020). Changes in the Arctic Ocean carbon cycle with diminishing ice cover. *Geophys. Res. Lett.* 47 (12), e2020GL088051. doi: 10.1029/2020GL088051

DeGrandpre, M., Lai, C., Timmermans, M., Krishfield, R., Proshutinsky, A., and Torres, D. (2019). Inorganic Carbon and pCO_2 Variability during ice formation in the Beaufort Gyre of the Canada Basin. *J. Geophys. Res. Oceans* 124 (6), 4017–4028. doi: 10.1029/2019JC015109

Dickson, A. (1990). Standard potential of the reaction: $AgCl(s)+12H_2(g) =Ag(s)+HCl(aq)$, and and the standard acidity constant of the ion HSO_4^- in synthetic sea water from 273.15 to 318.15 K. *J. Chem. Thermodyn* 22, 113–127. doi: 10.1016/0021-9614(90)90074-Z

Dickson, A., and Millero, F. (1987). A comparison of the equilibrium constantsfor the dissociation of carbonic acid in seawater media. *Deep Sea Res. Part A Oceanographic Res. Papers* 34, 1733–1743. doi: 10.1016/0198-0149(87)90021-5

Egleston, E. S., Sabine, C. L., and Morel, F. M. M. (2010). Revelle revisited: Buffer factors that quantify the response of ocean chemistry to changes in DIC and alkalinity. *Glob. Biogeochem. Cycles.* 24, GB1002. doi: 10.1029/2008GB003407

Fransson, A., Chierici, M., and Nojiri, Y. (2009). New insights into the spatial variability of the surface water carbon dioxide in varying sea ice conditions in the Arctic Ocean. *Cont Shelf Res.* 29, 1317–1328. doi: 10.1016/j.csr.2009.03.008

Fransson, A., Chierici, M., Skjelvan, A., Olsen, P., Assmy, A., Peterson, G., et al. (2017). Effects of sea-ice and biogeochemical processes and storms on under-ice water fCO_2 during the winter-spring transition in the high Arctic Ocean: implications for sea-air CO_2 fluxes. *J. Geophys. Res. Oceans* 122, 5566–5587. doi: 10.1002/2016JC012478

Friedlingstein, P., Jones, M., O' Sullivan, M., Andrew, R., Bakke, D., and Hauck, J. (2022). Global carbon budget 2021. *Earth Syst. Sci. Data.* 14, 1917–2005. doi: 10.5194/essd-14-1917-2022

Garcia-Soto, C., Cheng, L., Caesar, L., Schmidtko, S., Jewett, E., Cheripka, A., et al. (2021). An overview of ocean climate change indicators: sea surface temperature, ocean heat content, ocean pH, dissolved oxygen concentration, arctic sea ice extent, thickness and volume, sea level and strength of the AMOC (Atlantic meridional overturning circulation). *Front. Mar. Sci.* 21, 8–2021. doi: 10.3389/fmars.2021.642372

Geilfus, N., Carnat, G., Papakyriakou, T., Tison, J., Else, B., Thomas, H., et al. (2012). Dynamics of pCO_2 and related air-ice CO_2 fluxes in the Arctic coastal zone (Amundsen Gulf, Beaufort Sea). *J. Geophys. Res.* 117, 1–15. doi: 10.1029/2011JC007118

Harry, Y., Mcsween, J. R., Taylor, L. A., and Stolper, E. M. (1979). Carbon dioxide in the ocean surface: the homogeneous buffer factor. *Science.* 204, 1203–1205. doi: 10.1126/science.204.4398.1203

Islam, F., DeGrandpre, M., Beatty, C., Timmermans, M., Krishfield, R., Toole, J., et al. (2017). Sea surface pCO_2 and O_2 dynamics in the partially ice-covered Arctic Ocean. *J. Geophys. Res.* 122, 1425–1438. doi: 10.1002/2016JC012162

Japan Meteorological Agency/Japan. (2013). *JRA-55: Japanese 55-year reanalysis, daily 3-hourly and 6-hourly data* (Boulder, CO: Research Data Archive, National Center for Atmospheric Research, Computational and Information Systems Laboratory).

Jeong, S., Bloom, A., Schimel, D., Sweeney, C., Parazoo, N., Medvigy, D., et al. (2018). Accelerating rates of Arctic carbon cycling revealed by long-term atmospheric CO_2 measurements. *Sci. Adv.* 4 (7), eaao1167. doi: 10.1126/sciadv.aao1167

Lindsay, R., and Schweiger, A. (2015). Arctic sea ice thickness loss determined using subsurface, aircraft, and satellite observations. *Cryosphere* 9 (1), 269–283. doi: 10.5194/tc-9-269-2015

Manizza, M., Follows, M., Dutkiewicz, S., Menemenlis, D., Hill, C., and Key, R. (2013). Changes in the arctic ocean CO_2 sink, (1996-2007): a regional model analysis. *Global Biogeochem. Cycles* 27, 1108–1118. doi: 10.1002/2012GB004491

Manizza, M., Menemenlis, D., Zhang, H., and Miller, C. (2019). Modeling the recent changes in the Arctic Ocean CO_2 sink, (2006-2013). *Global Biogeochem Cycles* 33 (3), 420–438. doi: 10.1029/2018GB006070

Mehrbach, C., Culberson, C., Hawley, J., and Pytkowicx, R. (1973). Measurement of the apparent dissociation constants of carbonic acid in seawater at atmospheric pressure. *Limnol. Oceanogr.* 18, 897–907. doi: 10.4319/lo.1973.18.6.0897

Mortenson, E., Steiner, N., Monahan, A., Hayashida, H., Sou, T., and Shao, A. (2020). Modeled impacts of sea ice exchange processes on Arctic Ocean carbon uptake and acidification, (1980-2015). *J. Geophys. Res. Oceans* 125, e2019JC015782. doi: 10.1029/2019JC015782

Nomura, D., Eicken, H., Gradinger, R., and Shirasawa, K. (2010). Rapid physically driven inversion of the air-sea ice CO_2 flux in the seasonal landfast ice off Barrow, Alaska after onset of surface melt. *Cont Shelf Res.* 30, 1998–2004. doi: 10.1016/j.csr.2010.09.014

Ouyang, Z., Li, Y., Qi, D., Zhong, W., Murata, A., Nishino, S., et al. (2022). The changing CO_2 sink in the Western Arctic Ocean from 1994 to 2019. *Global Biogeochem Cycles* 36 (1), e2021GB007032. doi: 10.1029/2021GB007032

Ouyang, Z., Qi, D., Chen, L., Takahashi, T., Zhong, W., DeGrandpre, M., et al. (2020). Sea-ice loss amplifies summertime decadal CO_2 increase in the western Arctic Ocean. *Nat. Clim Chang* 10, 678–684. doi: 10.1038/s41558-020-0784-2

Pierrot, D., Lewis, E., and Wallace, D. (2006). *MS Excel program developed for CO_2 system calculations. Carbon Dioxide Information Analysis Center, Oak Ridge National Laboratory* (Oak Ridge: U.S. Department of Energy). doi: 10.3334/cdiac/otg.co2sys_xls_cdiac105a

Pipko, I., Pugach, S., Semiletov, I., Anderson, L., Shakhova, N., Gustafsson, Ö., et al. (2017). The spatial and inter-annual dynamics of the surface water carbonate system and air-sea CO_2 fluxes in the outer shelf and slope of the Eurasian Arctic Ocean. *Ocean Sci.* 13, 997–1016. doi: 10.5194/os-13-997-2017

Polyakov, I., Rippeth, T., Fer, I., Alkire, M., Baumann, T., Carmack, E., et al. (2020). Weakening of cold halocline layer exposes sea ice to oceanic heat in the Eastern Arctic Ocean. *J. Clim.* 33 (18), 8107–8123. doi: 10.1175/JCLI-D-19-0976.1

Qi, D., Chen, B., Chen, L., Lin, H., Gao, Z., Sun, H., et al. (2020). Coastal acidification induced by biogeochemical processes driven by sea-ice melt in the western Arctic ocean. *Polar Sci.* 23, 100504. doi: 10.1016/j.polar.2020.100504

Qi, D., Ouyang, Z., Chen, L., Wu, Y., Lei, R., Chen, B., et al. (2022b). Climate change drives rapid decadal acidification in the Arctic Ocean from 1994 to 2020. *Science* 377 (6614), 1544–1550. doi: 10.1126/science.abo0383

Qi, D., Wu, Y., Chen, L., Cai, W., Ouyang, Z., Zhang, Y., et al. (2022a). Rapid acidification of the arctic Chukchi Sea waters driven by anthropogenic forcing and biological carbon recycling. *Geophys. Res. Lett.* 49, e2021GL097246. doi: 10.1029/2021GL097246

Riedel, A., Michel, C., Gosselin, M., and Leblanc, B. (2008). Winter-spring dynamics in sea-ice carbon cycling in the coastal Arctic Ocean. *J. Mar. Syst.* 74, 918–932. doi: 10.1016/j.jmarsys.2008.01.003

Schuster, U., McKinley, G., Bates, N., Chevallier, F., Doney, S., Fay, A., et al. (2013). An assessment of the Atlantic and Arctic sea-air CO_2 fluxes 1990-2009. *Biogeosciences* 10, 607–627. doi: 10.5194/bg-10-607-2013

Screen, J., and Simmonds, I. (2010). The central role of diminishing sea ice in recent Arctic temperature amplification. *Nature* 464 (7293), 1334–1337. doi: 10.1038/nature09051

Semiletov, I., Makshtas, A., and Akasofu, S. (2004). Atmospheric CO_2 balance: The role of Arctic sea ice. *Geophys. Res. Lett.* 31, L05121. doi: 10.1029/2003GL017996

Shepherd, A., Ivins, E., Barletta, V., Bentley, M., Bettadpur, S., Briggs, K., et al. (2012). A reconciled estimate of ice-sheet mass balance. *Science* 338 (6111), 1183–1189. doi: 10.1126/science.1228102

Sun, H., Gao, Z., Peng, L., Xiu, P., and Chen, L. (2017). Evaluation of the net CO_2 uptake in the Canada Basin in the summer of 2008. *Hai Yang Xue Bao.* 36, 1–7. doi: 10.1007/s13131-017-1028-9

Tu, Z., Le, C., Bai, Y., Jiang, Z., Wu, Y., Ouyang, Z., et al. (2021). Increase in CO_2 uptake capacity in the Arctic Chukchi Sea during summer revealed by satellite-based estimation. *Geophys. Res. Lett.* 48, e2021GL093844. doi: 10.1029/2021GL093844

Uppstrom, L. (1967). "Analysis of boron in seawater by a modified curcumin method," in *Marine chemistry, vol. 1 (Analytical methods), 2nd ed*, vol. 1972 . Ed. D. F. Martin (New York: Marcei. Dekker. Inc), 389.

Wanninkhof, R. (2014). Relationship between wind speed and gas exchange over the ocean revisited. *Limnol Oceanogr. Methods* 12, 351–362. doi: 10.4319/lom.2014.12.351

Wanninkhof, R., Pierrot, D., Sullivan, K., Mears, P., and Barbero, L. (2022). Comparison of discrete and underway CO_2 measurements: inferences on the temperature dependence of the fugacity of CO_2 in seawater. *Mari Chem.* 247, 104178. doi: 10.1016/j.marchem.2022.104178

Weiss, R. (1974). Carbon dioxide in water and seawater: the solubility of a nonideal gas. *Mar. Chem.* 2, 203–215. doi: 10.1016/0304-4203(74)90015-2

Xu, A., Jin, M., Wu, Y., and Qi, D. (2023). Response of nutrients and primary production to high wind and upwelling favorable wind in the Arctic Ocean: A modeling perspective. *Front. Mar. Sci.* 10, 1065006. doi: 10.3389/fmars.2023.1065006

Yang, W., Wu, Y., Cai., W., Ouyang, Z., Zhuang, Y., Chen, L., et al. (2023). Rapid changes in the surface carbonate system under complex mixing schemes across the Bering Sea: a comparative study of a forward voyage in July and a return voyage in September 2018. *Front. Mar. Sci.* 10, 1107646. doi: 10.3389/fmars.2023.1107646

Yasunaka, S., Murata, A., Watanabe, E., Chierici, M., Fransson, A., Heuven, S., et al. (2016). Mapping of the air-sea CO_2 flux in the Arctic Ocean and its adjacent seas: Basin-wide distribution and seasonal to interannual variability. *Polar Res.* 10, 323–334. doi: 10.1016/j.polar.2016.03.006

Yasunaka, S., Siswanto, E., Olsen, A., Hoppema, M., Watanabe, E., Fransson, A., et al. (2018). Arctic Ocean CO_2 uptake: an improved multiyear estimate of the air-sea CO_2 flux incorporating chlorophyll a concentrations. *Biogeosciences* 15, 1643–1661. doi: 10.5194/bg-15-1643-2018

Zheng, Z., Luo, X., Wei, H., Zhao, W., and Qi, D. (2021). Analysis of the seasonal and interannual variations of air-sea CO_2 flux in the Chukchi Sea using a coupled ocean-sea ice-biogeochemical model. *J. Geophys. Res. Oceans* 126, e2021JC017550. doi: 10.1029/2021JC017550

frontiers | Frontiers in Marine Science

TYPE Original Research
PUBLISHED 21 May 2024
DOI 10.3389/fmars.2024.1379673

OPEN ACCESS

EDITED BY
Tommaso Tesi,
National Research Council (CNR), Italy

REVIEWED BY
Fangjian Xu,
Hainan University, China
Shengfa Liu,
Ministry of Natural Resources, China
Bernhard Diekmann,
Alfred Wegener Institute Helmholtz Centre for Polar and Marine Research (AWI), Germany

*CORRESPONDENCE
Qian Ge
qge@sio.org.cn

RECEIVED 02 February 2024
ACCEPTED 30 April 2024
PUBLISHED 21 May 2024

CITATION
Chen D, Ge Q, Lei Z, Zhou B and Han X (2024) Glacial activity and paleoclimatic evolution records in the Cosmonaut Sea since the last glacial maximum.
Front. Mar. Sci. 11:1379673.
doi: 10.3389/fmars.2024.1379673

Glacial activity and paleoclimatic evolution records in the Cosmonaut Sea since the last glacial maximum

Dong Chen[1,2], Qian Ge[1,2*], Ziyan Lei[3], Bingfu Zhou[1,2] and Xibin Han[1,2]

[1]Key Laboratory of Submarine Geosciences, Ministry of Natural Resources, Hangzhou, China, [2]Second Institute of Oceanography, Ministry of Natural Resources, Hangzhou, China, [3]Department of Oceanography and Coastal Science, Louisiana State University, Baton Rouge, LA, United States

This research explored the origin and paleoenvironmental significance of sediments from the Cosmonaut Sea, Antarctica, focusing on the period since the Last Glacial Maximum (LGM, 26,000 cal a BP). Sediment samples from core ANT37-C5/6-07 were subjected to AMS^{14}C dating, clay-mineral assemblage analysis, grain size evaluation, and geochemical testing. Results indicated illite as the dominant clay mineral (average 46%), followed by kaolinite (22%) and smectite (21%), with chlorite (11%) being the least abundant. Comparison with previous studies suggested that these sediments are largely derived from weathered material from Prydz Bay and Enderby Land coastal regions. The study of mineral ratios, geochemical elements, and sediment grain size, alongside δ^{18}O values from the East Antarctica EDML ice core, revealed that the ice sheet in the study area retreated around 18600 cal a BP, melted more markedly during 16800-15000 cal a BP, tended to expand during 14800-13500 cal a BP, and then the ice sheet remained in a state of retreat until it expanded again around 5000 cal a BP. It is largely synchronous with the phased changes in the Antarctic climate since the LGM (26ka) of the Cosmonaut Sea. Notably, the sediment record aligns with major paleoclimatic events, including Heinrich Stadial 1 and the Younger Dryas in the northern hemisphere and the Antarctic cold reversal, reflecting a climatic 'seesaw' effect. These findings suggest that the sedimentary record in the Cosmonaut Sea is a sensitive indicator of climatic conditions, highlighting a history of glacial movements and revealing East Antarctica's climatic fluctuations. Additionally, the research indicates that the regional ice sheet is more sensitive to climatic changes than previously believed, underscoring its instability.

KEYWORDS

Cosmonaut Sea, clay minerals, last glacial maximum, paleoclimate, sediment sources

Highlights

- Sources of sediment from core ANT37-C5/6-07 were analyzed;
- The warm and cold variations in the study area were reconstructed;
- Clay minerals and geochemical elements in the Antarctic sediments are good indicators of provenance and paleoclimate.

1 Introduction

Climate change on Earth has been significant in the last century, mainly characterized by global warming, which has led to the retreat of glaciers, the rise of the snow line, and the rise of the sea level at high latitudes. Being one of the most responsive areas to global climate change and a vital region for the global exchange of CO_2 between sea and air, the Southern Ocean is influential in that alterations in its climate and environment directly influence the thickness of the ice sheet and the extent of sea-ice coverage. These changes, in turn, affect ocean circulation and sea-level height, and they play a significant role in the global carbon cycle (Legendre, 1998; Collier et al., 2000; Leonardo et al., 2000). Therefore, historical changes in the Antarctic paleo-ice sheet provide insights into past climatic variations and sea-level fluctuations. Being the largest solid water reservoir on Earth, the Antarctic ice sheet constitutes approximately 90% of the world's land ice and 80% of the world's total freshwater (Ju, 2019). Satellite observations indicate melting of the Antarctic ice sheet in recent decades has contributed to a global sea-level rise of 7.6 ± 3.9 mm. The pace of sea-ice loss is progressively accelerating, and climate models predict a reduction in the sea-ice extent by approximately one-third by the end of this century (Turner et al., 2017; Rignot et al., 2019). The melting of the Antarctic ice sheet has affected the distribution of sea ice in the Southern Ocean, which, in turn, has affected ocean-air exchange, the global heat balance, and ocean circulation. Therefore, comprehending the mechanisms of interaction between the climate and glaciers in the Southern Ocean is crucial for obtaining insights into the future of the Antarctic and global climate.

Environmental changes in East and West Antarctica are showing distinct trends. Recent satellite observations indicate rising temperatures and melting sea ice in the West Antarctica, while sea ice in the East Antarctica remains relatively stable. Many scholars have conducted extensive research on the Antarctic climate, sea ice, and productivity (Bonn et al., 1998; Shepherd et al., 2004; Ducklowa et al., 2008). However, studies based on satellite observations typically only capture short-term changes in sea ice. Research on longer timescales often involves reconstructing paleo-topographic features or using proxies from marine sediments. For example, Kim et al. (2021) examined the effect of El Niño-Southern Oscillation and Circumpolar Deep Water on ice-shelf melting in the Amundsen Sea. They conducted their analysis by examining total organic carbon, total sulfur, and biogenic silicon in sediments from the Amundsen Sea. Pedro et al. (2011) explored the coupling of millennial-scale climate changes in the Antarctica and Greenland using five high-resolution Antarctic ice-core records and examining changes in global methane concentrations. Crosta et al. (2008) reconstructed climate change in the East Antarctica since the Holocene by analyzing the response of diatom species in the East Antarctic cores to seasonal climate changes.

Clay minerals in Antarctic sediments have been the focus of extensive research by scholars as a valuable tool for reconstructing paleoclimatology and interpreting sedimentary sources and processes (e.g. Biscaye, 1965; Chamley, 1997). For instance, Ehrmann et al. (1992) synthesized findings from various scholars on Antarctic clay minerals, revealing distinct clay-mineral assemblages in sediments from different seas. Understanding the variations in these assemblages and their influencing factors is essential for deciphering Antarctic paleoclimatology and changes in ice sheets.

The Cosmonaut Sea is situated in the northwestern part of the East Antarctic Enderby Land, spanning from 30°E to 60°E. It is bordered by the Reeser-Larsen Sea to the west and the Cooperative Sea to the east. Three bays, namely Lützow-Holm Bay, Casey Bay, and Amundsen Bay, are arranged from west to east. This region serves as a crucial junction for polar circulation, where dynamic physical processes like current flows and the formation and dissolution of polynyas occur. Here, the interplay between sea ice and the ocean is a dominant force in shaping the Antarctic ecosystem. The currents, sea ice and surface productivity in this area have also been analysed and studied by previous authors. Williams et al. (2010) conducted an analysis based on the BROKE-WEST survey, examining the large-scale circulation, water masses, and fronts on the inner shelf slope and the surface of upwelling areas in the Cosmonaut Sea. They observed that the sea ice in the region is complex and highly variable, characterized by multiple polynyas. Additionally, the study found that the region's dynamics are influenced by several currents: the eastward-flowing Antarctic Circumpolar Current (ACC) to the north and the westward-flowing Coastal Current and Antarctic Slope Current (ASC) to the south (see Figure 1). Additionally, the seasonal flow of Antarctic Bottom Water exists at the base of the region, and two large-scale circulations, the Prydz Bay circulation in the east and the East Weddell circulation in the west (Bibik et al., 1988), contribute to the dynamic oceanic system. And the Cosmonaut Sea is very active in physical processes, with large-scale latitudinal and meridional ocean circulation patterns, annual formation and disappearance of sea ice, and pronounced seasonal surface water mass transitions (Gloersen et al., 1993; Bindoff et al., 2000; Williams et al., 2008). Li et al. (2021) reveal the climatic response of the ice-proximal environment to the melting of the ice sheet from the Last Glacial Maximum (LGM) to Holocene based on diatom data from sediments. The knowledge of the Cosmonaut Sea in the East Antarctica is limited by previous studies, in particular, studies of the Astronaut Sea have focused on hydrology and biology, and the sedimentary record of the Cosmonaut Sea through inorganic geochemistry is relatively scarce. This research gap emphasizes the necessity of gaining a deeper understanding of the importance of the Southern Ocean

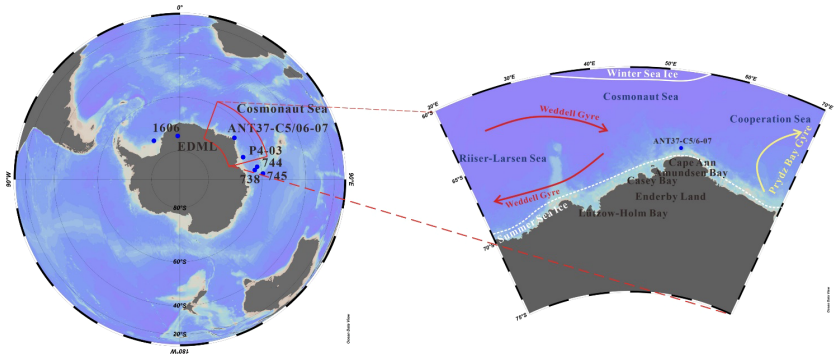

FIGURE 1
Map of the currents and core locations. The map on the left side is an overall view of the Antarctica. The map on the right side is a detailed one of the study area. The arrows represent the currents. The yellow arrow represents the Prydz Bay Gyre, the red arrows represent the Weddell Sea Gyre, the blue arrow represents ASC, the purple arrow represents ACC, the white dashed line is the summer sea-ice line, and the white solid line is the winter sea-ice line.

mineral assemblages in Antarctic paleoclimatology and glacial reconstruction, and investigating climate and sea-ice changes in the Cosmonaut Sea can significantly contribute to comprehending environmental changes in the broader Antarctica. Hence, this study focused on marine sediments from core ANT37-C5/6-07 in the Cosmonaut Sea (Figure 1) to reconstruct the paleoclimatic evolutionary history since the Last Glacial Maximum (LGM) in the East Antarctica through the analysis of clay-mineral assemblages and their integration with variations in grain size and geochemical elements.

2 Materials and methods

The samples were collected from core ANT37-C5/6-07 (52° 35.69'E, 65°21.27'S; Figure 1; recovery length: 378 cm), which was obtained during the 37th Chinese Antarctic Expedition in 2021. This station is situated in the Cosmonaut Sea at a water depth of 2825 m. For this study, a 91-cm-long sample at the top was chosen from the initial section. The sediments in this core exhibit an olive-green color and consist of silty mud that is weakly cohesive. Owing to the lack of calcareous fossils in the sediments, sediments from the Antarctic marginal sea are usually dated using the AMS^{14}C method, which uses the acid-insoluble organic fraction from the sediments (Licht and Andrews, 2002; Hillenbrand et al., 2010; Hu et al., 2022), and ages determined by this method are usually considered reliable (Licht and Andrews, 2002). Therefore, we selected samples from five layers (Table 1) for AMS^{14}C dating at the Beta Analytic Inc, USA.

The pretreatment, separation, preparation, and X-ray diffraction (XRD) analysis of clay mineral samples were conducted at the Key Laboratory of Submarine Geosciences, Ministry of Natural Resources in Hangzhou, Zhejiang Province. The remaining samples, extracted from grain-size fractions smaller than 2 μm using Stokes low of sedimentation, were then transformed into oriented slices for XRD analyses. The clay-mineral profiles were analyzed and calculated using Jade 6.0. Qualitative analysis was conducted through a comprehensive comparison of the characteristics of the three oriented-sheet diffraction peaks. Semi-quantitative analysis was performed using the weighting coefficients determined by Biscaye (1965). The result for illite crystallinity was determined by averaging four calculations for each sample, with error control maintained within 3%. Ninety-one samples were analyzed with a sampling interval of 1 cm.

Grain size analysis was conducted using a laser-particle-size analyzer. The laser grain size analysis was performed using a Malvern 2000 particle-size analyzer at the Key Laboratory of Submarine Geosciences, Ministry of Natural Resources in Hangzhou, Zhejiang Province. Ninety-one samples were analyzed with a sampling interval of 1 cm.

TABLE 1 Ages of the sediments from core ANT37-C5/6-07.

Station	Sample layer (cm)	Age of AMS^{14}C/a	Calibrated age/cal BP	Age of old carbon/a	Calendar ages /cal BP
ANT37-C5/6-07	0–1	5300 ± 30	2118	2118	0
ANT37-C5/6-07	11–12	13,230 ± 30	11,486	2118	9368
ANT37-C5/6-07	44–45	18,210 ± 80	17,774	2118	15,656
ANT37-C5/6-07	67–68	19,810 ± 60	19,280	2118	17,162
ANT37-C5/6-07	90–91	27,830 ± 120	28,116	2118	25,998

Geochemical elements analysis was also conducted at the Key Laboratory of Submarine Geosciences, Ministry of Natural Resources in Hangzhou, Zhejiang Province. We weighed 40 mg of whole rock powder in a polytetrafluoroethylene sample cartridge. We added 0.5 ml of HNO_3 and 1.0 ml of HF. Then, we sealed the cartridge with a steel sleeve and placed it in an oven at 195°C for 3 d. We steamed the sample bomb containing the digestion solution on a hot plate until the salt was wet. Next, we added 1 ml of HNO_3 and 4 ml of 18.2 MΩ pure water to the bomb. We resealed the bomb and placed it in a 190° C oven for 12 h of closed digestion. We removed the inner liner after cooling. Thermo Fisher's ICAP-RQ ICP-MS instrument was used to analyze the samples. The samples were collected at a 1-cm interval, and a total of 91 samples underwent testing and analysis.

3 Results

3.1 Chronology

Table 1 presents the results of AMS ^{14}C dating for the five layers. Results from acid-insoluble organic matter dating in sediments using the AMS^{14}C method are usually affected by old carbon and therefore need to be calibrated. After calibration with the Calib 8.2.0 program (Stiver and Reimer, 1993) using the Marine20 dataset (Heaton et al., 2020) and adopting an ΔR value of 1120 for carbon-reservoir correction, the top age of the core was determined to be 2118 cal a BP, and the bottom age as 28,116 cal a BP (Yoshida and Moriwaki, 1979; Takano et al., 2012). In line with previous studies (Pudsey et al., 2006; Andrews et al., 2017; Hu et al., 2022), we generally performed age correction by subtracting the age at the top of the core. Owing to the proximity of the core ANT37-C5/6-07 sediments to the study location of Hu et al. (2022), we also treated the surface deposits as modern, resulting in an age of 0 cal a BP at the core's top and an old carbon age of 2118 a. Corrections involved subtracting the old carbon age and making appropriate adjustments to derive the final calendar age. The sediment-age framework for core ANT37-C5/6-07 referenced the work of Hu et al. (2023) (Figure 2).

3.2 Clay minerals

Figure 3 illustrates the contents and variations of clay minerals from core ANT37-C5/6-07. Among the clay minerals, illite exhibits the highest content, ranging from 29% to 61%, with an average of 45.98%. Illite content exhibits significant fluctuations between 40 and 60 cm, with minor changes from 0 to 40 cm. The overall variation in smectite content is relatively insignificant, ranging from 12% to 35%, averaging at 21%. Observable peaks and valleys are present in the curves to depict its content change, predominantly occurring at depths between 40 and 60 cm. Kaolinite content ranges from 15% to 30%, averaging at 22%. Below 60 cm, its content is relatively lower; however, above 60 cm, it increases and exhibits fluctuations. Chlorite content ranges from 7% to 16%, averaging at 11%. It is lower and more stable compared with the others. Overall, the fluctuation is minimal below 60 cm, with slight fluctuations observed above 60 cm. The highest content is situated at approximately 40 cm. Illite crystallinity varies from 0.31°Δ2θ to 0.53°Δ2θ. Small variations are observed below 60 cm and above 40 cm, all below 0.4°Δ2θ, indicating better crystallization. Larger variations are noted from 40 to 60 cm, exceeding 0.4°Δ2θ and indicating worse overall crystallization. The chemical index of illite ranges from 0.02 to 0.21, with a mean value of 0.06. Overall, all values are less than 0.1, with a peak around 45 cm, indicating enhanced chemical weathering. However, the overall trend suggests weathering predominantly dominated by physical weathering and controlled by cold and dry climatic conditions in the Antarctica.

3.3 Grain size

Figure 4 illustrates the vertical variation of grain size characteristic parameters in core ANT37-C5/6-07. By using the Udden-Wentworth grain-size classification method (Gladstone et al., 2001), we selected three grain-size parameters: the percentage content of grain-size fractions less than 4 μm, 4–63 μm, and greater than 63 μm. These parameters represent the percentage content of the clay, silt, and sand fractions in the samples. Silt dominated the sediments in this core,

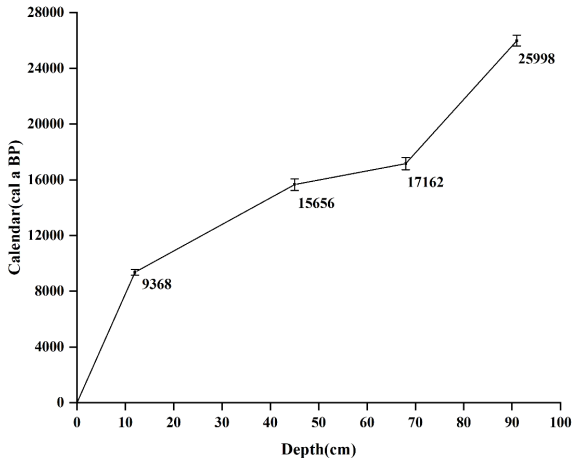

FIGURE 2
Calibrated calendar ages for the top 91 cm of core ANT37-C5/6-07.

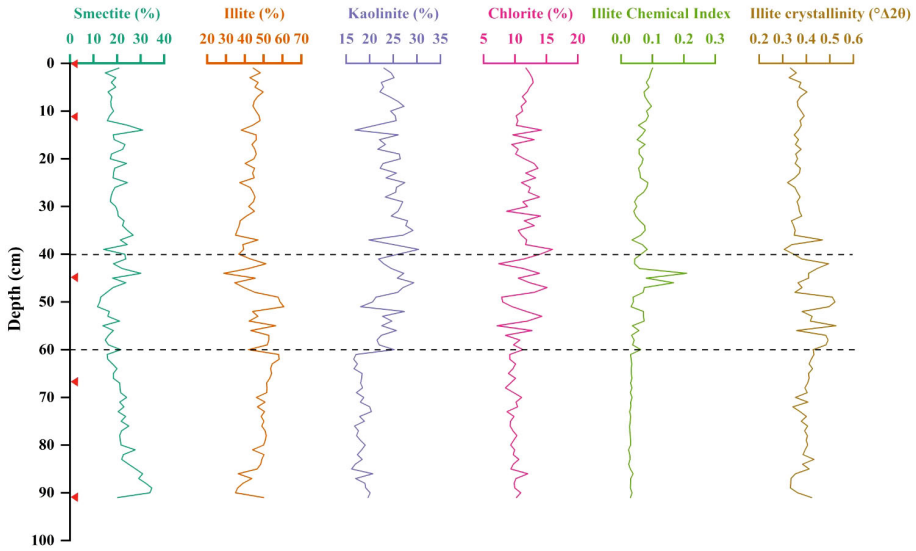

FIGURE 3
Characteristics of clay-mineral assemblages and their vertical variations in core ANT37-C5/6-07. The red triangles are age marker points.

with the average percentage of clay-component contents at 21.0% (7.1–32.2%), the average percentage of silt component contents at 58.0% (34.3–67.2%), and the average percentage of sand-component contents at 21.0% (2.4–51.9%). The variations in silt- and clay-component contents were similar but were opposite to those of sand-component contents. The mean grain size (Mz) ranged from 7.2 μm to 90.5 μm, experiencing more frequent fluctuations between 45 cm and 91 cm and then stabilizing and increasing above 45 cm. In addition, the grain size characteristics of sediments can reflect hydrodynamic conditions and ice-rafted debris content variations (Bischof et al., 1996; Chen et al., 2014). However, using grain size data to infer depositional environments introduces some uncertainty. To mitigate this, a statistical approach—grain size-standard deviation—is often applied to enhance the interpretation of grain size data (Chen et al., 2013). This method's analysis (Figure 5) reveals three significant deviation peaks at 14.6 μm, 58.3 μm, and 1230 μm, along with three minor peaks at 0.22 μm, 25.4 μm, and 406.1 μm in the sediment of core ANT37-C5/6-07. Thus, the sediment can be

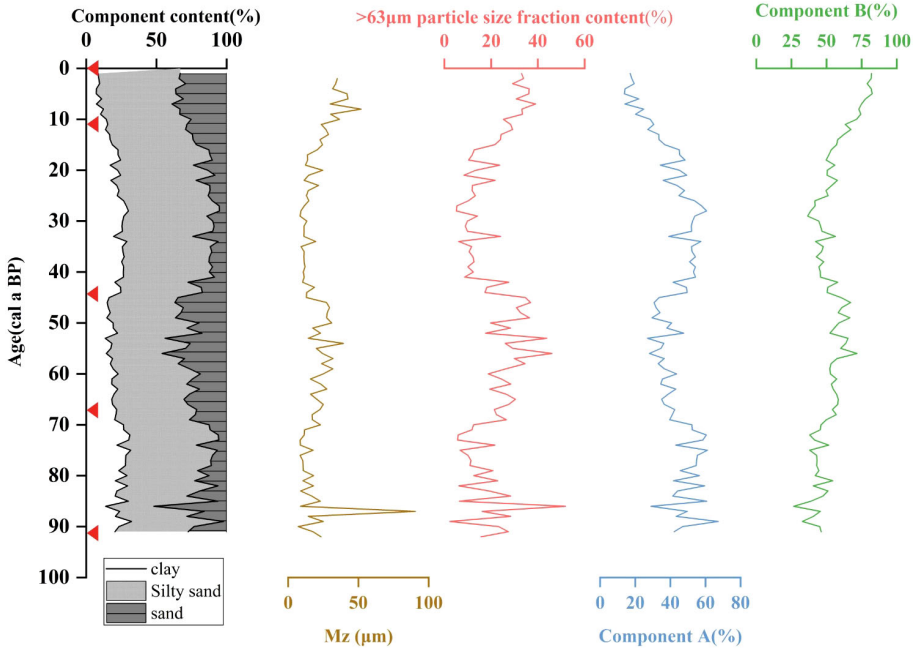

FIGURE 4
Vertical variations in the characterization of grain size in core ANT37-C5/6-07. The red triangles are age marker points.

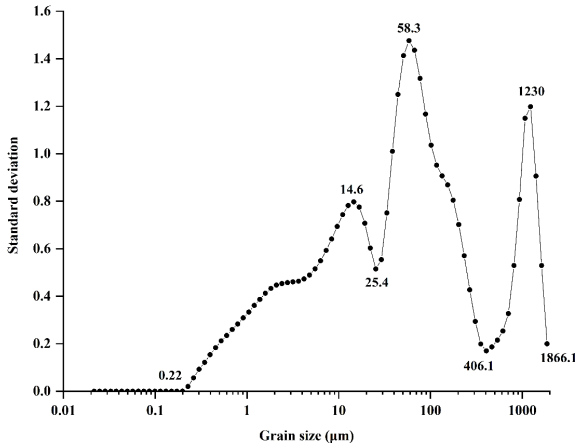

FIGURE 5
Grain size standard deviation diagram of the sediments in core ANT37-C5/6-07.

classified into three environmentally sensitive grain size groups: 0.22–25.4 μm (component A), 25.4–406.1 μm (component B), and 406.1–1866.1 μm (component C). Among these, component C is minor and exhibits a standard deviation near zero, rendering its discussion irrelevant.

3.4 Geochemical elements

Table 2 presents the results of elemental analyses for the sediments in core ANT37-C5/6-07. The contents of Al_2O_3 and Fe_2O_3 are the highest. Aluminum is commonly considered an element enriched by terrestrial-source debris. Its coefficient of variation is very small (0.06), making it suitable as a standardized element to mitigate the influence of terrestrial-source debris on elemental content. The results reveal a high coefficient of variation for the redox-sensitive element Mo and an elevated content of Ba among the trace elements in core ANT37-C5/6-07. The average concentrations are 231.73 ppm for total rare-earth elements (REE), 213.09 ppm for light rare-earth elements (LREE), and 18.64 ppm for heavy rare-earth elements (HREE). The trends reflect a remarkable accumulation of LREE. The alterations in the characteristics of certain elements in the sediment samples from core ANT37-C5/6-07 are illustrated in Figure 6. The variations in the characteristics of elements in the sediments manifested in two distinct phases: the last glacial period and the Holocene, exhibiting significant cyclic fluctuations. Notably, except for the elements Ba and Mn, a sudden change occurred in the other elements at around 46 cm. The characteristics of terrestrial enrichment elements depicted in Figure 6, including Ti, Al, Fe, K, P, and Mg, exhibit a similarity to the trend of changes in other elemental characteristics and show a positive correlation. Conversely, Si and Ba display a negative correlation.

4 Discussion

4.1 Origin of sediments

Sediments in high-latitude marine environments are frequently transported by glaciers and ocean currents, encapsulating valuable insights into alterations in source areas and depositional processes. As

TABLE 2 Statistical characterization of the main and trace elements contents of the sediments from core ANT37-C5/6-07.

Elements	Mean value	Standard deviation	Variation coefficient	Elements	Mean value	Standard deviation	Variation coefficient
Al_2O_3 (%)	13.40	0.83	0.06	Mo (ppm)	0.59	0.38	0.64
TFe_2O_3 (%)	7.45	0.63	0.08	Ni (ppm)	52.73	8.34	0.16
K_2O (%)	2.89	0.16	0.06	Ba (ppm)	845.25	112.12	0.13
MgO (%)	2.87	0.26	0.09	U (ppm)	1.88	0.62	0.33
TiO_2 (%)	0.76	0.04	0.05	Th (ppm)	19.63	1.56	0.08
CaO (%)	2.58	0.27	0.10	ΣREE (ppm)	231.73	14.97	0.06
P_2O_5 (%)	0.14	0.01	0.06	ΣLREE (ppm)	213.09	14.61	0.07
MnO (%)	0.10	0.03	0.27	ΣHREE (ppm)	18.64	0.93	0.05
Co (ppm)	19.36	1.91	0.10				

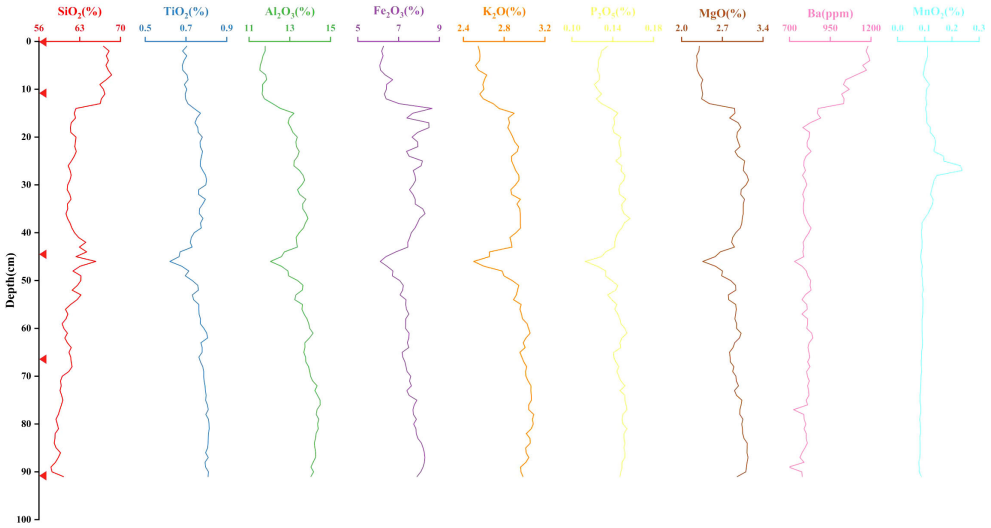

FIGURE 6
Characteristics of longitudinal variation of elements in core ANT37-C5/6-07. The red triangles are age marker points.

highlighted earlier, the clay-mineral composition and characteristics of impeccably preserved sediments bear information regarding depositional sources and climatic changes. However, discussions regarding the sediment source based solely on clay-mineral characteristics may be prone to bias owing to the influence of multiple mechanisms (Singer, 1984; Yemane et al., 1996). And REEs have been widely used as useful and reliable provenance proxy for terrigenous sediments from different regions (Taylor and McLennan, 1985; Xu et al., 2021). Therefore, based on the analysis of the characteristics of the clay-mineral assemblage, combined with the REE characteristics of the sediments, and compared with the characteristics in the sediments of the neighboring seas, we could identify the origin of sediments in core ANT37-C5/6-07.

The analysis of previous experimental results (Figure 3) showed that illite dominated as the clay mineral in core ANT37-C5/6-07. This dominance can be attributed to the terrestrial physical weathering and glacial abrasion processes characteristic of high-latitude regions. Illite primarily originates from the physical weathering of metamorphic and sedimentary rocks in the surrounding land. Experimental results show that the average illite crystallinity is less than 0.4°Δ2θ, indicating superior crystallization. Additionally, the illite chemical-weathering index (<0.2) suggests that the illite is mainly from physical weathering. Notably, Trail and McLeod (1969) observed that the region is predominantly composed of migmatite and gneiss. They further noted that substantial quantities of readily weatherable hydrocarbon source rocks can contribute to the presence of illite and chlorite. Smectite is typically considered a product of seafloor weathering of volcanic material, as observed in sediments from the Ross Sea. This volcanic material originates from the nearby McMurdo volcano (Jung et al., 2021). Smectite has also been identified in some Antarctic soils (Claridge, 1965), suggesting its potential presence in sediments due to the transport of ancient, loosely weathered products and soils into the ocean by glaciers or turbidity currents. Kaolinite typically forms through the chemical weathering of rocks in warm, humid temperate-to-tropical climates. However, in the cold, arid climate of the Antarctic continent, characterized by weak chemical weathering, glaciers likely transported kaolinite from the soils and loose sediments of coastal plains from the Mesozoic to the Tertiary (Hambrey et al., 1991). Ehrmann et al. (1992) identified the presence of high levels of kaolinite in sediments from the Oligocene period, coinciding with the formation of ice sheets in the East Antarctica. After the ice sheet formed, unconsolidated debris was transported away from the continents, leaving glaciers to primarily erode unweathered rock, which resulted in only a small quantity of kaolinite being produced. Additional kaolinite likely resulted from the weathering of preexisting kaolinite-bearing sediments and the erosion of ancient soils (Trail and McLeod, 1969). Moreover, the Lambert Glacier and Emery Ice Shelf in the Prydz Bay were found to be filled with older kaolinite. When the glacier melted, the older kaolinite beneath was exposed, and subsequent weathering and erosion contributed to the kaolinite content.

Sediment provenance is further examined by considering the potential source areas of the four clay minerals and analyzing the clay-mineral assemblages. Given that both illite and chlorite result from physical weathering (Ehrmann et al., 1992), we combined their contents as a composite end member to explore their potential source regions. This analysis involved comparing them with clay mineral characteristics of other marine sediments that may share the same sediment source station (Ehrmann, 1991; Melles, 1991; Dai et al., 2016) and integrating this information with the current characteristics of the study area. The source analysis triangulation for clay minerals is shown in Figure 7. The comparison of results reveals that the clay mineral assemblages in core ANT37-C5/6-07 exhibit a distinct signature, which only partially matches that of the clay mineral assemblages from core P4-03 in Prydz Bay. This suggests that the primary source of clay minerals in core ANT37-C5/6-07 is likely nearby Enderby Land, with a portion also possibly originating from the coastal land along Prydz Bay. Referring to the core locations and current characteristics illustrated in Figure 1, both cores fell within the influence of the eastward ASC. The ASC, driven by the horizontal gradient pressure of the Antarctic Slope

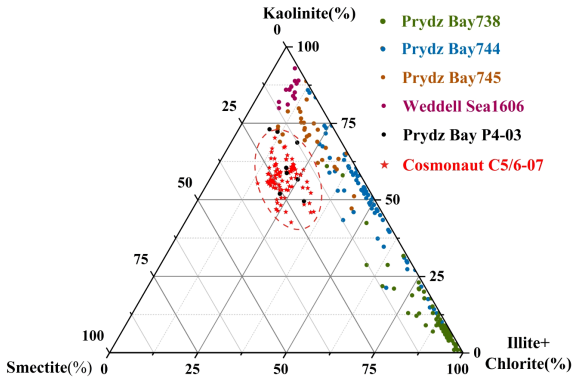

FIGURE 7
Triangulation of clay-mineral source analysis diagram showing clay mineral assemblages from sediments in core ANT37-C5/6-07 compared to those from the ODP sites 738, 744, and 745 at Australia-Antarctic Basin (Ehrmann and Grobe, 1991), site P4-03 at Prydz Bay (Dai et al., 2016), and site 1606 at Weddell Sea (Melles, 1991). The red dash line represents the range of similarity in clay-mineral characteristics.

Peak, exhibits a high flow velocity, reaching a maximum of 25 cm/s and being particularly active at a water depth of 750–1250 m. Below this depth, the flow velocity gradually decreases, facilitating the deposition of detrital material (Hunt et al., 2007; Williams et al., 2010). As both cores are situated at water depths below 2500 m, their clay-mineral assemblages are significantly influenced by the ASC. Consequently, we propose that the sediments in core ANT37-C5/6-07 are partly derived from rocks weathered on the continental shelf of Prydz Bay, transported by the ASC. Additionally, some sediments are believed to originate from coastal Enderby Land. To elucidate the sediment origin further, we selected REE as proxy indicators for compositional analysis. REE is typically associated with source rocks owing to their low reactivity. However, the fractionation of REE during deposition is influenced by multiple factors. Notably, a grain size effect has been observed in REE, often leading to enrichment in fine-grained material (Cullers et al., 1987). Additionally, study results confirm the reactivity of REE during chemical weathering, where the intensity of chemical weathering can affect their composition. Moreover, REE is influenced by mineral adsorption, and research has indicated that the composition of REE is also affected by ferromanganese oxides. Correlation analysis of the REE content of the sediments with Mz, the illite chemical index indicating chemical weathering intensity, and the $(Fe_2O_3+MnO)/Al_2O_3$ value representing ferromanganese oxide content (Dou et al., 2012) reveals that the REE content in core ANT37-C5/6-07 exhibits a weak correlation with these three factors (Figure 8). This suggests that the variation in REE features is primarily influenced by the source. Therefore, the sediment source can be inferred based on the and considering light and heavy rare-earth fractionation features, such as $(La/Sm)_N$ and $(Gd/Yb)_N$.

REE compositions in chondrite meteorites are believed to be undifferentiated. Analyzing the chondrite-normalized REE partitioning patterns can thus provide a clearer understanding of the differentiation characteristics of the sample's REE (Boynton, 1984). We compared the REE compositions in the core ANT37-C5/6-07 sediments with those in the potential source area to try to analyze the source of the sediments (Shi et al., 1998; Chen et al., 2015; Li et al., 2017; Xiu et al., 2017). The REE compositions in the core ANT37-C5/6-07 sediments, as shown in the chondrite-normalized partitioning patterns (Figure 9), display a marked enrichment in Light REE (LREE) and a depletion in Heavy REE (HREE). This pattern aligns with terrestrial source characteristics, suggesting a significant terrestrial influence, particularly from nearby Enderby Land. In contrast, the REE abundance in the sediments from the Antarctic Peninsula and Ross Island differs markedly, indicating a distinct geological origin (Shi et al., 1997; Chen et al., 2015). Moreover, the sediments in core ANT37-C5/6-07 show a higher REE content compared to those from the Ross Sea (Xiu et al., 2017). The similarity in LREE levels and the deficit in ΣHREE compared to the Enderby Land metamorphic rocks, along with distinct positive Ce anomalies and negative Eu anomalies, reflect the underlying bedrock composition, primarily ancient metamorphic rocks such as gneisses and mafic rocks (Sheraton et al., 1984; Tingey, 1991; Stagg et al., 2004). These features, supported by the bedrock characteristics in Prydz Bay and Enderby Land, suggest a mixed sediment source for core ANT37-C5/6-07.

The normalized ratios $(La/Sm)_N$ and $(Gd/Yb)_N$ indicate the fractionation levels of light and heavy rare-earth elements, respectively. A higher $(La/Sm)_N$ ratio signifies greater enrichment

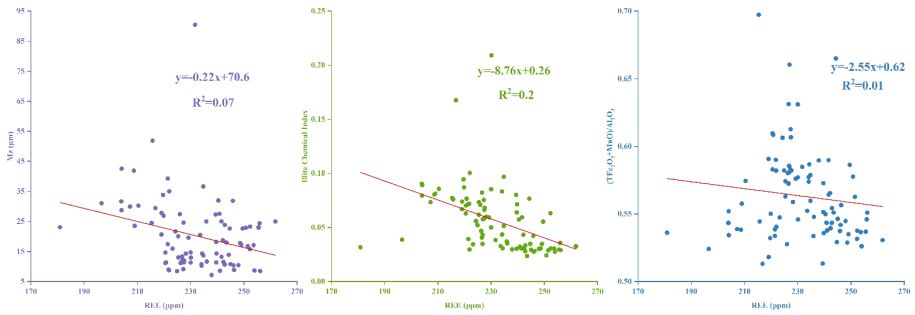

FIGURE 8
Correlations of REE with Mz, ferromanganese oxides, and chemical-weathering intensity in the sediments of core ANT37-C5/6-07.

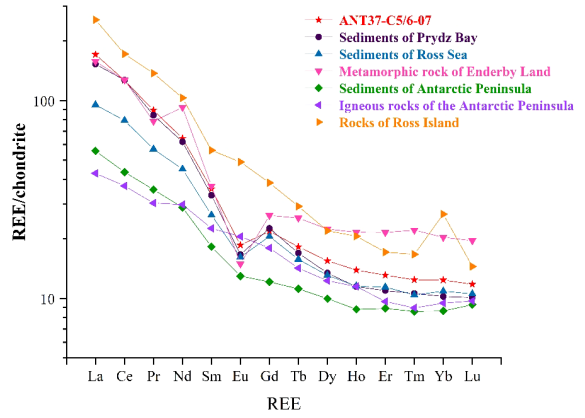

FIGURE 9
Chondrite-normalized partitioning pattern of REE for core ANT37-C5/6-07 and sediments from the Prydz Bay (Li et al., 2017), the Ross Sea (Xiu et al., 2017), sediments from the Antarctic Peninsula (Chen et al., 2015), metamorphic rocks of the Enderby Land (Suzuki et al., 1999), igneous rocks of the Antarctic Peninsula (Chen et al., 2015), and igneous rocks of the Ross Island (Shi et al.1998).

in LREEs, while a lower $(Gd/Yb)_N$ ratio points to greater HREE enrichment. By comparing the REE ratios in the sediments to those in potential source rocks, we can assess the fractionation between HREEs and LREEs. In core ANT37-C5/6-07 sediments (refer to Figure 10), the $(La/Sm)_N$ and $(Gd/Yb)_N$ ranges overlap with those from the Enderby Land Metamorphic Rocks and Prydz Bay sediments. This overlap suggests that these locations are the primary sources, as supported by the REE partitioning patterns observed.

In conclusion, the integrated analysis results of clay-mineral assemblages and REE composition strongly suggest that the predominant source of sediments in the study area is coastal land of Prydz Bay and Enderby Land. We consider that the sediments primarily originate from coastal-land weathering, transported into the ocean through processes like glacial or turbidite deposition, and subsequently carried by the ASC before settling at this specific station.

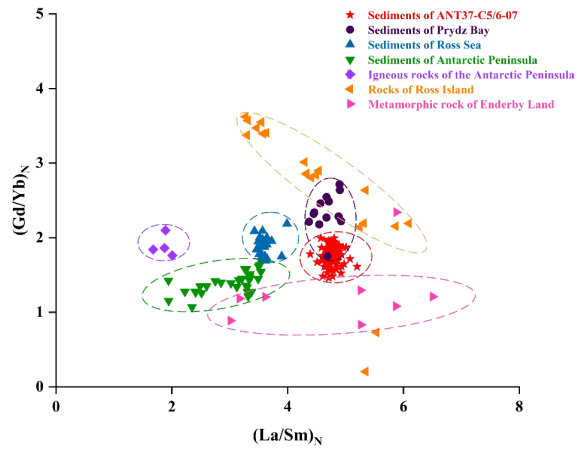

FIGURE 10
Discrimination diagrams for determination of provenances of sediments in core ANT37-C5/6-07, by comparing with $(La/Sm)_N$ and $(Gd/Yb)_N$ characteristics of the Prydz Bay (Li et al., 2017), sediments of the Ross Sea (Xiu et al., 2017), metamorphic rock of the Enderby Land (Suzuki et al., 1999), sediments of the Antarctic Peninsula, igneous rocks of the Antarctic Peninsula (Chen et al., 2015), and rocks of the Ross Island (Shi et al., 1997).

4.2 Paleoclimatic significance since LGM

Clay-mineral assemblages in marine sediments from distinct regions convey varied climatic information. Considering the stability of ASC influencing the deposition of core ANT37-C5/6-07 (Williams et al., 2010), we propose that alterations in the clay-mineral characteristics of the sediments may indirectly indicate paleoclimatic changes. Drawing from prior studies, we propose that the smectite in the study area may have an authigenic origin, potentially affecting the accuracy of the paleoclimate information it contains (Iacoviello et al., 2010). In contrast, kaolinite originates from old kaolinite buried under glaciers or formed through chemical weathering under warm and humid climatic conditions, signifying a warm climate. Illite and chlorite result from physical weathering, typically indicating dry and cold climates. Thus, the (illite + chlorite)/kaolinite value can serve as a proxy indicator of paleoclimatology, reflecting the shift between warm and cold climates in the source area (Yang et al., 2022). Combined with other paleoclimatic proxies, we can further elucidate the reasons for the alteration of clay-mineral assemblages and changes in depositional processes to reconstruct the paleoclimatology of the source region.

The geochemical elemental characteristics of the sediments bear information about paleoenvironmental changes. The contents of various grain size fractions were analyzed through an R-type factor analysis with the sediment elements at this station (Table 3). The chosen rotation method for factor analysis was the maximum-variance rotation method, leading to the identification of two primary factors, F1 and F2. Examination of Table 3 reveals that the variance factor of F1 was larger than that of F2, signifying that F1 predominantly influenced the composition of sediment elements. The TiO_2, Al_2O_3, Fe_2O_3, MgO, K_2O, P_2O_5, and clay fractions displayed high positive loadings, denoting their typical characteristics as terrigenous inputs. The iron could be correlated with chlorite, illite, and smectite, while potassium was primarily linked to potassium feldspar and illite. The F2 factor has positive high loadings only for MnO and chalk, which may indicate that Mn is more likely to be in the silty sand grain fraction relative to the other elements (Zhang, 2011). The SiO_2 and barium constitute components of marine-derived sediments, and SiO_2 levels could be associated with diatoms. Previous research has demonstrated that climatic variations can influence the timing and extent of sea-ice coverage in the Southern Ocean, subsequently influencing the photosynthesis of surface phytoplankton (Wong et al., 1999; Ducklowa et al., 2008). Therefore, biogenic barium (Ba_{bio}) and Si/Al were chosen as paleo-productivity indicators to indirectly infer information on climate warming and cooling. The Ba_{bio} was calculated using the following formula (Bonn et al., 1998):

TABLE 3 Results of R-type factor analysis of elements and grain size fractions from core ANT37-C5/6-07.

	F1	F2	Factor	Percentage of variance	Accumulated %
SiO_2	-0.968	0.008	F1	62.857	62.857
TiO_2	0.904	0.121	F2	20.601	83.457
Al_2O_3	0.98	-0.061			
Fe_2O_3	0.846	0.261			
MnO	-0.169	0.67			
MgO	0.953	0.179			
K_2O	0.966	-0.04			
P_2O_5	0.861	0.221			
Ba	-0.827	-0.004			
Clay	0.759	0.527			
Silty sand	0.094	0.943			
Sand	-0.483	-0.829			

$$Ba_{bio} = Ba_{tatal} - Al_{sed} \times (Ba/Al)_{ter}$$

where $(Ba/Al)_{ter}$ represents the abundance of barium in the terrestrial crust and has a value of 0.0051 (Taylor, 1964).

Combined with the previous section, the grain size composition and characteristics of marine sediments can indirectly reflect the hydrodynamic strength at the time of deposition, currents and other changes in the depositional environment (Hall et al., 2011). Compared with component A, the content of component B is higher, and the change of the content B shows an obvious positive correlation with the average grain size change of the sediment in the core ANT37-C5/06-07, which indicates that the change of the content B influences the overall change of the grain size of the sediment, and it is more sensitive to the environmental changes. Therefore, this paper suggests that component B can be used as a proxy indicator for changes in the depositional environment, and that the grain size components A and B correspond to the environmentally sensitive clay and silt, which to some extent can be indicative of weak and strong hydrodynamic conditions.

The ebb and flow of glaciers are deeply intertwined with shifts in climate patterns. Studies, including Stammerjohn et al. (2015), have demonstrated that rising temperatures significantly influence ice melt. This melting corresponds with periods of glacial retreat, often associated with warmer climates, which in turn fosters the emergence of open oceanic environments and an increase in surface productivity. In contrast, cooler climates are marked by a reduction in this productivity due to expansive sea-ice coverage. The presence of coarser grain sizes in sediment, like those greater than 63 μm, 125 μm, and 150 μm, is frequently interpreted as an indicator of increased ice-rafted debris (Chen et al., 2006), reflecting such climatic shifts. Within the specific environmental context of the area under study, it is plausible that the kaolinite found originates from the physical weathering and erosion of ancient, glacier-buried deposits, as indicated by its concentration. Notably, this kaolinite content aligns with the >63 μm grain size fraction, providing a sedimentary record that can be used to trace historical glacial movements.

To unravel the history of climate in Antarctica, we turned to ice cores, which are rich archives of past climatic conditions. In this study, the analysis went further, incorporating additional proxies; we delved into the intricate details of sedimentary records from core ANT37-C5/6-07. We scrutinized the variations in the composition of clay minerals, their relative proportions, the Ba_{bio}, the silicate-to-aluminum ratio (Si/Al), the >63 μm grain size fractions, and the component B. These sedimentary parameters were cross-referenced with the oxygen isotope data ($\delta^{18}O$) from the EDML ice core, which was obtained near our study site (as illustrated in Figure 1; Epica Community Members, 2006). Our comprehensive approach allowed us to piece together a dynamic history of hydrodynamics, paleoproductivity, and ice cover in the region. Through this lens, we discerned four distinct periods alternating between warmer and cooler climates (labeled P1 through P4). Moreover, we pinpointed the timing of these local environmental shifts in relation to broader global climatic events, as depicted in Figure 11.

During the period from 26,000 to 18,600 cal a BP, the (illite + chlorite)/kaolinite value was relatively high, and the kaolinite content was low. These features suggest a cold climate, weak chemical weathering intensity, and the reburial of older kaolinite due to the re-formation of the ice sheet. And content of component B is consistently low, indicating a less hydrodynamic depositional environment. This may be due to the fact that the exchange between the upper and lower water column was inhibited during that period due to sea ice cover. Concurrently, reduced values of Ba_{bio} and the Si/Al value point to diminished marine surface productivity, attributable to the sea ice extent. Marked variations in the >63μm grain size fraction, representing ice-rafted debris, were observed throughout this interval. Complementing these findings, the persistently low $\delta^{18}O$ values in the EDML ice core corroborate a colder climate and intensified glacial conditions. The alignment of these conditions with the Last Glacial Maximum (LGM) confirms

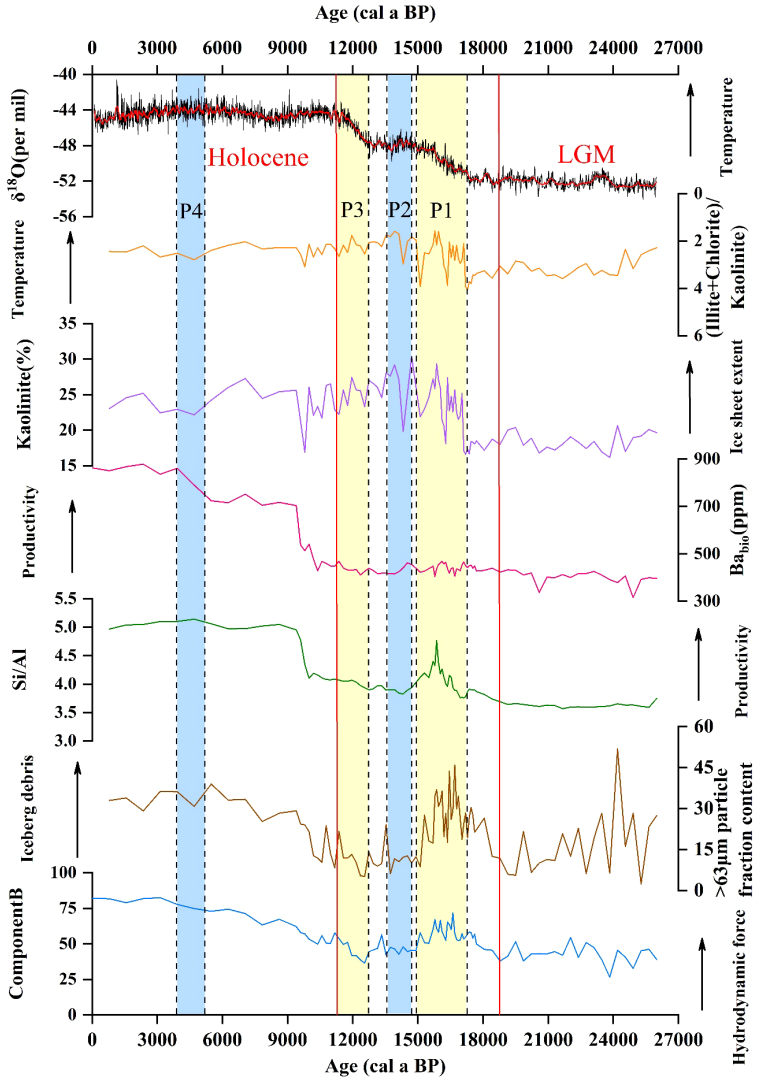

FIGURE 11
Changes in clay-mineral assemblages, Ba_{bio}, Si/Al, component B, content of >63-μm grain size fractions in the core ANT37-C5/6-07 sediments, and $\delta^{18}O$ of the EDML ice cores (Epica Community Members, 2006). The red line demarcates the LGM and Holocene phases, with the blue and yellow areas representing the cooler and warmer phases (P1-P4), respectively.

the chronology posited by Huybrechts (2002). Additionally, the shifts in these indicators denote that the study area commenced the Last Deglaciation around 18,600 cal a BP.

During the interval from 16,800 to 15,000 cal a BP (P1), a notable trend was observed: a decline in the (illite + chlorite)/kaolinite value to a nadir coincided with a significant rise in the $\delta^{18}O$ values of the EDML ice cores. Concurrently, the content of component B showed an upward tendency. These trends collectively suggest a warming climate. In this phase, the >63 μm grain size fraction, initially increased and then declined, mirroring the glacier retreat that first released and later reduced the transport of such debris to the study area. This glacial retreat also facilitated enhanced phytoplankton photosynthesis and wind-stressed upwelling, intensifying surface-layer productivity and hydrodynamic conditions. Additionally, weathering and erosion exposed older kaolinite previously under the ice sheet, resulting in a significant increase in the kaolinite content. However, there was no significant change in Ba_{bio}, an indicator of productivity. This was attributed to a warming climate. The sudden increase in surface productivity led to the deposition of settled organic matter that consumes large amounts of oxygen, creating an anoxic environment and resulting in low levels of Ba_{bio} (Hu et al., 2023).

The subsequent period between 14,800 and 13,500 cal a BP (P2) was characterized by an opposite trend: the (illite + chlorite)/kaolinite value ascended, $\delta^{18}O$ values dropped, and the >63 μm grain size fraction markedly escalated, while kaolinite content diminished. Si/Al, Ba_{bio}, and component B contents were comparatively low, suggesting a cooling climate, a surge in ice-rafted debris due to new ice sheet formation, and the reburial of kaolinite. And the new ice sheet resulted in restricted vertical

mixing in the water column, weaker hydrodynamics, and reduced surface productivity.

From 12,800 to 11,400 cal a BP (P3), a warming climate was once again indicated by a decrease in the (illite + chlorite)/kaolinite value, a rise in kaolinite and component B content, a decline in the >63μm fraction, and the increase in $\delta^{18}O$. Conversely, the Si/Al value and Ba_{bio} content remained relatively stable, implying lower temperatures during this warm period compared to the previous warm period. Studies by Borchers et al. (2016) in the nearby Burton Basin in East Antarctica also indicated that the ice shelf front started to retreat from the site around 12,800 cal a BP, evidencing warming during this period.

The sedimentary record in core ANT37-C5/6-07 provides a detailed account of the Antarctic climate transition from colder to warmer conditions following the Last Glacial Maximum (LGM). This transition in Antarctica was distinct from that in the Northern Hemisphere, largely because the extensive landmass of the Northern Hemisphere experienced more rapid warming during the initial phase of the last deglaciation. This led to increased ice meltwater influx into the North Pacific, causing a weakening of the Atlantic Meridional Overturning Current and consequent heat accumulation in the Southern Ocean. This heat accumulation, in turn, warmed the Antarctic climate, establishing a temperature gradient between the North and South Poles, an effect known as the Bipolar Seesaw (Broecker, 1998; Wang et al., 2015). Compared to previous studies in the East Antarctic (Borchers et al., 2016; Yang et al., 2021), the geochemical proxies in the Cosmonaut Sea, particularly the shifts in (illite + chlorite)/kaolinite values, Ba_{bio} content, Si/Al, and the content of component B in core ANT37-C5/6-07, provide a clear timeline for the Antarctic ice sheet's response to these climatic shifts. Notably, the warming in Antarctica from 16,800 cal a BP to 15,000 cal a BP (P1) occurred concurrently with the Heinrich Stadial 1 (HS1) in the Northern Hemisphere, whereas the cooler phase from 14,800 cal a BP to 13,500 cal a BP (P2) aligns with the Antarctic Cold Reversal (ACR). This latter period saw significant glacial expansion in the Ross Sea, further evidencing the frigid conditions in Antarctica (Huang et al., 2016). Following this, the period from 12,800 to 11,400 cal a BP (P3) signifies a warming phase post-ACR, which overlaps with the Younger Dryas (YD) cooling event in the Northern Hemisphere (Alley et al., 2003).

From 11,400 cal a BP to 5,000 cal a BP, the climate data from core ANT37-C5/6-07 show a phase of relative climatic stability and warming in Antarctica. The ratio of (illite + chlorite) to kaolinite was consistently low, reflecting stable conditions, while the $\delta^{18}O$ values showed minimal fluctuations, indicating steady climatic conditions. The low content of >63μm particles, representing ice-rafted debris, along with stable kaolinite content, suggests a constant source and reduced glacial activity. This period saw significant increases in Si/Al values, Ba_{bio}, and component B content, pointing to diminished sea ice, enhanced water column exchange, and heightened surface plankton photosynthesis, culminating in increased productivity. These conditions mark the gradual climatic shift into the Holocene, characterized by overall warming (Bentley et al., 2009). Post-ACR, the climate witnessed a warming trend, with only minor fluctuations. However, between 5,000 cal a BP and 4,000 cal a BP (P4), a slight cooling is observed, as the (illite + chlorite)/kaolinite value increased, and kaolinite content decreased, which is in line with the $\delta^{18}O$ records. Despite this cooling signal, the sedimentary record from the Antarctic Peninsula by Shevenell et al. (1996) confirms a warmer paleoclimate overall for this period. Notably, Si/Al and Ba_{bio} levels remained high, indicating sustained productivity, a phenomenon attributed to the reduced influence of sea ice and increased significance of solar irradiance in the post-Holocene warm climate (Hu et al., 2023). After this colder climatic phase, the (illite + chlorite)/kaolinite value remained low and stable, while the value of Si/Al, the content of Ba_{bio} and component B were high. This indicates that the Antarctica has generally been characterized by warmer conditions and the hydrodynamic is strong, surface productivity is high in the study area, collectively, these indicators suggest the initiation of a climatically suitable period in the Antarctica.

In summary, the variations in clay mineral assemblages, grain size distributions, and elemental compositions within core ANT37-C5/6-07 from the Cosmonaut Sea have proven to be effective indicators of the historical dynamics of the ice sheet since the Last Glacial Maximum (LGM). Comparative analysis with prior studies in West Antarctica (Long et al., 2024) and East Antarctica, including future projections (Borchers et al., 2016; Yang et al., 2021), reveals that the ice sheet in our study area exhibits heightened sensitivity to climatic shifts. This sensitivity allows for more precise dating of climatic events in East Antarctica. Our findings challenge the notion of stability in the East Antarctic ice sheet as proposed by Rignot et al. (2019), suggesting that there remains a considerable risk of ice-shelf collapse under ongoing global warming.

5 Conclusions

Our comprehensive study and analysis of clay minerals, grain sizes, and elemental characteristics in the sediments from core ANT37-C5/6-07 in the Cosmonaut Sea have led to the following primary conclusions:

(1) The integration of clay mineral assemblages and REE profiles in the sediment points to a predominant influence of rock weathering from Prydz Bay and Enderby Land coastlines, indicating these areas as the main sediment sources.

(2) Based on the (illite + chlorite)/kaolinite value, content of Ba_{bio} and cpmponent B, Si/Al value, content of >63μm grain size fractions in the sediments of core ANT37-C5/6-07, and the $\delta^{18}O$ record of the EDML ice core, we found that the ice sheet in the study area retreated around 18600 cal a BP, had significant ablation during 16800-15000 cal a BP (P1) and 12800-11400 cal a BP (P3), and expanded during 14800-13500 cal a BP (P2) and 5000-4000 cal a BP (P4). It is largely

synchronous with the phases of climate changes in the Cosmonaut Sea since the LGM (26 ka). These findings align with previous Antarctic studies, offering evidence for understanding the climatic response of the Cosmonaut Sea and the East Antarctic region to global changes.

Data availability statement

The original contributions presented in the study are included in the article/supplementary material. Further inquiries can be directed to the corresponding author.

Author contributions

DC: Writing – original draft, Writing – review & editing. QG: Funding acquisition, Investigation, Project administration, Supervision, Writing – review & editing. ZL: Investigation, Supervision, Visualization, Writing – review & editing. BZ: Writing – review & editing. XH: Formal analysis, Investigation, Resources, Writing – review & editing.

Funding

The author(s) declare financial support was received for the research, authorship, and/or publication of this article. This work was funded by the Impact and Response of Antarctic Seas to Climate Change (IRASCC). This project provided us with cruise and funding for sampling and analysis.

Acknowledgments

We are grateful to the crew and researchers of the 37th Chinese Antarctic Expedition for the collection of samples and to the Chinese Arctic and Antarctic Administration and Polar Research Institute of China for their support and assistance.

Conflict of interest

The authors declare that the research was conducted in the absence of any commercial or financial relationships that could be construed as a potential conflict of interest.

Publisher's note

References

Alley, R. B., Marotzke, J., Nordhaus, W. D., Overpeck, J. T., Peteet, D. M., Pielke, R. A., et al. (2003). Abrupt climate change. *Science* 299, 2005–2010. doi: 10.1126/science.1081056

Andrews, J. T., Domack, E. W., Cunningham, W. L., Leventer, A., Licht, K. J., Jull, A. J., et al. (2017). Problems and possible solutions concerning radiocarbon dating of surface marinesediments, ross sea, Antarctica. *Quater. Res.* 52, 206–216. doi: 10.1006/qres.1999.2047

Bentley, M. J., Hodgson, D. A., Smith, J. A., Cofaigh, C. Ó., Domack, E. W., Larter, R. D., et al. (2009). Mechanisms of Holocene palaeoenvironmental change in the Antarctic Peninsula region. *Holocene* 19, 51–69. doi: 10.1177/0959683608096603

Bibik, V. A., Maslennikov, V. V., Pelevin, A. S., Polonsky, V. E., and Solyankin, E. V. (1988). "The current system and the distribution of waters of different modifications in the Cosmonaut Sea," in *Interdisciplinary investigations of pelagic ecosystem in the commonwealth and cosmonaut seas* (VNIRO Publishers, Moscow), 16–43

Bindoff, N. L., Rosenberg, M. A., and Warner, M. J. (2000). On the circulation and water masses over the Antarctic continental slope and rise between 80 and 150 E. *Deep Sea Res. Part II: Topical Stud. Oceanogr.* 47, 2299–2326. doi: 10.1016/S0967-0645(00)00038-2

Biscaye, P. E. (1965). Mineralogy and sedimentation of recent deep-sea clay in the Atlantic ocean and adjacent seas and oceans. *Geol. Soc. America Bull.* 76, 803–832. doi: 10.1130/0016-7606(1965)76[803:MASORD]2.0.CO;2

Bischof, J., Clark, D. L., and Vincent, J. S. (1996). Origin of ice-rafted debris: Pleistocene paleoceanography in the western Arctic Ocean. *Paleoceanography* 11, 743–756. doi: 10.1029/96PA02557

Bonn, W. J., Gingele, F. X., Grobe, H., Mackensen, A., and Fütterer, D. K. (1998). Palaeoproductivity at the Antarctic continental margin: Opal and barium records for the last 400 ka. *Palaeogeogr. Palaeoclimatol. Palaeoecol.* 139, 195–211. doi: 10.1016/S0031-0182(97)00144-2

Borchers, A., Dietze, E., Kuhn, G., Esper, O., Voigt, I., Hartmann, K., et al. (2016). Holocene ice dynamics and bottom-water formation associated with Cape Darnley polynya activity recorded in Burton Basin, East Antarctica. *Mar. Geophys. Res.* 37, 49–70. doi: 10.1007/s11001-015-9254-z

Boynton, W. V. (1984). Cosmochemistry of the rare earth elements: meteorite studies. *Develop. Geochem.* 2, 63–114. doi: 10.1016/B978-0-444-42148-7.50008-3

Broecker, W. S. (1998). Paleocean circulation during the last deglaciation: a bipolar seesaw. *Paleoceanography* 13, 119–121. doi: 10.1029/97PA03707

Chamley, H. (1997). *Clay Mineral Sedimentation in the Ocean. In: Soils and Sediments* Vol. 623, 269-302 (Springer Berlin Heidelberg). doi: 10.1007/978-3-642-60525-3_13

Chen, Z. H., Chen, Y., Wang, R. J., Huang, Y. H., Liu, X. D., Wang, L., et al. (2014). Ice-rafted detritus events and paleoceanographic records in tne bering basin since last deglaciation. *Chin. J. Polar Res.* 26, 17. doi: 10.13679/j.jdyj.2014.1.017

Chen, Z. H., Huang, Y. H., Tang, Z., Wang, H. Z., Ge, S. L., Fang, X. S., et al. (2015). Rare earth elements in the offshore surface sediments of the northeastern Antarctic Peninsula and their implications for provenance. *Mar. Geol. Quater. Geol.* 35, 145–155. doi: 10.3724/SP.J.1140.2015.03145

Chen, Q., Liu, D. Y., Chen, Y. J., Shen, X. H., Jiang, J. J., Li, X., et al. (2013). Comparative analysis of grade-standard deviation method and factors analysis method for environmental sensitive factor analysis. *Earth Environ.* 41, 319–325. Available at: http://ir.yic.ac.cn/handle/133337/6562.

Chen, Z., Shi, X., Cai, D., Han, Y., and Yang, Z. (2006). Organic carbon and nitrogen isotopes in surface sediments from the western Arctic Ocean and their implications for sedimentary environments. *Haiyang Xuebao* 25, 16. doi: 10.3321/j.issn:0253-4193.2006.06.009

Claridge, G. G. C. (1965). The clay mineralogy and chemistry of some soils from the Ross dependency, Antarctica. *New Z. J. Geol. Geophys.* 8, 186–220. doi: 10.1080/00288306.1965.10428107

Collier, R., Dymond, J., Honjo, S., Manganini, S., Francois, R., and Dunbar, R. (2000). The vertical flux of biogenic and lithogenic material in the Ross Sea: moored sediment

trap observations 1996-1998. *Deep Sea Res. Part II: Topical Stud. Oceanogr.* 47, 3491–3520. doi: 10.1016/S0967-0645(00)00076-X

Crosta, X., Denis, D., and Ther, O. (2008). Sea ice seasonality during the Holocene, Adélie Land, East Antarctica. *Mar. Micropaleontol.* 66, 222–232. doi: 10.1016/j.marmicro.2007.10.001

Cullers, R. L., Barrett, T., Carlson, R., and Robinson, B. (1987). Rare-earth element and mineralogic changes in Holocene soil and stream sediment: a case study in the Wet Mountains, Colorado, USA. *Chem. Geol.* 63, 275–297. doi: 10.1016/0009-2541(87)90167-7

Dai, Q. Q., Wang, B. S., and Zhang, Y. P. (2016). Clay mineral composition of the Prydz Bay and its Climate implications. *Mar. Geol. Front.* 32, 6. doi: 10.16028/j.1009-2722.2016.0200

Dou, Y. G., Li, J., and Li, Y. (2012). Rare earth element compositions and provenance implication of surface sediments in the eastern Beibu Gulf. *Geochimica* 41, 147–157. doi: 10.3969/j.issn.0379-1726.2012.02.006

Ducklowa, H. W., Ericksona, M., Kellyb, J., Montes-Hugo, M., Ribic, C. A., Smith, R. C., et al. (2008). Particle export from the upper ocean over the continental shelf of the west Antarctic Peninsula: A long-term record 1992–2007. *Deep Sea Res. Part II: Topical Stud. Oceanogr.* 55, 2118–2131. doi: 10.1016/j.dsr2.2008.04.028

Ehrmann, W. U. (1991). Implications of sediment composition on the southern kerguelen plateau for paleoclimate and depositional environment. *Proc. ocean drill. Program Sci. results* 119, 185–210. doi: 10.2973/odp.proc.sr.119.121.1991

Ehrmann, W. U., and Grobe, H. (1991). Cyclic sedimentation at sites 745 and 746. *Proc. Ocean Drill. Program Sci. Results* 119, 225–237. doi: 10.2973/odp.proc.sr.119.123.1991

Ehrmann, W. U., Melles, M., Kuhn, G., and Grobe, H. (1992). Significance of clay mineral assemblages in the Antarctic Ocean. *Mar. Geol.* 107, 249–273. doi: 10.1016/0025-3227(92)90075-S

Epica Community Members (2006). One-to-one coupling of glacial climate variability in Greenland and Antarctica. *Nature* 444, 195–198. doi: 10.1038/nature05301

Gladstone, R. M., Bigg, G. R., and Nicholls, K. W. (2001). Iceberg trajectory modeling and meltwater injection in the Southern Ocean. *J. Geophys. Res. Atmosph.* 106, 19903–19915. doi: 10.1029/2000JC000347

Gloersen, P., Campbell, W. J., Cavalieri, D. J., Comiso, J. C., Parkinson, C. L., and Zwally, H. J. (1993). Satellite passive microwave observations and analysis of Arctic and Antarctic sea ice 1978–1987. *Ann. Glaciol.* 17, 149–154. doi: 10.3189/S0260305500012751

Hambrey, M. J., Ehrmann, W., and Larsen, B. (1991). Cenozoic glacial record of the Prydz Bay continental shelf, East Antarctica. *Proc. ocean drill. Program Sci. results* 119, 77–132. doi: 10.2973/odp.proc.sr.119.200.1991

Heaton, T. J., Köhler, P., Butzin, M., Bard, E., Reimer, R. W., Austin, W. E., et al. (2020). Marine20—The marine radiocarbon age calibration curve (0–55,000 cal BP). *Radiocarbon* 62, 779–820. doi: 10.1017/RDC.2020.68

Hillenbrand, C. D., Smith, J. A., Kuhn, G., Esper, O., Gersonde, R., Larter, R. D., et al. (2010). Age assignment of a diatomaceous ooze deposited in the western Amundsen Sea Embayment after the Last Glacial Maximum. *J. Quater. Sci.: Published Quater. Res. Assoc.* 25, 280–295. doi: 10.1002/jqs.1308

Hu, B. Y., Long, F. J., Han, X. B., Zhang, Y. C., Hu, L. M., Xiang, B., et al. (2022). The evolution of paleoproductivity since the Middle Holocene in the Cosmonaut Sea, Antarctic. *Earth Sci. Front.* 29, 113–122. doi: 10.13745/j.esf.sf.2022.1.12

Hu, L. M., Zhang, Y., Wang, Y. Z., Ma, P. Y., Wu, W. D., Ge, Q., et al. (2023). Paleoproductivity and deep-sea oxygenation in Cosmonaut Sea since the Last Glacial Maximum: Impact on atmospheric CO_2. *Front. Mar. Sci.* 10. doi: 10.3389/fmars.2023.1215048

Huang, M. X., Wang, R. J., Xiao, W. S., Wu, L., and Chen, Z. H. (2016). Retreat process of Ross ice shelf and Hydrodynamic changes on northwestern Ross continental shelf since the Last Glacial. *Mar. Geol. Quater. Geol.* 36, 97–108. doi: 10.16562/j.cnki.0256-1492.2016.05.010

Hunt, B. P. V., Pakhomov, E. A., and Trotsenko, B. G. (2007). The macrozooplankton of the cosmonaut sea, east Antarctica (30°E–60°E), 1987–1990. *Deep Sea Res. Part I: Oceanogr. Res. Pap.* 54, 1042–1069. doi: 10.1016/j.dsr.2007.04.002

Huybrechts, P. (2002). Sea-level changes at the lgm from ice-dynamic reconstructions of the Greenland and antarctic ice sheets during the glacial cycles. *Quater. Sci. Rev.* 21, 203–231. doi: 10.1016/S0277-3791(01)00082-8

Iacoviello, F., Giorgetti, G., Memmi, I. T., and Nieto, F. (2010). "Authigenic and detrital smectites in Cenozoic marine sediments from McMurdo continental margin (Antarctica)," in *International Polar Year - Oslo Science conference 2010*. Available at: https://www.researchgate.net/publication/294729284_Authigenic_and_detrital_smectites_in_Cenozoic_marine_sediments_from_McMurdo_continental_margin_Antarctica.

Ju, M. S. (2019). *Late Quaternary cyclic variations of ice sheet and oceanography in the Amundsen Sea sector, Antarctica* (First Institute of Oceanography, MNR)

Jung, J., Ko, Y., Lee, J., Yang, K., Park, Y. K., Kim, S., et al. (2021). Multibeam bathymetry and distribution of clay minerals on surface sediments of a small bay in Terra Nova bay, Antarctica. *Minerals* 11, 72. doi: 10.3390/min11010072

Kim, S. Y., Lim, D., Rebolledo, L., Park, T., Esper, O., Muñoz, P., et al. (2021). A 350-year multiproxy record of climate-driven environmental shifts in the Amundsen Sea Polynya, Antarctica. *Global Planet. Change* 205, 103589. doi: 10.1016/j.gloplacha.2021.103589

Legendre, L. (1998). Flux of particulate organic material from the euphoric zone of ocean: Estimation phytoplankton biomass. *J. Geophys. Res.* 103, 2897–2903. doi: 10.1029/97JC02706

Leonardo, L., Mauro, F., Mariangela, R., and Cristina, B. (2000). Particle fluxes and biogeochemical processes in an area influenced by seasonal retreat of the ice margin (northwestern Ross Sea, Antarctic). *J. Mar. Syst.* 27, 221–234. doi: 10.1016/S0924-7963(00)00069-5

Li, G. G., Ji, Y. J., Li, Y. H., Leng, Q. N., Bu, R. Y., and Li, Y. X. (2017). Geochemical characteristics of rare earth elements in the sediments of Prydz Bay, Antarctica. *Chin. J. Polar Res.* 29, 23. doi: 10.13679/j.jdyj.2017.1.023

Li, Q. M., Xiao, W. S., Wang, R. J., and Chen, Z. H. (2021). Diatom based reconstruction of climate evolution through the Last Glacial Maximum to Holocene in the Cosmonaut Sea, East Antarctica. *Deep Sea Res. Part II: Topical Stud. Oceanogr.* 194, 104960. doi: 10.1016/j.dsr2.2021.104960

Licht, K. J., and Andrews, J. T. (2002). The ^{14}C record of late pleistocene ice advance and retreat in the central ross sea, Antarctica. *Arctic Antarctic Alpine Res.* 34, 324–333. doi: 10.1080/15230430.2002.12003501

Long, F. J., Xiang, B., Wang, Y. Z., Zhang, Y. C., Hu, L. M., Sun, X., et al. (2024). Evolution of paleoproductivity in the Antarctica Ross Sea since the Last Glacial Maximum. *Mar. Geol. Quater. Geol.* 44, 109–120. doi: 10.16562/j.cnki.0256-1492.2022111601

Melles, M. (1991). Late Quaternary paleoglaciology and paleoceanography at the continental margin of the southern Weddell Sea, Antarctica. *Polarstern Abstr.* 6, 128–129. doi: 10.2312/BzP_0081_1991

Pedro, J. B., Ommen, T. D. V., Rasmussen, S. O., Morgan, V. I., and Delmotte, M. (2011). The last deglaciation: timing the bipolar seesaw. *Climate Past* 7, 397–430. doi: 10.5194/cp-7-671-2011

Pudsey, C. J., Murray, J. W., Appleby, P., and Evans, J. (2006). Ice shelf history from petrographic and foraminiferal evidence, Northeast Antarctic Peninsula. *Quater. Sci. Rev.* 25, 2357–2379. doi: 10.1016/j.quascirev.2006.01.029

Rignot, E., Mouginot, J., Scheuchl, B., Broeke, M. V. D., and Morlighem, M. (2019). Four decades of antarctic ice sheet mass balance from 1979–2017. *Proc. Natl. Acad. Sci.* 116, 201812883. doi: 10.1073/pnas.1812883116

Shepherd, A., Wingham, D., and Rignot, E. (2004). Warm ocean is eroding west antarctic ice sheet. *Geophys. Res. Lett.* 31, 1-4. doi: 10.1029/2004GL021106

Sheraton, J. W., Black, L. P., and McCulloch, M. T. (1984). Regional geochemical and isotopic characteristics of high-grade metamorphics of the Prydz Bay area: the extent of Proterozoic reworking of Qrchaean continental crust in East Antarctica. *Precambrian Res.* 26, 169–198. doi: 10.1016/0301-9268(84)90043-3

Shevenell, A. E., Domack, E. W., and Kernan, G. M. (1996). Record of Holocene palaeoclimate change along the Antarctic Peninsula: evidence from glacial marine sediments, Lallemand Fjord. *Pap. Proc. R. Soc. Tasmania* 130, 55–64. doi: 10.26749/rstpp.130.2.55

Shi, L., Xie, G. H., and Li, H. M. (1997). Trace element geochemistry of the volcanic rocks from the Taylor Valley and Ross Islands, Antarctica. *Geochimica* 13, 11. doi: 10.1088/0256-307X/16/9/027

Singer, A. (1984). The paleoclimatic interpretation of clay minerals in sediments—a review. *Earth Sci. Rev.* 21, 251–293. doi: 10.1016/0012-8252(84)90055-2

Stagg, H. M. J., Colwel, J. B., Direen, N. G., O'brien, P. E., Bernardel, G., Borissova, I., et al. (2004). Geology of the continental margin of Enderby and Mac. Robertson Lands, East Antarctica: insights from a regional data set. *Mar. Geophys. Res.* 25, 183–219. doi: 10.1007/s11001-005-1316-1

Stammerjohn, S. E., Maksym, T., Massom, R. A., Lowry, K. E., Arrigo, K. R., Yuan, X., et al. (2015). Seasonal sea ice changes in the Amundsen Sea, Antarctica, over the period of 1979–2014. *Elem.: Sci. Anthropocene* 3, 55. doi: 10.12952/journal.elementa.000055

Stiver, M., and Reimer, P. J. (1993). Extended ^{14}C data base and revised Calib 3.0 ^{14}C age calibration program. *Radiocarbon* 35, 215–230. doi: 10.1017/S0033822200013904

Suzuki, S., Hokada, T., Ishikawa, M., and Ishizuka, H. (1999). Geochemical study of granulites from Mt. Riiser-Larsen, Enderby Land, East Antarctica: Implication for protoliths of the Archean Napier Complex. *Polar Geosci.* 12, 101–125. doi: 10.15094/00003045

Takano, Y., Tyler, J. J., Kojima, H., Yokoyama, Y., Tanabe, Y., Sato, T., et al. (2012). Holocene lake development and glacial-isostatic uplift at Lake Skallen and Lake Oyako, Lützow-Holm Bay, East Antarctica: Based on biogeochemical facies and molecular signatures. *Appl. Geochem.* 27, 2546–2559. doi: 10.1016/j.apgeochem.2012.08.009

Taylor, S. R., and McLennan, S. M. (1985). The continental crust: its composition and evolution. *J. Geol.* 94, 57–72. doi: 10.1016/0031-9201(86)90093-2

Tingey, R. J. (1991). The regional geology of Archean and Proterozoic rocks in Antractica. *geol. Antarctica*, 1–73. Available at: http://search.proquest.com/georef/docview/50177959/13223285216616C858/15?accountid=14245.

Trail, D. S., and McLeod, I. R. (1969). Geology of the Lambert Glacier region. In: C. Craddock (Editor), *Geologic Maps of Antarctica, 11* (Antarctic Map Folio Ser., 12). (Am. Geogr.Soc., New York).

Turner, J., Phillips, T., Marshall, G. J., Hosking, J. S., and Deb, P. (2017). Unprecedented springtime retreat of antarctic sea ice in 2016: Antarctic Sea ice retreat. *Geophys. Res. Lett* 44, 6868-6875. doi: 10.1002/2017GL073656

Wang, Z., Zhang, X., Guan, Z., Sun, B., Yang, X., and Liu, C. (2015). An atmospheric origin of the multi-decadal bipolar seesaw. *Sci. Rep*. 5 (8909), 1-5. doi: 10.1038/SREP08909

Williams, G. D., Nicol, S., Aoki, S., Meijers, A. J. S., Bindoff, N. L., Iijima, Y., et al. (2010). Surface oceanography of BROKE-West, along the Antarctic margin of the south-west Indian Ocean (30–80°E). *Deep Sea Res. Part II: Topical Stud. Oceanogr*. 57, 738–757. doi: 10.1016/j.dsr2.2009.04.020

Williams, G. D., Nicol, S., Raymond, B., and Meiners, K. (2008). Summertime mixed layer development in the marginal sea ice zone off the Mawson coast, East Antarctica. *Deep Sea Res. Part II: Topical Stud. Oceanogr*. 55, 365–376. doi: 10.1016/j.dsr2.2007.11.007

Wong, C. S., Whitney, F. A., Crawford, D. W., Iseki, K., Matear, R. J., Johnson, W. K., et al. (1999). Seasonal and interannual variability in particle fluxes of carbon, nitrogen and silicon from time series of sediment traps at Ocean Station P 1982–1993: relationship to changes in subarctic primary productivity. *Deep Sea Res. Part II: Topical Stud. Oceanogr*. 46, 2735–2760. doi: 10.1016/S0967-0645(99)00082-X

Xiu, C., Chen, X. X., Zhou, M. J., Meina, X., Zhang, X., and Xing, J. (2017). REE geochemical characteristics of core R11 in the Ross Sea Antarctic. *Mar. Geol. Front*. 33, 1–8. doi: 10.16028/j.1009-2722.2017.05001

Xu, F. J., Hu, B. Q., Zhao, J. T., Liu, X. T., Xu, K. H., Xiong, Z. F., et al. (2021). Provenance and weathering of sediments in the deep basin of the northern South China Sea during the last 38 kyr. *Mar. Geol.* 440, 106602. doi: 10.1016/j.margeo.2021.106602

Yang, J. Y., Jiang, F. Q., Yan, Y., Zheng, H., and Chang, F. M. (2022). Provenance and paleoclimatic significance of clay minerals from Izu-Ogasawara Ridge since Pliocene. *Earth Sci. Front.* 29, 73–83. doi: 10.13745/j.esf.sf.2022.1.8

Yemane, K., Kahr, G., and Kelts, K. (1996). Imprints of post-glacial climates and palaeogeography in the detrital clay mineral assemblages of an Upper Permian fluviolacustrine Gondwana deposit from northern Malaw. *Palaeogeogr. Palaeoclimatol. Palaeoecol.* 125, 27–49. doi: 10.1016/S0031-0182(96)00023-5

Yoshida, Y., and Moriwaki, K. (1979). *Some consideration on elevated coastal features and their dates around syowa station, Antarctica* (Memoirs of National Institute of Polar Research) 13, 220–226.

Zhang, J. R. (2011). Element features in different grain size fractions of lacustrine sediment and their environmental implication: A case study of Huangqihai Lake. *Acta Sedimentol. Sin.* 29, 381–387. doi: 10.1007/s11589-011-0776-4

frontiers | Frontiers in Marine Science

TYPE Original Research
PUBLISHED 28 June 2024
DOI 10.3389/fmars.2024.1361892

OPEN ACCESS

EDITED BY
Zhifang Xiong,
Ministry of Natural Resources, China

REVIEWED BY
Xiaoxu Shi,
Southern Ocean Science and Engineering Guangdong Laboratory (Zhuhai), China
Jindong Jiang,
Ministry of Natural Resources, China

*CORRESPONDENCE
Xufeng Zheng
xufengzheng@hainanu.edu.cn

RECEIVED 27 December 2023
ACCEPTED 24 May 2024
PUBLISHED 28 June 2024

CITATION
Li N, Zheng X, Su T, Ma X, Zhu J and Cheng D (2024) A key hub for climate systems: deciphering from Southern Ocean sea surface temperature variability.
Front. Mar. Sci. 11:1361892.
doi: 10.3389/fmars.2024.1361892

A key hub for climate systems: deciphering from Southern Ocean sea surface temperature variability

Ninghong Li[1], Xufeng Zheng[2]*, Ting Su[3], Xiao Ma[4], Junying Zhu[2] and Dongdong Cheng[1]

[1]State Key Laboratory of Marine Resource Utilization in South China Sea and School of Information and Communication Engineering, Hainan University, Haikou, China, [2]State Key Laboratory of Marine Resource Utilization in South China Sea and School of Marine Science and Engineering, Hainan University, Haikou, China, [3]School of Information and Communication Engineering, Hainan University, Haikou, China, [4]State Key Laboratory of Satellite Ocean Environment Dynamics, Second Institute of Oceanography, Ministry of Natural Resources, Hangzhou, China

The Southern Ocean connects the Pacific, Atlantic, and Indian Oceans, serving as a key hub for the global overturning circulation. The climate of the Southern Ocean is closely linked to the low-latitude equatorial Pacific, as well as the high-latitude regions of the North Atlantic, making it an important component of the global climate system. Due to the interactions of various processes such as atmospheric, oceanic, and ice cover, the Southern Ocean exhibits a complex and variable sea surface temperature structure. Satellite observations indicate that since 1980, the sea surface temperature of the Southern Ocean has been cooling, contrary to the global warming trend. However, due to the relatively short length of satellite observations, the specific mechanisms are not yet clear. Here, we used the EOF method to analyze sea surface temperature data since 1870 (HadISST1 and ERSSTV5), with three main separated modes explaining over 70% of the sea temperature variability. Among them, the first mode shows widespread positive sea surface temperature anomalies in the Southern Ocean, with a time series change consistent with global temperature anomalies, representing a mode of global warming. The second mode corresponds to the Atlantic Multidecadal Oscillation (AMO) but with a lag of approximately 4 years. The third mode is consistent with the variability of the El Niño-Southern Oscillation (ENSO). Furthermore, our study indicates that despite the ongoing global warming since 1980, the negative phase of AMO and positive phase of ENSO may counteract the effects of global warming, leading to an overall cooling trend in the sea surface temperature of the Southern Ocean.

KEYWORDS

Southern Ocean, empirical orthogonal function, sea surface temperature, AMO, ENSO

1 Introduction

The continuous emission of greenhouse gas into the atmosphere since the industrial revolution results in the rise of global temperature (IPCC, 2021). The ocean acting as a regulator of the climate system can slow down the warming of the global atmospheric surface temperature by absorbing excess heat due to its vast area and large heat capacity (Cheng et al., 2019). Over the past few decades, the ocean has absorbed more than 90% of the excess heat from the energy imbalance and more than half of the globally increased ocean heat is stored in the Southern Ocean (Rye et al., 2014).

The Southern Ocean has a unique and complex ocean dynamic environment, where different ocean processes influence the heat absorption and redistribution (Rintoul, 2018). Observations show that the warming in the Southern Ocean are not uniform and vary in different regions. The most significant warming areas are mainly concentrated in the Indian Ocean sectors of the Southern Ocean, followed by the Pacific Ocean sectors, while the Atlantic Ocean sectors of the Southern Ocean has relatively smaller warming amplitudes (Purkey and Johnson, 2010; Schmidtko et al., 2014; Cheng et al., 2020). Furthermore, the Southern Ocean is connected to the Pacific, Indian, and Atlantic Oceans. The distribution and variation of heat in the Southern Ocean can not only influence the climate changes in other ocean basins but also be affected by the climate and ocean processes of other ocean basins through atmospheric bridges and other mechanisms (Li et al., 2014; Liu et al., 2018).

Reanalysis data show that the fastest warming region in the Southern Ocean from 1979 to 2001 is located between 40°S and 45°S, followed by the area near 60°S, with slower warming in other regions (Fogt and Bromwich, 2006). Moreover, buoy data has revealed that since the 1950s, the warming of sub-surface waters in the Southern Ocean has been significantly higher than in most other global ocean regions, with the warming occurring near the Antarctic Circumpolar Current (ACC) (Gille, 2002). Other studies utilizing observational data collected since the 1960s have similarly shown that upper ocean waters in mid-latitudes of the Southern Ocean are rapidly warming, accompanied by surface water freshening (Böning et al., 2008; Wijffels et al., 2008). However, some studies have found that south of 60°S in the Southern Ocean, there is a weaker or cooling trend in surface warming (Purkey and Johnson, 2010; Schmidtko et al., 2014). Recent work based on satellite observation revealed slight cooling trend since 1980 contrary to the global warming trend (Yang et al., 2023). However, the satellite observation is too short to elucidate the specific mechanisms contributing to this cooling trend. Here, we utilize data spanning from 1870 to 2022, totaling 153 years, to decompose various modes of Southern Ocean SST using Empirical Orthogonal Function (EOF) analysis. Our work aims to investigate the main mechanisms influencing the distribution and changes in Southern Ocean SST based on the spatial characteristics of temperature anomalies associated with different modes and their temporal trends. Based on above results, we proposed that despite the ongoing global warming since 1980, the negative phase of AMO and positive phase of ENSO may counteract the effects of global warming, leading to an overall cooling trend in the sea surface temperature of the Southern Ocean.

2 Data and methods

This study utilized sea surface temperature analyses from the Hadley Centre Sea ice and SST data set version 1(HadISST1) and Extended Reconstructed Sea Surface Temperature version 5 (ERSSTV5) datasets for Empirical Orthogonal Function (EOF) analysis. HadISST1 primarily consists of satellite observations, but data prior to the satellite era were reconstructed using ship-based measurements, which have uncertainty due to sparse coverage (Kennedy, 2014). Therefore, the ERSSTV5 dataset was used for additional comparison. HadISST1 dataset including monthly observations from 1870 to the present employs a standard method for calculating SST and undergoes quality control and correction processes based on observational data (Rayner et al., 2003). We choose the SST for latitude range of 40°S to 75°S and longitude range of 180° to -180°from January 1870 to December 2022 with a spatial resolution of 1° × 1° and a temporal resolution of monthly intervals for EOF analyses. The ERSSTV5 dataset is reconstructed by combining data from ships, buoys, satellite measurements, and other observation platforms. The spatial resolution of ERSSTV5 is approximately 2° × 2°. The selected time range and temporal resolution are consistent with HadISST1. To process the data, we first calculated anomalies relative to the annual mean sea surface temperature and then performed the EOF analysis. Moreover, we compare the time series of our extracted SST modes with climate index, i.e., AMO, ENSO, to infer their potential driving mechanisms. The AMO index was calculated based on the SST anomalies averaged over the North Atlantic region (0°-60°N, 80°W-0°) (Zhang and Delworth, 2007) and the Southern Oscillation Index (SOI) was used as an indicator of ENSO.

3 Results and discussion

EOF analysis conducted on the area-weighted annual mean observed Sea Surface Temperature data south of 40°S for the HadISST1 spanning the years 1870 to 2022 reveals that the primary EOF mode (EOF1, Figure 1A) of HadISST1 exhibits predominantly positive values across the entire region south of 40°S, with minor cooling anomalies observed in the Bellingshausen Sea and Amundsen Sea. The first principal component (PC1,

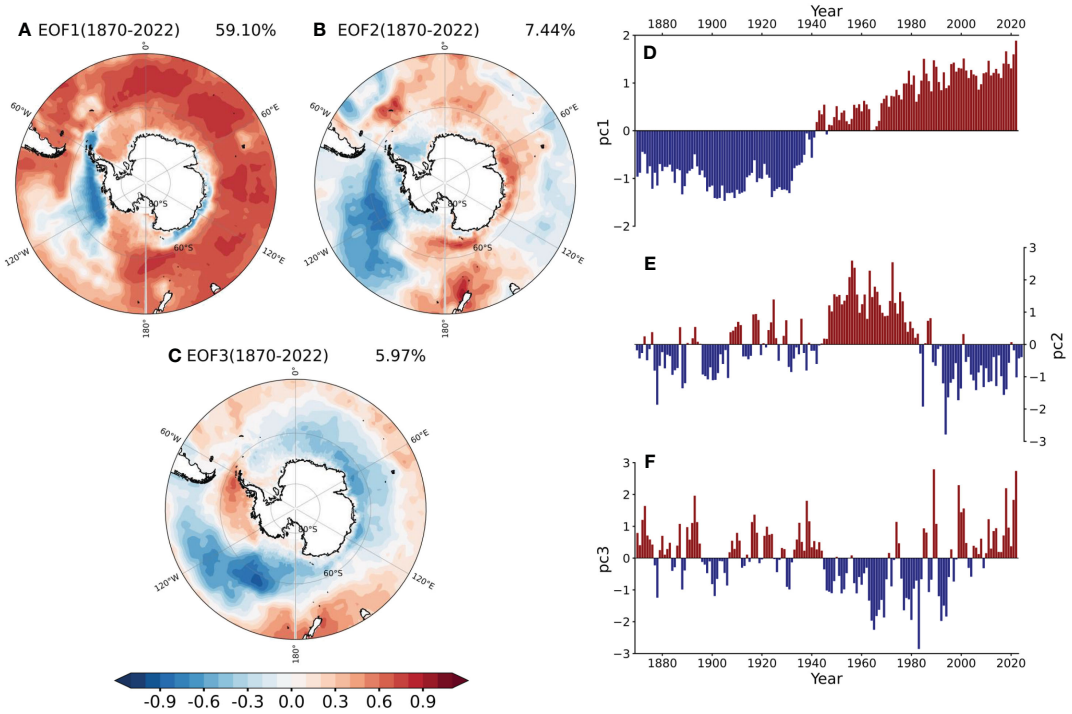

FIGURE 1
(HadISST1 dataset) EOF analysis results of sea surface temperature in the Southern Ocean from 1870 to 2022. **(A–C)** show the spatial temperature anomaly distribution (corresponding to positive PC values) and the contribution rate for EOF1, EOF2, and EOF3, respectively. Red indicates positive anomalies, while blue indicates negative anomalies. **(D–F)** show the corresponding time series fluctuations for each mode, with temperature anomalies reversed when PC values are negative.

Figure 1D) exhibits a significant increasing trend, particularly noticeable after 1942, and its temporal variability is highly correlated with Global Temperature Anomaly (correlation coefficient, R=0.84, p<0.01). The dominant spatio-temporal SST variability in ERSSTV5 (Figure 2) closely resembles that of HadISST1. The observed SST pattern in the Southern Ocean is primarily characterized by widespread warming, which explains half of the total variance (59.1% for HadISST1 and 43.33% for ERSSTV5). Furthermore, the regression coefficients between the Global Temperature Anomaly and SST of HadISST1 demonstrate a similar pattern to that of Empirical Orthogonal Function 1 (EOF1) (Figures 3A, B). Due to the utilization of distinct data sources, analysis procedures, and historical bias corrections by HadISST1 and ERSSTV5, the strong agreement between them provides assurance in interpreting this phenomenon as indicative of "global warming".

The second EOF (EOF2, Figure 1B) of HadISST1, accounting for 7.4% of the total variance, displays a symmetric pattern characterized by positive anomalies predominantly in regions linked to the South Atlantic, along the coast of New Zealand, the Ross Sea, and the Antarctic ice edge. Conversely, negative anomalies are observed in the Bellingshausen Sea and Amundsen Sea. The second principal component (PC2, Figure 1E) displays significant interdecadal variability, exhibiting prominent positive anomalies between 1940 and 1980 and negative anomalies from 1980 to 2022. The spatial and temporal variability of the EOF2 and its corresponding principal component in the HadISST1 dataset closely resemble the EOF3 of ERSSTV5 (Figure 2C), which accounts for 7.31% of the total variance in ERSSTV5.

The regression coefficients between AMO and SST of HadISST1 exhibit similar pattern as EOF2. Furthermore, the temporal variation of PC2 is highly correlated to AMO. In short, EOF2 of HadISST1 and EOF3 of ERSSTV5 are mainly dominated by the AMO Figures 3C, D.

However, it should be noted that the AMO leads the PC2 of HadISST1 by approximately 4 years (Figure 4). The delayed impact of AMO on SST in the Southern Ocean could be attributed to the gradual propagation of Rossby waves. The AMO is the primary mode of interannual sea surface temperature variability in the Atlantic Ocean, exhibiting a period of around 60 years (Schlesinger and Ramankutty, 1994). The AMO can impact the Southern Ocean by modifying circulation patterns in the North Atlantic (Simpkins et al., 2016). The positive phase of the AMO is associated with the strengthening of North Atlantic eddies and the circulation in the Celtic Sea, leading to the generation of remote Rossby waves in the Southern Ocean. These Rossby waves disturb the circulation patterns in the Southern Ocean, consequently altering the

10.3389/fmars.2024.1361892

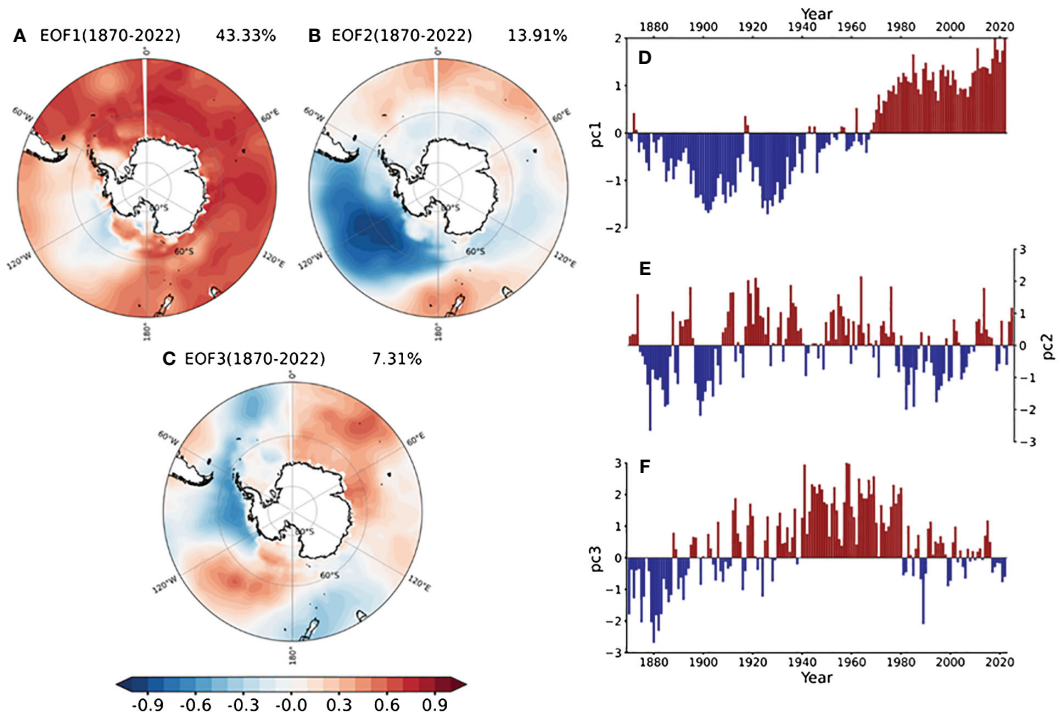

FIGURE 2
(ERSSTV5 dataset) EOF analysis results of sea surface temperature in the Southern Ocean from 1870 to 2022. **(A–C)** show the spatial temperature anomaly distribution (corresponding to positive PC values) and the contribution rate for EOF1, EOF2, and EOF3, respectively. **(D–F)** show the corresponding time series fluctuations for each mode.

distribution of SST and heat transport (Simpkins et al., 2014). The delayed response of the Southern Ocean SST to the AMO can be explained by the time needed for distant atmospheric teleconnections to occur and the sluggish propagation of Rossby waves, which can take several years to reach the Southern Ocean (Zhang et al., 2017). Moreover, the Southern Ocean is situated at high latitudes south of the equator, and its distinctive seasonal distribution may lead to a delay in the expression of the AMO signal in the SST of the Southern Ocean. The seasonal fluctuations and specific features necessitate a prolonged period for the Southern Ocean to react to the AMO signal.

The EOF3 of HadISST1 (Figure 1C), explaining 5.97% of the total variance, shows positive anomalies in the peripheral areas of the Southern Ocean, particularly between latitudes 50°S and 40°S, as well as in the Bellingshausen Sea and the Amundsen Sea. Conversely, negative anomalies are observed in the waters off the western coast of Australia and in the southern Indian Ocean, displaying a symmetrical pattern. The principal component PC3 (Figure 1F), which displays significant interannual variability, is strongly correlated with the El Niño-Southern Oscillation (ENSO index, SOI). In addition, the regression coefficients between SOI and SST in HadISST1 exhibit a similar pattern to the EOF3 of HadISST1. Therefore, we suggest that this SST pattern is primarily influenced by ENSO Figures 3E, F.

Previous research has demonstrated that the ENSO can impact the Southern Ocean. ENSO events lead to convective heating in the tropical atmosphere, causing abnormal pressure changes that move towards the south and east. These pressure fluctuations interact with the Amundsen Sea Low (ASL) system, affecting SST in the Southern Ocean through wind-induced and thermodynamic reactions. This effect is also apparent in simulations of future climate change (Li, 2000; Ciasto and England, 2011; Wang et al., 2022). ENSO events can induce anomalous variations in sea surface temperatures in the equatorial Pacific, subsequently influencing sea surface temperatures in the Southern Ocean via ocean currents.

During El Niño events, the elevated SST in the central-eastern equatorial Pacific induce alterations in atmospheric circulation, causing a rise in SST in the eastern sector of the Southern Ocean. Conversely, during La Niña events, the reduction in SST in the central-eastern equatorial Pacific leads to a decline in SST in the eastern part of the Southern Ocean (Wang et al., 2017; Ferster et al., 2018). These changes align with the temperature anomalies identified in EOF3 (Figure 1C). Consequently, the findings of the third mode further substantiate the impact of ENSO events on temperature fluctuations in the Southern Ocean, albeit the contribution is relatively minor.

10.3389/fmars.2024.1361892

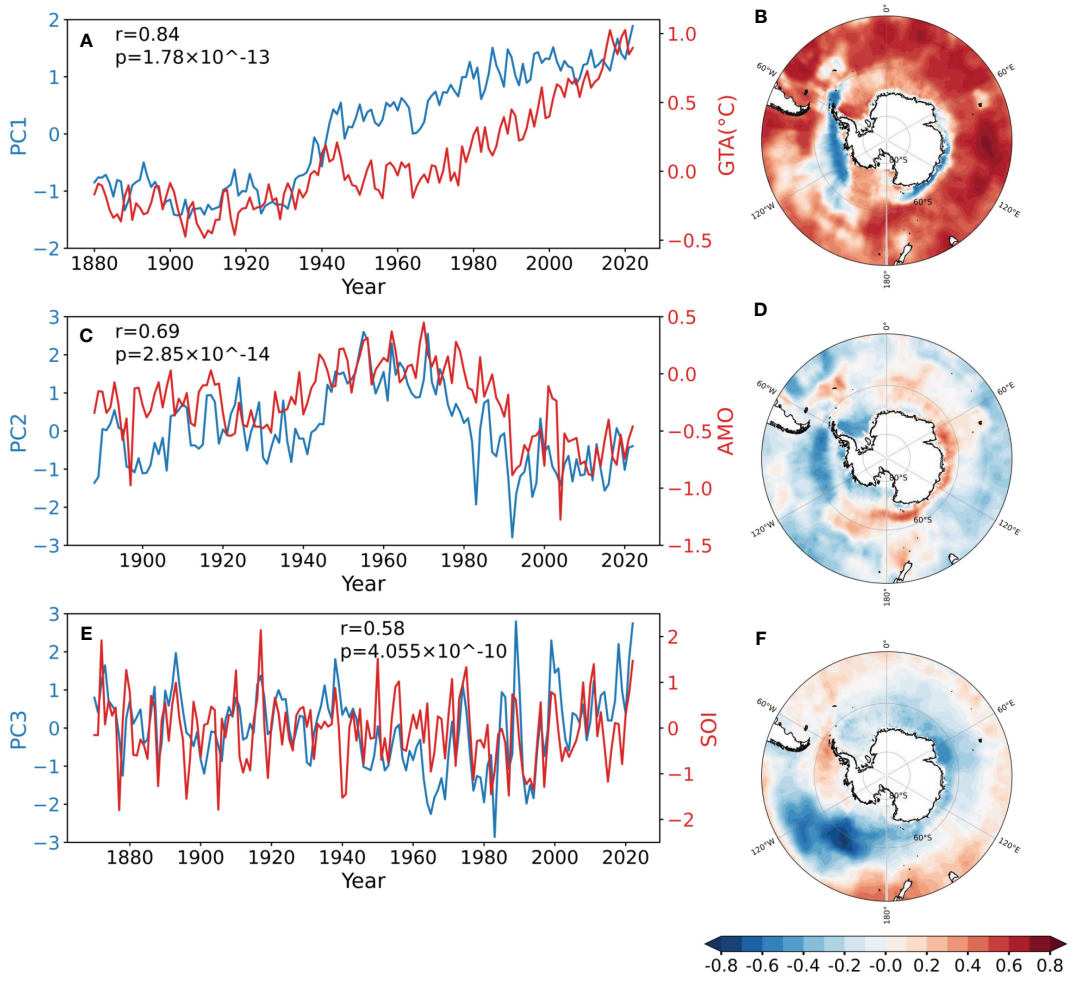

FIGURE 3
(HadISST1 dataset) Spatial correlation between relevant indicators and sea surface temperature in the Southern Ocean in the EOF analysis from 1870 to 2022. **(A, C, E)** show the correlation analysis between GTA (Global Temperature Anomaly), AMO, SOI, and PC1, PC2, PC3, respectively, in terms of time scale. **(B, D, F)** show the spatial correlation distribution between Southern Ocean SST and GTA, AMO, SOI, respectively.

Both HadISST1 and ERSSTV5 dataset clearly reveal the dominant role of global warming on the SST of the Southern Ocean over the past century (Figures 1, 2). This warming anomaly is more obvious after 1942. However, recent studies based on satellite data have shown a cooling trend in the Southern Ocean since 1982 (Yang et al., 2023), which appears to contradict to the warming trend indicated by EOF1. According to our results, the PC2 of HadISST1 and PC3 of ERSSTV5, which were interpreted as SST mode influenced by AMO here, shifted to negative phase after approximately 1980. Therefore, we propose that the negative phase of AMO since 1980 will possibly offset the warming trend and resulting in cooling trending in the Southern Ocean.

4 Summary

The SST in the Southern Ocean plays a crucial role in the global climate system, and its variations are influenced by multiple factors. By analyzing the HadISST1 and ERSSTV5 datasets (Figure 5) from 1870 to 2022 using the EOF method, we found that the spatiotemporal characteristics of Southern Ocean SST are closely related to global temperature anomalies, the AMO, and the ENSO. Global temperature anomalies are identified as the primary driver of Southern Ocean SST changes, exhibiting a persistent increasing trend. In addition, both AMO and ENSO have significant impacts on Southern Ocean SST, with a lagged response of four years to AMO. The contributions of these two modes differ between the two datasets, possibly due to variations in data sources and resolutions. Specifically, since 1980, there has been a clear global warming trend; however, the negative phase of AMO and the positive phase of ENSO may have counteracted the effects of global warming, leading to a cooling trend in Southern Ocean SST since 1980. These findings suggest that global warming, AMO, and ENSO are the primary factors influencing Southern Ocean SST variations.

10.3389/fmars.2024.1361892

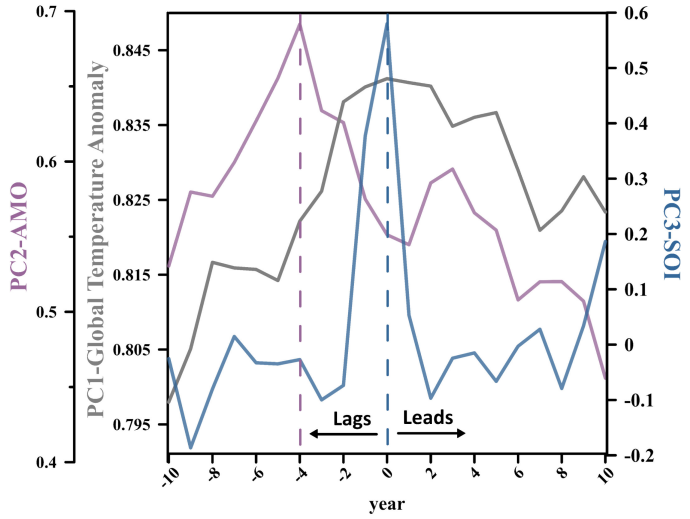

FIGURE 4
(HadISST1 dataset) Delayed and advanced correlations between various indicators and their corresponding time series in the EOF analysis from 1870 to 2022. The negative axis represents PC lagging behind the corresponding indicator, while the positive axis represents PC leading. The vertical axis represents the correlation coefficient, and the gray and blue dashed lines represent the maximum correlation.

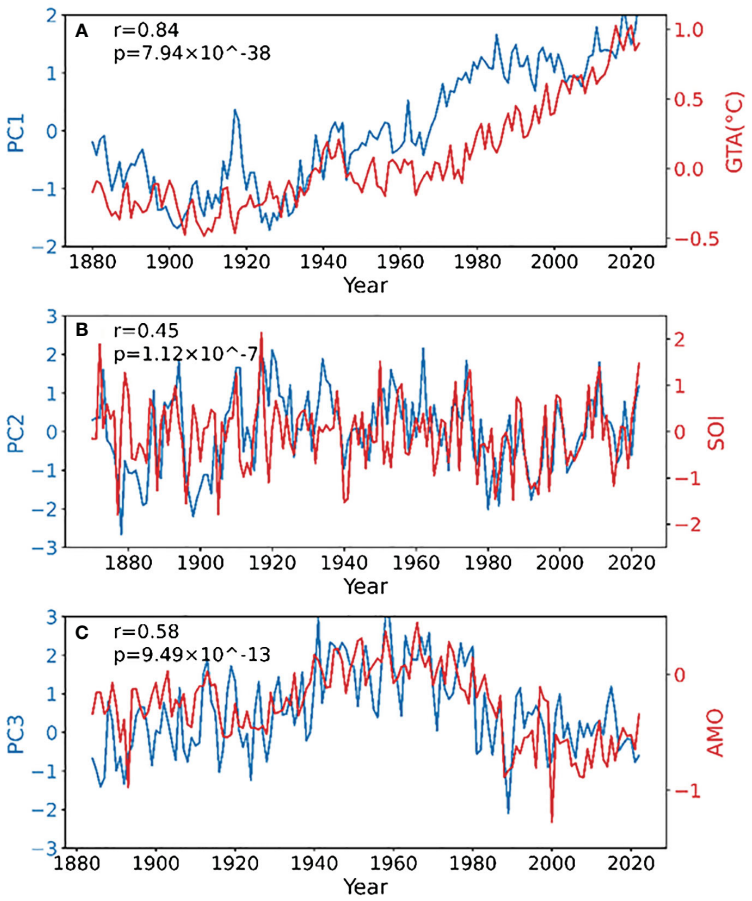

FIGURE 5
(ERSSTV5 dataset) Correlation between PC and relevant indicators in EOF analysis from 1870 to 2022. The correlation between **(A)** PC1 and GTA, **(B)** PC2 and AMO, **(C)** PC3 and SOI.

Data availability statement

The original contributions presented in the study are included in the article/supplementary material, further inquiries can be directed to the corresponding author.

Author contributions

NL: Writing – original draft. XZ: Writing – original draft. TS: Writing – original draft. XM: Writing – original draft. JZ: Writing – original draft. DC: Software, Writing – review & editing.

Funding

The author(s) declare financial support was received for the research, authorship, and/or publication of this article. This research is funded by Hainan Province's Key Research and Development Project (ZDYF2022SHFZ091), the National Natural Science Foundation of China (42276061), Hainan University Collaborative Innovation Centre Project (XTCX2022HYB08).

Conflict of interest

The authors declare that the research was conducted in the absence of any commercial or financial relationships that could be construed as a potential conflict of interest.

Publisher's note

All claims expressed in this article are solely those of the authors and do not necessarily represent those of their affiliated organizations, or those of the publisher, the editors and the reviewers. Any product that may be evaluated in this article, or claim that may be made by its manufacturer, is not guaranteed or endorsed by the publisher.

References

Böning, C. W., Dispert, A., Visbeck, M., Rintoul, S. R., and Schwarzkopf, F. U. (2008). The response of the Antarctic Circumpolar Current to recent climate change. *Nat. Geosci.* 1, 864–869. doi: 10.1038/ngeo362

Cheng, L., Abraham, J., Hausfather, Z., and Trenberth, K. E. (2019). How fast are the oceans warming? *Science* 363, 128–129. doi: 10.1126/science.aav7619

Cheng, L., Abraham, J., Zhu, J., Trenberth, K. E., Fasullo, J., Boyer, T., et al. (2020). Record-setting ocean warmth continued in 2019. *Adv. Atmospheric Sci.* 37, 137–142. doi: 10.1007/s00376-020-9283-7

Ciasto, L. M., and England, M. H. (2011). Observed ENSO teleconnections to Southern Ocean SST anomalies diagnosed from a surface mixed layer heat budget. *Geophysical Res. Lett.* 38, L09701-1-L09701-5. doi: 10.1029/2011GL046895

Ferster, B. S., Subrahmanyam, B., and Macdonald, A. M. (2018). Confirmation of ENSO-Southern Ocean teleconnections using satellite-derived SST. *Remote Sens.* 10, 331. doi: 10.3390/rs10020331

Fogt, R. L., and Bromwich, D. H. (2006). Decadal variability of the ENSO teleconnection to the high-latitude South Pacific governed by coupling with the southern annular mode. *J. Climate* 19, 979–997. doi: 10.1175/JCLI3671.1

Gille, S. T. (2002). Warming of the southern ocean since the 1950s. *Science* 295, 1275–1277. doi: 10.1126/science.1065863

IPCC. (2021). Climate change 2021—The physical science basis. *Chem. Int.* 43, 22–23. doi: 10.1515/CI-2021-0407

Kennedy, J. J. (2014). A review of uncertainty in *in situ* measurements and data sets of sea surface temperature. *Rev. Geophysics* 52, 1–32. doi: 10.1002/rog.v52.1

Li, X., Holland, D. M., Gerber, E. P., and Yoo, C. (2014). Impacts of the north and tropical Atlantic Ocean on the Antarctic Peninsula and sea ice. *Nature* 505, 538–542. doi: 10.1038/nature12945

Li, Z. X. (2000). Influence of Tropical Pacific El Nino on the SST of the Southern Ocean through atmospheric bridge. *Geophysical Res. Lett.* 27, 3505–3508. doi: 10.1029/1999GL011182

Liu, F., Lu, J., GAruba, O., Leung, L. R., Luo, Y., and Wan, X. (2018). Sensitivity of surface temperature to oceanic forcing via q-flux Green's function experiments. Part I: Linear response function. *J. Climate* 31, 3625–3641. doi: 10.1175/JCLI-D-17-0462.1

Purkey, S. G., and Johnson, G. C. (2010). Warming of global abyssal and deep Southern Ocean waters between the 1990s and 2000s: Contributions to global heat and sea level rise budgets. *J. Climate* 23, 6336–6351. doi: 10.1175/2010JCLI3682.1

Rayner, N., Parker, D. E., Horton, E. B., Folland, C. K., Alexander, L. V., Rowell, D. P., et al. (2003). Global analyses of sea surface temperature, sea ice, and night marine air temperature since the late nineteenth century. *J. Geophysical Research: Atmospheres* 108. doi: 10.1029/2002JD002670

Rye, C. D., Naveira Garabato, A. C., Holland, P. R., Meredith, M. P., George Nurser, A. J., Hughes, C. W., et al. (2014). Rapid sea-level rise along the Antarctic margins in response to increased glacial discharge. *Nat. Geosci.* 7, 732–735. doi: 10.1038/ngeo2230

Rintoul, S. R. (2018). "The global influence of localized dynamics in the Southern Ocean.", *Nature*, 558 (7709), 209-218. doi: 10.1038/s41586-018-0182-3

Schlesinger, M. E., and Ramankutty, N. (1994). An oscillation in the global climate system of period 65–70 years. *Nature* 367, 723–726. doi: 10.1038/367723a0

Schmidtko, S., Heywood, K. J., Thompson, A. F., and Aoki, S. (2014). Multidecadal warming of Antarctic waters. *Science* 346, 1227–1231. doi: 10.1126/science.1256117

Simpkins, G. R., Mcgregor, S., Taschetto, A. S., Ciasto, L. M., and England, M. H. (2014). Tropical connections to climatic change in the extratropical Southern hemisphere: the role of Atlantic SST trends. *J. Climate* 27, 4923–4936. doi: 10.1175/JCLI-D-13-00615.1

Simpkins, G. R., Peings, Y., and Magnusdottir, G. (2016). Pacific influences on tropical atlantic teleconnections to the southern hemisphere high latitudes. *J. Climate* 29, 6425–6444. doi: 10.1175/JCLI-D-15-0645.1

Wang, G., Cai, W., Santoso, A., Wu, L., Fyfe, J. C., Yeh, S., et al. (2022). Future Southern Ocean warming linked to projected ENSO variability. *Nat. Climate Change* 12, 649–654. doi: 10.1038/s41558-022-01398-2

Wang, C., Deser, C., Yu, J., Dinezio, P., and Clement, A. (2017). ""El Niño and southern oscillation (ENSO): a review," in *Coral reefs of the eastern tropical Pacific: Persistence and loss in a dynamic environment*, 8, 85–106.

Wijffels, S. E., Willis, J., Domingues, C. M., Barker, P., White, N. J., Gronell, A., et al. (2008). Changing expendable bathythermograph fall rates and their impact on estimates of thermosteric sea level rise. *J. Climate* 21, 5657–5672. doi: 10.1175/2008JCLI2290.1

Yang, H., Gerrit, L., Christian, S., Qiang, W., Xin, H. R., Xiaoxu, S., et al. (2023). Satellite-observed strong subtropical ocean warming as an early signature of global warming. *Commun. Earth Environ.* 4. doi: 10.1038/s43247-023-00839-w

Zhang, R., and Delworth, T. L. (2007). Impact of the Atlantic multidecadal oscillation on North Pacific climate variability. *Geophysical Res. Lett.* 34, L23708-1-L23708-6. doi: 10.1029/2007GL031601

Zhang, L., Delworth, T. L., and Zeng, F. (2017). The impact of multidecadal Atlantic meridional overturning circulation variations on the Southern Ocean. *Climate Dynamics* 48, 2065–2085. doi: 10.1007/s00382-016-3190-8

frontiers | Frontiers in Marine Science

TYPE Original Research
PUBLISHED 20 September 2024
DOI 10.3389/fmars.2024.1428621

OPEN ACCESS

EDITED BY
Jun Zhao,
Ministry of Natural Resources, China

REVIEWED BY
Ruifeng Zhang,
Shanghai Jiao Tong University, China
Cunde Xiao,
Beijing Normal University, China

*CORRESPONDENCE
Jeremy D. Owens
jdowens@fsu.edu

RECEIVED 06 May 2024
ACCEPTED 26 July 2024
PUBLISHED 20 September 2024

CITATION
Kenlee B, Owens JD, Raiswell R, Poulton SW, Severmann S, Sadler PM and Lyons TW (2024) Long-range transport of dust enhances oceanic iron bioavailability.
Front. Mar. Sci. 11:1428621.
doi: 10.3389/fmars.2024.1428621

Long-range transport of dust enhances oceanic iron bioavailability

Bridget Kenlee[1], Jeremy D. Owens[2]*, Robert Raiswell[3], Simon W. Poulton[3], Silke Severmann[4], Peter M. Sadler[1] and Timothy W. Lyons[1]

[1]Department of Earth and Planetary Sciences, University of California, Riverside, Riverside, CA, United States, [2]Department of Earth, Ocean & Atmospheric Science, Florida State University National High Magnetic Field Laboratory, Tallahassee, FL, United States, [3]School of Earth and Environment, University of Leeds, Leeds, United Kingdom, [4]Department of Marine and Coastal Sciences, Rutgers University, New Brunswick, NJ, United States

Wind-borne dust supply of iron (Fe) to the oceans plays a crucial role in Earth's biogeochemical cycles. Iron, a limiting micronutrient for phytoplankton growth, is fundamental in regulating ocean primary productivity and in turn the global carbon cycle. The flux of bioavailable Fe to the open ocean affects oscillations in atmospheric CO_2 due to its control on inorganic carbon fixation into organic matter that is eventually exported to the sediments. However, the nature of dust-delivered Fe to the ocean and controls on its bioavailability remain poorly constrained. To evaluate the supply of wind-borne bioavailable Fe and its potential impact on Fe-based climate feedbacks over the last 120,000 years, we examine sediment profiles from four localities that define a proximal to distal transect relative to Saharan dust inputs. Bulk δ^{56}Fe isotope compositions (average = -0.05‰) and Fe_T/Al ratios suggest crustal values, thus pointing to a dominant dust origin for the sediments at all four sites. We observed no variability in grain size distribution or in bioavailable Fe supply at individual sites as a function of glacial-versus-interglacial deposition. Importantly, there is no correlation between sediment grain size and Fe bioavailability. Spatial trends do, however, suggest increasing Fe bioavailability with increasing distance of atmospheric transport, and our sediments also indicate the loss of this Fe and thus potential bioavailability utilization once deposited in the ocean. Our study underscores the significance of Fe dynamics in oceanic environments using refined speciation techniques to elucidate patterns in Fe reactivity. Such insights are crucial for understanding nutrient availability and productivity in various ocean regions, including the Southern Ocean, where wind-delivered Fe may play a pivotal role. It is expected that dust delivery on glacial-interglacial timescales would be more pronounced in these high-latitude regions. Our findings suggest that studies linking Fe availability to marine productivity should benefit significantly from refined Fe speciation approaches, which provide insights into the patterns and controls on Fe reactivity, including atmospheric processing. These insights are essential for understanding the impacts on primary production and thus carbon cycling in the oceans and consequences for the atmosphere.

KEYWORDS

iron, dust, isotopes, productivity, glacial-interglacial

1 Introduction

As the dominant source of iron (Fe) to the open oceans (Fung et al., 2000), wind-borne (aeolian) dust is an integral part of Earth's climate system. Iron, an essential micronutrient, plays an important role in regulating the oceanic biological pump due to its limited bioavailability for phytoplankton in large regions of the ocean (Martin and Fitzwater, 1988; Jickells et al., 2005). Consequently, Fe bioavailability exerts a strong control on levels of atmospheric carbon dioxide (CO_2) and climate on global scales (Joos et al., 1991; Baker et al., 2003; Boyd and Ellwood, 2010). North Africa is one of the primary sources of dust to Earth's atmosphere, where it is subsequently deposited in the oceans and on continents (Engelstaedter et al., 2006). Downwind from North Africa, dust-driven fertilization may enhance long-term productivity in Western Atlantic regions including Amazon rain forests and Floridian, Bahamian, and Caribbean coral reefs and water columns (Shinn et al., 2000; Muhs et al., 2007; Bristow et al., 2010; Prospero and Mayol-Bracero, 2013; Swart et al., 2014; Yu et al., 2015). More generally, transport-dependent enhancement of iron bioavailability may have been a factor in determining the loci of primary productivity in the oceans throughout Earth's history.

Importantly, not all dust-borne Fe is bioavailable in the ocean, and the processes that enhance Fe bioavailability are not well understood. Atmospheric deposition of Fe in the open ocean is predominantly via fine-grained iron (oxyhydr)oxide (mostly as grain coatings) and silicate minerals (Raiswell and Canfield, 2012). Previous studies have suggested that the chemical properties of Fe in atmospheric dust are often grain size-dependent (Hand et al., 2004; Baker and Jickells, 2006; Ooki et al., 2009). Furthermore, with longer transport times in the atmosphere, Fe solubility (and consequently Fe bioavailability) should increase via atmospheric processing, principally involving acid production via photochemistry (Hand et al., 2004). The signatures of these processes, however, are yet to be explored systematically in modern sediments using carefully calibrated iron extraction techniques or other chemical fingerprints. Instead, past studies have often characterized potentially soluble iron (Fe_{Sol}) as bioavailable Fe, emphasizing reactive minerals such as ferrihydrite (Wells et al., 1983; Fan et al., 2006). However, ferrihydrite is thermodynamically unstable and will transform into more stable phases on diagenetic timescales, including (oxyhydr)oxides such as goethite, hematite, and magnetite, or other secondary phases such as pyrite and Fe-carbonates. The critical implication is that measured values for the residual, most reactive phases in sediment cores may underestimate the total original reactive Fe pool (Schwertmann et al., 2004).

Here, we have adopted a scheme for iron speciation that is more inclusive of Fe phases that may have been bioavailable prior to transformations in seawater and early lithification. We define a broader array of Fe mineral pools as being highly reactive (Fe_{HR}) because their precursors may have initially been bioavailable. These mineral phases consist of (a) carbonate Fe (plus weakly bound, surface Fe); (b) amorphous and crystalline Fe oxides and (oxyhydr) oxides such as ferrihydrite, goethite, and hematite; (c) magnetite Fe; and (d) pyrite (Poulton and Canfield, 2005). We normalize Fe_{HR} to total Fe (Fe_T) to identify relative enrichments or deficiencies in the Fe_{HR} pool compared to the entire Fe contents. These Fe_{HR}/Fe_T ratios are robust against potential artifacts of dilution (e.g., by carbonate or biogenic silica), which can otherwise obscure interpretations of absolute concentrations. It is important to note that substantial portions of all these phases may have formed by mineral transformation of initially soluble and bioavailable precursor phases following deposition (Benner et al., 2002). Therefore, Fe_{HR} effectively serves as upper limit proxy for the residual concentration of the initial bioavailable Fe (Sur et al., 2015; Sardar Abadi et al., 2020). While this approach may overestimate the original bioavailable Fe pool due to inputs such as detrital magnetite, it provides a comprehensive baseline against which enrichments and depletions in formerly bioavailable forms can be assessed. This approach is conservative, in terms of percentages, because percent loss from Fe_{HR} would be low relative to the loss from the smaller amount of the most soluble original Fe (Fe_{Sol}). However, sediment cores are unlikely to contain significant amounts of these original phases due to expected rapid diagenetic transformations, which contribute to the various Fe_{HR} pools.

Several recent studies have addressed the controls and distribution of recent aeolian bioavailable Fe in the oceans and subsequent climate feedbacks (Lis et al., 2015; Shoenfelt et al., 2018; Thöle et al., 2019), including grain size controls on aerosol Fe solubility (Baker and Jickells, 2006; Mackie et al., 2006; Trapp et al., 2010), but none has focused on characterization, spatial trends, and grain size relationships as preserved in marine sediments over glacial-interglacial cycles. To isolate trends in aeolian bioavailable iron in marine sediments, four sample locations that preserve marine sedimentary records of African dust export were strategically selected from International Ocean Discovery Program sites (IODP or previous iterations of the program—ODP and initial IODP) to provide a wide spatial distribution in the Northern Atlantic Ocean from core repositories (Figure 1) from the last glacial period to present (about the last 120,000 years). We use bulk Fe isotopes to identify the potential end-member sources to these sites. Additionally, we examined grain size characteristics and quantified various Fe pools to assess controls on bioavailable Fe distribution. We document that dust-borne Fe at distal sites experiences enhanced atmospheric processing, leading to an increase in Fe_{Sol}, which was readily available to primary producers (Hassler et al., 2011; Borchardt et al., 2019). Instantaneous consumption of Fe_{Sol} could have stimulated primary productivity. The net effect would be increases in the overall impact with increasing distance from the Saharan source, which may also reduce Fe delivery to the sediments.

2 Material and methods

2.1 Study sites

The four locations studied are sites 658 (21°N, 19°W) and 659 (18° N, 21°W) from ODP expedition 108, located on top of the Cape Verde

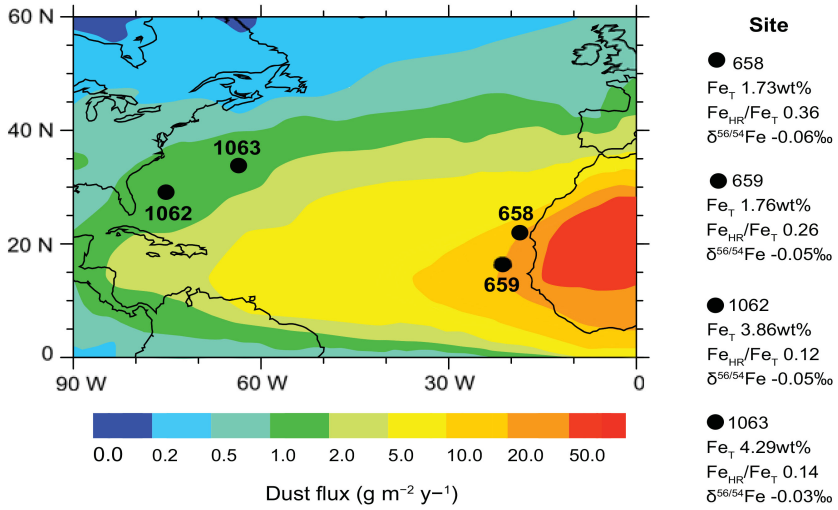

FIGURE 1
Locations of IODP sites 658, 659, 1062 and 1063 with Fe data. Base map shows estimates for dust deposition (g m^{-2} y^{-1}) — specifically transport of African dust across the surface ocean. Dust flux data are from Jickells et al. (2005), Mahowald et al. (1999), and Ginoux et al. (2001); all other data are from this study. Highly reactive Fe (Fe_{HR}) for each site is normalized to total Fe (Fe_T) to distinguish relative enrichments or deficiencies in the Fe_{HR} pool. Also shown are the Fe isotope compositions ($\delta^{56}Fe$) to constrain different sources of Fe.

Plateau near the northwest African continental margin, and sites 1062 (28°N, 74°W) and 1063 (33°N, 57°W) from the sediment drifts of the western North Atlantic Ocean as part of ODP Leg 172. The sites were selected because they span a wide portion of the Northern Atlantic Ocean (Figure 1). The marine sedimentary records of North African dust export offer the advantage of continuous sedimentation (Tiedemann et al., 1989; Giosan et al., 2002). These sites range from proximal to distal relative to the Sahara Dust Corridor source region. The average time resolution of the four records is about 4 kyr/sample covering the last glacial period to present (over the last 120,000 years) (Supporting Information).

2.2 Dust deposition average

Calculations of dust deposition (g m^{-2} y^{-1}) were obtained from the average of three models (Mahowald et al., 1999; Ginoux et al., 2001; Jickells et al., 2005) (Supplementary Table S7) to represent our best approximations of dust delivery.

2.3 Grain size analysis

Grain size distribution (GSD) in marine sediments are often used as a measure of dust delivery (Blott and Pye, 2001; Harrison et al., 2001; Baker et al., 2006; Ooki et al., 2009). Samples were dried at 80°C. Dry sieving was carried out for 15 minutes using a tapping sieve shaker (RO-TAP) equipped with a set of stainless-steel sieves. Short sieving times prevented the formation of aggregates due to electrostatic interactions and interparticle cohesion. Each fraction was weighed and recorded. Particle size distribution is represented graphically using a cumulative distribution curve and the D value method (S. J. Blott and Pye, 2001) from GRADISTAT (Blott, 2000). Samples were divided into >45µm (bulk), 45 to 20µm, and<20µm size fractions.

2.4 Iron speciation and iron isotope analysis

We used a state-of-the-art sequential Fe extraction procedure modified from Poulton and Canfield (2005) to characterize the Fe phases present ($Fe_{Na\text{-}Ac}$, Fe_{Dith}, and Fe_{Ox}), including minerals that might have formed diagenetically from initially bioavailable Fe. All Fe extracts were analyzed by inductively coupled plasma-mass spectrometry (ICP-MS; Agilent 7500ce) with H_2 and He modes in the collision cell, diluted with trace-metal grade 2% HNO_3 to enhance Fe detection by reducing interferences, thereby improving the accuracy of analytical results.

A multi-acid digest was performed to determine total solid-phase iron (Fe_T) and aluminum (Al) concentrations. Dried samples were ashed at 550°C, and a standard three-step digestion was performed using trace metal grade HF, HNO_3, and HCl at 140°C. This way, the potential bioreactivity of the Fe can be expressed as a fraction of the total Fe pool. Final concentrations were determined using the same ICP-MS. Reference standards SDO-1 (Devonian Ohio Shale) and SCO-1 (Cody Shale) were digested and analyzed in parallel with the sample extractions and yielded errors of less than<4%.

Splits from the multi-acid digest were used to measure the Fe isotope composition of the bulk sample ($\delta^{56}Fe_T$). Iron isotopes were analyzed at all four sites, resulting in total of 38 isotopic analyses (Supplementary Table S11) Anion exchange resin and a standard ion chromatography protocol were used for Fe separation to eliminate matrix effects (Skulan et al., 2002; Arnold et al., 2004). Column yields were carefully monitored using the Ferrozine

colorimetric method with UV-Vis spectrophotometry (λ = 562 nm) (Viollier et al., 2000) before and after chromatographic purification, ensuring only samples with yields ≥95% were used for isotopic analysis. Isotopic compositions were measured on a Neptune Thermo Scientific MC-ICP-MS (Multiple Collector-Inductively Coupled Plasma-Mass Spectrometer) at Rutgers University, applying the method of Arnold et al. (2004). Samples were introduced as a 1 ppm solution using a cyclonic spray chamber. Mass bias during the analysis was corrected using a Cu elemental spike, and standard reference material IRMM-014 served as a bracketing standard between each sample for accurate mass bias correction. The blank procedure involved spiking the blanks post-column separation to prevent overestimation of the procedure blank from incomplete spike recovery, ensuring accurate accounting of any blank contributions and preventing inaccuracies in the final results. The iron isotope composition (δ^{56}Fe) is defined as follows:

$$\delta^{56}\,Fe_{‰} = \left[\frac{(^{56}Fe/^{54}Fe)_{sample}}{(^{56}Fe/^{54}Fe)_{IRMM-14}}\right] - 1 \text{ x } 1,000,$$

where the δ^{56}Fe is reported relative to IRMM-014 reference material. The measured Fe isotope composition of IRMM-014 is $\delta^{56}Fe_T$ =-0.09‰ on this scale, with an internal precision of ±0.06‰ (2σ).

2.5 Carbon concentrations

Sedimentary total carbon (TC) was analyzed by combustion using an Eltra CS-500 carbon-sulfur analyzer. Total inorganic carbon (TIC) was determined by acidification of a split of the sample. Total organic carbon (TOC) content was calculated as the difference between TC and TIC. The Eltra limestone geostandards AR4007 and AR4011 were analyzed routinely, with values falling within reported ranges and deviating less than<5%. Geo-reference standards AR4007 (carbon = 7.58%) and AR4011 (carbon = 8.91%) were used for analytical calibration and quality control. Calcium carbonate concentrations ($CaCO_3$), as weight percent (wt. %), were calculated from the measured TIC content assuming that all evolved CO_2 was derived from the dissolution of $CaCO_3$:

$$CaCO_3(wt.\%) = TIC\ x\ 8.33\ (wt.\%)$$

Standard $CaCO_3$ (>99.9% calcium carbonate, Fisher Scientific) was used during individual batches of analyses to confirm accuracy and instrument performance before, during, and after each run (with reproducibility better than 3%). No correction was made for the presence of other carbonate minerals.

2.6 Statistical analysis

The analysis of variance (ANOVA), the F-test, and t-tests were conducted to determine whether there is a significant difference of bioavailable Fe distribution between proximal and distal sites and to assess any dependence of Fe_{HR}/Fe_T with grain size (Montgomery et al., 2009; Haynes, 2013). The 95% confidence interval was used in all analyses (see Supplementary Information for grouping rationale and sensitivity analyses).

2.7 Aerosols optical properties

Aerosol optical depth (AOD) data are from the MIRS—Multi-angle Imaging SpectroRadiometer (https://misr.jpl.nasa.gov/getData/accessData/). These data provide a benchmark for calibrating models and interpreting sediment records that span long-term geological timescales. The averaged concentration of AOD between 2009-2019 over the North Atlantic Ocean was utilized to provide an estimate of atmospheric African dust deposition to the North Atlantic Ocean. Modern AOD data help bridge temporal scales, offering historical perspectives on changes in dust patterns and aerosol loading, while sediment cores offer long-term insights into dust deposition and iron (Fe) content over glacial-interglacial cycles.

2.8 The ecoGEnIE model

To model the relationship between Fe flux and primary productivity dynamics, we used the ecoGEnIE paleoclimate model, an extension of cGEnIE—a carbon-centric, Grid Enabled Integrated Earth system model featuring comprehensive marine biogeochemical uptake (Ward et al., 2018). ecoGEnIE incorporates a scheme for plankton ecology (ECOGEM) with a size-dependent control on the plankton biogeochemical function (Ward et al., 2018). This addition allows for a better representation of biodiversity, including ecosystem shifts in response to environmental forcing. ecoGEnIE provides dynamic simulations of nutrient usage in response to availability. For our purposes, we used cGEnIE/ecoGEnIE default configurations (Ridgwell and Hargreaves, 2007).

3 Results and discussion

3.1 Iron supply from the North African dust to the North Atlantic Ocean

Iron isotope data (δ^{56}Fe) can be a powerful way to constrain the Fe sources to the oceans over Earth history (Beard et al., 2003; Waeles et al., 2007; Owens et al., 2012; Conway et al., 2019). The average bulk δ^{56}Fe values for samples from all four sites (-0.05 ± 0.02‰; 2-standard deviations) is consistent with continentally derived dust (Figure 1, Supplementary Table S1) given the similarity to the δ^{56}Fe composition of most silicate rocks (Beard et al., 2003; Dauphas and Rouxel, 2006; Waeles et al., 2007; Conway and John, 2014). The Fe_T/Al ratio of 0.55 ± 0.02 also overlaps with the mean Fe_T/Al ratio for terrigenous sediments and average continental crust (0.55 ± 0.11; Martinez et al., 2007), suggesting no significant hydrothermal contribution, which typically has a δ^{56}Fe similar to crustal values but has a Fe_T/Al >2.00 (Clarkson

et al., 2014; Raiswell et al., 2018a). Our average Al/Ti ratio of 18.9 ± 0.78 is also consistent with an aeolian origin for our samples (Yarincik et al., 2000).

The potential Fe bioavailability can be explored by speciation studies, which are broadly linked to Fe phases in the sample (Shi et al., 2009). The concentrations of Fe extracted using sodium acetate ($Fe_{Na\text{-}Ac}$) comprised 0.5-2.9 wt.% of Fe_T (Supplementary Tables S2a-d, S3a-d). Although Poulton and Canfield (2005) used $Fe_{Na\text{-}Ac}$ to remove carbonate-bound Fe, their data show that minor amounts are also removed from iron-bearing silicates. We confirmed this possibility by extracting a range of Fe-bearing silicates with sodium acetate (Supplementary Table S4), suggesting that acetate removes a minor fraction of Fe from such minerals—potentially from weakly bound surface sites (Heron et al., 1994; Raiswell et al., 2018b). This silicate-associated pool has been documented to be readily bioavailable (Shoenfelt et al., 2017) because Fe(II)-rich silicate minerals can enhance diatom growth as well as photosynthetic efficiency. However, this silicate-bound Fe fraction is very small relative to the other potentially bioavailable pools we now discuss. A dithionite Fe extraction (Fe_{Dith}), dominantly representing Fe (oxyhydr)oxide minerals, removed 8.6 to 21.6 wt.% of Fe_T (Supplementary Tables S2a-d, S3a-d). Previous studies have considered Fe_{Dith} to be an effective measure of potentially bioavailable iron from aeolian dust particles (Fan et al., 2006; Baker and Croot, 2010). An oxalate Fe extraction (Fe_{Ox}) mainly targets Fe in magnetite and ranges from 5.4-12.1 wt.% of Fe_T (Supplementary Tables S2a-d, S3a-d). If delivered unaltered to the ocean, rather than forming during diagenesis, magnetite would likely represent refractory (insoluble) iron in surface seawaters.

On the broadest scales, an overall increase in atmospheric dust deposition occurs during glacial intervals due to an expansion in the source areas (Mahowald et al., 1999) and stronger winds (McGee et al., 2010) that consequently influence the supply of bioavailable Fe to the open ocean. However, at low latitudes, there is no significant glacial-interglacial trend in dust input (Maher et al., 2010). Iron bioavailability in marine systems is linked to complexation with prokaryotic-released organic compounds, such as siderophores, polycarboxylate ligands (Barbeau, 2006; Shaked and Lis, 2012), and saccharides (Hassler et al., 2011). Thus, a fraction of this delivered Fe pool should be bioavailable. Our analyses of Fe_T, Fe_{HR}/Fe_T, and total organic carbon (TOC) at each site have limited to no statistically relevant stratigraphic variation over the last glacial period to the present ($p>0.05$) (Figure 2, Supplementary Tables S10a-d). Further, the TOC contents argue against productivity that is enhanced in one interval relative to the other (glacial versus interglacial). This combination of data suggests that there is little or no temporal variation at low latitudes on glacial-interglacial timescales. Importantly, however, past studies have suggested that downwind locations may be impacted biologically by the enhanced solubility of delivered Fe, such as the Bahamas and Amazon region (Shinn et al., 2000; Muhs et al., 2007; Bristow et al., 2010; Muhs et al., 2012; Prospero and Mayol-Bracero, 2013; Swart et al., 2014; Yu et al., 2015). Consistent with this possibility, our data document a

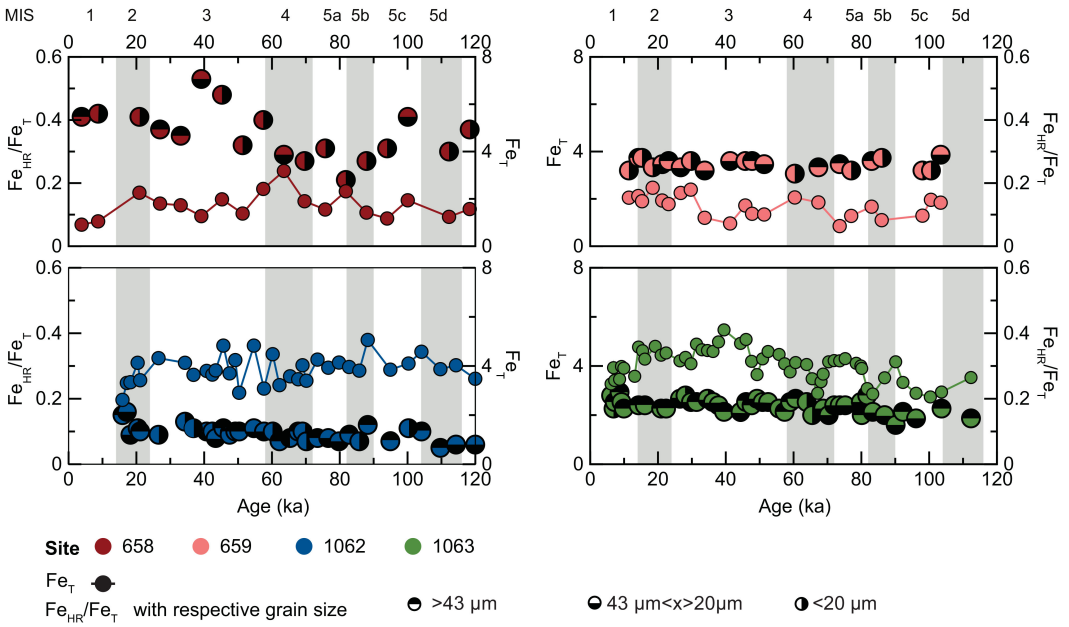

FIGURE 2
Age profiles for iron (Fe) in IODP cores 658 (red), 659 (orange), 1062 (blue), and 1063 (green) showing glacial-interglacial relationships. Gray bars indicate climatic events of importance for the Last Glacial Period (extending back ~ 120,000 years) as recorded in polar ice cores. MIS refers to marine isotope stages. Total Fe (Fe_T) is shown as filled, connected circles for each site. Highly reactive (Fe_{HR}) consists of carbonate Fe (plus weakly bound surface Fe); amorphous and crystalline Fe oxides and (oxyhydr)oxides such as ferrihydrite, goethite, and hematite; and magnetite Fe. Fe_{HR} data are normalized to total Fe (Fe_T) to distinguish relative enrichments or deficiencies in the Fe_{HR} pool. FeHR/Fe_T ratios are expressed in terms of grain size populations.

transport-dependent process that would also be relevant to other regions, such as the south Atlantic, and time intervals that are characterized by Fe limitation. Moreover, our data suggest atmospheric pathways to enhanced reactivity that are relatively constant, at least at low latitude, under glacial versus interglacial global climatic regimes (see discussions below). The glacial-interglacial uniformity we observe implies consistency in sourcing and processing during transport despite temporal differences in weathering relationships in the source regions and wind patterns, among other varying controls (McGee et al., 2013). Additional work is necessary to demonstrate whether the observed relationship is the same for all source regions and latitudes. Importantly, however, this surprising result is likely to influence future climate models for this region and potentially beyond.

3.2 Downcore Fe geochemistry and grain size distribution

The bioavailable Fe supply in sediments as a function of grain size distribution (GSD) during glacial-interglacial periods could have important impacts on marine primary productivity (Mahowald et al., 2014). Therefore, we determined the GSD at all four sites by dry sieving (Supplementary Figure S1, Supplementary Table S5). A statistical one sample t-Test was carried out for all four sites to test the variability of GSD during glacial and interglacial periods, (n=128; Figure 2 and Supplementary Table S9). The p-values for proximal sites 658 and 659 are 0.88 and 0.76, respectively, and 0.72 and 0.19 for distal sites 1062 and 1063, respectively. The end member p-values suggest that variability in GSD over glacial-interglacial timescale is not statistically significant for any of the four sites, consistent with previous findings that the flux of low-latitude Saharan dust does not vary significantly over these timescales (Maher et al., 2010; Skonieczny et al., 2019).

Previous work has suggested that Fe bioavailability is grain size-dependent, primarily due to the greater surface-area-to-volume relationship of small grains of atmospheric dust (Mahowald et al., 2018). Greater relative surface areas for small-sized particles could support proportionally larger surface alteration during transport and associated coatings of soluble Fe. To test for statistically significant differences of bioavailable Fe distribution for GSD in our drill-core sediment samples, Fe_{HR}/Fe_T (n=394) were compared using an analysis of variance (ANOVA) and a t-test (see Supplementary Information for grain size rationale and sensitivity analyses). We found no statistically significant differences in Fe_{HR}/Fe_T with grain size at a given location (Supplementary Tables S8a-d). For example, the ANOVA for site 658 shows no significant dependence ($p<0.05$), with an f-critical value of $2.80e^{-4}$ and a p-value of 1.0 among the various grain sizes. The ANOVA data for site 659 have an f-critical value of 1.13 and a p-value of 0.33, which is also not significant at $p<0.05$. Sites 1062 and 1063 also show no significant dependence at $p<0.05$, with f-critical values of 1.12 and 0.99 and p-values of 0.33 and 0.37 for sites 1062 and 1063, respectively. The negligible variability in potentially bioavailable Fe distribution as a function of GSD in these sediments from each site is likely due, at least in part, to the particles having experienced many series of aggregation and disaggregation as they settled through the water column (Bacon et al., 1985)—thus the larger particles in the sediments are mostly aggregates of finer original materials (Anderson et al., 2016) but initially were larger but through disaggregation and then aggregation have been modified. Consistent with the possibility, our the Fe_{HR}/Fe_T ratios of larger grains are similar to those of smaller particles i.e. showing no significant locality relation between GSD and Fe geochemistry (Supplementary Figure S3). Importantly, the results from these cores do not suggest there is a statistical difference in grain size variations related to in Fe reactivity among grains of differing primary size.

3.3 Spatial trends in potentially bioavailable Fe distribution

North African dust is carried great distances over thousands of kilometers, as would be true for any ocean basin. Because atmospheric transport is a size-selective process (Pye, 1989), proximal and distal Fe dust can be distinguished by the grain-size distributions related to distance from the source, whereby dust particle size decreases with increasing distance (Mahowald et al., 2014). Average particle size distributions for our samples show a decrease of ~20% in grain size (Supplementary Table S5) and a corresponding increase of ~30% in surface area (Supplementary Table S6) from proximal to distal sites. Small particles have a longer lifetime in the atmosphere and thus experience enhanced atmospheric processing (chemical and/or photochemical), likely leading to an increase in the solubility (Fe_{Sol}) of Fe_{HR} (Spokes et al., 1994; Desboeufs et al., 2001; Shi et al., 2009). This suggests these grains are disaggregated primary grains where the finer distal grains (as suggested by grain size analyses) have traveled farther - increasing processing time. Thus, these finer distal grains have high surface are-to-volume ratios, which also favors the extent of processing.

Our measurements show a systematic decrease in Fe_{HR}/Fe_T from proximal to distal sites (Figure 3A). Importantly, suggestions of lower total Fe concentrations at proximal sites (Figure 3B) mostly reflect increased carbonate dilution at those locations. Detailed insight into Fe behavior is provided by our Fe_{Dith} data, which show the greatest decrease, from 21.5 wt.% and 15.5 wt.% of Fe_T at proximal sites 658 and 659, respectively, to 9.0 wt.% at both distal sites (1062 and 1063; Supplementary Tables S2a-d and S3a-d). We suggest that our Fe_{HR}/Fe_T ratios decrease with increasing transport due to enhanced Fe solubility via atmospheric reactions (Oakes et al., 2012), leading to dissolution in seawater and likely uptake of the bioavailable Fe by primary producers in the surface ocean at these distal sites. Bioavailable Fe delivery and utilization from primary producers has been observed in this general region of the Atlantic previously (Borchardt et al., 2019) and has been suggested for transport of Fe to oligotrophic lakes in Spain (Bhattachan et al., 2016). Modern dust transport from the Saharan desert to the Atlantic shows seasonal differences. In the boreal summer, the trade winds typically carry dust from northern Africa to the Caribbean, while in winter, transport shifts south toward the

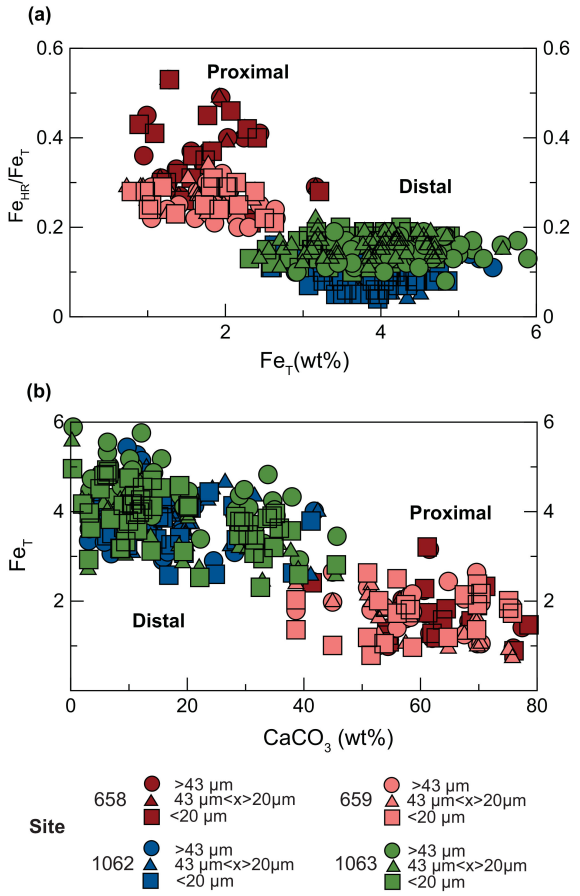

FIGURE 3
(A) Fe_{HR}/Fe_T versus Fe_T for proximal (658-red and 659-orange) and distal (1062-blue and 1063-green) sites. Note the systematic decrease in Fe_{HR}/Fe_T from proximal to distal sites. **(B)** Fe_T versus $CaCO_3$ for proximal and distal sites. The effects of carbonate dilution on Fe_T are confirmed by a steep inverse relationship between Fe_T and $CaCO_3$ content across all sites and in all size fractions. Samples with grain size >45µm (bulk), 45 to 20µm, and<20µm are shown as a circles, triangles, and squares, respectively. There is no significant difference in Fe_{HR}/Fe_T among the grain size populations from a given site.

Amazon Basin (Bakker et al., 2019). This relationship indicates that the central and western Sahara are significant dust sources in the productive summer, while the Sahel region contributes more dust to the Caribbean during the winter. (Figure 4A). Furthermore, the aerosol optical depth (AOD) decreases progressively from the Sahara Desert to the open ocean. Continued research on seasonal dust transport variation is crucial for a comprehensive understanding of these dynamics and the seasonal impacts, particularly since these may evolve due to climate change. The ecoGEnIe model suggests significant increases in Fe flux (Figure 4B) in these distal locations, underscoring the significant role of dust deposition. This scenario, based on limited data, is thought provoking and highlights an area of research that should be explored. Evaluating our experiments, we confirm that lower Fe concentrations may indeed reflect higher carbonate dilution in these specific locations. However, full quantification of the loss of soluble Fe and the role of transport in Fe bioavailability will require more information about the North African dust source region (Huneeus et al., 2011; McGee et al., 2013), post-depositional processing of the Fe (Bressac and Guieu, 2013; Meskhidze et al., 2019), biogeochemical conditions of the surface seawater (Boyd and Ellwood, 2010), and atmospheric processes (Baker and Croot, 2010).

Further, it is important to consider alternative interpretations of our data. For example, the Fe content of analyzed dust samples could decrease downwind of North Africa, as described by Zhang et al. (2015), due to selective, progressive loss of heavier hematite-rich grains through gravitational settling during transport in the atmosphere. In truth, many of our observations are consistent with this possibility, and it may play a role, but there are other observations that are less consistent. First, it is not clear that the trend observed in Fe deposition in Zhang et al. (2015) is an expression of hematite availability. Other Fe phases, in particular Fe (oxyhydr)oxides, are likely a substantial part of the Fe pool in the dust—both as original constitutes from the source region and as products of atmospheric reactions. Importantly, these phases are approximately half as dense as crystalline hematite and would be decidedly less vulnerable to differential settling effects during transport. Moreover, soil hematite, the likely source of dust, would also be less dense than well-crystallized hematite, and these Fe phases are likely to be only a small part of the total grain mass (discrete Fe oxide grains are rare; Poulton and Raiswell, 2005). Further, hematite and other Fe(III) phases are often present as coatings on aluminosilicate grains that tend, if anything, to have lower densities than other silicates.

Our detailed speciation provides additional insight. Specifically, we see the same distal trends in our data from the acetate extraction, which does not target hematite but instead extracts more reactive, less dense Fe (oxyhydr)oxide phases. Finally, we also do not observe a difference in Fe chemistry as a function of grain size, in contrast to expected transport-related physical sorting that is controlled by grain size and/or density. These observations do not preclude other important processes, but they do leave us with our interpretation as the most parsimonious explanation of the full range of observations.

4 Conclusion

The potential effects of iron fertilization via dust delivery likely scale (although perhaps not linearly) with the total dust input and the proportion of bioavailable (soluble) Fe present. Our results show that while dust fluxes decrease with transport distance, the solubility/bioavailability of the associated iron increases downwind as a consequence of greater transport distance and thus greater time of exposure to atmospheric photochemical reactions that favor transformation to more soluble Fe(III) phases as conceptualized in Figures 5A–F. The decrease in Fe_{HR}/Fe_T ratios in downwind sediments fingerprints a loss of bioavailable Fe upon deposition due to dissolution. Despite lower dust fluxes compared to upwind sites (Figure 4A),

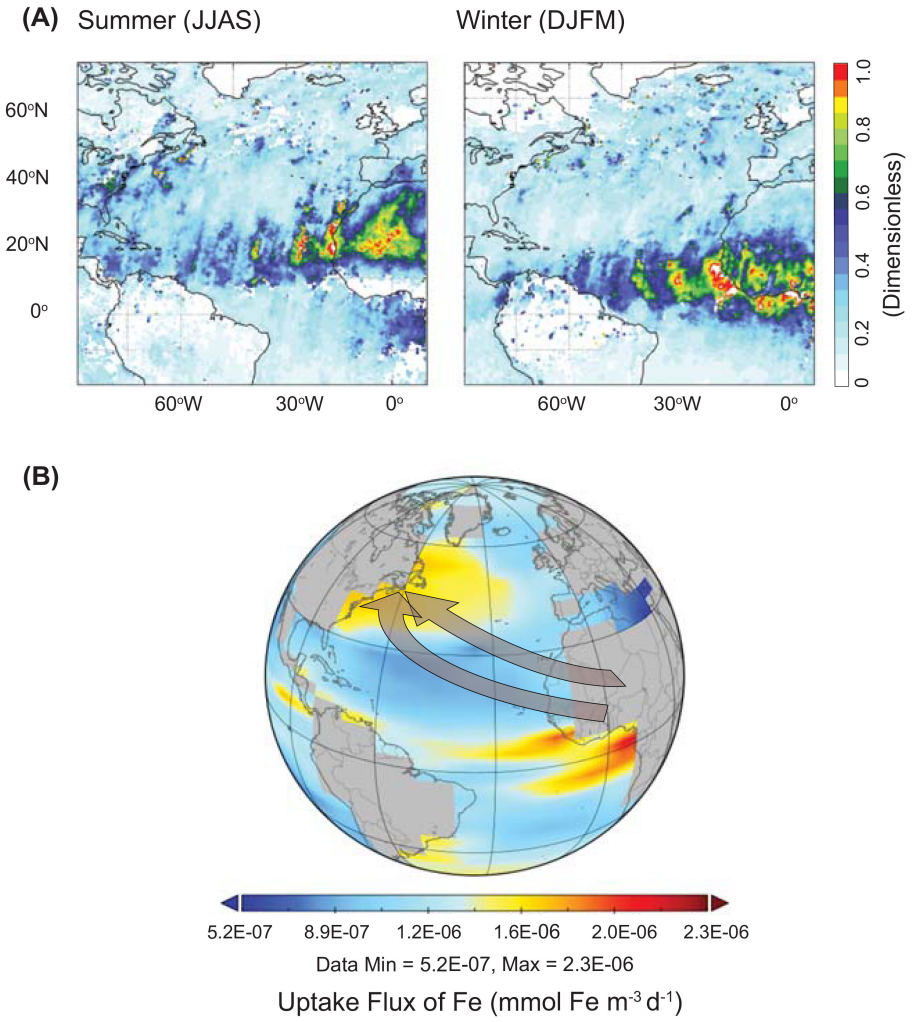

FIGURE 4
(A) Modern dust transport over the North Atlantic Ocean. Map of dust aerosol optical depth (AOD) over the North Atlantic showing the transport of African dust across the North Atlantic Ocean during the boreal summer [June-July-August-September (JJAS)] and boreal winter [December-January-February-March (DJFM)]. AOD is a measure of the extinction of the solar beam by dust and haze. It is a dimensionless number that is related to the amount of aerosol in the vertical column of atmosphere over the observation location. **(B)** Uptake of Fe flux modeled using ecoGEnIE. Gray arrow indicates the African dust that are carried from Northern Africa across the Atlantic Ocean.

our data are consistent with the idea of downwind loci of elevated bioavailability of the iron that stimulated primary productivity (Figure 4B). This enhanced reactivity at distal sites is likely more important than the consequences of more abundant inputs of less-soluble Fe upwind. Previous studies have suggested enhanced biological activity linked to these Fe patterns, including microbial response in the surface layers (Borchardt et al., 2019), nitrogen fixation of the North Atlantic Ocean (Moore et al., 2009), carbonate production in Bahamas (Shinn et al., 2000), growth of the coral reefs in the Caribbean (Swart et al., 2014), and the fertilization of Amazon region (Bristow et al., 2010). For instance, Swart et al. (2014) argued for dust-related stimulation of Fe-limited nitrogen-fixing cyanobacteria in the Bahamas leads to local drawdown of CO_2 and carbonate precipitation.

In summary, distal sites exhibit lower dust fluxes and total Fe delivery but higher reactivity compared to proximal locations that are dominated by relatively insoluble phases (Bhattachan et al., 2016), so that even high total dust fluxes would result in relatively low delivery of bioavailable Fe. In contrast, the distal sites receive less dust, but the Fe is highly soluble and bioavailable because of distance-dependent transport processing in the atmosphere. This Fe, we argue, is lost upon deposition in the ocean, which results in the lower residual ratio of reactive to total iron in the sedimentary record compared to the sediments of the proximal sites. Beyond recent impacts in the North Atlantic, our findings suggest that enhanced of Fe bioavailability at distal sites could help explain patterns of biological activity and organic accumulation relative to dust source in other regions throughout Earth history (Sardar Abadi et al., 2020). Our study emphasizes the significance of exploring Fe speciation to improve our understanding of Fe dynamics across various temporal scales, including glacial-interglacial periods. This

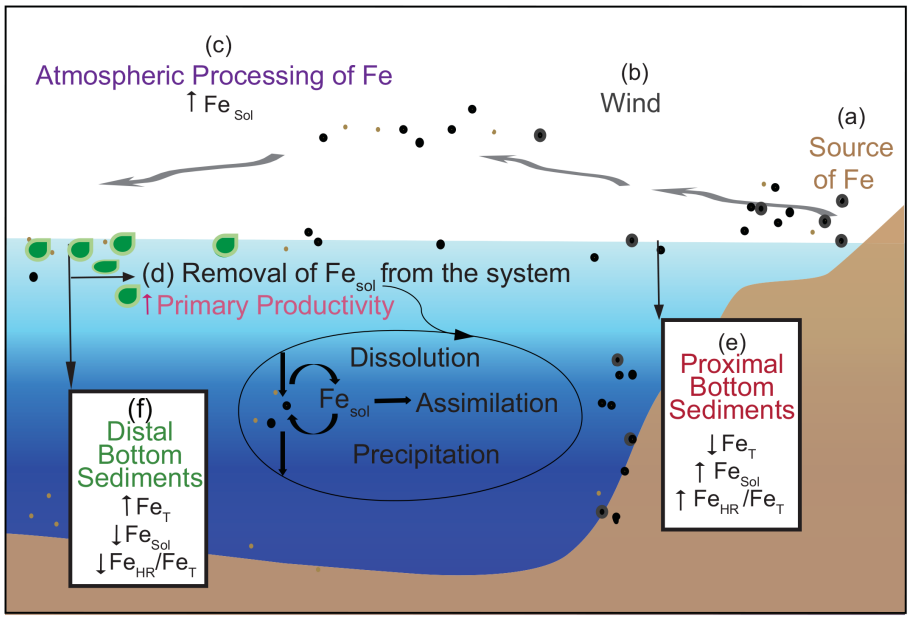

FIGURE 5
Generalized schematic of the iron biogeochemical cycle. The major source of Fe in the open ocean is dust delivered by the atmosphere. Fe_T: total, Fe_{HR}: highly reactive Fe (at least partly bioavailable Fe at the time of deposition), and Fe_{Sol}: soluble Fe (bioavailable Fe that is readily used for primary productivity). **(A)** Source of dust is from the Sahara Desert. **(B)** Wind eroding soils containing Fe oxides and silicates leads to transport of the dust seaward. Coarse particles will sink rapidly, while smaller particles will travel further in the atmosphere and remain in the surface ocean longer. **(C)** Atmospheric processing can increase Fe solubility and bioavailability. **(D)** In the ocean, Fe_{Sol} is removed from the system via dissolution and is assimilated by the phytoplankton. The dissolved Fe does not remain in solution in oxic seawater since oxidation to Fe(III) is rapid, and seawater is close to saturation with iron(oxyhydr)oxides. **(E)** Sediments of proximal sites show relatively low values for Fe_T due to carbonate dissolution and relatively high Fe_{Sol} and Fe_{HR}/Fe_T. **(F)** Sediments at distal sites show decreases of Fe_{Sol} due to its dissolution and removal by primary producers in the surface ocean, leading to low values for Fe_{Sol} and Fe_{HR}/Fe_T in the underlying sediments.

insight contributes significantly to broader understandings of oceanic and atmospheric carbon cycling. Hopefully, similar studies will be undertaken in other regions, particularly in the Southern Ocean, where nutrient availability may be abundant but primary production is constrained by the availability of reactive Fe. These sites would be influenced strongly by dust and processes analogous to those discussed in this study.

Data availability statement

The original contributions presented in the study are included in the article/Supplementary Material. Further inquiries can be directed to the corresponding author.

Author contributions

BK: Conceptualization, Data curation, Formal analysis, Investigation, Methodology, Project administration, Supervision, Validation, Visualization, Writing – original draft. JO: Conceptualization, Formal analysis, Investigation, Methodology, Supervision, Validation, Visualization, Writing – review & editing. RR: Conceptualization, Formal analysis, Methodology, Writing – review & editing. SP: Formal analysis, Methodology, Writing – review & editing. SS: Methodology, Writing – review & editing. PS: Formal analysis, Methodology, Writing – review & editing. TL: Conceptualization, Formal analysis, Funding acquisition, Investigation, Methodology, Resources, Supervision, Validation, Visualization, Writing – review & editing.

Funding

The author(s) declare financial support was received for the research, authorship, and/or publication of this article. This work was supported by grants from the National Science Foundation (EAR-2026926), NASA Exobiology 80NSSC18K1532 and 80NSSC23K0346, and Alfred P. Sloan Foundation FG-2020-13552 (JO). Funding was also provided (TL) through the NASA Astrobiology Institute under Cooperative Agreement No. NNA15BB03A issued through the Science Mission Directorate, NASA Interdisciplinary Consortia for Astrobiology Research (ICAR), and the Geobiology and Low-Temperature Geochemistry Program of the National Science Foundation.

Conflict of interest

The authors declare that the research was conducted in the absence of any commercial or financial relationships that could be construed as a potential conflict of interest.

The author(s) declared that they were an editorial board member of Frontiers, at the time of submission. This had no impact on the peer review process and the final decision.

Publisher's note

Supplementary material

The Supplementary Material for this article can be found online at: https://www.frontiersin.org/articles/10.3389/fmars.2024.1428621/full#supplementary-material

References

Anderson, R., Cheng, H., Edwards, R., Fleisher, M., Hayes, C., Huang, K.-F., et al. (2016). How well can we quantify dust deposition to the ocean? *Philos. Trans. R. Soc. A: Mathematical Phys. Eng. Sci.* 374, 20150285.

Arnold, G. L., Weyer, S., and Anbar, A. (2004). Fe isotope variations in natural materials measured using high mass resolution multiple collector ICPMS. *Analytical Chem.* 76, 322–327. doi: 10.1021/ac034601v

Bacon, M. P., Huh, C.-A., Fleer, A. P., and Deuser, W. G. (1985). Seasonality in the flux of natural radionuclides and plutonium in the deep Sargasso Sea. *Deep Sea Res. Part A. Oceanographic Res. Papers* 32, 273–286. doi: 10.1016/0198-0149(85)90079-2

Baker, A. R., and Croot, P. L. (2010). Atmospheric and marine controls on aerosol iron solubility in seawater. *Mar. Chem.* 120, 4–13. doi: 10.1016/j.marchem.2008.09.003

Baker, A. R., and Jickells, T. D. (2006). Mineral particle size as a control on aerosol iron solubility. *Geophysical Res. Lett.* 33(17). doi: 10.1029/2006GL026557

Baker, A. R., Jickells, T. D., Witt, M., and Linge, K. L. (2006). Trends in the solubility of iron, aluminium, manganese and phosphorus in aerosol collected over the Atlantic Ocean. *Mar. Chem.* 98, 43–58. doi: 10.1016/j.marchem.2005.06.004

Baker, A. R., Kelly, S. D., Biswas, K. F., Witt, M., and Jickells, T. D. (2003). Atmospheric deposition of nutrients to the Atlantic Ocean. *Geophysical Res. Lett.* 30 (24). doi: 10.1029/2003GL018518

Bakker, N., Drake, N., and Bristow, C. S. (2019). Evaluating the relative importance of northern African mineral dust sources using remote sensing. *Atmospheric Chem. Phys.* 19, 10525–10535. doi: 10.5194/acp-19-10525-2019

Barbeau, K. (2006). Photochemistry of organic iron(III) complexing ligands in oceanic systems. *Photochem. Photobiol.* 82, 1505–1516. doi: 10.1562/2006-06-16-IR-935

Beard, B. L., Johnson, C. M., Skulan, J. L., Nealson, K. H., Cox, L., and Sun, H. (2003a). Application of Fe isotopes to tracing the geochemical and biological cycling of Fe. *Chem. Geol.* 195, 87–117. doi: 10.1016/S0009-2541(02)00390-X

Beard, B. L., Johnson, C. M., Von Damm, K. L., and Poulson, R. L. (2003b). Iron isotope constraints on Fe cycling and mass balance in oxygenated Earth oceans. *Geology* 31, 629–632. doi: 10.1130/0091-7613(2003)031<0629:IICOFC>2.0.CO;2

Benner, S. G., Hansel, C. M., Wielinga, B. W., Barber, T. M., and Fendorf, S. (2002). Reductive dissolution and biomineralization of iron hydroxide under dynamic flow conditions. *Environ. Sci. Technol.* 36, 1705–1711. doi: 10.1021/es0156441

Bhattachan, A., Reche, I., and D'Odorico, P. (2016). Soluble ferrous iron (Fe (II)) enrichment in airborne dust. *J. Geophysical Res.: Atmospheres* 121, 10–153. doi: 10.1002/2016JD025025

Blott, S. (2000). Grain size distribution and statistics package for the analysis of unconsolidated sediments by sieving or by laser granulometer. *Grandistat* 26, 1237–1248.

Blott, S. J., and Pye, K. (2001). GRADISTAT: A grain size distribution and statistics package for the analysis of unconsolidated sediments. *Earth Surface Processes Landforms* 26(11):1237–1248. doi: 10.1002/esp.261

Borchardt, T., Fisher, K. V., Ebling, A. M., Westrich, J. R., Xian, P., Holmes, C. D., et al (2019). Saharan dust deposition initiates successional patterns among marine microbes in the Western Atlantic. *Limnol. Oceanogr.* 65(1):191-203. doi: 10.1002/lno.11291

Boyd, P., and Ellwood, M. (2010). The biogeochemical cycle of iron in the ocean. *Nat. Geosci.* 3, 675. doi: 10.1038/ngeo964

Bressac, M., and Guieu, C. (2013). Post-depositional processes: What really happens to new atmospheric iron in the ocean's surface? *Global biogeochemical cycles* 27, 859–870. doi: 10.1002/gbc.20076

Bristow, C. S., Hudson-Edwards, K. A., and Chappell, A. (2010). Fertilizing the Amazon and equatorial Atlantic with West African dust. *Geophysical Res. Lett.* 37(14). doi: 10.1029/2010GL043486

Clarkson, M., Poulton, S., Guilbaud, R., and Wood, R. (2014). Assessing the utility of Fe/Al and Fe-speciation to record water column redox conditions in carbonate-rich sediments. *Chem. Geol.* 382, 111–122. doi: 10.1016/j.chemgeo.2014.05.031

Conway, T. M., Hamilton, D. S., Shelley, R. U., Aguilar-Islas, A. M., Landing, W. M., Mahowald, N. M., et al. (2019). Tracing and constraining anthropogenic aerosol iron fluxes to the North Atlantic Ocean using iron isotopes. *Nat. Commun.* 10, 2628. doi: 10.1038/s41467-019-10279-w

Conway, T. M., and John, S. G. (2014). Quantification of dissolved iron sources to the North Atlantic Ocean. *Nature* 511, 212. doi: 10.1038/nature13482

Dauphas, N., and Rouxel, O. (2006). Mass spectrometry and natural variations of iron isotopes. *Mass Spectrometry Rev.* 25, 515–550. doi: 10.1002/mas.20078

Desboeufs, K., Losno, R., and Colin, J.-L. (2001). Factors influencing aerosol solubility during cloud processes. *Atmospheric Environ.* 35, 3529–3537. doi: 10.1016/S1352-2310(00)00472-6

Engelstaedter, S., Tegen, I., and Washington, R. (2006). North African dust emissions and transport. *Earth-Sci. Rev.* 79, 73–100. doi: 10.1016/j.earscirev.2006.06.004

Fan, S.-M., Moxim, W. J., and Levy, H. (2006). Aeolian input of bioavailable iron to the ocean. *Geophysical Res. Lett.* 33(7). doi: 10.1029/2005GL024852

Fung, I. Y., Meyn, S. K., Tegen, I., Doney, S. C., John, J., and Bishop, J. (2000). Iron supply and demand in the upper ocean (vol 14, pg 281, 2000). *Global biogeochemical cycles* 14, 697–700. doi: 10.1029/2000gb900001

Ginoux, P., Chin, M., Tegen, I., Prospero, J., Holben, B., Dubovik, O., et al. (2001). Global simulation of dust in the troposphere: Model description and assessment. *J. Geophys. Res.* 106, 255–220.

Giosan, L., Flood, R. D., Grützner, J., and Mudie, P. (2002). Paleoceanographic significance of sediment color on western North Atlantic drifts: II. Late Pliocene–Pleistocene sedimentation. *Mar. Geol.* 189, 43–61. doi: 10.1016/S0025-3227(02)00322-5

Hand, J. L., Mahowald, N. M., Chen, Y., Siefert, R. L., Luo, C., Subramaniam, A., et al. (2004). Estimates of atmospheric-processed soluble iron from observations and a global mineral aerosol model: Biogeochemical implications. *J. Geophysical Research-Atmospheres* 109(D17). doi: 10.1029/2004JD004574

Harrison, S. P., Kohfeld, K. E., Roelandt, C., and Claquin, T. (2001). The role of dust in climate changes today, at the last glacial maximum and in the future. *Earth-Sci. Rev.* 54, 43–80. doi: 10.1016/S0012-8252(01)00041-1

Hassler, C. S., Schoemann, V., Nichols, C. M., Butler, E. C. V., and Boyd, P. W. (2011). Saccharides enhance iron bioavailability to Southern Ocean phytoplankton. *Proc. Natl. Acad. Sci. United States America* 108, 1076–1081. doi: 10.1073/pnas.1010963108

Haynes, W. (2013). "Student's t-test," in *Encyclopedia of Systems Biology* (New York, NY: Springer), 2023–2025.

Heron, G., Crouzet, C., Bourg, A. C., and Christensen, T. H. (1994). Speciation of Fe (II) and Fe (III) in contaminated aquifer sediments using chemical extraction techniques. *Environ. Sci. Technol.* 28, 1698–1705. doi: 10.1021/es00058a023

Huneeus, N., Schulz, M., Balkanski, Y., Griesfeller, J., Prospero, M., Kinne, S., et al. (2011). Global dust model intercomparison in AeroCom phase I. *Atmospheric Chem. Phys.* 11, 7781–7816. doi: 10.5194/acp-11-7781-2011

Jickells, T. D., An, Z. S., Andersen, K. K., Baker, A. R., Bergametti, G., Brooks, N., et al. (2005). Global iron connections between desert dust, ocean biogeochemistry, and climate. *Science* 308, 67–71. doi: 10.1126/science.1105959

Joos, F., Sarmiento, J. L., and Siegenthaler, U. (1991). Estimates of the effect of Southern Ocean iron fertilization on atmospheric CO2 concentrations. *Nature* 349, 772. doi: 10.1038/349772a0

Lis, H., Shaked, Y., Kranzler, C., Keren, N., and Morel, F. M. (2015). Iron bioavailability to phytoplankton: an empirical approach. *ISME J.* 9, 1003. doi: 10.1038/ismej.2014.199

Mackie, D., Peat, J., McTainsh, G., Boyd, P., and Hunter, K. (2006). Soil abrasion and eolian dust production: Implications for iron partitioning and solubility. *Geochem. Geophys. Geosystems* 7(12). doi: 10.1029/2006GC001404

Maher, B., Prospero, J., Mackie, D., Gaiero, D., Hesse, P. P., and Balkanski, Y. (2010). Global connections between aeolian dust, climate and ocean biogeochemistry at the present day and at the last glacial maximum. *Earth-Sci. Rev.* 99, 61–97. doi: 10.1016/j.earscirev.2009.12.001

Mahowald, N., Albani, S., Kok, J. F., Engelstaeder, S., Scanza, R., Ward, D. S., et al. (2014). The size distribution of desert dust aerosols and its impact on the Earth system. *Aeolian Res.* 15, 53–71. doi: 10.1016/j.aeolia.2013.09.002

Mahowald, N. M., Hamilton, D. S., Mackey, K. R., Moore, J. K., Baker, A. R., Scanza, R. A., et al. (2018). Aerosol trace metal leaching and impacts on marine microorganisms. *Nat. Commun.* 9, 1–15. doi: 10.1038/s41467-018-04970-7

Mahowald, N., Kohfeld, K., Hansson, M., Balkanski, Y., Harrison, S. P., Prentice, I. C., et al. (1999). Dust sources and deposition during the last glacial maximum and current climate: A comparison of model results with paleodata from ice cores and marine sediments. *J. Geophysical Research-Atmospheres* 104, 15895–15916. doi: 10.1029/1999JD900084

Martin, J. H., and Fitzwater, S. E. (1988). Iron deficiency limits phytoplankton growth in the north-east Pacific subarctic. *Nature* 331, 341. doi: 10.1038/331341a0

Martinez, N. C., Murray, R., Thunell, R. C., Peterson, L. C., Muller-Karger, F., Astor, Y., et al. (2007). Modern climate forcing of terrigenous deposition in the tropics (Cariaco Basin, Venezuela). *Earth Planetary Sci. Lett.* 264, 438–451. doi: 10.1016/j.epsl.2007.10.002

McGee, D., Broecker, W. S., and Winckler, G. (2010). Gustiness: The driver of glacial dustiness? *Quaternary Sci. Rev.* 29, 2340–2350. doi: 10.1016/j.quascirev.2010.06.009

McGee, D., deMenocal, P. B., Winckler, G., Stuut, J. B. W., and Bradtmiller, L. I. (2013). The magnitude, timing and abruptness of changes in North African dust deposition over the last 20,000yr. *Earth Planetary Sci. Lett.* 371-372, 163–176. doi: 10.1016/j.epsl.2013.03.054

Meskhidze, N., Völker, C., Al-Abadleh, H. A., Barbeau, K., Bressac, M., Buck, C., et al. (2019). Perspective on identifying and characterizing the processes controlling iron speciation and residence time at the atmosphere-ocean interface. *Mar. Chem.* 217, 103704. doi: 10.1016/j.marchem.2019.103704

Montgomery, D. C., Runger, G. C., and Hubele, N. F. (2009). *Engineering statistics* (Wiley, New York, NY: John Wiley & Sons).

Moore, C. M., Mills, M. M., Achterberg, E. P., Geider, R. J., LaRoche, J., Lucas, M. I., et al. (2009). Large-scale distribution of Atlantic nitrogen fixation controlled by iron availability. *Nat. Geosci.* 2, 867–871. doi: 10.1038/ngeo667

Muhs, D. R., Budahn, J. R., Prospero, J. M., and Carey, S. N. (2007). Geochemical evidence for African dust inputs to soils of western Atlantic islands: Barbados, the Bahamas, and Florida. *J. Geophysical Res.* 112(F2). doi: 10.1029/2005JF000445

Muhs, D. R., Budahn, J. R., Prospero, J. M., Skipp, G., and Herwitz, S. R. (2012). Soil genesis on the island of Bermuda in the Quaternary: The importance of African dust transport and deposition. *J. Geophysical Res.: Earth Surface* 117(F3). doi: 10.1029/2012JF002366

Oakes, M., Ingall, E., Lai, B., Shafer, M., Hays, M., Liu, Z., et al. (2012). Iron solubility related to particle sulfur content in source emission and ambient fine particles. *Environ. Sci. Technol.* 46, 6637–6644. doi: 10.1021/es300701c

Ooki, A., Nishioka, J., Ono, T., and Noriki, S. (2009). Size dependence of iron solubility of Asian mineral dust particles. *J. Geophysical Research-Atmospheres* 114 (D3). doi: 10.1029/2008JD010804

Owens, J. D., Lyons, T. W., Li, X. N., Macleod, K. G., Gordon, G., Kuypers, M. M. M., et al. (2012). Iron isotope and trace metal records of iron cycling in the proto-North Atlantic during the Cenomanian-Turonian oceanic anoxic event (OAE-2). *Paleoceanography* 27(3). doi: 10.1029/2012PA002328

Poulton, S. W., and Canfield, D. E. (2005). Development of a sequential extraction procedure for iron: implications for iron partitioning in continentally derived particulates. *Chem. Geol.* 214, 209–221. doi: 10.1016/j.chemgeo.2004.09.003

Poulton, S. W., and Raiswell, R. (2005). Chemical and physical characteristics of iron oxides in riverine and glacial meltwater sediments. *Chem. Geol.* 218, 203–221. doi: 10.1016/j.chemgeo.2005.01.007

Prospero, J. M., and Mayol-Bracero, O. L. (2013). Understanding the transport and impact of African dust on the Caribbean basin. *Bull. Am. Meteorological Soc.* 94, 1329–1337. doi: 10.1175/BAMS-D-12-00142.1

Pye, K. (1989). "Processes of fine particle formation, dust source regions, and climatic changes," in *Paleoclimatology and Paleometeorology: Modern and Past Patterns of Global Atmospheric Transport* (Springer), 3–30.

Raiswell, R., and Canfield, D. E. (2012). The iron biogeochemical cycle past and present. *Geochemical Perspect.* 1, 1–220. doi: 10.7185/geochempersp.1.1

Raiswell, R., Hardisty, D. S., Lyons, T. W., Canfield, D. E., Owens, J. D., Planavsky, N. J., et al. (2018a). The iron paleoredox proxies: A guide to the pitfalls, problems and proper practice. *Am. J. Sci.* 318, 491–526. doi: 10.2475/05.2018.03

Raiswell, R., Hawkings, J., Elsenousy, A., Death, R., Tranter, M., and Wadham, J. (2018b). Iron in glacial systems: Speciation, reactivity, freezing behaviour and alteration during transport. *Front. Earth Sci.* 6, 222. doi: 10.3389/feart.2018.00222

Ridgwell, A., and Hargreaves, J. (2007). Regulation of atmospheric $CO_{2\ by}$ deep-sea sediments in an Earth system model. *Global Biogeochemical Cycles* 21(2). doi: 10.1029/2006GB002764

Sardar Abadi, M., Owens, J. D., Liu, X., Them, T. R., Cui, X., Heavens, N. G., et al. (2020). Atmospheric dust stimulated marine primary productivity during Earth's penultimate icehouse. *Geology.* 48, 247-251. doi: 10.1130/G46977.1

Schwertmann, U., Stanjek, H., and Becher, H.-H. (2004). Long-term in *vitro* transformation of 2-line ferrihydrite to goethite/hematite at 4, 10, 15 and 25 C. *Clay Minerals* 39, 433–438. doi: 10.1180/0009855043940145

Shaked, Y., and Lis, H. (2012). Disassembling iron availability to phytoplankton. *Front. microbiol.* 3, 123. doi: 10.3389/fmicb.2012.00123

Shi, Z. B., Krom, M. D., Bonneville, S., Baker, A. R., Jickells, T. D., and Benning, L. G. (2009). Formation of iron nanoparticles and increase in iron reactivity in mineral dust during simulated cloud processing. *Environ. Sci. Technol.* 43, 6592–6596. doi: 10.1021/es901294g

Shinn, E. A., Smith, G. W., Prospero, J. M., Betzer, P., Hayes, M. L., Garrison, V., et al. (2000). African dust and the demise of Caribbean coral reefs. *Geophysical Res. Lett.* 27, 3029–3032. doi: 10.1029/2000GL011599

Shoenfelt, E. M., Sun, J., Winckler, G., Kaplan, M. R., Borunda, A. L., Farrell, K. R., et al. (2017). High particulate iron (II) content in glacially sourced dusts enhances productivity of a model diatom. *Sci. Adv.* 3, e1700314. doi: 10.1126/sciadv.1700314

Shoenfelt, E. M., Winckler, G., Lamy, F., Anderson, R. F., and Bostick, B. C. (2018). Highly bioavailable dust-borne iron delivered to the Southern Ocean during glacial periods. *Proc. Natl. Acad. Sci.* 115, 11180–11185. doi: 10.1073/pnas.1809755115

Skonieczny, C., McGee, D., Winckler, G., Bory, A., Bradtmiller, L., Kinsley, C., et al. (2019). Monsoon-driven Saharan dust variability over the past 240,000 years. *Sci. Adv.* 5, eaav1887. doi: 10.1126/sciadv.aav1887

Skulan, J. L., Beard, B. L., and Johnson, C. M. (2002). Kinetic and equilibrium Fe isotope fractionation between aqueous Fe(III) and hematite. *Geochimica Cosmochimica Acta* 66, 2995–3015. doi: 10.1016/S0016-7037(02)00902-X

Spokes, L. J., Jickells, T. D., and Lim, B. (1994). Solubilisation of aerosol trace metals by cloud processing: A laboratory study. *Geochimica Cosmochimica Acta* 58, 3281–3287. doi: 10.1016/0016-7037(94)90056-6

Sur, S., Owens, J. D., Soreghan, G. S., Lyons, T. W., Raiswell, R., Heavens, N. G., et al. (2015). Extreme eolian delivery of reactive iron to late Paleozoic icehouse seas. *Geology* 43, 1099–1102. doi: 10.1130/G37226.1

Swart, P. K., Oehlert, A., Mackenzie, G., Eberli, G. P., and Reijmer, J. (2014). The fertilization of the Bahamas by Saharan dust: A trigger for carbonate precipitation? *Geology* 42, 671–674. doi: 10.1130/G35744.1

Thöle, L. M., Amsler, H. E., Moretti, S., Auderset, A., Gilgannon, J., Lippold, J., et al. (2019). Glacial-interglacial dust and export production records from the Southern Indian Ocean. *Earth planetary Sci. Lett.* 525, 115716. doi: 10.1016/j.epsl.2019.115716

Tiedemann, R., Sarnthein, M., and Stein, R. (1989). Climatic changes in the western Sahara: Aeolo-marine sediment record of the last 8 million years (sites 657-661). *Proc. ocean drilling program Sci. results* 108, 241-277. College Station, Tex.: Ocean Drilling Program.

Trapp, J. M., Millero, F. J., and Prospero, J. M. (2010). Trends in the solubility of iron in dust-dominated aerosols in the equatorial Atlantic trade winds: Importance of iron speciation and sources. *Geochem. Geophys. Geosystems* 11(3). doi: 10.1029/2009GC002651

Viollier, E., Inglett, P., Hunter, K., Roychoudhury, A., and Van Cappellen, P. (2000). The ferrozine method revisited: Fe (II)/Fe (III) determination in natural waters. *Appl. geochemistry* 15, 785–790. doi: 10.1016/S0883-2927(99)00097-9

Waeles, M., Baker, A. R., Jickells, T., and Hoogewerff, J. (2007). Global dust teleconnections: aerosol iron solubility and stable isotope composition. *Environ. Chem.* 4, 233–237. doi: 10.1071/EN07013

Ward, B. A., Wilson, J. D., Death, R. M., Monteiro, F. M., Yool, A., and Ridgwell, A. (2018). EcoGEnIE 1.0: plankton ecology in the cGEnIE Earth system model. *Geoscientific Model. Dev.* 11, 4241–4267. doi: 10.5194/gmd-11-4241-2018

Wells, M. L., Zorkin, N. G., and Lewis, A. (1983). The role of colloid chemistry in providing a source of iron to phytoplankton. *J. Mar. Res.* 41, 731–746. doi: 10.1357/002224083788520478

Yarincik, K., Murray, R., and Peterson, L. (2000). Climatically sensitive eolian and hemipelagic deposition in the Cariaco Basin, Venezuela, over the past 578,000 years: Results from Al/Ti and K/Al. *Paleoceanography* 15, 210–228. doi: 10.1029/1999PA900048

Yu, H., Chin, M., Yuan, T., Bian, H., Remer, L. A., Prospero, J. M., et al. (2015). The fertilizing role of African dust in the Amazon rainforest: A first multiyear assessment based on data from Cloud-Aerosol Lidar and Infrared Pathfinder Satellite Observations. *Geophysical Res. Lett.* 42, 1984–1991. doi: 10.1002/2015GL063040

Zhang, Y., Mahowald, N., Scanza, R., Journet, E., Desboeufs, K., Albani, S., et al. (2015). Modeling the global emission, transport and deposition of trace elements associated with mineral dust. *Biogeosciences.* 12, 5771-5792. doi: 10.5194/bgd-11-17491-2014

frontiers | Frontiers in Marine Science

TYPE Original Research
PUBLISHED 07 October 2024
DOI 10.3389/fmars.2024.1474189

OPEN ACCESS

EDITED BY
Khan M. G. Mostofa,
Tianjin University, China

REVIEWED BY
Rui Bao,
Ocean University of China, China
Shuting Liu,
Kean University, United States
Xiting Liu,
Ocean University of China, China

*CORRESPONDENCE
Haisheng Zhang
zhangsoa@sio.org.cn
Jun Zhao
jzhao@sio.org.cn

†These authors have contributed equally to this work

RECEIVED 01 August 2024
ACCEPTED 17 September 2024
PUBLISHED 07 October 2024

CITATION
Yang D, Chen W, Huang W, Zhang H, Han Z, Lu B and Zhao J (2024) Spatial and historical patterns of sedimentary organic matter sources and environmental changes in the Ross Sea, Antarctic: implication from bulk and *n*-alkane proxies. *Front. Mar. Sci.* 11:1474189. doi: 10.3389/fmars.2024.1474189

Spatial and historical patterns of sedimentary organic matter sources and environmental changes in the Ross Sea, Antarctic: implication from bulk and *n*-alkane proxies

Dan Yang[1†], Wenshen Chen[2†], Wenhao Huang[1,3], Haisheng Zhang[1*], Zhengbing Han[1], Bing Lu[1] and Jun Zhao[1*]

[1]Key Laboratory of Marine Ecosystem Dynamics, Second Institute of Oceanography, Ministry of Natural Resources, Hangzhou, China, [2]Zhuhai Central Station of Marine Environmental Monitoring, State Oceanic Administration, Zhuhai, China, [3]School of Ocean Sciences, China University of Geosciences, Beijing, China

Organic carbon (OC) burial in the Antarctic marginal seas is essential for regulating global climate, particularly due to its association with ice shelf retreat. Here, we analyzed total OC (TOC), total nitrogen (TN), radiocarbon isotope, *n*-alkanes and relative indicators in surface and core sediments from the Ross Sea, West Antarctica. Our aim was to investigate spatial and historical changes in OC sources, and to explore the influencing factors and implications for ice shelf retreat since the last glacial maximum (LGM). Our results revealed distinct spatial patterns of OC sources as indicated by *n*-alkane indicators in surface sediments. In the Western Ross Sea, *n*-alkanes predominantly originated from phytoplankton and bacteria, as evidenced by their unimodal distribution, low carbon preference index (CPI) of short-chain *n*-alkanes (CPI_L = 1.41 ± 0.30), and low terrestrial/aquatic ratio (TAR = 0.22 ± 0.14). In the Southwest Ross Sea, *n*-alkanes were derived from marine algae and terrestrial bryophytes, indicated by bimodal distribution, low ratio of low/high molecular-weight *n*-alkanes (L/H = 0.62 ± 0.21), low CPI of long-chain *n*-alkanes (CPI_H = 1.18 ± 0.16), and high TAR (1.26 ± 0.66). In contrast, the Eastern Ross Sea exhibited *n*-alkanes that were a combination of phytoplankton and dust from Antarctic soils and/or leaf waxes from mid-latitude higher plant, as suggested by both unimodal and bimodal distributions, high L/H (1.60 ± 0.58) and CPI_H (2.04 ± 0.28), and medium TAR (0.61 ± 0.30). Geologically, during the LGM (27.3 – 21.0 ka before present (BP)), there was an increased supply of terrestrial OC (TOC/TN = 13.63 ± 1.29, bimodal distribution of *n*-alkanes with main carbon peaks at nC_{17}/nC_{19} and nC_{27}). From 21.0 to 8.2 ka BP, as glaciers retreated and temperatures rose, the proportion of marine *n*-alkanes significantly increased (TOC/TN = 9.09 ± 1.82, bimodal distribution of *n*-alkanes with main carbon peaks at nC_{18}/nC_{19} and nC_{25}). From 8.2 ka BP to the present, as the ice shelf continued to retreat to its current position, the marine contribution became dominant (TOC/TN = 8.18 ± 0.51,

unimodal distribution of *n*-alkanes with main carbon peak at $nC_{17}/nC_{18}/nC_{19}$, and low TAR (0.41 ± 0.32)). This research has significant implications for understanding the variations in Antarctic OC sources and their climatic impacts in the context of accelerated glacier melting.

KEYWORDS

Ross Sea, marine sediments, *n*-alkanes, organic matter, environment change

1 Introduction

Marine sediments, located at the interface of the hydrosphere, biosphere and lithosphere, serve a critical function as carbon reservoirs, facilitating the deposition, burial, and preservation of organic matter (LaRowe et al., 2020). The total organic carbon (TOC) in marine sediments primarily comprises various components, including lipids, proteins, carbohydrates, and humic substances (Burdige, 2007; Lomstein et al., 2012; Dittmar and Stubbins, 2014). The origins of TOC from different sources, including marine, terrestrial and bacterial origins, are often a key concern of research (Didyk et al., 1978; Gustafsson et al., 2009; Bianchi and Canuel, 2011). Traditional parameters used to characterize organic matter, such as the molar ratio of TOC to total nitrogen (TN) (Mayer, 1994; Zhang et al., 2023) and the carbon and nitrogen isotopes of organic matter ($\delta^{13}C$, $\delta^{15}N$) (Das et al., 2007; Wu et al., 2020), provide valuable insights into the main sources of TOC but exhibit limitations regarding source specificity. Given the complex nature of TOC sources, more precise methods, such as the chemical biomarker approach, are essential for tracing the origins of specific TOC components (Bianchi and Canuel, 2011; Gal et al., 2022). Chemical biomarkers are organic compounds found within the environmental matrix that can be linked back to their biological sources (Eglinton and Calvin, 1967; Meyers, 2003) and the prevailing climatic conditions at the time of their formation (Liu and An, 2020). Despite undergoing significant geochemical transformations like oxidation and reduction during early diagenesis over extended periods, these biomarkers retain the carbon chain structures of their parent molecules (Bianchi et al., 2016), making them valuable indicators of material sources.

N-alkanes, which are saturated straight-chain hydrocarbons typically ranging from nC_{14} to nC_{34} in length, are abundant in marine sediments, resistant to degradation and source-specific, making them effective biomarkers (Zhao et al., 2022). In contrast, some biomarkers such as lignin, may have certain regional limitations. For instance, lignin is commonly utilized in mid- and low-latitude seas, but is challenging to apply in Antarctica due to the absence of vascular plants (Bianchi and Canuel, 2011). Various organisms, including algae, aquatic macrophytes, terrestrial plants and bacteria, can synthesize *n*-alkanes. In marine sediments, *n*-alkanes are derived from autochthonous sources, such as algae and bacteria, and allochthonous inputs from terrestrial plants (Eglinton and Eglinton, 2008). Distinct compositional patterns exist among different sources: medium to short-chain even *n*-alkanes (nC_{12} to nC_{22}, mainly nC_{16} and nC_{18}) originate from bacteria (Grimalt and Albaigés, 1987); medium to short-chain odd *n*-alkanes (nC_{13} to nC_{21}, mainly nC_{15}, nC_{17} and nC_{19}) are produced by marine algae (Blumer et al., 1971); medium-chain odd *n*-alkanes (mainly nC_{23} and nC_{25}) are derived from mosses (Baas et al., 2000; Bingham et al., 2010); and long-chain *n*-alkanes (nC_{25} to nC_{34}, with a predominance of nC_{27}, nC_{29} and nC_{31}) mainly come from terrestrial higher plants (Eglinton and Calvin, 1967; Wang et al., 2021). Various proxies based on *n*-alkanes of different carbon chain lengths have been developed, such as the terrestrial/aquatic ratio (TAR) (Meyers, 1997), the low molecular-weight (nC_{13} to nC_{21}) to high molecular-weight *n*-alkanes (nC_{25} to nC_{34}) (L/H), and the long-chain and short-chain carbon preference index (CPI_H and CPI_L) (Eglinton and Calvin, 1967; Cranwell et al., 1987). These proxies are valuable indicators for elucidating the sources, composition, and distribution of organic carbon in sedimentary environments (Zhao et al., 2018). *N*-alkanes also respond to variations in climate and environmental conditions (Liu and An, 2020), with the distribution patterns exhibiting systematic changes across different stages of sedimentary geological evolution (Hanisch et al., 2003; Li et al., 2008). For instance, the collective abundance of nC_{21} to nC_{33} significantly increased during glacial periods and decreased during interglacial periods, reflecting alterations in terrestrial material input (Ikehara et al., 2000; Ternois et al., 2001). Consequently, *n*-alkanes present in sediment cores serve as valuable proxies for reconstructing past environmental changes in marine ecosystems.

Antarctica, particularly West Antarctica, is currently experiencing a critical phase of accelerated glacial melting and significant environmental changes (The IMBIE Team, 2018;

Abbreviations: OC, organic carbon; TOC, total organic carbon; TN, total nitrogen; $\delta^{13}C$, $\delta^{15}N$, stable isotopes of carbon and nitrogen; $\Delta^{14}C$, radiocarbon isotope; L/H, low/high molecular-weight *n*-alkanes; CPI, carbon preference index; CPI_L, CPI of short-chain (or low molecular-weight) *n*-alkanes; CPI_H, CPI of long-chain (or high molecular-weight) *n*-alkanes; TAR, terrestrial/aquatic ratio; LGM, last glacial maximum; BP, before present; RSP, Ross Sea Polynya; MSP, McMurdo Sound Polynya; TNBP, Terra Nova Bay Polynya; M_Z, mean particle size; σ, sorting coefficient; SK, skewness; K_G, kurtosis; CHINARE, Chinese National Antarctic Research Expedition.

Naughten et al., 2023). These alterations have resulted in shifts in the community structure and biomass of phytoplankton and zooplankton in West Antarctica (Lin et al., 2021; Yang et al., 2022; Trinh et al., 2023). The Ross Sea is a key region in West Antarctica, with significant regional variations in hydrodynamic conditions (Wu et al., 2024) that have potential implications for organic matter preservation (Eusterhues et al., 2003; Keil and Mayer, 2014). Furthermore, the Ross Sea is undergoing modifications in sea ice extent, primary productivity, and plankton populations (Orr et al., 2005; Matson et al., 2011; Smith et al., 2012; Kim et al., 2023), all of which influence the quantity and composition of organic matter in sediments. Previous research has examined the composition and distribution of *n*-alkanes in various substrates, including microbial mats, mosses, lichens (Chen et al., 2019a, 2021), soils (Matsumoto et al., 2010), suspended particulates (Tao et al., 2022) and sediments (Kvenvolden et al., 1987; Venkatesan, 1988; Duncan et al., 2019; Chen, 2020) in the Ross Sea. For example, Kvenvolden et al. (1987) reported that *n*-alkanes in near-surface sediments in the Western Ross Sea primarily originate from two sources: both primary and reworked marine materials, and aged organic matter redeposited from terrestrial plants. Duncan et al. (2019) observed that C_{29} *n*-alkanes dominated in late Miocene sediments, while C_{27} *n*-alkanes dominated in the Oligocene, suggesting the influence of climate change on vegetation evolution. Chen (2020) found that long-chain *n*-alkanes (nC_{27} to nC_{35}) in a 330,000-year-old deep-sea core from the Ross Sea fan area mainly come from Antarctic soils, and long-distance transport of dust from mid-latitude terrestrial sources, plant leaf waxes. Despite these studies, there remains a significant gap in comprehensive research on the sources of *n*-alkanes in surface sediments. Additionally, studies on the characteristics of *n*-alkanes in the Ross Sea since the last glacial maximum (LGM) and their response to changes in ice shelves are notably insufficient.

In this study, we analyzed grain size, TOC, TN, radiocarbon isotopes ($\Delta^{14}C$) and *n*-alkanes in 18 surface sediments and one sediment core collected from the Ross Sea. We calculated parameters related to hydrodynamic conditions and traced the sources of TOC and *n*-alkanes. We specifically addressed the following three issues: 1. to investigate spatial distribution variances and influencing factors of hydrodynamic conditions, OC content and sources in surface sediments; 2. to examine spatial distribution variances in the sources of *n*-alkanes in surface sediments; 3. to assess the impact of changes in the ice shelf on *n*-alkane characteristics since the LGM.

2 Study area and sample collection

2.1 Study area

The Ross Sea is located at the southwestern boundary of the Antarctic continent within the Pacific sector of the Southern Ocean, and is the second largest bay in this region, covering an area of approximately 750,000 km² (Smith et al., 2012). It is bordered by Marie Byrd Land to the east, the Transantarctic Mountains and Victoria Land to the west, and to the south, it adjoins the Ross Ice Shelf, which is the largest ice shelf in the world, spaning about 500,000 km². The Ross Sea is a vital source region for Antarctic Bottom Water (Whitworth and Orsi, 2006). Sea ice distribution in the Ross Sea displays significant seasonal fluctuations, with polynyas like the Ross Sea Polynya (RSP), McMurdo Sound Polynya (MSP), and Terra Nova Bay Polynya (TNBP) forming earlier in the summer along the front of the Ross Ice Shelf and the coast of Victoria Land, primarily due to katabatic wind (Parish et al., 2006; Tamura et al., 2008). The Ross Sea boasts high primary productivity, contributing approximately one-third of the Southern Ocean's primary productivity (Arrigo et al., 2008a, 2008b), and hosts a thriving ecosystem. Notably, the Adélie penguin population in the Ross Sea represents one-third of the global population (Xu et al., 2021).

The Ross Sea continental shelf is geographically divided into Eastern and Western regions by approximately 180° longitude, with water depths ranging from less than 500 m to over 1000 m. The eastern shelf is predominantly characterized by a broad basin and gently undulating shoals, while the western shelf features narrow basins and more pronounced undulating shoals (Halberstadt et al., 2016; Gales et al., 2021; Ha et al., 2022). TOC in the surface sediments of the Ross Sea primarily originates from upper ocean primary production (DeMaster et al., 1996; Langone et al., 1998) based on biomarker compounds (Song et al., 2019), OC/TN ratio and $\delta^{13}C$ (Xiu et al., 2017). The southwestern Ross Sea, including RSP and MSP, exhibits high content of biogenic components (OC, TN, and opal) and represents a distinct environment setting compared to the western Ross Sea (Zhou et al., 2022). Based on the differences in the geographic location and biogenic components, our sediment samples were categorized into three distinct groups: Southwest, Western and Eastern (Figure 1, Supplementary Table S1).

2.2 Sample collection

Eighteen surface sediments were collected during the 31st and 32nd Chinese National Antarctic Research Expeditions (CHINARE-31 and -32) (Figure 1). They were collected by a box sampler, and the 0 – 1 cm sediment layer was taken as the surface sample. A gravity core sediment sample at station JB03 (170.698°E, 75.804°S, water depth = 615 m) within the southern Joides Trough were collected during CHINARE-31. The total length of the sediment core was 130 cm, and was divided at 2 cm intervals. All samples were frozen at –20°C, brought back to the laboratory and kept frozen at –20°C until analysis.

3 Analytical methods

3.1 Sediment particle size analysis

The particle size of sediment samples was determined using a laser particle size analyzer (range 0.02 to 4000 μm, Mastersizer 3000, UK, the precision is better than 1%). Ca. 1.0 to 2.0 g untreated wet sediment samples was placed into beakers with a small amount

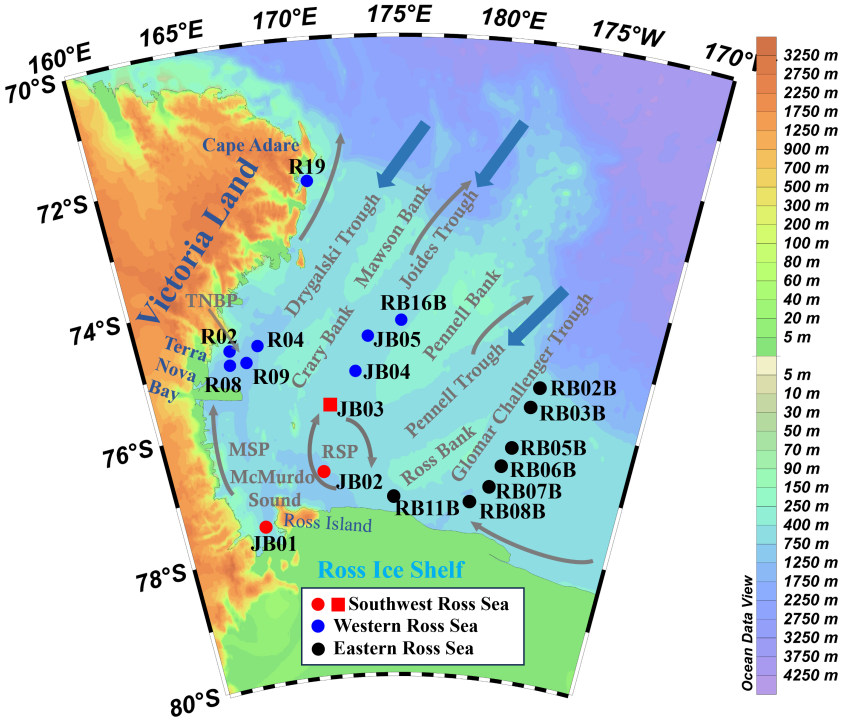

FIGURE 1
Surface sediment samples (dots) from Southwest (in red), Western (in blue) and Eastern (in black) Ross Sea, the sediment core sample (square), with water depth (values in legend) and circulation patterns (arrows) (Pillsbury and Jacobs, 1985; Dinniman et al., 2003; Smith et al., 2012). TNBP, Terra Nova Bay Polynya; RSP, Ross Sea Polynya; MSP, McMurdo Sound Polynya.

of deionized water to soak the samples. A small amount of 30% hydrogen peroxide (H_2O_2) was added until no bubbles were produced to remove sedimentary organic matter. 0.25 mol/L of dilute HCl was added to remove carbonates in the sample, followed by 20 mL of a 1 mol/L $NaCO_3$ solution, and the beaker was placed into a constant temperature water bath at 85°C for 4 h. Deionized water was added and the solution was stirred with a glass rod, left to stand for 24 h, and the supernatant collected. This step was repeated for 3 times, until the washing produced a neutral pH solution. 1 mL of 0.5 mol/L sodium hexametaphosphate was added to the combined supernatant as a dispersive substance, and a suspension was formed by ultrasonic oscillation for 120 s. The suspension was collected and particle sizes were measured on the instrument.

Sediment samples were separated into 3 standard size fractions: sand (> 63 μm), silt (4 – 63 μm), and clay (< 4 μm). Based on the φ values (φ_5, φ_{16}, φ_{25}, φ_{50}, φ_{75}, φ_{84}, φ_{95}) corresponding to the 5%, 16%, 25%, 50%, 75%, 84%, and 95% points on the cumulative probability curve, the mean particle size (M_Z), sorting coefficient (σ), skewness (SK) and kurtosis (K_G) were calculated to characterize the sedimentary environment (Folk and Ward, 1957). Generally, Mz is constrained by a value of 4 φ, with values greater than 4 φ indicating a low-energy sedimentary environment, while values less than 4 φ suggesting a high-energy environment. A smaller σ value denotes better sediment sorting. SK is used to measure the symmetry of particle size frequency distribution. Furthermore, a smaller K_G value reflects a broader distribution in the sharpness of the grain size frequency curve (see Supplementary Text S1 for indicative meanings of the above parameters).

$$M_z = \frac{\varphi_{16} + \varphi_{50} + \varphi_{84}}{3}$$

$$\sigma = \frac{\varphi_{84} - \varphi_{16}}{4} + \frac{\varphi_{95} - \varphi_5}{6.6}$$

$$SK = \frac{\varphi_{16} + \varphi_{84} - 2\varphi_{50}}{2(\varphi_{84} - \varphi_{16})} + \frac{\varphi_5 + \varphi_{95} - 2\varphi_{50}}{2(\varphi_{95} - \varphi_5)}$$

$$K_G = \frac{\varphi_{95} - \varphi_5}{2.44(\varphi_{75} - \varphi_{25})}$$

3.2 TOC and TN content

TOC and TN contents of the samples were determined by an elemental analyzer (Elementar Vario MICRO cube, Germany). TOC determination requires acid removal of inorganic carbon, while TN does not (Schubert and Nielsen, 2000). Briefly, 0.5 g of lyophilized and ground sediment samples were weighed into 15 mL glass test tubes, 10 mL of a 1 M HCl solution was added and stirred, and the tubes were placed in a constant temperature water bath at 50°C for 48 h (Faust et al., 2021). The samples were then centrifuged (2500 r/min, 5 min) and the supernatant poured into a new glass container. The samples were rinsed with distilled water until a neutral pH was achieved, and finally the samples were lyophilized in a freeze-dryer and weighed. The decarbonated samples were accurately weighed (30.0 ± 0.2 mg) into tin capsules for analysis.

The sediment standard sample GB07314 (offshore marine sediments, The State Bureau of Quality and Technical Supervision of China) was analyzed in parallel as a quality control standard, with replicate measurements varying by less than 1%.

3.3 AMS^{14}C analysis

$\Delta^{14}C$ of TOC from 11 sub-samples (i.e., 0 – 2, 2 – 4, 18 – 20, 54 – 56, 68 – 70, 72 – 74, 78 – 80, 102 – 104, 110 – 112, 112 – 114, and 128 – 130 cm) of the core sediment were analyzed using a 250 KeV NEC single stage particle accelerator at Beta Analysis Laboratory in the USA. Results are ISO/IEC-17025:2017 accredited. Briefly, the samples were subjected to ultrasonic mixing and screening to remove impurities. Inorganic carbon was eliminated through pickling, and graphite targets were prepared for testing in an accelerator mass spectrometer. The standard was NIST SRM-4990C (oxalic acid). The analytical precision for $\Delta^{14}C$ measurements is typically < 5‰.

3.4 *N*-alkanes

Ca. 3.0 to 6.0 g of lyophilized and ground sediment samples were accurately weighed and loaded into the extraction cell of a rapid solvent extractor (ASE-350, USA), and hexadecane deuterium ($nC_{24}D_{50}$) was added as an internal standard. Organic matter extracts were obtained by introducing dichloromethane and methanol (9:1, v:v) to the cell and heating at 100°C for 5 min, followed by extraction for 10 min. The heating and extraction were repeated 3 times. The extracts were initially concentrated by rotary evaporation, followed by evaporation under a steady stream of N_2. When the volumes were < 10 mL, the extracts were transferred to 10 mL glass bottles and evaporated with N_2 until dry. Next, a 6% potassium hydroxide in methanol solution was added and ultrasonicated for 10 min. The hydrolysate was removed by adding 4 mL of hexane and waiting for the polar and non-polar layers to separate. The non-polar layer was removed and transferred to a 20 mL glass bottle. The extraction was repeated 4 times, with all extracts combined in the new container. 0.2 mL of the combined organic matter extract was sub-sampled and dried under N_2, re-constituted in a known quantity of hexane, and then separated on an activated silica gel column. The non-polar components were obtained by leaching with *n*-hexane.

An Agilent gas chromatograph (Agilent 6890N, USA) with a flame ionization detector (GC-FID) was used for *n*-alkane analysis. The GC was equipped with an HP-1 (dimethylpolysiloxane) column (50 m × 0.32 mm × 0.17 μm). Analytical conditions were as follows: inlet temperature 310°C, FID detector temperature 320°C, carrier gas (N_2) flow rate 1.2 mL/min. The GC oven initial temperature was 60°C, which was held for 1 min before increasing to 200°C at a rate of 10°C/min. The temperature was then increased to 300°C at a rate of 5°C/min, and then to 310°C at a rate of 5°C/min, where it was held for 15 min. An example *n*-alkane chromatogram with relative abundance (station RB08B) was shown in Supplementary Figure S1. The retention time of target compounds was determined by comparing the retention time of 34 *n*-alkanes in a mixed standard (nC_7 to nC_{40}). The relative response values of each component peak of the mixed standard and the $nC_{24}D_{50}$ internal standard peak were applied to the peak areas of the target compounds to quantify their abundance. Yields of *n*-alkanes were normalized to the mass of sediment extracted, and values are expressed as ng/g.

L/H, TAR (Meyers, 1997), CPI_H and CPI_L (Eglinton and Calvin, 1967; Cranwell et al., 1987) were calculated based on the content of *n*-alkanes of different carbon numbers (see Supplementary Text S2 for indicative meanings of the above parameters):

$$L/H = \sum nC_{13\sim21}/\sum nC_{22\sim34}$$

$$TAR = (C_{27} + C_{29} + C_{31})/(C_{15} + C_{17} + C_{19})$$

$$CPI_H = 1/2[(C_{25} + C_{27} + C_{29} + C_{31} + C_{33} + C_{35})/(C_{24} + C_{26} + C_{28} + C_{30} + C_{32} + C_{34}) + (C_{25} + C_{27} + C_{29} + C_{31} + C_{33} + C_{35})/(C_{26} + C_{28} + C_{30} + C_{32} + C_{34} + C_{36})]$$

$$CPI_L = 1/2[(C_{15} + C_{17} + C_{19} + C_{21})/(C_{14} + C_{16} + C_{18} + C_{20}) + (C_{15} + C_{17} + C_{19} + C_{21})/(C_{16} + C_{18} + C_{20} + C_{22})]$$

3.5 Statistical analyses

A Pearson correlation analysis and a two-tailed test of significance were performed using the statistical software SPSS (Version 25) to determine relationships between the measured parameters. Statistically, significant differences were identified using one-way analysis of variance with a 95% confidence interval ($p < 0.05$).

4 Results

4.1 Chronostratigraphic framework

A reliable chronostratigraphic framework based on TOC should consider marine reservoir effects (Andrews et al., 1999; Pudsey et al., 2006) and fossil carbon contamination from glacial erosion on the Antarctic continent (Hillenbrand et al., 2010). A marine reservoir age of 825 a was referenced from Anderson et al. (2014) and Huang et al. (2016). A fossil carbon contamination age of 3045 a was referenced from station ATN31-JB06 (173.907°E, 74.473°S, water depth = 567 m) (Huang et al., 2016; Fan et al., 2021) due to the absent of foraminifera in JB03. Calendar ages were determined using the 7.10 software and Marine 13 program (http://calib.org/calib/calib.html). Linear interpolation and extrapolation were employed to establish a chronological framework, resulting in an age of 27.3 ka BP at the bottom of core JB03. The different depth intervals (0 – 72, 72 – 78 and 78 – 130 cm) corresponded to the Holocene (11.7 – 0 ka BP), the last deglaciation (21.0 – 11.7 ka BP) and the LGM (27.3 – 21.0 ka BP), respectively (Table 1; Figure 2). Sedimentation rates for each layer were calculated using 11 age control points and the interpolation method. The sedimentation

TABLE 1 Dating results and calculated sedimentation rate for core JB03.

Depth	Measured 14C age	Fossil carbon age	Marine reservoir age	Calendar age	Sedimentation rate	Chronology
cm	a BP	a	a	a BP	(cm/ka)	
0 – 2	4470 ± 30	3045	825	600		Holocene
2 – 4	4774 ± 30	3045	825	904	6.58	
18 – 20	6950 ± 30	3045	825	3080	7.35	
54 – 56	12655 ± 30	3045	825	8785	6.31	
68 – 70	14730 ± 30	3045	825	10860	6.75	
72 – 74	15720 ± 30	3045	825	11850	4.04	Deglaciation
78 – 80	28950 ± 30	3045	825	25080	0.45	LGM
102 – 104	31010 ± 30	3045	825	27140	11.7	
110 – 112	31090 ± 30	3045	825	27220	100	
112 – 114	31095 ± 30	3045	825	27225	400	
128 – 130	31140 ± 30	3045	825	27270	356	

rate for the interval 0 – 72 cm ranged from 6.31 to 7.35 cm/ka. The age difference between 78 – 80 cm and 72 – 74 cm layers was as high as 13.2 ka, and the lowest sedimentation rate for the whole core was calculated to be 0.45 cm/ka. Layers between 102 – 130 cm exhibited extremely high sedimentation rate, up to > 100 cm/ka (Table 1; Figure 2).

4.2 Particle size components

The composition of sand, silt and clay in surface sediments of the Ross Sea varied from 4.03% to 56.7%, 37.1% to 78.3% and 6.16% to 35.4%, respectively (Supplementary Table S1; Figures 3A–C). Spatially, the proportions of sand and silt did not exhibit significant ($p > 0.05$) differences among the three regions, while clay content in the Eastern sediment (27.0% ± 4.74%) was significantly ($p < 0.01$) higher than that in the Southwest and Western sediments (11.8% ± 0.25% and 13.0% ± 5.34%). Following Folk (1980) sediment classification method, the predominant sediment type in the study area was clayey silt, mainly located in Cape Adare and Glomar Challenger Trough. This was followed by sandy silt, distributed in Joides Trough and Drygalski Trough. Silty sand sediment was present at stations R02 and R08 near Terra Nova Bay, while silt sediment was at stations JB01 and JB03 in McMurdo Sound and Joides Trough (Supplementary Figure S2). Hydrodynamic indicators, including M_Z, σ, SK, and K_G, ranged from 4.17 to 7.00 φ, 1.63 to 2.44, –0.17 to 0.37 and 0.82 to 1.04, respectively (Supplementary Table S1; Figures 3D–G). The M_Z in the Eastern sediment (6.75 ± 0.21 φ) was significantly ($p < 0.01$) higher than that in the Southwest and Western sediments (5.70 ± 0.24 φ and 5.42 ± 0.68 φ), while σ, SK and K_G did not show significant ($p > 0.05$) differences among the three regions.

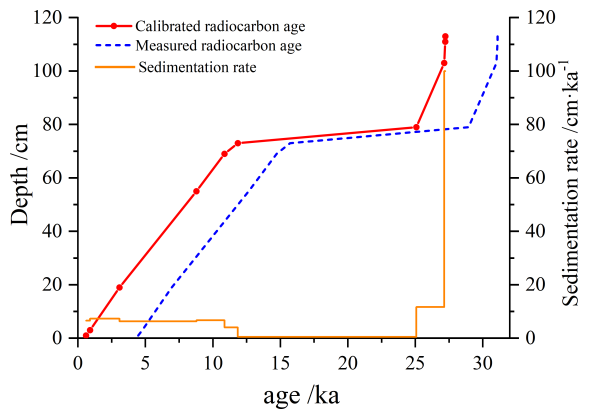

FIGURE 2
The measured ages, corrected ages and sedimentation rates in Core JB03 based on AMS^{14}C results.

4.3 TOC, TN and TOC/TN ratio

The TOC content of surface sediment samples ranged from 0.40% to 1.34% (wt%), which is consistent with the ranges of previous studies (0.2% to 2%) (Langone et al., 1998; Andrews et al., 1999; Chen et al., 2019b). Spatially, TOC content in the Southwest sediment (1.08% ± 0.23%) was significantly ($p < 0.05$) higher than that in the Eastern sediments (0.62% ± 0.21%), and intermediate in the Western sediments (0.82% ± 0.24%) (Supplementary Table S1; Figure 3H). TN content ranged from 0.07% to 0.23%, showing a similar spatial distribution pattern to TOC content (Figure 3I). A significant positive correlation was observed between TOC and TN content ($r = 0.99$, $p < 0.001$, Figure 4A). The TOC/TN ratio varied from 5.57 to 7.00, with no significant differences observed among the three regions (6.62 ± 0.19, 6.35 ± 0.28 and 6.28 ± 0.49 in the Southwest, Western and Eastern Ross Sea sediments, respectively) (Supplementary Table S1; Figure 3J).

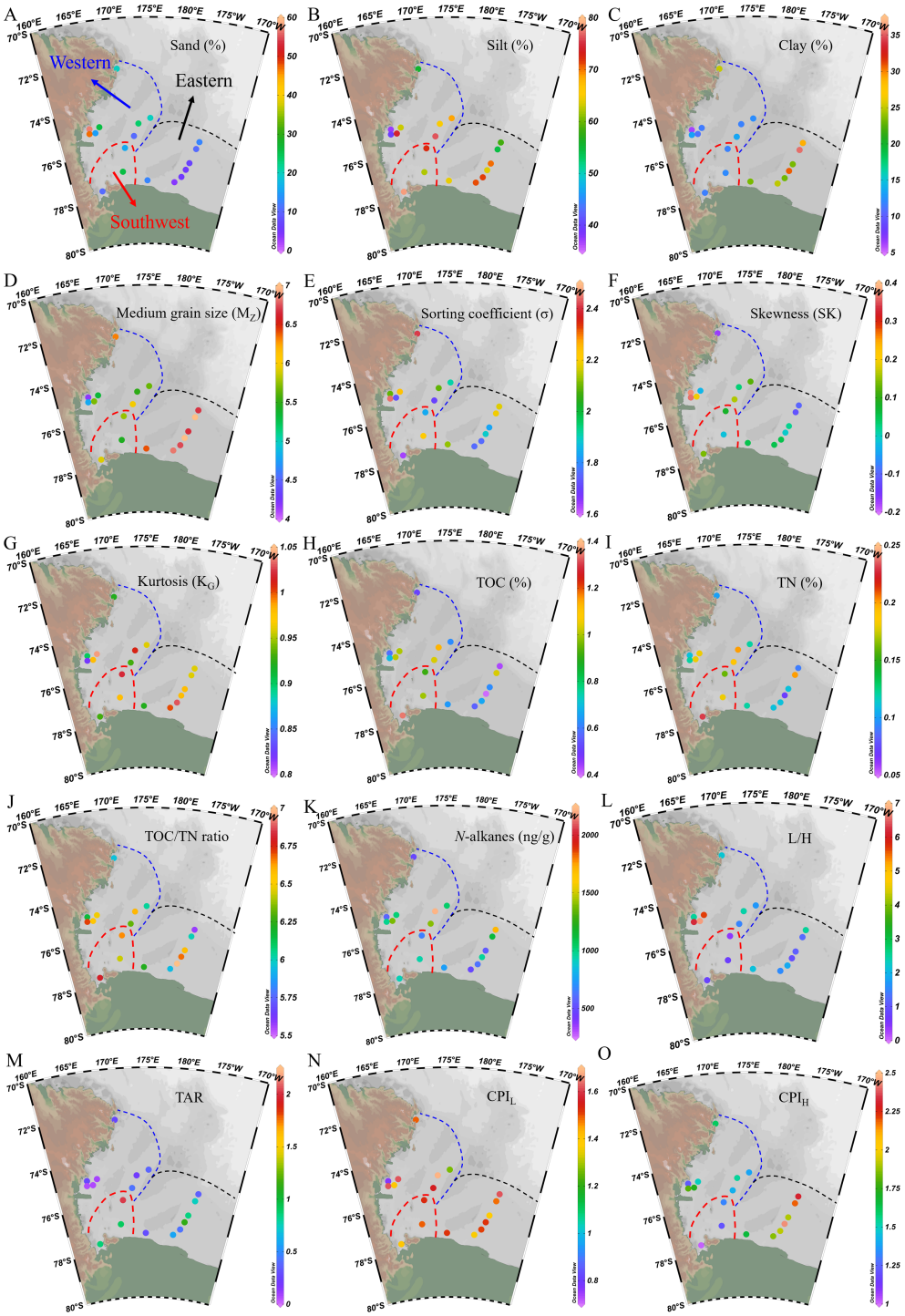

FIGURE 3
Spatial distribution of **(A)** sand (%), **(B)** silt (%), **(C)** clay (%), **(D)** mean particle size (M_Z), **(E)** sorting coefficient (σ), **(F)** skewness (SK), **(G)** kurtosis (K_G), **(H)** TOC (%), **(I)** TN (%), **(J)** TOC/TN ratio, **(K)** total content of *n*-alkanes (ng/g), **(L)** ratio of low molecular-weight (nC_{13} – nC_{21}) to high molecular-weight *n*-alkanes (nC_{25} – nC_{34}) (L/H), **(M)** terrestrial/aquatic ratio (TAR), **(N, O)** long-chain and short-chain carbon preference index (CPI_H and CPI_L) in surface sediments of the Ross Sea.

In the JB03 core sediments, TOC content ranged from 0.43% to 1.85%, while TN content ranged from 0.03% to 0.23%. Similar to the surface sediments, a significant positive correlation between TOC and TN was noted in the core sediments (r = 0.97, $p < 0.001$, Figure 4B). The TOC/TN ratio ranged from 6.91 to 16.81 (Supplementary Table S2). In the downcore profiles, TOC decreased from 1.56% ± 0.30% during the period of 0.6 – 8.2 ka BP to 0.74% ± 0.12% during 21.0 – 27.3 ka BP, while the TOC/TN ratio increased from 8.18 ± 0.51 to 13.63 ± 1.29 (Figure 5).

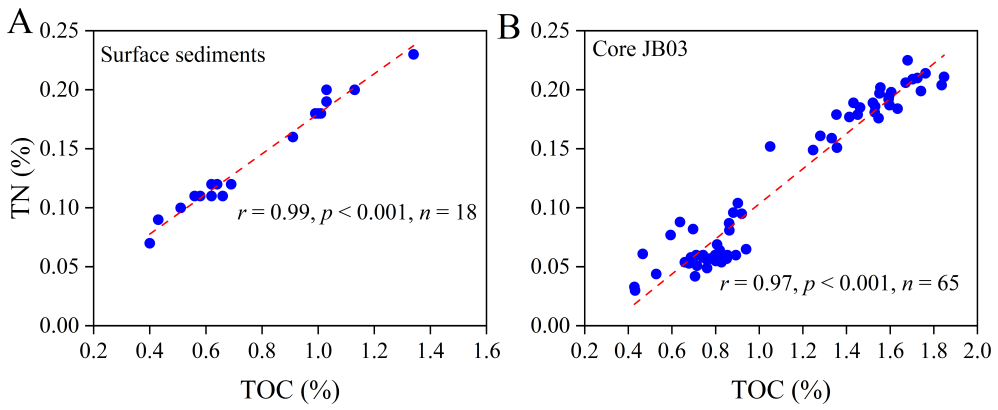

FIGURE 4
Diagrams of the relationship between TOC content and TN content in **(A)** surface sediments and **(B)** core JB03 of the Ross Sea.

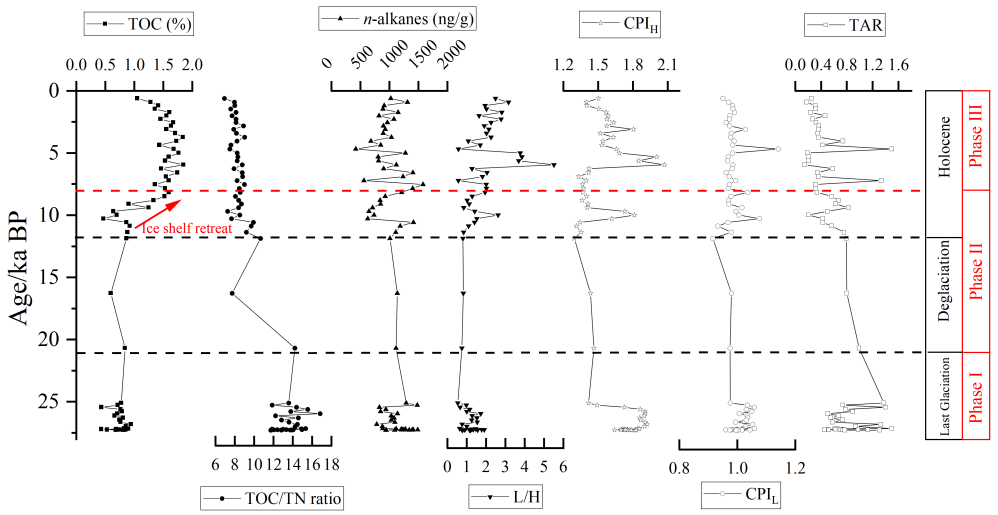

FIGURE 5
Downcore variability of TOC (%), TN (%), TOC/TN ratio, *n*-alkanes (ng/g), low molecular-weight (nC_{13} – nC_{21}) to high molecular-weight *n*-alkanes (nC_{25} – nC_{34}) (L/H), terrestrial/aquatic ratio (TAR), long-chain and short-chain carbon preference index (CPI_H and CPI_L) in core JB03 since LGM.

4.4 *N*-alkanes

The concentration of *n*-alkanes in the surface sediments of the Ross Sea varied from 482 to 2221 ng/g, with higher values found in the Glomar Challenger Trough and Joides Trough (stations RB02B and JB05), and the lowest concentration found near Cape Adare (station R19) (Figure 3K). The carbon chain lengths of *n*-alkanes ranged from nC_{12} to nC_{35}, characterized by a unimodal distribution with main carbon peak at nC_{17} or nC_{19} in Western Ross Sea (Figure 6A), a bimodal distribution with main carbon peaks at nC_{19} and nC_{25} in the Southwest Ross Sea (Figure 6B), and a combination of unimodal and bimodal distributions with main carbon peaks at nC_{17} or nC_{19} and nC_{27} in the Eastern Ross Sea (Figure 6C**)**. The L/H ranged from 0.38 to 6.72, being significantly ($p < 0.05$) higher of Western sediments (3.60 ± 2.18) than those in Southwest and Eastern sediments (0.62 ± 0.21 and 1.60 ± 0.58) (Figure 3L). The TAR varied from 0.07 to 2.03, significantly ($p < 0.01$) higher in the Southwest sediments (1.26 ± 0.66) than in the Western and Eastern sediments (0.22 ± 0.14 and 0.61 ± 0.30) (Figure 3M). *N*-alkanes exhibited odd carbon dominance (CPI_L = 1.26 to 1.68), except for station R02, which displayed an even carbon distribution (CPI_L = 0.76) (Figure 3N). The CPI_H ranged from 1.01 to 2.43, being highest in the Eastern sediments (2.04 ± 0.28), lowest in the Southwest sediments (1.18 ± 0.16), and intermediate in the Western sediments (1.52 ± 0.19) (Figure 3O; Supplementary Table S1).

In core JB03, the *n*-alkane content ranged from 416 to 1577 ng/g, exhibiting a slight increasing trend downcore, which contrasts with TOC profile (Figure 5). The carbon chain lengths extended from nC_{13} to nC_{33}, displaying a unimodal distribution with nC_{17}, nC_{18} or nC_{19} as main carbon peaks during 0.6 – 8.2 ka BP (Figure 6D), bimodal distribution with main carbon peaks as nC_{18}/nC_{25} and nC_{19}/nC_{25}

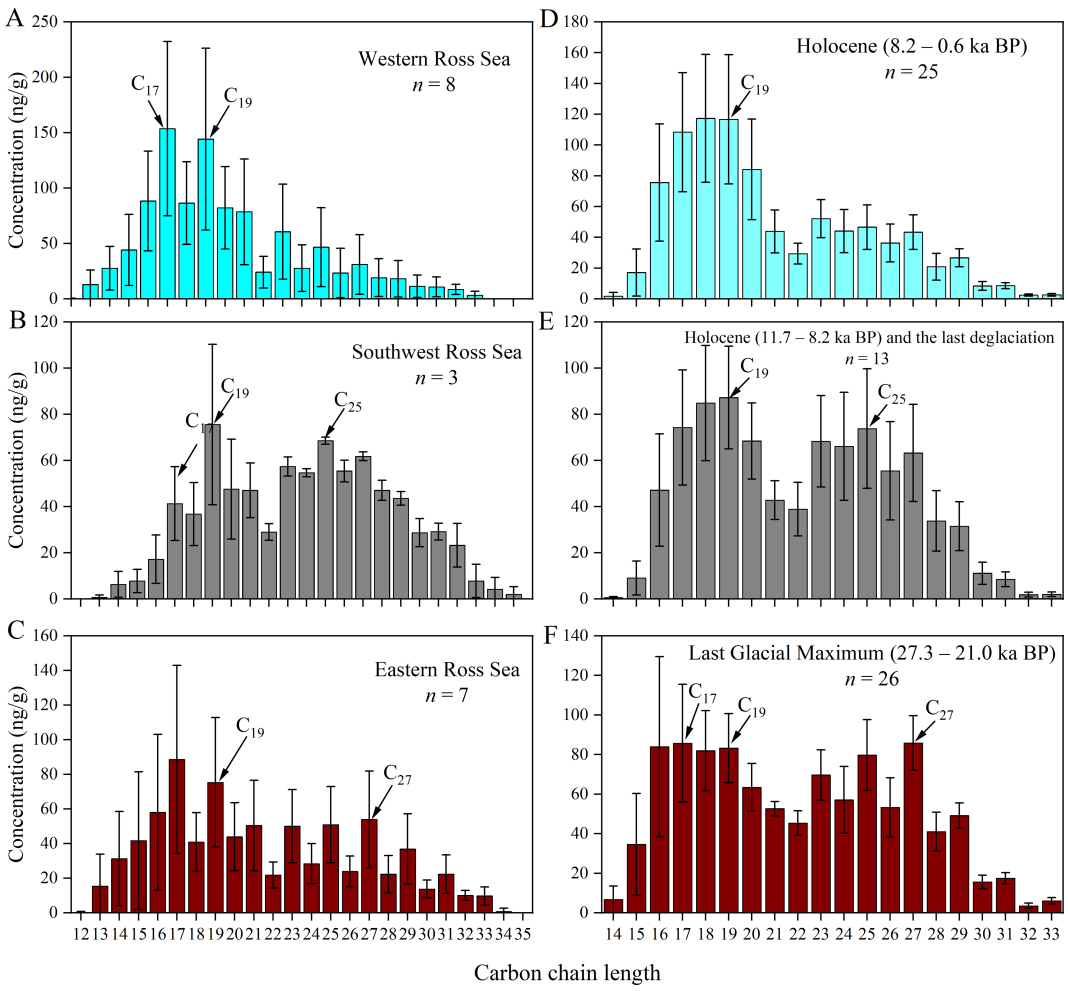

FIGURE 6
Abundance of *n*-alkanes in **(A)** Western, **(B)** Southwest, **(C)** Eastern surface sediment and **(D)** Holocene (8.2 – 0.6 ka BP), **(E)** early Holocene (11.7 – 8.2 ka BP) and the last deglaciation, **(F)** Last Glacial Maximum (27.3 – 21 ka BP) in core JB03. The error bars are the standard deviations of measured abundances in samples.

during 8.2 – 21.0 ka BP (Figure 6E), and bimodal distribution with main carbon peaks of nC_{17} or nC_{19} and nC_{27} during 21.0 – 27.3 ka BP (Figure 6F). The source indices, including the L/H, TAR, CPI_L and CPI_H, ranged from 0.53 to 5.50, 0.14 to 1.50, 0.92 to 1.14 and 1.29 to 2.07, respectively (Supplementary Table S2). Downcore analysis revealed that the L/H decreased from 2.27 ± 1.07 during 0.6 – 8.2 ka BP to 1.17 ± 0.37 during 21.0 – 27.3 ka BP. Conversely, TAR increased from 0.41 ± 0.32 to 0.83 ± 0.31, while CPI_L and CPI_H did not show significant downcore trends (Figure 5).

5 Discussion

5.1 Sedimentary environment and organic matter source pattern in the surface sediments

5.1.1 Sedimentary environment

M_z values were > 4.00, σ values were > 1.00 and K_G values generally fell within the mid-peak range of 0.90 – 1.11 for surface sediments in the study area. These findings indicate poor sediment sorting characteristic of a low-energy, hydrodynamic stable sedimentary environment (Folk and Ward, 1957). This aligns with the characteristics of an ice-sea environment dominated by physical weathering processes, such as abrasion and sediment extraction (Wang et al., 2016). Meanwhile, a significant positive correlation was observed between M_z and clay content ($r = 0.88$, $p < 0.01$, Figure 7A), while a significant negative correlation was noted between M_z and SK ($r = -0.71$, $p < 0.01$, Figure 7B), consistent with the sediment type distribution trends. High M_z values were exhibited in Glomar Challenger Trough with high clay content, predominantly chalky texture, and SK values generally less than 0 (Supplementary Figure S2). Previous studies based on radioisotope analysis (Licht and Hemming, 2017; Shao et al., 2022 and references therein) and sediment mineralogical composition (Andrews and LeMasurier, 2021) have shown that sediments in the Eastern Ross Sea are from both Edward VII Land and Marie Byrd Land, while in the Western Ross Sea, sediments originate predominantly from Victoria Land. Weaker hydrodynamic conditions lead to *in situ* deposition of coarse-grained material, while fine-clay minerals may

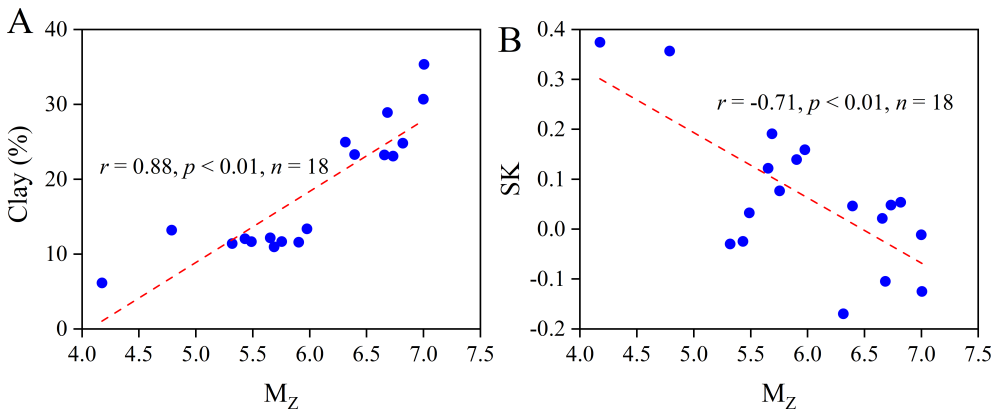

FIGURE 7
Diagrams of the relationship between M_z and **(A)** clay content, **(B)** SK in the surface sediments of the Ross Sea.

be transported over long distances to Glomar Challenger Trough. Conversely, stations at TNBP, particularly station R02, exhibited the highest sand content (56.7%), the lowest M_z (4.17) and the most positive SK (0.37), indicating the impact from terrestrial sand and gravel carried by sea ice ablation and/or relatively stronger coastal currents (DeMaster, 1992; Orsi et al., 1995).

5.1.2 Spatial distribution and source difference of TOC

A common source for TOC and TN in the surface sediments of the study area was indicated by a significant positive correlation between TOC and TN content (Figure 4A), in line with findings from previous studies (DeMaster et al., 1996; Langone et al., 1998; Xiu et al., 2017). Studies have shown that the TOC/TN ratio varies significantly depending on the source of organic matter. For instance, the TOC/TN ratio ranges from 2.3 to 3.7 from marine microbial sources (Lee and Fuhrman, 1987; Coffin and Cifuentes, 1993), 3 to 8 from protein-rich marine organic matter (Redfield et al., 1963; Meyers, 1994), and > 12 from lignin- and cellulose-rich terrestrial higher plants (Sampei and Matsumoto, 2001). In this study, the TOC/TN ratio in the surface sediments was at 6.37 ± 0.37, showing no significant difference ($p > 0.1$) among the three regions (Supplementary Table S1; Figure 3J), comparable to the ratios reported in previous studies of particulate matter in the euphotic zone of the Ross Sea (6.5 on average, Fabiano et al., 1993), sediments (6.5 to 7.0 on average, Wakeham and Mcnichol, 2014; DeMaster et al., 1996), and was also close to the Redfield ratio (Redfield et al., 1963). A recent study found that TOC/TN ratio and σ are significantly correlated in the East China Sea, a large river dominated marginal sea, indicating that the TOC/TN ratio could be affected by the grain size, with potential to inferring the evolution of the sedimentary environments (Zhang et al., 2023). However, no significant ($p > 0.05$) correlation was found between the TOC/TN ratio and σ in the surface sediments of Ross Sea. Therefore, these results suggest that surface OC in the Ross Sea primarily originates from epipelagic phytoplankton production.

The spatial distribution of TOC exhibited a pattern of high in the west and low in the east, consistent with findings from previous studies (Andrews et al., 1999; Chen et al., 2019b; Zhou et al., 2022). This distribution discrepancy can be attributed to two factors. Firstly, the formation of polynyas and open seas occurs earlier in the summer in the Southwest and Western Ross Sea due to katabatic wind, with polynyas even observable in winter. In contrast, in the Eastern Ross Sea, the formation of open seas is delayed until later in the summer season. Chlorophyll a concentrations throughout the Ross Sea exceed 5 μg/L in December, and then decrease to < 2 μg/L in January and February. However, in the Western Ross Sea, particularly at the RSP location, chlorophyll a levels remain above 5 μg/L throughout the austral summer (Smith and Kaufman, 2018; Smith, 2022). This extended period of elevated productivity contributes to a higher accumulation of TOC in the sediments of the southwestern region. Secondly, sedimentation rates are significantly higher in the Southwest and Western Ross Sea than the Eastern (DeMaster et al., 1996). For instance, the sedimentation rate was 6.58 cm/ka on the top of core JB03 in this study, and was 8 cm/ka on the top of core RB16C from Joides Trough, Western Ross Sea (Song et al., 2019). In contrast, sedimentation rates on the Eastern Ross Sea shelf typically range from 1 to 2 cm/ka (DeMaster et al., 1996; Cui et al., 2021). High sedimentation rates facilitate the bypassing of OC early diagenesis, leading to its burial in anaerobic sediments and enhancing preservation potential (Smith et al., 2015; Faust et al., 2021). Notably, station R02 in TNBP exhibited low clay (6.16%) and TOC content (0.58%). Despite being in a highly productive area, the retention of clay fraction is poor due to strong hydrodynamic conditions, whereas clay minerals promote organic matter preservation through physical or chemical adsorption owing to their large specific surface area (Eusterhues et al., 2003; Keil and Mayer, 2014; Wu et al., 2024).

5.1.3 Spatial distribution and source difference of *n*-alkanes

Concentrations of *n*-alkanes were slightly higher in the Western Ross Sea (1136 ± 548 ng/g) than in the Southwest and Eastern Ross Sea (837 ± 161 and 884 ± 431 ng/g). The *n*-alkanes in Western Ross Sea exhibited a unimodal distribution, with main carbon peak at nC_{17} or nC_{19} (Figure 6A), a weak odd-carbon preference (CPI_L = 1.41 ± 0.30) and the lowest TAR (0.22 ± 0.14) (Supplementary Table S1). These

results suggest that *n*-alkanes are mainly derived from marine algae and bacteria in the upper ocean, consistent with the results of TOC/TN ratio.

The *n*-alkanes in the Southwest Ross Sea exhibited a bimodal distribution with main carbon peaks at nC_{19} and nC_{25} (Figure 6B), a low L/H (0.62 ± 0.21), low CPI_H values (1.18 ± 0.16) and the highest TAR value (1.26 ± 0.66) (Supplementary Table S1). Previous research has demonstrated that marine phytoplankton can produce significant quantities of medium- and long-chain alkyl lipids with low CPI values (e.g., Volkman et al., 1998). Additionally, *n*-alkanes from peat moss (*Sphagnum*) are characterized by a high abundance of nC_{23} and nC_{25} (Baas et al., 2000; Bingham et al., 2010). A TAR > 1 typically indicates a higher proportion of terrestrial OC input, while a TAR < 1 suggests a predominance of marine-derived sources (Meyers, 1997). In the Southwest Ross Sea, the presence of medium- and long-chain *n*-alkanes, without an odd-over-even carbon preference, suggests a mixture of contributions from marine algae and terrestrial mosses. This finding is consistent with the results of Tao et al. (2022), which showed that a CPI_H ~1 in suspended particulates from the Southwest Ross Sea, indicating the contribution of terrestrial organic matter.

The *n*-alkanes in the Eastern Ross Sea stations exhibited combination of unimodal and bimodal distributions, with main carbon peaks at nC_{17} or nC_{19} and nC_{27}, respectively (Figure 6C). The Eastern Ross Sea is characterized by the highest CPI_H values (2.04 ± 0.28) and moderate L/H and TAR values (1.60 ± 0.58 and 0.61 ± 0.30) compared to the Western and Southwest Ross Sea (Supplementary Table S1). This suggests that short-chain *n*-alkanes possibly originate from phytoplankton, while long-chain *n*-alkanes may come from terrestrial sources such as higher plant fragments. Previous research has shown that medium- and long-chain *n*-alkanes are more prevalent than short-chain *n*-alkanes in McMurdo Dry Valleys soils, with main carbon peaks at nC_{23}, nC_{25} and nC_{27}, and CPI_H values from 2.0 to 2.6. These *n*-alkanes are mainly from lichens and higher vascular plant fragments from pre-glacial periods, specifically the Miocene to Pliocene epochs (Matsumoto et al., 1990a, 1990b, 2010). Given the similarities in *n*-alkane characteristics between surface sediments in the Eastern Ross Sea and soils from the McMurdo Dry Valleys, it is suggested that long-chain *n*-alkanes may could have been transported over long distances by ocean currents. Furthermore, research indicates that dust from mid-latitude land areas and plant leaf waxes could be carried long distances through the atmosphere to the Southern Ocean, utilizing lipid biomarkers and compound-specific stable carbon isotope ratios of *n*-alkanes in aerosols (Bendle et al., 2007; Jaeschke et al., 2017). These materials may serve as sources of long-chain *n*-alkanes in Eastern Ross Sea sediments and may undergo degradation during transport, thus altering the original *n*-alkanes signature (CPI_H > 30 to 2.04 ± 0.28) (Bray and Evans, 1961; Naafs et al., 2019).

It is important to note that there are certain differences in the organic matter sources in the surface sediments in the Ross Sea based on the TOC/TN ratio and *n*-alkane related parameters. The TOC/TN indicates the general characteristics of organic matter sources but lacks specificity regarding source identification (Mayer, 1994; Bianchi and Canuel, 2011). In contrast, although *n*-alkanes constitute a minor fraction of TOC, they are more stable and encompass a broader range of sources, thereby providing more detailed insights into the origins of organic matter. By combining bulk OC and *n*-alkanes, we can achieve a more comprehensive and nuanced understanding of the sources of organic matter in Antarctic sediments.

5.2 Changes in *n*-alkane sources since the LGM and implications for ice shelf retreat

5.2.1 Impacts of ice shelf retreat on sedimentary age

The sedimentation rate of core JB03 during the LGM, deglaciation and Holocene differed significantly from those of neighboring cores (Huang et al., 2016; Song et al., 2019; Zhao et al., 2017), suggesting that sedimentary environments are influenced by ice shelf retreat and display considerable spatial variability. The sedimentation rate in the 102 – 130 cm layer (27.1 – 27.3 ka BP, during the LGM) was extremely high at 100 cm/ka (Figure 2 and Supplementary Table S2), in contrast to the northern cores (e.g., 3 – 4 cm/ka for JB06 and ~26 cm/ka for RB16C) (Huang et al., 2016; Song et al., 2019). The Ross Ice Shelf was expanding during the LGM, with the northernmost position of the grounding line at 74°S, as determined from seismic and multibeam data analyses (Ship et al., 1999; Halberstadt et al., 2016) and grain-size sedimentary sequences (Anderson et al., 2014; Huang et al., 2016; Zhao et al., 2017). While Huang et al. (2016) suggested that the ice shelf did not reach the seafloor at JB06 (~74.5°S), the notably high sedimentation rate observed in this study implies that the more southerly JB03 (~75.8°S) may have experienced grounding events during the LGM, rapidly accumulating sediment of equivalent or older age from the surrounding area.

An extremely low sedimentation rate (0.45 cm/ka) was recorded during the last deglaciation period (72 – 78 cm, 21.0 – 11.9 ka BP), significantly lower than the neighboring cores (~15 cm/ka for JB06 and ~10 cm/ka for RB16C) during the same timeframe (Huang et al., 2016; Song et al., 2019). Given that this period was characterized by a predominantly sub-glacial sedimentary environment (McKay et al., 2012), the absence of a stratigraphic record between 72 – 78 cm could be attributed to ice sheet collapse scouring or interruptions in sedimentation due to ice sheet coverage.

During the early Holocene (11.9 – 8.2 ka BP), the sedimentation rate increased to 6.75 cm/ka, similar to rates observed in northern cores (e.g., ~5 cm/ka for JB06 and ~3 cm/ka for RB16C) (Huang et al., 2016; Song et al., 2019). Sedimentary phase sequences and foraminifera radiocarbon dating indicated that the Ross Ice Shelf retreated rapidly during 11 – 10 ka BP (McKay et al., 2008). Finocchiaro et al. (2005) reported the presence of a patchy diatom-rich soft mud layer dating to 9.5 – 9.4 ka BP in Cape Hallett Bay, suggesting early Holocene warming and open ocean conditions. Subsequently, sandy mud deposition during 8.0 – 7.8 ka BP indicated a rapid landward retreat of regional glaciers.

Consequently, due to the ongoing retreat of the ice shelf, station JB03 transitioned from a sub-glacial sedimentary environment to a marine setting.

After 8.2 ka BP, the ice shelf continued its retreat towards Ross Island (McKay et al., 2016). During this period, the sedimentation rate was stable at 6.71 ± 0.39 cm/ka, comparable to rates observed in the northern cores, such as 7 cm/ka for JB06 and RB16C (Huang et al., 2016; Song et al., 2019). Ice core $\delta^{18}O$ records suggested that the Ross Sea experienced its second warm period of the Holocene from 7 to 5 ka BP (Masson-Delmotte et al., 2000). Station JB03 displayed a seasonal sea ice period sedimentary characteristics.

5.2.2 Changes in TOC and *n*-alkane sources at different historical stages

Based on the TOC content, TOC/TN ratio, *n*-alkane characteristics and calculated indices, the sedimentary record of JB03 can be divided into three phases. Phase I extended from 78 to 130 cm (LGM period); Phase II ranged from 52 to 78 cm (the last deglaciation and 11.9 – 8.2 ka BP in the early Holocene period); and Phase III was found at depths shallower than 52 cm (8.2 – 0.6 ka BP during the Holocene period) (Figure 5). Significant variations in sedimentary environments and their associated TOC and *n*-alkane sources were observed across these phases in the Ross Sea.

During Phase I, TOC content was the lowest (0.74% ± 0.12%), while the TOC/TN ratio was the highest (13.63 ± 1.29). The *n*-alkane distribution was predominantly bimodal, with main carbon peaks at nC_{17} or nC_{19} and nC_{27} (Figure 6F), and exhibited the highest CPI_H (1.78 ± 0.12) and TAR (0.83 ± 0.31), and lowest L/H (1.17 ± 0.37) (Figure 5), indicating a predominance of terrestrial OC inputs. This could be due to disturbed and redeposited sediments caused by ice-shelf grounding, potentially mixed with fragments of higher vascular plants from pre-glacial periods (e.g., Oligocene and Miocene) (Duncan et al., 2019), as discussed in section 5.2.1.

The TOC content of Phase II sediments (0.90% ± 0.30%) was slightly higher than that of Phase I, exhibiting a significant increasing trend in TOC content between 11.9 – 8.2 ka BP (Figure 5 red arrow). The TOC/TN ratio (9.09 ± 1.82) indicated a mixture of OC from phytoplankton (3 – 8) and higher plants (>12) (Figure 5). The *n*-alkane distribution was mainly bimodal, with main carbon peaks at nC_{18}/nC_{25} and nC_{19}/nC_{25}, differing from Phase I (Figure 6E). The CPI_H (1.46 ± 0.16) and TAR (0.62 ± 0.21) were slightly lower than those of Phase I (Figure 5). These results suggest a mixture of inputs from both marine and terrestrial sources (Anderson et al., 2014; Huang et al., 2016; Zhao et al., 2017). Overall, our findings align with historical data (see section 5.2.1), indicating a notable increase in marine-derived *n*-alkanes due to glacier retreat, rising temperatures, and enhanced productivity during the early Holocene. Additionally, there was an increase in terrestrial input from mosses, lichens and other land sources (Kvenvolden et al., 1987), alongside a decrease in the ancient organic matter proportions.

The sediments in Phase III exhibited the highest TOC content (1.56% ± 0.30%) and the lowest TOC/TN ratio (8.18 ± 0.51) compared to the other two phases (Figure 5). The *n*-alkanes in Phase III closely resembled those found in modern surface sediments, showing mainly a unimodal distribution with nC_{17}, nC_{18} or nC_{19} as main carbon peaks (Figure 6D). Furthermore, the odd-carbon predominance of short chains was not obvious (CPI_L = 0.99 ± 0.04), while the TAR (0.41 ± 0.32) was significantly lower compared to Phase I and Phase II (0.81 ± 0.33 and 0.55 ± 0.18, respectively). Conversely, and L/H (2.27 ± 1.07) was significantly higher than in Phase I and II (1.17 ± 0.37, 1.19 ± 0.50, respectively) (Figure 5). These findings suggest that the *n*-alkanes in the sediment are primarily derived from marine phytoplankton and bacteria after approximately 8 ka BP (Song et al., 2019; Xiu et al., 2017). As discussed in section 5.2.1, the ice shelves had receded to near Ross Island around 8 ka BP, establishing a seasonal sea-ice environment similar to present conditions, characterized by high productivity and a predominant contribution from marine sources.

6 Conclusion

The overall sorting of surface sediments in the Ross Sea was poor, indicating a low-energy and hydrodynamically stable sedimentary environment. TOC was mainly derived from upper ocean phytoplankton, with a distribution trend showing higher concentrations in the west and lower in the east. This variation was related to higher sedimentation rates and longer periods of primary productivity accumulation in the west. Significant regional differences in the sources of *n*-alkanes in modern surface sediments were identified, with the Western region mainly derived from phytoplankton and bacteria, the Southwest region from a mixture of phytoplankton and terrestrial mosses, and the Eastern region from a combination of phytoplankton, terrestrial soil/low-latitude higher plant leaf waxes. The *n*-alkane characteristics in the Western Ross Sea core were basically consistent with the history of ice shelf dynamics, showing a high terrestrial input signal before 21.0 ka BP during the ice shelf expansion. From 21.0 to 11.7 ka BP, while the ice shelf retreated, the JB03 site remained beneath the ice shelf, resulting in very low sedimentation rates. From 11.7 to 8.2 ka BP, as temperatures rose and glaciers continued to retreat, *n*-alkanes exhibited characteristics of mixed terrestrial and marine source inputs. Since 8.2 ka BP, as the glaciers retreated to Ross Island, marine-derived *n*-alkanes have dominated in the sediment. This study provides insights into the changes in organic matter properties resulting from the accelerated melting of the Antarctic ice shelf.

Data availability statement

The original contributions presented in the study are included in the article/Supplementary Material. Further inquiries can be directed to the corresponding authors.

Author contributions

DY: Data curation, Formal analysis, Investigation, Methodology, Writing – original draft, Writing – review & editing. WC: Data curation, Investigation, Methodology, Software,

Writing – original draft, Writing – review & editing. WH: Data curation, Formal analysis, Methodology, Writing – original draft, Writing – review & editing. HZ: Conceptualization, Funding acquisition, Project administration, Resources, Supervision, Writing – review & editing. ZH: Data curation, Software, Writing – original draft. BL: Conceptualization, Validation, Writing – review & editing. JZ: Conceptualization, Funding acquisition, Project administration, Supervision, Writing – original draft, Writing – review & editing.

Funding

The author(s) declare financial support was received for the research, authorship, and/or publication of this article. This work was supported by the National Natural Science Foundation of China (Grant Nos. 42076243, 41976228 and 41976227), the National Key Research and Development Program of China (Grant No. 2022YFE0136500) and National Polar Special Program "Impact and Response of Antarctic Seas to Climate Change" (Grant Nos. IRASCC 01-01-02A and 02-02).

Acknowledgments

Appreciation goes to the personnel who participated in CHINARE-31 and -32 and the crew of *R/V Xuelong* for their hard work in collecting sediment samples. We would like to express our sincere thanks to the Polar Specimen Museum of the Polar Research Institute of China for providing sediment samples.

Conflict of interest

The authors declare that the research was conducted in the absence of any commercial or financial relationships that could be construed as a potential conflict of interest.

Publisher's note

Supplementary material

The Supplementary Material for this article can be found online at: https://www.frontiersin.org/articles/10.3389/fmars.2024.1474189/full#supplementary-material

References

Anderson, J. B., Conway, H., Bart, P. J., Witus, A. E., Greenwood, S. L., McKay, R. M., et al. (2014). Ross Sea paleo-ice sheet drainage and deglacial history during and since the LGM. *Quat. Sci. Rev.* 100, 31–54. doi: 10.1016/j.quascirev.2013.08.020

Andrews, J. T., Domack, E. W., Cunningham, W. L., Leventer, A., Licht, K. J., Timothy Jull, A. J., et al. (1999). Problems and possible solutions concerning radiocarbon dating of surface marine sediments, Ross Sea, Antarctica. *Quat. Res.* 52, 206–216. doi: 10.1006/qres.1999.2047

Andrews, J. T., and LeMasurier, W. (2021). Resolving the argument about volcanic bedrock under the West Antarctic Ice Sheet and implications for ice sheet stability and sea level change. *Earth Planet. Sci. Lett.* 568, 117035. doi: 10.1016/j.epsl.2021.117035

Arrigo, K. R., Van Dijken, G., and Long, M. (2008a). Coastal Southern Ocean: A strong anthropogenic CO_2 sink. *Geophys. Res. Lett.* 35, L21602. doi: 10.1029/2008gl035624

Arrigo, K. R., Van Dijken, G. L., and Bushinsky, S. (2008b). Primary production in the Southern Ocean 1997-2006. *J. Geophys. Res.-Oceans* 113, C08004. doi: 10.1029/2007jc004551

Baas, M., Pancost, R., Geel, B., and Sinninghe-Damste, J. (2000). A comparative study of lipids in Sphagnum species. *Org. Geochem.* 31, 535–541. doi: 10.1016/S0146-6380(00)00037-1

Bendle, J., Kawamura, K., Yamazaki, K., and Niwai, T. (2007). Latitudinal distribution of terrestrial lipid biomarkers and n-alkane compound-specific stable carbon isotope ratios in the atmosphere over the western Pacific and Southern Ocean. *Geochim. Cosmochim. Acta* 71, 5934–5955. doi: 10.1016/j.gca.2007.09.029

Bianchi, T., and Canuel, E. (2011). *Chemical Biomarkers in Aquatic Ecosystems* (Princeton, New Jersey: Princeton University Press), 396pp. doi: 10.1515/9781400839100

Bianchi, T., Schreiner, K., Smith, R., Burdige, D., Woodard, S., and Conley, D. (2016). Redox effects on organic matter storage in coastal sediments during the holocene: A biomarker/proxy perspective. *Annu. Rev. Earth Planet. Sci.* 44, 295–319. doi: 10.1146/annurev-earth-060614-105417

Bingham, E., Mcclymont, E., Väliranta, M., Mauquoy, D., Roberts, Z., Chambers, F., et al. (2010). Conservative composition of *n*-alkane biomarkers in Sphagnum species: Implications for palaeoclimate reconstruction in ombrotrophic peat bogs. *Org. Geochem.* 41, 214–220. doi: 10.1016/j.orggeochem.2009.06.010

Blumer, M., Guillard, R. R. L., and Chase, T. (1971). Hydrocarbons of marine phytoplankton. *Mar. Biol.* 8, 183–189. doi: 10.1007/BF00355214

Bray, E. E., and Evans, E. D. (1961). Distribution of n-paraffins as clue to recognision of source beds. *Geochim. Cosmochim. Acta* 22, 2–15. doi: 10.1016/0016-7037(61)90069-2

Burdige, D. J. (2007). Preservation of organic matter in marine sediments: Controls, mechanisms, and an imbalance in sediment organic carbon budgets? *Chem. Rev.* 107, 467–485. doi: 10.1021/cr050347q

Chen, W., Yu, P., Han, X., Zhao, J., and Pan, J. (2019b). Contents and distribution of GDGTs in surface sediments of Ross Sea, Antarctic and their environmental significances (in Chinese with English abstract). *J. Mar. Sci.* 37, 30–39. doi: 10.3969/j.issn.1001-909X.201

Chen, X. (2020). *Carbon and hydrogen istope of* n*-alkyl lipids in lacustrine and ocean sediments from Ross Sea, Antarctica and paleoclimatic implications (in Chinese with English abstract)* (Doctor, Hefei: University of Science and Technology of China).

Chen, X., Liu, X., Jia, H., Jin, J., Kong, W., and Huang, Y. (2021). Inverse hydrogen isotope fractionation indicates heterotrophic microbial production of long-chain n-alkyl lipids in desolate Antarctic ponds. *Geobiology* 19, 394–404. doi: 10.1111/gbi.12441

Chen, X., Liu, X., Wei, Y., and Huang, Y. (2019a). Production of long-chain n-alkyl lipids by heterotrophic microbes: New evidence from Antarctic lakes. *Org. Geochem.* 138, 103909. doi: 10.1016/j.orggeochem.2019.103909

Coffin, R., and Cifuentes, L. A. (1993). *Handbook of methods in aquatic microbial ecology*. Eds. P. F. Kemp, B. F. Sherr, E. B. Sherr and J. J. Cole (Boca Raton, Florida, USA: Lweis), 663–675.

Cranwell, P. A., Eglinton, G., and Robinson, N. (1987). Lipids of aquatic organisms as potential contributors to lacustrine sediments—II. *Org. Geochem.* 11, 513–527. doi: 10.1016/0146-6380(87)90007-6

Cui, C., Tang, Z., Rebesco, M., De Santis, L., Li, Z., Wang, X., et al. (2021). Sedimentary records of enhanced deep ventilation during the last deglaciation in the Ross Sea, Southern Ocean (in Chinese with English abstract). *Quat. Sci.* 41, 678–690. doi: 10.11928/j.issn.1001-7410.2021.03.05

Das, S., Routh, J., Roychoudhury, A., and Klump, J. (2007). Elemental (C, N, H and P) and stable isotope ($\delta^{15}N$ and $\delta^{13}C$) signatures in sediments from Zeekoevlei, South Africa: A record of human intervention in the lake. *J. Paleolimnol.* 39, 349–360. doi: 10.1007/s10933-007-9110-5

DeMaster, D. J. (1992). Cycling and accumulation of biogenic silica and organic matter in high-latitude environments: the Ross Sea. *Oceanography* 5, 146–153. doi: 10.5670/oceanog.1992.03

DeMaster, D. J., Ragueneau, O., and Nittrouer, C. A. (1996). Preservation effciencies and accumulation rates for biogenic silica and organic C, N, and P in high-latitude sediments: The Ross Sea. *J. Geophys. Res.-Oceans* 101, 18501–18518. doi: 10.1029/96JC01634

Didyk, B. M., Simoneit, B. R. T., Brassell, S. C., and Eglinton, G. (1978). Organic geochemical indicators of palaeoenvironmental conditions of sedimentation. *Nature* 272, 216–222. doi: 10.1038/272216a0

Dinniman, M., Klinck, J., and Smith, W. (2003). Cross-shelf exchange in a model of Ross Sea circulation and biogeochemistry. *Deep Sea Res. II Top. Stud. Oceanogr.* 50, 3103–3120. doi: 10.1016/j.dsr2.2003.07.011

Dittmar, T., and Stubbins, A. (2014). "Dissolved organic matter in aquatic systems," in *Treatise on Geochemistry, 2nd ed.*, vol. 12 . Eds. H. D. Holland and K. K. Turekian (Amsterdam, Netherlands: Elsevier), 125–156. doi: 10.1016/B978-0-08-095975-7.01010-X

Duncan, B., Mckay, R., Bendle, J., Naish, T., Inglis, G. N., Moossen, H., et al. (2019). Lipid biomarker distributions in Oligocene and Miocene sediments from the Ross Sea region, Antarctica: Implications for use of biomarker proxies in glacially influenced settings. *Palaeogeogr. Palaeoclimatol. Palaeoecol.* 516, 71–89. doi: 10.1016/j.palaeo.2018.11.028

Eglinton, G., and Calvin, M. (1967). Chemical fossils. *Sci. Am.* 216, 32–43. doi: 10.1038/scientificamerican0167-32

Eglinton, T., and Eglinton, G. (2008). Molecular proxies for paleoclimatology. *Earth Planet. Sci. Lett.* 275, 1–16. doi: 10.1016/j.epsl.2008.07.012

Eusterhues, K., Rumpel, C., Kleber, M., and Kögel-Knabner, I. (2003). Stabilisation of soil organic matter by interactions with minerals as revealed by mineral dissolution and oxidative degradation. *Org. Geochem.* 34, 1591–1600. doi: 10.1016/j.orggeochem.2003.08.007

Fabiano, M., Povero, P., and Danovaro, R. (1993). Distribution and composition of particulate organic matter in the Ross Sea (Antarctica). *Polar Biol.* 13, 525–533. doi: 10.1007/BF00236394

Fan, J., Wang, R., Ding, X., and Wu, L. (2021). Benthic foraminifera assemblages and their response to ice shelf changes in the Joides trough of the Ross Sea, Antarctica since the last glacial period (in Chinese with English abstract). *Acta Microbiol. Sin.* 38, 93–111. doi: 10.16087/j.cnki.1000-0674.2021.01.009

Faust, J. C., Tessin, A., Fisher, B. J., Zindorf, M., Papadaki, S., Hendry, K. R., et al. (2021). Millennial scale persistence of organic carbon bound to iron in Arctic marine sediments. *Nat. Commun.* 12, 275. doi: 10.1038/s41467-020-20550-0

Finocchiaro, F., Langone, L., Colizza, E., Fontolan, G., Giglio, F., and Tuzzi, E. (2005). Record of the early Holocene warming in a laminated sediment core from Cape Hallett Bay (Northern Victoria Land, Antarctica). *Glob. Planet. Change* 45, 193–206. doi: 10.1016/j.gloplacha.2004.09.003

Folk, R. L. (1980). *Petrology of sedimentary rocks* (Austin: Hemphill publishing company).

Folk, R. L., and Ward, W. C. (1957). Brazos river bar: A study in the significance of grain size parameters. *J. Sediment. Res.* 27, 3–26. doi: 10.1306/74D70646-2B21-11D7-8648000102C1865D

Gal, J.-K., Kim, B., Joo, H., Shim, C., Lee, B., Kim, I.-N., et al. (2022). Spatial distribution and origin of organic matters in an Arctic fjord system based on lipid biomarkers (*n*-alkanes and sterols). *Environ. Res.* 205, 112469. doi: 10.1016/j.envres.2021.112469

Gales, J., Rebesco, M., Santis, L. D., Bergamasco, A., Colleoni, F., Kim, S., et al. (2021). Role of dense shelf water in the development of Antarctic submarine canyon morphology. *Geomorphol.* 372, 107453. doi: 10.1016/j.geomorph.2020.107453

Grimalt, J., and Albaigés, J. (1987). Sources and occurrence of C_{12}-C_{22} n-alkane distributions with even carbon-number preference in sedimentary environments. *Geochim. Cosmochim. Acta* 51, 1379–1384. doi: 10.1016/0016-7037(87)90322-X

Gustafsson, O., Kruså, M., Zencak, Z., Sheesley, R., Granat, L., Engström, J., et al. (2009). Brown clouds over south asia: biomass or fossil fuel combustion? *Science* 323, 495–498. doi: 10.1126/science.1164857

Ha, S., Colizza, E., Torricella, F., Langone, L., Giglio, F., Kuhn, G., et al. (2022). Glaciomarine sediment deposition on the continental slope and rise of the central Ross Sea since the Last Glacial Maximum. *Mar. Geol.* 445, 106752. doi: 10.1016/j.margeo.2022.106752

Halberstadt, A. R. W., Simkins, L. M., Greenwood, S. L., and Anderson, J. B. (2016). Past ice-sheet behaviour: Retreat scenarios and changing controls in the Ross Sea, Antarctica. *Cryosphere.* 10, 1003–1020. doi: 10.5194/tc-10-1003-2016

Hanisch, S., Ariztegui, D., and Püttmann, W. (2003). The biomarker record of Lake Albano, central Italy - Implications for Holocene aquatic system response to environmental change. *Org. Geochem.* 34, 1223–1235. doi: 10.1016/S0146-6380(03)00118-9

Hillenbrand, C.-D., Smith, J. S., Kuhn, G., Esper, O., Gersonde, R., Larter, R. D., et al. (2010). Age assignment of a diatomaceous ooze deposited in the western Amundsen Sea Embayment after the Last Glacial Maximum. *J. Quat. Sci.* 25, 280–295. doi: 10.1002/jqs.1308

Huang, M., Wang, R., Xiao, W., Wu, L., and Chen, Z. (2016). Retreat process of ross ice shelf and hydrodynamic changes on northwestern Ross continental shelf since the last glacial (in Chinese with English abstract). *Mar. Geol. Quat. Geol.* 36, 97–108. doi: 10.16562/j.cnki.0256-1492.2016.05.010

Ikehara, M., Kawamura, K., Ohkouchi, N., Murayama, M., Nakamura, T., and Taira, A. (2000). Variations of terrestrial input and marine productivity in the Southern Ocean (48°S) during the last two deglaciations. *Paleoceanography* 15, 170–180. doi: 10.1029/1999PA000425

Jaeschke, A., Wengler, M., Hefter, J., Ronge, T., Geibert, W., Mollenhauer, G., et al. (2017). A biomarker perspective on dust, productivity, and sea surface temperature in the Pacific sector of the Southern Ocean. *Geochim. Cosmochim. Acta* 204, 120–139. doi: 10.1016/j.gca.2017.01.045

Keil, R., and Mayer, L. M. (2014). "Mineral matrices and organic matter," in *Treatise on Geochemistry, 2nd ed.*, vol. 12 . Eds. H. D. Holland and K. K. Turekian (Amsterdam, Netherlands: Elsevier), 337–359. doi: 10.1016/B978-0-08-095975-7.01024-X

Kim, J., La, H. S., Kim, J.-H., Jo, N., Lee, J., Kim, B., et al. (2023). Spatio-temporal variations in organic carbon composition driven by two different major phytoplankton communities in the Ross Sea, Antarctica. *Sci. Total Environ.* 891, 164666. doi: 10.1016/j.scitotenv.2023.164666

Kvenvolden, K. A., Rapp, J. B., Golan-Bac, M., and Hostettler, F. D. (1987). Multiple sources of alkanes in Quaternary oceanic sediment of Antarctica. *Org. Geochem.* 11, 291–302. doi: 10.1016/0146-6380(87)90040-4

Langone, L., Frignani, M., Labbrozzi, L., and Ravaioli, M. (1998). Present-day biosiliceous sedimentation in the Northwestern Ross Sea, Antarctica. *J. Mar. Syst.* 17, 459–470. doi: 10.1016/S0924-7963(98)00058-X

LaRowe, D. E., Arndt, S., Bradley, J. A., Estes, E. R., Hoarfrost, A., Lang, S. Q., et al. (2020). The fate of organic carbon in marine sediments - New insights from recent data and analysis. *Earth-Sci. Rev.* 204, 103146. doi: 10.1016/j.earscirev.2020.103146

Lee, S., and Fuhrman, J. (1987). Relationships between biovolume and biomass of naturally derived marine bacterioplankton. *Appl. Environ. Microbiol.* 53, 1298–1303. doi: 10.1128/AEM.53.6.1298-1303.1987

Li, L., Wang, H., and Wang, P. (2008). Molecular Organic Geochemical Record of Paleoenvironmental Changes of Core 17937 in Northern South China Sea Since 40 ka (in Chinese with English abstract). *Earth Sci.-J. China Univ. Geosci.* 33, 793–799.

Licht, K. J., and Hemming, S. R. (2017). Analysis of Antarctic glacigenic sediment provenance through geochemical and petrologic applications. *Quat. Sci. Rev.* 164, 1–24. doi: 10.1016/j.quascirev.2017.03.009

Lin, Y., Moreno, C., Marchetti, A., Ducklow, H., Schofield, O., Delage, E., et al. (2021). Decline in plankton diversity and carbon flux with reduced sea ice extent along the Western Antarctic Peninsula. *Nat. Commun.* 12, 4948. doi: 10.1038/s41467-021-25235-w

Liu, J., and An, Z. (2020). Leaf wax n-alkane carbon isotope values vary among major terrestrial plant groups: Different responses to precipitation amount and temperature and implication for paleoenvironmental reconstruction. *Earth-Sci. Rev.* 202, 103081. doi: 10.1016/j.earscirev.2020.103081

Lomstein, B. A., Langerhuus, A. T., D'hondt, S., Jorgensen, B. B., and Spivack, A. J. (2012). Endospore abundance, microbial growth and necromass turnover in deep sub-seafloor sediment. *Nature* 484, 101–104. doi: 10.1038/nature10905

Masson-Delmotte, V., Vimeux, F., Jouzel, J., Morgan, V., Delmotte, M., Ciais, P., et al. (2000). Holocene climate variability in Antarctica based on 11 ice-core isotopic records. *Quat. Res.* 54, 348–358. doi: 10.1006/qres.2000.2172

Matson, P., Martz, T., and Hofmann, G. (2011). High-frequency observations of pH under Antarctic sea ice in the southern Ross Sea. *Antarct. Sci.* 1, 607–613. doi: 10.1017/S0954102011000551

Matsumoto, G. I., Akiyama, M., Watanuki, K., and Torii, T. (1990a). Unusual distributions of long-chain n-alkanes and n-alkenes in Antarctic soil. *Org. Geochem.* 15, 403–412. doi: 10.1016/0146-6380(90)90167-X

Matsumoto, G. I., Hirai, A., Hirota, K., and Watanuki, K. (1990b). Organic geochemistry of the McMurdo Dry Valleys soil, Antarctica. *Org. Geochem.* 16, 781–791. doi: 10.1016/0146-6380(90)90117-I

Matsumoto, G. I., Honda, E., Sonoda, K., Yamamoto, S., and Takemura, T. (2010). Geochemical features and sources of hydrocarbons and fatty acids in soils from the McMurdo Dry Valleys in the Antarctic. *Polar Sci.* 4, 187–196. doi: 10.1016/j.polar.2010.04.001

Mayer, L. M. (1994). Surface area control of organic carbon accumulation in continental shelf sediments. *Geochim. Cosmochim. Acta* 58, 1271–1284. doi: 10.1016/0016-7037(94)90381-6

McKay, R., Dunbar, G., Naish, T., Barrett, P., Carter, L., and Harper, M. (2008). Retreat history of the Ross Ice Sheet (Shelf) since the Last Glacial Maximum from deep-basin sediment cores around Ross Island. *Palaeogeogr. Palaeoclimatol. Palaeoecol.* 260, 245–261. doi: 10.1016/j.palaeo.2007.08.015

McKay, R., Golledge, N. R., Maas, S., Naish, T., Levy, R., Dunbar, G., et al. (2016). Antarctic marine ice-sheet retreat in the Ross Sea during the early Holocene. *Geology* 44, 7–10. doi: 10.1130/G37315.1

McKay, R., Naish, T., Powell, R., Barrett, P., Scherer, R., Talarico, F., et al. (2012). Pleistocene variability of Antarctic Ice Sheet extent in the Ross Embayment. *Quat. Sci. Rev.* 34, 93–112. doi: 10.1016/j.quascirev.2011.12.012

Meyers, P. (1994). Preservation of elemental and isotopic source identification of sedimentary organic matter. *Chem. Geol.* 144, 289–302. doi: 10.1016/0009-2541(94)90059-0

Meyers, P. (1997). Organic geochemical proxies of paleoceanographic, paleolimnologic, and paleoclimatic processes. *Org. Geochem.* 27, 213–250. doi: 10.1016/S0146-6380(97)00049-1

Meyers, P. A. (2003). Applications of organic geochemistry to paleolimnological reconstructions: a summary of examples from the Laurentian Great Lakes. *Org. Geochem.* 34, 261–289. doi: 10.1016/S0146-6380(02)00168-7

Naafs, B. D. A., Inglis, G., Blewett, J., Mcclymont, E., Lauretano, V., Xie, S., et al. (2019). The potential of biomarker proxies to trace climate, vegetation, and biogeochemical processes in peat: A review. *Glob. Planet. Change* 179, 57–79. doi: 10.1016/j.gloplacha.2019.05.006

Naughten, K. A., Holland, P. R., and De Rydt, J. (2023). Unavoidable future increase in West Antarctic ice-shelf melting over the twenty-first century. *Nat. Clim. Change.* 13, 1222–1228. doi: 10.1038/s41558-023-01818-x

Orr, J., Fabry, V., Aumont, O., Bopp, L., Doney, S., Feely, R., et al. (2005). Anthropogenic ocean acidification over the twenty-first century and its impact on calcifying organisms. *Nature* 437, 681–686. doi: 10.1038/nature04095

Orsi, A. H., Whitworth, T., and Nowlin, W. D. (1995). On the meridional extent and fronts of the antarctic circumpolar current. *Deep Sea Res. I Oceanogr. Res. Pap.* 42, 641–673. doi: 10.1016/0967-0637(95)00021-W

Parish, T. R., Cassano, J. J., and Seefeldt, M. W. (2006). Characteristics of the Ross Ice Shelf air stream as depicted Antarctic Mesoscale Prediction System simulations. *J. Geophys. Res.* 111, D12109. doi: 10.1029/2005JD006185

Pillsbury, R., and Jacobs, S. (1985). Preliminary observations from long-term current meter moorings near The Ross Ice Shelf, Antarctica. *Antarct. Res. Ser.* 43, 87–107. doi: 10.1029/AR043p0087

Pudsey, C., Murray, J., Appleby, P., and Evans, J. (2006). Ice shelf history from petrographic and foraminiferal evidence, Northeast Antarctic Peninsula. *Quat. Sci. Rev.* 25, 2357–2379. doi: 10.1016/j.quascirev.2006.01.029

Redfield, A. C., Ketchum, B. H., and Richards, F. A. (1963). The influence of organisms on the composition of sea-water. *Sea* 2, 26–77.

Sampei, Y., and Matsumoto, E. (2001). C/N ratios in a sediment core from Nakaumi Lagoon, southwest Japan - Usefulness as an organic source indicator. *Geochem. J.* 35, 189–205. doi: 10.2343/geochemj.35.189

Schubert, C. J., and Nielsen, S. B. (2000). Effects of decarbonation treatments on $\delta^{13}C$ values in marine sediments. *Mar. Chem.* 72, 55–59. doi: 10.1016/s0304-4203(00)00066-9

Shao, H., He, J., Wu, L., and Wei, L. (2022). Elemental and Sr–Nd isotopic compositions of surface clay-size sediments in the front end of major ice shelves around Antarctica and indications for provenance. *Deep Sea Res. II Top. Stud. Oceanogr.* 195, 105011. doi: 10.1016/j.dsr2.2021.105011

Ship, S., Anderson, J., and Domack, E. (1999). Late Pleistocene-Holocene retreat of the West Antarctic Ice-Sheet system in the Ross Sea: Part 1 - Geophysical results. *Geol. Soc Am. Bull.* 111, 1486–1516. doi: 10.1130/0016-7606(1999)111<1486:LPHROT>2.3.CO;2

Smith, W. (2022). Primary productivity measurements in the Ross Sea, Antarctica: a regional synthesis. *Earth Syst. Sci. Data* 14, 2737–2747. doi: 10.5194/essd-14-2737-2022

Smith, R. W., Bianchi, T. S., Allison, M., Savage, C., and Galy, V. (2015). High rates of organic carbon burial in fjord sediments globally. *Nat. Geosci.* 8, 450–453. doi: 10.1038/ngeo2421

Smith, W., and Kaufman, D. (2018). Climatological temporal and spatial distributions of nutrients and particulate matter in the ross sea. *Prog. Oceanogr.* 168, 182–195. doi: 10.1016/j.pocean.2018.10.003

Smith, W. O. J., Sedwick, P. N., Arrigo, K. R., Ainley, D. G., and Orsi, A. H. (2012). The ross sea in a sea of change. *Oceanography* 25, 90–103. doi: 10.5670/oceanog.2012.80

Song, L., Han, X., Li, J., Gao, S., Liu, G., and Long, P. (2019). Western Ross Sea sedimentary environment reconstruction since the Last Glacial Maximum based on organic carbon and biomarker analyses (in Chinese with English abstract). *Haiyang Xuebao* 41, 52–64. doi: 10.39698/j.issn.0253-4193.2019.09.005

Tamura, T., Ohshima, K. I., and Nihashi, S. (2008). Mapping of sea ice production for Antarctic coastal polynyas. *Geophys. Res. Lett.* 35, L07606. doi: 10.1029/2007GL032903

Tao, S. Q., Li, Y. H., Tang, Z., Ye, X., Sun, H., Gao, Z. Y., et al. (2022). Composition of organic materials and the control factors of suspended particulates in the surface water of the Ross Sea-Amundsen Sea in marginal sea of the southwestern Antarctic in austral summer 2019-2020 (in Chinese with English abstract). *Mar. Geol. Quat. Geol.* 42, 24–38. doi: 10.16562/j.cnki.0256-1492.2022022101

Ternois, Y., Kawamura, K., Keigwin, L., Ohkouchi, N., and Nakatsuka, T. (2001). A biomarker approach for assessing marine and terrigenous inputs to the sediments of Sea of Okhotsk for the last 27,000 years. *Geochim. Cosmochim. Acta* 65, 791–802. doi: 10.1016/S0016-7037(00)00598-6

The IMBIE Team (2018). Mass balance of the antarctic ice sheet from 1992 to 2017. *Nature* 558, 219–222. doi: 10.1038/s41586-018-0179-y

Trinh, R., Ducklow, H., Steinberg, D., and Fraser, W. (2023). Krill body size drives particulate organic carbon export in West Antarctica. *Nature* 618, 526–530. doi: 10.1038/s41586-023-06041-4

Venkatesan, M. (1988). Organic geochemistry of marine sediments in Antarctic region: Marine lipids in McMurdo Sound. *Org. Geochem.* 12, 13–27. doi: 10.1016/0146-6380(88)90270-7

Volkman, J., Barrett, S., Blackburn, S., Mansour, M., Sikes, E., and Gelin, F. (1998). Microalgal biomarkers: A review of recent research developments. *Org. Geochem.* 29, 1163–1179. doi: 10.1016/S0146-6380(98)00062-X

Wakeham, S., and Mcnichol, A. (2014). Transfer of organic carbon through marine water columns to sediments - Insights from stable and radiocarbon isotopes of lipid biomarkers. *Biogeosciences* 11, 6895–6914. doi: 10.5194/bg-11-6895-2014

Wang, H., Chen, Z., Wang, K., Liu, H., Tang, Z., and Huang, Y. (2016). Characteristics of heavy minerals and grain size of surface sediments on the continental shelf of Prydz Bay: implications for sediment provenance. *Antarct. Sci.* 28, 103–114. doi: 10.1017/s0954102015000498

Wang, Y., Huang, Y., Tian, J., Li, C., Yu, K., Zhang, M., et al. (2021). A sediment record of terrestrial organic matter inputs to Dongting Lake and its environmental significance from 1855 to 2019. *Ecol. Indic.* 130, 108090. doi: 10.1016/j.ecolind.2021.108090

Whitworth, T., and Orsi, A. H. (2006). Antarctic Bottom Water production and export by tides in the Ross Sea. *Geophys. Res. Lett.* 331, L12609. doi: 10.1029/2006GL026357

Wu, L., Li, L., Wang, R., Shao, H., Chen, Y., Lin, Z., et al. (2024). Grain-size, coarse fraction lithology and clay mineral compositions of surface sediments from Ross Sea, Antarctica: implications for their provenance and delivery mode. *Front. Mar. Sci.* 10. doi: 10.3389/fmars.2023.1324391

Wu, C., Wang, G., Li, J., Li, J., Cao, C., Ge, S., et al. (2020). The characteristics of atmospheric brown carbon in Xi'an, inland China: sources, size distributions and optical properties. *Atmos. Chem. Phys.* 20, 2017–2030. doi: 10.5194/acp-20-2017-2020

Xiu, C., Huo, S., Zhao, M., Zhang, X., Xing, J., and Xu, M. (2017). GeochemicaI characteristics and source of organic carbon and nitrogen in the coIumn sediments from the Ross Sea, Antarctica (in Chinese with English abstract). *Mar. Geol. Quat. Geol.* 37, 83–90. doi: 10.16562/j.cnki.0256-1492.2017070201

Xu, Q., Yang, L., Gao, Y., Sun, L., and Xie, Z. (2021). 6,000-year reconstruction of modified circumpolar deep water intrusion and its effects on sea ice and penguin in the ross sea. *Geophys. Res. Lett.* 48, e2021GL094545. doi: 10.1029/2021GL094545

Yang, G., Atkinson, A., Pakhomov, E., Hill, S., and Racault, M. F. (2022). Massive circumpolar biomass of Southern Ocean zooplankton: Implications for food web structure, carbon export, and marine spatial planning. *Limnol. Oceanogr.* 67, 1–15. doi: 10.1002/lno.12219

Zhang, M., Liu, X., Xu, F., Li, A., Gu, Y., Chang, X., et al. (2023). Organic carbon deposition on the inner shelf of the East China sea constrained by sea level and climatic changes since the last deglaciation. *J. Ocean Univ. China* 22, 1300–1312. doi: 10.1007/s11802-023-5476-x

Zhao, R., Chen, Z., Liu, H., Tang, Z., Huang, Y., Li, Y., et al. (2017). Sedimentary record and paleoceanographic implications of the core on the continental shelf off the Ross Sea since 15 ka (in Chinese with English abstract). *Haiyang Xuebao* 39, 78–88. doi: 10.3969/j.issn.0253-4193.2017.05.008

Zhao, M., Sun, H., Liu, Z., Qian, B., Chen, B., Yang, M., et al. (2022). Organic carbon source tracing and the BCP effect in the Yangtze River and the Yellow River: Insights from hydrochemistry, carbon isotope, and lipid biomarker analyses. *Sci. Total Environ.* 812, 152429. doi: 10.1016/j.scitotenv.2021.152429

Zhao, B., Zhang, Y., Huang, X., Qiu, R., Zhang, Z., and Meyers, P. (2018). Comparison of n -alkane molecular, carbon and hydrogen isotope compositions of different types of plants in the Dajiuhu peatland, central China. *Org. Geochem.* 124, 1–11. doi: 10.1016/j.orggeochem.2018.07.008

Zhou, Z., Xiao, W., Wang, R., and Teng, Y. (2022). Distribution patterns of biogenic components in surface sediments of the Ross Sea and their environmental implications (in Chinese with English abstract). *Mar. Geol. Quat. Geol.* 42, 12–23. doi: 10.16562/j.cnki.0256-1492.2021093002

Frontiers in Marine Science

Explores ocean-based solutions for emerging global challenges

The third most-cited marine and freshwater biology journal, advancing our understanding of marine systems and addressing global challenges including overfishing, pollution, and climate change.

Discover the latest Research Topics

See more →

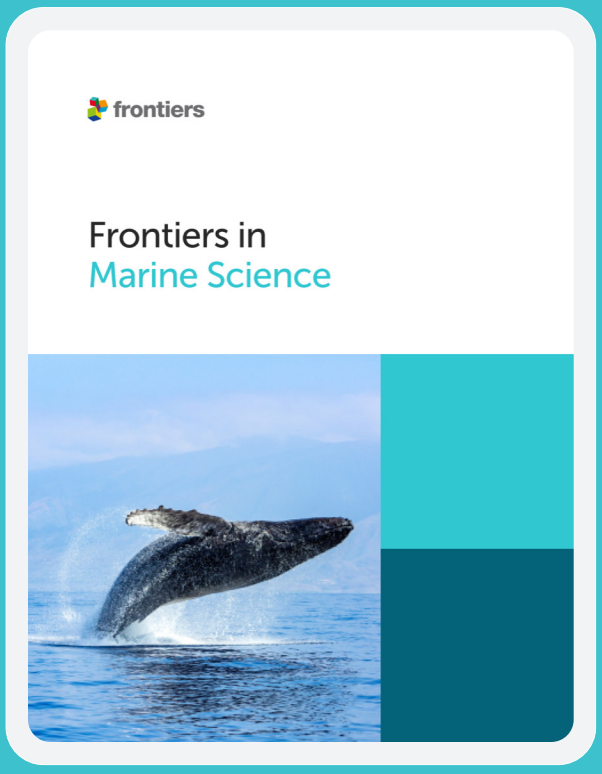

Frontiers

Avenue du Tribunal-Fédéral 34
1005 Lausanne, Switzerland
frontiersin.org

Contact us

+41 (0)21 510 17 00
frontiersin.org/about/contact